2018

Deformation Mechanisms and Strain Localization in the Mafic Continental Lower Crust

Degli Alessandrini, Giulia

UNIVERSITY OF
PLYMOUTH

DEFORMATION MECHANISMS AND STRAIN LOCALIZATION IN THE MAFIC CONTINENTAL LOWER CRUST

by

GIULIA DEGLI ALESSANDRINI

A thesis submitted to the University of Plymouth
in partial fulfilment of the degree of

DOCTOR OF PHILOSOPHY

School of Geography, Earth and Environmental Sciences

2018

AKNOWLEDGMENTS

Firstly, I would like to thank my supervisory team, Luca Menegon, Arjan Dijkstra and Mark Anderson, for all the fruitful scientific discussions and guidance. In particular Luca Menegon, who has followed and helped my personal and academic growth in the four years I was his student. An acknowledgment goes also to Nadia Malaspina and Marco Beltrando for their contributions, and to Gustavo Viegas and Francesco Giuntoli for their frequent scientific discussions and exchange of ideas.

I would also like to acknowledge all academic and support staff, for their excellent support during analyses. This includes Roy Moate and all the staff of the Plymouth University Electron Microscopy Centre, Cees-Jan De Hoog of the NERC Ion Microprobe Facility in Edinburgh, Andrea Risplendente and the Microprobe team of the Universita' degli Studi di Milano, and Alex Taylor of the Consolidated Radio-isotope Facility in Plymouth.

In addition, I would like to thank all those great people I met in Plymouth and shared many good moments with, laughed with, partied with, played music with, camped with, bbq-ed with, and … drank with (JSV forever)! You all made Plymouth a better place, and I hope the friendships we made will last the years and distance. In particular, a thank you to Christian Marien for tolerating me for so long, to Gustavo Viegas for being Gustavo and to Camille Dusseaux for always inviting me for dinner and music sessions.

A special thank you goes to my awesome housemates, Madeleine Vickers (with whom I roughly shared an impressive 26'280 hours of my life), Hoayda Darkal, Alex Dawson, Ester Garcia x2, Francesca Prando, Mike Bedington and Camille Visinand. You have been my family in Plymouth, and I have shared my best times with you. I will never forget this.

Another special thank you goes to Michele Locatelli, with whom I shared many moments, dreams and obstacles, and of whom I have great admiration and esteem.

A dedicated thank you goes also to Filippo and Erminia degli Alessandrini for their kindness and support during my fieldwork in the Italian Alps. Your hospitality was a precious help.

Finally, a massive thank you to my parents and sister Claudia, who were always there to give me love and support, help me follow my dreams and build my future. This work is dedicated to you.

This PhD scholarship has been funded by a FP7 Marie Curie Career Integration Grant to Luca Menegon (grant agreement PCIG13-GA-2013-618289) and by Plymouth University. This PhD would have not been the same without the financial support of Sandra Grubissich and Andrea degli Alessandrini.

AUTHOR'S DECLARATION

At no time during the registration for the degree of Doctor of Philosophy has the author been registered for any other University award without prior agreement of the Doctoral College Quality Sub-Committee.

Work submitted for this research degree at the University of Plymouth has not formed part of any other degree either at the University of Plymouth or at another establishment.

This study was financed by a studentship from the University of Plymouth and by the FP7 Marie Curie Career Integration Grant to Luca Menegon (grant agreement PCIG13-GA-2013-618289), and carried out in collaboration with the University of Plymouth.

A programme of advanced study was undertaken, which included Research Skills and Research Methods modules. Relevant scientific seminars and conferences were regularly attended at which work was often presented; relevant training and workshops were also attended; several papers were prepared for publication.

Publications:

- Degli Alessandrini G, Menegon L, Malaspina N, Dijkstra AH, Anderson MW (2017) "Creep of mafic dykes infiltrated by melt in the lower continental crust (Seiland Igneous Province, Norway)" Lithos 274-275, 169-187.

Presentation at conferences:

- Degli Alessandrini G, Menegon L, Giuntoli F (2017) "Protracted weakening during lower crustal shearing along an extensional shear zone", TSG and EGU 2017

- Degli Alessandrini G, Menegon L, N. Malaspina, Dijkstra AH, Anderson MW (2016) "Mineral reactions and strain localization in a sheared mafic granulite infiltrated by melt (Seiland Igneous Province, Norway), TSG and EGU 2016

- Degli Alessandrini G, Menegon L, M. Beltrando, Dijkstra AH, Anderson MW (2016) "Metamorphic reactions, grain size reduction and deformation of mafic lower crustal rocks", EGU 2016

- Degli Alessandrini G, Menegon L, N. Malaspina, Dijkstra AH, Anderson MW (2015), "Deformation mechanisms of pyroxenes in a sheared mafic granulite from the Seiland Igneous Province", EGU 2015

- Degli Alessandrini G, Menegon L, N. Malaspina, Dijkstra AH, Anderson MW (2015) "Melt-rock interaction during viscous creep of a mafic granulite", MSG 2015

- Degli Alessandrini G, Menegon L, N. Malaspina (2015) "Deformation mechanisms of clino- and orthopyroxene in a sheared mafic granulite from the Seiland Igneous Province (northern Norway)", TSG 2015

Word count of main body of thesis: 44264

Signed 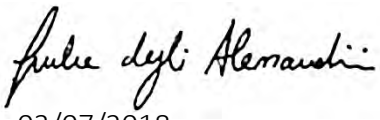

Date 03/07/2018

DEFORMATION MECHANISMS AND STRAIN LOCALIZATION IN THE MAFIC CONTINENTAL LOWER CRUST

Giulia degli Alessandrini

ABSTRACT

The rheology and strength of the lower crust play a key role in lithosphere dynamics, influencing the orogenic cycle and how plate tectonics work. Despite their geological importance, the processes that cause weakening of the lower crust and strain localization are still poorly understood. Through microstructural analysis of naturally deformed samples, this PhD aims to investigate how weakening and strain localization occurs in the mafic continental lower crust. Mafic granulites are analysed from two unrelated continental lower crustal shear zones which share comparable mineralogical assemblages and high-grade deformation conditions (T > 700 °C and P > 6 Kbar): the Seiland Igneous Province in northern Norway (case-study 1) and the Finero mafic complex in the Italian Southern Alps (case-study 2).

Case-study 1 investigates a metagabbroic dyke embedded in a lower crustal metasedimentary shear zone undergoing partial melting. Shearing of the dyke was accompanied by infiltration of felsic melt from the adjacent partially molten metapelites. Findings of case-study 1 show that weakening of dry and strong mafic rocks can result from melt infiltration from nearby partially molten metasediments. The infiltrated melt triggers melt-rock reactions and nucleation of a fine-grained (< 10 µm average grain size) polyphase matrix. This fine-grained mixture deforms by diffusion creep, causing significant rheological weakening.

Case-study 2 investigates a lower crustal shear zone in a compositionally-layered mafic complex made of amphibole-rich and amphibole-poor metagabbros. Findings of case-study 2 show that during prograde metamorphism (T > 800 °C), the presence of amphibole undergoing dehydration melting reactions is key to weakening and strain localization. Dehydration of amphibole generates fine-grained symplectic intergrowths of pyroxene + plagioclase. These reaction products form an interconnected network of fine-grained (< 20 µm average grain size) polyphase material that deforms by diffusion creep, causing strain partitioning and localization in amphibole-rich layers. Those layers without amphibole fail to produce an interconnected network of fine grained material. In this layers, plagioclase deforms by dislocation creep, and pyroxene by microfracturing and neocrystallization.

Overall, this PhD research highlights that weakening and strain localization in the mafic lower crust is governed by high-T mineral and chemical reactions that drastically reduce grain size and trigger diffusion creep.

CONTENTS

FIGURES AND TABLES

1 INTRODUCTION

1.1 RESEARCH TOPIC

The rheological behaviour of the continental lower crust exerts a fundamental control on processes such as the depth of earthquakes, the rate of post- and inter-seismic deformation and the viscous (de)coupling between the crust and the mantle (e.g. Bürgmann and Dresen, 2008; Handy and Brun, 2004; Maggi et al., 2000; Wright et al., 2013). Despite the recent results of Hacker et al. (2015), the composition, structure and rheology of the lower crust are still underexplored. In the past, it was widely assumed that the ductile lithosphere, i.e. the lower crust and the lithospheric mantle, deformed homogeneously. Nowadays, a wealth of field examples, laboratory experiments, analogue models, numerical models and rheological calculations have proven that deformation in the lower crust and mantle can localize along shear zones, and that deformation in the ductile regime is far from being homogeneously distributed (Brodie and Rutter, 1987a; Handy et al., 2007; Poirier, 1980; Ramsay, 1980; Rutter et al., 2001; Vauchez et al., 2012; White et al., 1980). Shear zones are zones of weakness where strain localizes, therefore the presence of these structures profoundly modifies the overall strength of the lithosphere (e.g. Bürgmann and Dresen, 2008; Fossen and Cavalcante, 2017; Handy et al., 2007; Holyoke and Tullis, 2006; Vauchez et al., 2012). The recognition of shear zones within the ductile lithosphere has raised the fundamental question of *how* and *where* these structures nucleate and evolve; in other words how and where weakening and strain localization is achieved in the ductile lithosphere.

A number of geological processes and conditions have been identified as responsible for weakening (i.e. strain softening - Hobbs et al., 1990) in the ductile lithosphere: 1)

geometric softening, 2) grain size reduction, 3) fracturing, 4) syn-kinematic metamorphic reactions (reaction softening), 5) water-induced weakening (including hydrolytic weakening), 6) melt-induced weakening, 7) lithological heterogeneities and 8) shear heating (Poirier, 1980; White et al., 1980, in Burlini and Bruhn, 2005). These will be addressed with more detail in Chapter 2, section 2.4.

In the absence of any of the above weakening processes/conditions the strength of the lower crust would be governed solely by the yield strength of its constituting minerals (e.g. Handy et al., 2007). However, owing to the above, the strength of the lower crust can be substantially weaker in shear zones. While the weakening effect of these naturally-occurring processes/conditions has been well studied for the middle-crust and the brittle-ductile transition - particularly for quartzo-feldspathic rocks (e.g. Fitz Gerald and Stünitz, 1993; Gueydan et al., 2003; Hippertt and Hongn, 1998; Kilian et al., 2011; Mancktelow and Pennacchioni, 2004; Menegon et al., 2008; Pennacchioni and Mancktelow, 2007; Simpson, 1985; Viegas et al., 2016)-, the roles of each of these weakening processes/conditions in polyphase mafic rocks of the lower crust are less understood. The present scientific challenge is to understand which of these processes can occur in lower crustal settings (and where), and, if more than one of these can occur simultaneously, which one is responsible for the greatest weakening. Ultimately, it is the most efficient process, or combination of processes, that determines where shear zones nucleate and evolve in the lower crust.

Assessing the rheology and weakening mechanisms of the lower crust comes with a number of intrinsic challenges. The first challenge is that most of the above-mentioned natural processes/conditions depend on each other. Therefore, the different causes of weakening are difficult to separate and quantify. For instance, grain size reduction has

been recognized as one of the (if not the) most important weakening mechanism (e.g. Brodie and Rutter, 1987; de Ronde et al., 2005; Kanagawa et al., 2008; Kenkmann and Dresen, 2002; Kilian et al., 2011; Kruse and Stünitz, 1999; Mehl and Hirth, 2008; Newman et al., 1999; Pearce et al., 2011; Pearce and Wheeler, 2011; Poirier, 1980; Raimbourg et al., 2008; Rutter and Brodie, 1988; Stünitz, 1998; Stünitz and Tullis, 2001; Urai et al., 1986; White et al., 1980), but *how* grain size reduction is achieved in the lower crustal and mantle is still a matter of debate: some authors have invoked dynamic recrystallization (e.g. Platt, 2015; Platt and Behr, 2011), others invoked fracturing through a transiently seismic lower crust (e.g. Austrheim, 2013, 1987; Menegon et al., 2013; Okudaira et al., 2015) and others metamorphic reactions (e.g. Brodie and Rutter, 1985, 1987b; de Ronde et al., 2005; Kenkmann and Dresen, 2002; Newman et al., 1999; Stünitz and Tullis, 2001; White and Knipe, 1978). However, weakening through dynamic recrystallization requires an already established shear zone, and does not explain how shear zones *nucleate*. Seismicity induced fracturing requires earthquake- propagation to lower crustal levels and strong rocks capable of sustaining high differential stresses until rupture (Menegon et al., 2017; Okudaira et al., 2015). Finally, metamorphic reactions require either a pressure and/or temperature perturbation, or the addition of (an external?) fluid to the system (Etheridge et al., 1983; Jamtveit et al., 2016; Vernon and Clarke, 2008). The above example intends to convey that there is no fixed recipe as to what causes weakening in the lower crust. Weakening by grain size reduction can be intrinsically linked to the process of dynamic recrystallization, fracturing, syn-kinematic metamorphic reactions, or any combination or interference of these.

The second challenge is that the composition and structure of the lower crust is still under discussion (e.g. Christensen and Mooney, 1995; Hacker et al., 2015; Rudnick and Fountain, 1995; Rudnick and Gao, 2003; Wedepohl, 1995); and these uncertainties pose

a major limitation in the understanding of its strength. As will be briefly addressed in Chapter 2, Section 2.1, the lower crust has been found to be spatially and temporally heterogeneous in lithology, metamorphic grade, fluid content/distribution and temperature (Bürgmann and Dresen, 2008). This heterogeneity results in different rheological behaviours and strengths, so that the lower crust can be ductile (and weak) at times, while brittle (and strong) at other times. In fact, both brittle and ductile behaviours have been reported, with convincing evidence and reasoning on both sides (see Chapter 2, section 2.2). Authors in favour of a strong (brittle) lower crust bring evidence of large parts of it being composed of mechanically strong, dry granulites (Jackson et al., 2004; Maggi et al., 2000) that are incapable of deforming by crystal plastic flow (Austrheim, 2013; Fagereng, 2013; Menegon et al., 2011, 2017). This idea is supported by lower crustal pseudotachylites (Austrheim, 2013; Menegon et al., 2017) and fits with the identification of lower crustal tremors/earthquakes (Fagereng, 2013; Jackson, 2002). Other authors instead bring evidenceof a weak lower crust, causing shear zones and strain localization (Burov, 2011; Getsinger et al., 2013; Handy and Brun, 2004; Kenkmann and Dresen, 2002; Wang et al., 2012). Unravelling where, when and under what conditions the lower crust behaves elastically or plastically, strong or weak, is one of the present scientific challenges.

From the above, the lower crust appears to be a highly complex system in terms of rheology, and further work is needed to understand how weakening occurs in natural lower crustal rocks. Through microstructural analysis of natural samples, this PhD aims to contribute to the understanding of the weakening mechanisms responsible for strain localization in shear zones of the mafic lower crustal rocks.

1.2 RESEARCH AIMS AND STRATEGY

The main objective of this work is to investigate the grain-scale processes and deformation mechanisms of mafic granulites, in order to evaluate how strain localises in the lower levels of the continental crust and assess how different geological factors (i.e. water content, presence of melt, metamorphic reactions, grain size reduction) influence this process. This aim is achieved by coupling field-based structural observations with detailed quantitative microstructural analysis of mafic lower crustal shear zones. The approach combines textural characterization of the samples -through crystallographic orientation analysis of the rock's constituting minerals- , with chemical characterization. This microstructural approach has the intent to fully describe lower crustal shear zones within mafic lithologies.

This research utilises naturally-deformed samples, which retain a wealth of textural and chemical information that are challenging to reproduce in experimental setups. In addition, natural samples retain clues of the complex processes that occur in the lower crust, such as strain partitioning and localization in different lithologies (so that the range of related microstructures and deformation mechanisms can be documented), protracted weakening (through changes in mineral chemistry), syn-kinematic metamorphic reactions and fluid-rock interactions.

The focus of this research are mafic granulites because this rock type can be considered representative of the lower crust (Rudnick and Fountain, 1995; Rudnick and Gao, 2003). Mafic granulites (mainly metagabbros) are sampled from two unrelated continental lower crustal shear zones which share comparable mineralogical assemblages and high-grade deformation conditions (temperature > 700°C and pressure > 6 Kbar): the Seiland

Igneous Province in northern Norway (case study 1) and the Finero mafic complex in the Ivrea-Verbano Zone, Italian Southern Alps (case study 2) (Fig. 1.1).

Fig. 1.1

Simplified map of Europe showing the geographical locations of the two case studies (boxed, in red). The Seiland Igneous Province (case study 1) is in northern Norway; the Finero mafic complex (case study 2) is in the Ivrea-Verbano Zone, Italian Southern Alps.

Both complexes shared a history of magmatic underplating with emplacement of gabbroic plutons, followed by orogenic collision and exhumation of lower crustal units (see Sections 4.1 and 5.1 for geological setting). In both cases, the investigated lower crustal units escaped the tectono-metamorphic overprints of their respective orogenies (the Caledonian orogeny and the Alpine orogeny), allowing a window on pre-collisional lower crustal deformation. In addition, both shear zones most likely deformed under

melt-present conditions, making them informative examples of melt-present deformation in mafic lithologies of the lower crust.

Despite the above analogies, the two case studies differ in their nature: in the Seiland Igneous Province, the investigated mafic granulites are metagabbroic dykes embedded in a lower crustal metasedimentary shear zone; whereas in the Finero mafic complex, the mafic granulites derive from a shear zone that developed within a layered gabbroic intrusion.

Both case studies are analysed following the same methodological approach, which consists of detailed chemical and textural (i.e. crystallographic orientation) investigations on representative thin-sections, utilising a range of micro-analytical techniques and procedures. These include optical microscopy and Scanning Electron Microscopy (SEM) for microstructural characterization, Electron Microprobe Analysis (EMPA) for quantitative mineral chemistry, X-ray fluorescence (XRF) for bulk rock chemistry, Electron Backscatter Diffraction (EBSD) for characterization of crystallographic preferred orientations, and Secondary Ion Mass Spectrometry (SIMS) for quantification of trace amounts of water stored in nominally anhydrous minerals. Quantitative microstructural parameters, i.e. grain size, aspect ratios and area% of minerals are obtained using image-analysis techniques (Heilbronner and Barrett, 2013), whereas the pressure-temperature conditions of deformation, the metamorphic reactions and the shear zone evolution are constrained through thermodynamic modelling using Perple_X (Connolly, 1990). Particular focus is given to grain-scale deformation mechanisms of individual mineral phases and to the rheological behaviour of the polyphase aggregate, as it is widely known that deformation mechanisms control bulk-rock rheology (e.g. Rutter et al., 2001). Furthermore, particular effort is made to constrain the P-T conditions of deformation,

the changes in mineral chemistry during deformation and the chemical reactions, as these are seen as important aspects of deformation.

All of the above investigations aim to address the following key questions:

1) What are the deformation mechanisms in mafic polyphase rocks deforming at lower crustal conditions?
2) What is the rheological effect of metamorphic reactions in mafic lithologies of the lower crust?

and, ultimately,

3) How is weakening and strain localization achieved in the mafic lower crust?

1.3 STRUCTURE OF THESIS

This thesis focuses on the grain-scale processes responsible for weakening and strain localization in the mafic lower crust, with special regard to the rheological effect of metamorphic reactions. The investigated sheared mafic rocks are sampled from two distinct lower crustal units in the Norwegian Caledonides (Seiland Igneous Province) and in the Italian Southern Alps (Finero mafic complex, Ivrea Zone). The particularities of each study area requires each location to be presented, analysed and discussed separately. This thesis is therefore structured as two stand-alone case-studies, which together serve as natural examples of weakening and strain localization of mafic lower crustal rocks. A brief background on relevant aspects of the research topic is given in Chapter 2. The two case studies are investigated using a combination of analytical techniques and procedures, which are detailed in Chapter 3. The Seiland Igneous Province case-study (case-study 1) is presented in Chapter 4, whereas the Finero case-study (case-study 2) is

presented in Chapter 5. The Seiland Igneous Province case-study has been published in *Lithos* as *Degli Alessandrini et al. (2017)* with title: *Creep of mafic dykes infiltrated by melt in the lower continental crust (Seiland Igneous Province)*. Co-authors of this publication are Luca Menegon (University of Plymouth), Nadia Malaspina (University of Milano Bicocca), Arjan Dijkstra (University of Plymouth) and Mark Anderson (University of Plymouth). Chapter 6 ends this work with some final remarks and conclusions. The Appendices at the back of the thesis incorporate additional information and results that have been omitted in the main chapters.

2 BACKGROUND KNOWLEDGE ON THE RESEARCH TOPIC

This chapter touches on some key aspects related to lower crustal deformation. Concepts and terminology presented here will be discussed and applied in the two case-studies that follow in Chapters 4 and 5. Thus, the aim of this chapter is to provide the interested reader with some background knowledge on the most relevant aspects related to this PhD research.

2.1 STRUCTURE AND COMPOSITION OF THE LOWER CRUST

What is known about the composition of the deeper portions of the crust relies on exhumed crustal sections, xenoliths, and on a combination of indirect evidence, mainly from seismic surveys, surface heat flows and geochemical studies (Kay and Kay, 1981, Hacker 2015). There is a wide consensus that the lower crust is lithologically heterogeneous, mainly consisting of granulite facies rocks of mafic to intermediate composition (Christensen and Fountain, 1975, Rudnick and Fountain, 1995, Rudnick and Gao, 2014) (Fig. 2.1).

Mafic granulites are high-grade metamorphic rocks typically resulting from dehydration melting of amphibolites, or, alternatively, from metamorphic re-equilibration of magmatic gabbroic intrusions (Harley, 1989; Ellis, 1987). Mafic granulites are primarily composed of plagioclase, clinopyroxene, orthopyroxene and garnet, but can contain variable amounts of amphibole, k-feldspar, quartz, ilmenite and olivine (Vernon and

Clarke, 2008a). Their composition approaches that of primitive mantle-derived basaltic magmas – i.e. metagabbro. Lower crustal rocks with intermediate compositions approach the composition of diorites (Rudnick and Fountain, 1995). Typical mafic granulites are therefore anhydrous rocks and, when undeformed, medium to coarse grained with a granoblastic fabric. The transition from amphibolites to granulites is commonly associated with prograde (melting) reactions that consume amphibole and stabilize pyroxene (both orthopyroxene and clinopyroxene) (e.g. Palin et al., 2016). In mafic rocks, this transition occurs gradually, which means that amphibole can coexist as a metastable phase, together with pyroxenes and partial melt, at granulitic conditions (Palin et al., 2016). Furthermore, the mineral assemblage in (mafic) granulites is dependent on pressure. Medium-P granulites are characterized by the association clinopyroxene + orthopyroxene + plagioclase ± olivine ± amphibole; whereas high-P granulites are characterized by clinopyroxene + garnet. The transition to a high-P assemblage is accompanied by orthopyroxene + plagioclase instability forming garnet (and an Al content increase in pyroxene). The appearance of garnet and disappearance of orthopyroxene coincides with an increase in P (typical of high-P granulite field: Harley 1989, Brown 2007; Palin et al. 2016).

Based on outcrop extents and on their expected high heat production, metapelites are only considered to be a minor component of lower crustal levels (Rudnick and Fountain, 1995). Indeed, calculations from Christensen and Mooney (1995) suggest that 93% of the lower crust consists of mafic lithologies (amphibolites, mafic granulites and mafic-garnet granulites) and the remaining 7% consists of tonalitic gneisses (Rudnick and Gao, 2003). In over-thickened crust (e.g. in orogenic belts), high pressure eclogites can be found associated with granulites (e.g. Austrheim, 2013). Not everyone agrees on these

compositions: Hacker et al (2015) claims that the lower crust could be less mafic than commonly believed, due to dynamic processes of crustal differentiation which brings changes in density and buoyancy, causing "relamination" and compositional refinements.

Studies of exhumed sections of the lower crust suggest that the lower crust is compositionally layered, with an upper portion consisting of felsic granulites and metasediments and a lower portion consisting of layered intermediate-to-mafic granulites, pyroxenites and peridotites (Rudnick and Fountain, 1995). Granulites are thought to form either by dehydration partial melting (Palin et. al 2016), ingress of CO_2 rich fluids/brines (Harlov, 2012; Touret, 2009) or by magmatic underplating, as in the Ivrea-Verbano lower crustal section in northern Italy (Voshage et al., 1990; Rivalenti et al., 1975), where case-study 2 of this PhD is located.

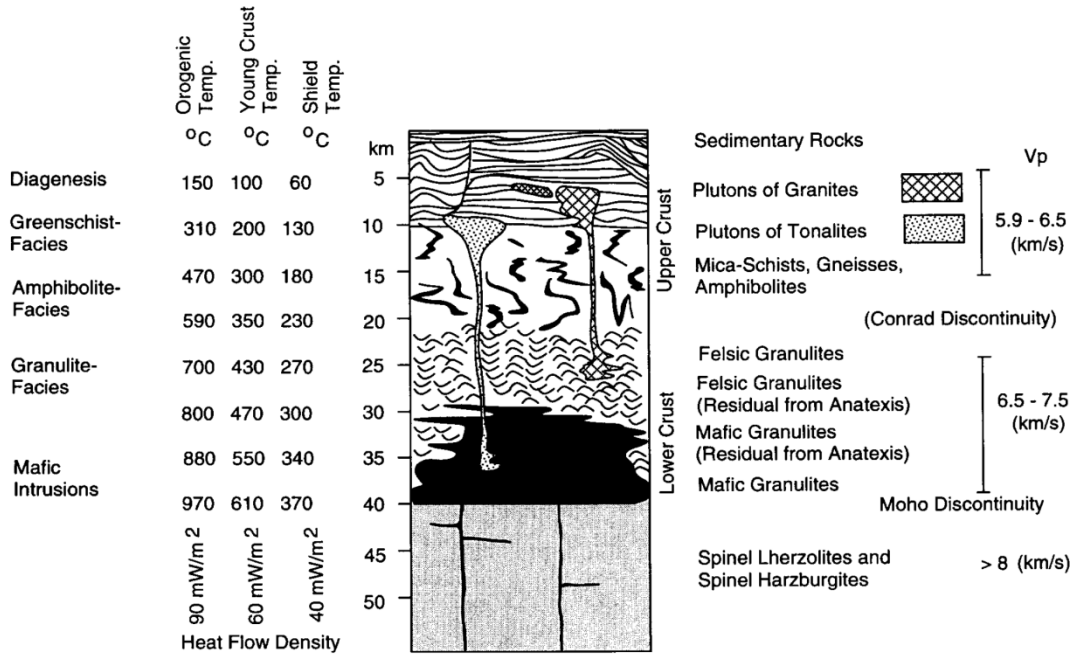

Fig. 2.1

Schematic profile across the continental crust from Hans Wedepohl (1995).

2.2 STRENGTH OF THE LOWER CRUST: WEAK VS. STRONG

Lithospheric strength profiles (also known as strength envelopes) are models that describe how strength in the lithosphere changes with depth (Fig. 2.2 and Fig. 2.3). For low temperatures (< ca. 500 °C) and confining pressures corresponding to shallow crustal levels, the maximum differential stress that rocks can sustain is defined by Byerlee's law of frictional sliding (on favourably oriented pre-existing fractures with no pore-fluid pressure) or alternatively by the Mohr-Coulomb or Griffith failure criteria (for intact rocks) (Byerlee, 1978; Kohlstedt et al., 1995; Ranalli, 1995). Under such conditions, deformation is in the brittle regime and is governed by fracturing and frictional sliding, with final products being brittle fault rocks - e.g., gouges, cataclasites and pseudotachylites (Rutter et al., 2001). With increasing confining pressure, the differential stress required for failure increases (almost) linearly until the brittle-ductile transition in the middle crust (Fig. 2.2) (Handy et al., 2007). For higher temperatures, normally corresponding to middle and lower crust (ca. 500°C), deformation is described by a power-law equation of the form

$$\dot{\varepsilon} = A\,\sigma^{n} \exp\left(\frac{-Q}{RT}\right) \qquad (Eq.\,2.1)$$

This simplified equation relates stress to strain rate, where $\dot{\varepsilon}$ is strain rate, σ is the differential stress raised to the stress exponent n, A is a constant, Q is the activation enthalpy, R is the gas constant and T is temperature (e.g. Karato, 2008). This equation is here mentioned to introduce strength profiles; the same equation will be discussed in more detail in Section 2.3 in the context of diffusion creep and dislocation creep.

Power law equations of the form of Eq. 2.1 are derived from laboratory rock deformation experiments. For the continental lithosphere, the crust's power-law is

typically modelled according to experimentally derived wet-quartz rheology whereas the lithospheric mantle is modelled according to olivine rheology (Kohlstedt et al., 1995). In such a simplified lithospheric strength profile, these power-laws translate in portions of the lithosphere deforming in the ductile manner (Fig. 2.3).

From the analysis of a simplified strength profile, such as that of Fig. 2.3, it is intuitive that crustal levels deforming by power-law creep are generally weaker than levels deforming by cataclasis (if we exclude the first few km below the surface). This implies a weak lower crust and a strong middle crust (corresponding to the transition between the brittle and ductile regimes), and an important strength contrast at the Moho (given by a large difference in plastic creep strength between quartz and olivine) (e.g. Kohlstedt et al., 1995; Handy and Brun, 2004).

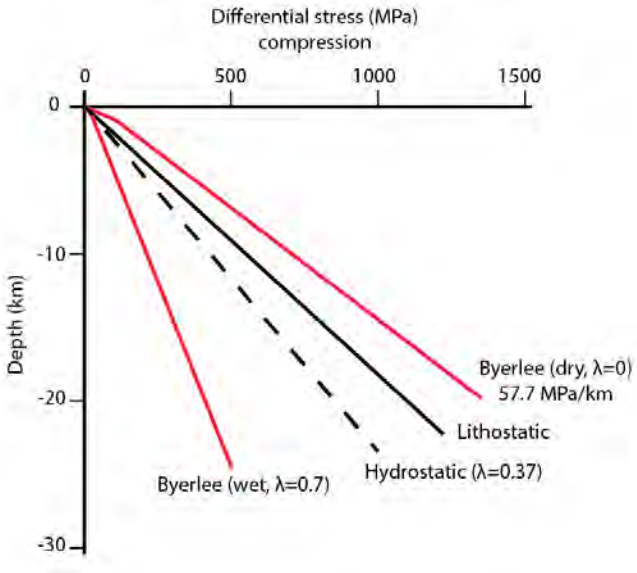

Fig. 2.2

Strength profile of brittle upper-crust based on Byerlee laws of frictional sliding (Byerlee, 1978). Sketch modified after Burov (2011), showing rock strengths for different pore fluid pressures (λ) in a compressive regime.

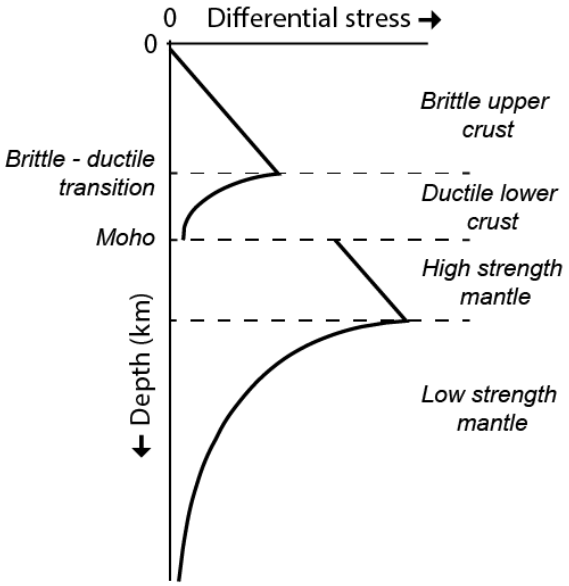

Fig. 2.3

Simplified lithospheric strength profile, showing a brittle upper crust, a ductile lower crust and a high strength mantle. This sketch has no rheological significance as it serves as an example.

Since the concept of lithospheric strength profile was first introduced in the 1970's (Goetze and Evans, 1979; Kirby, 1980), lithospheric models have been constantly improved to account for differences in (1) tectonic regimes, (2) geothermal profiles, (3) water contents, (4) melt contents, (5) deformation mechanisms and (6) different lithology (as in the constituting minerals) (e.g. Burlini and Bruhn, 2005). All these parameters influence the constitutive laws from which the strength profiles are constructed. The tectonic regime (i.e. the stress field) affects the slope of the Byerlee curve and therefore the position of the brittle-ductile transition: in a compressive regime this is located at shallower depth and occurs at higher differential stresses than in extension (Handy et al., 2007). Differences in the geothermal profile, water content, melt content (if any), and lithology produces different stress-strain rate power-law curves, with important consequences on the resulting lithospheric strengths profiles.

Indeed, two end-member models emerge when using different flow-law parameters and boundary conditions: 1) a model with a weak lower-crust sandwiched between a strong upper-crust and mantle (known as the "Jelly sandwich" model) and 2) a model with a strong crust overlying a weak mantle (known as the "Crème brulée" model); Bürgmann and Dresen, 2008). The two models are illustrated in Fig. 2.4. The first model (the Jelly sandwich model) has been constructed assuming a wet lower crust (by using a wet-feldspar flow law), whereas the second model (the Crème brulée model) has been constructed assuming a high geotherm in the mantle (which makes temperature at the Moho higher, thus modifying the dry olivine flow law) and a dry lower crust (using the dry-feldspar flow law) (Fig. 2.4).

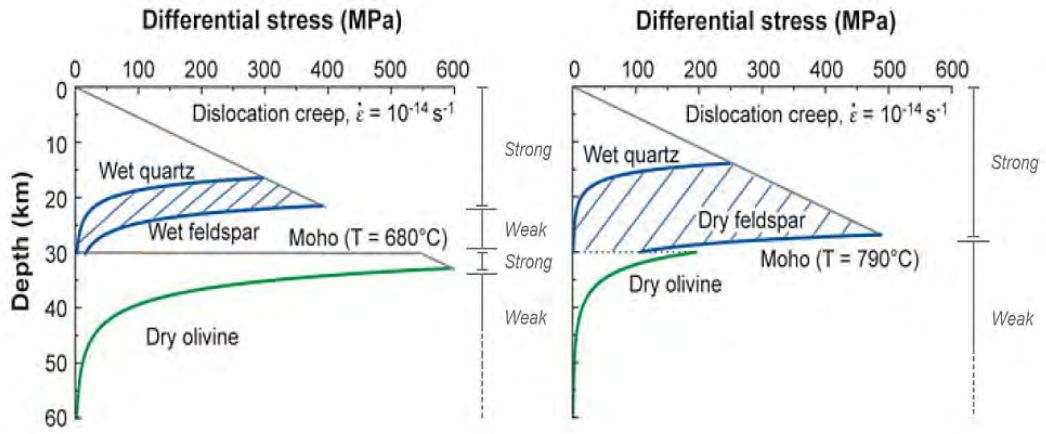

Fig. 2.4

Continental strength profiles, modified from Bürgmann and Dresen (2008). The left profile, with a strong upper crust and mantle and a weak lower crust, is known as the "Jelly sandwich" model. The right profile, with a strong lower crust and a weak upper mantle, is known as the "Crème brulée" model. The two models clearly underline the importance of temperature, water content and lithology in determining the model's outcome. For the flow law parameters used in the models, refer to Burgmann and Dresen (2008). See text for more details.

In the first model the lower crust is rheologically “weak”, whereas in the second model it is “strong”. The “Jelly sandwich” model is supported by geophysical observations, numerical and analogue models and by indications of decoupling at the Moho. Tectonic modelling shows that the lithosphere requires a relatively strong mantle and a relatively weak lower crust for plate tectonics to operate (Handy and Brun, 2004). The “Crème brulée” model is supported by earthquake focal depths distributions and gravimetric anomalies, indicating that the lower crust is elastic and stronger compared to the underlying aseismic upper mantle (Maggi et al., 2000; Jackson, 2002). The authors in favour of this model argue that the long-term strength of the lithosphere resides in the seismogenic layer which extends down to the lower crust. The mantle is (almost) aseismic and weaker due to its high thermal regime (Maggi et al., 2000; Jackson, 2002). This model fits well with mechanically strong dry granulites residing in the lower crust (Jackson, 2002). A strong lower crust has typically been explained with large parts of it being dry, thus incapable of deforming by crystal plastic flow (Jackson et al., 2004; Fitz Gerald et al., 2006; Menegon et al., 2011; Austrheim, 2013; Menegon et al., 2017).

More recently, Burov (2010) has analysed the plausibility of each model and argued in favour of the “Jelly sandwich” model with a weak lower crust and a strong upper mantle. According to this author’s thermal and mechanical modelling of the lithosphere, “the mantle is strong and capable of supporting stresses and geological loads” for long time scales. In his work Burov (2010) also points out that the seismogenic thickness does not coincide with the elastic thickness, making it incorrect to link earthquake distributions to elastic strength as suggested in Jackson (2002). Furthermore, “seismicity is an indicator of frictional instability rather than strength; the mantle could still be

strong despite being aseismic" (Maggi et al., 2000). Also, a strong lower crust does not necessarily imply a weak upper mantle (Burov, 2010).

From the above models, it is clear that the greatest controversies are related to the lower crust, and that the rheological behavior of this layer is critical for understanding the overall strength of the continental lithosphere. Current lithospheric models, constructed using experimentally-derived flow laws of single minerals, do not account for the complex processes that occur in the lower crust, such as strain partitioning, syn-kinematic metamorphic reactions and fluid-rock interactions. In addition, these models consider the lower crust as a mechanical layer with homogeneous properties, even though strain localization in lower-crustal shear zones clearly indicates the opposite (e.g. Kruse and Stünitz, 1999; Kanagawa et al., 2008; Rutter and Brodie, 1988). Therefore, additional studies such as this research project are needed to improve our understanding of the rheology and strength of the continental lower crust.

2.3 DEFORMATION MECHANISMS AND RHEOLOGY

Rocks in the ductile regime deform according to two deformation mechanisms: 1) power-law dislocation creep and 2) diffusion creep (e.g. Karato, 2008). Each mechanism is described by a characteristic flow law, starting from the general equation that relates stress to strain:

$$\dot{\varepsilon} = A\,\sigma^{n}\,d^{-m}\,f_{H2O}^{r}\exp\left(-\frac{Q_d + PV}{RT}\right) \quad (Eq.\,2.2)$$

In this equation, $\dot{\varepsilon}$ is strain rate, σ is the differential stress, n is the stress exponent, A is the material constant, d is grain size, m is the grain size exponent, $f^{r}H_2O$ is the fugacity of water raised to the water exponent r, Q is activation energy, R is the gas constant, T

is temperature, P is the mean stress and V is the activation volume (Blenkinsop, 2000; De Bresser et al., 2001; Karato, 2008; Mehl and Hirth, 2008; Karato, 2010b). Often the term PV is ignored due to its small contribution (Blenkinsop, 2000) and the term $f^r H_2O$ applies if water is considered. In case of melt-assisted creep, the melt fraction ϕ is used in place of the term $f^r H_2O$.

2.3.1 DISLOCATION CREEP

Dislocation creep is a means to produce crystal plastic deformation through motion of dislocations in a crystal lattice (Nicolas, 1976). Dislocations migrate through the crystallographic lattice to reduce the density of dislocations and hence minimize the energetic state of strained minerals. Dislocations glide or climb through the crystal lattice along specific crystallographic planes (slip planes) and directions (defined by the Burgers vector), which together define a slip system. Minerals normally have more than one slip system; which slip system gets activated depends on crystallography, temperature, stress state (differential stress and orientation of stress field relative to the slip plane), activation energy (E or Q) and strain rate (Poirier, 1985).

Dislocation climb (in edge-dislocations) and cross slip (in screw-dislocations) are ways of bypassing impurities of the crystallographic lattice and allow easy glide (Poirier, 1985). Dislocation glide assisted by dislocation climb is termed dislocation creep. If the temperature of the system is too low for dislocation climb, then dislocation glide is inefficient, leading to a build-up of dislocations, increased strain in the lattice and eventually fracture. If recovery is efficient, dislocations either move through the grain or arrange in dislocation walls forming subgrains (Vernon, 2004).

Typical microstructural evidence for dislocation creep is (1) a strong crystallographic preferred orientation (CPO) (2) strained grains resulting from high dislocation densities displaying subgrains or sweeping extinction and (3) dynamic recrystallization.

Dynamic recrystallization is a recovery mechanism associated with dislocation creep that forms new grains either by SGR (subgrain rotation) or GBM (grain boundary migration) (Hirth and Tullis, 1992). SGR forms new grains by progressive rotation of subgrain walls until the misorientation angle between two subgrains becomes greater than a threshold, usually 10°. This results in small strain-free grains with slightly different orientations in respect to the parent grain. GBM instead forms new grains by migration of a grain with lower dislocation density into a grain with greater dislocation density, consuming the latter (Blenkinsop, 2000; Karato, 2008).

For dislocation creep, Equation 2.2 becomes:

$$\dot{\varepsilon}_{disl} = A\,\sigma^{n}\,\exp\left(\frac{-Q_c}{RT}\right) \quad (Eq.\,2.3)$$

This equation is also known as power-law creep, because of a non-linear relationship between stress and strain rate (non-Newtonian flow, variable effective viscosity). The stress exponent n is usually between 3 and 5. Dislocation creep is grain size insensitive, and requires low stress and higher temperatures and slower strain rates than dislocation glide (Blenkinsop, 2000; Karato, 2008).

Slip systems in mafic minerals of the lower crust

Dislocation glide or creep in minerals occurs on a combination of slip systems, with the dominant slip system(s) being the one(s) energetically most favourable. A slip system is defined by a crystallographic plane (slip plane, or glide plane) and a direction (Burgers vector). Slip systems are commonly written with the slip planes in round brackets and

the slip directions in square brackets (e.g. (100)[001]). This section summarises the most common, or dominant, slip systems identified in literature for mafic minerals of the lower crust. The diagram at the end of the section, Fig. 2.5, serves as a visual reference for the crystallographic planes and direction discussed below.

Pyroxenes

In pyroxenes, dislocation glide in the (001) crystallographic plane is not possible because the chains of tetrahedral SiO_4 align along the [001] axis. This means that glide planes must all be in zone with the [001] axis (Raterron et al., 2014). Despite many different slip systems can be activated in pyroxene, the (100)[001] seems to be the most common, both for clinopyroxene and orthopyroxene. Interestingly, exsolution lamellae in both clinopyroxenes and orthopyroxenes occurs parallel to the (100) crystallographic plane, suggesting that this plane is weak. Also twinning observed in clinopyroxene seem to preferentially occur along the (100) planes (Deer et al., 2013).

Clinopyroxene (Diopside)

Most of what is known on clinopyroxene slip systems derives from studies of mantle rocks or from experiments simulating mantle conditions. In fact, a great deal of literature on pyroxene deformation derives from eclogites or peridotites (Bascou et al., 2002 and reference therein).

Nevertheless, the most commonly observed slip systems in clinopyroxenes are (100)[001], {110}[001] and {1-10}½<110>, which combined can result in an L-type CPO with (010) planes parallel to the foliation and [001] directions parallel to the lineation (e.g Godard and van Roermund, 1995; Bascou et al., 2001; Bystricky and Mackwell, 2001; Bascou et al., 2002; Ulrich and Mainprice, 2005; Raterron et al., 2014). Subgrain

boundaries have been reported parallel to {110}, (100), (010) and (001) planes (Passchier and Trouw, 2005). Twinning of clinopyroxene occurs along the (100) planes and, less frequently, along the (001) planes. Exsolution can occur parallel to (100) and (001), but at temperatures above 700–750°C only along (100) (Deer et al., 2013). Diopside also has a good cleavage along {110} (Deer et al., 2013).

Orthopyroxene

Dislocation glide for orthopyroxene occurs preferentially on the (100)[001], (100)[010] and (010)[001] slip systems (Dornbusch et al., 1994; Passchier and Trouw, 2005; Raimbourg et al., 2008). Subgrain boundaries are often parallel to (100), (010) and (001). Deformed orthopyroxene can form clinopyroxene exsolution lamellae parallel to (100). It is not uncommon to find elongated ribbons of orthopyroxene, both in the mantle and lower crust (Hanmer, 2000; Ishii and Sawaguchi, 2002; Sawaguchi and Ishii, 2003; Raimbourg et al., 2008; 2011).

Plagioclase

Above 600 ^{o}C, crystal plasticity becomes relevant, and plagioclase easily undergoes dynamic recrystallization. A rather large number of slip systems have been identified for plagioclase. The most common are the (010)[001], (010)[100], (001)[100] and (001)½<110>, but slip on (001)½<1-10> and {111}<110> were also reported (Kruze et al. 2001, Kanagawa et al., 2008; Mehl and Hirth, 2008, Satsukawa et al. 2013, Pearce et al. 2011, Morales et al., 2011). Several authors have reported elongated plagioclase ribbons, with (010) twins oriented at low angles (ca. 10°) with the long dimension of the elongate grain (e.g. Hanmer, 2000). Deformation twins, undulose extinction and deformation bands are common in such ribbons.

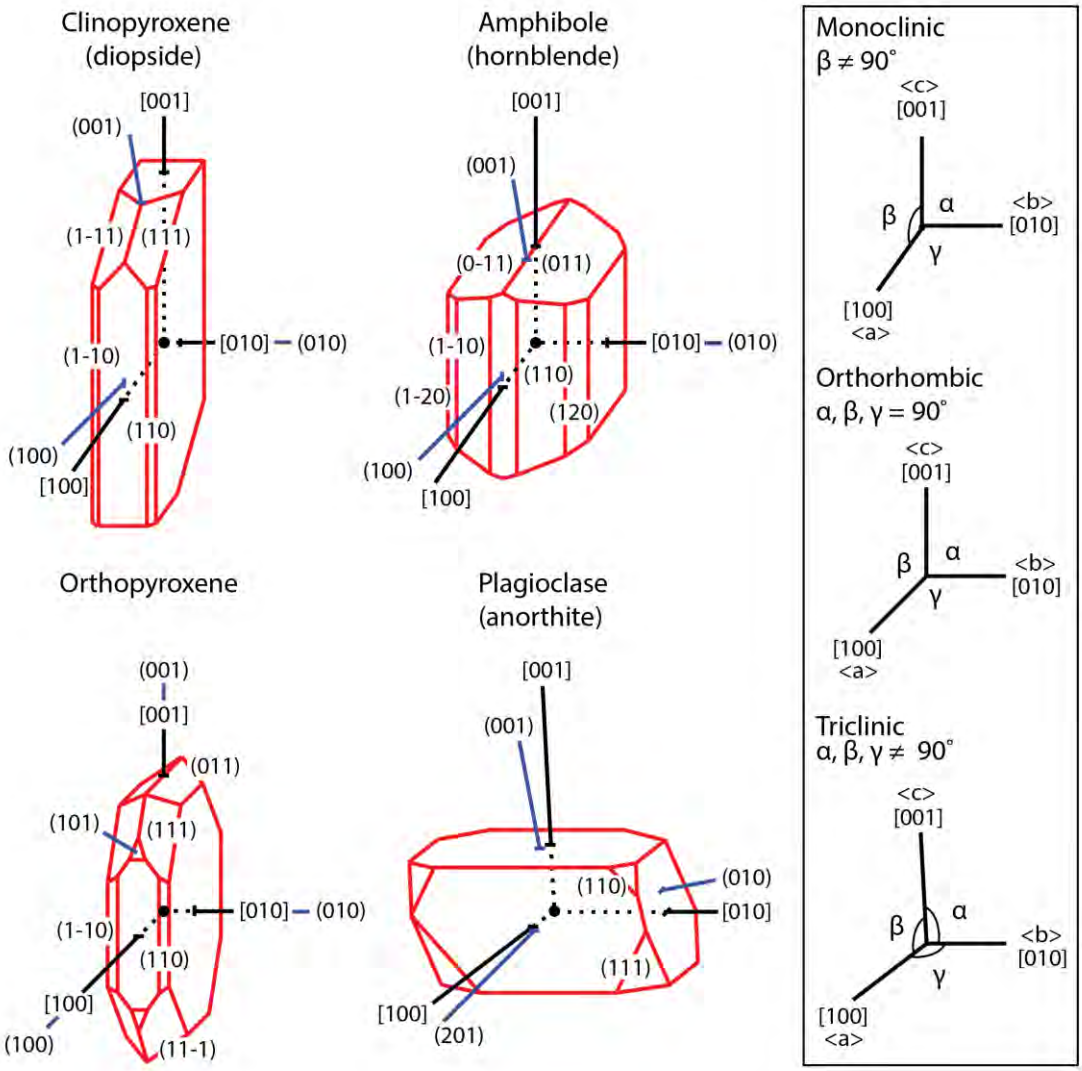

Fig. 2.5

Diagram showing the main crystallographic axes and planes in clinopyroxene, amphibole, orthopyroxene and plagioclase minerals. The crystallographic reference frame for each mineral is shown in black, and the poles to planes are shown in blue. Crystallographic indices of axes and planes are given in square and round brackets respectively. Clinopyroxene and amphibole have a monoclinic symmetry, while orthopyroxene is orthorhombic and plagioclase is triclinic. Clinopyroxene, amphibole and orthopyroxene diagrams are modified after Klein et al. (2002) and plagioclase is modified from https://www.mindat.org/min-246.html. Crystal's morphology can vary and crystal faces can be larger or smaller from the given examples.

2.3.2 *DIFFUSION CREEP (GRAIN SIZE SENSITIVE CREEP)*

Diffusion of intracrystalline point defects and of chemical components (also known as diffusion creep) can occur along grain boundaries (Coble creep) or within the grain lattice (Nabarro-Herring creep) (Nicolas and Poirier, 1976). Coble creep and Nabarro-Herring creep can operate simultaneously, but Coble creep is predominant at lower temperatures, whereas Nabarro-Herring creep occurs at higher temperatures. Grain size is very important for the efficiency of diffusion, therefore diffusion creep is a grain size sensitive mechanism. The smaller the grain size, the greater the efficiency of diffusion. Solid-state diffusion (as opposed to fluid-assisted) operates at a granular scale which means that diffusion pathways are short and chemical mobility is limited (Blankishop 2000). Fluid assisted diffusion instead occurs through a grain boundary fluid (water or melt), whereby material is dissolved from sites of high normal compressive stress and deposited at sites of low stress (Vernon, 2004). Fluid assisted diffusion creep is also known as solution-precipitation creep.

Diffusion creep is concomitant with grain-boundary sliding, as the latter preserves grain-boundary cohesion as the grains change shape (as described by Lifshitz, 1963, Raj and Ashby, 1971) (Fig. 2.6). The combination of diffusion creep and grain boundary sliding is commonly known as grain-size sensitive creep (GSSC). Grain-size sensitive creep occurs in fine-grained materials under high temperature conditions and is characteristic of high strain rates and low differential stresses (e.g. Karato, 2010a). This mechanism is generally accepted to operate in the lower crust and mantle and is considered an important deformation mechanism in shear zones with fine grained polyphase aggregates (Kanagawa et al., 2008; Kenkmann and Dresen, 2002; Kilian et al., 2011; Kruse and Stünitz, 1999; Mehl and Hirth, 2008; Newman et al., 1999; Pearce and

Wheeler, 2011; Raimbourg et al., 2008; Rutter and Brodie, 1988; Stünitz, 1998; Stünitz and Tullis, 2001). A switch from dislocation creep to diffusion creep is associated with a dramatic weakening (Pearce and Wheeler, 2011).

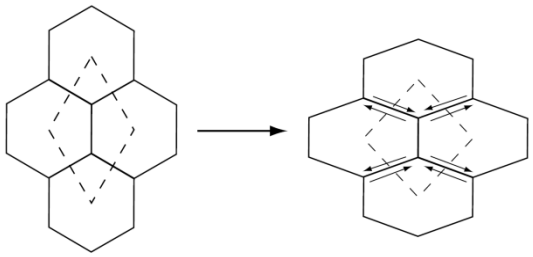

Fig. 2.6

Diagram from Karato (2008) illustrating how grain boundary sliding is necessarily associated with diffusion creep.

Provided that no post-tectonic annealing occurs, diffusion creep in rocks results in a microstructure with fine-grained (in the order of tens of microns), strain-free crystals and absence of a crystallographic preferred orientation (Tullis and Yund, 1991; Blenkinsop, 2000). These microstructural features can be observed and quantified using optical and SEM techniques, of which Electron Backscatter Diffraction (EBSD) technique is the most advanced and useful.

For diffusion creep, Equation 2.2 becomes:

$$\dot{\varepsilon}_{diff} = A\,\sigma^{n}\,d^{-m}\exp\left(\frac{-Q_d}{RT}\right) \quad (Eq.\,2.4)$$

Stress and strain rate are linearly dependent (as the stress exponent n =1, Newtonian flow) and the strain rate is inversely proportional to grain size, with grain size exponent m = 2-3 (Karato, 2010b).

2.4 MECHANISMS OF WEAKENING AND STRAIN LOCALIZATION IN THE LOWER CRUST

It is now established that deformation localizes along discrete structures (i.e. high strain zones or shear zones) and these determine the bulk strength of the lithosphere (e.g. Bürgmann and Dresen, 2008; Fossen and Cavalcante, 2017; Handy et al., 2007; Holyoke and Tullis, 2006; Vauchez et al., 2012). This is valid for different scales, from mm-scale intracrystalline shear zones to lithospheric-scale shear zones. The strength of the rock and ultimately the strength of the lithosphere depend on the strength of these "weak" layers. A number of processes have been considered responsible for localized weakening: fracturing, grain size reduction, syn-kinematic metamorphic reactions, presence of fluids, presence of melt and lithological heterogeneities (e.g. Burlini and Bruhn, 2005). Determining which process is most relevant is still a matter of debate. Almost certainly, it is a combination of these processes that cause weakening and strain localization. These will be briefly discussed below.

2.4.1 THE EFFECT OF GRAIN-SIZE REDUCTION

Grain size reduction is commonly observed in deformed zones at all lithospheric levels, suggesting that there is an intimate connection between grain size and localization of deformation (e.g. White et al., 1980; Tullis et al., 1982; Tullis and Yund, 1985; Rutter and Brodie, 1988). This has led many authors to investigate grain size reduction and how it links to stress and strain rate, using both experimental and theoretical approaches. It is now widely accepted that grain size reduction is a major cause of rheological weakening and strain localization (e.g. Rutter and Brodie, 1988; Rutter et al.,

2001, Platt and Behr 2011, Karato 2008, Raimbourg et al 2008). The underlying idea is that grain size reduction triggers a switch in deformation mechanism from grain size insensitive creep (dislocation creep) to grain size sensitive creep (diffusion creep). The latter deformation mechanism requires lower differential stresses to deform at a given strain rate – i.e. it is weaker – thus promoting strain localization (e.g. Rutter and Brodie, 1988; 2004).

Different mechanisms have been proposed to explain grain size reduction: (1) dynamic recrystallization (bulging, subgrain rotation,; and grain boundary migration) (Hirth and Tullis, 1992; Platt and Behr, 2011), (2) metamorphic reactions (e.g. Newman et al., 1999) and (3) fracturing (Handy and Stünitz, 2002; Stünitz et al., 2003; Menegon et al., 2013).

While many authors agree that a switch in deformation mechanism triggered by grain size reduction *by dynamic recrystallization* is an important mechanism for weakening, causing "profound modifications of both the microstructure and the rheology of rocks in the upper half of the lithosphere" (Platt and Behr, 2011), some such as De Bresser et al. (2001) reason against. In fact, De Bresser et al. (2001) suggest that dynamic recrystallization cannot cause a switch from grain size insensitive creep to grain size sensitive because of grain growth. It follows that dynamic recrystallization cannot be responsible for drastic weakening unless grain growth is inhibited, and other processes such as metamorphic reactions (e.g. Newman et al., 1999; see Section 2.4.2) or brittle fracturing (Menegon et al., 2013) must be taken into consideration.

From analysis of natural samples of fine-grained shear zones, Brodie and Rutter (1987b) suggest that the fine grained aggregate was produced by dehydration reactions.

Building up on this, Handy and Stünitz (2002) proposed a combination of anhydrous fracturing and syn-tectonic metamorphic reactions as means to produce ultra-fine grained mylonites, associated with fluid infiltration.

2.4.2 THE EFFECT OF METAMORPHIC REACTIONS

Metamorphic reactions occur when one or more phases are in thermodynamic disequilibrium with the surroundings. Disequilibrium is normally achieved either through changes in P-T conditions (Newman et al., 1999; Stünitz and Tullis, 2001) or through chemical instabilities driven by the addition of a fluid (usually hydrous fluid) or melt to the system (Etheridge et al., 1983). Changes in P-T conditions occur, for example, during exhumation along crustal scale shear zones (decrease in P-T) or during magmatic underplating (increase in T). Presence of water or melt in shear zones is common as these are permeable pathways for fluids also in the lower crust (Austrheim, 1987; Mancktelow, 2006; Menegon et al., 2015). Both water and melt enhance diffusion and this is a likely trigger of metamorphic reactions (Burlini and Bruhn, 2005).

Syn-tectonic metamorphic reactions can significantly contribute in weakening and strain localization via nucleation of a fine grained aggregate that deforms by grain size sensitive creep (Rutter and Brodie, 1988; Kenkmann and Dresen, 2002; de Ronde et al., 2005), Newmann et al., 1999, Stunitz and Tullis 2001). The reaction products not only are fine-grained, but are also strain-free and with a degree of phase mixing (Kenkmann and Dresen, 2002). It is generally accepted that phase mixing plays an important role of weakening, because pinning of second phases prevents grain growth and thus stabilizes the fine aggregate microstructure (Evans et al., 2001).

In addition to grain-size reduction, metamorphic reactions can form mechanically weaker products (such as serpentine from olivine, or micas from feldspar) that contribute in reducing the rock's strength.

2.4.3 THE EFFECT OF WATER

Water can promote weakening in multiple ways: it can trigger metamorphic reactions, increase the efficiency of dislocation creep and grain boundary diffusion, and cause partial melting by lowering the solidus of minerals (Blenkinsop, 2000).

Intracrystalline water in NAMs (nominally anhydrous minerals: quartz, feldspars, olivine, pyroxenes) is known to significantly reduce mineral strengths by promoting climb and hence dislocation creep (hydrolytic weakening: Griggs, 1967, Kohlstedt, 2006), and to influence the activity of slip systems (Jung et al., 2006). Experimental studies of the effect of water on pyroxenites indicate that water can substantially increase dislocation creep rates in clinopyroxenes (Chen et al., 2006).

Presence of water at grain boundaries facilitates diffusion (via dissolution and precipitation), grain boundary migration (GBM) and grain boundary sliding (Mancktelow and Pennacchioni, 2004, Karato, 2008). In addition, grain boundary water can promote metamorphic reactions through enhanced chemical diffusion. However, the low porosity of high-grade rocks of the lower crust do not allow large quantities of interstitial grain boundary water to freely circulate, which means that "this type" of water in the lower crust is scarce, and unevenly distributed (e.g. Yadley 1997, Weinberg and Hasalova 2015).

One way of bringing water at depth is through shear zones, owing to their enhanced interconnected porosity and permeability (Austrheim, 1987; Mancktelow, 2006; Menegon et al., 2015). The presence of syn-kinematic amphibole in lower crustal shear zones (e.g. Vauchez et al., 2012; Getsinger et al., 2013) confirm that water preferentially localized along shear zones (Austrheim, 2013; Getsinger et al., 2013) and suggest the importance of fluids during shearing also at these depths.

Fracturing is an efficient way to increase the permeability of rocks and to facilitate fluid infiltration, mineral reactions and deformation even at lower crustal conditions (e.g. Austrheim, 1987, 2013, Menegon et al., 2013, Okudaira et al.,2015). Extensive fracturing under granulite facies conditions has been interpreted as indicative of high creep strength of the granulites (Austrheim, 2013; Jackson et al., 2004; Okudaira et al., 2015) that enable in situ stresses to reach magnitudes sufficient for fracture. Austrheim (2013) suggests that ingress of fluid in the lower crust occurs after seismicity-induced fracturing of dry and strong granulites.

Aqueous fluid infiltration can trigger metamorphic reactions (typically hydration reactions). Austrheim (2013) suggests that the most important metamorphic reactions in the lower crust (i.e. the granulite - eclogite, the gabbro-eclogite and the eclogites-amphibolite transitions) are all triggered by hydrous fluids. Heterogeneous distribution of fluids result in a rheological contrast between dry and wet mineralogies, and this triggers localized shearing (Austrheim, 2013; Getsinger et al., 2013).

Another source of water in the lower crust is through dehydration reactions consuming biotite and/or amphibole (e.g. Fyfe, 1973). Water released during these reactions

lowers the solidus and this can lead to partial melting (for a review, see Weinberg and Hasalova 2015).

2.4.4 *THE EFFECT OF MELT*

Partial melting is another fluid-related process that has a strong influence on the mechanical behaviour of rocks, where the melt weakening effect has been demonstrated in experimentally and naturally deformed rocks of felsic and mafic compositions representative of the lower crust (Dimanov et al., 1998, 2000; Rosenberg and Handy 2005; Rosenberg et al 2007; Rutter and Neumann, 1995; Van der Molen and Paterson, 1979; Yoshinobu and Hirth, 2002; Zhou et al., 2012, 2017).

The strength of partially molten aggregates decreases by introducing a phase with lower viscosity (the melt) to the system (e.g. Rosenberg 2007). According to Rosenberg and Handy, 2005, the greatest strength drop occurs when melt wets the majority of grain boundaries to form an interconnected melt network. In crustal systems, this typically happens for melt fractions >= 7% (Rosenberg and Handy, 2005). Weakening effect is explained by an increased contribution of melt assisted grain boundary sliding and diffusion creep (e.g. Dell'Angelo et al., 1987; Rosenberg and Berger, 2001; Rutter et al., 2006).

For large fractions of melt (melt volumes between 20%-50%, Rosenberg and Handy 2007), the strength of the rock is not determined any longer by the solid-bearing framework but by the melt portion. As melt has a significantly lower viscosity than the solid minerals, the bulk strength drops a few orders of magnitude (Rosenberg and Handy, 2005). The percentage of melt necessary for a switch from the solid-bearing to the melt-bearing framework is known as the critical melt fraction (CMF), also known as

the rheological critical melt percentage (RCMP), and is generally estimated above 30% melt (e.g. Burlini and Bruhn, 2005). This value essentially separates the fields of solid-state flow and magmatic flow.

For more modest amounts of melt fraction (typically lower than 7% for crustal material: Rosenberg and Handy, 2005), melt affects rheology much like the hydrous fluids discussed in Section 2.4.3. The most important effect is enhancing grain boundary diffusivity (Karato, 2008). In addition, melt can produce chemical disequilibrium with the rock, leading to the development of fine-grained reaction products able to deform by grain size sensitive creep (Dijkstra et al., 2002; Závada et al., 2007; Zhou et al 2017).

3 METHODS

This chapter describes the analytical techniques and procedures employed in this PhD thesis. The aim of this chapter is to provide the reader with a brief background overview of the analytical instrumentation, with details of sample preparation, of the operating conditions and of data processing. For more in-depth details on the principles behind the analytical techniques, the interested reader should refer to the following sources: Al-Merey et al. (2005), Connolly (1990), Engler and Randle (2009), Heilbronner and Barrett (2014), Higgins (2006), Lloyd et al. (1997) Prior et al. (2009, 1999), Reed (2005). For an account of the research strategy and choice of techniques please refer back to Chapter 1, section 1.2.

3.1 FIELD WORK AND SAMPLE PREPARATION

For case-study 1, a suite of samples from the Seiland Igneous Province (Norway) were readily available from the department for study. For case-study 2, a 10-days field campaign was taken in the Ivrea zone (Finero mafic-ultramafic complex) in June 2014 for structural measurements and collection of samples across a lower crustal shear zone. Shear zone rocks were sampled from high and low strain domains and where lithological differences were observed. Structural profiles were drawn across the shear zone to accompany sampling. In addition, all samples were oriented in the field according to the orientation of foliation (dip/dip direction) and stretching lineation (trend/plunge), and these orientations were marked on each sample. Sample details, together with the GPS coordinates, can be found in the Appendix, Appx.1. Geological maps of the study areas

were compiled using Esri ArcGIS and modified to incorporate stereoplots of structural data and samples GPS locations (Fig. 5.1 and Fig. 5.2).

In the laboratory, rock samples were cut perpendicular to foliation and parallel to stretching lineation to make polished thin sections (Fig. 3.1). Thin sections were oriented with the Z axis pointing towards the pole of the foliation and with the X axis pointing to the plunging direction of stretching lineation. These Z and X directions correspond to the Z and X direction of the finite strain ellipsoid. The microstructural investigations at the base of this PhD thesis were done on a selection of representative thin sections. Before further investigations, all thin sections were studied under the polarized light microscope for groundwork mineral identification and for large-scale imaging of the microstructure (useful for navigation on the SEM and also for image analysis).

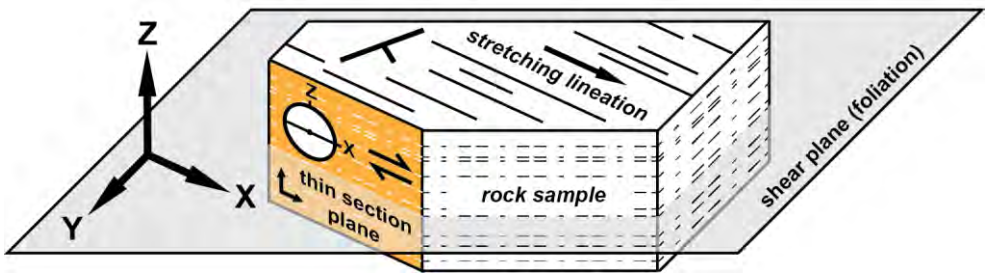

Fig. 3.1

Schematic diagram of the reference system used throughout in this thesis. Rock samples were cut perpendicular to the foliation and parallel to the stretching lineation, and labelled X (direction of stretching lineation) and Z (pole to the foliation plane). The XZ plane (shown in orange) was made into thin sections. All microstructural analysis, unless stated otherwise, relate to this reference system, including pole figures (see section 3.4.2).

After mechanical polishing down to 30 µm thickness, thin sections analysed with Electron Backscatter Diffraction (EBSD) technique were chemo-mechanically polished with a

colloidal silica suspension to remove the damage induced by mechanical polishing, and to obtain a homogeneous flat surface (see Section 3.4). Colloidal silica polishing is an essential step for quality EBSD results, as topography causes beam shadows when the sample surface is tilted at 70° from the horizontal position. Colloidal silica polishing was done with a Bühler Vibromet ® vibratory polishing machine for a duration of ca. two hours per sample. The samples were then immediately rinsed with deionized water and placed in an ultrasound bath for 1-2 minutes. This assured that no colloidal silica could crystallize on the surface of the sample upon drying.

Thin sections used for SEM-based analysis were coated with a thin carbon film (ca. 20 nm) to avoid electrical charging effects that may occur during the interaction of the electron beam with a non-conductive sample surface.

Specially-prepared thin-sections were made for SIMS analyses by specialists at the Ion Microprobe Facility in Edinburgh. Samples were polished using Alumina powder. The rock chips were glued to the supporting glass with a water-free epoxy. The samples were coated with a thin gold film (<0.02 µm) to prevent charging, and mounted on an aluminium sample-holder using Indium (soft metal, free of H^+).

3.2 Microstructural Analysis

The petrography and microstructure of sheared mafic rocks were studied on polished thin sections. Individual grains and mineral aggregates were manually outlined from optical and SEM backscatter electron images, and the resulting microstructural maps were processed using the image analysis software Fiji (ImageJ) (http://fiji.sc/Fiji) to derive: (1) grain-size (defined as the diameter of the equivalent circle); (2) grain/aggregate aspect ratio; and (3) relative phase abundances, following the approach

of Heilbronner and Barrett (2014). Grain size and shapes yield important information on the deformation mechanism (grain size sensitive vs. grain size insensitive creep), whereas phase abundances is useful to quantify the mineralogical proportions in the rock.

3.3 Scanning Electron Microscopy (SEM) – BSE, EDS

The Scanning Electron Microscope (SEM) was used for high-magnification imaging and semi-quantitative chemical analysis. SEM analyses were done at the Plymouth Electron Microscopy Centre using either the JEOL 6610 VP-SEM or the JEOL 7001 FEG-SEM.

In the SEM, electrons are produced in an electron gun either by thermo-emission from a tungsten filament or by emission from an electrostatic field (field emission gun) (e.g. Reed, 2005). The electrons are accelerated by an electric potential difference (ΔV), resulting in a high energy monochromatic electron beam. This is focused perpendicular to the sample through a series of electromagnetic lenses and apertures that reduce the diameter of the beam. The sample is mounted horizontally on a sample-holder and placed on a movable stage that allows lateral analysis and beam focus. The whole system is kept under vacuum to avoid interaction of the beam with a medium such as air gas and water vapor. The volume of sample that interacts with the beam depends on the energy of the beam (given by the applied voltage) and by the composition of the material. Typically a beam generated by 15 kV voltage gives an interaction volume of about 1 µm diameter. The interaction of the electron beam with the sample results in both electron signals and electromagnetic radiations (Fig. 3.2).

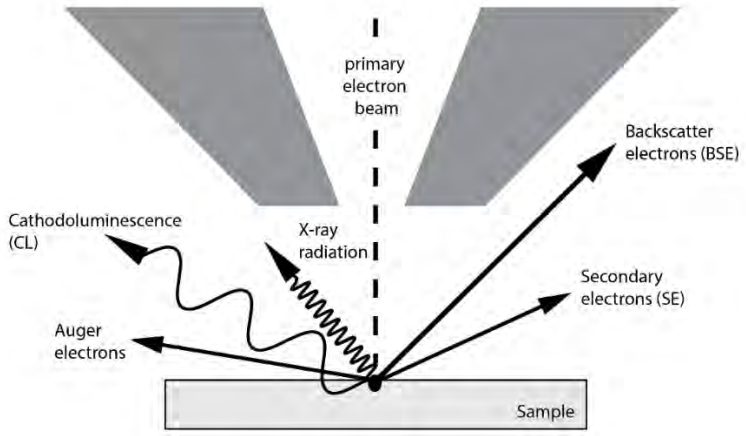

Fig. 3.2

Cartoon of signals emitted by the electron beam interacting with the sample's surface, based on the signals described in Reed (2005).

The electron signals are 1) Backscattered electrons (BSE), 2) Secondary electrons (SE) and 3) Auger electrons (not discussed here) (Fig. 3.2). When the electron beam interacts with the sample's atoms it produces elastic and inelastic scattering of electrons. Parts of the scattered electrons are absorbed by the sample, while part are scattered back out of the sample (the latter are known as backscattered electrons). BSE are high energy backscattered electrons, while SE are low energy forescattered electrons (<50 eV). BSE and SE are used for electron images, obtained by scanning the electron beam line by line over an area of the sample. SE is better suited to image the morphology and/or topography of the sample's surface, while BSE gives images based on the composition (i.e. based on the element's atomic number Z). The BSE are electrons scattered by atoms, so the more electrons an atom contains the higher the probability of elastic scatter. Therefore, the higher the atomic number the better the BSE signal. In a backscattered electron image, the average atomic number Z is imaged as shades of grey with the light shades having higher atomic numbers than the darker ones. This produces grey-scale

electron images where differing compositions are identified by different grey tones. BSE imaging is a fundamental microstructural investigation tool in this thesis.

In addition to the electronic signals, the sample also produces electromagnetic signals, which are of most interest for chemical analysis of the sample. These electromagnetic signals are 1) Characteristic X-ray radiations and 2) Cathodoluminescence - CL (not discussed here).

Characteristic X-ray radiation is formed by the ionization of the electrons in the atoms: the electron beam removes electrons from the inner orbitals of atoms, causing electrons to move from the outer orbitals of atoms to the inner orbitals where the electrons were expelled (Fig. 3.3).

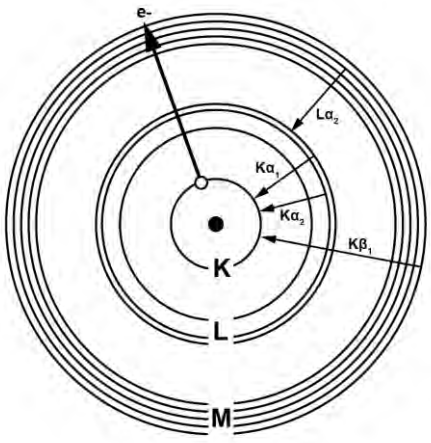

Fig. 3.3

Schematic diagram of the atom's K, L, and M shells, modified after Reed 2006. Electrons are expelled from inner orbitals, causing outer electrons to move in their place. The difference in energy (keV) between the two orbitals is given off as X-ray photons of specific energy.

The difference in energy resulting from this electron movement is emitted as X-rays photons (and Auger electrons). Each element emits a characteristic set of X-rays that

depends on which orbital the element was expelled from, and from which orbital the electron transfers. For example, if the X-ray signal comes from the K orbital there is a K radiation and if it comes from the L orbital there is an L radiation. α, β and γ refer to the intensity of the signal, where α is the highest intensity (Fig. 3.3).

EDS (Energy Dispersive Spectroscopy) analysis is a semi-quantitative analysis that simultaneously identifies elements from the spectrum of measured X-rays. From the spectrum, EDS can detect major elements and their relative concentrations (Fig. 3.4). Common rock-forming minerals are reconstructed based on the elements they contain and on the intensity of the signals (height of the spectrum peaks), which are then translated into relative element quantities. EDS is a semi-quantitative analysis because it is not sensitive enough to reveal minor and trace elements. In addition, if standards are lacking the instrument is not calibrated, which means that the intensity of the signal does not directly correlate with weight %. Nevertheless, due to the speed of acquisitions, EDS is a very practical semi-quantitative tool, used in this thesis for point analysis (for semi-quantitative mineral composition) and major element map distributions (e.g Fig. 5.12a).

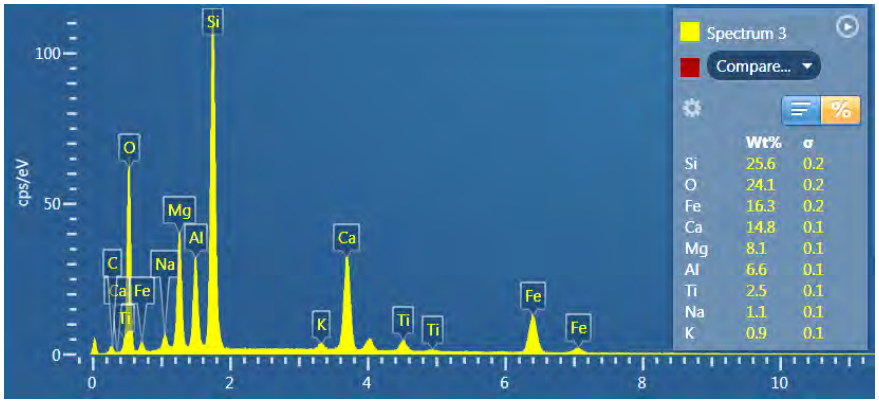

Fig. 3.4

EDS spectrum of amphibole, using Oxford Instruments Aztec software. Different peaks of the same element represent energies from different atomic shells.

3.4 ELECTRON BACKSCATTER DIFFRACTION (EBSD)

Electron Backscatter Diffraction (EBSD) is a SEM based analytical technique that measures crystallographic orientations of any crystalline material, providing textural/crystallographic information of polycrystalline samples (Engler and Randle, 2009; Prior et al., 1999, 2009). The technique exploits the electrons that are backscattered from minerals when they are probed with an electron beam. When the beam interacts with the atomic structures of the mineral, emitted electrons are diffracted according to Bragg's law:

$$n\lambda = 2dsin\theta \qquad (Eq.\ 3.1)$$

where λ is the wavelength of the incident beam, d is the distance between atomic planes, n is the order of reflection and θ is the Bragg's angle (Bragg and Bragg, 1913). Any diffraction that does not obey Bragg's law is destructive, meaning that interfering waves cancel each other out. Therefore, only specific angles of diffraction, characteristic of a specific set of lattice planes, get preserved. In three dimensions, the trajectories of diffracted electrons define two cones, named the Kossel cones (Prior et al., 1999, 2009). Diffracted electrons hit the EBSD detector (a phosphor screen), producing a pattern of lines, known as Kikuchi bands, that are specific of a crystallographic orientation (Nishikawa and Kikuchi, 1928) (Fig. 3.5). The pattern is then recorded by a CCD (charge-coupled device) camera. Given a known crystal structure, the pattern depends on the orientation in space of the crystal. The acquisition software recognizes the pattern (based on the angles and position of Kikuchi bands) and compares it with theoretical match units of specific mineral phases derived from their lattice parameters. The process of attributing a specific crystallographic orientation to a mineral phase is referred to as

"indexing". Indexing translates the Kikuchi pattern into a set of three rotation angles, known as Euler angles, which together define the crystallographic orientation in a 3D space (Engler and Randle, 2009). This way, the orientation of each point is described by three rotations angles, required to bring the crystallographic orientation to coincide with the sample's reference frame. There are different rotation conventions to match the crystal's orientation with the sample's reference frame, and here the Bunge convention is used (Bunge, 1982).

Accuracy of indexing is expressed by the Mean Angular Deviation (MAD), which corresponds to the angular deviation of the indexed pattern from the theoretical match unit. Accuracy of EBSD is typically on the order of 1-2°, and modern EBSD systems can get to < 0.5°. EBSD patterns are measured in raster mode using a predefined distance (step-size). Scanning across an area produces maps where each pixel is a crystallographic orientation.

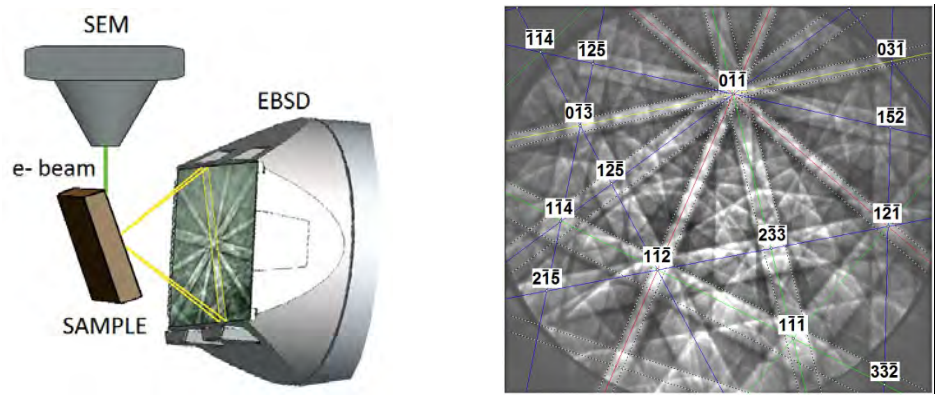

Fig. 3.5

Sketch modified after Oxford Instruments: http://www.oxford-instruments.com/ schematically showing the set-up for EBSD analysis, with the sample tilted at 70° to the horizontal position. Diffracted electrons hit the EBSD detector (a phosphor screen), producing a pattern of lines (known as Kikuchi bands) that is specific of a crystallographic orientation. An example of EBSD pattern is given on the right (for quartz). Where Kikuchi bands intersect there is a crystallographic axis.

EBSD data is essentially an orientation matrix (expressed as three rotation angles – Euler angles) that relates the orientation of the crystal lattice to the sample's X-Y-Z reference frame. This orientation matrix can be visualized in different ways; the most common being EBSD maps where each pixel (positioned in the X-Y coordinates in the sample's reference frame; Z is the pole to the X-Y surface) represents an orientation of the crystals lattice. In alternative, crystallographic planes or directions can be plotted in stereographic projections, commonly referred to as pole figures (see section 3.4.2 below). EBSD data can also be processed to extract other quantitative information such as grain size, misorientation angles between two pixels or between set of pixels (within grains or at grain boundaries), misorientations angles of all pixels from one specific orientation, and misorientations angles from one of the sample's reference directions X, Y or Z (Lloyd et al., 1997; Prior et al., 2009; Wheeler et al., 2001). EBSD analysis is a key tool for the understanding of deformation mechanisms and other metamorphic processes in polyphase rocks (Prior et al., 2009).

3.4.1 EBSD DATA ACQUISITION

EBSD analyses were performed on the JEOL 6610 VP-SEM at the Electron Microscopy Centre of Plymouth University. EBSD maps were acquired on the same polished thin sections used for light microscopy and for electron microprobe analysis. EBSD-quality polishing is essential for quality data acquisition, as the technique requires a perfectly flat surface for diffraction patterns to be detected. Therefore, chemo-mechanical polishing up to nano-scale using colloidal silica is required (see section 3.1). The thin sections were left uncoated during acquisition of EBSD patterns. Working conditions were 20 kV accelerating voltage, 50 Pa vacuum (low-vacuum mode), a working distance between 18

and 23 mm, and a 70° sample tilt. EBSD patterns were acquired in a rectangular grid mode using a step size between 0.6 µm and 4 µm depending on the main target of the analysis (fine-grained matrix vs. large porphyroclasts). Diffraction patterns were automatically indexed using Oxford Instruments Aztec software. Raw indexing rate ranged from 72% to 95%.

3.4.2 EBSD DATA PROCESSING

The quality of the EBSD data depends on a number of factors, including the quality of the sample's polished surface, the operational settings of the SEM and the efficiency of the pattern-matching algorithm (e.g. Prior et al. 2009). Wrong indexing (i.e. mis-indexing of EBSD patterns) and non-indexing (i.e. no matching of EBSD pattern) can occur to some extent, particularly with phases exhibiting low crystal symmetries, and in proximity of grain boundaries (e.g. Prior et al. 2009). Fortunately, most of these errors can be corrected with a data cleaning routine. Here, EBSD results were processed with Oxford Instrument HKL Channel 5 software. Raw EBSD maps were cleaned of misindexed and non-indexed data points using the routine of "spike removal" and "extrapolation of zero solutions", following the procedure tested by Prior et al. (2002). The former removes pixels (data points) with mismatching orientation with the surrounding pixels, whereas the latter extrapolates the orientation of unindexed pixels based on average orientations of the neighbour data points. EBSD data can be presented in multiple ways, and each map or plot is useful for different purposes. The following section briefly explains the EBSD maps and plots presented in this thesis, and examples of each are given in Fig. 3.6.

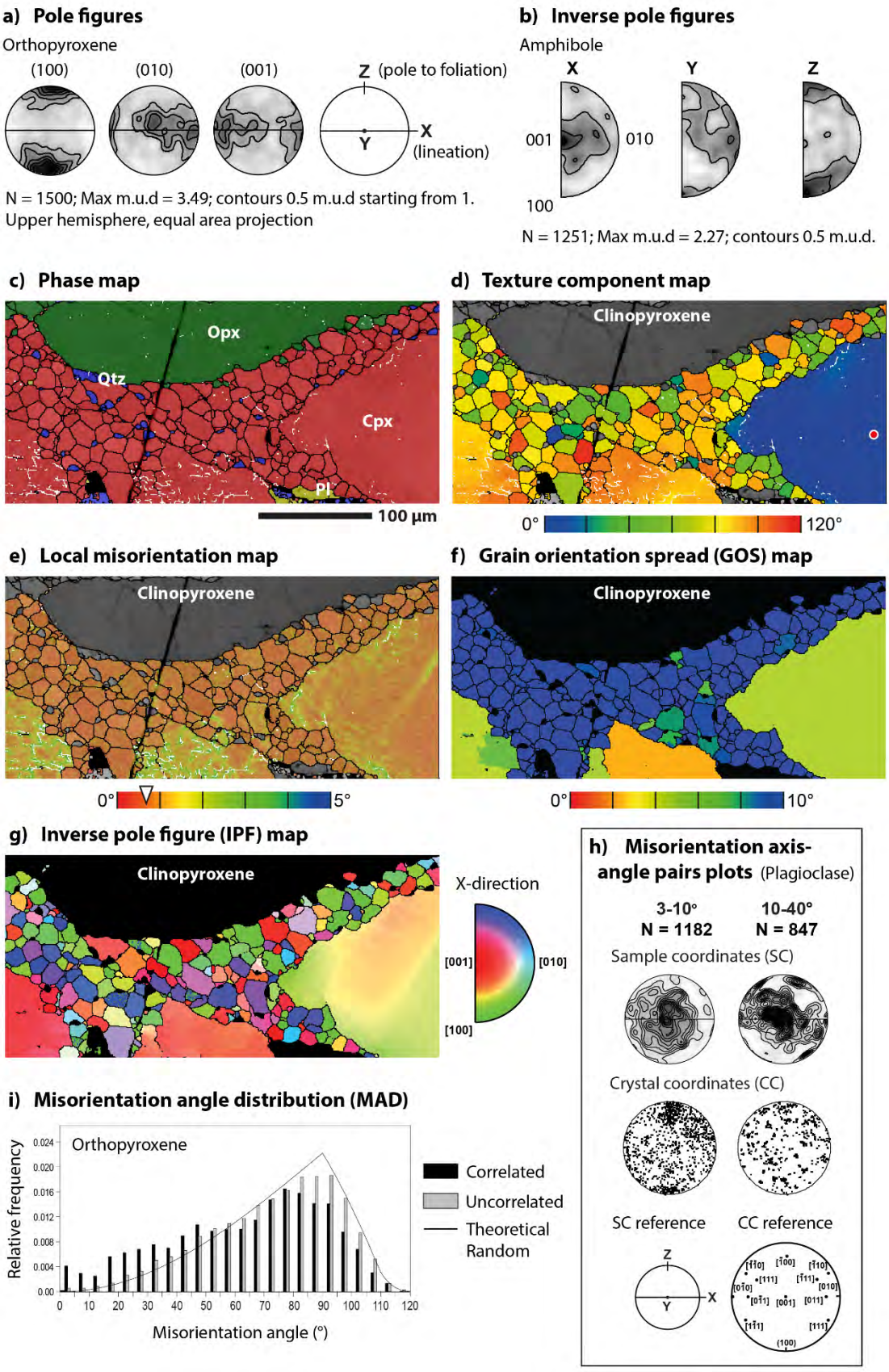

Fig. 3.6

Examples of the different types of EBSD plots and maps employed in this thesis. Please refer to the text for explanations.

Pole figures:

Pole figures are stereographic projections which plot crystallographic directions or poles to crystallographic planes in the sample's X-Y-Z reference frame (Fig. 3.6a). As such, pole figures are useful to quantify texture. For each mineral phase, a series of crystallographic directions are plotted. The choice of crystallographic planes and directions to plot depends on the crystal symmetry and on the known slip systems from literature. Owing to - and depending on – the crystal symmetry, some crystallographic planes and directions are symmetrically equivalent (these are known as family of planes or directions). For instance, the (100), (010) and (001) planes in the cubic crystal system are symmetrically equivalent, which means that the pole figures are identical. As a rule of thumb, the lower the symmetry the less the symmetrically equivalent planes. For plagioclase, pertaining to the triclinic crystal system, no crystallographic planes or directions are equivalent, if not for the -1 inversion.

All pole figures presented in this work are referenced with the pole to the mylonitic foliation (sample's Z direction) pointing upwards and the mineral lineation (sample's X direction) horizontal. These correspond to the Z and X directions of the finite strain ellipsoid. In addition, all pole figures - unless stated otherwise - are plotted as one point per grain (abbreviated as OPPG), to avoid the effect of grain size on textural strength determination.

Texture strength (as in orientation distribution density) is expressed through the m.u.d (multiples of uniform distribution) value, calculated from one point per grain datasets using a Gaussian Half Width of 15°. The m.u.d. is a statistical expression of the strength of texture (as in the distribution of orientations), whereby the higher the m.u.d the more

pronounced the texture. It is however important to specify that the m.u.d is relative to each dataset, as its value depends also on the Gaussian Half Width and on the number of points in the dataset (e.g. Skemer et al., 2005). Clearly, the fewer the points the less representative the texture. For datasets with a considerable number of points (i.e. ca. > 300 points or grains as one point per grain), pole figures are contoured using 0.5 m.u.d intervals with the first contour being 1 m.u.d. Instead, datasets with only few points (i.e. < 300 points, or grains as one point per grain) are left without contours. The latter is because small datasets are more prone to statistical errors in m.u.d calculation, causing the tendency to over-calculate (and contour) local maxima defined by a clustering of a limited number of points, with the risk of concealing a potential "real" texture. The J-index parameter (where 1 = random orientations and ∞ = single crystal), calculated using a Gaussian Half Width of 15° and a Spherical Harmonic Order of 10, was also used to quantify the strength of the texture (Bunge, 1982).

Inverse pole figure plots:

Inverse Pole figures are stereographic projections of the crystallographic reference frame (Fig. 3.6b). These are used to plot all crystallographic directions that align with one of the sample's reference directions. In other words, the sample's X, Y or Z directions are plotted in the crystallographic reference frame. Owing to crystal symmetry, only a portion of the crystallographic coordinate system needs to be shown.

Misorientation angle distribution graph (MADs):

This graph shows the frequency distributions of misorientation angles, as defined by Wheeler et al. (2001) (Fig. 3.6i). Two types of misorientations are considered, one between neighbouring pixels (correlated misorientations) and the other between two unrelated pixels (uncorrelated misorientations). These are plotted against the theoretical

curve for a random orientation of points that is specific of the crystal symmetry (Wheeler et al., 2001) using a 5° increment binning. A minimum angle of 3° is considered to avoid angular errors (given by accuracy of EBSD indexing) (e.g. Prior et al., 1999). The graph can be computed using the whole dataset, or in alternative, using only one point per boundary (abbreviated as OPPB).

Misorientation axis-angle pairs plots:

These plots are another way of visualizing the misorientations between neighbouring pixels. Misorientations can be selected according to their angle, and plotted in both the sample's reference frame (the same reference of pole figure plots) and the crystal's reference frame (the same reference of inverse pole figure plots) (Fig. 3.6h).

EBSD maps:

All EBSD results (maps and pole figures) are presented with the pole to the mylonitic foliation (Z direction) pointing upwards. Grains are conventionally defined when entirely surrounded by a 10° misorientation boundary, and these boundaries are shown in black. Properties such a grain size and shape can be calculated from grains defined in the above manner. One point per grain (OPPG) orientation is calculated as the average orientation of all the pixels in the grain. Polysynthetic albite twin boundaries are defined by a 180° rotation (± 10°) about the (010) axis, and these boundaries are not considered as grain boundaries. Grains with an area smaller than 5 pixels are also discarded from the dataset so to minimize misindexing errors. Low angle (3 - 10°) boundaries are shown in white. The maps that follow all derive from the original EBSD dataset, from which different parameters are extracted.

Phase map:

The phase map assigns each phase a different colour. This map is only used to visualize the spatial distribution of phases in the analysed regions (Fig. 3.6c).

Texture component map:

This map is colour coded according to the misorientation angle with respect to a chosen reference point (a reference orientation) within the map (Fig. 3.6d). The misorientation angles are calculated as the smallest angular differences (considering symmetry) between the chosen reference point and each other pixel of the same phase. The map is useful to spatially visualize the degree of misorientations from the chosen point, and is here used as an aid to understand intracrystalline lattice distortions and recrystallization mechanisms.

Local misorientation map:

This map is colour coded according to the degree of misorientation between each pixel and its neighbouring cluster of pixels within a radius of 7x7 pixels (Fig. 3.6e). The maximum misorientation used is 5°. The map highlights the presence of deformation substructures within the grain, such as subgrain walls. This map differs from the subgrains boundaries map, as the misorientation is computed across more pixels rather than taking the misorientation angle between two neighbouring pixels. The algorithm calculates the average misorientation between each pixel and the surrounding pixels within the assigned radius, and assigns the mean value to that pixel. The pixel is then colour coded according to its mean misorientation value. This highlights gradual lattice bending that is in the order of few microns, rather than one-pixel angle jumps, and can therefore resolve the presence of substructures more effectively.

Grain Orientation Spread (GOS) map:

This map colour codes grains according to the mean of all the misorientations within each grain (Fig. 3.6f). This map can therefore be used as a tool to discern the recrystallized grains from the relic (parent) grains, based on the degree of intracrystalline lattice distortion in each grain (Cross et al., 2017). GOS lower than 3° are to be considered "misorientation-free" for the accuracy of EBSD indexing (Prior et al., 1999); whereas large GOS (> 40° ?) should be interpreted with caution as they can be the result of e.g. twinning.

Inverse pole figure map:

This map is colour coded according to which crystallographic axis is aligned with one of the samples' directions (either the X, Y or Z) (Fig. 3.6g). Each crystallographic axis is represented by a colour, given in a colour legend.

3.5 Electron Microprobe Analyser (EMPA)

The Electron Microprobe (EMP) is designed for quantitative chemical analysis of major and trace elements (e.g. Reed, 2005). Like the SEM, it works on the principle that a focused electron beam interacting with a solid matter emits electrons and X-rays of characteristic energies (see section 3.3). By measuring the intensities of the emitted X-rays, it is possible to quantify the elements in the substance analyzed. The great advantage of the microprobe over an analytical SEM lies in the quality and number of X-ray detectors. SEMs are usually equipped with an EDS (Energy Dispersive Spectroscopy) detector: a Si-drift detector (SDD). This crystal absorbs all the incoming X-rays and gets ionized producing electrical pulses, which are amplified and analyzed by a multichannel analyzer. Microprobes are instead equipped with 4+ WDS (Wavelength Dispersive Spectroscopy) detectors. EDS measures X-rays intensities simultaneously whereas WDS measures X-rays wavelengths one at a time. The WDS uses different diffraction-crystals

(LIF, PET, TAP, LDE) to transform the incoming multi-wave radiation in monochromatic radiation that is diffracted according to Bragg's law (Eq. 3.1, see section 3.4). The geometry of the crystal and the detector are arranged so that they are always at the same distance, defining a circle of constant radius (the Rowland Circle). As the crystal and detector move, the angle of incidence of the incoming X-rays changes allowing for detection of different wavelengths. WDS has a very high-spectral resolution where signal to background ratio is much better than for EDS, giving better detection limits and allowing for minor and trace elements quantification.

Elements concentrations are calculated by comparing the signal's intensities with that of standards. The intensity of the signal is the number of counts per second measured by the WDS detectors. In first approximation (corrections have to be applied), the concentration C of an element (element wt%, e.g. Fe) is:

$$C_{Fe,x} = \frac{I_{Fe,x}}{I_{Fe,std}} C_{Fe,std} \qquad \text{(Eq. 3.2)}$$

where *I* is the intensity of the element in the substance *X* and in the standard *std*, and *C* is the concentration. Therefore, calibration of the machine by measurement of standards is required before each quantitative analysis.

3.5.1 EMPA DATA ACQUISITION

Major element mineral chemistry was measured with the JEOL 8200 Super Probe electron microprobe analyser (EMPA) at the Department of Earth Sciences, University of Milan, Italy, by Andrea Risplendente. Thin sections were carbon-coated. Working conditions were 15 kV accelerating voltage, 5 nA current, 1 µm beam diameter, 10 mm working distance, using wavelength dispersive spectrometry (WDS) and natural silicates

as standards. A PhiRhoZ routine was used for matrix correction. Potassic feldspar was analysed with a defocussed beam to prevent K devolatilisation during the analyses. Mineral analyses were always assisted by BSE images to inspect the microstructural site. The following elements were measured: Si, Ti, Al, Fe, Mn, Mg, Ca, Na, K, Cr (or P) and converted in the oxides SiO_2, TiO_2, Al_2O_3, FeO(tot), MnO, MgO, CaO, Na_2O, K_2O, Cr_2O_3 (or P_2O_5), expressed as wt%. The microprobe was also used to acquire microprobe elemental maps.

3.5.2 EMPA DATA PROCESSING

Microprobe chemical results were given as oxide wt%. To reconstruct the mineral compositions, oxide wt% were converted into the corresponding moles of ions (by dividing by the molecular weight and multiplying by the number of atoms), which were then normalized based on the number of ions in the mineral formula unit. All minerals were normalised based on the number of cations unless stated otherwise (pyroxene 4, amphibole 13, plagioclase 5 and garnet 8). The end-members compositions were computed as ratios of the cations. The Mg# was calculated from formula unit as

$$Mg\# = \frac{Mg}{Mg+Fetot} * 100 \quad \text{(Eq. 3.3)}$$

XMapTools version 2.4 (Lanari et al., 2014) was used as a tool to reconstruct a local chemical composition from one of the microprobe maps. Phase density corrections were applied, following Lanari and Engi (2017).

Some major element geochemical data was plotted using the GeoChemical Data toolkit (GCDkit) (Janoušek et al., 2006). Plots using the GCDkit toolkit are cited in the figure captions.

3.6 X-RAY FLUORESCENCE (XRF)

The X-Ray Fluorescence (XRF) technique was used to determine the bulk chemical composition of a selection of rock samples by giving the concentrations of each element in the form of wt% oxides or ppm. The XRF operates with an X-ray beam generated in a Rhodium X-ray tube. When X-rays hit the sample, some are absorbed by the sample giving fluorescence and some are scattered. Fluorescence is the result of the interaction between high-energy X-rays and the atoms of the substance. If the X-ray has sufficient energy to overcome the electron's binding energy, ionization occurs. The difference in energy resulting from ionization is emitted as X-rays fluorescence with characteristic energies, making it possible to distinguish between different elements. The fluorescence X-rays have lower energies (and larger wavelength) than the primary radiation. The intensity of the signal sent to the detector is a function of the number of photons emitted, thus to the quantity of the element in the sample. Light elements are very difficult to detect with XRF because most of the radiation is not absorbed and does not produce fluorescence. The XRF analysis is done at a constant temperature and in a vacuum chamber, reason for which gases and liquids cannot be measured easily. Analysis can be made either from glass-beads (pills) or from powder. The bead has the advantage of being chemically more homogeneous than the corresponding powder.

A representative and homogeneous powder is the starting material for XRF analysis. This is obtained by crushing and grinding (milling) the rock sample until it becomes a fine powder. Two slightly different preparatory procedures were used between case study 1 and 2, due to the different locations of analyses. The crushing and milling was done at Plymouth University laboratories using a mechanical crusher and an automated miller. The samples were first crushed to a fine gravel using ceramic crushing plates and then

milled for cycles of 10 minutes in an agate mortar. The ceramic plates and the agate mortar were cleaned with water and a cycle of quartz chipping grinding after each sample to keep cross-contamination to the minimum.

For the Norwegian samples (case study 1), XRF bulk rock analysis was performed using the WDS Philips PW2400 sequential spectrometer installed at the University of Padova. Major and trace elements were measured on glass beads. Instrumental precision was within 0.6 % for major elements, and within 3 % for trace elements. Reference standards were natural geological samples (Geostandards Newsletter, Vol. XVIII, Special Issue, July 1994, K. Govindaraju, ed.). The powder was placed in a furnace at 860 °C for 20 minutes and at 980 °C for 2 hours to dehydrate the sample of its volatile component and to determine the loss on ignition (LOI). The LOI is the difference in weight between the pre-dried and dried samples, reported as % of the original weight. The volatile-free powder is then molten at 1150 °C to produce a glass bead. To lower the rock's melting point, the powder was mixed with Lithium-tetraborate ($Li_2B_4O_7$) in the proportion 1:10. The Lithium-tetraborate does not influence the XRF analysis because it is composed of light elements that cannot be measured.

For the Ivrea samples (case study 2), XRF bulk-rock compositions were measured at the Plymouth University's Consolidated Radio-isotope Facility (CORIF) using the PANalytical Wavelength Dispersive XRF (Axios Max) spectrometer, by Dr. Alex Taylor. Major and trace elements were measured on glass beads. To make the beads, the powders were pre-dried overnight at 105 °C to get rid of atmospheric moisture. These were then mixed with Lithium-tetraborate flux ($Li_2B_4O_7$) in the proportion 1:10 (9 g of Lithium-tetraborate, 0.9 g sample-powder) and with 300 µl of non-wetting agent (Lithium

Iodide), before being placed in the melting furnace (PANalytical Eagon 2 fusion system) at 1200 °C.

The LOI was calculated by measuring the difference in weight of a portion of sample powder (ca. 10-20 g) before and after placing it in a furnace at 1050 °C for 3 hours. The powders (including the crucibles) were measured 3 times in succession using a microgram weight balance with 4 digits precision; and the measurements were then averaged. In between measures, the samples were stored in a desiccator to avoid moisture from the atmosphere increasing the weight. The LOI was used as an indication of the volatile component of the rock.

3.7 Secondary Ion Mass Spectrometry (SIMS)

Secondary Ion Mass Spectrometry (SIMS) is an analytical technique used to measure in situ trace quantities (ppm quantities) of elements in a substance. The analyzed substance is placed in high vacuum and bombarded by a high-energy beam of negatively charged oxygen ions ($^{16}O^-$). Interaction of the ion beam with the sample results in the generation of secondary ions that are expelled from the surface of the sample. These are removed from the sample's surface (by an extraction lens with a strong potential difference) and conveyed through a series of lenses to the mass spectrometer. The mass spectrometer is composed of 1) an electrostatic energy analyzer and 2) a mass analyzer. The former filters out unwanted low energy ions, whereas the latter deflects the ions using a strong magnetic field, according to their mass to charge ratio. This way, the mass analyzer isolates the ions of interest that are then measured by a detector and transformed in an electric signal. The element concentration is quantified based on the number of counts per seconds measured by the detector.

In this project, SIMS was used to measure ppm quantities of hydrogen in nominally anhydrous minerals (NAMs) as a proxy for intracrystalline water content. Intracrystalline hydrogen content was measured on polished thin sections using the Cameca ims-4f Secondary Ion Mass Spectrometry (SIMS) at the NERC Ion Microprobe Facility in Edinburgh, under the supervision of Dr. J.C.M De Hoog (Fig. 3.7).

Fig. 3.7

Cameca ims-4f SIMS of the NERC Ion Microprobe Facility in Edinburgh.

Prior to analysis the samples were placed in an oven at 105°C for 30 minutes to remove surface humidity. The samples were then coated with a thin gold film (< 0.02 µm) to prevent charging, and kept in the SIMS chamber under high vacuum conditions (5 x 10^{-9} Torr) for > 48 hours. Analyses were performed with a 5 nA primary beam of $^{16}O^-$ ions accelerated to 14.5 kV. To reduce the risk of surface contamination, the first few nm of surface material were removed by sputtering the spot for 4 minutes while rastering the beam (25 µm grid) before each measurement. Measurements were acquired using a

beam spot size of 20 µm (± 5 µm). Each analysis consisted of 20 repeats (cycles) which measured the isotopes ^{1}H, ^{23}Na, ^{30}Si, ^{39}K and ^{49}Ti for the Norwegian sample (case study 1); and 20 repeats (cycles) which measured the isotopes ^{1}H, ^{7}Li, ^{23}Na, ^{26}Mg, ^{30}Si, ^{39}K, ^{42}Ca and ^{88}Sr for the Finero samples (case study 2). For hydrogen only the last 15 cycles were averaged as ^{1}H signals usually dropped during the first cycles before stabilizing. Probing locations were identified and imaged beforehand and particular attention was taken to avoid cracks, grain-boundaries and alterations, as these could contain free water molecules. A basaltic glass standard St81A9 (Lesne et al., 2011) was used to calibrate the water content, whereas an anhydrous olivine standard (Kilbourne Hole) was used to correct for background ^{1}H signals. The measured background signals were equivalent to 12 wt ppm H_2O for the Norwegian sample (case study 1) and < 5 wt ppm H_2O for the Finero samples (case-study 2). These values were subtracted to the measurements. Water contents were also calibrated to take mineralogy into account, by multiplying the water concentrations by *2.11 for clinopyroxene and *0.92 for orthopyroxene (Dr. J.C.M De Hoog personal communication). No calibration is to date available for plagioclase. SiO_2 wt% contents measured from microprobe analyses were used as internal standards, whereas the other oxides (e.g. CaO) were calculated as ratios of the SiO_2 wt% content, using the following:

$$CaO\ (wt\%)_{(a)} = \frac{42Ca/30Si_{\ (a)}}{42Ca/30Si_{\ (st)}}(measured) * \frac{CaO(wt\%)_{\ (st)}}{SiO2(wt\%)_{\ (st)}}(literature) * SiO2(wt\%)_{(a)}$$

(Eq. 3.4)

where (a) is the analysis, and (st) is the basaltic glass standard St81A9.

3.8 THERMODYNAMIC MODELLING

Thermodynamic modelling is a powerful tool for calculating phase equilibria in the P-T-X space (X = composition), given a starting bulk composition and a set of boundary constrains. This is done through modelling programs such as Perple_X (Connolly, 1990) that compute phase-equilibria based on thermodynamic principles. Typical outputs of thermodynamic modelling programs are pseudosections, i.e. diagrams showing stability fields of different phase assemblages in the P-T-X space. In 2D diagrams, one of the three variables is kept constant and the other two vary between the chosen boundaries. Pseudosections are particularly useful to predict 1) the P-T conditions of stability of a specific mineral assemblage in a rock with a given bulk composition, 2) changes in the mineral assemblage with changing metamorphic conditions (T-X or P-X diagrams), and 3) changes in chemical composition of minerals in the P-T space (mineral isopleths). In addition, pseudosections can be used to model melt-rock interactions (to find the stable mineral assemblage when mixing a melt composition with a rock composition), and to reconstruct the P-T path of a rock. In this project, thermodynamic modelling is used for all the above, with the objective of constraining the ambient conditions (P, T, X) of deformation and infer the metamorphic evolution of the shear zone. Owing to constant upgrades in software versions and databases, the two case studies have used different thermodynamic databases and solution models, as described below.

Case study 1 (Norway) pseudosections were obtained using Perple_X version 667 thermodynamic modelling package (Connolly, 1990) using the 9 components NCKFMASHT (Na_2O-CaO-K_2O-FeO-MgO-Al_2O_3-SiO_2-H_2O-TiO_2) system and using the input bulk-rock compositions obtained through XRF and from the literature (Menegon et al., 2011) (see Chapter 4, Table 4.1). The FeO content was kept as total iron.

The models ran with the thermodynamic database and equation of state for H_2O of Holland and Powell (1998, upgraded 2002), using the following solution models: olivine, orthopyroxene, clinopyroxene, garnet, phengite, feldspar, biotite (Holland and Powell, 2003, 1998, 1996) and amphibole (Dale et al., 2005). The models were obtained in collaboration with Dr. Nadia Malaspina.

Case-study 2 (Finero) pseudosections were obtained using Perple_X version 675 thermodynamic modelling package (Connolly, 1990) using the 10 components NCKFMASHTO (Na_2O-CaO-K_2O-FeO-MgO-Al_2O_3-SiO_2-H_2O-TiO_2-O_2) system, and using the input bulk-rock compositions obtained through XRF and through microprobe maps recalculations using XMapTools (Lanari et al., 2014) (see Chapter 5, Table 5.2).

The models ran with the thermodynamic database of Holland and Powell (2011), with the following solution models: augite, horneblende, metabasic melt (Green et al., 2016); orthopyroxene, garnet, biotite, chlorite (White et al., 2014); spinel (for magnetite) (White et al., 2002); epidote (Holland and Powell, 2011); olivine (Holland and Powell, 1998) and feldspar (Fuhrman and Lindsley, 1988). Ilmenite was treated as a pure end-member phase. The oxidation state (O_2 content, which controls Fe^{3+}/Fe^{2+} ratios) was set to a fixed value of 0.4 wt% O_2, implying that 25% of the total FeO content is Fe^{3+}. Water was at first estimated from the LOI, but the results did not match with the observed phase assemblages and mineral chemistries. The water contents were therefore set to 0.1 wt% and 0.2 wt% for samples F10B and F20A respectively. The recently published melt model of Green et al. (2016), used for the Finero case-study, allows for the first time for partial melting equilibria to be calculated for metabasic rocks (Green et al., 2016).

4 CASE STUDY 1: SHEARED MAFIC DYKES IN THE SEILAND IGNEOUS PROVINCE (NORWEGIAN CALEDONIDES)

The first case study investigates a sheared mafic dyke from the Seiland Igneous Province (Northern Norway). The dyke deformed together with the surrounding metasedimentary sequence undergoing dehydration melting (Elvevold et al., 1994; Menegon et al., 2011), making this an ideal system to study deformation mechanisms and weakening processes of mafic lower crustal rocks under melt-present conditions.

This study has been published in the journal *Lithos* as *Degli Alessandrini et al. (2017)*, thus most of the content of this chapter is shared with the publication. This chapter however features additional figures, a more comprehensive methodology (presented in Chapter 3), updated SIMS results (sections 4.5 and 4.9, on account of new mineral corrections made available after publication) and a revisited section 4.10.

4.1 GEOLOGICAL SETTING: THE SEILAND IGNEOUS PROVINCE

The Seiland Igneous Province of the north Norwegian Caledonides is a suite of mafic, ultramafic and alkaline deep-seated intrusions emplaced in the lower continental crust during pre-Caledonian rifting at 570-520 Ma (Elvevold et al., 1994; Roberts et al., 2006) (Fig. 4.1). The Seiland Igneous Province is part of the Kalak Nappe Complex of the north-Norwegian Caledonides (Roberts et al., 2006 and references therein); however, it largely escaped the tectono-metamorphic Caledonian overprint, the evidence of which is

possibly restricted to narrow localized shear zones within the gabbros (Elvevold et al., 1994). In the Øksfjord peninsula (Fig. 4.1 and Fig. 4.2a), gabbroic bodies intruded high grade metasedimentary rocks (paragneisses and metapelites; Fig. 4.1 in orange) presumably belonging to the Eidvågeid Sequence found some 50 km farther NE within the Kalak Nappe Complex (Elvevold et al., 1994; Reginiussen et al., 1995) (Fig. 4.1).

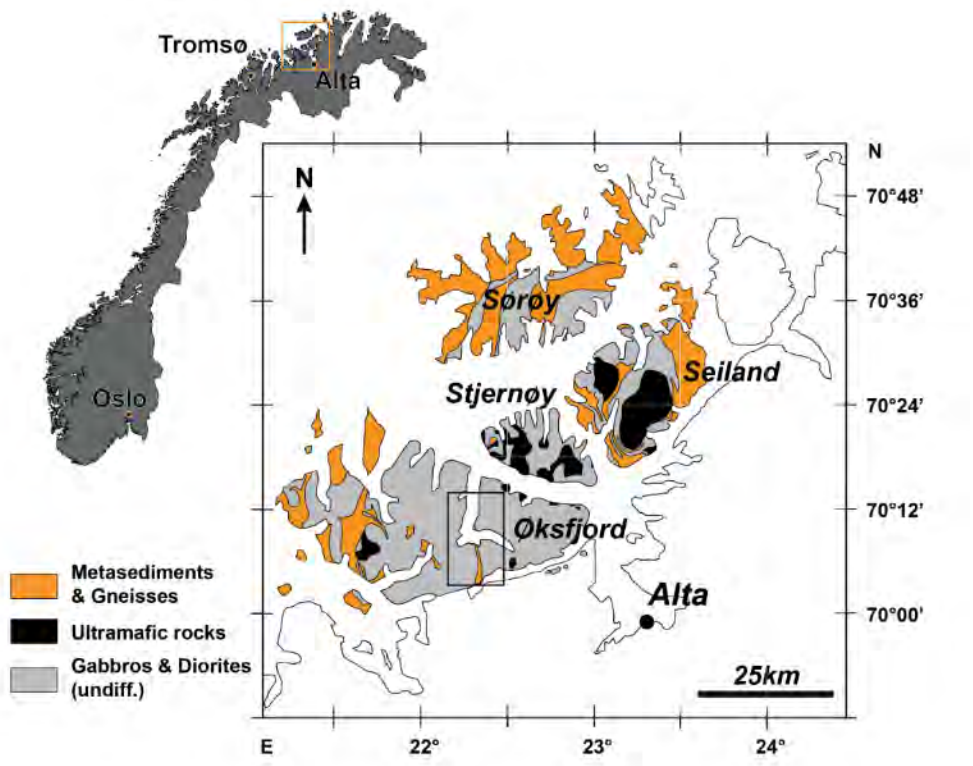

Fig. 4.1

Simplified Geological map of the Seiland Igneous Province, showing the main lithological divisions. Metasediments are shown in orange. Modified after Reginiussen et al. (1995). Detail of study area in box (Fig. 4.2).

The metasediments contain multiple sets of mafic dykes that intruded the sequence at different stages of the prolonged tectonomagmatic evolution of the Seiland Igneous Province (Reginiussen et al., 1995). These dykes were classified by Reginiussen et al. (1995) as pre-kinematic, syn-kinematic and post-kinematic dykes based on their

structural and chemical signatures. In this context, pre-kinematic means that the dykes predate the pervasive shearing event that results from the emplacement of the Seiland Igneous Province bodies (Reginiussen et al., 1995). Emplacement of gabbroic bodies was accompanied by contact metamorphism, partial melting and shearing of the host rocks, which produced a steeply dipping N-S trending gneissic to mylonitic foliation in both the metasediments and the intercalated dykes (Elvevold et al., 1994; Menegon et al., 2011).

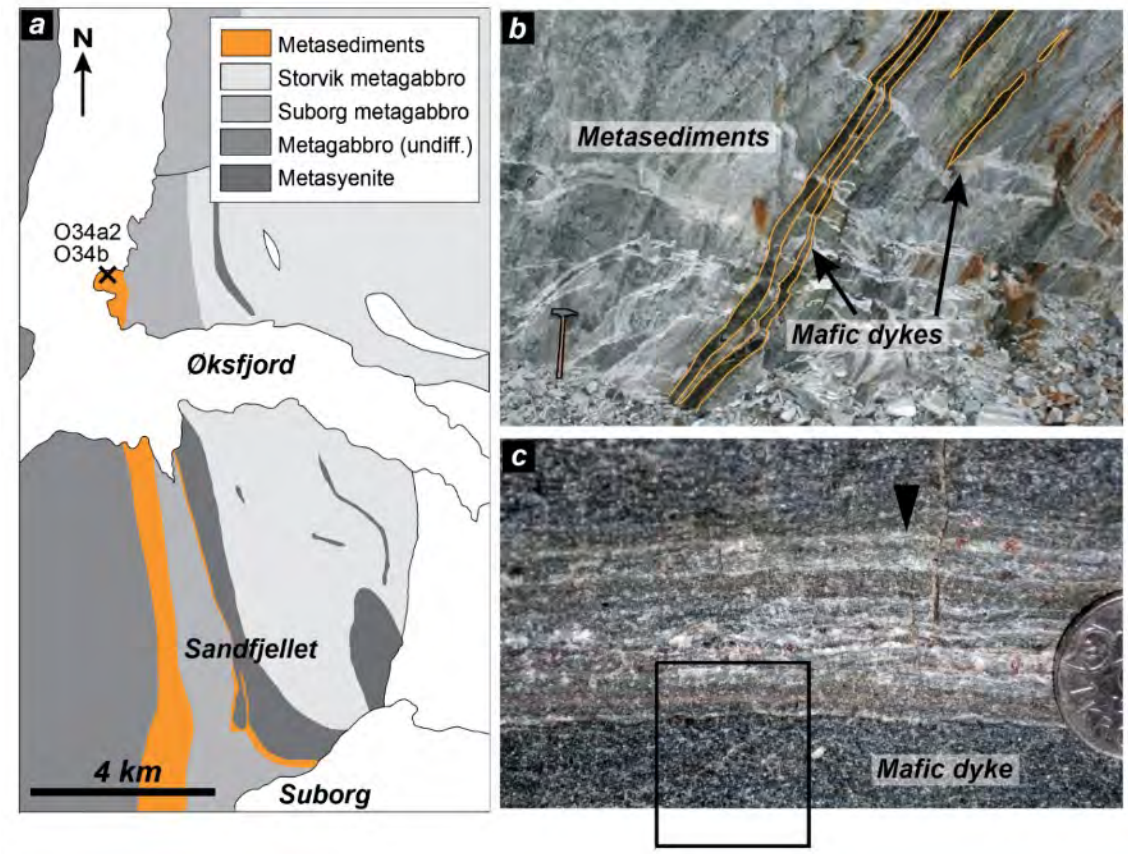

Fig. 4.2

(a) Detail of the geological map of Øksfjord peninsula, modified after Elvevold et al. (1994) and Reginiussen et al. (1995). The mafic dykes were sampled in the paragneisses of the Bardineset locality (sample O34b, GPS coordinates relative to WGS 84, zone 34 W, 0549420 E, 7783845 N). (b) Outcrop of sample O34b: sheared metasedimentary sequence (light grey) with mafic dykes (contoured dark layers) at Bardineset locality. Foliation is steeply dipping to the WSW. Hammer for scale. (c) Detail of mafic dyke with felsic bands and veinlets (indicated by black arrow). Approximate location of thin section O34b. Coin (1.6 cm diameter) for scale.

The mylonitic foliation contains a stretching lineation plunging moderately to the NW and kinematic indicators are consistent with a top-down-to-NW sense of shear. The shear fabric formed during isobaric cooling and granulite facies re-equilibration from peak conditions of T = 930°C - 960°C, P = 5.5 - 7 kbar to T = 700 - 750°C, P = 5 - 7 kbar (Elvevold et al., 1994). The mylonitic foliation is parallel to a primary magmatic layering locally preserved in the gabbros, and this has been taken as indicative of protracted syn- to post-intrusive deep crustal shearing (Elvevold et al., 1994; Roberts et al., 2006).

The analysed samples are pre-kinematic mafic dykes in metapelites from the Bardineset locality (GPS UTM coordinates relative to WGS84: zone 34 W, 0549420 E, 7783845 N) (Fig. 4.2a). In the outcrop, the dykes are dark foliated layers ranging in thickness from < 1 cm to about 2 m (Fig. 4.2b). The dykes are concordant with the dominant N-S striking foliation in the area and also exhibit a well-developed NW-plunging stretching lineation.

Solid state shearing conditions in the metapelites were estimated from thermodynamic modelling of syn-kinematic mineral assemblages at T = 760 °C - 820 °C and P = 7.5 – 9.5 kbar (Menegon et al., 2011). Partial melting during shearing of the metasedimentary sequence is evident from segregated leucosome-rich domains. Melt segregations occur from outcrop- to thin-section scale, with Menegon et al. (2011) demonstrating that melting and shearing in the metapelites were coeval. Thermodynamic modelling and microstructural analysis indicated that about 5-7 vol% of melt was present in the metapelites during shear deformation at the estimated P, T conditions (Menegon et al., 2011). During shearing, felsic melt from the metapelites infiltrated the adjacent mafic dykes as evident from thin leucosome veinlets in the dykes (Fig. 4.2c and Fig. 4.3).

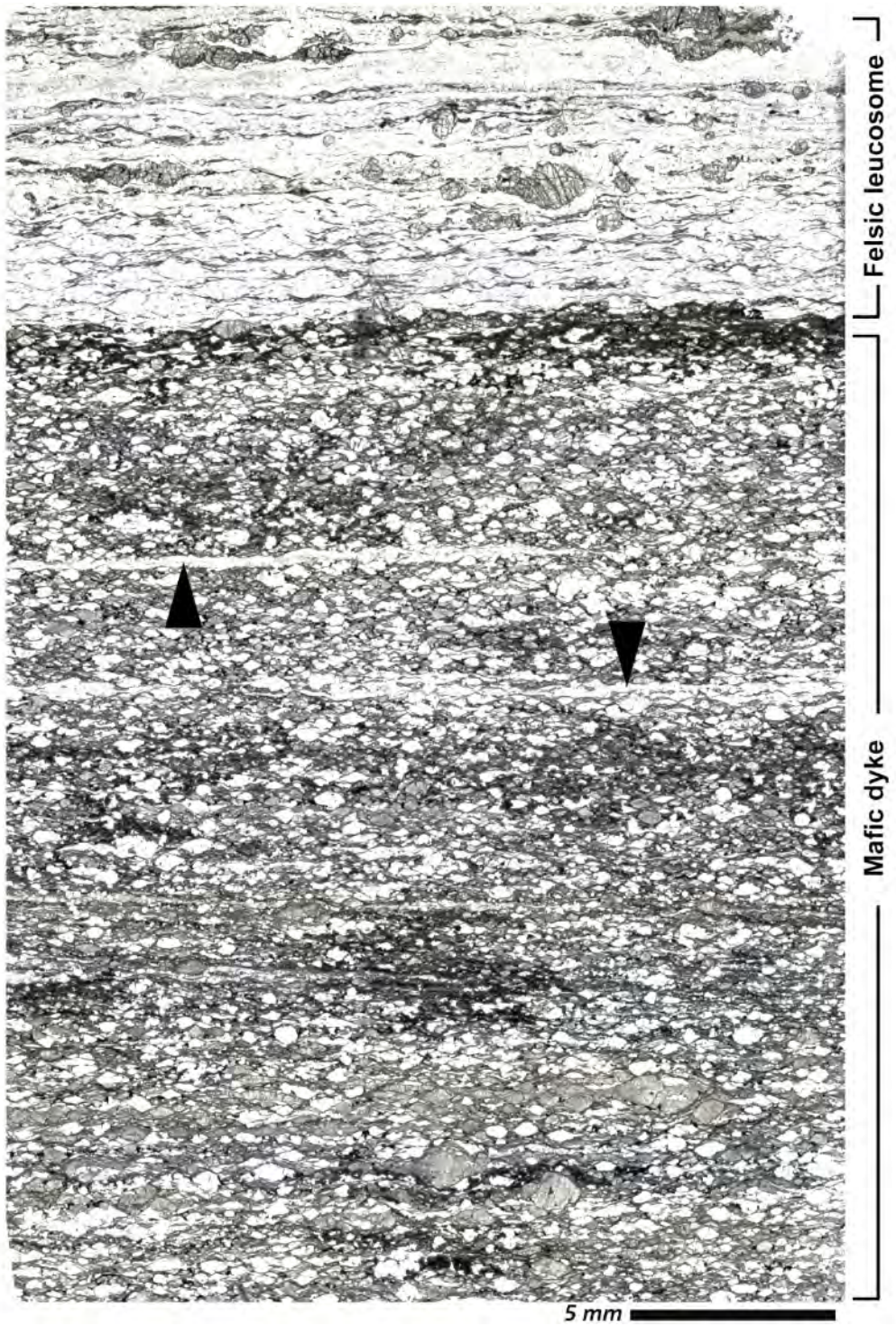

Fig. 4.3

Optical micrograph (thin section montage) of the sheared mafic dyke (sample O34b), with mm-thick felsic veinlets indicated by black arrows. Felsic leucosome in the upper portion. Clear grains are mostly plagioclase porphyroclasts and quartz ribbons, whereas light brown grains are pyroxenes. Black patches are rich in garnet coronas and opaques (magnetite, ilmenite). Sinistral sense of shear.

RESULTS

4.2 DYKE'S MICROSTRUCTURE

The sheared mafic dyke is a SCC'-type mylonite with a porphyroclast-in-mixture texture, consisting of clinopyroxene, orthopyroxene and plagioclase porphyroclasts embedded in a fine grained polyphase mixture of clinopyroxene + orthopyroxene + plagioclase + quartz + ilmenite ± K-feldspar ± apatite (Fig. 4.4: porphyroclasts – Fig. 4.5: fine mixture). Locally, plagioclase porphyroclasts are rimmed by garnet + ilmenite coronas. The sense of shear is sinistral, and corresponds to the top-down-to-NW sense of shear observed in the field. Porphyroclasts range in size from 25 to 650 μm and form 43% of the area fraction of the mylonite; the remaining 57% is formed by the fine-grained polyphase mixture. Plagioclase, orthopyroxene and clinopyroxene and plagioclase form 57%, 26% and 17% of the porphyroclast area fraction of the rock, respectively, whereas the fine-grained mixture consists of 38% plagioclase, 25% orthopyroxene, 17% clinopyroxene, 9% quartz, 6% ilmenite, 1% K-feldspar and 2-3% apatite, with some local garnet overgrowth. Thus, the overall phase abundances (by area) in the sheared dyke (porphyroclasts + mixture) are as follows: 46% plagioclase, 25% orthopyroxene, 17% clinopyroxene, 5% quartz, 3% ilmenite, 1% apatite, 0.6% K-feldspar, ca. 2% garnet. Hydrous phases (amphibole, biotite) have not been observed in the microstructure.

Felsic veinlets, typically < 1 mm thick, are locally found along the mylonitic foliation of the dyke (Fig. 4.2c and Fig. 4.3). The mineral assemblage in the veinlets consists of K-feldspar, quartz, plagioclase ± garnet ± orthopyroxene (Fig. 4.6). K-feldspar can be indicative of former melt (e.g. Holness and Sawyer, 2008), when it is found as (1) thin (< 50 μm thick)

monomineralic grain boundary films; (2) irregularly-shaped patches containing small (< 20 µm) rounded grains of quartz and plagioclase completely surrounded by K-feldspar; and (3) as K-feldspar rich patches in cuspate-lobate embayments around garnet porphyroblasts. Similar microstructures, attributed to dehydration melting of biotite, were described from the Bardineset sheared felsic migmatites in Menegon et al. (2011) and are also observed in this study (Fig. 4.6c).

Fig. 4.4 (next page)

Microstructural overview of the mafic dyke: micrographs (optical + backscatter electron-BSE), showing orthopyroxene, clinopyroxene and plagioclase porphyroclasts wrapped by a fine-grained polyphase matrix of orthopyroxene, quartz, clinopyroxene, ilmenite and plagioclase; Sinistral sense of shear; Mineral abbreviations: Pl - Plagioclase, Opx - orthopyroxene, Cpx - clinopyroxene, Qtz - quartz, Grt - garnet, Ilm - ilmenite, Kf - k-feldspar, Ap apatite. (a) BSE image, showing elongated single-grain orthopyroxenes, reaching aspect ratios of 12:1. (b) BSE image, showing boudinaged orthopyroxene and clinopyroxene porphyroclasts (boudin necks, white arrows). (c-f): Microstructural details of mylonite, optical images, plane polarised light.

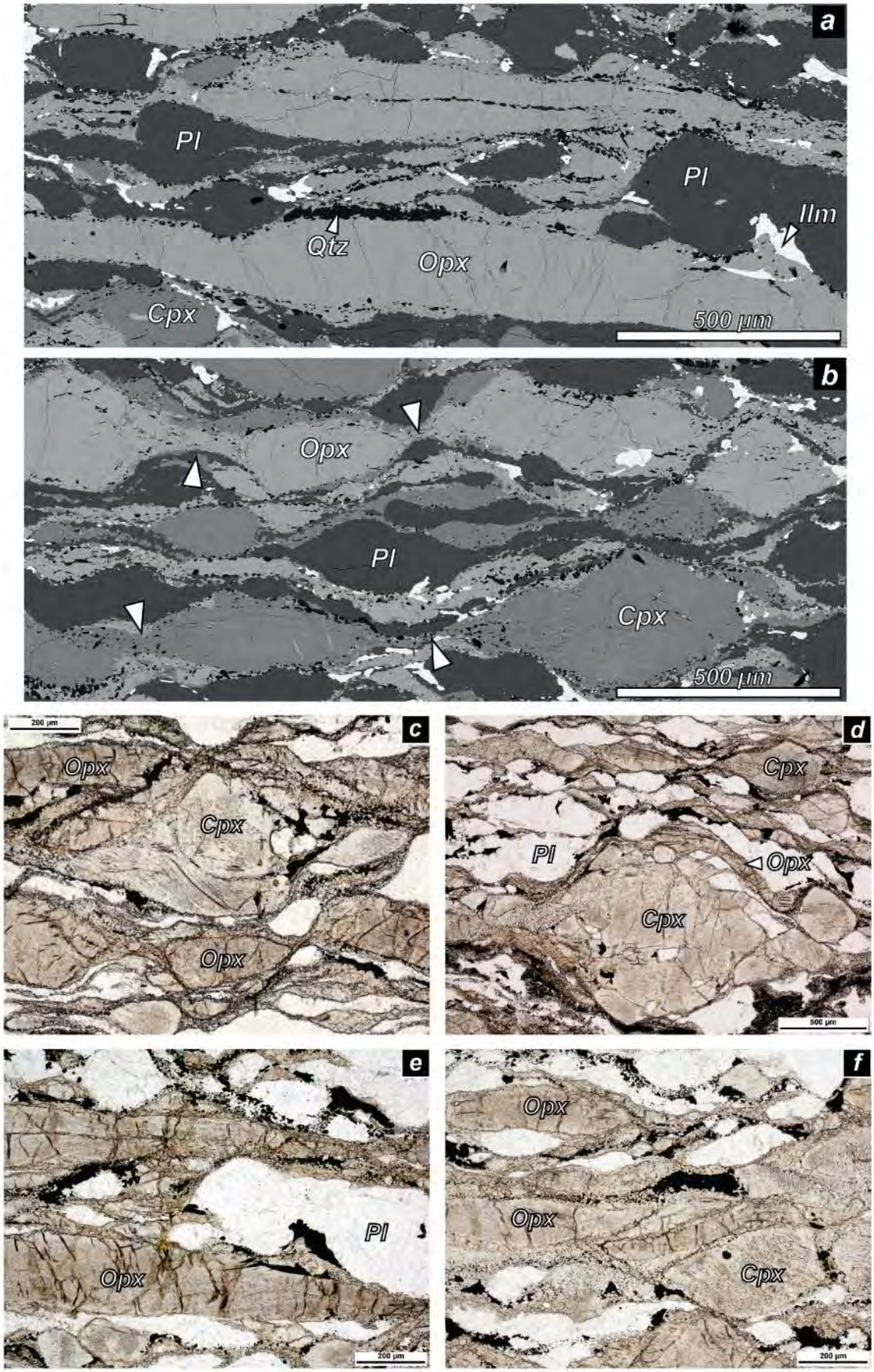
a
Pl
Pl
Ilm
Qtz
Opx
Cpx
500 µm
b
Opx
Pl
Cpx
500 µm
200 µm
c
Opx
Cpx
Opx
d
Cpx
Pl
Opx
Cpx
500 µm
e
Pl
Opx
200 µm
f
Opx
Opx
Cpx
200 µm

Fig. 4.4

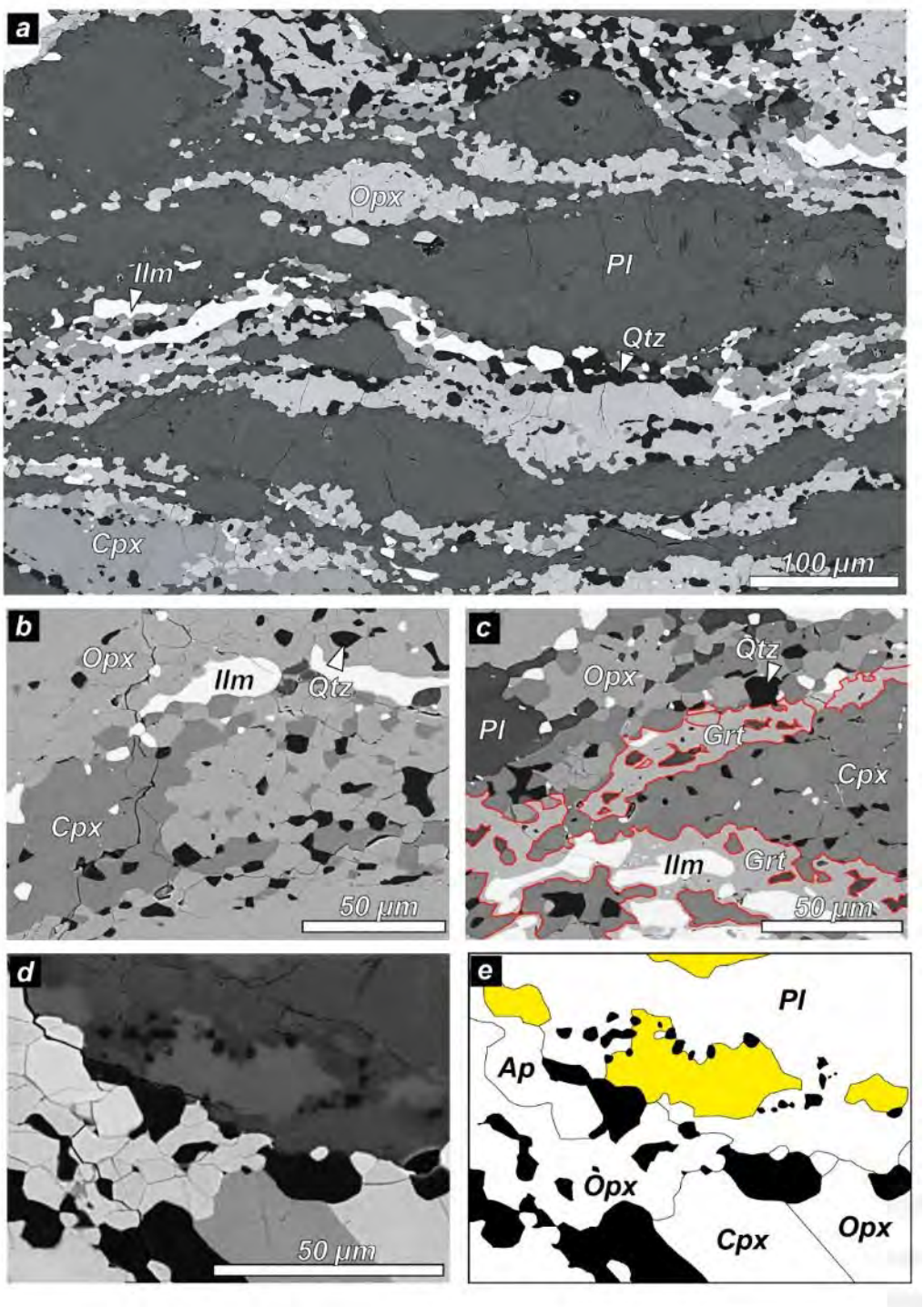

Fig. 4.5

(a) Backscatter electron (BSE) image of the fine-grained polyphase aggregate of Cpx + Opx + Pl + Qtz + Ilm ± Kf ± Ap, sinistral sense of shear (b-c) Details of polyphase aggregate of Cpx + Opx + Pl + Qtz + Ilm (± Kf ± Ap). Garnet + ilmenite locally overgrows on the aggregate as shown by red contours in c. Note the grain size consistently below 10 µm. (d-e) Irregularly shaped patches of K-feldspar associated with plagioclase and quartz; e is the outline of d showing K-feldspar in yellow and quartz in black.

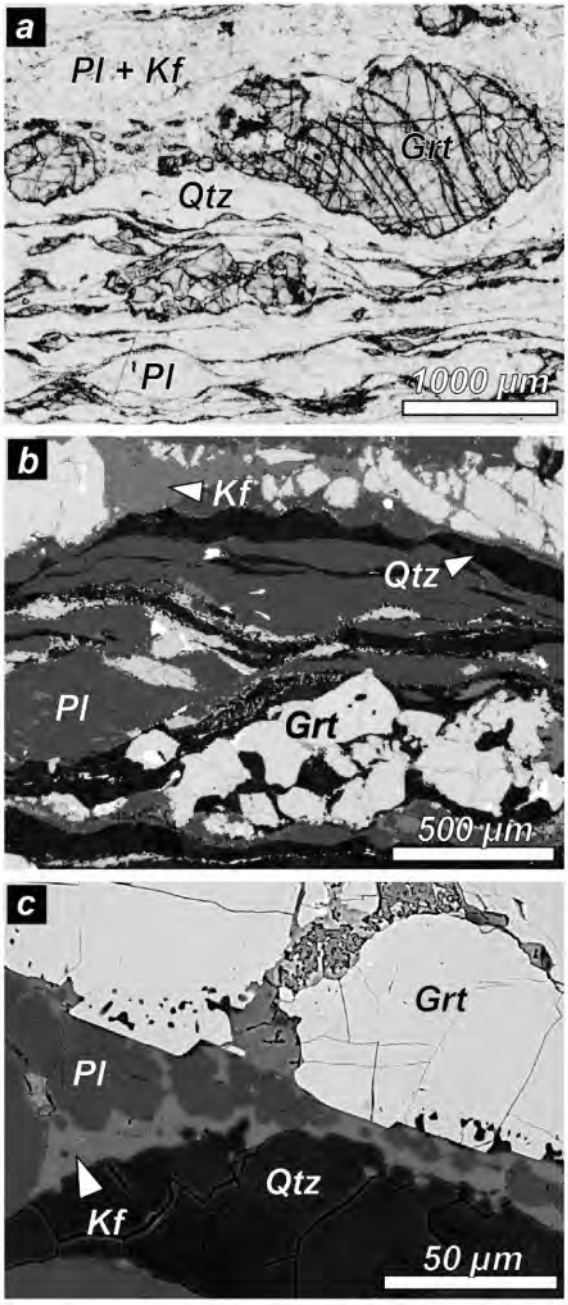

Fig. 4.6

Optical + backscatter electron (BSE) images of the felsic leucosome in contact with the mafic dyke. Sinistral sense of shear. (a-b) Large (up to 2mm) garnet porphyroclasts wrapped by a matrix of quartz, k-feldspar and plagioclase +- orthopyroxene. (a) optical image; plane polarised light (b) BSE image (c) Pools of former melt are preserved as K-feldspar surrounding rounded plagioclase and quartz grains; BSE image.

4.2.1 PORPHYROCLASTS

Orthopyroxene porphyroclasts are typically lenticular, but can occur as elongated single-grain ribbons parallel to the foliation, with aspect ratios up to 12:1 (Fig. 4.4a). Some are boudinaged, with the fine-grained polyphase mixture filling the boudin necks (Fig. 4.4b). Orthopyroxene grains can contain thin (< 1 µm) exsolution lamellae of clinopyroxene (Fig. 4.7c, d). In porphyroclasts with high aspect ratios (>3:1) the lamellae are oriented at low angles to the crystal elongation; whereas in more equant porphyroclasts no lamellae are observed (Fig. 4.7e, f).

Clinopyroxene porphyroclasts vary from ca. 30 µm to ca. 300 µm in size and commonly display low to moderate aspect ratios (> 80% below 3:1). Most porphyroclasts show strong crystal distortions in the form of undulose extinction and misorientation bands (Fig. 4.8a, b). In addition, they are characterized by different sets of exsolution lamellae of orthopyroxene. The latter are variably oriented with respect to the crystal elongation andare often bent, providing further evidence of strain and crystal distortion within the porphyroclasts (Fig. 4.8g). As for orthopyroxene, clinopyroxene porphyroclasts show boudinage and pinch and swell microstructures, with the fine-grained polyphase aggregate filling the boudin necks (Fig. 4.4b). Individual fragments of the same porphyroclast can be easily identified under the optical microscope by the same extinction position and interference colours. Clinopyroxene fragments are frequently crosscut by cracks filled by recrystallized fine-grained clinopyroxene (11 µm average grain size) (Fig. 4.8f, h and Fig. 4.15a, b). These bands are dominantly monomineralic with only minor amounts of other phases (quartz, orthopyroxene, plagioclase or ilmenite).

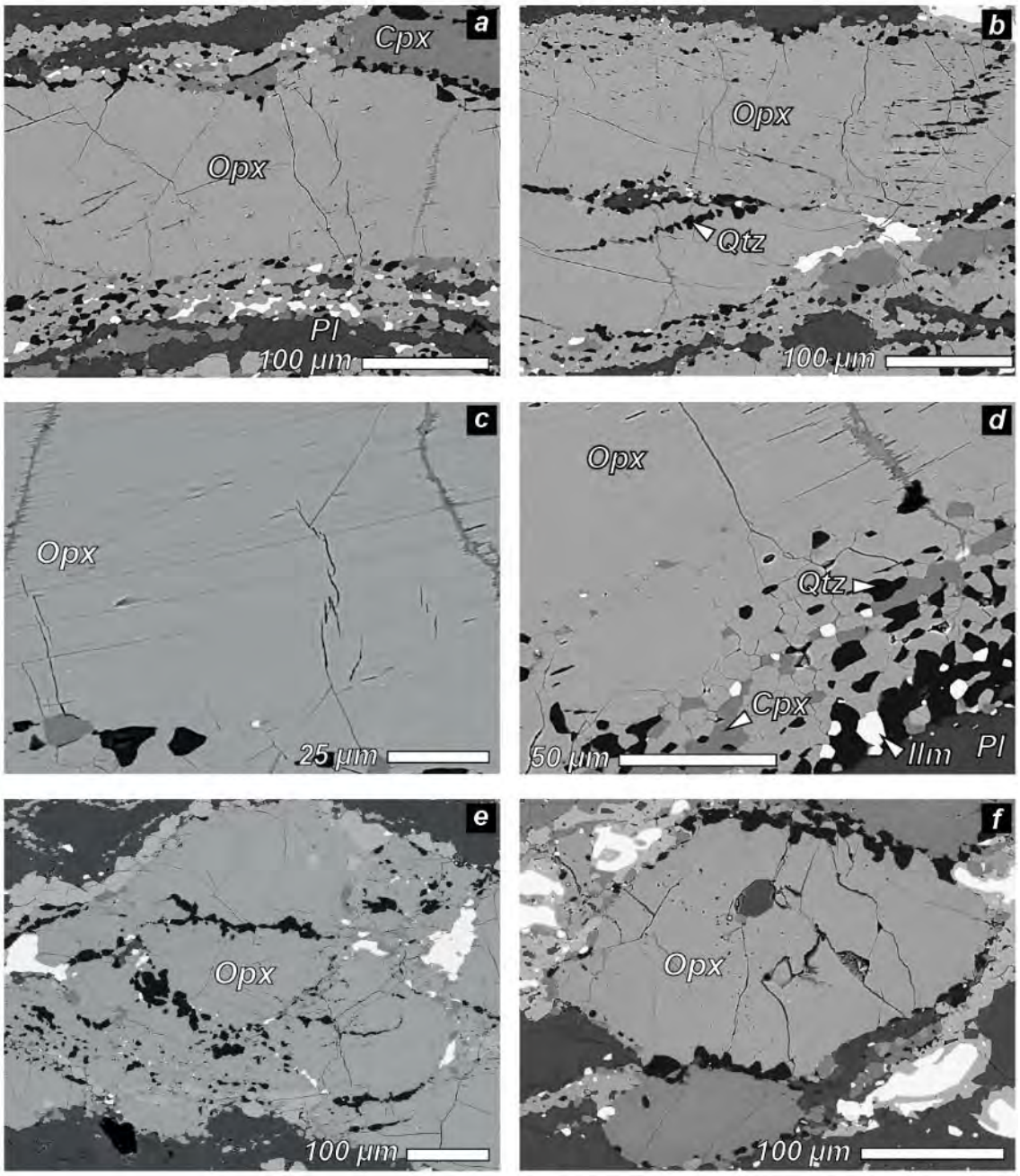

Fig. 4.7

Micrographs (BSE) of orthopyroxene porphyroclasts. (a-b) examples of variably elongated porphyroclasts, surrounded by a fine-grained polyphase aggregate of orthopyroxene, quartz, clinopyroxene and ilmenite. (c-d). Details of fine (<1 µm) exsolution lamellae in elongated orthopyroxene ribbons. These lamellae are mostly oriented subparallel to the crystal long axis. (e-f) Example of equant-shaped orthopyroxenes with no visible exsolution lamellae.

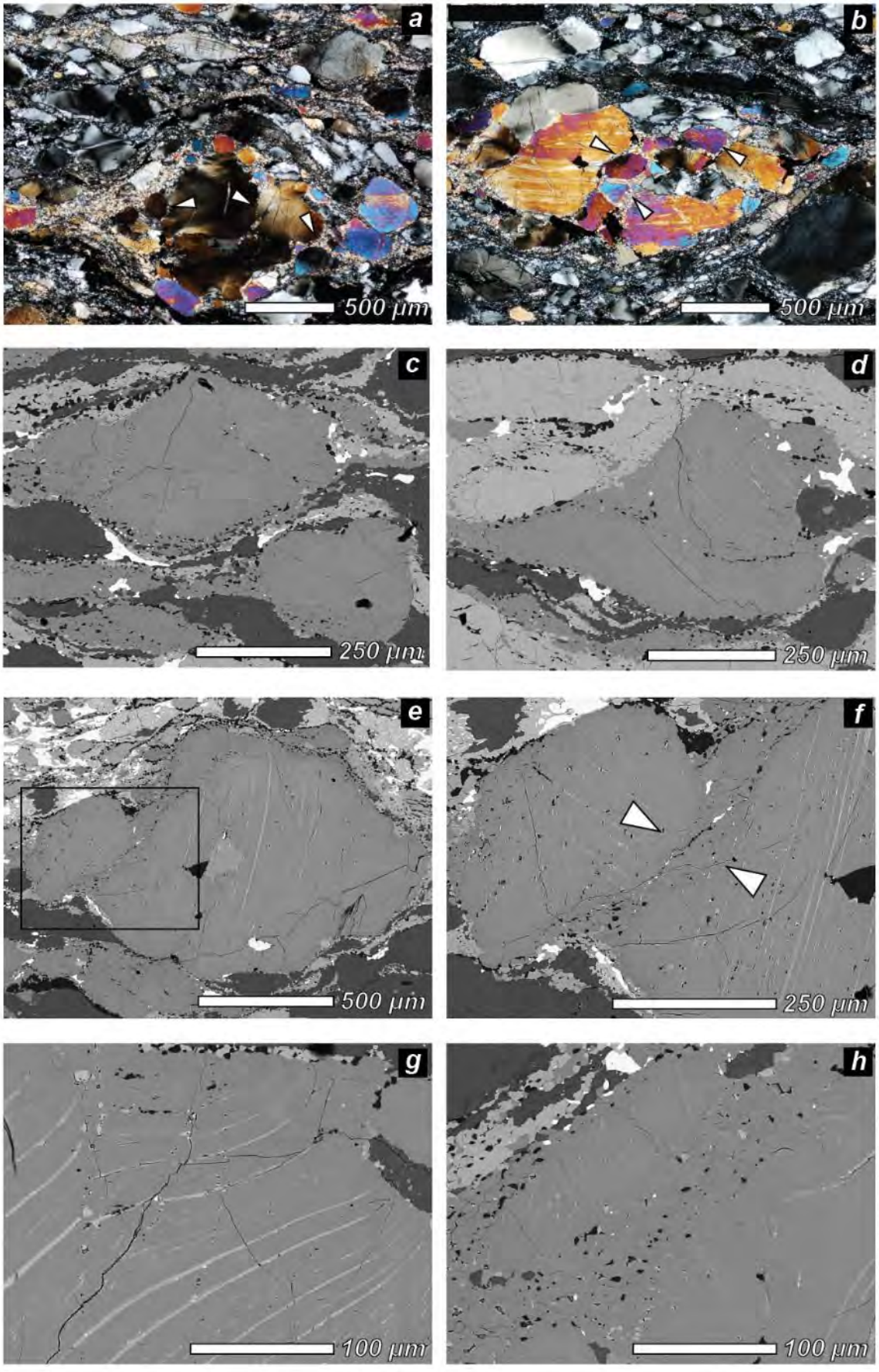

Fig. 4.8

Fig. 4.8 (previous page)

Micrographs (optical + BSE) of clinopyroxene porphyroclasts. (a-b) Clinopyroxene porphyroclasts showing undulose extinction, exsolution lamellae and intracrystalline bands of recrystallized pyroxene. The latter are marked by white arrows. Optical micrographs in crossed polars. (c-e) BSE micrographs, showing typical lenticular clinopyroxene porphyroclasts with different sets of orthopyroxene exsolution lamellae, commonly bent. A close-up of such exsolution lamellae is given in (g). (f) and (h) show clinopyroxene fragments crosscut by an intracrystalline band of fine grained material. (f) is a detail of (e).

Plagioclase porphyroclasts are lenticular with low aspect ratios (77% below 3:1) and display crystal distortions in the forms of undulose extinction, bent twins and deformation bands (Fig. 4.9). Similar to clinopyroxene, plagioclase is often crosscut by intracrystalline bands filled by small recrystallized grains of plagioclase. The fractures occur with a wide range of orientations, and synthetic and antithetic bookshelf geometries are common (Fig. 4.9a). Such fractures are often parallel to the sinistral C' shear bands observed at the thin section scale. In addition, plagioclase porphyroclasts are locally rimmed by garnet + ilmenite coronas growing at the expense of plagioclase (Fig. 4.9e).

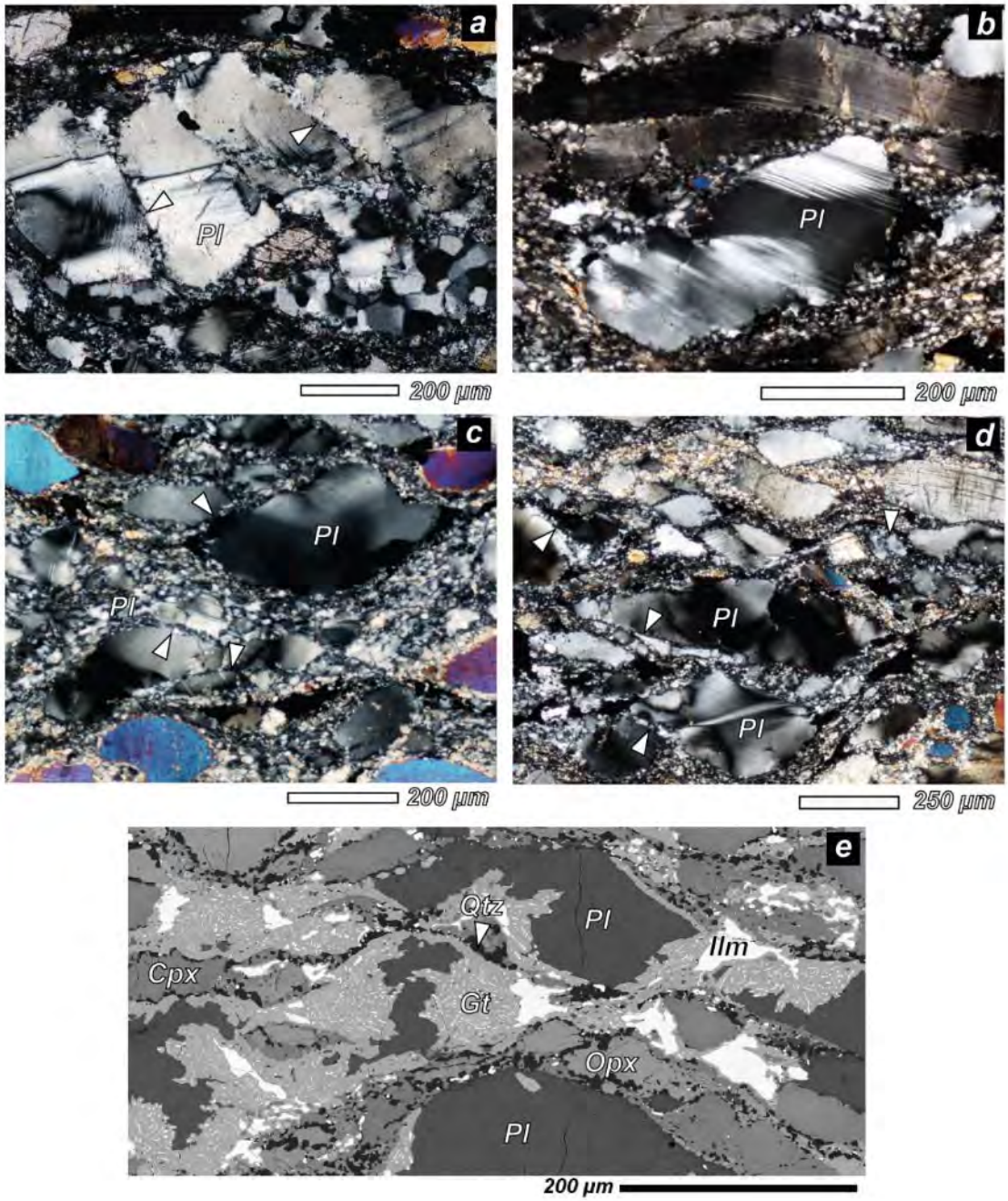

Fig. 4.9

Micrographs (optical + BSE) of plagioclase porphyroclasts. Sinistral sense of shear. (a-d) Plagioclase porphyroclasts, with evidence of undulose extinction, deformation twins and intracrystalline bands of recrystallized plagioclase. Intracrystalline bands are marked by white arrows. Optical micrographs in crossed polars. (e) plagioclase porphyroclasts, locally rimmed by garnet + ilmenite coronas growing at the expenses of plagioclase. BSE micrograph.

4.2.2 FINE-GRAINED POLYPHASE MIXTURE

Porphyroclasts are embedded in a fine-grained mixture of clinopyroxene + orthopyroxene + plagioclase + quartz + ilmenite ± K-feldspar ± apatite. The grain-size is consistently less than 10 µm (average 4-7 µm) (Fig. 4.5 and Fig. 4.10). The relative phase abundances vary locally, depending on the phase surrounded by the aggregate. Aggregates around orthopyroxene porphyroclasts are dominated by a mixture of orthopyroxene and quartz, while aggregates around clinopyroxene porphyroclasts by a mixture of clinopyroxene and quartz. Exsolution lamellae have not been observed in the fine-grained ortho- and clinopyroxene of the mixture.

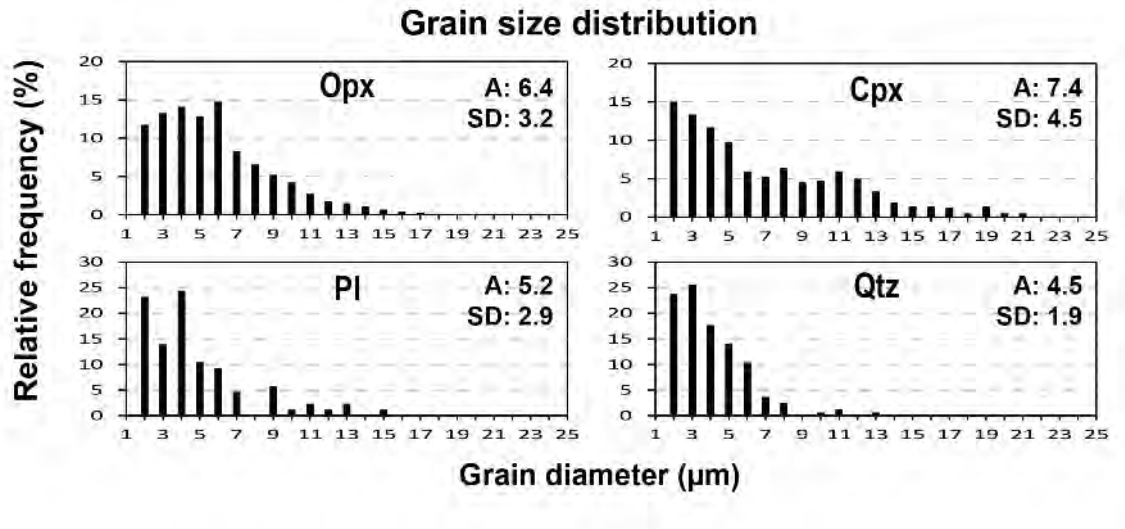

Fig. 4.10

Grain size distribution of orthopyroxene, plagioclase, clinopyroxene and quartz in the fine-grained polyphase aggregate. Mean (A) and Standard Deviation (SD) is given on the side. Grain size is consistently below 10 µm for all phases.

The fine-grained aggregate is locally overgrown by garnet + ilmenite (Fig. 4.5c), which also form rims around plagioclase porphyroclasts (Fig. 4.9e). K-feldspar is found in minute

quantities, where it often forms irregularly-shaped patches containing rounded grains of plagioclase and quartz entirely surrounded by K-feldspar (Fig. 4.5d, e). These patches are similar to those occurring in the felsic veinlets (Fig. 4.6c).

4.3 DYKE'S CHEMISTRY

4.3.1 BULK-ROCK CHEMISTRY

The bulk rock composition (major elements) of the sheared mafic dyke is reported in Table 4.1. Two domains were analysed: one that included felsic leucosome veinlets and one that did not.

Wt%	O34b without felsic	O34b with felsic portion	Menegon et al. 2011 Leucosome-rich domain	Menegon et al. 2011 Leucosome-poor domain	Reginiussen et al. 1995 Pre-kinematic 574C
SiO_2	47.39	52.12	66.05	66.04	45.91
Al_2O_3	14.13	15.04	15.90	16.13	12.92
Fe_2O_3	16.18	13.66	4.39	6.22	13.04
MnO	0.26	0.24	0.06	0.04	0.19
MgO	7.25	5.67	4.28	4.13	11.19
CaO	10.07	8.07	2.49	2.38	11.48
Na_2O	1.11	1.84	1.45	1.37	0.65
K_2O	0.13	0.8	3.22	1.86	0.75
TiO_2	3.14	2.5	0.22	0.13	2.33
P_2O_5	0.4	0.25	0.11	0.09	0.35
LOI	0.03	0.03	1.83	1.61	-
Tot	**100.06**	**100.19**	**98.1700**	**98.39**	**98.81**

Table 4.1

Bulk-rock composition (major elements, oxide wt%) of the sheared mafic dyke (O34b), with and without felsic portion, compared with leucosome compositions of Menegon et al. (2011) and with Reginiussen et al. (1995) most-mafic dyke (574C) of the same suite of sample O34b.

The analysis that includes the felsic portion shows contamination of the pristine dyke by felsic melt, resulting in SiO_2 and Al_2O_3 enrichment and in a corresponding Fe_2O_3 (as total iron), MgO and CaO depletion (Fig. 4.11). Bulk compositions are compared with felsic

leucosomes sampled by Menegon et al. (2011) in adjacent migmatitic metapelites and with the pre-kinematic mafic dykes of Reginiussen et al. (1995). All the compositions grossly correlate in a linear trend. Sample O34b (with and without felsic portion) lies on a mixing trend between the pre-kinematic dykes and felsic leucosome produced by dehydration melting of the host metapelites.

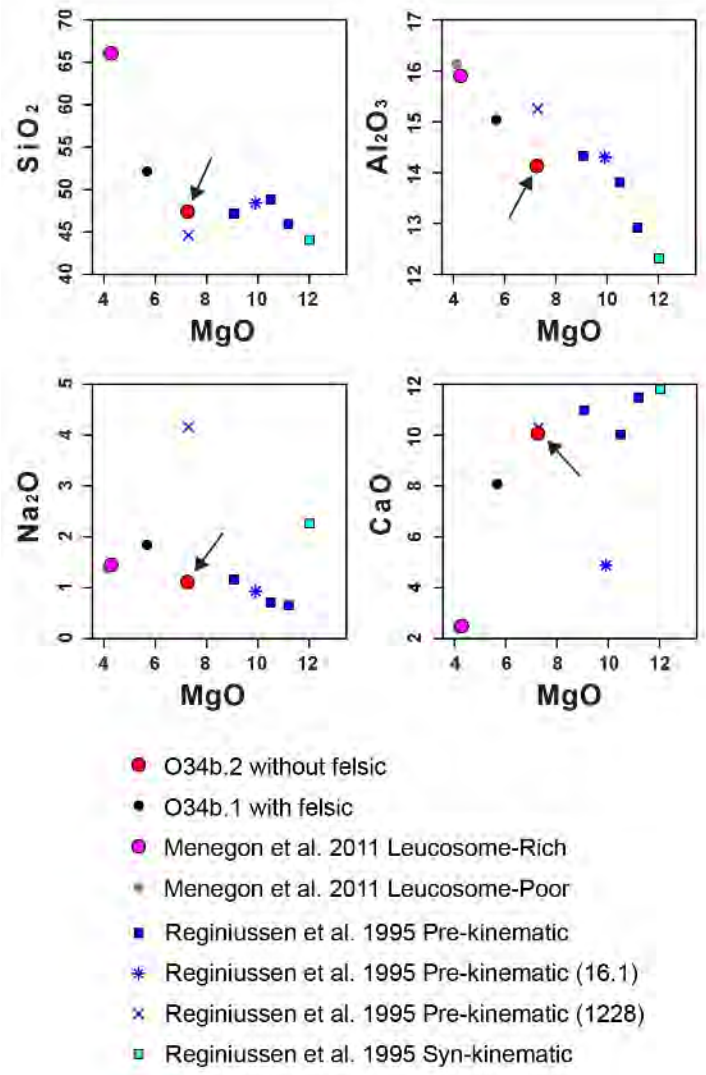

Fig. 4.11

Plots of MgO versus SiO_2, Al_2O_3, Na_2O and CaO wt% of bulk-rock chemical compositions. The mafic dyke O34b (without felsic leucosome veinlets) shown in red is compared with the felsic leucosomes sampled by Menegon et al. (2011) from adjacent migmatitic metapelites and with mafic pre-kinematic dykes reported by Reginiussen et al. (1995). Bulk rock chemical compositions are also given in Table 4.1.

4.3.2 MINERAL CHEMISTRY

Table 4.2 reports major element microprobe analysis of porphyroclastic and fine-grained clinopyroxene, orthopyroxene and plagioclase. Porphyroclasts are homogeneous in composition and do not display chemical variations between cores and rims. Clinopyroxenes have an average diopside composition of $[Ca_{0.47},Mg_{0.35},Fe_{0.18}]SiO_3$, orthopyroxenes have an average composition of En50 $[Ca_{0.01},Mg_{0.50},Fe_{0.49}]SiO_3$ and plagioclases have an average composition of An_{77}: $(Na_{0.22},Ca_{0.77})(Al_{1.75,}Si_{2.23})O_8$. In pyroxenes, only minor compositional variations occur between the porphyroclasts and the small grains in the mixture. The clinopyroxenes and the orthopyroxenes in the fine grained mixture have average compositions of $[Ca_{0.47},Mg_{0.36},Fe_{0.17}]SiO_3$ and $[Ca_{0.01},Mg_{0.50},Fe_{0.49}]SiO_3$) respectively. In contrast, plagioclase in the mixture displays chemical variations ranging from An_{60} to An_{90} (Table 4.2 and Fig. 12).

	Opx porphyro.					Opx matrix					
wt%	opx-p-12	opx-p-13	opx-p-14	opx-p-34	opx-p-59	opx-m-11	opx-m-15	opx-m-17	opx-m-35	opx-m-44	opx-m-16
SiO_2	51.3	51.3	51.2	51.1	51.7	50.3	51.0	51.1	51.3	51.5	51.9
TiO_2	0.0	0.1	0.0	0.1	0.1	0.1	0.1	0.1	0.0	0.1	0.1
Al_2O_3	0.9	0.9	1.0	1.0	0.9	1.7	1.2	1.4	1.3	1.1	1.1
Fe_2O_3	30.0	30.1	30.0	29.5	29.5	30.5	29.3	29.1	29.1	29.1	29.5
MnO	0.6	0.6	0.7	0.6	0.6	0.6	0.6	0.5	0.5	0.6	0.6
MgO	16.9	17.0	17.0	17.2	16.9	16.1	16.7	16.6	17.3	17.5	16.7
CaO	0.4	0.4	0.5	0.5	0.5	0.5	0.4	0.4	0.3	0.3	0.4
Na_2O	0.0	0.0	0.0	0.0	0.0	0.0	0.0	0.0	0.0	0.0	0.0
K_2O	0.0	0.0	0.0	0.0	0.0	0.0	0.0	0.0	0.0	0.0	0.0
P_2O_5	0.0	0.0	0.0	0.0	0.0	0.0	0.0	0.0	0.0	0.0	0.0
Cr_2O_3	0.1	0.0	0.0	0.0	0.1	0.0	0.1	0.0	0.0	0.0	0.0
Tot	**100.36**	**100.42**	**100.39**	**100.06**	**100.25**	**99.80**	**99.28**	**99.13**	**99.89**	**100.12**	**100.35**
Si	1.97	1.98	1.97	1.97	1.99	1.96	1.98	1.99	1.98	1.98	2.00
Ti	0.00	0.00	0.00	0.00	0.00	0.00	0.00	0.00	0.00	0.00	0.00
Al	0.04	0.04	0.05	0.04	0.04	0.08	0.05	0.06	0.06	0.05	0.05
Fe tot	0.97	0.97	0.96	0.95	0.95	0.99	0.95	0.95	0.94	0.93	0.95
Mn	0.02	0.02	0.02	0.02	0.02	0.02	0.02	0.02	0.02	0.02	0.02
Mg	0.97	0.97	0.97	0.99	0.97	0.93	0.97	0.96	0.99	1.00	0.96
Ca	0.02	0.02	0.02	0.02	0.02	0.02	0.02	0.02	0.01	0.01	0.01
Na	0.00	0.00	0.00	0.00	0.00	0.00	0.00	0.00	0.00	0.00	0.00
K	0.00	0.00	0.00	0.00	0.00	0.00	0.00	0.00	0.00	0.00	0.00
Cr	0.00	0.00	0.00	0.00	0.00	0.00	0.00	0.00	0.00	0.00	0.00
P	0.00	0.00	0.00	0.00	0.00	0.00	0.00	0.00	0.00	0.00	0.00
SUM	**4.00**	**4.00**	**4.00**	**4.00**	**4.00**	**4.00**	**4.00**	**4.00**	**4.00**	**4.00**	**4.00**
Wo	0.9	0.9	1.0	1.0	1.0	1.1	0.8	0.8	0.7	0.6	0.8
En	49.6	49.7	49.7	50.5	50.0	47.9	50.0	50.0	51.1	51.5	49.9
Fs	49.5	49.4	49.3	48.6	49.0	51.0	49.3	49.2	48.2	47.9	49.3

	Pl porphyro.					Pl matrix					
wt%	pl-p-1	pl-p-2	pl-p-4	pl-p-5	pl-p-8	pl-m-40	pl-m-24	pl-m-25	pl-m-26	pl-m-27	pl-m-48
SiO_2	48.7	49.0	48.5	48.5	48.3	48.8	46.5	48.0	52.9	51.8	45.5
TiO_2	0.0	0.0	0.0	0.0	0.0	0.0	0.0	0.0	0.0	0.0	0.0
Al_2O_3	32.3	32.4	32.6	32.2	33.4	33.3	34.8	33.5	30.0	31.1	35.1
Fe_2O_3	0.1	0.1	0.2	0.1	0.1	0.3	0.1	0.3	0.3	0.4	0.6
MnO	0.0	0.0	0.0	0.0	0.0	0.0	0.0	0.0	0.0	0.0	0.0
MgO	0.0	0.0	0.0	0.0	0.0	0.0	0.0	0.0	0.0	0.0	0.0
CaO	15.9	15.7	16.1	15.9	15.7	15.5	17.0	15.9	12.1	13.1	17.7
Na_2O	2.6	2.6	2.5	2.7	2.5	2.3	1.7	2.4	4.4	3.8	1.1
K_2O	0.1	0.1	0.0	0.1	0.1	0.1	0.0	0.1	0.2	0.2	0.0
P_2O_5	-	-	-	-	0.2	0.1	0.2	0.3	0.2	0.2	0.2
Cr_2O_3	-	-	-	-	0.0	0.0	0.0	0.0	0.0	0.0	0.0
Tot	**99.57**	**99.93**	**99.96**	**99.46**	**100.35**	**100.42**	**100.29**	**100.43**	**100.08**	**100.68**	**100.26**
Si	2.24	2.24	2.22	2.24	2.20	2.22	2.13	2.19	2.39	2.34	2.18
Ti	0.00	0.00	0.00	0.00	0.00	0.00	0.00	0.00	0.00	0.00	0.00
Al	1.75	1.75	1.76	1.75	1.80	1.78	1.88	1.80	1.60	1.65	1.81
Fe tot	0.00	0.00	0.01	0.00	0.01	0.01	0.00	0.01	0.01	0.02	0.02
Mn	0.00	0.00	0.00	0.00	0.00	0.00	0.00	0.00	0.00	0.00	0.00
Mg	0.00	0.00	0.00	0.00	0.00	0.00	0.00	0.00	0.00	0.00	0.00
Ca	0.78	0.77	0.79	0.78	0.76	0.76	0.83	0.78	0.59	0.63	0.78
Na	0.23	0.23	0.22	0.24	0.22	0.20	0.15	0.21	0.38	0.34	0.21
K	0.00	0.01	0.00	0.00	0.01	0.00	0.00	0.00	0.01	0.01	0.00
Cr	-	-	-	-	0.00	0.00	0.00	0.00	0.00	0.00	0.00
P	-	-	-	-	0.01	0.00	0.01	0.01	0.01	0.01	0.01
SUM	**5.00**	**5.00**	**5.01**	**5.01**	**5.00**	**4.98**	**5.00**	**5.00**	**4.99**	**5.00**	**5.01**
An	76.9	76.7	77.9	76.4	77.3	78.6	84.4	78.5	59.9	64.7	78.6
Ab	22.6	22.8	21.8	23.1	22.1	20.9	15.4	21.1	39.2	34.3	21.1
Or	0.5	0.5	0.3	0.4	0.6	0.5	0.2	0.4	0.9	1.0	0.3

Table 4.2 (continued)

	Cpx porphyro.					Cpx matrix					
wt%	cpx-p-1	cpx-p-2	cpx-p-32	cpx-p-54	cpx-p-55	cpx-m-3	cpx-m-4	cpx-m-19	cpx-m-20	cpx-m-21	cpx-m-52
SiO_2	51.7	51.8	51.8	52.2	51.8	51.5	51.5	52.7	52.3	52.3	53.3
TiO_2	0.2	0.1	0.1	0.1	0.2	0.2	0.2	0.1	0.1	0.1	0.2
Al_2O_3	1.7	1.7	1.6	1.6	1.9	2.0	2.0	1.8	1.9	1.3	0.8
Fe_2O_3	11.1	10.6	11.3	11.3	11.1	11.3	11.1	9.5	10.4	11.0	9.1
MnO	0.2	0.2	0.2	0.2	0.3	0.3	0.2	0.2	0.2	0.3	0.2
MgO	11.7	11.8	11.6	11.6	11.6	11.5	11.4	12.2	11.8	12.1	13.4
CaO	21.8	22.0	21.9	21.8	22.1	21.9	22.0	22.3	22.1	22.0	22.6
Na_2O	0.4	0.5	0.4	0.5	0.4	0.4	0.4	0.5	0.5	0.4	0.4
K_2O	0.0	0.0	0.0	0.0	0.0	0.0	0.0	0.0	0.0	0.0	0
P_2O_5	0.3	0.2	0.3	0.3	0.3	0.3	0.2	0.2	0.2	0.3	0.3
Cr_2O_3	0.1	0.0	0.1	0.0	0.0	0.0	0.2	0.0	0.1	0.0	0
Tot	**99.28**	**98.94**	**99.37**	**99.63**	**99.60**	**99.48**	**99.08**	**99.56**	**99.64**	**99.75**	**100.14**
Si	1.96	1.97	1.97	1.98	1.96	1.95	1.96	1.98	1.97	1.97	1.99
Ti	0.01	0.00	0.00	0.00	0.00	0.01	0.01	0.00	0.00	0.00	0.00
Al	0.08	0.07	0.07	0.07	0.08	0.09	0.09	0.08	0.08	0.06	0.03
Fe tot	0.35	0.34	0.36	0.36	0.35	0.36	0.35	0.30	0.33	0.35	0.28
Mn	0.01	0.01	0.01	0.01	0.01	0.01	0.01	0.01	0.01	0.01	0.01
Mg	0.66	0.67	0.65	0.66	0.66	0.65	0.64	0.68	0.67	0.68	0.75
Ca	0.89	0.89	0.89	0.88	0.89	0.89	0.90	0.90	0.89	0.89	0.90
Na	0.03	0.04	0.03	0.03	0.03	0.03	0.03	0.04	0.04	0.03	0.03
K	0.00	0.00	0.00	0.00	0.00	0.00	0.00	0.00	0.00	0.00	0.00
Cr	0.00	0.00	0.00	0.00	0.00	0.00	0.00	0.00	0.00	0.00	0.00
P	0.01	0.01	0.01	0.01	0.01	0.01	0.01	0.01	0.01	0.01	0.01
SUM	**4.00**	**4.00**	**4.00**	**4.00**	**4.00**	**4.00**	**4.00**	**4.00**	**4.00**	**4.00**	**4.00**
Wo	46.7	47.1	46.7	46.5	47.1	46.9	47.4	47.8	47.4	46.4	46.7
En	34.8	35.3	34.4	34.6	34.5	34.2	34.0	36.4	35.3	35.4	38.6
Fs	18.5	17.7	18.8	18.9	18.4	18.9	18.6	15.8	17.3	18.2	14.7

Table 4.2

Selection of major element microprobe analysis of porphyroclastic and fine-grained clinopyroxene, orthopyroxene and plagioclase, with corresponding mineral formula unit recalculations. Pyroxenes are calculated based on 4 cations whereas plagioclase is calculated based on 8 oxygens. End members ratios are shown below each measurement: Wollastonite (Wo), Enstatite (En), Ferrosilite (Fs), Albite (Ab), Anorthite (An), Orthoclase (Or).

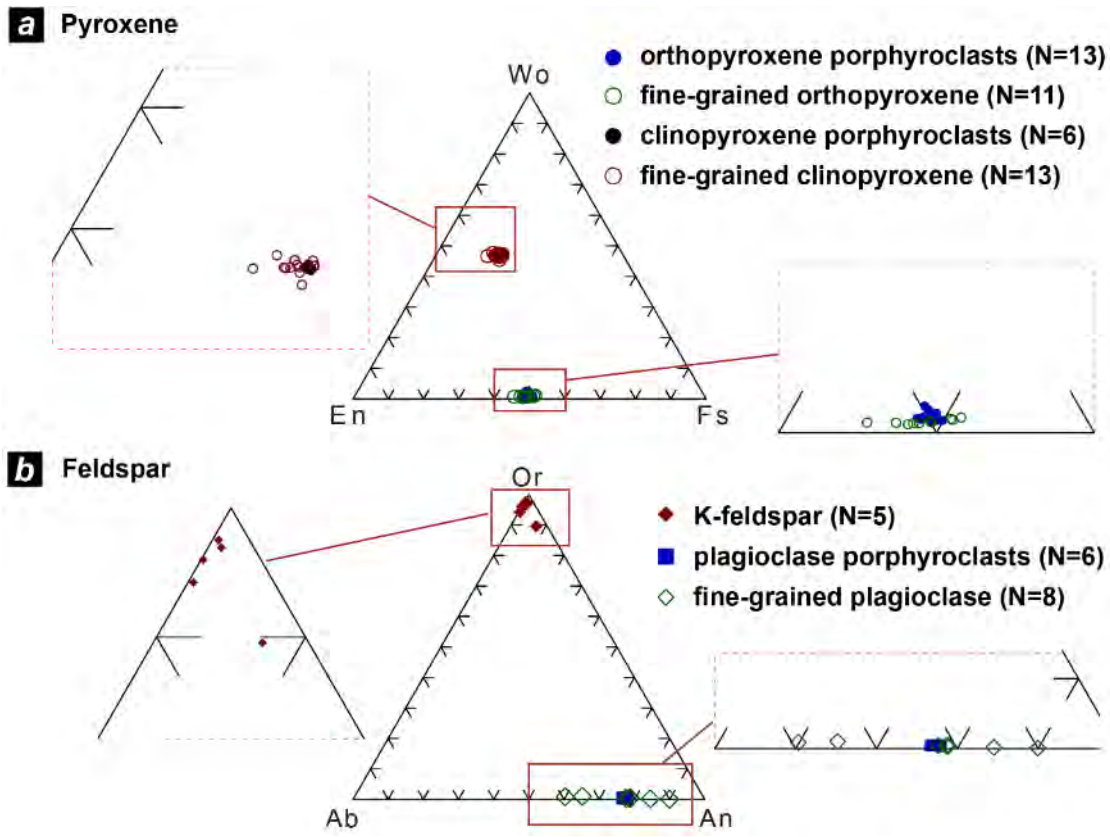

Fig. 4.12

Triangular plots of (a) pyroxene compositions and (b) feldspar compositions, derived from microprobe analysis of mineral phases. See also Table 4.2 for mineral compositions.

4.4 EBSD RESULTS

4.4.1 PORPHYROCLASTS

Orthopyroxene porphyroclasts are preferentially oriented with the [001] axes subparallel to the stretching lineation and the (100) planes subparallel to the foliation (Fig. 4.13d). Crystal distortion in orthopyroxene manifests as gradual increments of misorientation (< 3°), with cumulative misorientations across single porphyroclasts as large as 30° (Fig. 4.13c, profile A). The density of low angle boundaries (i.e. 3°-10°) in orthopyroxene porphyroclasts is very low, even in case of grains with high aspect ratios (Fig. 4.13a).

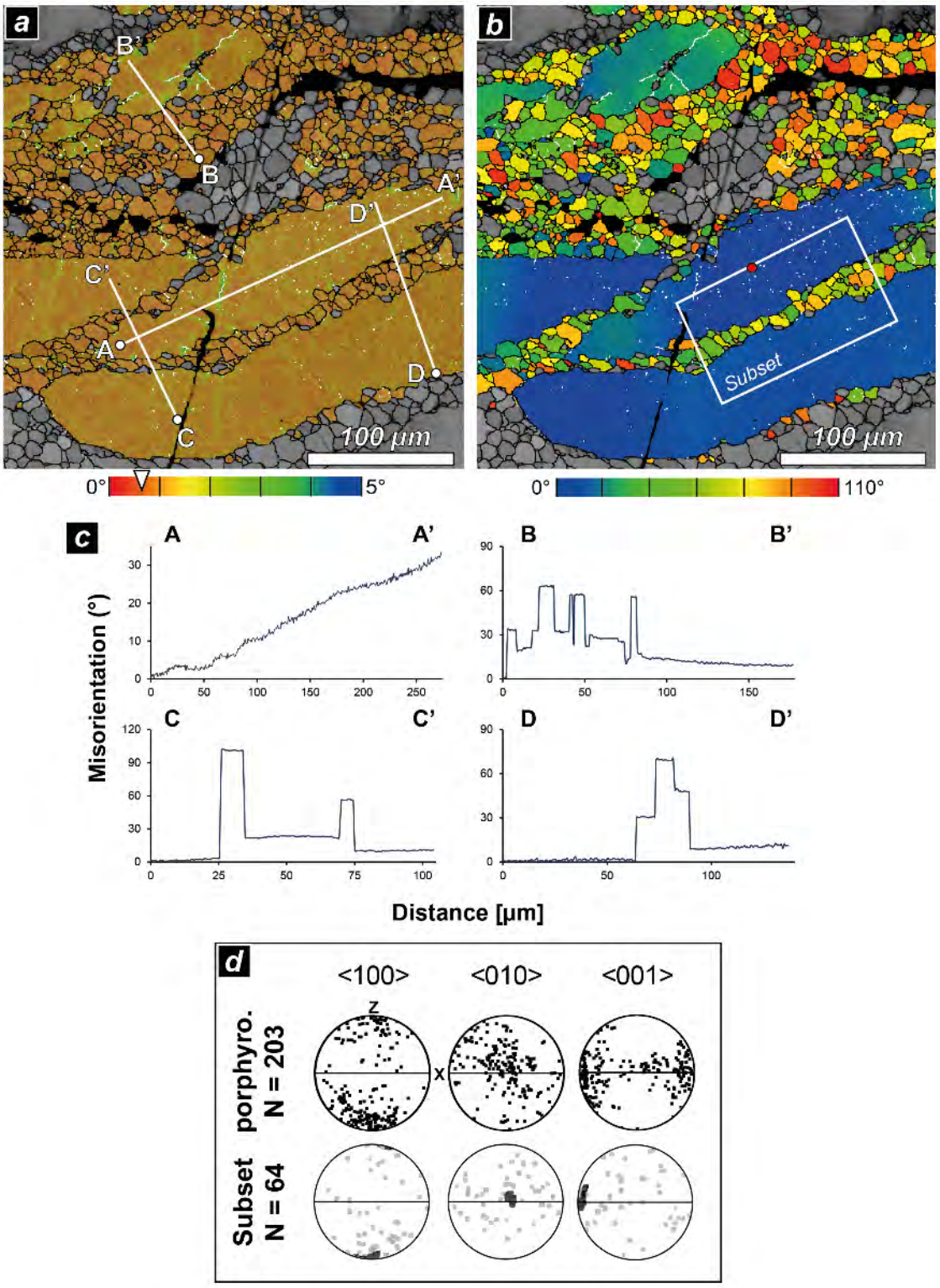

Fig. 4.13

EBSD analysis of orthopyroxene. (a) EBSD map of local misorientation, colour coded according to the degrees of misorientation between each pixel and its neighbouring clusters of pixels within an area of 7x7 pixels. Colour scale below. Low angle (3-10°) subgrain boundaries are shown in white; >10° grain boundaries in black. (b) EBSD map of texture component, colour coded according

to the misorientation from the red dot in large blue grain. Colour scale below; grains in grey are other phases. (c) Misorientation profiles relative to the first points (white dots). Trace of profiles are shown in (a). (d) Pole figures of orthopyroxene porphyroclasts (combination of all datasets, one-point-per-grain) and of the selected subset (white box in b). For the subset, the intracrystalline grains are shown in light grey and the porphyroclast in black. N is the number of grains. Upper hemisphere, equal area projection. See text for explanation.

This indicates limited subgrain development. The transition from orthopyroxene porphyroclasts to the fine-grained aggregate is marked by abrupt, large misorientation angles between the new grains and the neighbouring porphyroclast; as evident from the misorientation map and from the misorientation profiles of Fig. 4.13b (profiles B, C, D). In addition, the orientation of the fine-grained aggregate directly in contact with the porphyroclasts shows no host control (Fig. 4.13d, subset).

Clinopyroxene porphyroclasts do not display an obvious crystallographic preferred orientation (CPO), even though there is the tendency for the [001] axes to be aligned subparallel to the stretching lineation and for the (010) to be aligned subparallel to foliation (Fig. 4.14d). The density of low-angle boundaries (3-10˚) is highly variable: many porphyroclasts are essentially free of low-angle boundaries, while others show local evidence of substructures. As for the orthopyroxenes grains, the transition from the porphyroclasts to the small clinopyroxene grains is marked by abrupt misorientations, often > 80° (Fig. 4.14b). In addition, the fine-grained clinopyroxene grains in proximity of the porphyroclasts lack an evident CPO (Fig. 4.14c, subsets). The clinopyroxene grains in the matrix are mostly internally strain-free and do not contain evident substructures. Large misorientations between matrix grains are evident from the misorientation profile of Fig. 4.14b.

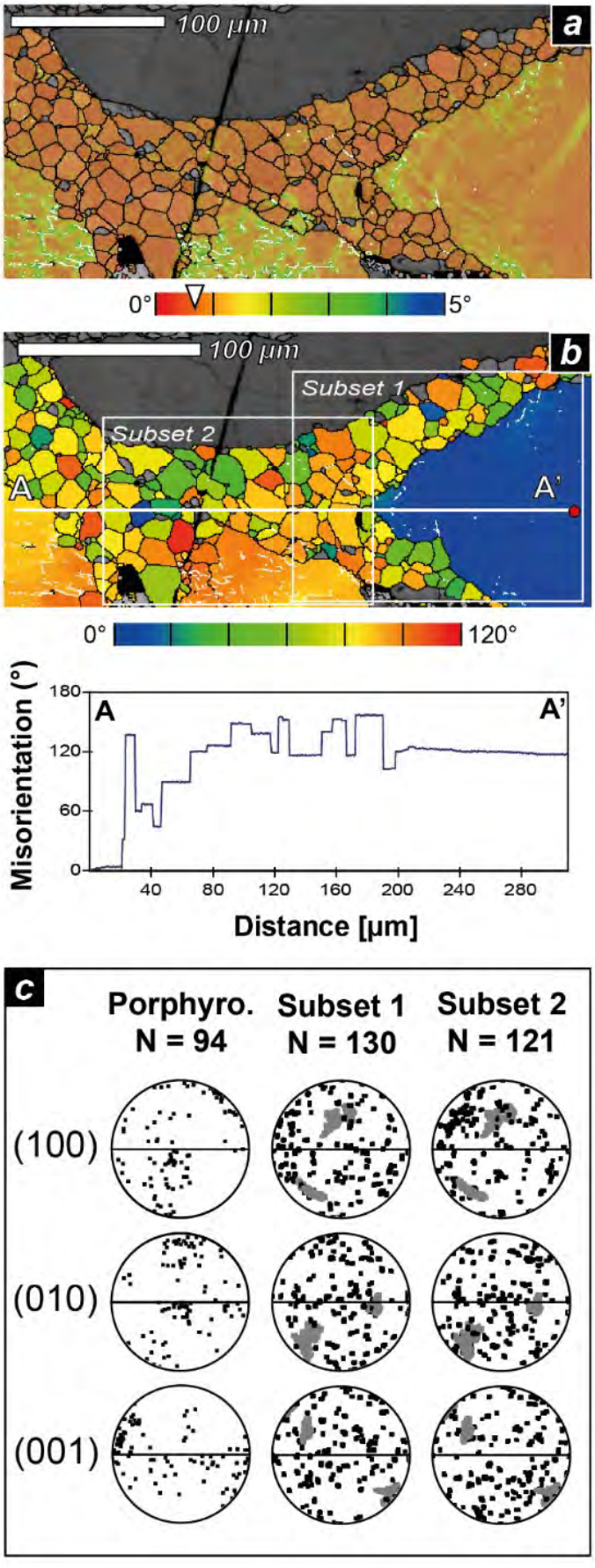
100 µm
a
0°
5°
100 µm
b
Subset 1
Subset 2
A
A'
0°
120°
Misorientation (°)
180
120
60
0
A
A'
40
80
120
160
200
240
280
Distance [µm]
c
Porphyro.
N = 94
Subset 1
N = 130
Subset 2
N = 121
(100)
(010)
(001)

Fig. 4.14

Fig. 4.14 (previous page)

EBSD analysis of clinopyroxene. (a) EBSD map of local misorientation; as in Fig. 4.13a. (b) EBSD map of texture component, colour coded according to the misorientation from the red dot. Colour scale below. Trace of misorientation profile A-A' is shown in white. Misorientations relative to the first point (A) (c) Pole figures of clinopyroxene porphyroclasts (combination of all datasets, one-point per grain) and of the selected subsets (white boxes in b). For the subsets, the intracrystalline grains are shown in black and the porphyroclast in light grey. N is the number of grains surrounding the porphyroclasts. Upper hemisphere, equal area projection. See text for explanation.

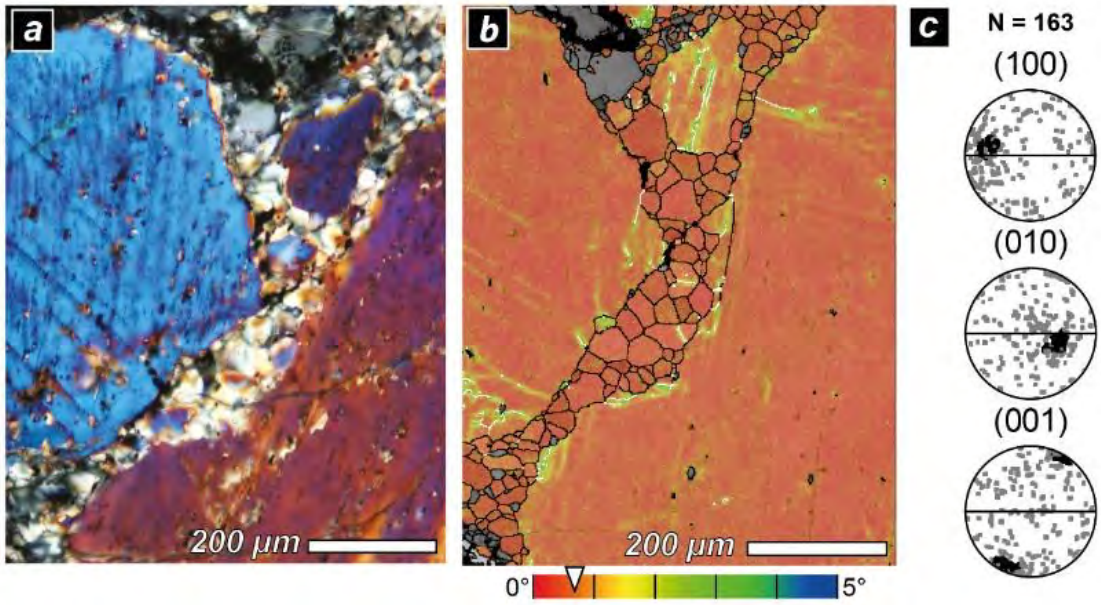

Fig. 4.15

EBSD analysis of an intracrystalline band in clinopyroxene porphyroclast. (a) Optical image in crossed polars. (b) EBSD map of local misorientation; as in Fig. 4.13a. (c) Pole figures of clinopyroxene – intracrystalline grains shown in grey, porphyroclast in black; data from image b. N is the number of intracrystalline grains. Upper hemisphere, equal area projection.

Clinopyroxene porphyroclasts are often crosscut by bands of fine-grained clinopyroxene (Fig. 4.15). While the porphyroclasts show large distortions adjacent to these bands, the small polygonal recrystallized grains in the bands are optically strain free. Once again, the

crystallographic orientation of the grains within the bands is unrelated to the orientation of the host porphyroclast (Fig. 4.15c). Minor low angle boundaries are visible in the porphyroclast in the area flanking the bands, while the interior of the porphyroclasts appear largely devoid. The new grains within the bands are strain free and without substructures (Fig. 4.15b).

Plagioclase porphyroclasts exhibit a weak CPO with (100) poles subparallel to lineation and (010) poles subnormal to foliation (Fig. 4.16c). Misorientation profiles across the length of lenticular porphyroclasts show strong crystal distortions with misorientations up to ca. 30° (Fig. 4.16b, profiles A-B). However, low-angle boundaries within the porphyroclasts' interior are scarce and preferentially cluster in regions adjacent to intracrystalline cracks and along porphyroclasts margins (Fig. 4.16a). Low-angle boundaries often define misorientation bands parallel to intracrystalline cracks filled with new grains. Misorientation bands occur also in conjugate sets symmetrically arranged with respect to the normal to the foliation plane (Fig. 4.16a).

Misorientation profiles across fine-grained bands separating porphyroclasts indicate that the misorientations are sharp, and that porphyroclasts on either side are highly misoriented (up to 150°) with respect to each other (Fig. 4.16b: profiles C-D). The regular jumps in misorientation along profile D is the result of twinning. In profile D, lattice distortion is mostly concentrated in proximity of the fine-grained band. As for ortho- and clinopyroxene, the crystallographic orientations of the small grains filling cracks and forming nearly mono-mineralic aggregates around porphyroclasts are unrelated to neighbouring porphyroclasts' orientation (Fig. 4.16c, subset). The recrystallized plagioclase grains have internal misorientation less than 1° and are strongly misoriented in respect to each other (Fig. 4.16b: profile E).

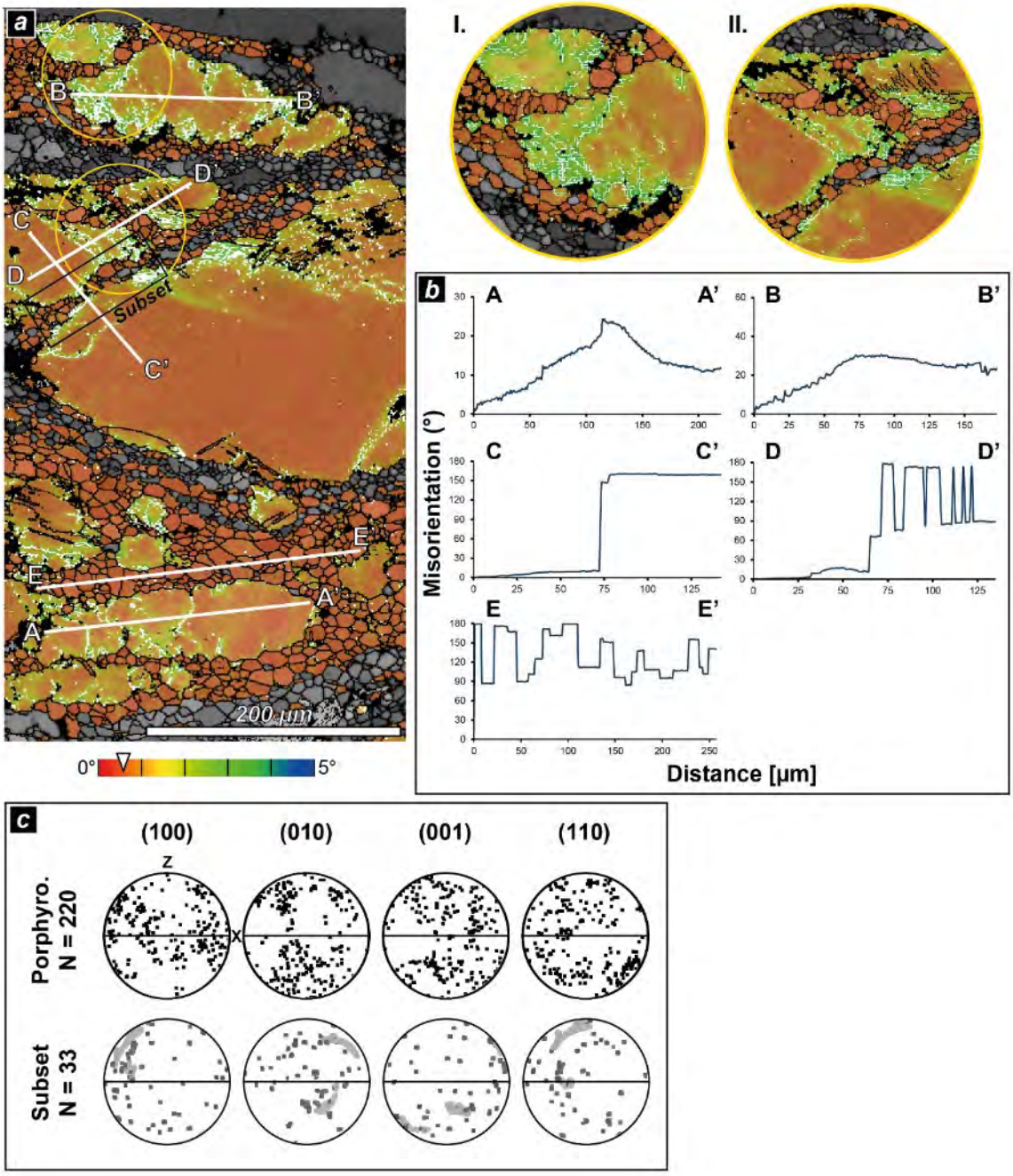

Fig. 4.16

EBSD analysis of plagioclase. (a) EBSD map of local misorientation; as in Fig. 4.13a. (b) Misorientation profiles relative to the first point. Trace of profiles are shown in (a). (c) Pole figures of plagioclase porphyroclasts (combination of all datasets, one-point-per-grain) and of the selected subset (white box in a). For the subsets, the crystallized grains are shown in dark grey and the porphyroclasts in light grey. N is the number of grains. Upper hemisphere, equal area projection.

4.4.2 FINE-GRAINED POLYPHASE MIXTURE

The crystallographic orientations of fine-grained orthopyroxene, clinopyroxene, plagioclase and quartz of the polyphase mixture were determined from the EBSD map shown in Fig. 4.17a. The same results were obtained from the analysis of other EBSD maps, so that the following description is considered representative of the crystallographic fabrics of the polyphase matrix.

In general, all phases of the polyphase mixture have a weak crystallographic preferred orientation (CPO) (max m.u.d < 3.5, J-index < 1.6) (Fig. 4.17b). The (100) planes and [001] directions of orthopyroxene form maxima parallel to the foliation plane and stretching lineation, respectively. These orientations overlap with that of the porphyroclasts (Fig. 4.13d). Clinopyroxene exhibits a weak L-type CPO (Helmstaedt et al., 1972) where the [001] axes are concentrated parallel to the stretching lineation, while the [010] axes form a girdle normal to the lineation (Fig. 4.14c). Poles to (100) planes cluster normal to the foliation and are rotated antithetically with respect to the sinistral sense of shear. This weak L-type CPO overlaps with that of the clinopyroxene porphyroclasts (Fig. 4.17c). The (110) planes of plagioclase form a weak maximum parallel to the foliation plane, while there is no clear maximum of crystallographic directions subparallel to the stretching lineation (Fig. 4.17b). Quartz c-axis CPO has a weak maximum (2.66 m.u.d, J-index 1.10) near the centre of the pole figure (Y direction) (Fig. 4.17b). The a-axes and the poles to the m-prismatic planes form weak maxima subparallel to the stretching lineation.

The misorientation angle distribution for uncorrelated pairs is remarkably close to the theoretical random curve for all the four analysed phases (Fig. 4.17c). The misorientation angle distribution for correlated pairs shows the following major deviations from the

random curve: (i) misorientations < 50° occur with a higher frequency than expected for a random distribution in orthopyroxene; (ii) misorientations < 80° and between 100° and 110° occur with a higher frequency than expected for a random distribution in clinopyroxene; (iii) misorientations < 20° and of 180° occur with a higher frequency than expected for a random distribution in plagioclase; and (iv) misorientations < 5° and of 60° occur with a higher frequency than expected for a random distribution in quartz. The peaks at 180° and 60° in plagioclase and quartz, respectively, are attributed to twinning.

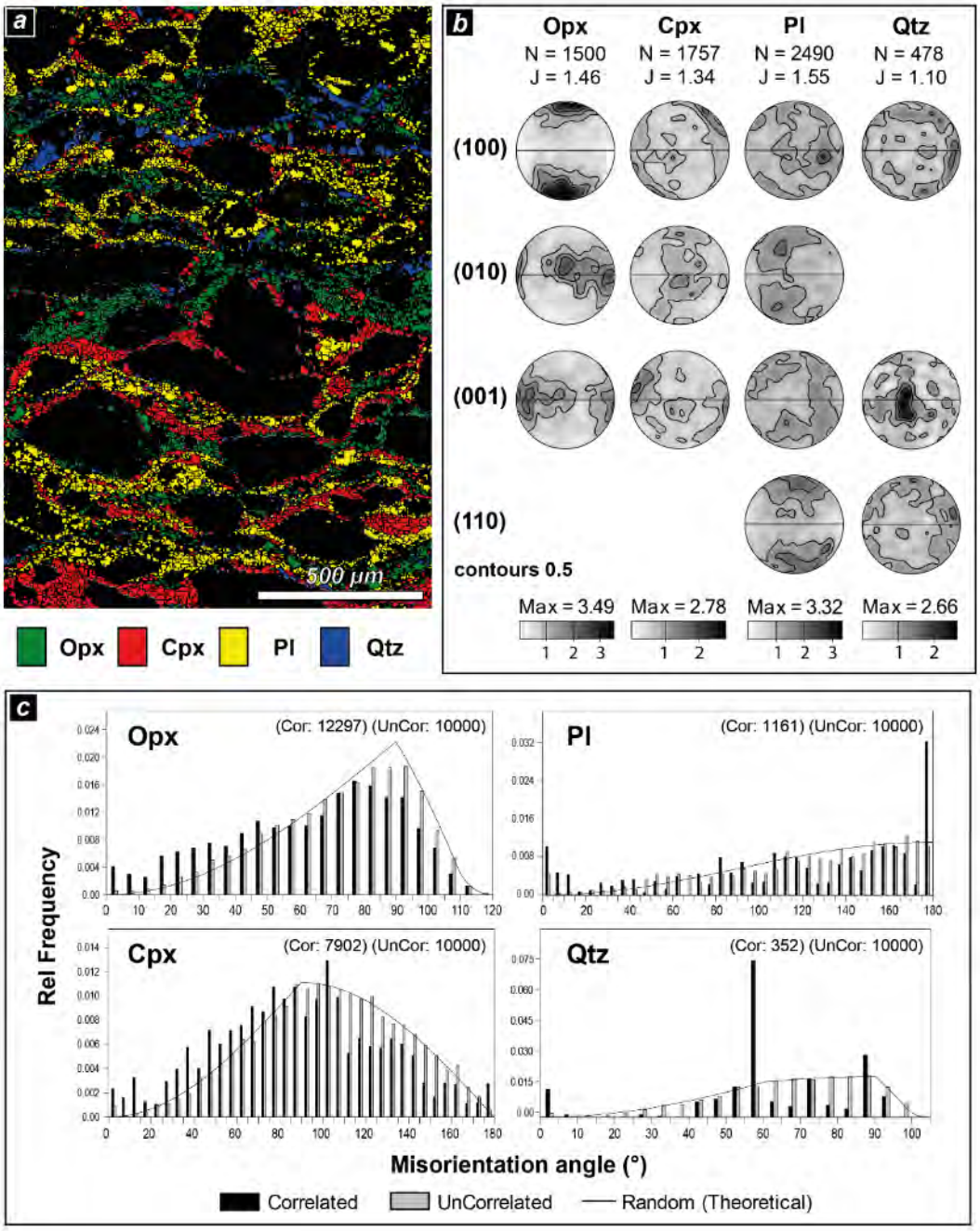

Fig. 4.17

EBSD analysis of the polyphase aggregate (a) EBSD phase-map of the fine polyphase aggregate. Green: orthopyroxene; blue: quartz; red: clinopyroxene; yellow: plagioclase. Black portions correspond to porphyroclasts (not analysed here) (b) Pole figures of the polyphase aggregate, one-point-per-grain. Upper hemisphere, equal area projection. Data is from (a), contoured using a half width of 15°. Strength of texture is given as m.u.d. (multiples of uniform distribution) and as J index. Contours have a step-size of 0.5, starting from 1.0 m.u.d. N is the number of grains. (c) Misorientation angle distributions for correlated and uncorrelated points, plotted against the theoretical random curve.

4.5 SIMS RESULTS: INTRACRYSTALLINE WATER CONTENT IN CLINO- AND ORTHOPYROXENE

Clino- and orthopyroxene porphyroclasts were analysed using SIMS to measure their intracrystalline water contents. These measurements were made to test whether different amounts of intracrystalline water could influence the ease of crystal plastic deformation, and explain the observed microstructural differences between clinopyroxene porphyroclasts - which are commonly dissected by intracrystalline fractures and boudinaged, - and orthopyroxene - which form strongly elongated monocrystalline ribbons.

Results are plotted as frequency distributions in Fig. 4.18a; while the complete table and the probing locations are supplied in the Appendix, Appx. 8. A total of 53 points were measured: 27 grains of orthopyroxene and 26 of clinopyroxene. The values differ from those reported by Degli Alessandrini et al. (2017) on account of the new mineral corrections made available for clino- and orthopyroxenes (J.C.M. De Hoog personal communication). Clinopyroxene grains water contents range between 80 and 357 wt ppm, with a mean of 159 ± 62 wt ppm (1StDev; n=26). Conversely, the majority of orthopyroxenes (22 out of 27) have water contents < 50 wt ppm, with only a smaller group of values > 100 wt ppm (Fig. 4.18a). After SIMS analysis each ion probe pit was inspected on SEM BSE images to check if anomalously high values of H contents resulted from the presence of cracks, grain boundaries or exsolution lamellae not detected during SIMS analysis. At the resolution of the SEM imaging all the pits looked clean, so that the measurements are taken as representative of real intracrystalline water contents. The mean water content in orthopyroxene grains is 17 ± 10 wt ppm (1StDev; n=22) if the

values greater than 100 wt ppm are excluded from the calculation. If these are accounted for, the average is 51 ± 80 wt ppm (1StDev; n=27). Based on the above, orthopyroxene contains considerably less intracrystalline water than clinopyroxene. No correlation was observed between the orthopyroxene grains aspect ratio and the intracrystalline water content (Fig. 4.18b). Highly elongated orthopyroxene grains were found to contain on average less water than rounded clinopyroxenes (Fig. 4.18b). A positive correlation exists between intracrystalline water content and the K_2O content that was simultaneously measured with SIMS (Fig. 4.18c).

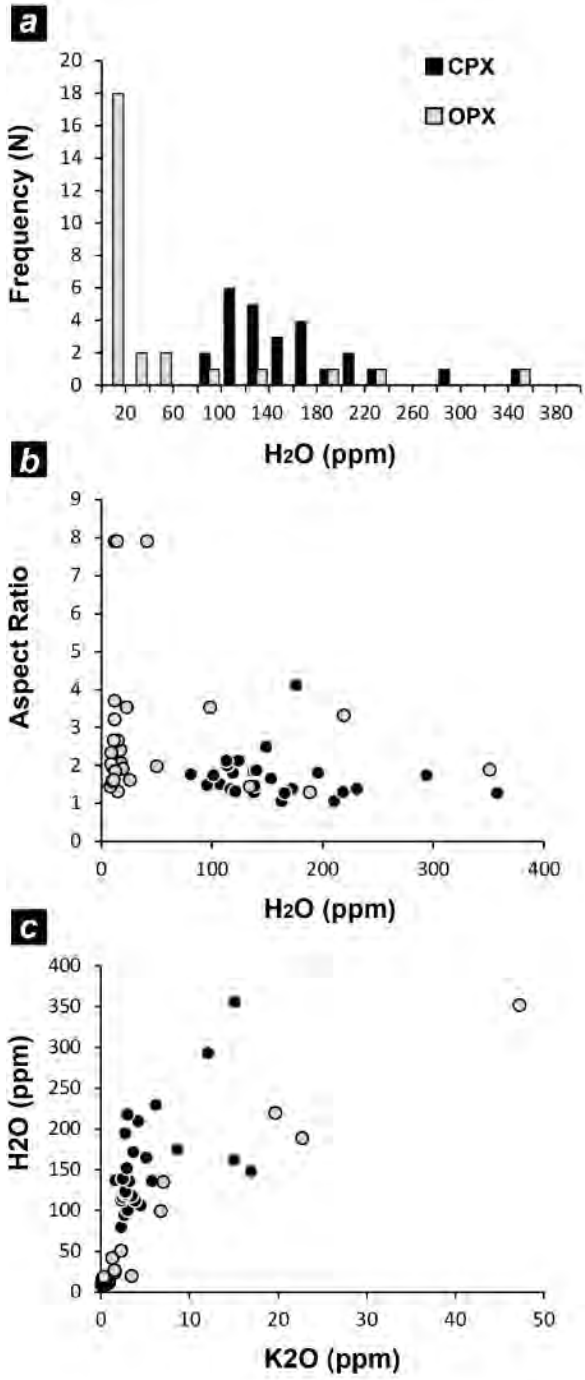

Fig. 4.18

Results from SIMS – intracrystalline water content in clinopyroxene (black) and orthopyroxene (grey) porphyroclasts. (a) Frequency histogram of intracrystalline water content. Frequency is given as number of measurements. (b) Intracrystalline water content versus grains' aspect ratio (c) K_2O content versus intracrystalline water content in pyroxenes.

DISCUSSION

4.6 P-T CONDITIONS OF DEFORMATION

To constrain the P-T conditions of deformation of the mafic dyke, two P-T isochemical sections (one at dry conditions and the other with 0.03 wt% H_2O) were constructed using Perple_X thermodynamic modelling package (Connolly, 1990). The input bulk composition is that of O34b.2 (without felsic veins) reported in Table 4.1, using the parameters described in Chapter 3, section 3.8. Results indicate that, at dry conditions, the mineral assemblage of the matrix (Opx + Pl + Cpx + Qtz + Ilm ± Kf) is stable for a wide range of P-T conditions. The previously estimated P, T conditions of 7 - 8 kbar, 760-820°C (Menegon et al., 2011) fall at the boundary of the stability field of the mineral assemblage calculated with Perple_X (Fig. 4.19a).

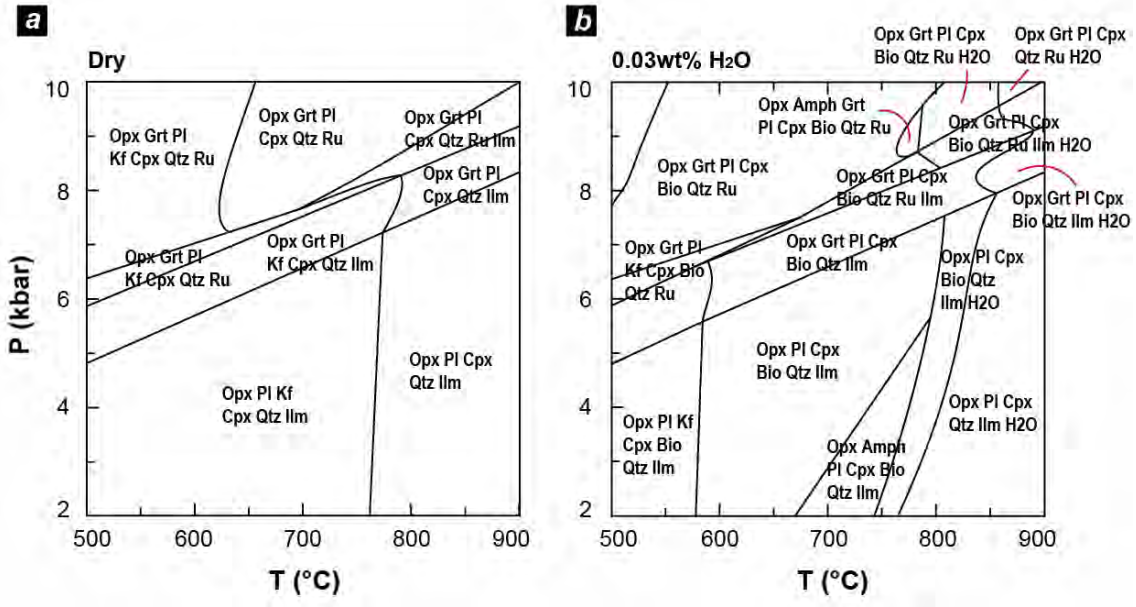

Fig. 4.19

Fig. 4.19 (previous page)

P-T isochemical section of the studied sample (composition of O34b without felsic portion of Table 4.1) at dry conditions and (b) the same P-T isochemical section with 0.03 wt.% H2O, corresponding to the LOI.

The P-T section also shows that garnet is stable at higher pressure, consistent with the textural position of garnet overgrowing the mylonitic fabric (Fig. 4.5c). Similar textural relationships, indicating a pressure increase in shear zones from the Seiland Igneous Province, were interpreted by Elvevold et al. (1994) as the result of localized Caledonian overprint. For comparison, the same isochemical section was calculated with 0.03 wt% H_2O, as measured from the LOI (Fig. 4.19b). This small amount of water thermodynamically stabilises biotite up to temperatures of 760-820°C in garnet-free assemblages, but biotite was not observed in the sheared dyke. Because biotite is not observed in the sheared dyke, 800°C is used as the equilibration temperature during mylonitization.

4.7 ORIGIN OF THE FINE-GRAINED POLYPHASE MIXTURE BY MELT-ROCK REACTION

In the Seiland Igneous Province, evidence of syn-kinematic melt infiltration from adjacent partially molten metapelites suggests that melt played an important role in the deformation of the mafic dykes. Petrographic evidence of melt-rock interaction is given by the occurrence of quartz and minor K-feldspar in the polyphase fine-grained mixture, together with orthopyroxene, clinopyroxene, plagioclase and ilmenite (Fig. 4.5d-e). This paragenesis excludes the possibility that the fine-grained mixture was produced by partial

melting of the dyke itself: partial melting of a gabbroic rock in the lower crust would require hydrous conditions, producing melts of plagiogranite to adakitic composition (e.g. Koepke et al., 2004; Sen and Dunn, 1994). Adakite usually contains phenocrysts of plagioclase, amphibole, mica, very rare orthopyroxene, and no clinopyroxene – substantially different to the observed assemblage. Furthermore, hydrous conditions are excluded since no hydrous minerals were observed. Therefore partial melting of the mafic dyke can be excluded, although it is not possible to predict whether melt-producing reactions occurred within the dyke when it reacted with felsic melt. Formation of the fine-grained mixture by extensive dynamic recrystallization of orthopyroxene, clinopyroxene and plagioclase porphyroclasts does not appear plausible because evidence of recovery (subgrain development) in the porphyroclasts is scarce (see section 4.4.1). Moreover, dynamic recrystallization alone cannot explain the presence of dispersed quartz and K-feldspar in the mixture. Therefore, based on microstructural, petrological and field evidence, it is proposed that the fine-grained polyphase mixture is the result of melt-rock reaction between the solid mafic dyke and the infiltrating felsic melt.

To test this hypothesis, Perple_X was used to model the mineral assemblage that would be thermodynamically stable when chemically mixing a pristine mafic dyke with a felsic melt (formed by syn-kinematic dehydration melting of the host metapelites). This scenario effectively corresponds to simple binary mixing between a mafic dyke and a leucosome. The result is shown as an isobaric T-X section (at P = 7 kbar), where X represents different proportions of chemical mixing between the mafic dyke (X = 0.00) and the felsic melt (X = 1.00) (Fig. 4.20a-b).

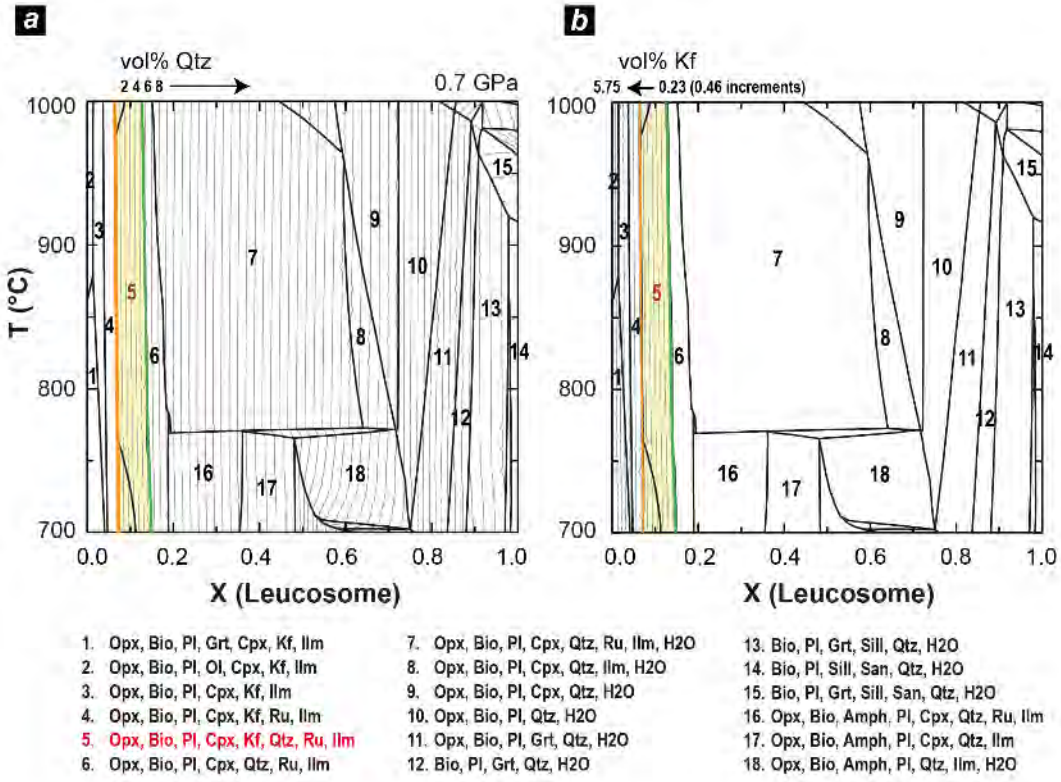

Fig. 4.20

(a-b) T-X section at 7 kbar pressure showing the mineralogical stability fields by mixing a pristine mafic dyke (X = 0.00; composition from Reginiussen et al. (1995); pre-kinematic dyke 574C) with a felsic leucosome (X= 1.00; composition from Menegon et al. (2011); leucosome-rich domain). Shaded yellow area is the T-X space where the observed syn-kinematic mineral assemblage is stable. Numbers refer to mineralogical assemblages given below. Grey lines correspond to vol.% of quartz (a) and K-feldspar (b). See text for discussion.

To construct this T-X section, the bulk-rock compositions of the least contaminated (pre-kinematic) dyke of Reginiussen et al. (1995) was used as one end member (X=0.00), and the felsic leucosome of Menegon et al. (2011) was used as the other (X=1.00). This approach is justified as the dyke O34b belongs to the pre-kinematic suite of Reginiussen et al. (1995) and its composition falls along the mixing line of these two end-members (Fig. 4.11). The composition of the infiltrating melt is taken to approximate the composition of the felsic leucosome. It is also assumed that most of infiltrating melt is

consumed in the reactions - that is little or no residual melt escaped. For this thermodynamic model, the same solid solution models and equation of state adopted for the P-T isochemical sections were used (see Chapter 3, section 3.8).

At X=0 (case scenario with no melt infiltration), the pristine dyke could be represented by the plagioclase + orthopyroxene + clinopyroxene porphyroclastic portion of sample O34b (Fig. 4.20a). Quartz is expected to form only when the dyke composition is mixed with (at least) 7 wt% of leucosome (X = 0.07). Further chemical mixing of the dyke with leucosome increases the modal proportion of quartz and decreases that of K-feldspar (Fig. 4.20a and b respectively). At 15 wt% leucosome mixing (X = 0.15), K-feldspar is in complete solid solution with plagioclase (and so disappears as an end-member phase). Therefore, the presence of both quartz and K-feldspar in the fine-grained polyphase aggregate suggests 7-15 wt% mixing of the leucosome with the dyke (Field 5, Fig. 4.20a-b). This range of mixing is further supported by the modal abundance of quartz and K-feldspar measured by image analysis (5% qtz, 0.16 Kfs), which matches that modelled in Fig. 4.20a; indicating around 10 wt% leucosome mixing during deformation. In addition to quartz and K-feldspar, 7-15 wt% of leucosome mixing stabilises also orthopyroxene, plagioclase, clinopyroxene, ilmenite, minor rutile and biotite (yellow field 5 of Fig. 4.20a-b). The latter mineral assemblage corresponds to the fine-grained polyphase aggregate observed in the mafic dyke (with the exception of biotite). From a thermodynamic point of view, even a small amount of water in the system (< 0.1 wt%) is sufficient to stabilise biotite as a hydrous phase, but this phase has not been identified in the sample. Considering an average density of 3.01 g/cm^3 for a basalt and of 2.69 g/cm^3 for a granite, 7-15 wt% of chemical mixing would correspond to about 9-11 vol% of felsic melt infiltrating the pristine mafic dyke during mylonitisation.

4.8 DEFORMATION MECHANISMS

4.8.1 CRYSTAL PLASTICITY VS. FRACTURING IN PORPHYROCLASTS

Elongated orthopyroxene porphyroclasts are interpreted to deform primarily by dislocation glide on the (100)[001] slip system, as evidenced by the widespread undulose extinction and crystal bending, by the high aspect ratios of these grains and by their CPO (Fig. 4.13). (100)[001] slip system is dominant in orthopyroxene, both in naturally and experimentally deformed samples under a wide range of P-T conditions, including those typical of the granulitic lower crust (e.g. Dornbusch et al., 1994; Hanmer, 2000; Kanagawa et al., 2008; Raimbourg et al., 2011, 2008). Evidence of subgrain development is scarce, and the transition porphyroclast-new grains is invariably characterized by large misorientations. Progressive accumulation of misorientation from the interior of porphyroclasts to the mantle of new grains were never observed. Thus, it is concluded that the new grains did not form by subgrain rotation recrystallization.

Clinopyroxene porphyroclasts show a weak L-type CPO, which could be consistent with simultaneous activation of {1-10}1/2<110>, {110}[001] and (100)[001] (Bascou et al., 2002). Local subgrain development is documented in Fig. 4.14a, where the porphyroclasts show polygonal regions separated by ca. 3° low-angle boundaries and a similar size of the new grains. Despite local presence of substructures in clinopyroxene porphyroclasts, the adjacent fine-grained aggregate is highly misoriented and without a CPO (Fig. 4.14c – subset 2). In addition, clinopyroxene porphyroclasts are frequently boudinaged and dissected by intracrystalline bands of fine-grained clinopyroxene (Fig. 4.15). The grains in these bands have a uniform grain size and resemble recrystallized aggregates. However, they do not display a CPO and their crystallographic orientation is

markedly different form that of the hosting porphyroclast. Furthermore, the porphyroclast-new grain transition is associated with large misorientation jumps, and the host porphyroclasts are typically devoid of low-angle boundaries. The few low-angle boundaries flanking the band of new grains in Fig. 4.15b can be interpreted as part of the "damage zone" associated with crack formation during fracturing (Stünitz et al., 2003; Trepmann et al., 2007). Taken all together, these observations suggest that subgrain rotation recrystallization was not the mechanism of formation of the intracrystalline bands. Therefore, these new grains are interpreted as the result of nucleation and growth from fractured fragments (e.g. Menegon et al., 2013; Stünitz et al., 2003; Trepmann et al., 2007). Given the similar chemical composition between new grains and host porphyroclast, grain growth was likely driven by the reduction in strain- and surface energy rather than in chemical energy (e.g. Stünitz, 1998). The above is consistent with the clinopyroxene porphyroclasts undergoing fracturing during deformation.

The weak CPO of plagioclase (i.e. alignment of (100) poles subparallel to lineation and (010) poles subnormal to foliation, Fig. 4.16c) may be attributed to dislocation glide on the (010)[100] slip system. However, the same CPO is often associated with magmatic flow (e.g. Morales et al., 2011) and it cannot be rule out that it represents a combined shape- and crystallographic fabric attained by plagioclase during magmatic flow in the dyke. Furthermore, evidence of dynamic recrystallization is scarce: low-angle boundaries mostly occur in proximity of intracrystalline bands, while the interior of the porphyroclasts are largely free of low-angle boundaries. This indicates that porphyroclasts are rather strong and with limited recovery (hence undulose extinction and deformation bands rather than pervasive subgrain development). Moreover, localized deformation bands often occur in conjugate sets, and synthetic and antithetic

fractured plagioclase porphyroclasts are common. The new grains within intracrystalline bands have large misorientations with each other and with the host porphyroclast. These microstructural features are consistent with nucleation and growth from fractured grains, which has been widely documented in high-grade feldspars both in experiments (Stünitz et al., 2003) and in nature (e.g. Menegon et al., 2013; Okudaira et al., 2015). To conclude, plagioclase deformed by dislocation glide plus fracturing, accompanied by nucleation and growth of new grains from fractured fragments, and that dynamic recrystallization was limited.

4.8.2 GRAIN SIZE SENSITIVE CREEP IN THE POLYPHASE MIXTURE

The similar grain size and shape of all phases and phase-mixing suggest that grain size sensitive creep was the dominant deformation mechanism in the polyphase matrix. At the given deformation temperatures (700-800°C), quartz and plagioclase are expected to be substantially weaker than ortho- and clinopyroxene in the dislocation creep regime (Bürgmann and Dresen, 2008 and reference therein). However, in the polyphase mixture, all of the phases appear equally competent and all show similar aspect ratios and grain sizes. Moreover, all the phases exhibit straight grain boundaries and no evidence for internal deformation, consistent with minor dislocation activity during the deformation of the small grains.

Individual phases in the polyphase mixture show weak CPOs and deviations from theoretical random distributions of the misorientation angle distributions for correlated grains (Fig. 4.17b and c). This indicates that some crystallographically-controlled process has contributed to the development of the microstructure of the mixture. The existence of a (weak) CPO in aggregates deforming in the grain size sensitive creep regime at mid-

to lower crustal conditions and in the upper mantle has been recognized elsewhere (e.g. plagioclase: Fukuda et al., 2012; Gómez-Barreiro et al., 2007; clinopyroxene: Godard and van Roermund, 1995; Mauler et al., 2000; orthopyroxene + olivine aggregates: Sundberg and Cooper, 2008). A CPO in fine-grained aggregates deforming by combined diffusion creep and grain boundary sliding in the presence of melt has been reported for K-feldspar (Negrini et al., 2014) and for forsterite + diopside aggregates (Miyazaki et al., 2013). The mechanism of formation of a CPO during diffusion creep involves a component of rigid-body rotation coupled with anisotropic diffusion rate leading to oriented grain growth, in which the crystallographic direction of faster diffusion/growth rate aligns with the instantaneous stretching axis during viscous flow (Bons and den Brok, 2000). In the ortho- and clinopyroxene fine grains of the sample, the alignment of (100) planes with the mylonitic foliation, and the alignment of the [001] axis with the stretching lineation can be explained as a shape fabric produced by oriented growth during syn-deformational melt-rock reaction and diffusion creep of the mixture. The [001] axis is the direction of faster diffusion rate in clinopyroxene (Mauler et al., 2000 and references therein). Likewise, the weak CPO of plagioclase is not interpretable in terms of known slip systems and is instead explained as a shape fabric produced during diffusion creep and rigid body rotation in the presence of melt. The misorientation angle distribution for correlated pairs for orthopyroxene, clinopyroxene and plagioclase lend further support to this interpretation, in that it shows high frequencies for misorientations between 10° and 50-80° (Fig. 4.17). This has classically been interpreted as the signature of grain boundary sliding that increases the misorientation between adjacent grains (Halfpenny et al., 2006; Miranda and Klepeis, 2016, and many others).

From the above, it is concluded that the polyphase mixture deformed primarily by diffusion creep, most likely during crystallization as melt-rock reaction products. Quartz may represent an exception to this interpretation, in that its weak c-axis CPO is consistent with the dominant activity of prism <a> slip system. Quartz CPO resulting from diffusion creep typically show c-axis maxima subparallel to the stretching lineation (Hippertt, 1994; Kilian et al., 2011; Viegas et al., 2016).

4.9 THE EFFECT OF INTRACRYSTALLINE WATER ON PYROXENE PLASTICITY

Water in nominally anhydrous minerals (NAMs) is known to be a weakening agent in deformation, promoting crystal plasticity (Griggs, 1967; Chen et al., 2006; Kohlstedt 2006). If the average crystal elongation is taken as a proxy for the amount of intracrystalline deformation, then clinopyroxene porphyroclasts are considerably less deformed than orthopyroxene porphyroclasts. Following this logic, if intracrystalline water was to promote crystal plasticity in pyroxenes, then elongated orthopyroxenes would be expected to retain more intracrystalline water than equant-shaped clinopyroxenes. However, SIMS results show that highly elongated orthopyroxene porphyroclasts can contain less water than relatively equant clinopyroxene grains. In fact, orthopyroxene porphyroclasts overall contain less water than clinopyroxene porphyroclasts, regardless of their aspect ratio (Fig. 4.18). Therefore, the different rheological behaviour of ortho- and clinopyroxene cannot be attributed to a preferential incorporation of intracrystalline water in orthopyroxene and to a related hydrolytic-weakening effect. The elongation of orthopyroxene porphyroclasts seems to be controlled by the presence of clinopyroxene exsolution lamellae along the (100) planes, which probably acted as planar defects capable of localizing deformation (Raimbourg et

al., 2008). Conversely, the multiple sets of exsolution lamellae in clinopyroxene may have effectively impeded the movement of dislocations, inhibiting efficient recovery in clinopyroxene. The positive correlation between K_2O and H_2O content reinforces the idea that orthopyroxene water contents are in general very low in high grade crustal rocks (< 100 wt ppm H_2O on average, e.g. Johnson, 2006) unless some microstructural and petrological modification has happened. It is here speculated that a coupled increase in K_2O and H_2O content reflects the infiltration of K-rich felsic melt (Menegon et al., 2011) from adjacent partially molten metapelites during shearing.

4.10 Rheological evolution of the sheared dykes

The above analysis supports the contention that viscous creep of the pristine dry mafic dyke was associated with melt infiltration and with melt-rock reactions, resulting in the formation of a fine-grained polyphase mixture that deformed by diffusion creep under granulite facies conditions. The presence of melt can have profound effects on the dyke's strength.

Using the constitutive equations for diffusion creep and dislocation creep of gabbroic rocks, and of their mineral constituents in melt-present conditions (see Chapter 2, section 2.3), it is possible to evaluate the role of melt infiltration and of melt-rock reactions on the rheological evolution of the sheared mafic dykes at the estimated deformation temperature of 800 °C.

The general flow laws for dislocation creep and diffusion creep are, respectively:

$$\dot{\varepsilon} = A\sigma^n \exp(-Q/RT) \qquad (Eq.\ 4.1)$$

$$\dot{\varepsilon} = A\sigma^n d^m \exp(-Q/RT) \qquad (Eq.\ 4.2)$$

where $\dot{\varepsilon}$ is strain rate, *A* an empirical constant, *σ* the differential stress, *n* the stress exponent, *d* the grain size, *m* the grain size exponent, *Q* the activation energy, *R* the gas constant, and *T* the temperature. In case of melt-assisted diffusion creep, the melt fraction ϕ is also included in (2) as a pre-exponential term (as in Dimanov et al., 1998). To model the rheological evolution of the sheared mafic dyke, the flow laws (*Eq. 4.1*) and (*Eq. 4.2*) were applied using the experimentally-derived flow laws and creep parameters listed in Table 4.3. Results are plotted in Fig. 4.21. For additional details on the flow laws, see Chapter 2, section 2.3: Eq. 4.1 corresponds to Eq. 2.2; Eq. 4.2 corresponds to Eq. 2.3.

Flow law	Material	Deformation mechanism	A (Pa^{-n} s^{-1})	log A	n	Q (kJ mol^{-1})	d (μm)	m	ϕ
Mackwell et al. (1998)	Dry Maryland diabase (56% plagioclase, 43% pyroxene)	Dislocation creep	8×10^6	-	4.7	485	-	-	-
Zhou et al. (2012)	Dry gabbro with < 1 vol% of melt	Dislocation creep	-	10.3	4	644	-	-	-
Dimanov et al. (1998)	Anorthite aggregates with up to 10 vol% of melt	Diffusion creep	-	1.09×10^{-15}	1	388	200	-2.7	0, 0.1
Dimanov and Dresen (2005)	Dry anorthite + diopside aggregates	Diffusion creep	1210	-	1	436	An 3.5 Di < 35	nd	-

Table 4.3

Flow law parameters used for Fig. 4.21, using the flow laws for dislocation creep and diffusion creep (Eq. 4.1 and Eq. 4.2 respectively).

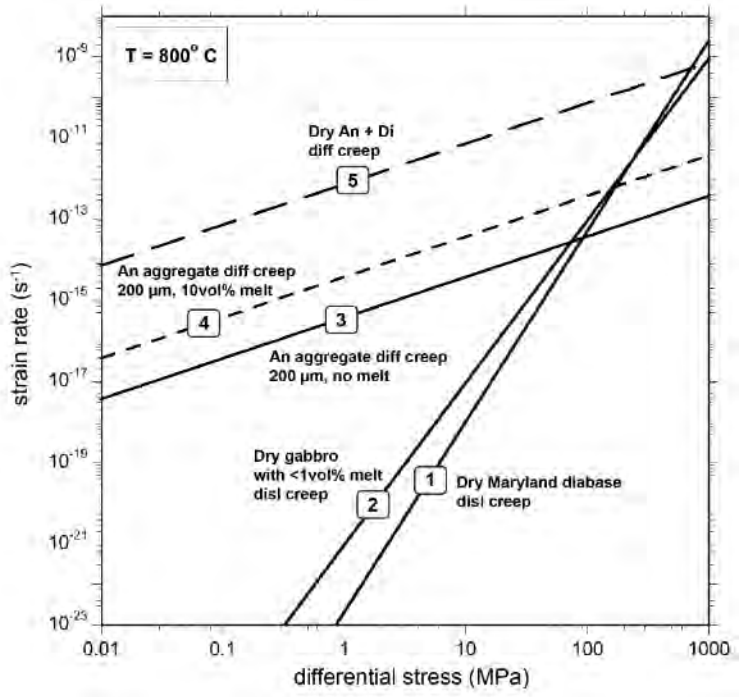

Fig. 4.21

Plot of strain rate (s^{-1}) versus differential stress (MPa) to model the rheology of the sheared mafic dyke. The following flow laws were used: dry diabase (1) (Mackwell et al., 1998) and dry gabbro with <1 vol.% melt (2) (Zhou et al., 2012) for dislocation creep; dry anorthite + diopside aggregate (5) (Dimanov and Dresen, 2005) and dry anorthite aggregate, 200 µm grain size - with (4) and without (3) 10 vol.% melt (Dimanov et al., 1998) for diffusion creep. See Table 4.3 for more details.

The rheology of the pristine mafic dyke was modelled using the dislocation creep flow law of dry Maryland diabase (Mackwell et al., 1998) (Fig. 4.21, curve 1). The latter assumes that the coarse-grained dyke initially deformed by dislocation creep without melt infiltration. Instead, to assess the weakening associated with < 1 vol% melt during dislocation creep deformation, the flow law of Zhou et al. (2012) was used (Fig. 4.21, curve 2).

In most experiments and theoretical models of melt-assisted deformation, creep is generally assumed to be linear viscous, with diffusion creep as the dominant deformation

mechanisms (Dimanov et al., 1998; Paterson, 2001). As a consequence, diffusion creep flow law is more suitable to describe the behaviour of natural rocks deforming under melt-present conditions. To model the rheology of a coarse-grained dyke infiltrated by 10 vol% melt, the flow law of Dimanov et al. (1998) for anorthite aggregates deforming by melt-assisted diffusion creep was used. This flow law aims to evaluate the rheology of the dyke in case melt-enhanced diffusion creep was triggered by melt-infiltration, without nucleation of a fine grained matrix (Fig. 4.21, curve 4). For comparison, the same flow law with 0 vol% melt is also shown (Fig. 4.21, curve 3). To model the rheology of the fine-grained polyphase matrix, the flow law of Dimanov and Dresen (2005) for dry anorthite-diopside aggregates deforming by diffusion creep was used (Fig. 4.21, curve 5). The latter flow law was derived for a 50:50 mixture of anorthite and diopside, where the average grain size of anorthite was 3.5 µm and the grain size of diopside was < 35 µm (Dimanov and Dresen, 2005).

Rheological calculations show that, for strain rates of 10^{-13} s^{-1} and for an average porphyroclast grain size of 200 µm, the weakening caused by infiltration of 10 vol% melt and a consequent switch from dislocation creep to melt-enhanced diffusion creep would not be dramatic (Fig. 4.21, curves 1 vs. 4). The melt-weakening effect would be more pronounced for slower strain rates and for smaller grain sizes, but a grain size of 200 µm was chosen as it is most representative of the porphyroclast fraction of the dyke. For a strain rate of 10^{-12} s^{-1}, diffusion creep in the presence of 10 vol% melt would require higher differential stresses than dislocation creep with or without < 1 vol% melt (Fig. 4.21, curves 1-2 and 4). Conversely, the weakening associated with activation of diffusion creep in the fine-grained reaction products would be dramatic (Fig. 4.21, curve 5). The differential stress required to sustain strain rates of 10^{-12} – 10^{-13} s^{-1} in the mixture by

diffusion creep would be < 2 MPa, 2 - 3 orders of magnitude smaller than the stress required to deform the dry mafic dyke by dislocation creep, and also considerably smaller than the stress required to deform the coarse-grained (200 μm) dyke by melt-enhanced diffusion creep. Therefore, the most prominent rheological effect of melt infiltration is a marked weakening by grain size reduction through nucleation of fine-grained reaction products that trigger diffusion creep.

Assuming a differential stress of ca. 100 MPa during shearing (from estimates of Menegon et al., 2011 in adjacent metapelites), diffusion creep in the fine-grained mixture would occur at 2.5 - 3.5 orders of magnitude faster strain rates than dislocation creep and melt-assisted diffusion creep of the porphyroclasts. The strain rates imposed by the matrix may have been too high for recovery to keep pace, so that porphyroclasts could have undergone local fracturing and boudinage. Similar effects of grain size reduction and strain rate enhancements through activation of diffusion creep, leading to non-uniform flow in natural mylonites, have been identified by White (1996). In the dyke, fracturing porphyroclasts could be the result of local stress concentrations imposed by diffusion creep in the mixture, as well as by the high pore-fluid pressures during infiltration of 10 vol% of melt. In light of this, it is worth noting that inter- and intragranular fractures often contain thin layers of reaction products that were here interpreted as evidence of former melt pathways.

SUMMARY

In the Seiland Igneous Province (northern Norway), lower crustal shearing of dry mafic dykes was accompanied by infiltration of felsic melt from adjacent partially molten metapelites. Shearing and partial melting were coeval and occurred at T of 800° C and P ≥ 7 kbar. The microstructural and rheological evolution during shearing of dry mafic dykes infiltrated by melt can be summarized as follows:

Porphyroclasts deformed by dislocation glide (only minor climb) with slip system (100)[001] for orthopyroxene, a combination of {1-10}1/2<110>, {110}[001] and (100)[001] for clinopyroxene and a possible (010)[100] for plagioclase. SIMS results indicate that strongly elongated orthopyroxene porphyroclasts can contain less water than relatively equant clinopyroxenes, suggesting that intracrystalline water has little effect on crystal plasticity in pyroxenes. In clinopyroxene and plagioclase, dislocation glide was accompanied by fracturing and growth of new grains from fractured fragments to form intracrystalline bands of small (< 10 μm) grains. Lattice distortion, deformation twinning, and no pervasive subgrains development in porphyroclasts indicated that the bulk of the fine-grained polyphase aggregate did not form by dynamic recrystallization, but rather by a combination of fracturing and melt-triggered chemical reactions.

Melt infiltration played an important role in the deformation of the mafic dyke, triggering chemical reactions and forming the bulk of the fine-grained polyphase aggregate. Thermodynamic models simulating chemical mixing of the pristine mafic dyke with felsic melt showed that ca. 10 vol% melt infiltration in the mafic dyke is capable of nucleating the observed fine-grained mixture of clinopyroxene + orthopyroxene + plagioclase +

quartz + ilmenite ± K-feldspar ± apatite. The fine-grained mixture (4-7 µm average grain size) formed interconnected weak layers that deformed by diffusion creep. The weak CPO of orthopyroxene, clinopyroxene and plagioclase is explained by oriented growth during diffusion creep, whereas quartz was found to deform dominantly by dislocation glide on the prism <a> slip system.

Rheological calculations of the mafic dyke, using appropriate flow laws for melt-present systems, showed that grain size reduction by melt-assisted chemical reactions is by far the most efficient weakening mechanism. Weakening due to grain size reduction largely exceeds that of melt-enhanced diffusion creep of an original coarse-grained dyke infiltrated by up to 10 vol% melt. This highlights the importance of grain size reduction relative to melt-enhanced diffusion creep alone (i.e. without the formation of the fine-grained aggregate).

5 CASE STUDY 2: THE PROVOLA SHEAR ZONE IN THE FINERO MAFIC COMPLEX (ITALIAN ALPS)

The second case study investigates a high-temperature shear zone hosted in the Finero mafic complex in the Ivrea-Verbano Zone, western Southern Alps (Italy). The Ivrea-Verbano zone is renown worldwide as one of the best preserved examples of continental lower crust which has experienced magmatic underplating (Quick et al., 1994, 2003; Rivalenti et al., 1975; Sinigoi et al., 1994; Voshage et al., 1990), and is one of the best natural laboratories to study the deformation processes active at lower crustal-upper mantle conditions (Brodie, 1980; Brodie and Rutter, 1985, 1987a; Kaczmarek and Tommasi, 2011; Kenkmann and Dresen, 2002; Mancktelow et al., 2002; Matysiak and Trepmann, 2012, 2015, Rutter et al., 2007, 1993, 2001; Stünitz, 1998; Tommasi et al., 2017; Ullemeyer et al., 2010).

5.1 GEOLOGICAL SETTING: THE IVREA ZONE AND THE FINERO MAFIC COMPLEX

The Ivrea-Verbano zone is a sliver of continental lower crust of the Adriatic plate, outcropping in the western Southern Alps (e.g. Schmid et al., 2004). It is bounded to the W-NW by the Insubric line, a section of the Periadriatic lineament (Schmid, 1993; Schmid et al., 2004), and to the E-SE by the Cossato-Mergozzo-Brissago (CMB) line, a regional shear zone of Permian age (Boriani et al., 1990a; Mulch et al., 2002) (Fig. 5.1). The Insubric line is a major Alpine structure which delimits the Southern Alps, of which the Ivrea-Verbano zone represents its continental lower basement, from the Austroalpine domain (e.g. Schmid et al., 2004). The CMB delimits the Ivrea-Verbano zone lower crustal units

from the adjacent Serie dei Laghi upper crustal units (Boriani et al., 1990a, 1990b). Part of the Ivrea-Verbano zone and the CMB line are truncated by the Pogallo line, interpreted as an extensional mid-crustal shear zone active in the Late Triassic - Early Jurassic (182Ma) (Mulch et al., 2002; Schmid et al., 1987) (Fig. 5.1).

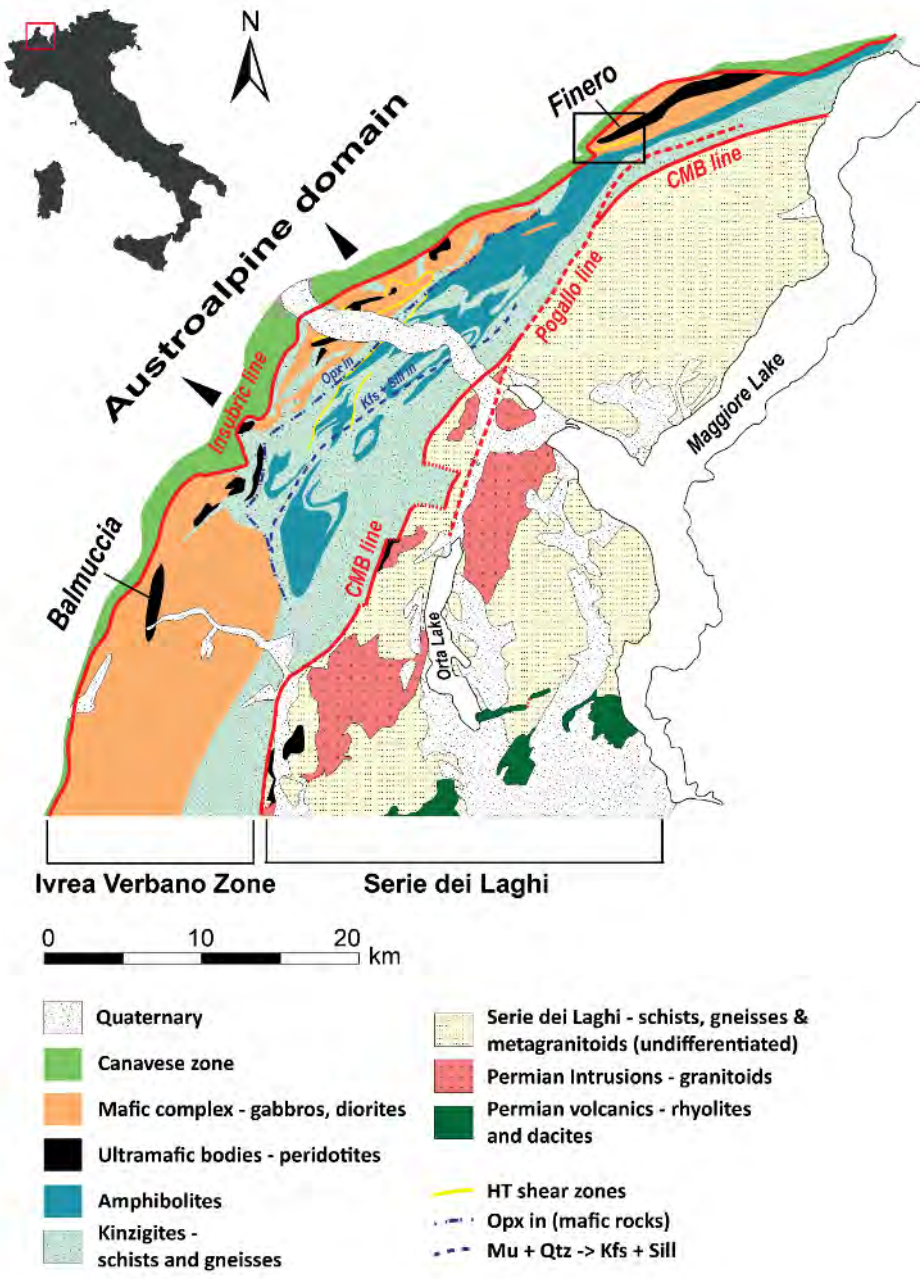

Fig. 5.1

Fig. 5.1 (previous page)

Simplified geological map of the Ivrea Zone, South-western Italian Alps, modified after Rutter et al. (2007) and references therein (central area), Boriani et al. (1995) (north-western area), Boriani and Giobbi (2004) (Serie dei Laghi) and Quick et al. (2009) (south-western area). The map shows the most important structural and lithological divisions. Study area (Fig. 5.2) is boxed. This map was compiled using Esri ArcGIS and later modified.

Internally, the Ivrea-Verbano Zone is subdivided into three main units: 1) the Kinzigite Formation, a metasedimentary sequence which comprises high-grade schists, paragneisses, amphibolites and calc-silicate rocks, 2) the Mafic Complex, a belt of mafic and ultramafic lithologies (mostly gabbroic-dioritic, with some ultramafic cumulates) (Rivalenti et al. 1975) and 3) the mantle peridotite lenses, preserved in the structurally deeper portions of the Mafic Complex near the Insubric Line (Quick et al., 1995; Rivalenti et al., 1975; Zingg et al., 1990) (Fig. 5.1). The Kinzigite formation represents the high-grade metasedimentary lower crustal basement, intruded by the gabbroic magmas of the Mafic Complex during the Permian magmatic event, at 300-280Ma (Peressini et al., 2007 and references therein). The peridotitic bodies are fault-bonded mantle slices tectonically incorporated in the lower crust (Quick et al., 1995).

The timings and kinematics of uplift, tilting and exposure of the Ivrea-Verbano to its current position are still under debate (for an overview, see Wolff et al., 2012). Traditionally, tilting and exhumation of the sequence has been explained as the result of polyphase Alpine transpressional tectonics, mostly along the Insubric Line (Handy and Zingg, 1991). However, more recent models explain the current configuration as the combined result of Mesozoic rift-related crustal thinning followed by Alpine continental collision, thereby recognising the importance of rift-inheritance (and hence of rift-related

structures) for the present-day architecture of the Alps (Beltrando et al., 2015; Mohn et al., 2014; Rutter et al., 2007; Wolff et al., 2012). The Finero mafic complex is the northernmost part of the mafic-ultramafic belt of the Ivrea-Verbano Zone (Quick et al., 2003; Rivalenti et al., 1981; Zingg, 1983) (Fig. 5.1). The complex is ca. 12 km long and 3 km wide (Steck and Tieche, 1976). In the Finero area, the complex forms an antiformal structure (Boriani et al., 1995; Steck and Tieche, 1976) which encloses a mantle peridotite body at its core, known as the Phlogopite Peridotite (Lu et al., 1997a; Siena and Coltorti, 1989; Zanetti et al., 2016). The complex is truncated in the NW by the Insubric Line, and grades in the SE into amphibolites, schists and gneisses of the metasedimentary Kinzigite formation (Fig. 5.1 and Fig. 5.2). More to the SE, the crustal sequence is truncated by the (presumed) Pogallo line and the CMB line. The metamorphic grade decreases steadily from granulite facies near the Insubric Line, to amphibolite facies towards the SE (e.g. Handy and Zingg, 1991; Kenkmann, 2000).

Fig. 5.2 (next page)

(a) Simplified geological map of the Finero mafic and ultramafic complex (after Boriani et al., 1995) showing the internal structural divisions and extent of the Provola shear zone in the study area. High strain domains, corresponding to the shear zone, are marked with dashed lines; the regional metamorphic fabric is marked with crosses. Stars indicate locations of profiles L12 and L32 (Fig. 5.5). Structural measurements (foliation dip-direction/dip and stretching lineation trend/plunge) are plotted in the stereonet insets (lower hemisphere, equal area projection; foliation as great circles; lineation as points); mean vectors of foliation (Fol.) and lineation (Lin.) are given below with n being the number of measurements. The main road, SP 75, is shown in yellow; the Cannobino stream in blue. Sample locations are shown in (b). GPS coordinates of sample location and structural measurements are given in the Appendix, Appx. 1. These maps were compiled using Esri ArcGIS, and subsequently modified to incorporate structural measurements and sample locations. Contour lines with elevation (meters above sea level) are shown in grey.

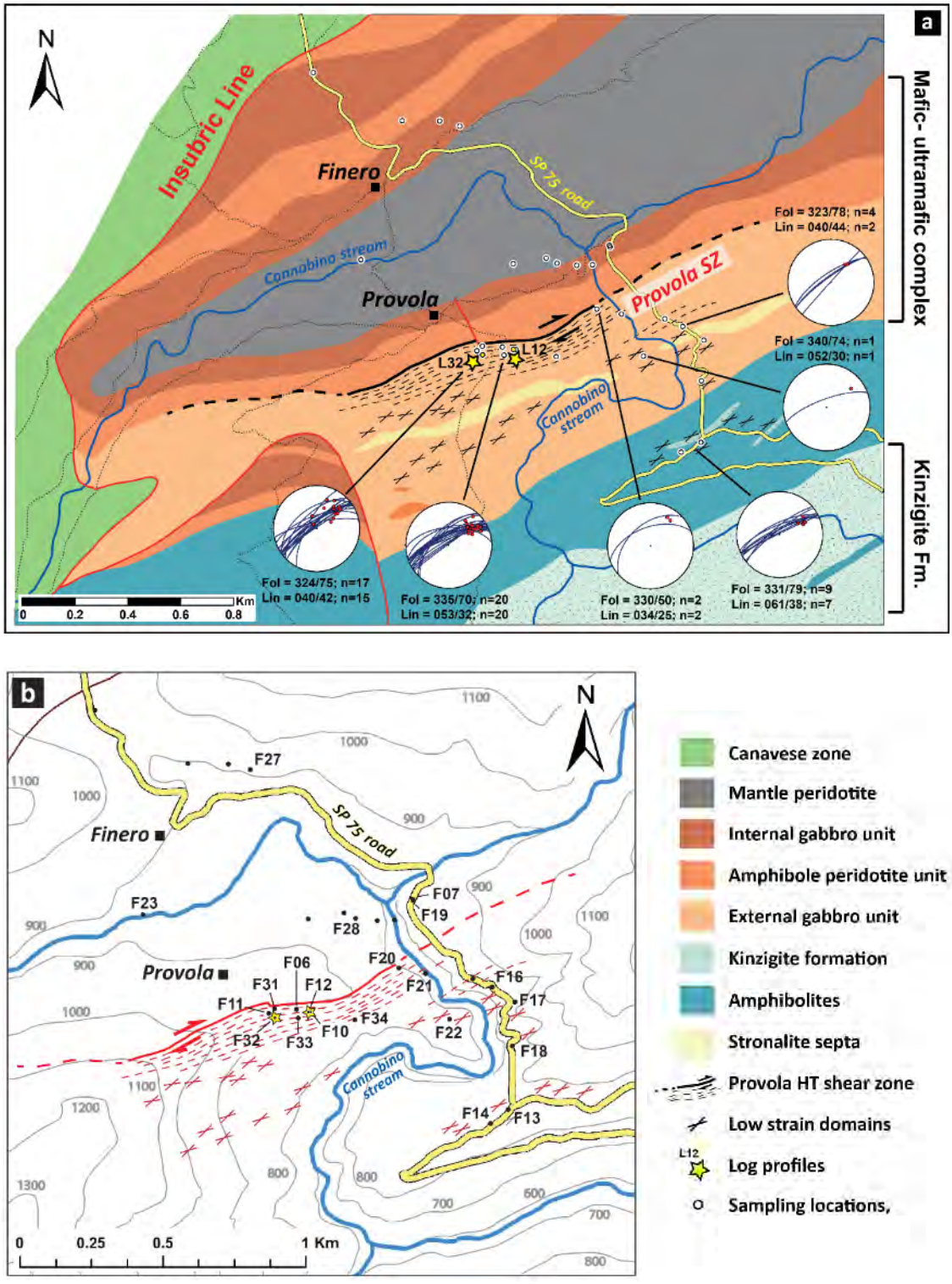
a
N
Insubric Line
Finero
SP 75 road
Cannobino stream
Provola
Provola SZ
L32
L12
Fol = 323/78; n=4
Lin = 040/44; n=2
Fol = 340/74; n=1
Lin = 052/30; n=1
Mafic- ultramafic complex
Kinzigite Fm.
Fol = 324/75; n=17
Lin = 040/42; n=15
Fol = 335/70; n=20
Lin = 053/32; n=20
Fol = 330/50; n=2
Lin = 034/25; n=2
Fol = 331/79; n=9
Lin = 061/38; n=7
Km
0 0.2 0.4 0.6 0.8
b
N
F27
Finero
SP 75 road
F23
F28
F07
F19
Provola
F06
F20
F31
F12
F21
F16
F11
F17
F34
F10
F22
F32
F33
F18
Cannobino stream
F14
F13
1100
1000
900
1200
1300
800
700
600
0 0.25 0.5 1 Km
Canavese zone
Mantle peridotite
Internal gabbro unit
Amphibole peridotite unit
External gabbro unit
Kinzigite formation
Amphibolites
Stronalite septa
Provola HT shear zone
Low strain domains
L12
Log profiles
Sampling locations,

Fig. 5.2

The internal architecture of the Finero mafic complex is divided in three units, comprising from base to top: 1) the Internal Gabbro (also known as the Layered Internal Zone), 2) the Amphibole Periodotite, and 3) the External Gabbro (Lu et al., 1997a; Zanetti et al., 2013- after Siena and Coltorti, 1989; U-Pb zircon age of 232 ± 3 Ma: Zanetti et al., 2013) (Fig. 5.2). The Internal Gabbro is a layered sequence of garnet-amphibole metagabbros, garnet hornblendites, pyroxenites, anorthosites and peridotites. The Amphibole Peridotite unit is a thick (ca. 300 m) sequence of amphibole bearing peridotites with subordinate pyroxenites and hornblendites; whereas the External Gabbro predominantly alternates amphibole-rich metagabbros with amphibole-poor metagabbros (for more details, see Langone et al., 2017). After emplacement in the lower crust, the complex experienced granulite-facies metamorphic re-equilibration (Sills, 1984; Steck and Tieche, 1976). The Internal Gabbro and the Amphibole Peridotite together preserve a cumulate nature: they are coarse grained, have a strong compositional layering, and are mostly undeformed. The External Gabbro instead is heterogeneously deformed and contains an anastomosing high-T shear zone, which is particularly well exposed near the village of Provola (Kenkmann, 2000; Kenkmann and Dresen, 2002; Mancktelow et al., 2002) and thus will be referred to as the Provola shear zone. The Provola shear zone is one of the high-T shear zones preserved in the lower crust that were first identified and characterized in the Ivrea Zone by Brodie and Rutter (Brodie, 1981; Brodie and Rutter, 1985, 1987b, 1987a; Rutter et al., 2007) and later investigated by a number of other authors (e.g. Kenkmann, 2000; Kenkmann and Dresen, 2002; Mancktelow et al., 2002; Snoke et al., 1999; Stünitz, 1998).

5.2 THE ANATOMY OF THE PROVOLA SHEAR ZONE: FIELD OBSERVATIONS

Field observations come from the south-western portion of the Finero mafic complex, covering an area ca. 1 km along and across strike SE of the village of Provola (Fig. 5.2a). This area displays readily accessible glacially polished outcrops, whereas east of the main provincial road SP-75 the outcrops are less accessible due to steep topography combined with thick vegetation (Fig. 5.3).

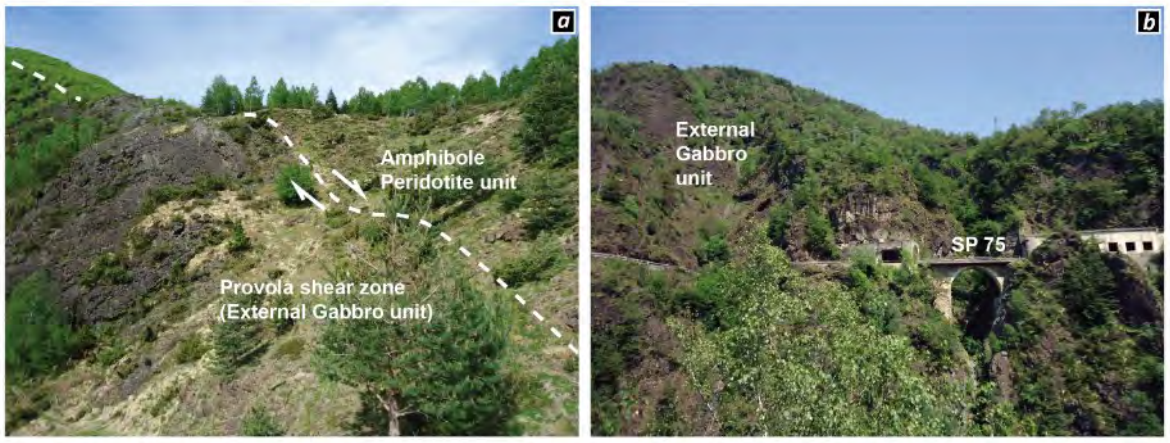

Fig. 5.3

(a) Panoramic view of the contact between the Amphibole Peridotite unit and the External Gabbro unit; UTM 32T 464483 E 5105408 N, looking W. (b) Panoramic view of the provincial road SP75 from across the Cannobino stream; UTM 32T 465016 E 5105374 N, looking E.

The Provola shear zone develops in the structurally-lowermost part of the External Gabbro unit, at the contact with the weakly deformed amphibole-peridotite unit of the mafic complex (Fig. 5.2a, and Fig. 5.4). Its northern boundary follows the contact with the Amphibole Peridotite unit, whereas its southern boundary is harder to assess due to its

anastomosing geometry. From field observations and sampling, the overall thickness of the shear zone (including low-strain lenses) is estimated to be approximately between 50 and 100 m. The Provola shear zone is a dextral shear zone with moderately plunging lineation (trend/plunge 046/36°, mean vector) and steeply dipping foliation (dip direction/dip 333/70°, mean vector) (for details, see Appendix, Appx. 1). The shear zone reworks both the mafic lithologies of the layered complex, and displays anastomosing patterns of (ultra)mylonitic high strain zones wrapping less foliated, weakly deformed low strain domains (Fig. 5.4).

The shear zone exploited the original compositional layering of the External Gabbro, which is locally defined by the alternation between amphibole-poor and amphibole-rich layers (Fig. 5.4). The reworking of the layered metagabbros results in a heterogeneously deformed sequence, where ultramylonitic high-strain zones preferentially localized in amphibole-rich layers (Fig. 5.4 and Fig. 5.5). Amphibole-rich and amphibole-poor domains responded differently to deformation, resulting in mineralogically-controlled strain partitioning and strain localization. This layering allows to study the shearing evolution from the incipient stages of deformation preserved in the low-strain domains to the evolved stages of deformation in the ultramylonitic layers.

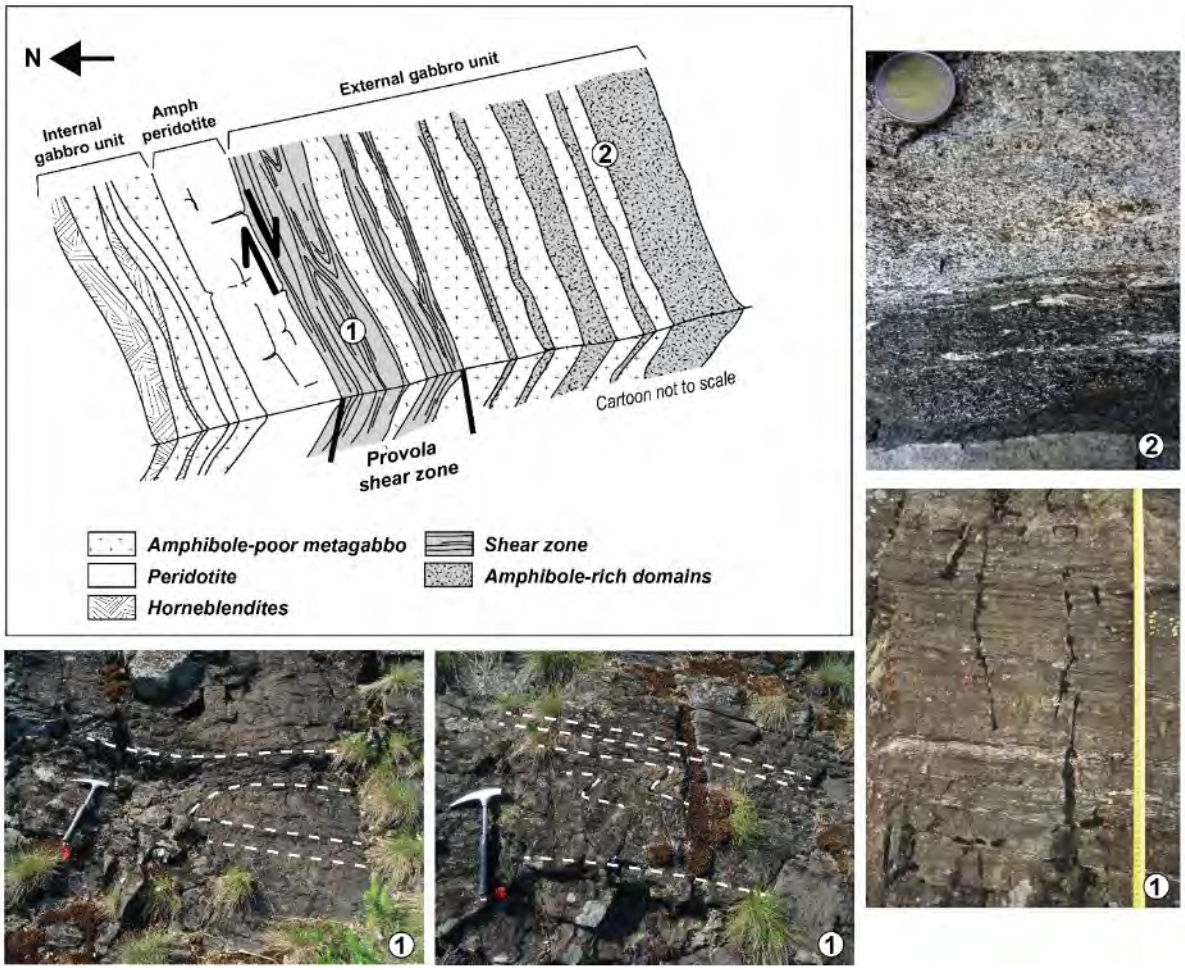

Fig. 5.4

Schematic structure (not to scale) and field photos illustrating the strain partitioning within the Finero mafic complex, with the Provola shear zone reworking the External Gabbro unit. The Provola shear zone, labelled (1) resides in the structurally-lowermost part of the External Gabbro unit, at the contact with the weakly deformed Amphibole Peridotite unit. The shear zone has an anastomosing pattern, with low-strain domains preserved as lenses within high-strain domains. The External Gabbro unit which hosts the Provola shear zone, labelled (2) is mainly a layered sequence of amphibole-rich and amphibole-poor metagabbros. The External Gabbro unit becomes progressively richer in amphibole going towards higher structural levels.

In the field, the shear zone outcrops as dark-brown/grey foliated rocks (Fig. 5.4). In the low-strain domains of the shear zone, the two metagabbroic lithologies display a rather similar protomylonitic texture with the main difference being the presence or absence of

amphibole, which is identifiable by its black colour and characteristic cleavage. In high-strain zones, the distinction between the two lithologies is more challenging due to reduced grain size and similar dark colours. Nevertheless, the two domains can still be recognised based on a number of characteristics. These were used to discern the different sheared layers in the field and construct schematic profiles of the shear zone (Fig. 5.5).

Amphibole-poor metagabbros are generally coarser-grained than their amphibole-rich counterparts, giving the rock a granular appearance. High-strain zones in amphibole-poor metagabbros commonly consist of banded mylonites, where plagioclase layers wrap around pyroxene-rich domains (Fig. 5.5, samples F12A, F12D, F32A, F32C; thin sections scans in the Appendix, Appx. 2). Thick packages of amphibole-poor metagabbros are intercalated by dark (almost black in outcrop) mm-to-cm thick amphibole-rich ultramylonitic levels, characterized by amphibole porphyroclasts in a homogeneous matrix not resolvable with the naked eye (Fig. 5.5, samples F12D, F32C, thin sections scans in the Appendix, Appx. 2). In addition, amphibole-poor domains are generally abundant in garnet porphyroclasts of variable sizes.

On the contrary, fine-grained, dark ultramylonites are very common in amphibole-rich layers (Fig. 5.5, samples F12F, F12E top, F12C, F10A3 thin sections scans in the Appendix, Appx. 2). As for the dark ultramylonitic intercalations in the amphibole-poor domains, the ultramylonite layers in the amphibole-rich domains are characterized by a fine-grained matrix not resolvable with the naked eye, which embeds isolated porphyroclasts of amphiboles, garnets and pyroxenes. Amphibole porphyroclasts are particularly useful to recognise this domain in the field, as they stand out from the homogeneous grey matrix

as black grains. Plagioclase does not wrap around pyroxene, but instead occurs as mm-thick ribbons elongate parallel to the ultramylonitic foliation (e.g. sample F12F). Garnets tend to concentrate in discrete bands parallel to the foliation, where they are found associated with plagioclase to make garnet-plagioclase lenses (Fig. 5.5, samples F12E, F10A3, F32C, blue arrows). Locally, amphibole ultramylonites grade into plagioclase-rich ultramylonites where amphibole is subordinate. The latter transition is easy to identify in the field, as the alternating sequence of dark amphibole and white plagioclase resembles a zebra-like pattern (Fig. 5.5, sample F10A1). Local greenschist facies overprint reworks the ultramylonites forming thin cataclasites layers that disrupt and rotate portions of the ultramylonitic foliation. These zones can be identified in the field by their light-grey/light-green tinge.

Fig. 5.5 (next pages)

Representative profiles across strike of the Provola shear zone, with corresponding field photos and samples. Thin-sections scans of the samples are shown next to the profiles. Amphibole-rich domains are marked with red arrows, amphibole-poor metagabbros with yellow arrows, and garnet bands with blue arrows. For way-point GPS coordinates, see Appendix, Appx. 1. See to text for further details.

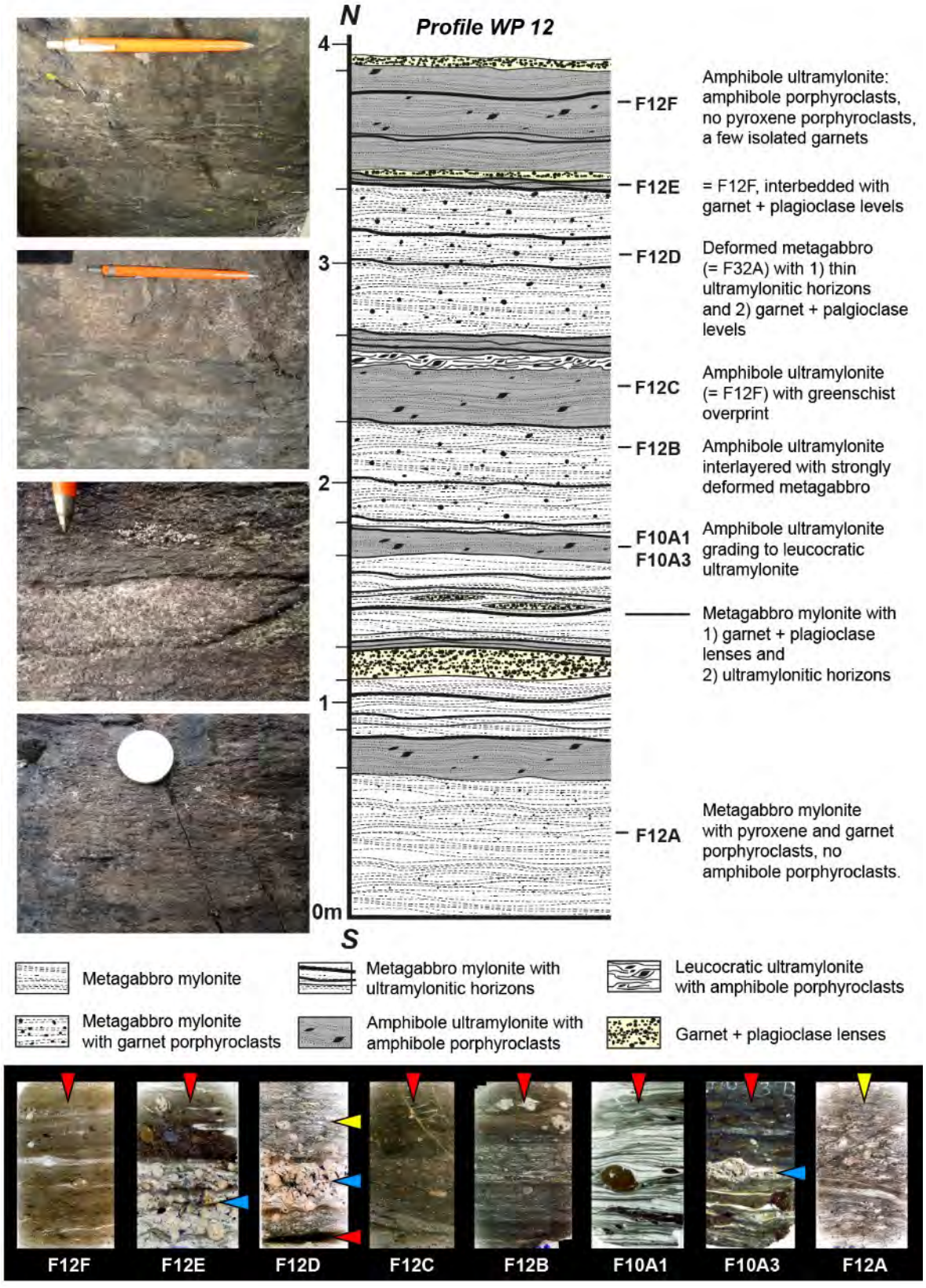

Fig. 5.5 (continued on next page)

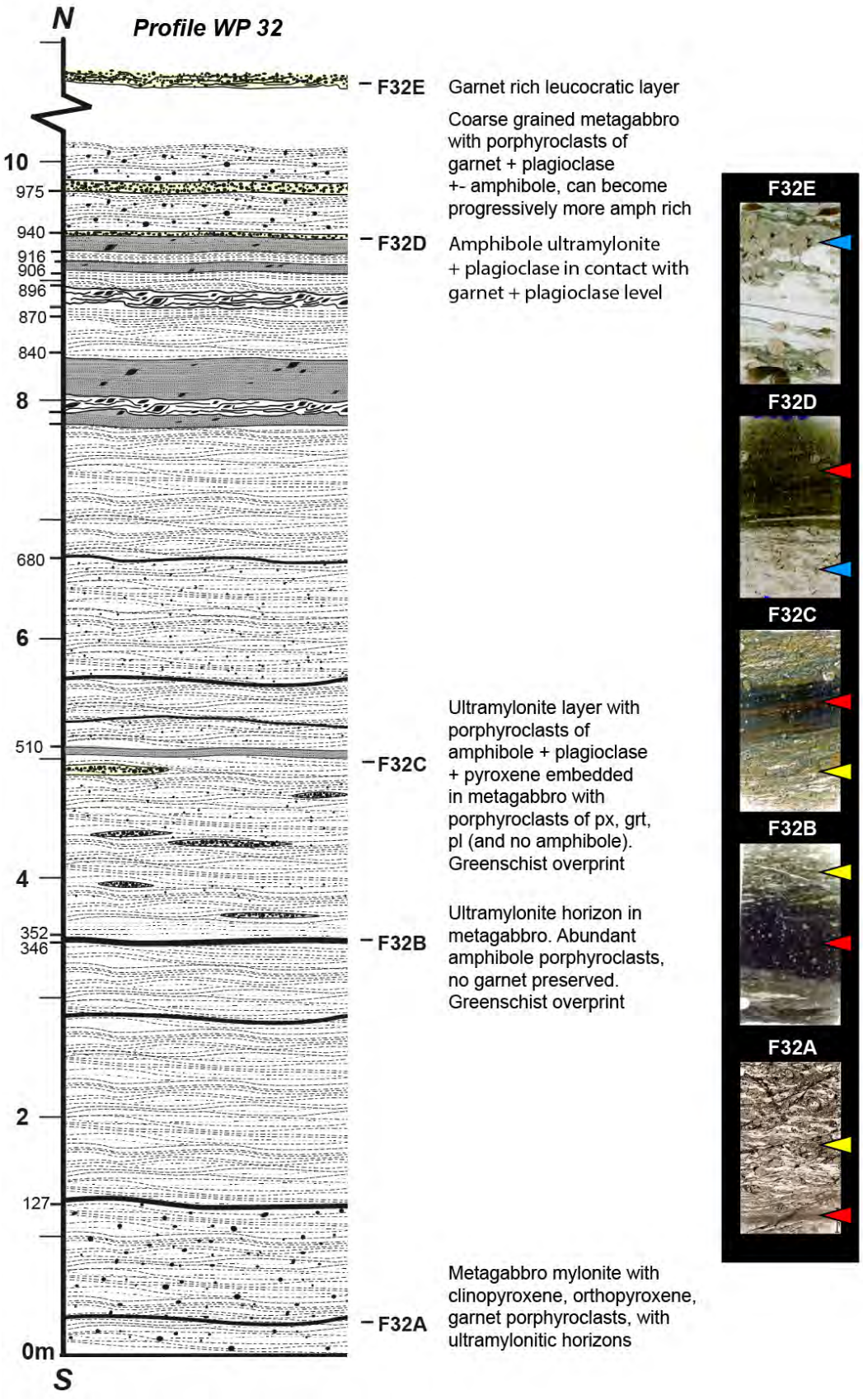

Fig. 5.5 (2nd page)

5.3 MICROSTRUCTURAL DOMAINS

Field observations indicate that high-strain ultramylonitic shear zones preferentially developed from an amphibole-rich protolith. At the scale of thin section, amphibole-rich domains can be identified by the widespread occurrence of amphibole *porphyroclasts*, which are lacking in amphibole-poor domains. Thus, in order to investigate the different microstructural evolution and rheological behaviour of amphibole-poor and amphibole-rich metagabbros, strain gradients in the two lithologies have been analysed separately and compared.

Based on mineralogical and microstructural criteria, four samples have been selected as representative of the deformation of the amphibole-poor metagabbroic domain: F22, F32A (mylonite portion), F10B (Fig. 5.6) and F20A (mylonite portion). Likewise, three samples were selected as representative of the deformation of the amphibole-rich domain: F33, F20A (ultramylonite portion) (Fig. 5.7) and F32A (ultramylonite portion). These variably deformed samples record different stages of microstructural evolution during shearing. Some samples (i.e. F20A and F32A) were sampled across the two domains and so contain both mylonites and ultramylonites, the former deriving from the amphibole-poor domain and the latter from the amphibole-rich domain. Scans of the complete thin sections are provided in the Appendix, Appx. 2, and a summary table describing the main features of the key samples is given in Table 5.1.

Table 5.1. Reference table summarising the key samples analysed and described in the following sections. Figures are cross-referenced for quick access.

Layer	Sample	Microstructure	Mineralogy	CPO		Def. mechanism
Amphibole-poor metagabbro	**F22 (protomylonite)** Fig. 5.6a Fig. 5.8 Fig. 5.9	Protomylonite with weak foliation, elongated Pl lenses alternating with porphyroclasts of Cpx, Opx and Grt and rare Am. Grt porphyroclasts are rimmed by Opx + Pl symplectites.	**Porphyroclasts:** Pl, Cpx, Opx, Grt, rare Am Ilm, Mt abundant in pressure shadows and shear bands	N.A.		Pl showing optical evidence of crystal plasticity + dynamic recrystallization. Opx elongated,
Amphibole-poor metagabbro	**F20A (mylonite)** Fig. 5.10 Fig. 5.11 **F32A (mylonite)** Fig. 5.6b Fig. 5.12 **F10B (mylonite)** Fig. 5.6c	Banded mylonite, made of alternating layers of Pl and Cpx. Pl is recrystallized. 2 generations of Cpx and Opx: porphyroclastic and neoblastic. Grt porphyroclasts are rimmed by Opx + Pl symplectites (Fig. 5.12d).	**Plagioclase layers:** Pl **Pyroxene layers:** Cpx (porphyro + neoblasts), Opx (porphyro + neoblasts), Mt, Ilm and Am between neoblasts **Porphyroclasts:** Grt, Cpx, Opx	**Plagioclase layer:** Fig. 5.31	Planes // fol. (010), (110), (011), (111) Dir // lin. [11-1], [-11-1], [01-1], [10-1] [100], [001]	Dislocation creep on multiple slip systems. Elongated grains consistent with slip system (010)[001].
				Pyroxene layer: Fig. 5.32	**Cpx:** [100] // to Y, (010) and (001) planes forming girdles. **Dispersed Am:** Planes // fol. (100) Dir // lin. [001]	No obvious slip system. Instead, evidence of microfracturing and neocrystallization

Table 5.1 (continued on next page)

Table 5.1 (2nd page)

Amphibole-rich metagabbro	**F33 (protomylonite)** Fig. 5.7a Fig. 5.14	Protomylonite with weak foliation, elongated lenses of Pl alternating with porphyroclasts of Cpx, Am, Grt and Opx. Am porphyroclasts are abundant, and are rimmed by Opx + Pl symplectites (Fig. 5.15).	**Porphyroclasts:** Pl, Am, Cpx, Opx, Grt, Ilm, Mt abundant in pressure shadows and shear bands	N.A.		Pl showing optical evidence of crystal plasticity + dynamic recrystallization. Am with limited fracturing and undulose extinction. No optical evidence of subgrain development in Am.
Amphibole-rich metagabbro	**F20A (ultramylonite)** Fig. 5.7b Fig. 5.18 Fig. 5.19 Fig. 5.20 **F32A (ultramylonite)** Fig. 5.18e Fig. 5.19	Ultramylonite made of a fine grained matrix of Pl, Cpx, Am, Opx, Mt, Ilm ± Ap, embedding large porphyroclasts of Am, Grt and Cpx. Am porphyroclasts are rimmed by Opx + Pl ± Am symplectites or Cpx + Pl ± Am symplectites (Fig. 5.22). Grt porphyroclasts are rimmed by Opx + Pl symplectites (Fig. 5.21).	**Ultramylonitic matrix:** Pl + Am + Cpx + Opx + Mt + Ilm ± Ap **Porphyroclasts:** Am, Grt, Cpx, rare Pl	**Plagioclase** Fig. 5.33	Planes // fol. (011), (111), minor (110) Dir // lin. [01-1], [-11-1], [11-1]	Diffusion creep + anisotrophic grain growth
				Amphibole Fig. 5.33 Fig. 5.34	Planes // fol. (100) Dir // lin. [001]	
				Clinopyroxene Fig. 5.33	Planes // fol. No main plane Dir // lin. No main direction	
				Orthopyroxene Fig. 5.33	Planes // fol. No main plane Dir // lin. No main direction	

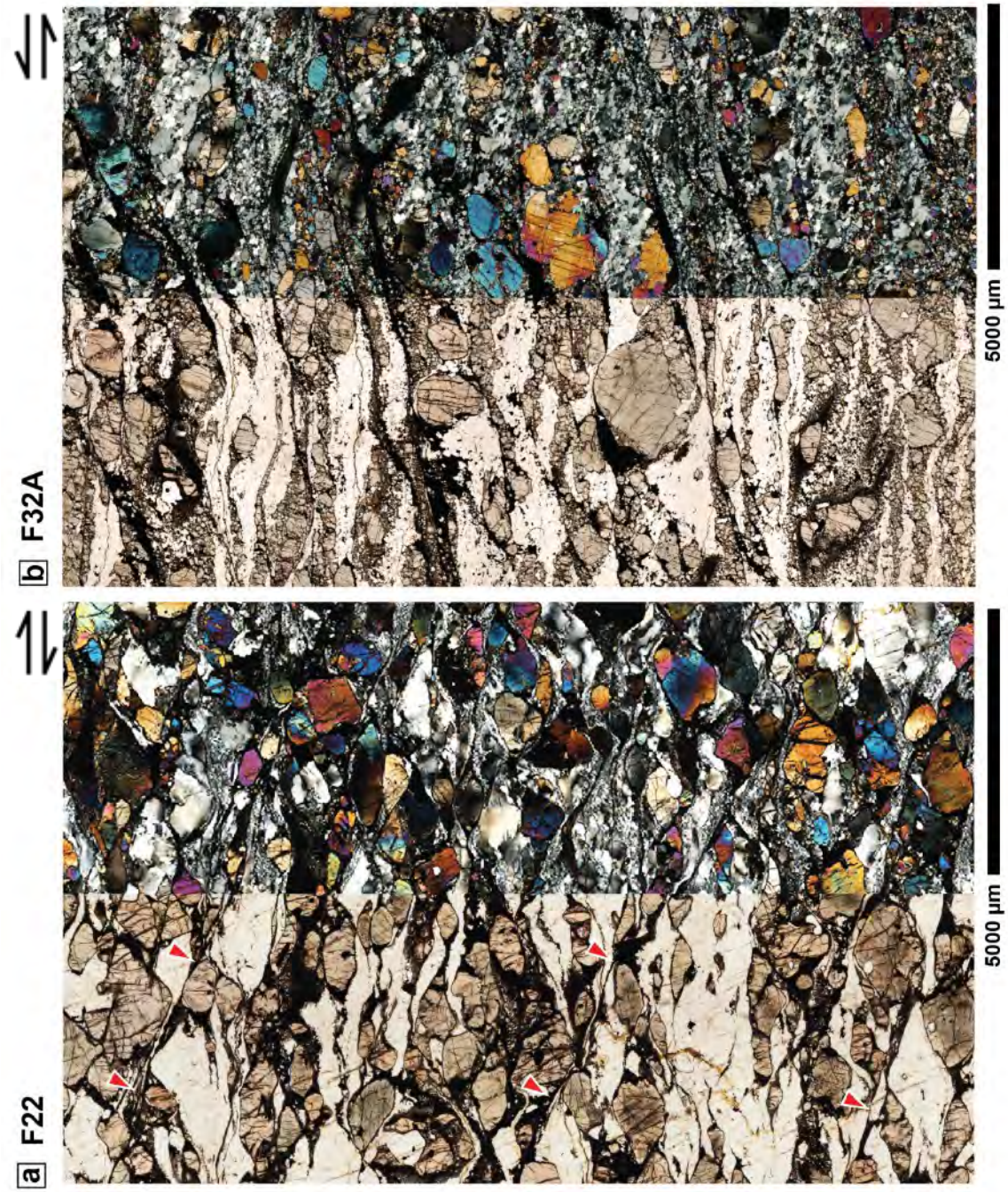

Fig. 5.6 (continue on next page)

Amphibole-poor domains. Light microscope images of portions of thin sections in plane polarised light (left) and in cross polars (right). (a) protomylonite sample F22; red arrows point to shear bands. (b) mylonite sample F32A (c) mylonite sample F10B.

Fig. 5.6 (2nd page)

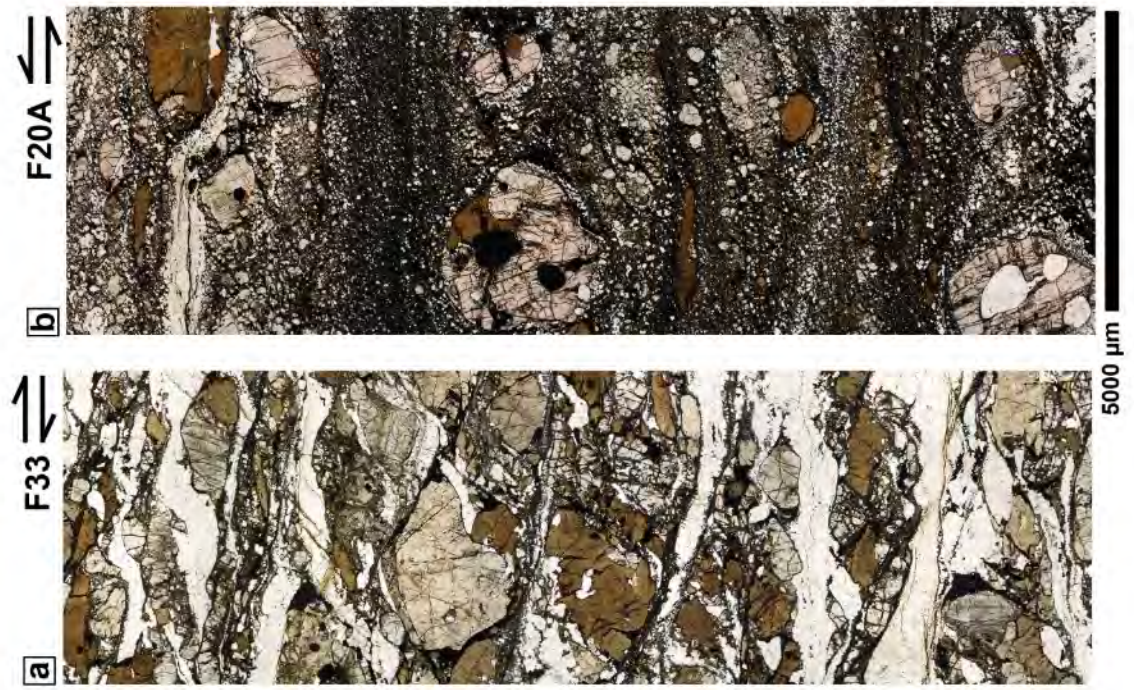

Fig. 5.7

Amphibole-rich domains. Light microscope images of portions of thin sections; in plane polarised light. (a) protomylonite sample F33 (b) ultramylonite sample F20A.

*5.3.1 AMPHIBOLE-POOR META*GABBROS

Protomylonites

Sample F22 (and sample F33, top portion) is the typical amphibole-poor metagabbro in its protomylonitic stage Fig. 5.6a; thin sections in Appendix, Appx. 2). This type of protomylonite is preserved in low strain domains (lenses) within the shear zone, and provides a snapshot of the starting material prior to deformation. The protomylonites deriving from amphibole-poor metagabbros are composed of plagioclase, clinopyroxene, orthopyroxene, garnet, magnetite and ilmenite. Pyroxene (clino and ortho), plagioclase and garnet form 55%, 40% and 4% of the porphyroclast area fraction of the rock, respectively. Amphibole is very rare (2% area fraction where most abundant), and is limited to local and isolated porphyroclasts or rare inclusions in pyroxenes.

The protomylonite is characterized by a weak foliation defined by polycrystalline elongated lenses of plagioclase that alternate with porphyroclasts of pyroxene and garnet (Fig. 5.6a and Fig. 5.8). C' shear bands, defined by a fine-grained assemblage of plagioclase, orthopyroxene, clinopyroxene, amphibole, and Fe-Ti oxides cut across the sample (Fig. 5.6a, and Fig. 5.8d-f, red arrows).

Except in C' shear bands, plagioclase forms essentially monophase ribbons where phase mixing is very limited. In such ribbons, plagioclase occurs as lenticular porphyroclasts displaying undulose extinctions and subgrains, surrounded by mantles of recrystallized grains (Fig. 5.8e-f). Intense grain size reduction is observed along the rims of plagioclase porphyroclasts' and in proximity of shear bands (Fig. 5.8c-f).

Orthopyroxene and clinopyroxene porphyroclasts show undulose extinction and no evidence of dynamic recrystallization or subgrain development (Fig. 5.8b-c). Instead, they are rimmed by some tens of μm thick aggregates of pyroxene + plagioclase + magnetite ± quartz (local), that in places join to form interconnected shear bands (Fig. 5.9e-f).

Garnet porphyroclasts are poikiloblastic with inclusions of plagioclase, clinopyroxene and ilmenite (Fig. 5.8a and Fig. 5.9b-c). They are characterized by a rim of symplectic orthopyroxene + plagioclase (symplectites are fine grained intergrowths of two or more phases) that is distributed also along the foliation (Fig. 5.9b-d). The rare amphibole porphyroclasts are characterized by a symplectic reaction rim of clinopyroxene + orthopyroxene + plagioclase ± Fe-Ti oxides ± amphibole (Fig. 5.9 g-h). Magnetite and to a lesser extent ilmenite concentrate along the pressure shadows of porphyroclasts and along shear bands (Fig. 5.6 and Fig. 5.8b-d).

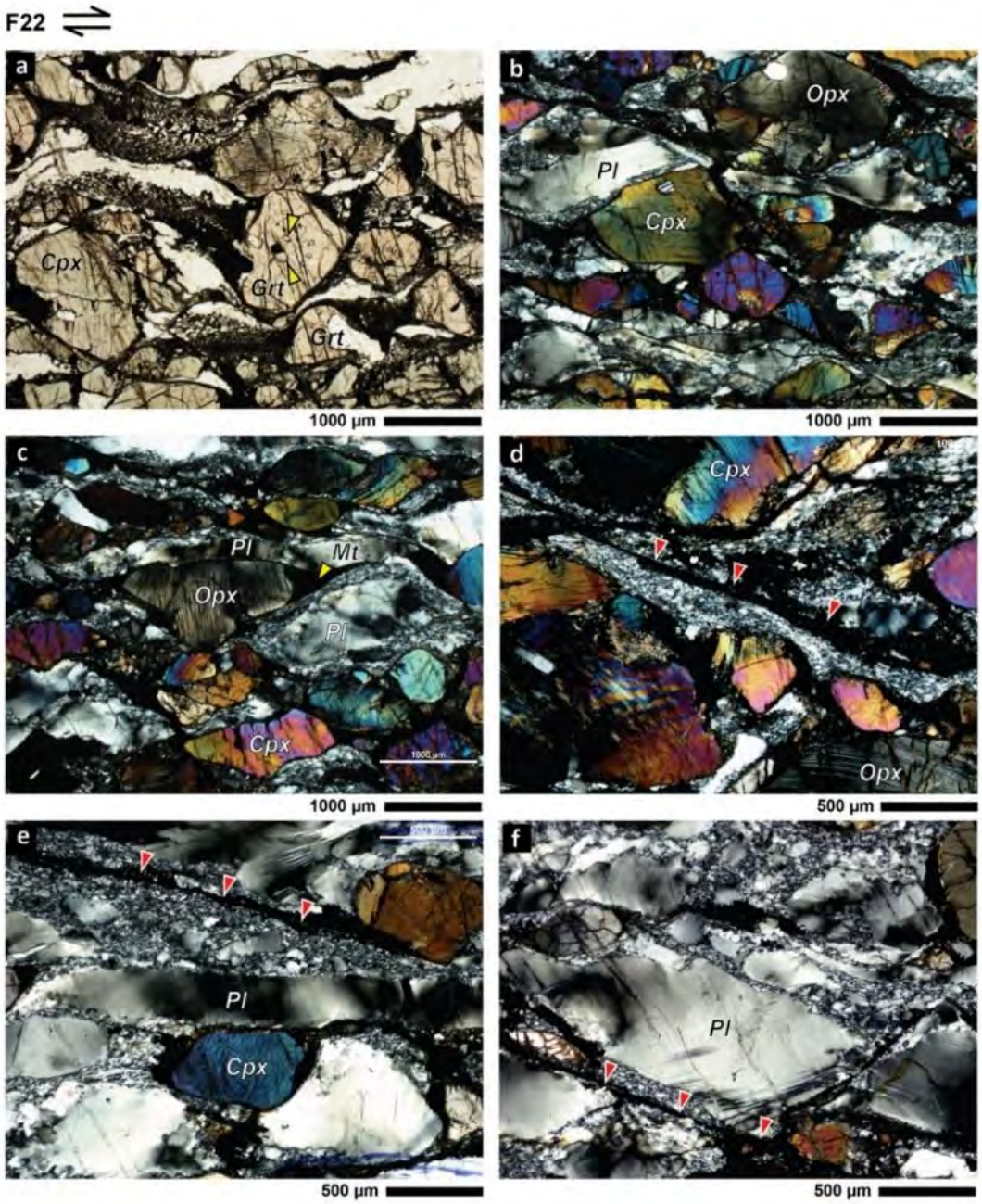

Fig. 5.8

Light microscope images of sample F22, showing the typical microstructure of amphibole-poor metagabbroic protomylonites; dextral sense of shear. Image (a) in plane polarised light; images (b-f) in crossed polars. (a) Garnet porphyroclasts with inclusions of clinopyroxene, ilmenite and plagioclase (yellow arrows); (b-c) Lenticular orthopyroxene and clinopyroxene porphyroclasts showing undulose extinction and no evidence of dynamic recrystallization or subgrains. Note the magnetite concentration along porphryoclasts' strain shadows (yellow arrow). (d-e) C' shear bands of fine grained material and oxides (red arrows). (e-f) Lenticular to elongated plagioclase porphyroclasts, surrounded by a matrix of recrystallized plagioclase.

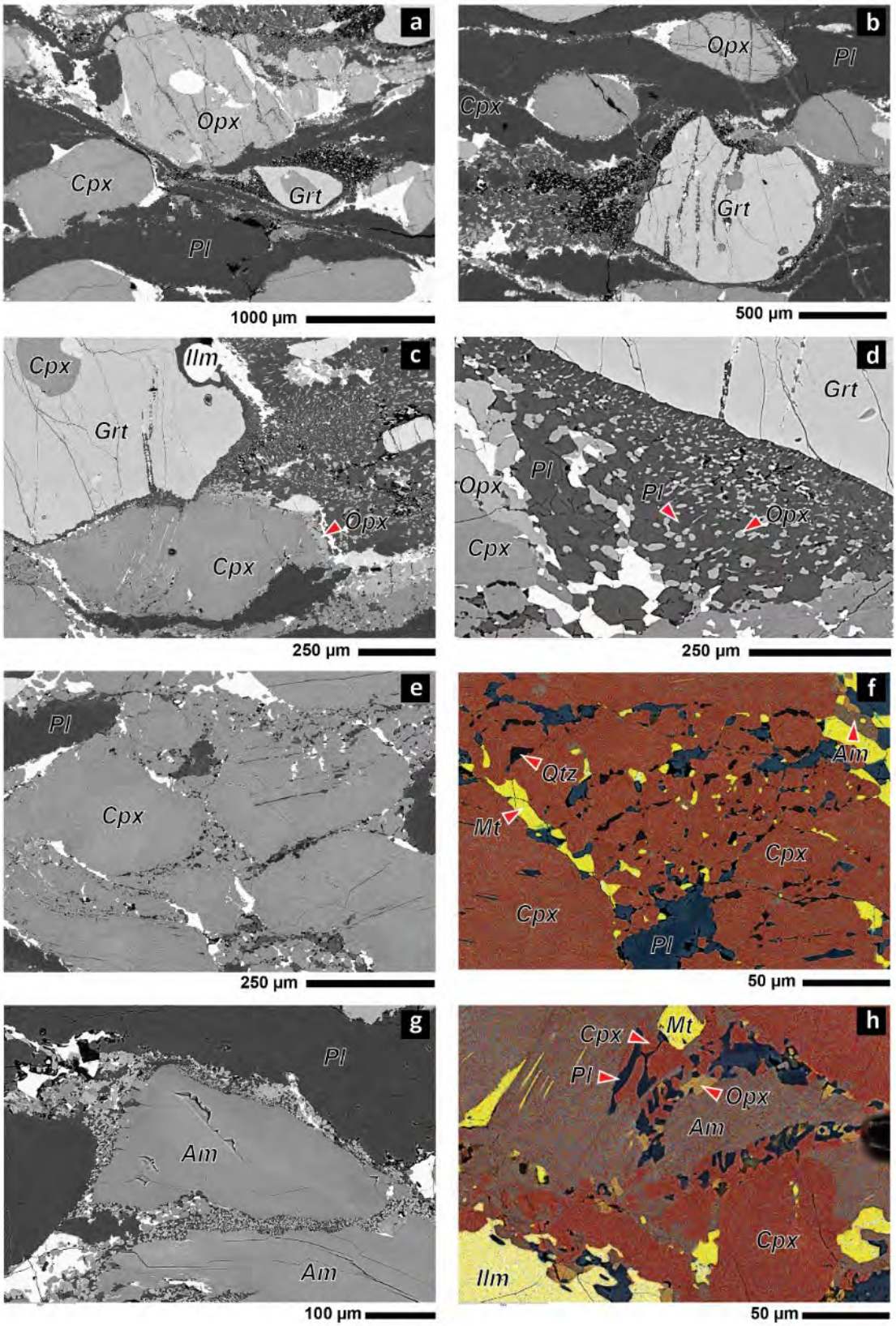
a
Opx
Cpx
Grt
Pl
1000 µm
b
Opx
Pl
Cpx
Grt
500 µm
c
Cpx
Ilm
Grt
Opx
Cpx
250 µm
d
Grt
Pl
Opx
Pl
Opx
Cpx
250 µm
e
Pl
Cpx
250 µm
f
Am
Qtz
Mt
Cpx
Cpx
Pl
50 µm
g
Pl
Am
Am
100 µm
h
Cpx
Mt
Pl
Opx
Am
Cpx
Ilm
50 µm

Fig. 5.9

Fig. 5.9 (previous page)

SEM backscatter electron images, showing microstructural details of amphibole-poor metagabbroic protomylonites (sample F22), dextral sense of shear. Images (f) and (h) are overlaid with EDS-derived phase maps. (a-d) Garnet porphyroclasts with inclusions, rimmed by symplectites of orthopyroxene + plagioclase. (e-f) Clinopyroxene porphyroclasts surrounded by neoblastic aggregates of clinopyroxene, with interstitial quartz, plagioclase and magnetite. (g-f) Rare amphibole porphyroclasts, mantled by reaction rims of clinopyroxene + orthopyroxene + plagioclase ± Fe-Ti oxides ± amphibole. Note the symplectic appearance of the reaction rim in (h).

Mylonites

Amphibole-poor metagabbroic mylonites are mineralogically banded rocks, composed of pyroxene-rich layers which alternate with monophase plagioclase layers, as in Kenkmann and Dresen, (2002). In the mineralogically banded domains, amphibole porphyroclasts are virtually absent. Typical amphibole-poor mylonites are the samples F32A, F10B, F20A-lower portion (Fig. 5.6b and c; also in Appendix, Appx. 2). The microstructures of these samples indicate that they experienced higher strain than the protomylonites (Fig. 5.6a vs. b-c). The porphyroclastic portion of the mylonite sample F20A is formed by 53% pyroxene, 0.5% amphibole and 46% garnet, measured as area fractions.

In amphibole-poor mylonites, plagioclase forms strongly elongate mono-mineralic layers parallel to the foliation (Fig. 5.6b-c and Fig. 5.10). These layers are made of recrystallized plagioclase containing relics of variably elongated porphyroclasts. Within plagioclase layers, mixing of plagioclase with other phases is very limited (Fig. 5.10 and Fig. 5.12: plagioclase in blue), so that the mineralogical banding is maintained also for samples exhibiting higher strain (e.g. sample F10B).

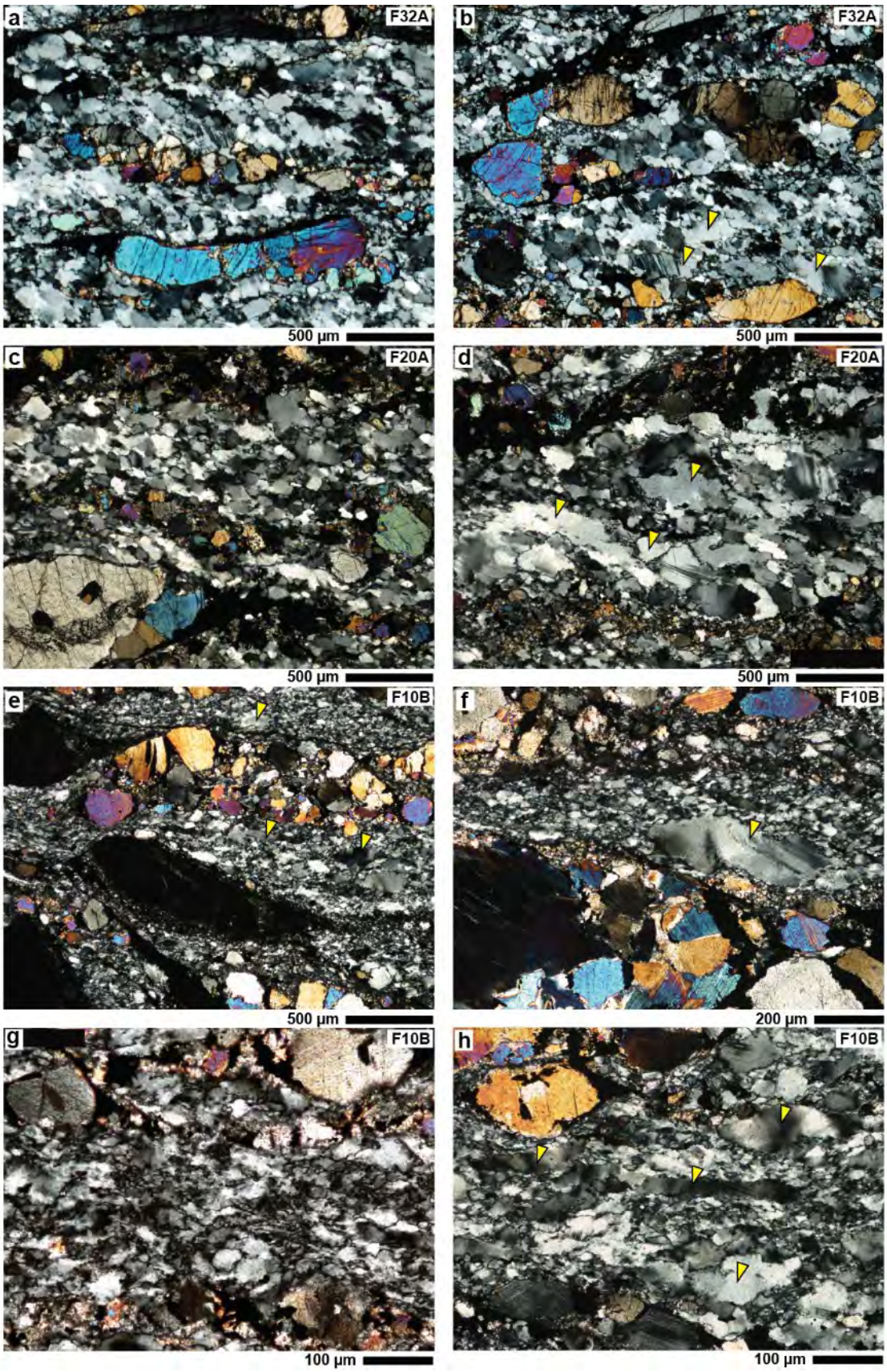
a
F32A
500 µm
b
F32A
500 µm
c
F20A
500 µm
d
F20A
500 µm
e
F10B
500 µm
f
F10B
200 µm
g
F10B
100 µm
h
F10B
100 µm

Fig. 5.10

Fig. 5.10 (previous page)

Light microscope images of plagioclase ribbons in amphibole-poor mylonites; crossed polars; sinistral sense of shear. Sample referenced on the top-right corner. Note the same scale on images (a-e). Yellow arrows point to variably elongated porphyroclast relics. Images (f-h) are close-up details.

Fig. 5.11 (next page)

Light microscope images of pyroxene-rich layers in amphibole-poor mylonites, showing pyroxene porphyroclasts mantled by aggregates of neoblastic clinopyroxenes. Plane light (left column) and crossed polaris (right column); sinistral sense of shear. Image (b) was analysed with EBSD (Fig. 5.32). Note the incipient microfracturing of pyroxene porphyroclasts (red arrows).

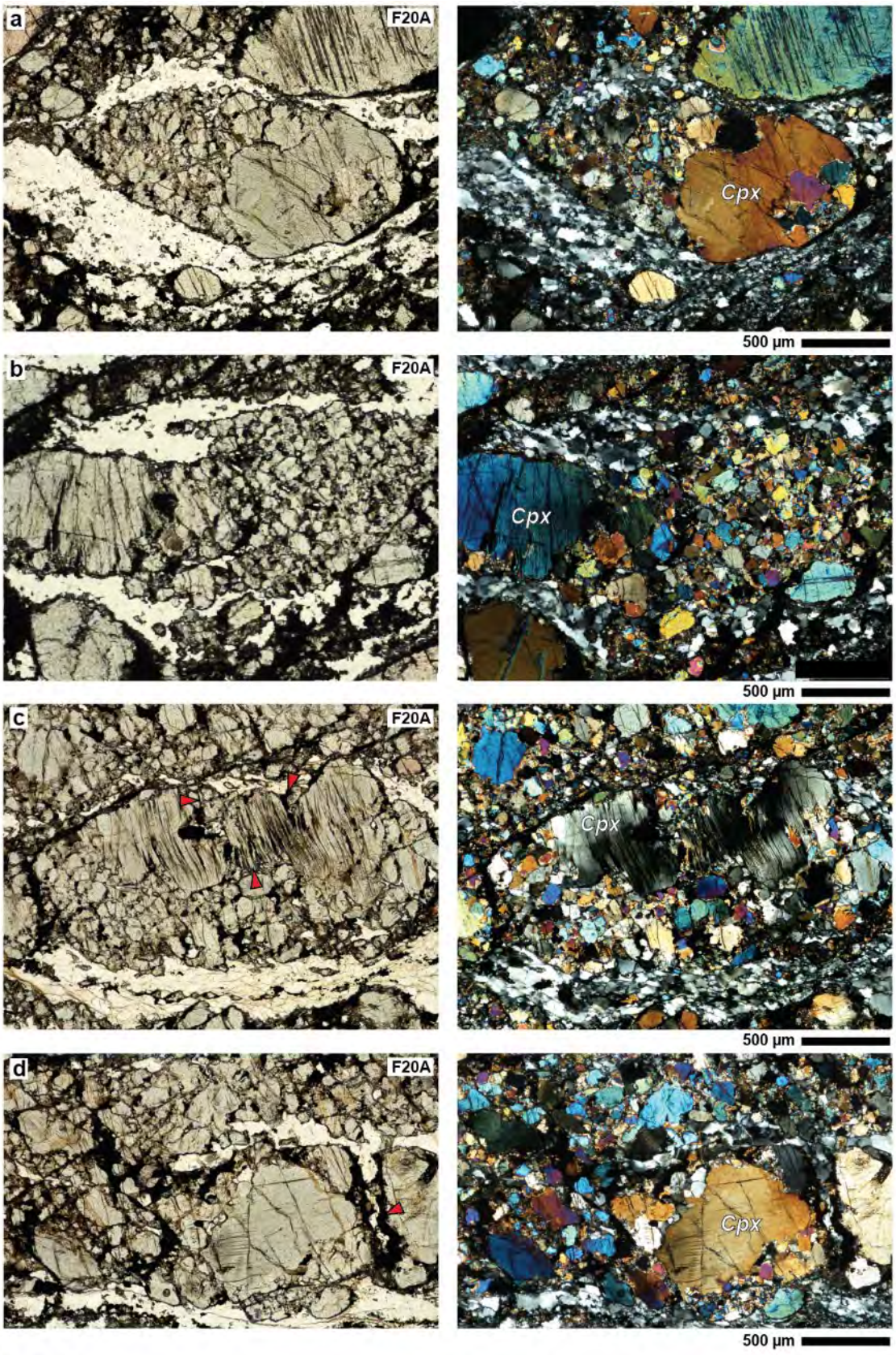
a
F20A
Cpx
500 µm
b
F20A
Cpx
500 µm
c
F20A
Cpx
500 µm
d
F20A
Cpx
500 µm

Fig. 5.11

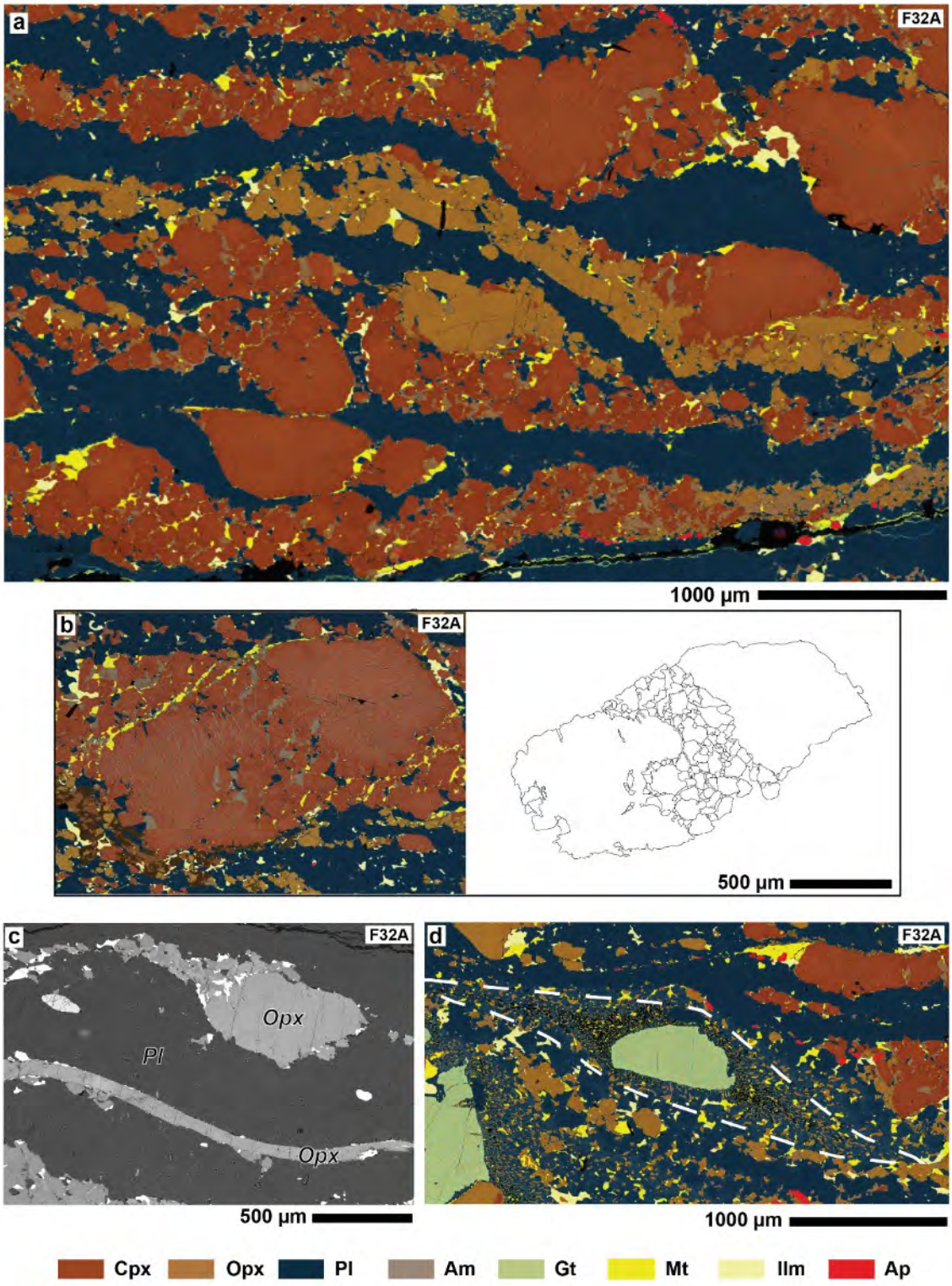

Fig. 5.12

SEM backscatter electron images showing microstructural details of amphibole-poor mylonites. SInistral sense of shear. (a) Overview of the microstructure. Stacked EDS elemental maps, evidencing chemical (thus mineralogical) differences; colour legend below. Note the pyroxene

porphyroclasts forming aggregates of secondary pyroxene, and the dispersed amphibole, plagioclase, magnetite and ilmenite in between. (b) Stacked EDS elemental maps with the same colour code, showing two clinopyroxene porphyroclastic fragments with an aggregate of secondary pyroxene in between. Note the different tones of orange between the porphyroclastic fragments and the neoblasts, highlighting differences in chemistry (porphyroclasts richer in Al_2O_3, see section 5.4.2 for mineral chemistry). The pyroxene aggregate also shows interstitial amphibole, plagioclase and magnetite; (c) BSE image of orthopyroxenes: lenticular grain above and elongated grain with high aspect-ratio below, surrounded by plagioclase. (d) Garnet porphyroclast rimmed by symplectites of orthopyroxene + plagioclase + ilmenite + magnetite. These symplectites developed in extensional quadrants during shearing, creating sigma-type, asymmetric (with respect to the shear plane) tails. These are shown by the white dashed line

Pyroxene-rich layers are made of clinopyroxene porphyroclasts and of aggregates of neoblastic clinopyroxene (Fig. 5.11 and Fig. 5.12a-b). Neoblastic plagioclase aggregates are found in strain shadows around clinopyroxene porphyroclasts, in thin bands and gaps separating adjacent fragments of porphyroclasts, and forming discontinuous layers parallel to the mylonitic foliation (Fig. 5.11 and Fig. 5.12a-b). Clinopyroxene neoblasts range in size from 15 µm to 280 µm (80 µm average grain size compared to > 750 µm average grain size of the porphyroclasts, as determined with image analysis; Fig. 5.13) and are arranged in closely packed polygonal aggregates. Dispersed plagioclase, secondary amphibole, and Fe-Ti oxides are usually found between the neoblasts (Fig. 5.11 and Fig. 5.12a-b).

Orthopyroxene porphyroclasts commonly develop elongated mono-crystalline ribbons with high aspect-ratios (up to 18:1) (Fig. 5.12c). As for clinopyroxene, lenticular orthopyroxenes are mantled by aggregates of neoblastic orthopyroxene, with dispersed plagioclase, amphibole and Fe-Ti oxides in between. Orthopyroxene neoblasts range in size from 20 µm to 220 µm (80 µm average grain size) (Fig. 5.13). During progressive

shearing, pyroxene porphyroclasts decrease in size and abundance, replaced by the neoblastic aggregates described above (Fig. 5.11 and Fig. 5.12a-b).

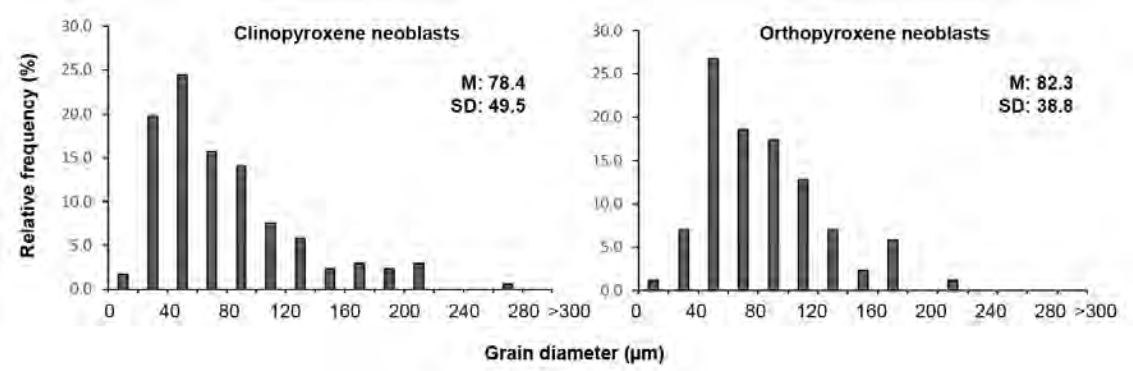

Fig. 5.13

Grain size distribution of clinopyroxene and orthopyroxene neoblasts in the pyroxene-rich layers of the mylonites. Sample F32A. Mean (M) and Standard Deviation (SD) is given on the side.

As in the protomylonites, garnet porphyroclasts are invariably rimmed by symplectites of orthopyroxene + plagioclase + ilmenite + magnetite. Symplectites are fine-grained vermicular intergrowths of two or more reaction products that form out of an unstable phase (Passchier and Trouw, 2005).These symplectites develop in the strain shadows of garnet porphyroclasts (i.e. in the extensional quadrants), creating sigma-type, asymmetric (with respect to the shear plane) tails (Fig. 5.12d). The microstructural position of these reactions indicate garnet breakdown during shearing. Similar asymmetric symplectites around garnets from lower crustal shear zones in metagabbros of the Ivrea Zone were described by Brodie (1995).

Fe and Fe-Ti oxides (magnetite - imenite) are ubiquitous in the mylonites, with the exception of the mono-phase plagioclase ribbons where they are practically absent (Fig.

5.12a). Magnetite and ilmenite are found within aggregates of neoblastic pyroxene, at porphyroclasts' strain shadows, between fractured grains, along shear bands and within the symplectites - all of which indicates that these oxides were syn-kinematic (Fig. 5.12).

5.3.2 AMPHIBOLE-RICH METAGABBROS

Protomylonites

Amphibole-rich metagabbros share the same metamorphic assemblage as the amphibole-poor metagabbros with the addition of abundant brown amphibole (Fig. 5.7a, and Fig. 5.14). In the protomylonitic stage represented by sample F33, the microstructures of plagioclase, pyroxenes, garnets and Fe-Ti oxides are identical to those described for the amphibole-poor metagabbro (see section 5.3.1; Fig. 5.8 and Fig. 5.9). Furthermore, C' shear bands of fine grained material are common (Fig. 5.14, red arrows).

Amphibole porphyroclasts are lenticular with abundant oxide inclusions and only limited undulose extinction (Fig. 5.14c, d). There is no optical evidence of subgrain development and no mantles of recrystallized grains around the porphyroclasts. Instead, porphyroclastic amphiboles are often rimmed by fine-grained symplectic intergrowths of pyroxene (both clino- and orthopyroxene) + plagioclase, ± Fe-Ti oxides and secondary amphibole (Fig. 5.15). Symplectic intergrowths, also known as symplectites, are fine-grained vermicular intergrowths of two or more reaction products that form out of an unstable phase (Passchier and Trouw, 2005). These fine grained, delicate structures are a key microstructural feature of amphibole-rich metagabbros, as will be discussed in

section 5.12. Pyroxene + plagioclase symplectites are best documented in the protomylonites, but they are also locally preserved in the ultramylonites.

Orthopyroxene + plagioclase intergrowths rimming amphibole porphyroclast in gabbroic shear zones (Anzola shear zone) were already identified in the Ivrea Zone by Brodie and Rutter (1985), who attributed these to post-deformation prograde reactions or alternatively to a drop in P_{H2O}.

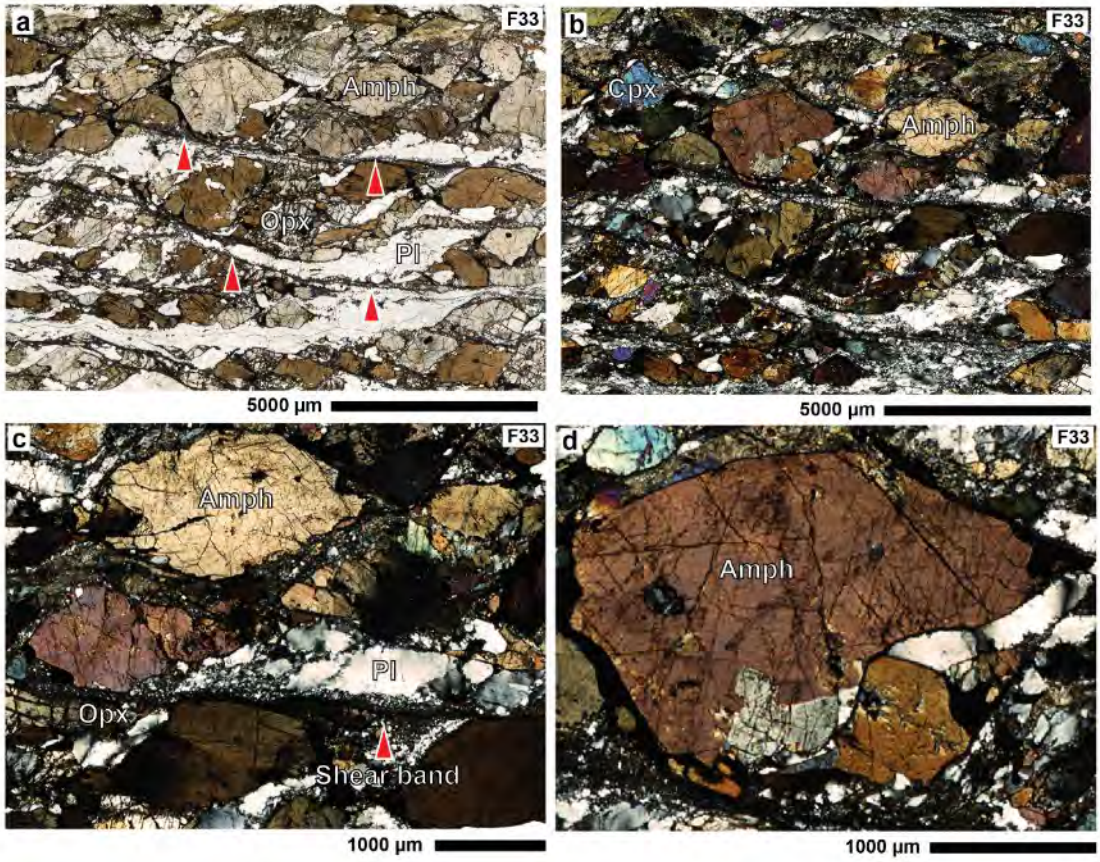

Fig. 5.14

Light microscope images of amphibole-rich protomylonites, sample F33. Dextral sense of shear. (a-b) overview of the microstructure in plane polarised light (see also Fig. 5.7a) and in crossed polars. Amphibole porphyroclasts are brown; shear bands are marked by red arrows. (c-d) details of amphibole porphyroclasts, showing minor undulose extinction and no optical evidence of subgrain development. Plagioclase porphyroclast relics are rimmed by fine grained recrystallized plagioclase; crossed polars.

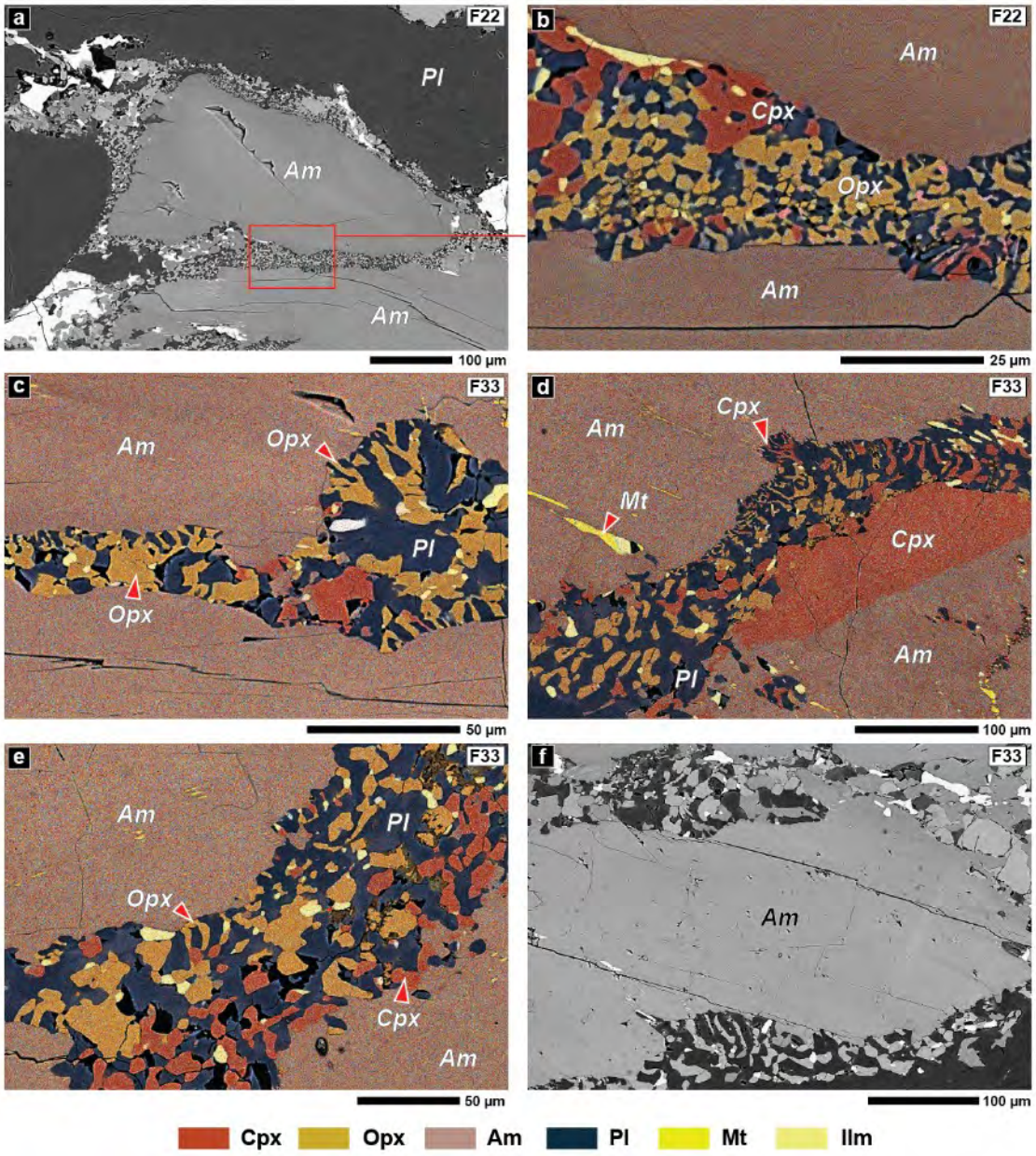

Fig. 5.15

SEM backscatter electron images of amphibole-derived symplectites preserved in the protomylonites. The symplectites are made of the assemblage clinopyroxene + orthopyroxene + plagioclase + ilmenite ± magnetite ± amphibole; black areas are voids. Samples referenced on the top-right; dextral sense of shear. Images (b-e) are overlaid with stacked EDS elemental maps, evidencing chemical (thus mineralogical) differences; colour legend below.

Ultramylonites

Ultramylonites are frequent in amphibole-rich metagabbros, and are characterized by isolated porphyroclasts of amphibole, garnet, orthopyroxene and clinopyroxene embedded in a fine-grained matrix of plagioclase + amphibole + clinopyroxene + orthopyroxene + ilmenite + magnetite ± apatite (Fig. 5.7b, Fig. 5.18, Fig. 5.19 and Fig. 5.20). The porphyroclastic portion of the ultramylonite of sample F20A is formed by 27% pyroxene, 20% amphibole and 53% garnet, calculated as area fractions. The porphyroclasts of pyroxene, amphibole and garnet are mostly rounded or lenticular, with average grain sizes of 635 µm, 480 µm and 1390 µm, respectively.

Phase proportions in the ultramylonitic matrix are variable within the different analysed sites; with plagioclase forming 26-59 area%, amphibole 22-32 area%, orthopyroxene 8-19 area%, clinopyroxene 7-28 area%, ilmenite 2-4 area% and magnetite 2-5 area% (Table 5.2). The fine-grained ultramylonitic matrix does not contain newly formed garnet. Owing to its larger sampling area, the phase proportions derived from the compositional map *F20A-map3* are taken as representative of the ultramylonitic phase proportions (*F20A-map3* is Fig. 5.20).

area%	EBSD F20A-map1	EBSD F20A map2	EBSD F32A - map1	F20A-map1	F20A-map3	F32A-map1	*Mean*
plagioclase	26.9	32.7	49.3	36.9	25.8	59.4	*38.5*
amphibole	31.2	22.3	24.5	24.7	32.4	23.0	*26.3*
orthopyroxene	13.5	7.8	7.5	18.6	10.9	5.9	*10.7*
clinopyroxene	22.2	28.1	16.8	15.3	22.1	6.9	*18.6*
ilmenite	3.2	4.1	1.8	2.3	4.2	1.9	*2.9*
magnetite	2.9	5.0	-	2.3	3.0	2.9	*3.2*

Table 5.2

Phase proportions in amphibole-rich metagabbroic ultramylonites, recalculated as area% from a selection of representative maps. The referenced maps are shown in the Appendix, Appx.3. F20A-map3 is shown in Fig. 5.20 .

Grain sizes in the ultramylonite are consistently below 20 µm on average for all phases (Fig. 5.16). Plagioclase has a small proportion of grains larger than 50 µm, with the largest measurement being 86 µm diameter. The phases in the fine-grained ultramylonitic matrix are well mixed, with the phase boundaries forming ca. 90 area% of the contacts, and the grain boundaries forming the remaining 10 area% (Fig. 5.17). Each phase analysed separately indicates that phase boundaries constitute more than ca. 83 area% of the grain contacts (Table in Fig. 5.17). Phase boundaries are mostly irregular and lobate. Amphibole is often found in contact with clinopyroxene grains.

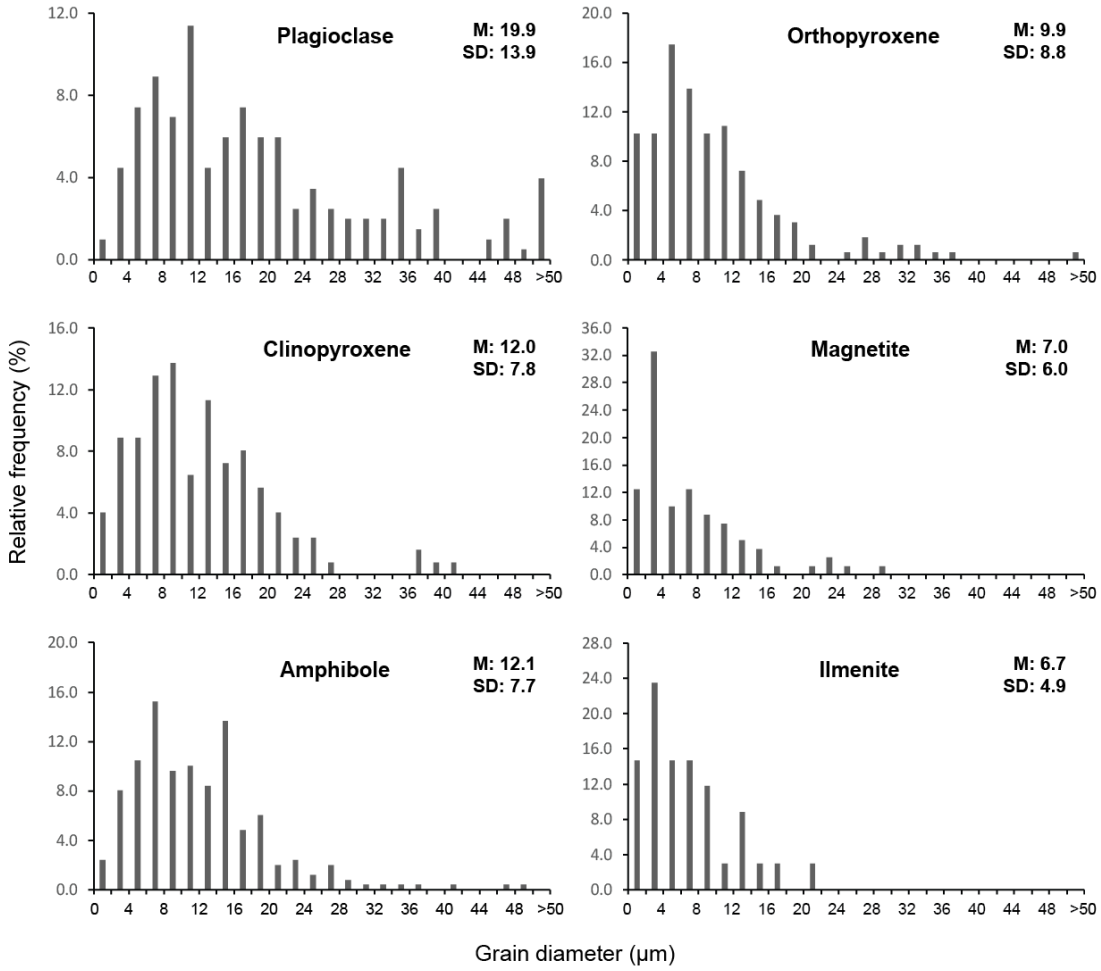

Fig. 5.16

Grain size distribution of plagioclase, clinopyroxene, amphibole, orthopyroxene, magnetite, and ilmenite in the ultramylonite. Sample F32A. Mean (M) and Standard Deviation (SD) is given on the side.

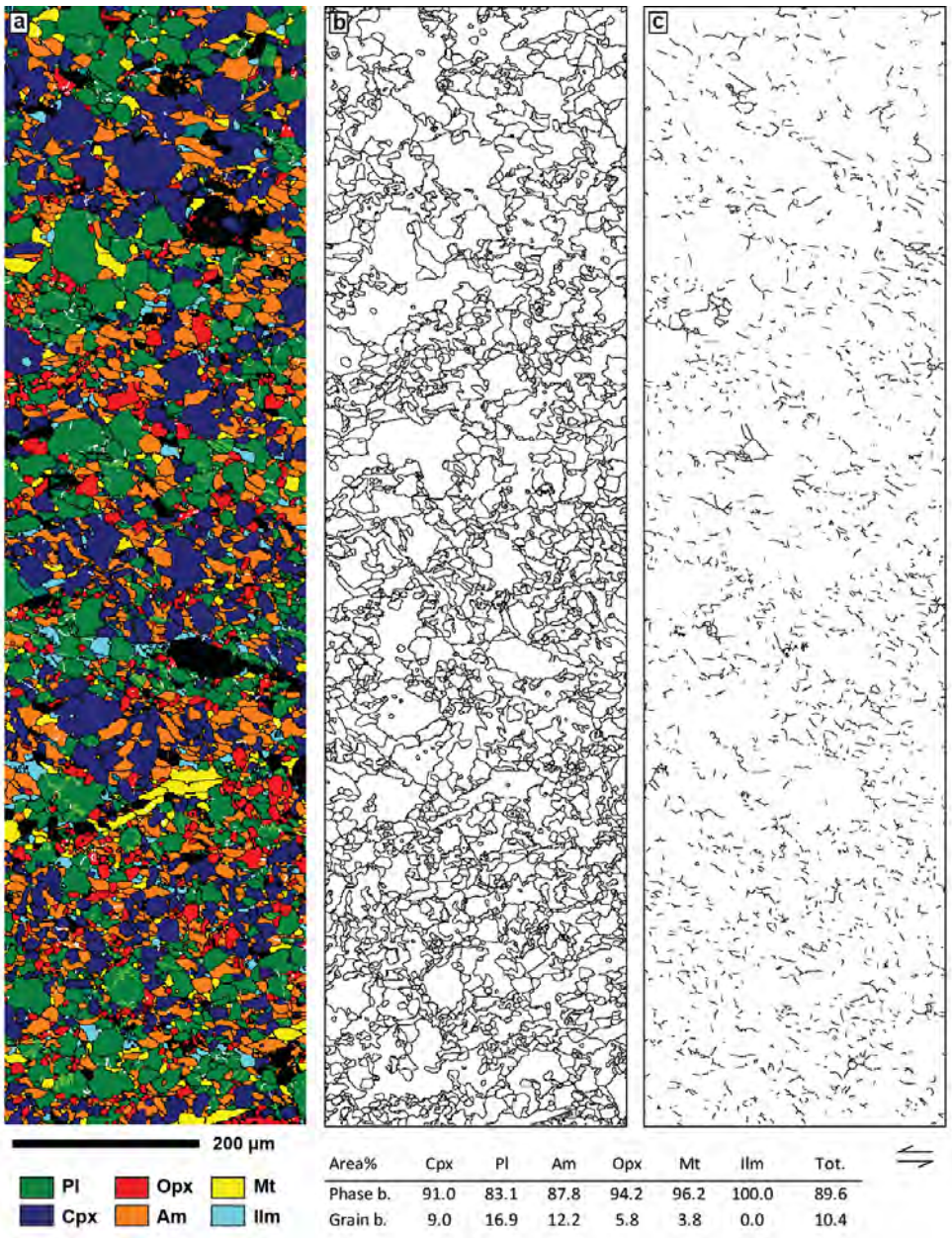

Area%	Cpx	Pl	Am	Opx	Mt	Ilm	Tot.
Phase b.	91.0	83.1	87.8	94.2	96.2	100.0	89.6
Grain b.	9.0	16.9	12.2	5.8	3.8	0.0	10.4

Fig. 5.17

Phase boundary and grain boundary distribution in the amphibole-rich ultramylonites. (a) EBSD-derived phase map (EBSD-F20A-map2) used for grain and phase boundary calculation. Different colours represent different mineral phases; colour legend below. Area fractions are calculated from pixel counts of boundaries, using Fiji (ImageJ). (b) Phase boundaries, all phases. (c) Grain boundaries, all phases. The grain boundaries are as defined for EBSD, i.e. for misorientations > 10°. The proportion of phase boundary to grain boundary (as area%) of each individual phase is given in the table below the figure. In (b) and (c), the phase boundaries and grain boundaries of all phases are shown together. Phase boundaries and grain boundaries of individual phases can be found in the Appendix, Appx. 4. Lines have been thickened after calculation, for display purpose.

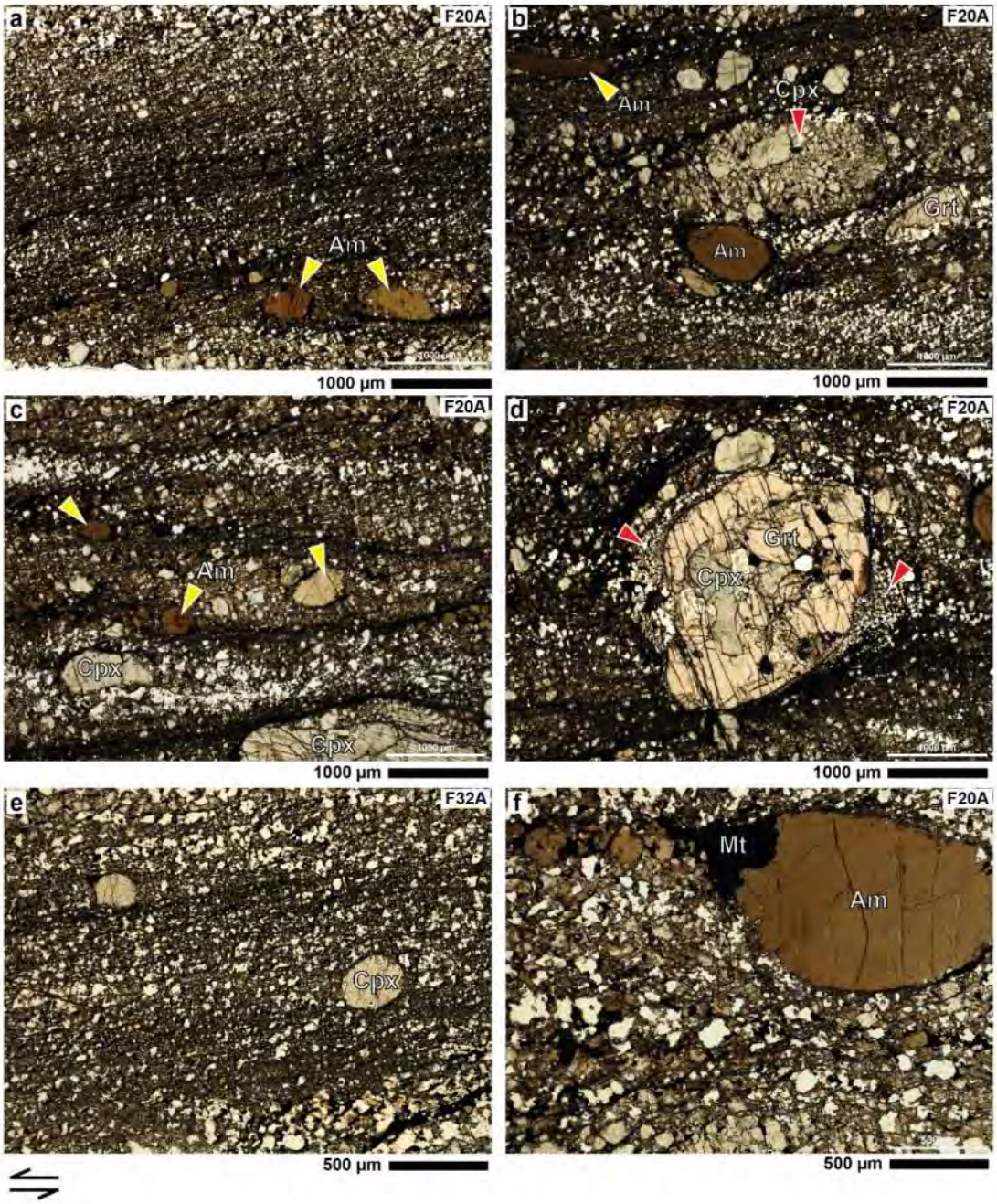

Fig. 5.18

(a-f) Light microscope images of amphibole-rich ultramylonites; samples F20A and F32A; plane polarised light; sinistral sense of shear. Brown amphiboles are widespread, both as porphyroclasts and as a fine grained phase in the ultramylonitic matrix. Some amphibole porphyroclasts are marked by yellow arrows. (b) Detail of ultramylonite showing a clinopyroxene aggregate lense (red arrow). (d) Detail of garnet porphyroclast preserved in the ultramylonite, with clinopyroxene inclusions, and with orthopyroxene + plagioclase symplectites preserved along strain shadows (red arrows). (e) ultramylonite of sample F32A, microstructurally analogous to (a). (f) Large amphibole porphyroclast in ultramylonite, with magnetite in the pressure shadow.

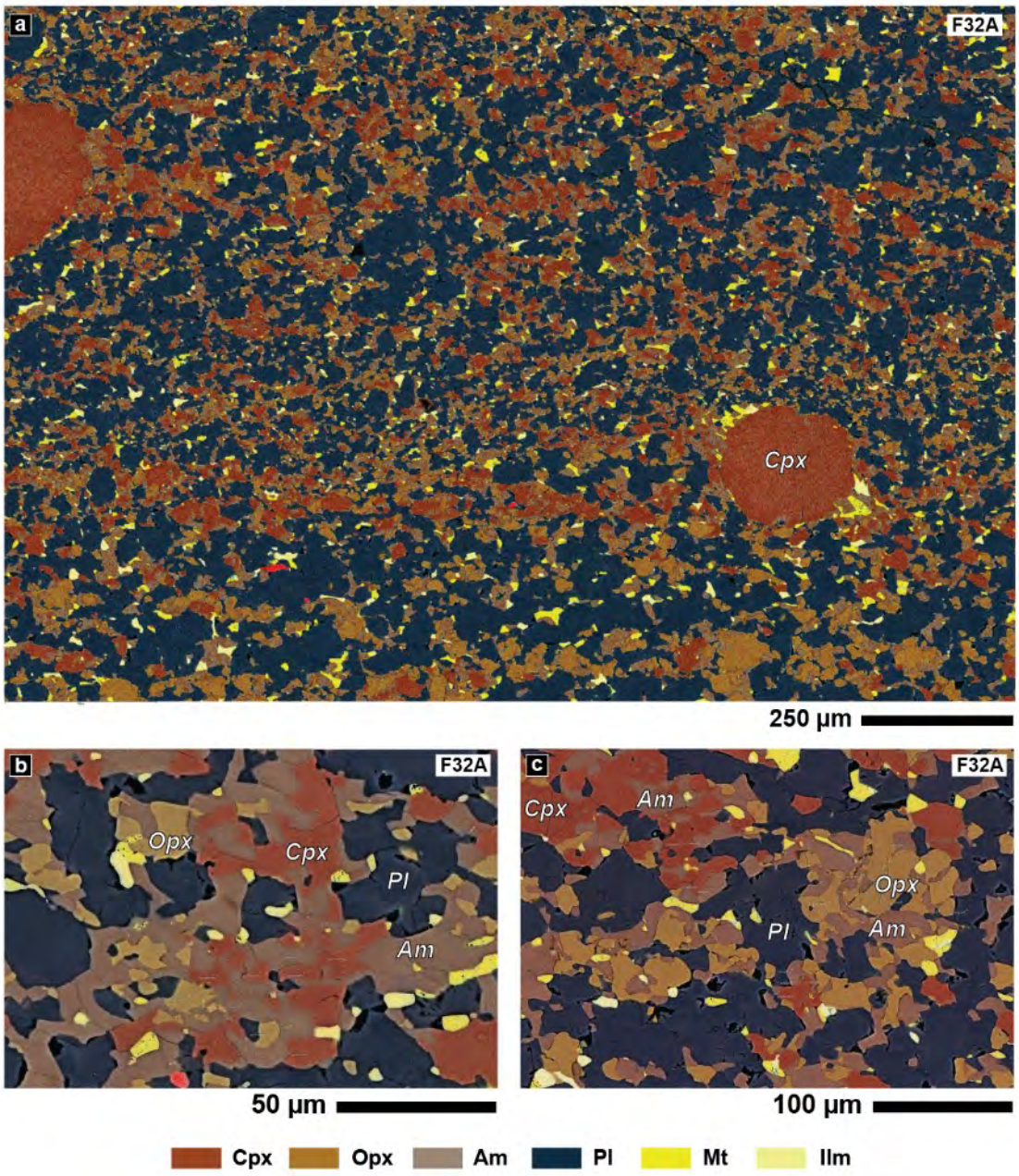

Fig. 5.19 (continued on next page)

SEM backscatter electron images, showing the typical microstructure of amphibole-rich metagabbroic ultramylonites. Samples referenced on the top right corners; sinistral sense of shear. Images (a-c) are overlaid with EDS elemental maps, evidencing chemical (and thus mineralogical) differences; colour legend below the figure. Note how clinopyroxene and amphibole can be distinguished in the EDS elemental maps, whereas in the backscatter images the two phases are indistinguishable owing to the similar grey tones. (a) Overview of the ultramylonitic microstructure. (b-c) Details of the microstructure, showing the spatial distribution of phases in the ultramylonite. (d-i) additional close-ups of the ultramylonites at different sites. Fig. 5.19 continued on next page…

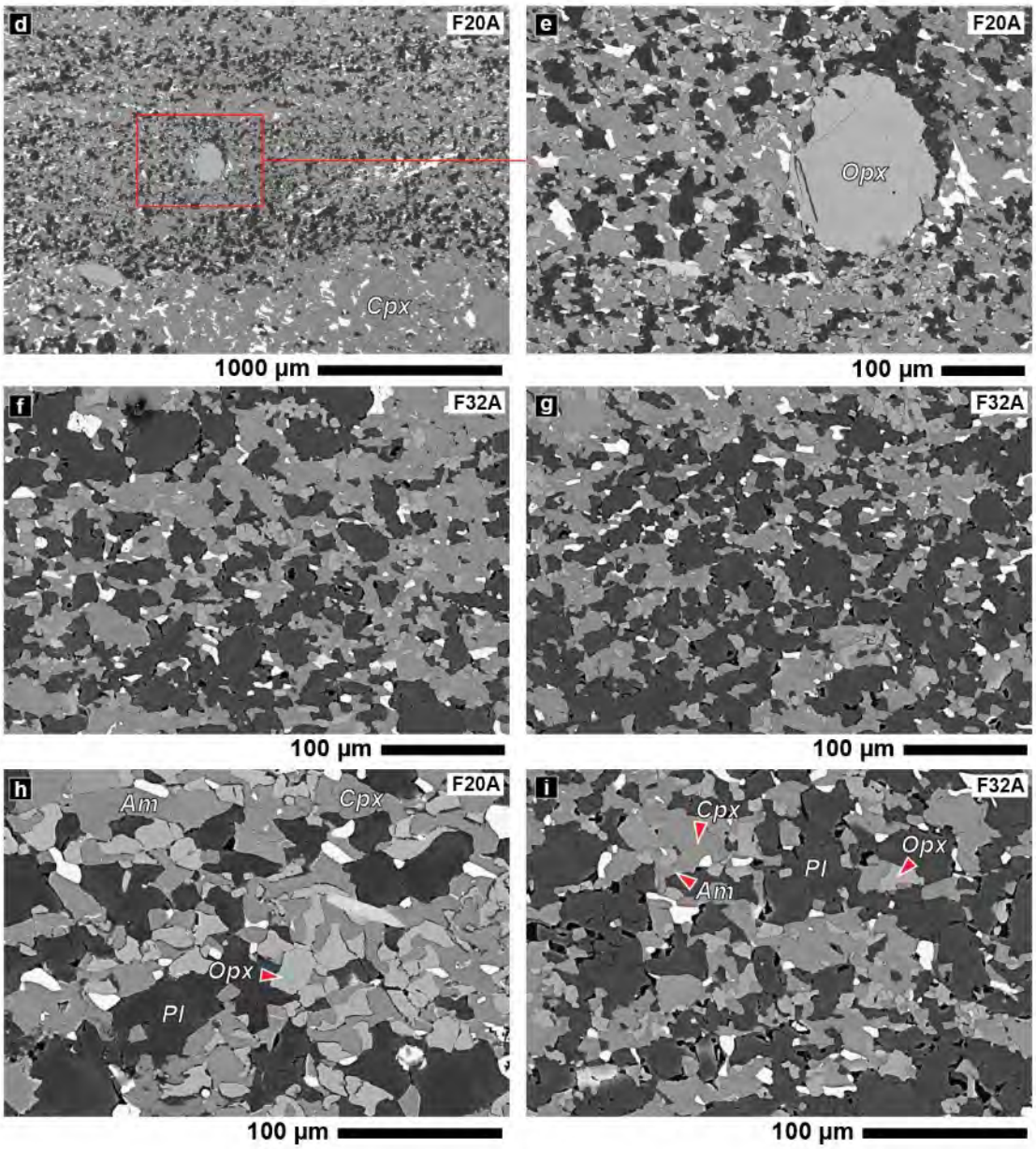

Fig. 5.19 (2nd page)

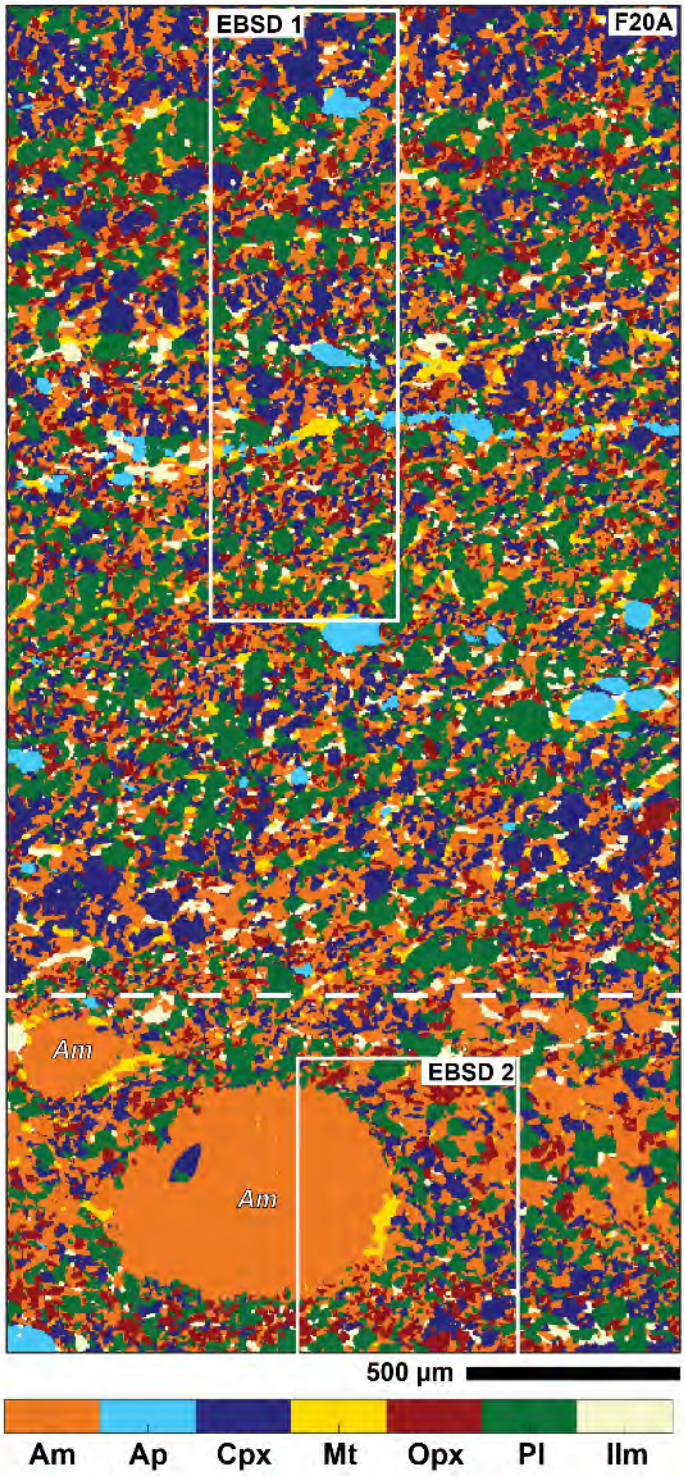

Fig. 5.20

Phase map reconstructed from the microprobe map F20A-map3, using XMapTools (Lanari et al., 2014). Locations of EBSD maps "EBSD-F20A-map1" and "EBSD-F20A-map2" in white boxes (see EBSD analysis, section 5.8). Colour legend below the figure. Phase proportions from this map (see Table 5.2) were calculated from the area above the dashed white line to exclude the porphyroclasts.

Within the ultramylonites, garnet porphyroclasts are rimmed by asymmetric orthopyroxene + plagioclase symplectites, or amphibole + plagioclase symplectites (Fig. 5.21). Both types of symplectites are preserved in pressure shadows of garnet porphyroclasts (extensional quadrants).

Amphibole porphyroclasts in the ultramylonites have irregular and lobate boundaries, locally rimmed by small (ca. 10 µm) grains of orthopyroxene + plagioclase (Fig. 5.22 d-f). Where best preserved, these rims resemble the symplectic intergrowths that occur in the amphibole-rich protomylonites around amphibole porphyroclasts (Fig. 5.15). Orthopyroxene + plagioclase ± amphibole intergrowths can also be found between amphibole porphyroclasts in contact or within fractured fragments (Fig. 5.22 a-c). Well preserved symplectic intergrowths in the ultramylonites are rare, but occasional vermicular symplectites of clinopyroxene + plagioclase ± orthopyroxene ± amphibole can be found preserved between amphibole porphyroclasts (Fig. 5.22a). Small grains of orthopyroxene (ca. 10 µm) locally overgrow the clinopyroxene + plagioclase ± amphibole symplectites (Fig. 5.22a).

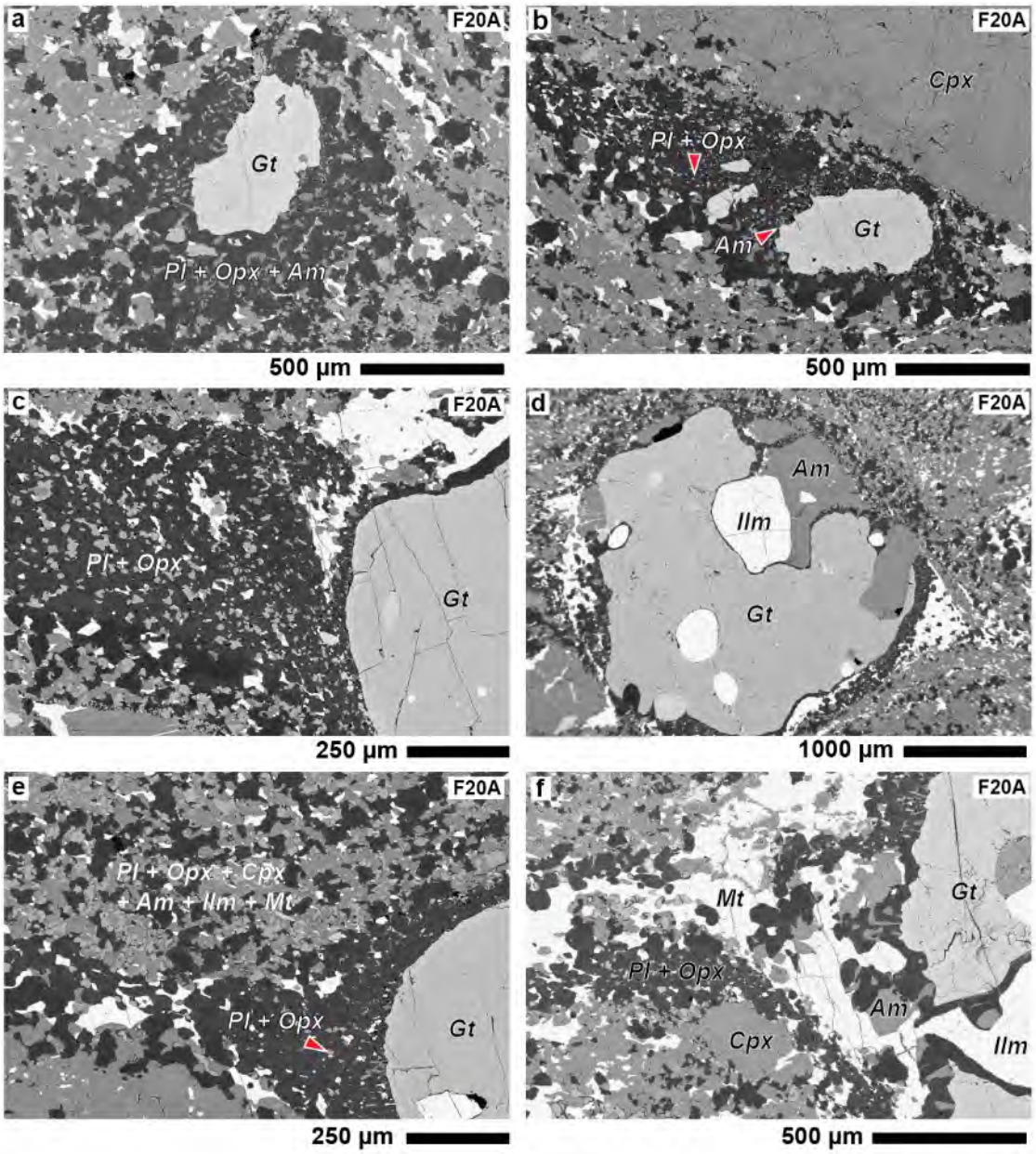

Fig. 5.21

SEM backscatter electron images of garnet porphyroclasts in the ultramylonites, rimmed by asymmetric orthopyroxene + plagioclase symplectites, or by amphibole + plagioclase symplectites, preserved in pressure shadows. Ultramylonite sample F20A; sinistral sense of shear.

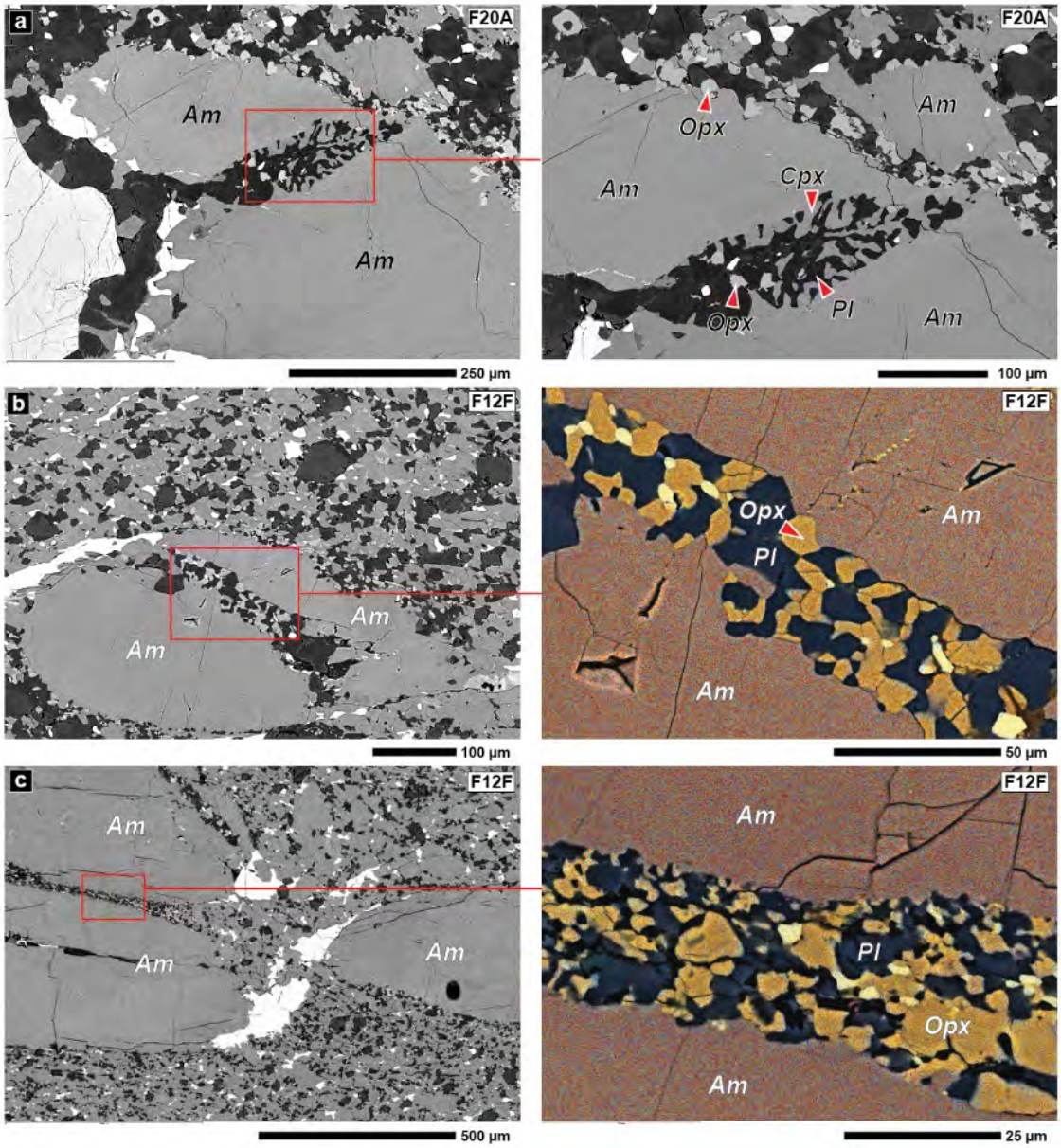

Fig. 5.22 *(continued on next page)*

SEM backscatter electron images of amphibole-derived intergrowths of clino/orthopyroxene + plagioclase, preserved in the amphibole-rich ultramylonites. Right column images are close-ups of left column; location is boxed. Images (b), (c) and (e) are overlaid with EDS elemental maps, evidencing chemical (and mineralogical) differences; colour legend below. Samples referenced on the top-right; sinistral sense of shear. (a-c) Clino/orthopyroxene + plagioclase intergrowths preserved between amphibole porphyroclasts, or within fractured fragments. (d-f) Clino/orthopyroxene + plagioclase intergrowths rimming amphibole porphyroclasts.

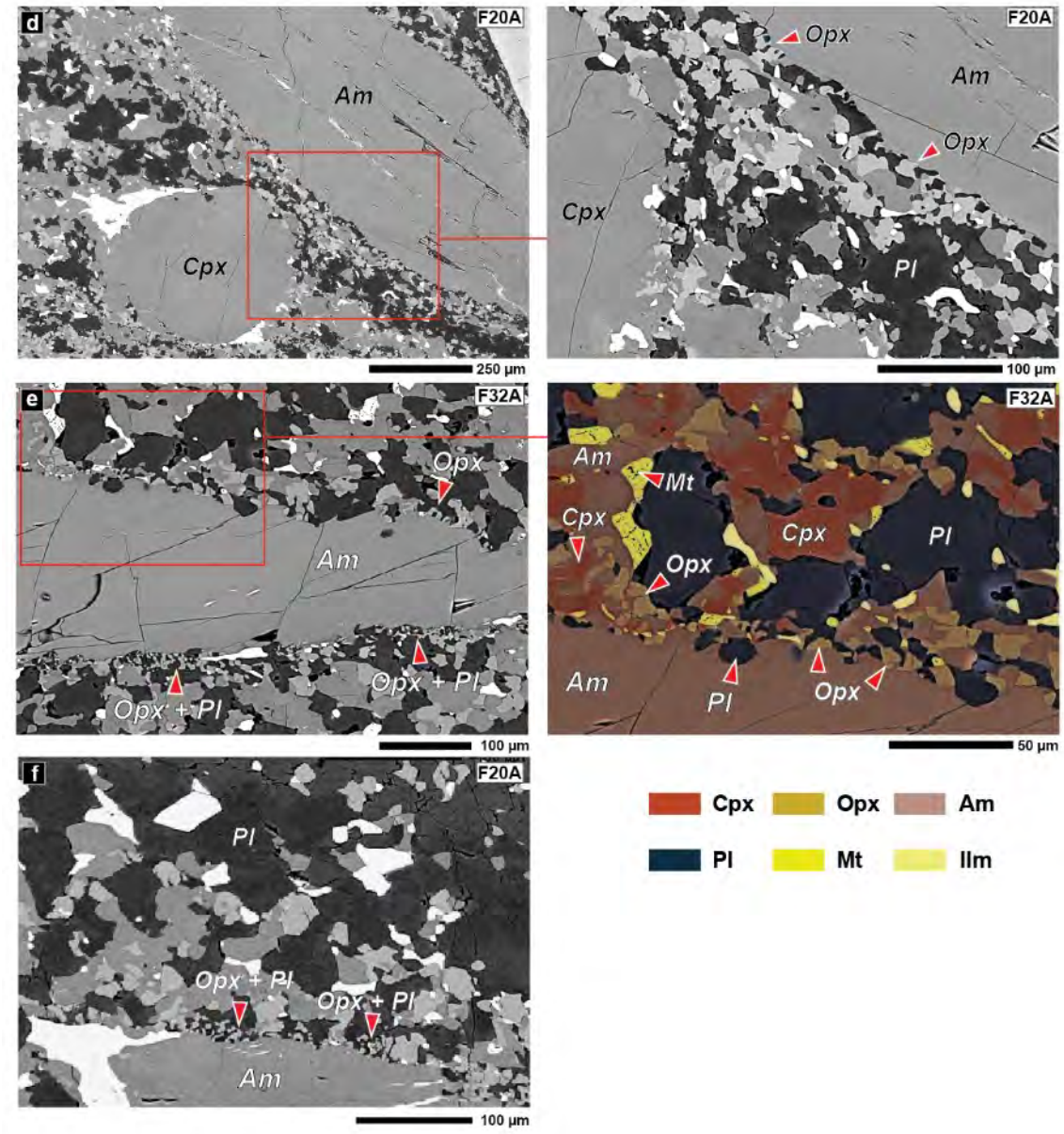

Fig. 5.22 (2nd page)

5.4 SHEAR ZONE CHEMISTRY

5.4.1 BULK-ROCK CHEMISTRY

Bulk-rock chemistry of the Finero metagabbros was analysed with XRF to constrain lithological differences within the shear zone and assess bulk compositional variations in relation to deformation. Furthermore, bulk-rock chemistry was used for thermodynamic modelling of the P-T conditions of shearing. Results are summarized in Table 5.3 and Fig. 5.23a. Six samples of metagabbros displaying variable degrees of deformation were analysed: five amphibole-poor and one amphibole-rich. Only one analysis of ultramylonites from amphibole-rich protoliths was possible due to technical difficulties in mechanically separating mm-cm ultramylonitic layers from the host rock. To account for this limitation, the bulk-rock chemistry of one ultramylonite (F20A) was reconstructed using XMapTools (Lanari et al., 2014) from the representative microprobe map of Fig. 5.20.

Bulk-rock chemical results indicate that chemical variability of major elements remains below 2 wt% (1St.Dev < 2 wt%) across the whole range of analysed samples (Table 5.3). Excluding water content (of which an estimate is given by the LOI), there is no significant difference in the chemistry of amphibole-poor and amphibole-rich portions. Comparison of our samples with others of Lu et al. (1997a) from the External Gabbro unit confirms chemical homogeneity throughout the complex, regardless of the degree of deformation and amphibole content (Fig. 5.23a vs. b). This is in line with previous findings that claimed that little or no metasomatism/crustal contamination occurred within the Finero mafic complex (Lu et al., 1997a, 1997b).

Protolith	Amphibole poor metagabbro					Amphibole rich metagabbro	
Sample	**F17**	**F14B**	**F22**	**F32A**	**F10B**	**F06D**	**F20A**
Rock type	metagabbro, slightly altered	metagabbro	protomylonite	mylonite	mylonite	ultramylonite	ultramylonite
Bulk rock OxWt%							
SiO2	43.35	44.17	45.86	45.11	44.70	44.39	44.90
TiO2	3.37	2.01	3.34	2.95	2.72	2.09	3.26
Al2O3	12.69	13.09	12.94	13.37	13.27	18.23	11.60
Fe2O3	17.53	16.44	17.02	16.67	16.50	12.91	16.16
Mn3O4	0.28	0.54	0.29	0.30	0.28	0.21	0.21
MgO	7.66	7.83	8.01	7.95	7.10	6.38	8.24
CaO	10.97	11.64	9.95	9.96	12.33	10.13	12.66
Na2O	2.24	2.74	2.03	2.17	1.80	2.75	2.07
K2O	0.09	0.62	0.02	0.08	0.08	0.45	0.14
P2O5	0.317	0.192	0.315	0.320	0.225	0.097	-
SO3	0.631	0.006	0.198	0.425	0.034	0.270	-
V2O5	0.103	0.075	0.101	0.084	0.088	0.064	-
Cr2O3	0.020	0.022	0.016	0.023	0.021	0.034	-
SrO	0.009	0.026	0.004	0.010	0.019	0.060	-
ZrO2	0.019	0.010	0.023	0.031	0.016	0.009	-
BaO	0.004	0.011	0.001	0.003	0.003	0.016	-
NiO	0.006	0.011	0.007	0.006	0.007	0.009	-
CuO	0.007	0.001	0.010	0.017	0.003	0.008	-
ZnO	0.015	0.021	0.016	0.034	0.015	0.015	-
PbO	0.002	0.006	0.004	0.003	0.008	0.008	-
Sum	**99.31**	**99.45**	**100.16**	**99.50**	**99.20**	**98.12**	**99.23**
FeO tot	15.78	14.79	15.32	15.00	14.85	11.61	14.54
MnO	0.26	0.51	0.27	0.28	0.26	0.20	0.20
LOI	**0.67**	**0.24**	**-0.06***	**0.30**	**0.09**	**0.97**	**0.77**

Table 5.3

*Bulk-rock chemistry (oxide wt%) analyses of a selection of amphibole-poor and amphibole rich metagabbros. Chemistry measured with XRF, excluding sample F2OA of which the chemistry was recalculated from the microprobe map shown in Fig. 5.20. Excluding sample F20A, the LOI was measured as the difference in weight before and after furnace heating (see Chapter 3, section 3.6 for further details). The negative LOI value * was interpreted as Fe oxidation reaction during combustion, thus this sample is interpreted to contain very low water contents. The LOI of sample F20A was calculated as 100 – sum of the elements. Additional XRF analyses can be found in the Appendix Appx. 5.*

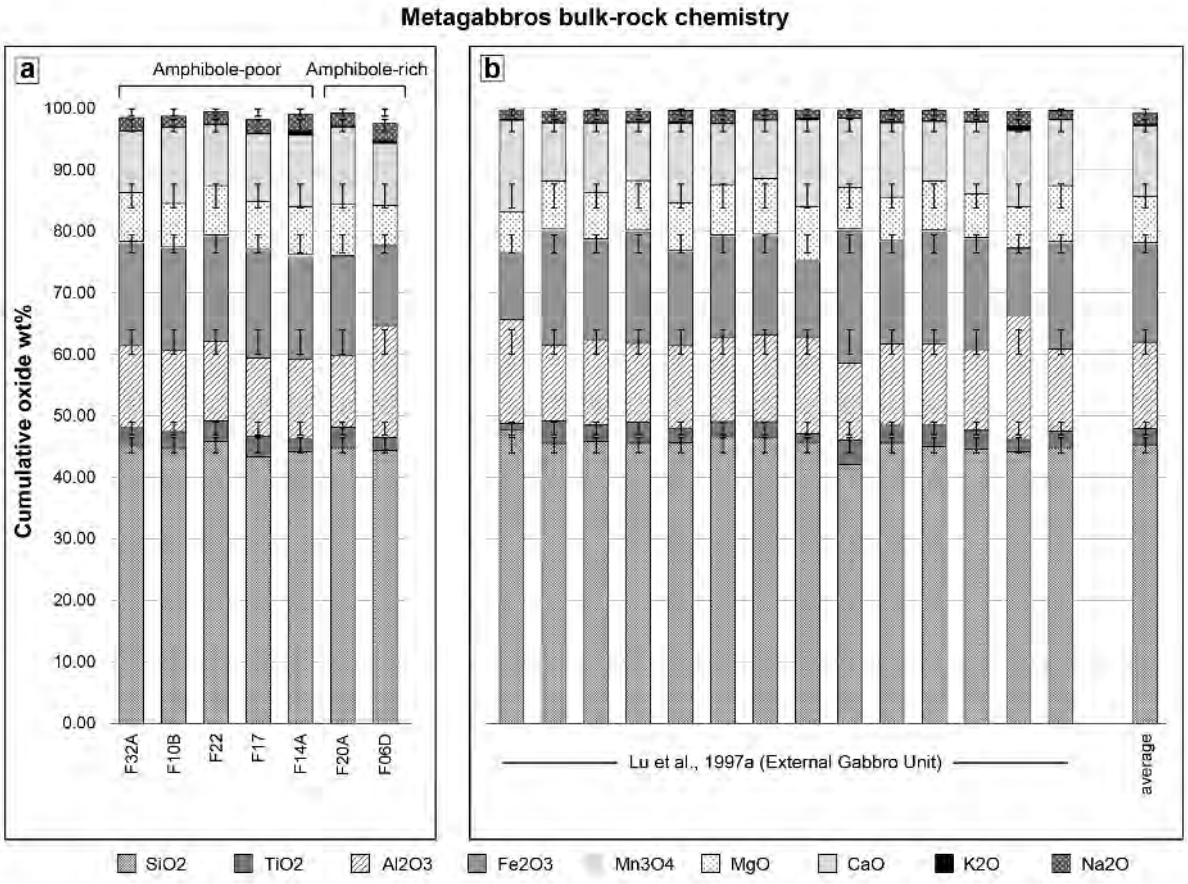

Fig. 5.23

Bulk-rock chemical composition (oxide wt% of major elements) of Finero metagabbros measured with XRF (excluding sample F20A which was recalculated from a Microprobe map) (a) Samples from this study, with corresponding data in Table 5.3; (b) samples from Lu et al., (1997) from the External Gabbro unit. The major elements' mean of both datasets, and associated error bars (1St. Dev), is shown on the right.

In addition to bulk-rock chemistry, 1) water content and 2) oxidation state are both controlling factors of the stable phase assemblages in mafic rocks (e.g. Palin et al., 2016 and reference therein). One way of estimating bulk-water content is through the LOI (loss on ignition), as water stored in the rock is released upon furnace heating (see Chapter 3, section 3.6 for details). Based on the LOI, amphibole-rich lithologies seem to have slightly higher water contents than their amphibole-poor counterparts (Table 5.3- LOI).

Water contents in the ultramylonite can be also derived based on the modal proportions of amphibole, using average water contents from Microprobe analysis. The average water content of fine-grained amphibole in the ultramylonite matrix is ca. 2.80 wt%, calculated as the difference between 100 and the sum of all elements measured (see section 5.4.2). From image analysis, the ultramylonite F20A is composed of ca. 32 area% amphibole (Table 5.2). Thus, based on these calculations, the water content in the ultramylonite would be ca. 0.9 wt%.

5.4.2 MINERAL CHEMISTRY

The compositions of the main minerals of the shear zone are summarized in Tables A, B, C, D and E, in the Appendix, Appx. 6. The tables are organized according to five subgroups that reflect the different microstructural positions of the minerals (and therefore the evolution of chemistry with shearing): A) porphyroclasts, B) neoblastic polygonal aggregates in the mylonites C) ultramylonitic matrix, D) symplectites, and E) dispersed-matrix grains. Neoblasts refer to the pyroxene grains found in the pyroxene-rich layers of mylonites (e.g. Fig. 5.11 and Fig. 5.12a-b). Ultramylonites refer to the grains in the ultramylonitic matrix only. Dispersed-matrix grains are the grains commonly found between neoblastic aggregates, or as fine grained material in shear bands. This division in subgroups is important because possible compositional variations between the different microstructural positions can be identified. Formula units of pyroxenes, amphiboles, plagioclases and garnets are recalculated based on 4, 13, 5 and 8 cations respectively. The magnesium number (Mg#) is calculated as $Mg/(Mg + Fe_{tot})$; the Fe^{3+} is calculated from stoichiometry, and the Mg oxide ratio is calculated as $MgO/(MgO + FeO_{tot})$ (Tables in Appendix, Appx. 6).

Overall, the mineral chemistries of pyroxenes and amphiboles shows a gradual but systematic increase in SiO_2, MgO and CaO, and a decrease in FeO, Al_2O_3, NaO and TiO_2 from porphyroclasts to syn-kinematic ultramylonitic grains (Fig. 5.24). This is most evident in clinopyroxenes and amphiboles, but orthopyroxenes also confirm this trend with an increase in MgO and SiO_2, and a decrease in FeO and Al_2O_3. All samples analysed here (F10B, F33, F32A, F20A, F10A3, F14A) show this trend and confirm previous studies on high-T shear zones of the Ivrea Zone (Brodie, 1981; Kenkmann, 2000; Kenkmann and Dresen, 2002; Stünitz, 1998).

(a) *Orthopyroxenes*

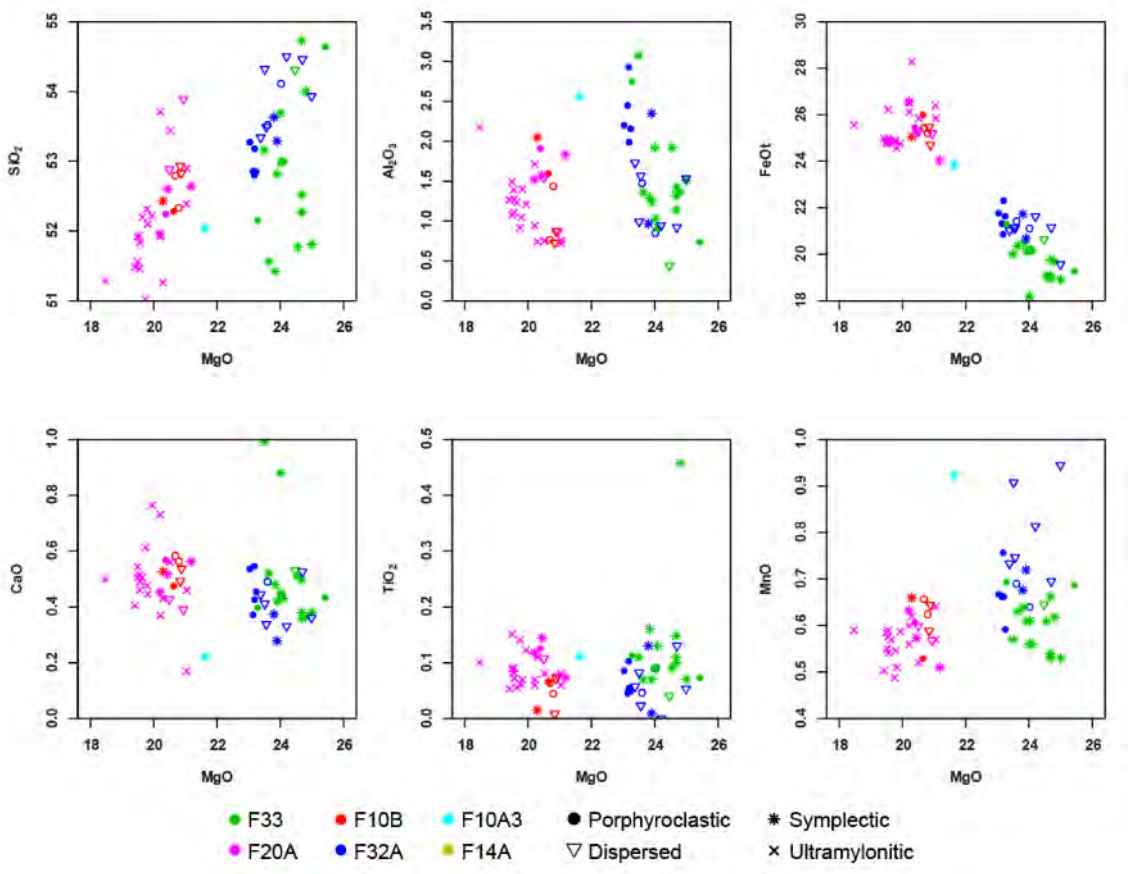

Fig. 5.24 (continued on next page)

(b) Clinopyroxenes

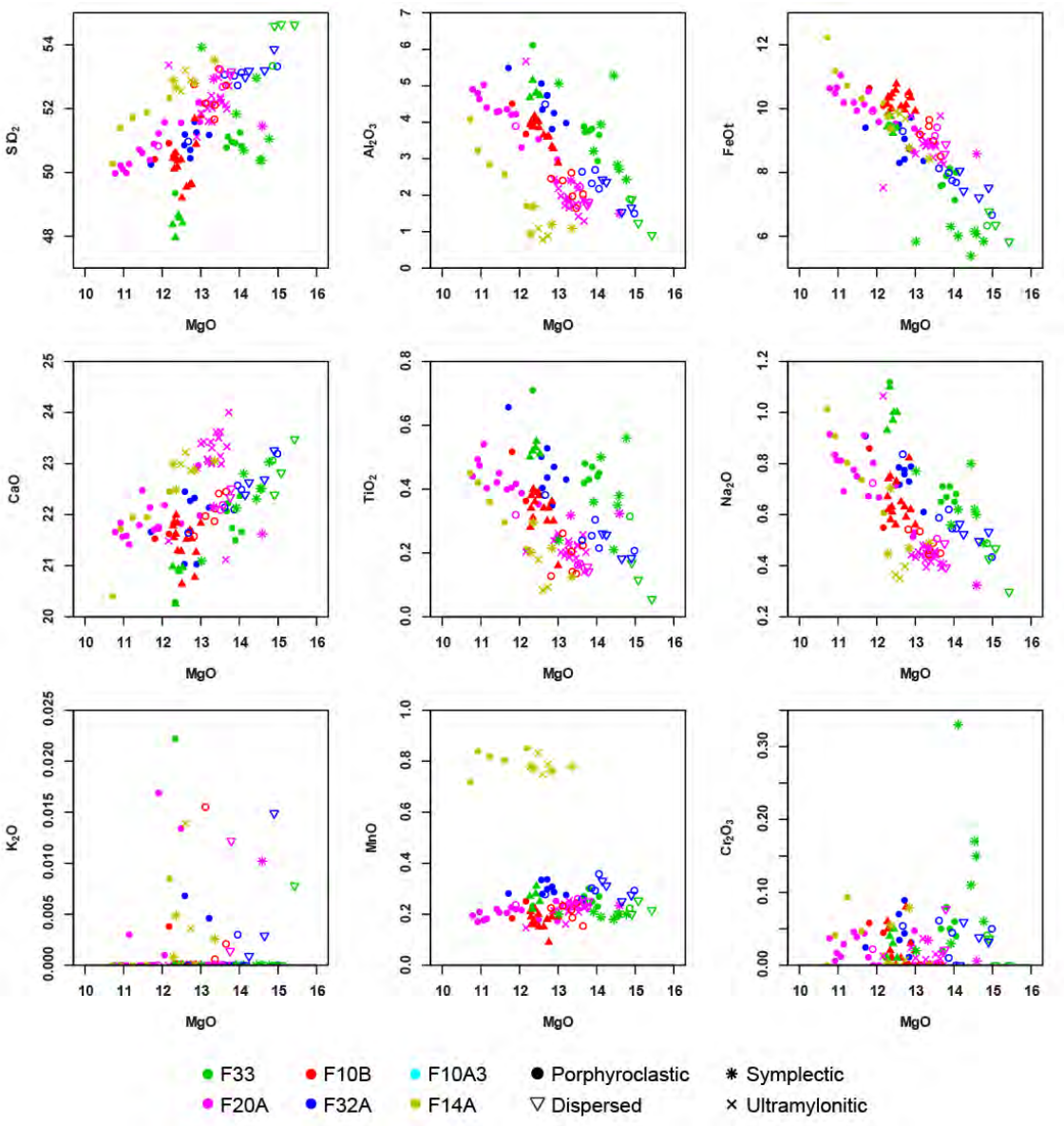

Fig. 5.24 (continued on next page)

(c) Amphiboles

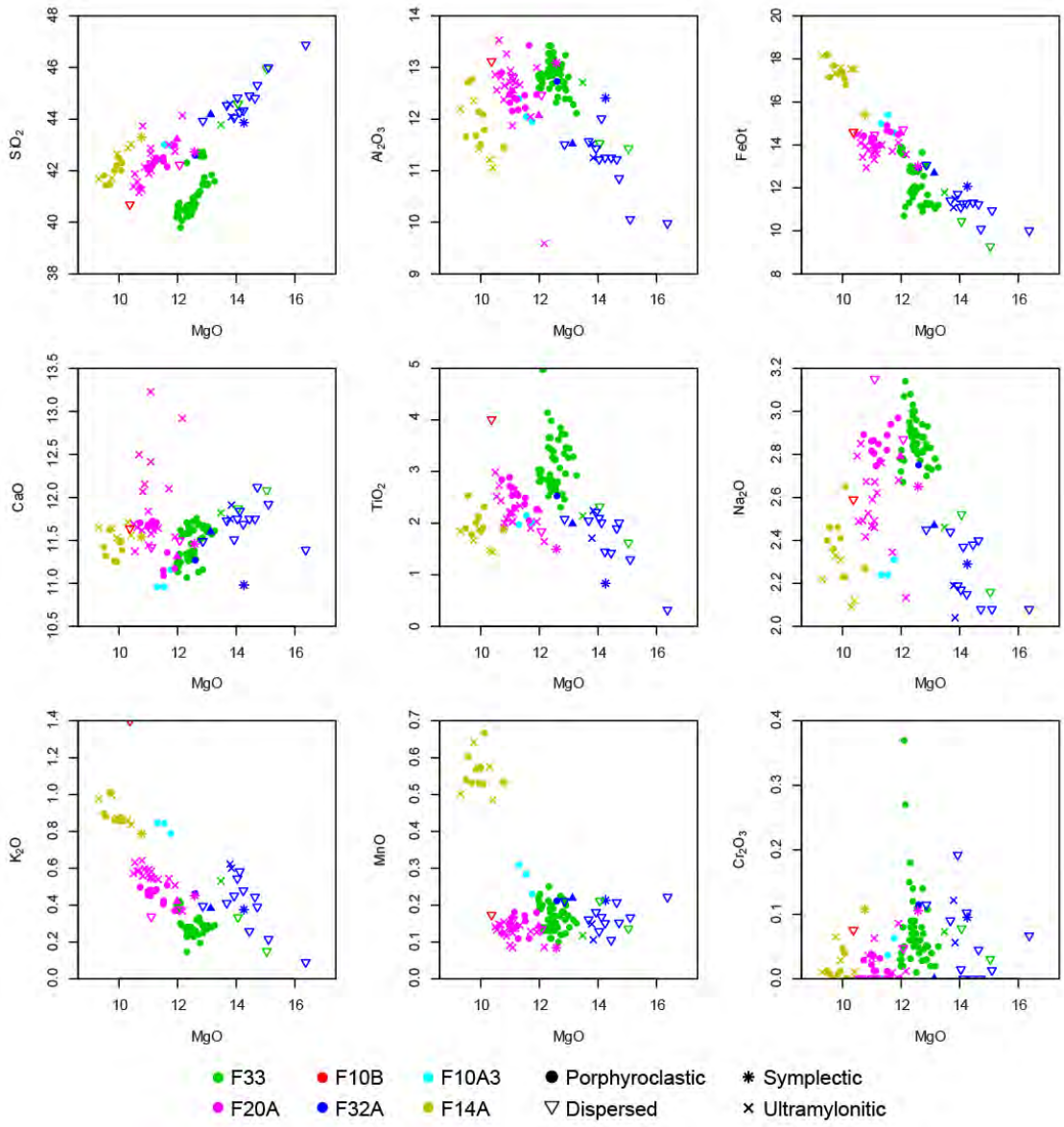

Fig. 5.24

Plots of MgO vs. major element oxides for orthopyroxene (a), clinopyroxene (b) and amphibole (c), from microprobe point analyses. Oxides in wt%. Different colours refer to different samples whereas different symbols refer to different microstructural positions – see legend below. Plots made with GCDkit 4.1 (Janoušek et al., 2006).

Plagioclase porphyroclasts and plagioclase inclusions in garnet porphyroclasts are andesines, with an anorthite content (An = Ca/[Ca+Na+K]) of An_{42}-An_{43} (Fig. 5.25 and Tables A-E in Appendix, Appx. 6). The composition of recrystallized plagioclase in mono-phase domains (of amphibole-poor metagabbros) ranges between An_{40}-An_{53}, with a mean of An_{48} (Fig. 5.26). Plagioclase in the ultramylonitic matrix ranges between An_{47}-An_{67}, with a mean of An_{50}. Symplectic plagioclase, derived from amphibole porphyroclasts, ranges between An_{44}-An_{78} with a mean of An_{52}; whereas symplectic plagioclase derived from garnet porphyroclasts ranges between An_{60}-An_{86}, with a mean value of An_{73}. Thus, undeformed plagioclase preserved as inclusions and as porphyroclasts in low strain domains is less anorthitic than the recrystallized plagioclase in mylonites, and even less anorthitic than the plagioclase in the ultramylonites and symplectites (Fig. 5.25). This compositional change corresponds to a progressive increase in CaO and Al_2O_3 contents.

Clinopyroxenes are diopsides, with mean compositions of $[Ca_{0.47},Mg_{0.37},Fe_{0.16}]SiO_3$ for porphyroclasts and inclusions in garnets; $[Ca_{0.46},Mg_{0.39},Fe_{0.14}]SiO_3$ for neoblastic aggregates; $[Ca_{0.48},Mg_{0.38},Fe_{0.14}]SiO_3$ for ultramylonitic clinopyroxene; and $[Ca_{0.48},Mg_{0.42},Fe_{0.11}]SiO_3$ for clinopyroxenes in amphibole-derived symplectites (Tables A-E in Appendix, Appx. 6). Already from the clinopyroxene end-member compositions, a slight decrease in the FeO content and a corresponding slight increase in the MgO content can be observed going from porphyroclasts to symplectites. However, changes in clinopyroxene chemistry are best seen using the Mg#. Clinopyroxenes show a progressive increase in Mg# from porphyroclasts to ultramylonite (Fig. 5.25). Clinopyroxene inclusions and clinopyroxene porphyroclasts have a mean Mg# of 70. The

neoblastic aggregates have a mean Mg# of 73, while the ultramylonites have a mean Mg# of 75. The clinopyroxene in symplectites have a mean Mg# of 80.

Orthopyroxenes are hypersthenes, with mean compositions of $[Ca_{0.01},Mg_{0.64},Fe_{0.35}]SiO_3$ for porphyroclasts; $[Ca_{0.01},Mg_{0.63},Fe_{0.36}]SiO_3$ for neoblastic aggregates; $[Ca_{0.01},Mg_{0.58},Fe_{0.41}]SiO_3$ for the ultramylonitic matrix; $[Ca_{0.01},Mg_{0.67},Fe_{0.32}]SiO_3$ for orthopyroxene in amphibole-derived symplectites and $[Ca_{0.01},Mg_{0.63},Fe_{0.36}]SiO_3$ for orthopyroxene in garnet-derived symplectites (Tables A-E in Appendix, Appx. 6). The mean Mg# is stable around ca. 64, except for orthopyroxene in amphibole-derived symplectites that shows a mean value of Mg# 68; and ultramylonitic orthopyroxene that shows a mean Mg# of 59 (Fig. 5.25). With the exception of orthopyroxenes from garnet-derived symplectites, the Al_2O_3 content decreases from ca. 3.0 wt % Al_2O_3 in porphyroclasts to 0.7 wt % Al_2O_3 in ultramylonitic matrix.

Amphibole porphyroclasts are classified as ferroanpargasites – pargasites – magnesio-hastingsites. The mean Mg# of amphibole inclusions and porphyroclasts is ca. 62, whereas that of the ultramylonite is Mg# 60 (Fig. 5.25). Amphibole from garnet symplectites and interstitial amphibole is Mg# 66-67 on average. The mean Al_2O_3 content is stable between 11.8-12.8 wt %, yet the ultramylonites record Al_2O_3 contents as low as 9.6 wt %. The CaO content of amphiboles increases from ca. 11.5 wt% of the inclusions and porphyroclasts to up to 13.2 wt% of the ultramylonitic amphiboles. The TiO2 content shows an increase from ca. 2.1 wt% of inclusions to up to 4.2 wt% of porphyroclasts, followed by a decrease to 2.2 wt % in the ultramylonites (Fig. 5.25).

Garnet porphyroclasts (cores) preserved in mylonites and ultramylonites are 0.53-0.54 Almandine, 0.27-0.28 Pyrope, 0.16-0.17 Grossular and 0.02 Spessartine in composition (Table A in Appendix, Appx. 6).

Fig. 5.25 (next pages)

Plot of mineral chemistry ranges for the different subgroups, as described in the text. The subgroups correspond to the ones of the Tables of Appendix, Appx 6. The bars indicate the range between the minimum and maximum values of each subgroup. The dots are the average values of each subgroup. The subgroup "rexx" stands for recrystallized plagioclase and neoblastic pyroxene; the subgroup "symplect" stands for symplectites and is divided between the amphibole derived symplectites (Am) and the garnet-derived symplectites (Grt).

CPX Mg#	Min	Mean	Max	Range
Inclusions	67.6	69.6	73.8	6.2
Porphyro	65.7	69.9	73.8	8.1
Rexx	68.7	73.5	80.0	11.4
Ultramyl	70.2	75.3	80.6	10.5
Symplect (Am)	72.8	80.0	82.7	9.9
Matrix	73.5	77.8	82.5	9.0

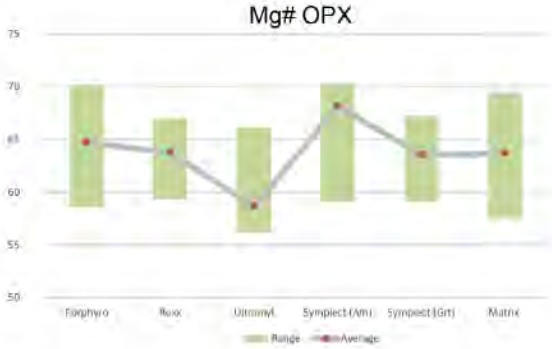

OPX Mg#	Min	Mean	Max	Range
Porphyro	58.6	64.7	70.2	11.6
Rexx	59.3	63.7	67.0	7.7
Ultramyl	56.1	58.6	66.1	10.0
Symplect (Am)	59.1	68.1	70.2	11.1
Symplect (Grt)	59.1	63.5	67.3	8.2
Matrix	57.6	63.6	69.5	11.9

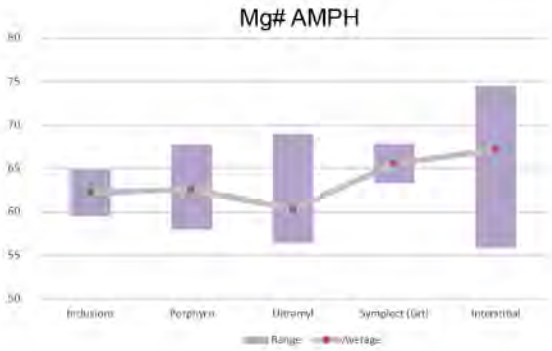

Amph Mg#	Min	Mean	Max	Range
Inclusions	59.5	62.2	64.8	5.4
Porphyro	58.0	62.5	67.8	9.8
Ultramyl	56.4	60.3	68.9	12.5
Symplect (Grt)	63.3	65.6	67.8	4.5
Interstitial	55.9	67.2	74.5	18.6

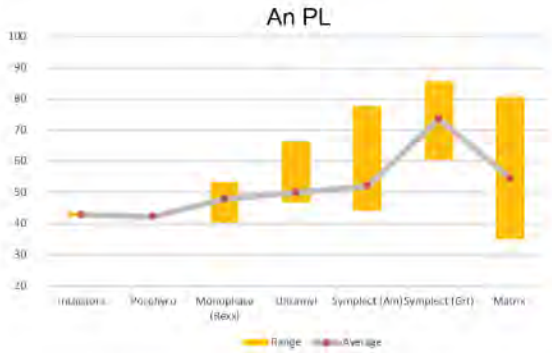

Plag An	Min	Mean	Max	Range
Inclusions	42.2	42.8	43.7	1.6
Porphyro	42.2	42.2	42.2	0.0
Monophase (Rexx)	40.3	47.8	53.4	13.1
Ultramyl	46.7	49.9	66.6	19.8
Symplect (Am)	44.2	52.0	77.7	33.5
Symplect (Grt)	60.3	73.4	85.7	25.5
Matrix	35.0	54.6	80.5	45.5

Fig. 5.25

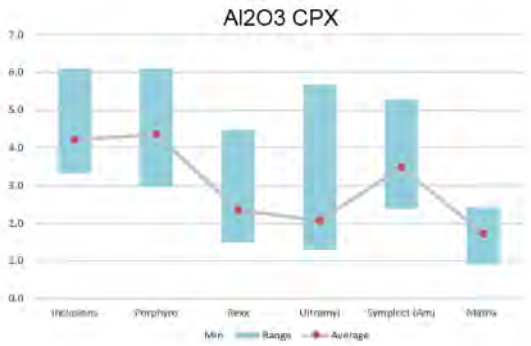

CPX Al2O3	Min	Mean	Max	Range
Inclusions	3.3	4.2	6.1	2.8
Porphyro	3.0	4.4	6.1	3.2
Rexx	1.5	2.3	4.5	3.0
Ultramyl	1.3	2.1	5.7	4.4
Symplect (Am)	2.4	3.5	5.3	2.9
Matrix	0.9	1.7	2.4	1.5

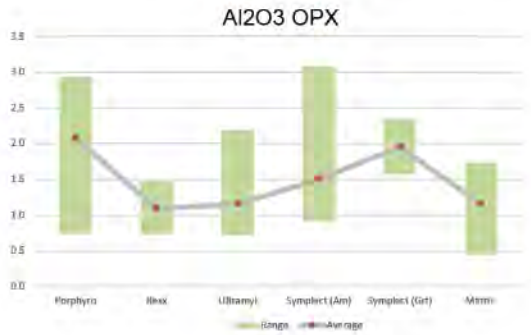

OPX Al2O3	Min	Mean	Max	Range
Porphyro	0.7	2.1	2.9	2.2
Rexx	0.7	1.1	1.5	0.7
Ultramyl	0.7	1.2	2.2	1.5
Symplect (Am)	0.9	1.5	3.1	2.2
Symplect (Grt)	1.6	1.9	2.4	0.8
Matrix	0.4	1.1	1.7	1.3

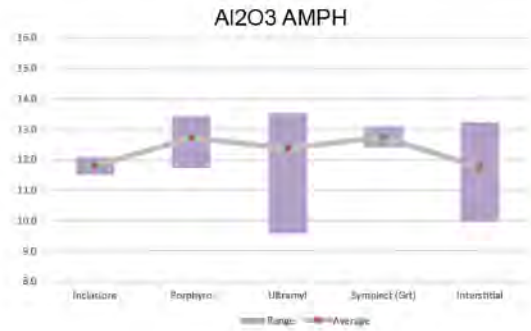

Amph Al2O3	Min	Mean	Max	Range
Inclusions	11.5	11.8	12.1	0.6
Porphyro	11.8	12.7	13.4	1.7
Ultramyl	9.6	12.4	13.5	3.9
Symplect (Grt)	12.4	12.8	13.1	0.7
Interstitial	10.0	11.7	13.2	3.3

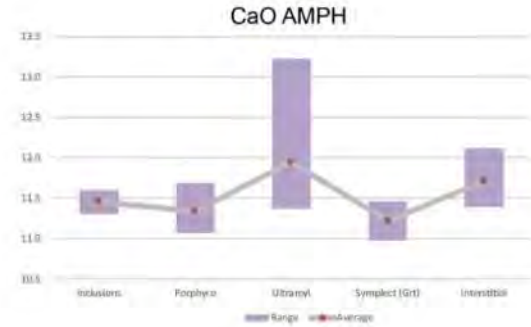

Amph CaO	Min	Mean	Max	Range
Inclusions	11.3	11.5	11.6	0.3
Porphyro	11.1	11.3	11.7	0.6
Ultramyl	11.4	12.0	13.2	1.9
Symplect (Grt)	11.0	11.2	11.5	0.5
Interstitial	11.4	11.7	12.1	0.7

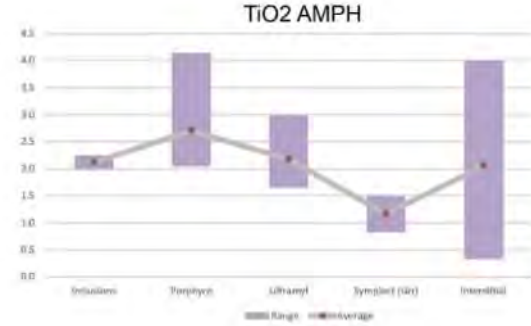

Amph TiO2	Min	Mean	Max	Range
Inclusions	2.0	2.1	2.3	0.3
Porphyro	2.1	2.7	4.2	2.1
Ultramyl	1.6	2.2	3.0	1.3
Symplect (Grt)	0.8	1.2	1.5	0.7
Interstitial	0.3	2.1	4.0	3.7

Fig. 5.25

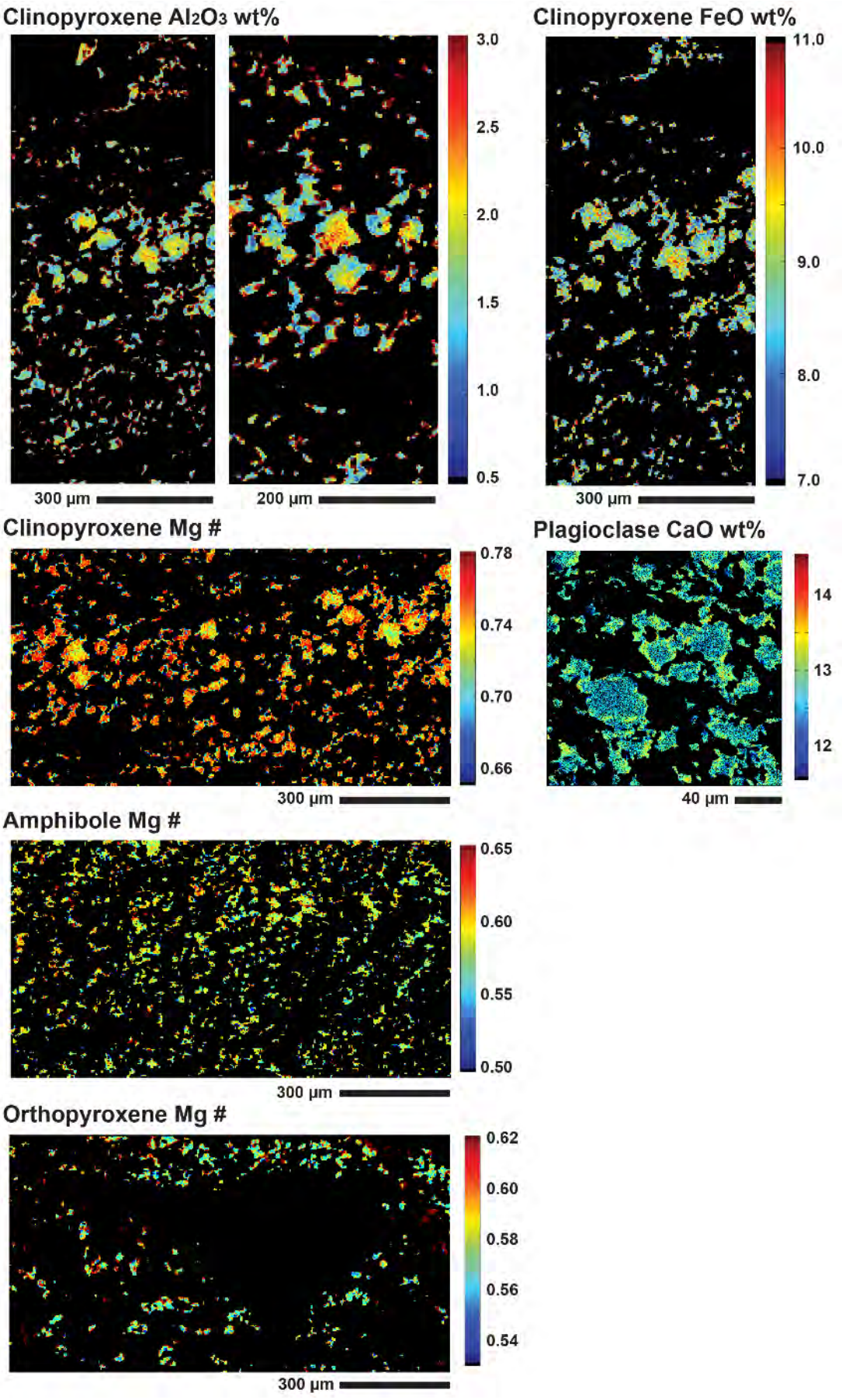

Fig. 5.26 (continued on next page)

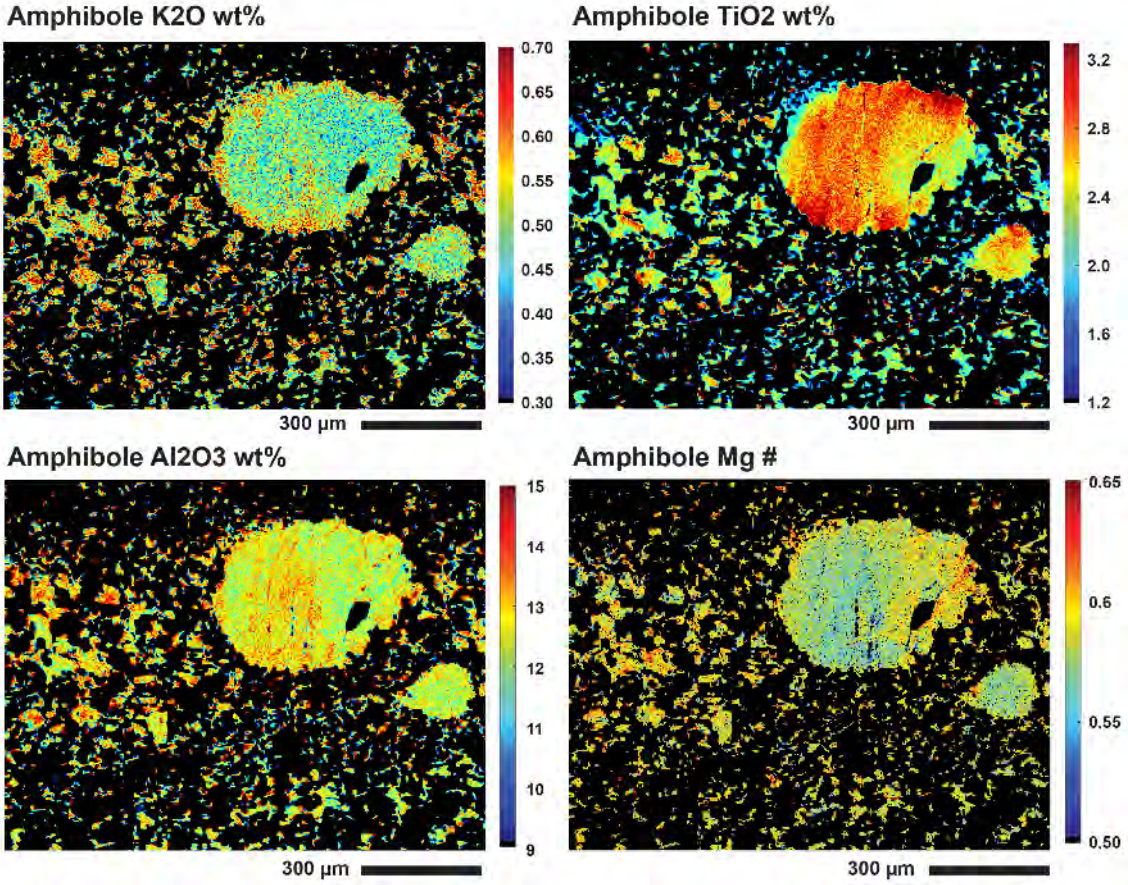

Fig. 5.26

Microprobe compositional maps of F20A ultramylonite, showing the element distribution (expressed as wt% oxide) of the minerals in the ultramylonite. Ultramylonitic clinopyroxenes show a chemical variation between cores and rims, with cores richer in Al_2O_3 and FeO than rims. The Mg# also increases from cores to rims. Ultramylonitic plagioclase show chemical variations, with rims richer in CaO than cores. Amphibole porphyroclasts preserved in the ultramylonite show a K2O-rich rim, and a localized TiO2 depletion.

5.5 THERMOBAROMETRIC ESTIMATES

Quantitative mineral chemistries measured with the microprobe (see section 5.4.2) were used to estimate the pressure and temperature conditions of stability of one or more mineral phases, using conventional geothermobarometry. In the Provola shear zone, pressure and temperature conditions of shearing were estimated using: (1) the barometer of Schmidt (1992) on amphiboles, (2) the thermometer of Holland and Blundy (1994) coupled with the barometer of Schmidt (1992) on amphibole-plagioclase pairs, (3) the thermobarometer of Ernst and Liu (1998) on amphiboles, and (4) the thermometers of Wood and Banno (1973), and Wells (1977) on clinopyroxene-orthopyroxene pairs. For comparison, temperature was also estimated using the QUILF software on clinopyroxene-orthopyroxene pairs (Frost and Lindsley, 1992; Lindsley and Frost, 1992).

The barometer of Schmidt (1992) is based on the Al-content in amphibole. The thermometers of Wood and Banno (1973) and Wells (1977) are based on Mg-Fe partitioning between clino- and orthopyroxene, whereas QUILF software is based on clinopyroxene-orthopyroxene net transfer (Lindsley and Frost, 1992; Mehl and Hirth, 2008). Garnet thermobarometers could not be used because garnet has been found only as porphyroclasts and not as a syn-kinematic phase in the shear zone. Thermobarometric results are summarised in Table 5.4 (amphibole; amphibole-plagioclase pairs), Fig. 5.27 (amphibole), and Table 5.5 (clinopyroxene-orthopyroxene pairs).

In the amphibole-rich metagabbros, amphiboles and amphibole-plagioclase pairs in the ultramylonite matrix indicate shearing temperatures of 778 – 858 °C (823 °C mean), and pressures of 6.2 - 8.2 kbar (7.4 kbar mean) (Table 5.4a). In the amphibole-poor

metagabbros, the amphibole-plagioclase pairs located between pyroxene neoblasts (the so-called “dispersed” grains; e.g. Fig. 5.12a) and the amphibole-plagioclase pairs in shear bands indicate pressures between 6.0 - 8.0 kbar (6.5 kbar mean), and temperatures between 825 - 964 °C (847 °C mean) (Table 5.4b). Thus, thermobarometry on amphibole-plagioclase pairs indicate pressures between 6.0 - 8.2 kbar and temperatures mainly between 780 – 960 °C for both amphibole-poor and amphibole rich metagabbros. The latter pressure-temperature range is also confirmed by the amphibole Al-Ti thermobarometry of Ernst and Liu (1998). Results using the Ernst and Liu (1998) thermobarometer are plotted in Fig. 5.27. Ernst and Liu (1998) thermobarometer has the advantage of not relying on amphibole-plagioclase equilibrium conditions, but is very sensitive to Ti content for temperature determination (Ernst and Liu, 1998).

In the amphibole-rich ultramylonites, clinopyroxene-orthopyroxene pairs indicate shearing temperatures mostly between 700 - 800 °C (mean values of 749 °C, 743 °C, and 708 °C, depending on the thermometer) (Table 5.5a). In the amphibole-poor mylonites, neoblastic clinopyroxene-orthopyroxene pairs indicate shearing temperatures between 745 – 870 °C (mean values of 831 °C, 839 °C and 745 °C, depending on the thermometer) (Table 5.5b). The thermometers of Wood and Banno (1973) and Wells (1977) using orthopyroxene-clinopyroxene pairs indicate a temperature difference of ca. 100 °C between amphibole-poor mylonites and amphibole-rich ultramylonites, from ca. 830 - 840 °C (mean values) of the mylonites to ca. 740 - 750 °C (mean values) of the ultramylonites (Table 5.5b). QUILF results instead indicate the same range of temperatures for both amphibole-poor and amphibole-rich domains.

To summarise, P-T results using a range of conventional geothermobarometers indicate P-T conditions of shearing ranging from upper amphibolite to lower-granulite facies (P = 6.0 – 8.0 kbar and T = 700-900 °C) for both amphibole-poor and amphibole-rich metagabbros.

(a) Amphibole-rich metagabbros				
Sample	**Rock type**	**Microstructural position**	**P (kbar) - Schmidt (92)**	**T (°C) Holland & Blundy (94)**
F33	protomylonite	porphyroclast	8.0	892
F33	protomylonite	porphyroclast	8.0	870
F33	protomylonite	porphyroclast	7.8	
F33	protomylonite	porphyroclast	7.8	875
F33	protomylonite	porphyroclast	7.7	
F33	protomylonite	porphyroclast	7.7	882
F33	protomylonite	porphyroclast	7.6	
F33	protomylonite	porphyroclast	7.5	
F33	protomylonite	porphyroclast	7.4	863
F33	protomylonite	porphyroclast	7.2	
F33	protomylonite	shear band	7.2	828
F33	protomylonite	shear band	6.3	814
F33	protomylonite	shear band	6.2	
F20A	ultramylonite	porphyroclast	8.0	
F20A	ultramylonite	porphyroclast	7.8	
F20A	ultramylonite	porphyroclast	7.5	
F20A	ultramylonite	porphyroclast	7.4	
F20A	ultramylonite	porphyroclast	7.4	
F20A	ultramylonite	porphyroclast	7.3	
F20A	ultramylonite	porphyroclast	7.3	
F20A	ultramylonite	porphyroclast	7.3	
F20A	ultramylonite	porphyroclast	7.2	
F20A	ultramylonite	porphyroclast	7.2	
F20A	ultramylonite	porphyroclast	7.1	
F20A	ultramylonite	porphyroclast	6.8	
F20A	ultramylonite	ultramylonite	8.2	858
F20A	ultramylonite	ultramylonite	8.1	808
F20A	ultramylonite	ultramylonite	7.9	794
F20A	ultramylonite	ultramylonite	7.9	845
F20A	ultramylonite	ultramylonite	7.8	852
F20A	ultramylonite	ultramylonite	7.6	793
F20A	ultramylonite	ultramylonite	7.6	838
F20A	ultramylonite	ultramylonite	7.6	
F20A	ultramylonite	ultramylonite	7.6	
F20A	ultramylonite	ultramylonite	7.6	834
F20A	ultramylonite	ultramylonite	7.6	824
F20A	ultramylonite	ultramylonite	7.6	854
F20A	ultramylonite	ultramylonite	7.5	849
F20A	ultramylonite	ultramylonite	7.5	852
F20A	ultramylonite	ultramylonite	7.5	785
F20A	ultramylonite	ultramylonite	7.2	
F20A	ultramylonite	ultramylonite	7.0	814
F20A	ultramylonite	ultramylonite	6.9	668
F20A	ultramylonite	garnet-derived symplectite	7.7	918
F10A3	ultramylonite	porphyroclast	7.2	
F10A3	ultramylonite	porphyroclast	6.8	
F10A3	ultramylonite	porphyroclast	6.8	
F32A	ultramylonite	porphyroclast	7.4	
F32A	ultramylonite	ultramylonite	6.6	778
F32A	ultramylonite	ultramylonite	6.4	
F32A	ultramylonite	ultramylonite	6.2	805

(b) Amphibole-poor metagabbros				
F20A	mylonite	porphyroclast	7.2	
F20A	mylonite	shear band	7.2	874
F32A	mylonite	porphyroclast	6.6	
F32A	mylonite	porphyroclast	6.4	
F32A	mylonite	dispersed	6.7	
F32A	mylonite	dispersed	6.4	
F32A	mylonite	dispersed	6.4	
F32A	mylonite	dispersed	6.3	847
F32A	mylonite	dispersed	6.2	860
F32A	mylonite	dispersed	6.1	825
F32A	mylonite	dispersed	6.1	
F32A	mylonite	dispersed	6.0	839
F32A	mylonite	shear band	6.2	836
F32A	mylonite	garnet-derived symplectite	7.0	958
F10B	mylonite	dispersed	8.0	964

Table 5.4

Thermobarometric estimates using the barometer of Schmidt (1992) on amphiboles, and the thermometer of Holland and Blundy (1994) coupled with the barometer of Schmidt (1992) on amphibole-plagioclase pairs. (a) amphibole-rich domains. (b) amphibole-poor domains. The amphibole measured in the amphibole poor domains is mostly dispersed amphibole found between pyroxene neoblasts or in shear bands.

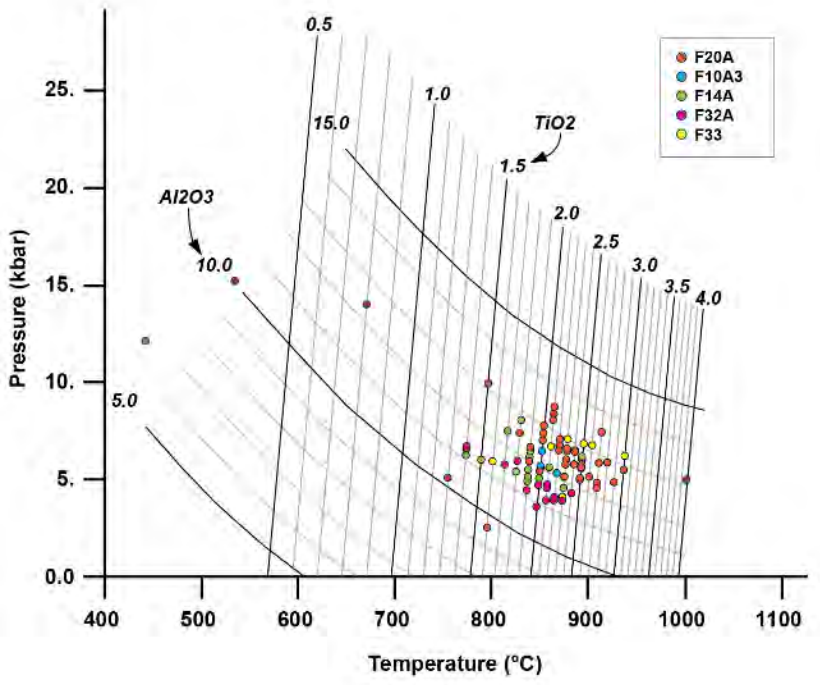

Fig. 5.27

Pressure-temperature results using Ti-Al thermobarometry in amphibole (Ernst and Liu, 1998).

(a) Amphibole-rich metagabbros						
Sample	**Rock type**	**Microstructural position**	**T (°C) Wood & Banno (73)**	**T (°C) Wells (77)**	**QUILF**	**QUILF uncertainty**
F33	protomylonite	shear band	855	852	780	13
F33	protomylonite	shear band	844	830	717	15
F20A	ultramylonite	ultramylonite	*879*	*922*	*698*	62
F20A	ultramylonite	ultramylonite	*672*	*638*	*585*	38
F20A	ultramylonite	ultramylonite	721	705	665	16
F20A	ultramylonite	ultramylonite	711	695	706	42
F20A	ultramylonite	ultramylonite	766	762	718	26
F20A	ultramylonite	ultramylonite	740	730	776	41
F20A	ultramylonite	ultramylonite	734	726	707	43
F20A	ultramylonite	ultramylonite	731	719	698	27
F20A	ultramylonite	ultramylonite	696	670	718	44
F20A	ultramylonite	ultramylonite	*881*	*929*	*734*	28
F20A	ultramylonite	ultramylonite	714	694	713	24
F20A	ultramylonite	ultramylonite	758	753	727	44
F20A	ultramylonite	ultramylonite	740	729	716	39
F20A	ultramylonite	ultramylonite	745	733	703	31
F20A	ultramylonite	ultramylonite	765	763	715	34
F20A	ultramylonite	ultramylonite	722	705	676	40
F20A	ultramylonite	ultramylonite	764	761	725	22
F20A	ultramylonite	ultramylonite	743	731	765	49
F20A	ultramylonite	amphibole-derived sympl.	839	865	748	21
		mean T (°C)	***749***	***743***	***708***	***36***
(b) Amphibole-poor metagabbros						
F20A	mylonite	shear band	829	851	707	18
F32A	mylonite	neoblasts	813	802	747	39
F32A	mylonite	neoblasts	840	838	754	16
F32A	mylonite	neoblasts	843	841	710	31
F32A	mylonite	neoblasts	817	803	738	31
F32A	mylonite	shear band	835	826	775	8
F10B	mylonite	neoblasts	842	868	769	31
F10B	mylonite	neoblasts	827	844	747	13
F10B	mylonite	neoblasts	826	846	735	20
F10B	mylonite	neoblasts	842	870	746	36
F10B	mylonite	neoblasts	824	844	762	14
		mean T (°C)	***831***	***839***	***745***	***23***

Table 5.5

Thermometric estimates using the thermometers of Wood and Banno (1973) and Wells (1977) on clinopyroxene-orthopyroxene pairs, and using QUILF software (Frost and Lindsley, 1992) on clinopyroxene-orthopyroxene pairs. (a) amphibole-rich domains. (b) amphibole-poor domains. Wood and Banno (1973) and Wells (1977) thermometers give a temperature difference of ca. 100 °C between the amphibole-poor mylonites and the amphibole-rich ultramylonites; whereas using QUILF the temperatures of the two domains overlap.

5.6 THERMODYNAMIC MODELLING

Thermodynamic modelling calculates phase equilibria in the P-T-X space (X = composition), given a starting bulk composition and a set of boundary constrains. Typical results of modelling are pseudosections, i.e. diagrams showing stability fields of different phase assemblages in a P-T space. These diagrams are therefore very useful to predict what minerals are stable, and with what compositions, at any point in the P-T space.

Thermodynamic modelling was used here to predict the P-T conditions of shearing, and infer from the models a possible P-T path of the shear zone. For the purpose, two P-T pseudosections were constructed: one for the amphibole-poor metagabbroic domain (mylonite F10B) and one for the amphibole-rich domain (ultramylonite F20A).

Using thermodynamic modelling to predict the P-T evolution of a shear zone is not always possible, because shear zones are often chemically-open systems and this means that the bulk chemistry changes over time. Here however, the bulk-rock chemistry was found to be the same regardless of the mineralogical differences (amphibole-rich vs. amphibole poor domains) or degree of deformation (mylonitic vs. ultramylonitic) (see Section 5.4.1). The system can therefore be considered a closed system, and thermodynamic modelling can be used as an investigative approach. Isochemical deformation is not uncommon during high temperature shearing at mid- to lower crustal conditions, and other studies have found the same bulk-rock chemistry between the undeformed host-rock and the shear zone, despite reporting differences in the microstructure and mineralogy (e.g. Brodie, 1981; Burg et al., 2005; Menegon et al., 2006; Pennacchioni and Mancktelow, 2007).

Results of thermodynamic modelling are displayed as P-T pseudosections showing the stability fields of different mineral assemblages for a given bulk-rock composition (Fig. 5.28a and b).

The P-T isochemical pseudosection of the amphibole-poor domain (sample F10B) shows that the mylonitic mineral assemblage (clinopyroxene, orthopyroxene, plagioclase, garnet, amphibole, ilmenite and magnetite) was stable between 650 - 950 °C and 6.5 - 9.7 kbar (shaded field, Fig. 5.28a). If melt is also considered, then this field expands also to field 3 (grey field, Fig. 5.28a). These P-T conditions partly overlap with those predicted by conventional thermobarometry (blue box, Fig. 5.28a). Amphibole is thermodynamically stable everywhere below the amphibole-out curve, despite the low water contents of the model (0.1 wt% H_2O), but only in minimal modal amounts (ca. 2 – 3 vol % as calculated from the modelling). Small quantities of amphibole are consistent with the presence of dispersed amphibole in pyroxene-rich layers.

Thermodynamic modelling was also used to estimate the pre-shearing P-T conditions, using the compositional isopleths of garnet porphyroclasts preserved in the mylonite sample F10B. The occurrence of porphyroclastic garnets in the shear zone indicates that the gabbro must have equilibrated under granulite-facies metamorphism before the onset of shearing (Sills, 1984). Results indicate that these garnet formed at 900 °C of temperature and 9.7 kbars of pressure (Fig. 5.29). The same garnet porphyroclasts are mantled by symplectites of orthopyroxene and plagioclase, indicating garnet instability during shearing. The granulite facies pre-shearing P-T conditions are shown in the pseudosections of Fig. 5.28 with a red box.

The P-T isochemical section of the amphibole-rich domain (sample F20A ultramylonite) indicates that the ultramylonitic mineral assemblage (clinopyroxene, orthopyroxene, amphibole, plagioclase, ilmenite and magnetite) was stable between ca. 800 – 900° C for pressures below 7 kbar (shaded field, Fig. 5.28b). In the ultramylonite, garnet porphyroclasts were unstable and reacted to form symplectites of orthopyroxene + plagioclase, indicating that shearing must have protracted at pressures below the garnet-out curve. If melt is also considered, then the P-T field expands also to higher temperatures (grey field, Fig. 5.28b). The P-T conditions predicted by the model partly overlap with those derived from conventional thermobarometry (blue box, Fig. 5.28b).

The position of the solidus curve (melt-in curve) in the P-T sections strongly depends on the total water content used in the model. If the P-T section F20A is modelled using 0.5 wt% H_2O, the solidus curve (the red melt-in curve) drops from ca. 920 °C to ca. 800 °C, while the amphibole-out curve remains at ca. 1000 °C (dashed red line, Fig. 5.28b). As a result, the stability field of the assemblage clinopyroxene + amphibole, melt, feldspar, magnetite and ilmenite widens, and orthopyroxene becomes stable for lower temperatures. From a modelling perspective, the addition of water also increases the modal amount of amphibole in the system.

a

F10B mylonite - 0.1 H2O, 0.4 O2.

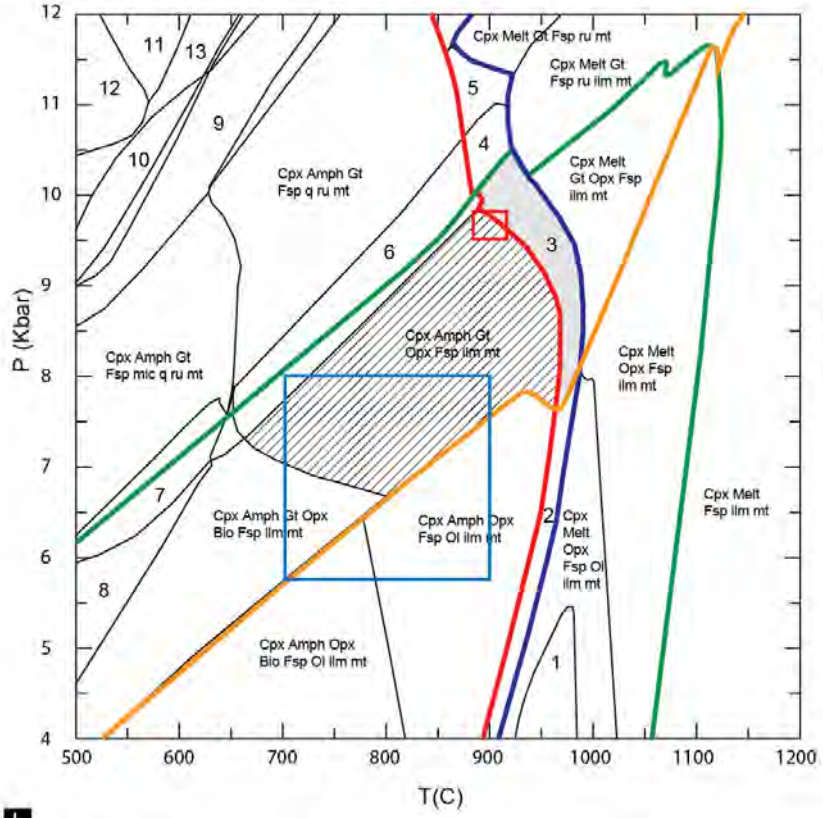

1 Cpx Melt Fsp Ol ilm mt
2 Cpx Amph Melt Opx Fsp Ol ilm m
3 Cpx Amph Melt Gt Opx Fsp ilm m
4 Cpx Amph Melt Gt Fsp ru ilm mt
5 Cpx Amph Melt Gt Fsp ru mt
6 Cpx Amph Gt Fsp q ru ilm mt
7 Cpx Amph Gt Opx Fsp mic q ilm
8 Cpx Amph Gt Opx Fsp mic ilm mt
9 Cpx Amph Ep Gt Fsp mic q ru mt
10 Cpx Amph Ep Gt Fsp mic q ru he
11 Cpx Ep Gt ky mic q ru
12 Cpx Amph Ep Gt ky mic q ru
13 Cpx Ep Gt Fsp mic q ru hem

b

F20A ultramylonite - 0.2 H2O, 0.4 O2.

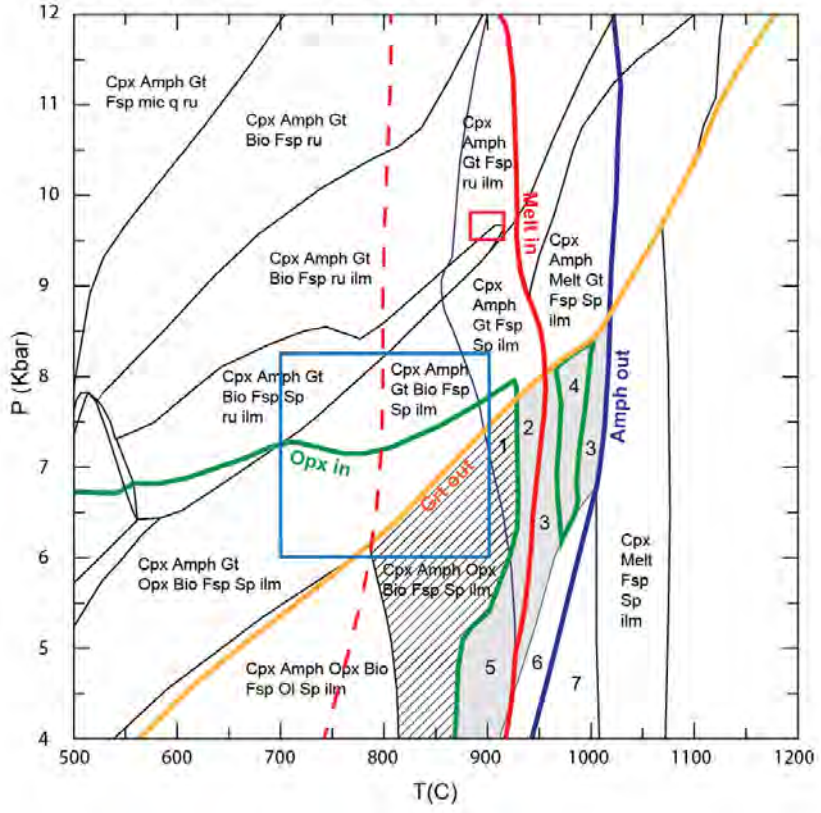

1 Cpx Amph Opx Fsp Sp ilm
2 Cpx Amph Fsp Sp ilm
3 Cpx Amph Melt Fsp Sp ilm
4 Cpx Amph Melt Opx Fsp Sp ilm
5 Cpx Amph Bio Fsp Sp ilm
6 Cpx Amph Melt Fsp Ol Sp ilm
7 Cpx Melt Fsp Ol Sp ilm

Fig. 5.28 (previous page)

Results from thermodynamic modelling. P-T isochemical sections showing the P-T stability boundaries for different mineral assemblages. Coloured lines are stability boundaries of the minerals: opx – green; grt – yellow; melt (solidus) – red; amph – blue. The red box in both pseudosections delimits the P-T conditions of granulite facies re-equilibration before the onset of shearing (see text for further details); the blue box in both pseudosections delimits the shearing conditions according to conventional thermobarometric results. The shaded fields are the samples' mineralogical assemblages. (a) P-T isochemical section of sample F10B (mylonite chemistry, with porphyroclasts), calculated using 0.1 wt% H_2O and O.4 wt% O_2. (b) P-T isochemical section of sample F20A (ultramylonite chemistry, without porphyroclasts), calculated using 0.2 wt% H_2O and O.4 wt% O_2 . The red dotted line is the solidus curve position using 0.5 wt% H_2O.

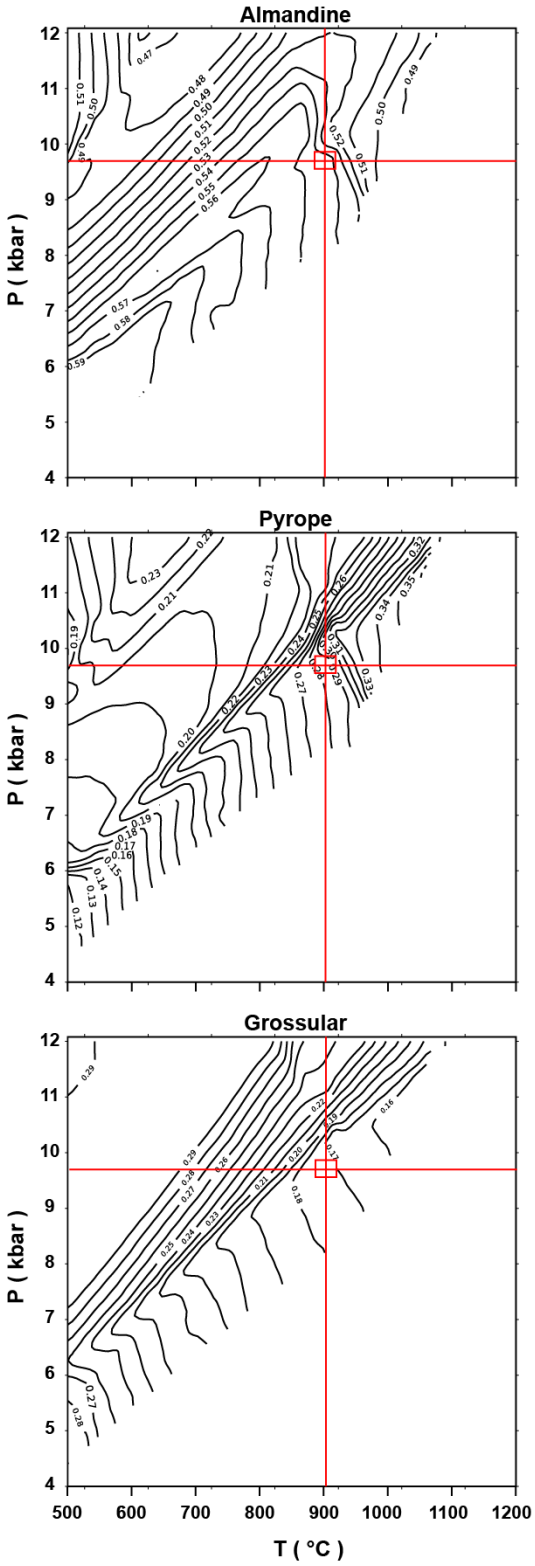

Fig. 5.29

Plots of compositional isopleths of garnet, computed from the pseudosection F10B. The composition of sample F10B garnets from microprobe (0.54 Almandine – 0.28 Pyrope – 0.17 Grossular) fall at 9.7 kbar pressure and 900°C temperature. These garnets record the granulite-facies re-equilibration before the onset of shearing.

5.7 P-T CONDITIONS OF SHEARING

Results from thermodynamic modelling and conventional geothermobarometry were combined to derive the P-T conditions of shearing and the possible P-T evolution experienced by the Provola shear zone.

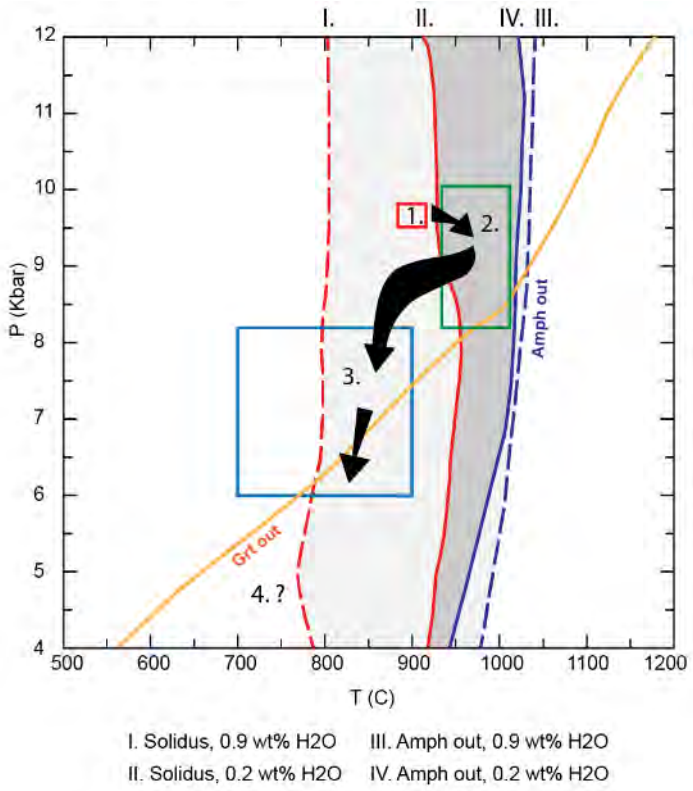

Fig. 5.30

P-T evolution of the Provola shear zone, derived from thermodynamic modelling and conventional thermobarometry. The evolution, corresponding to the stages 1. to 3. is described in the text. For reference, the solidus, the garnet and the amphibole stability curves are plotted. Solid lines are from the pseudosection F20A, modelled with 0.2 wt% H_2O. The dashed lines are from the pseudosection F20A modelled with 0.9 wt% H_2O. Note how the solidus drops substantially for increased water contents.

Based on the two methods, the following P-T evolution is proposed. Prior to shearing, the undeformed metagabbro equilibrated under granulitic conditions at 900°C and 9.7 kbar

(red box in Fig. 5.30; see also Fig. 5.28). This stage will be referred to as Stage 1. Stage 1 pressure and temperature conditions are derived from the composition of garnet porphyroclasts in the shear zone, which still preserve a poikiloblastic texture with inclusions of magmatic clinopyroxene and plagioclase (garnet examples: Fig. 5.12d; garnet composition: section 5.4.2; compositional isopleths in pseudosection: Fig. 5.29). Garnet growth is attributed to the post-intrusive granulite facies re-equilibration of the layered mafic sequence.

Stage 1 granulitic re-equilibration was followed by an increase in the temperature above the solidus, possibly coupled by a decrease in pressure (green box in Fig. 5.30). This will be referred to as Stage 2. In this stage of prograde metamorphism, magmatic amphiboles (i.e. the amphibole porphyroclasts in the amphibole-rich domains) were subject to dehydration melting reactions, forming peritectic phases and melt. The pyroxene + plagioclase ± amphibole symplectites replacing the magmatic amphiboles are considered the microstructural record of this temperature increase and of amphibole dehydration melting reactions (Fig. 5.22). In the modelled pseudosection F20A, the Al_2O_3 content of symplectic clinopyroxene, and the anorthitic content of symplectic plagioclase, both plot above the solidus (in Appendix, Appx. 9). Therefore, thermodynamic modelling suggests that stage 2 occurred above the solidus.

Stage 2 was followed by shearing and decompression, referred to as Stage 3 (blue box in Fig. 5.30; see also Fig. 5.28

). Decompression during shearing is supported by 1) the microstructure, showing syn-kinematic breakdown of garnet porphyroclasts into symplectites of orthopyroxene + plagioclase, indicating garnet instability during deformation (Fig. 5.21); by 2)

thermodynamic modelling, where garnet is predicted to be unstable for low P – high T conditions (below the garnet-out curve; Fig. 5.28); and by 3) the pressure range estimated by conventional geothermobarometry on amphiboles, indicating a pressure drop of ca. 2.2 kbar (blue box in Fig. 5.30; see also section 5.6).

Geothermobarometric estimates using plagioclase-hornblende pairs and orthopyroxene-clinopyroxene pairs indicate that Stage 3, for both amphibole-poor and amphibole-rich domains, occurred between 8 - 6 kbar and between 700 – 900 °C (blue boxes in Fig. 5.30; see also sections 5.5 and 5.6). In the pseudosections F10B (mylonite) and F20A (ultramylonite), modelled with 0.1 wt% and 0.2wt% H_2O respectively, Stage 3 P-T estimates obtained from conventional geothermobarometry plot below the solidus, suggesting that shearing occurred at subsolidus conditions – i.e. in the absence of melt.

However, sub-solidus shearing would not justify the peritectic products of amphibole-dehydration reactions found around amphibole porphyroclasts in the ultramylonites (Fig. 5.22). Furthermore, the P-T conditions of shearing predicted from conventional thermobarometry are very close the modelled solidus curve (blue box in Fig. 5.30; see also Fig. 5.28). The temperature of the modelled solidus strongly depends on the water content in the system, and this content is poorly constrained. It is in therefore possible that the amphibole-rich domains contained more than the 0.2 wt% H_2O used in the model, effectively reducing the temperature of the solidus. In the amphibole-rich pseudosection F20A, an increase of water content from 0.2 to 0.5 wt%, would shift the solidus curve to 800 °C, with the consequence of the thermobarometric estimates falling in the field of melting (dotter red line, Fig. 5.28b).

In summary, the above discussion evidences to two possible scenarios for stage 3 shearing and decompression:

1) Stage 3 shearing and decompression occurred at subsolidus conditions – i.e. in the absence of melt – for both amphibole-poor and amphibole-rich domains.

   or, in alternative,

2) Stage 3 shearing and decompression occurred at subsolidus conditions for amphibole-poor domains (as the water content in these rocks is minimal), and at suprasolidus conditions for amphibole-rich domains, owing to greater amounts of water "released" by amphibole dehydration melting. It is to clarify here that the P-T conditions of deformation of both the amphibole-poor and amphibole-rich metagabbros were found to be the same (as indicated by geothermobarometric estimates), and that this scenario only shifts the position of the solidus to lower temperatures in account of higher water contents in the amphibole-rich domains.

Based on the available evidence, both scenarios are equally possible. However, for the occurrence of amphibole-derived symplectites in the ultramylonites, I support the second scenario where shearing of amphibole-rich metagabbros occurred at supra-solidus conditions accompanied by dehydration melting reactions.

At the onset of shearing, both amphibole-poor and amphibole-rich domains deformed simultaneously, yet the presence or absence of amphibole was crucial for the deformation that followed. Shearing of amphibole-rich domains was accompanied by amphibole dehydration reactions, forming fine grained symplectites of clino-orthopyroxene + plagioclase ± amphibole + melt. Domains without amphiboles instead were devoid of the above reactions and thus deformed under solid state conditions. As a

result of amphibole dehydration melting reactions, the amphibole-rich portions formed ultramylonites such as F20A; whereas the amphibole-poor portions formed mylonites such as F10B.

All the above investigation assumes that melt remained in the system, in the form of reacted products (peritectic phases) and back-reacted products (secondary amphibole). If this was not the case, the system would be an open system and I would be unintentionally modelling a restitic portion. Thermodynamic modelling of shear zones is therefore appropriate only for systems that have experienced small melt volumes (below the melt interconnectivity threshold - ca. 7% melt fraction, according to Rosenberg and Handy 2005) and loses its significance for melt portions above ca. 10 wt%. It is here reasoned that the Finero ultramylonites were subject to small amounts of melt that remained in the system, based on the following lines of evidence:

1) The bulk composition of the amphibole-rich ultramylonite is substantially the same as the composition of the amphibole-poor mylonites (see section 5.4.1). Substantial melt removal form the system would have changed the chemistry in the ultramylonites.
2) Removal of melt from the system would have inhibited the formation of secondary amphibole upon cooling of the system past the solidus. Instead, there is widespread secondary amphibole in the ultramylonite, often preserved between pyroxenes. If the ultramylonitic amphibole was the result of externally-derived fluids, there would not be an explanation for pyroxene-symplectites out of amphibole porphyroclasts.

3) The melt in the system derives from in-situ dehydration melting of amphibole and thus the production of melt is limited by the abundance of primary amphibole, and by the rate of amphibole breakdown reactions.

The possibility that melt does not escape the system, causing back-reactions upon cooling was also proposed by Beard et al., (2004).

5.8 EBSD RESULTS: AMPHIBOLE-POOR VS. AMPHIBOLE-RICH DOMAINS

The EBSD technique was used for textural characterisation of sheared amphibole-poor and amphibole-rich domains, in order to document how these two microstructurally different domains were shearing, and decipher their deformation mechanisms and rheological responses. In the Provola shear zone, EBSD was used to measure the crystallographic orientations of clinopyroxene and plagioclase of amphibole-poor mylonites; and of amphibole, clinopyroxene, orthopyroxene and plagioclase of amphibole-rich ultramylonites. EBSD results were used to document the presence or absence of a CPO, determine plausible slip systems by comparison of measured CPOs with literature, assess the presence or absence of dynamic recrystallization and the degree of internal lattice distortions through misorientation analysis, and identify the dominant deformation mechanism. For details on the EBSD method, see Chapter 3, section 3.4. The sections that follow describe and interpret EBSD results of the main mineralogical phases of both amphibole-poor and amphibole-rich domains.

5.8.1 AMPHIBOLE-POOR MYLONITES

As seen in section 5.3.1, amphibole-poor mylonites are the deformed equivalents of amphibole-poor metagabbros. They are mineralogically banded rocks, made of alternating layers of plagioclase and pyroxene. The plagioclase ribbons are mostly monophase, whereas the pyroxene layers are mostly made up of pyroxene with secondary phases dispersed between. Both layers were analysed with EBSD, and the results and interpretations are presented below.

Plagioclase:

Plagioclase in the mono-phase ribbons of amphibole-poor mylonites displays a core-and-mantle structure with larger, sometimes elongated, grains (10-100 µm in F10B) surrounded by an aggregate of smaller recrystallized grains (< 10 µm in F10B) (Fig. 5.31c, d, e). The larger grains (parent grains) have a high density of low angle grain boundaries (3-10°, in white) and of polysynthetic twin boundaries (in yellow) (Fig. 5.31d). The presence and distribution of intracrystalline misorientation bands, with misorientation as low as 2-3°, is shown in the local misorientation map (Fig. 5.31e). The latter map highlights an abundance of substructures, and the incipient development of subgrains with sizes comparable to the finer recrystallized grains (Fig. 5.31e, white arrows).

The elongated plagioclase grain (marked with a star, Fig. 5.31d) has the [001] crystallographic axis oriented subparallel to the stretching lineation and the (010) plane oriented subparallel to the foliation (Fig. 5.31f).

Large plagioclase grains (> 10 µm) taken collectively display a CPO that differs from that of the elongated grain: the [001] alignment subparallel to the stretching lineation is replaced by a combination of other crystallographic directions (the [100], [01-1], [11-1] and [-11-1]); while the (010) plane alignment subparallel to the foliation is shared with the (110), (011), (111) planes. This is evident from comparison of pole figures; and from the girdle of the IPF-X direction (Fig. 5.31f vs. g; and i).

Recrystallized plagioclase grains (i.e. grains < 10 µm) have a well-defined CPO (4.22 m.u.d.) that matches that of the large parent grains (i.e. grains > 10 µm) (Fig. 5.31g vs. h). Planes (011), (010) and to a lesser extent (110) and (111) cluster subparallel to the

foliation plane; whereas the crystallographic directions [100], [01-1], [11-1] and [-11-1] cluster subparallel to the stretching lineation (Fig. 5.31h). Most of the other primitive planes (i.e. the (100), (101), (-110), (01-1), (10-1) and (-11-1)) form girdles. The same CPO can also be seen in the mylonite portion of sample F20A (Appendix, Appx. 7).

The inverse pole figure of the recrystallized plagioclase (grains < 10 μm) shows an alignment of [0-11] and [-1-11] (equal to [01-1] and [11-1] by inversion symmetry) directions with the stretching lineation (X direction); and an alignment of (011), (111), and (021) poles to planes with the pole to the foliation (Z direction) (Fig. 5.31i).

Misorientation angle-axis pairs of all plagioclase grains, for misorientation angles of 3-10°, and of 10-40°, indicate rotations around the centre of the pole figure (Y-direction of finite strain), corresponding to a girdle containing the [001], [100] and [-100] axis in crystal coordinates (Fig. 5.31j). For misorientations between 40-140°, there is no prevailing cluster of misorientation axis. For misorientation between 140-180°, the misorientation axes in sample coordinates form two clusters around the centre of the pole figure and one cluster near the pole to the mylonitic foliation. The latter cluster corresponds to the [010] axis, and is presumably associated with twinning.

The misorientation angle distribution for uncorrelated pairs of plagioclase approximates the theoretical random curve, with a minor excess of misorientation angles < 75° and > 140°, and a minor deficit for misorientation between 65° and 140° (Fig. 5.31j). Instead, the misorientation angle distribution for correlated pairs shows a marked deviation from the theoretical random curve, with an excess of misorientation angles < 60° and a deficit of misorientations for angles between 60° and 175°. The peak in misorientations at 180° is again attributed to twinning on the albite law.

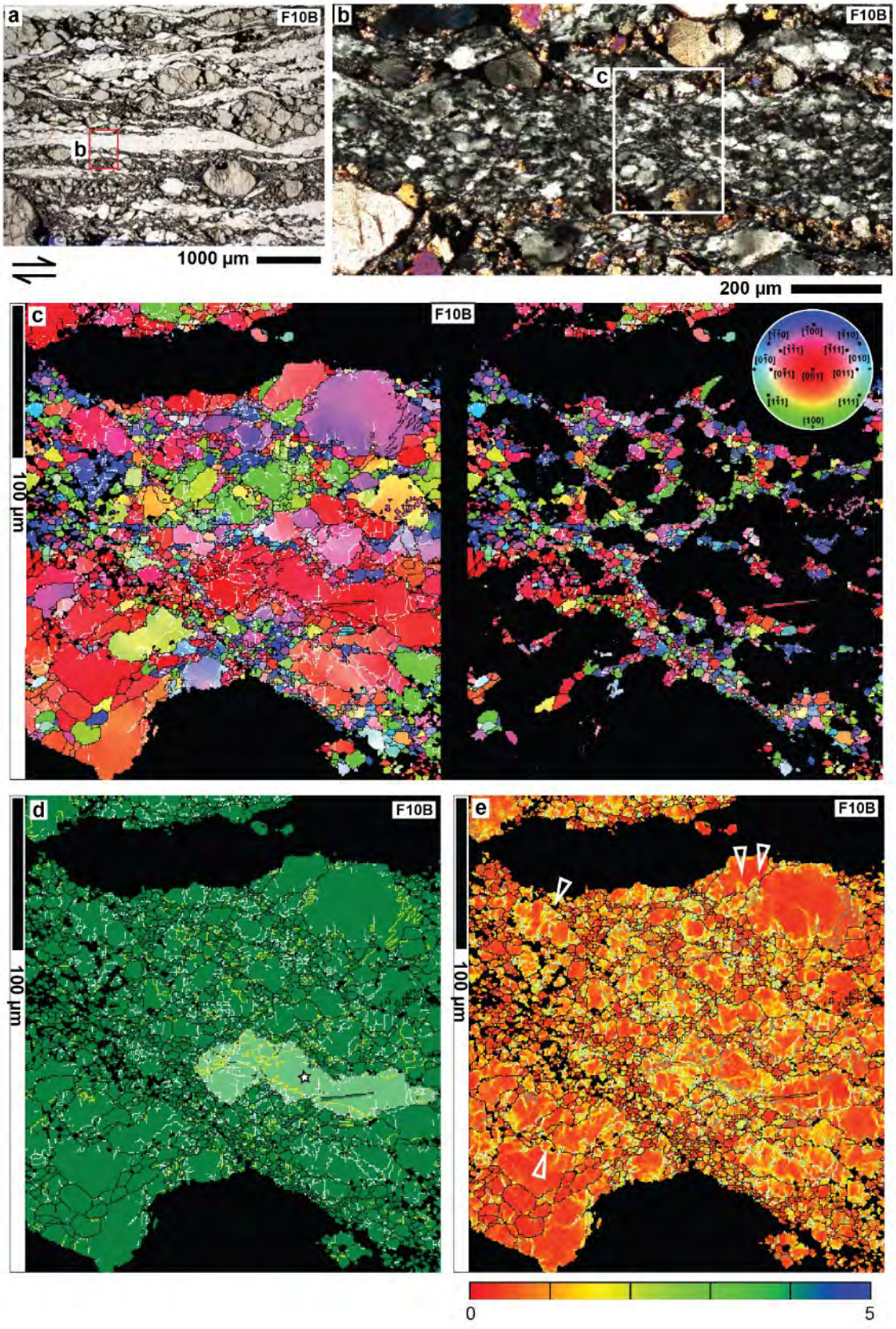
a
F10B
b
1000 µm
b
F10B
c
200 µm
c
F10B
100 µm
d
F10B
100 µm
e
F10B
100 µm
0
5

Fig. 5.31

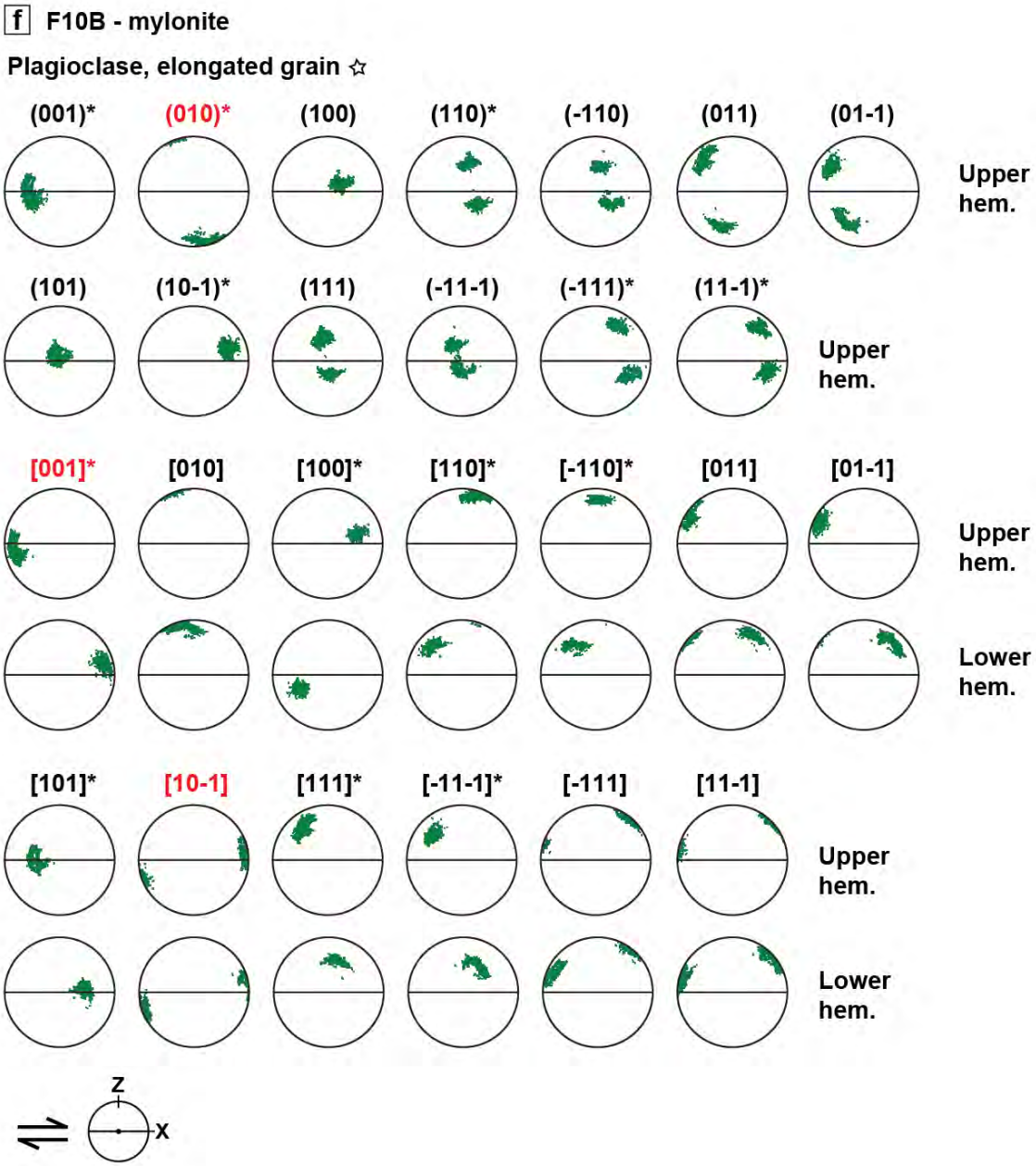

Fig. 5.31 *(continued)*

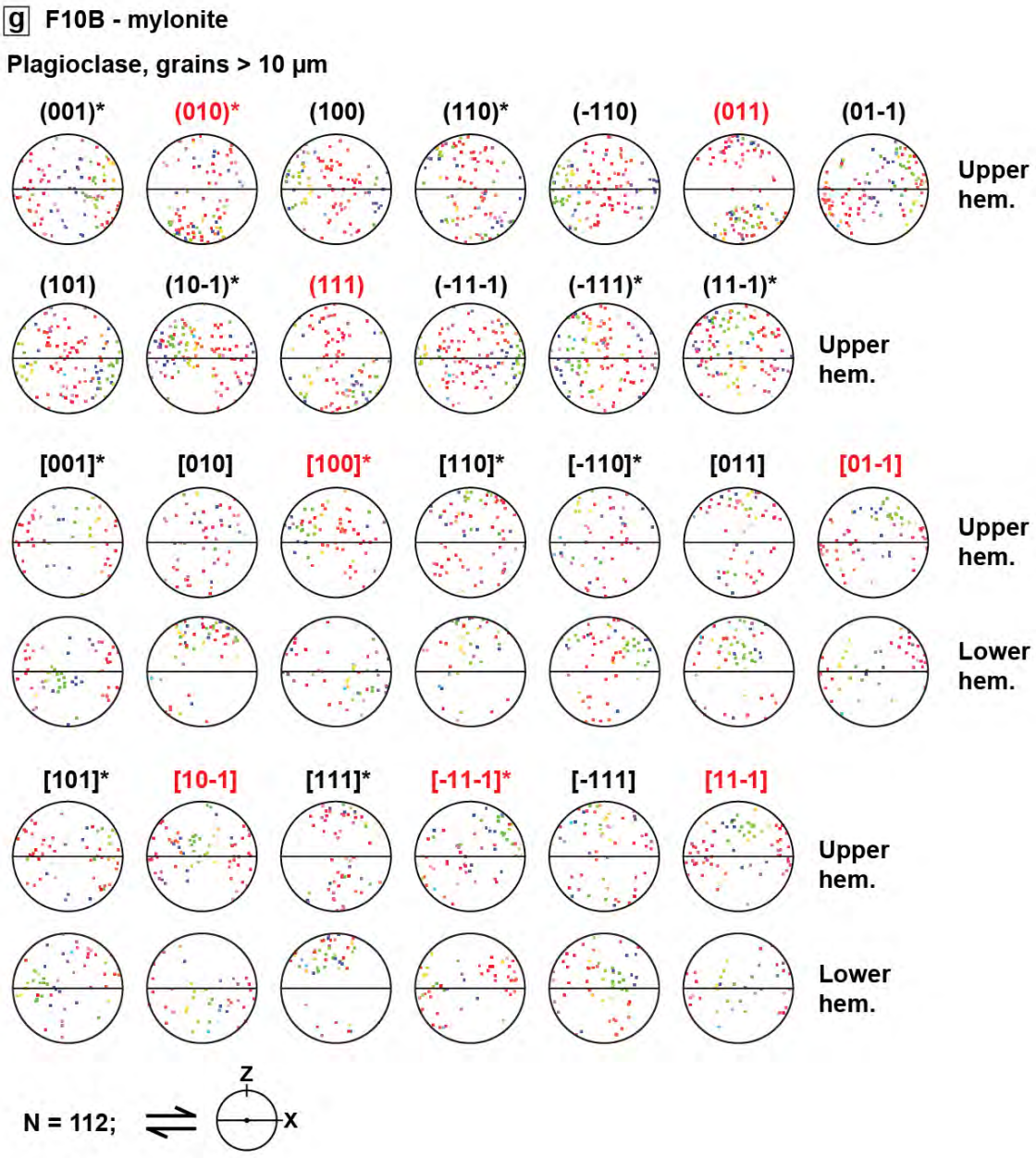

Fig. 5.31 *(continued)*

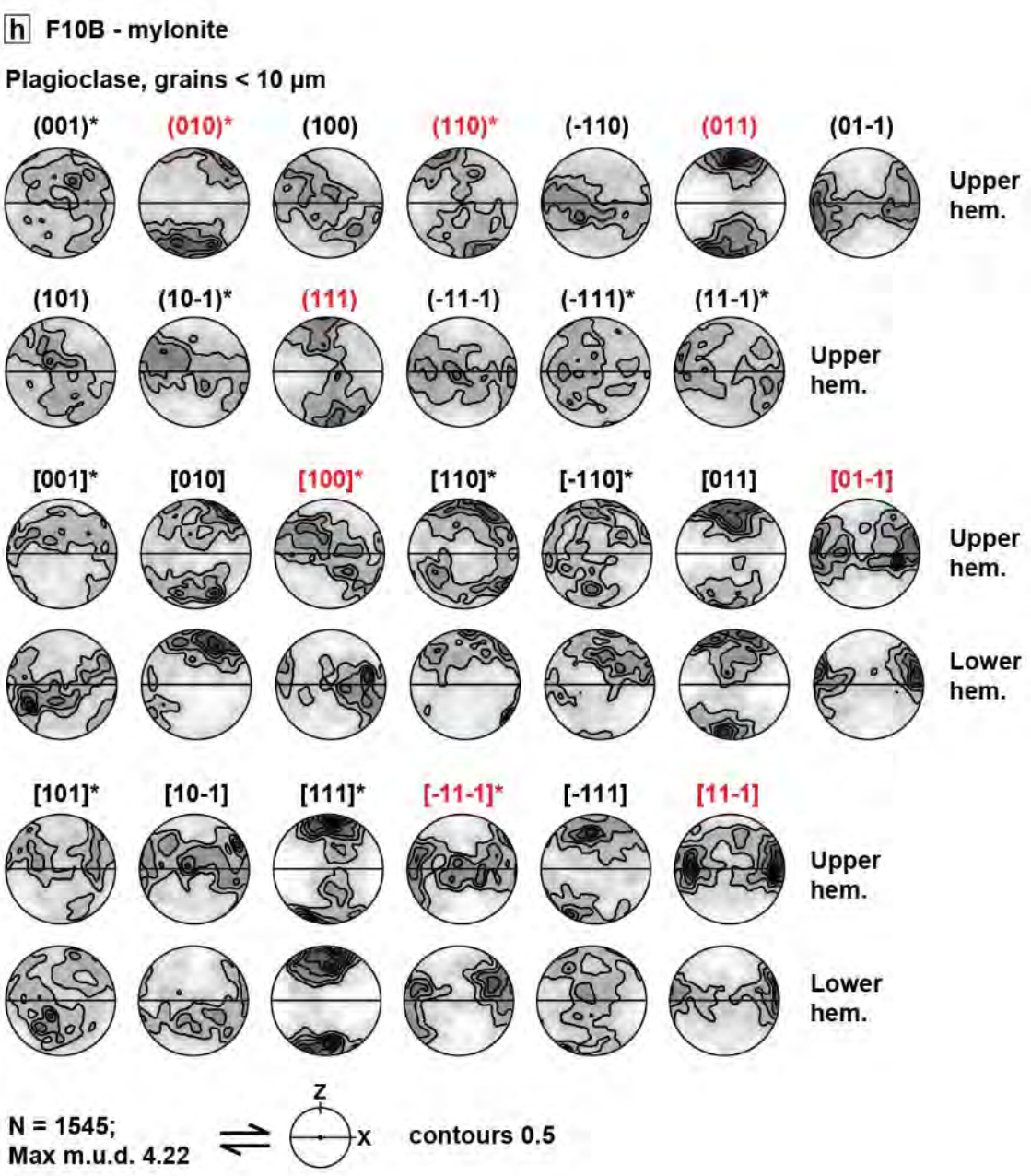

Fig. 5.31 *(continued)*

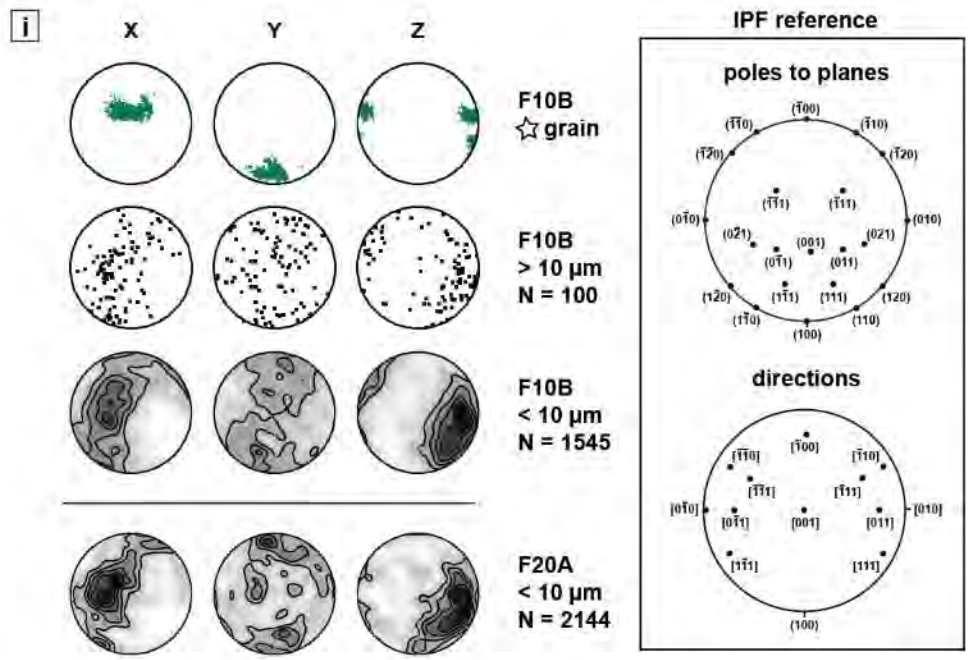
i
X
Y
Z
F10B
☆ grain
F10B
> 10 µm
N = 100
F10B
< 10 µm
N = 1545
F20A
< 10 µm
N = 2144
IPF reference
poles to planes
directions

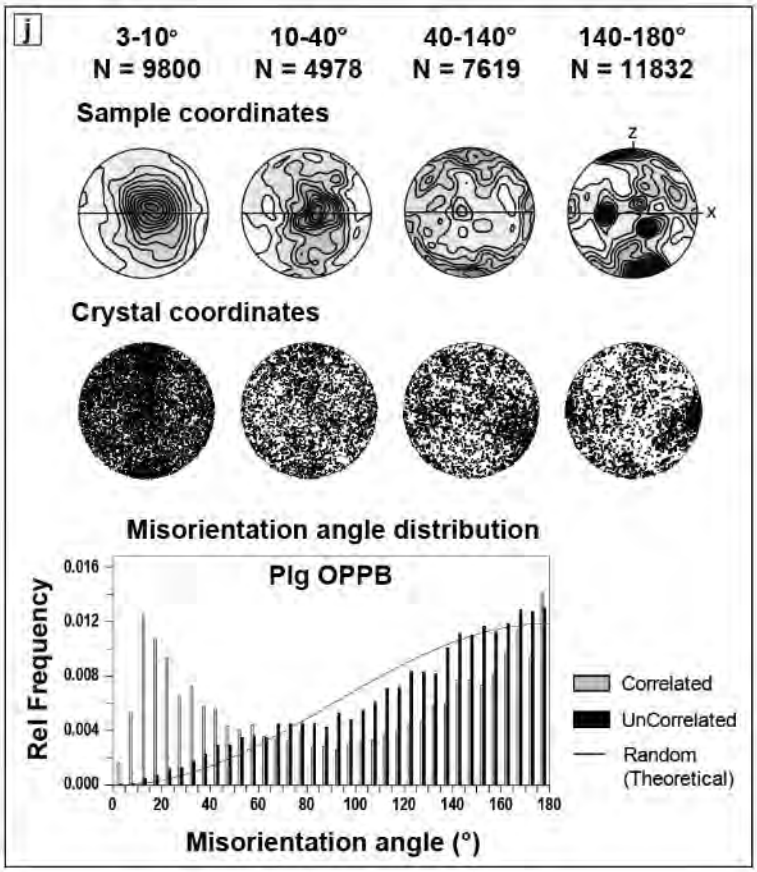
j
3-10°
N = 9800
10-40°
N = 4978
40-140°
N = 7619
140-180°
N = 11832
Sample coordinates
Z
X
Crystal coordinates
Misorientation angle distribution
Plg OPPB
Rel Frequency
0.016
0.012
0.008
0.004
0.000
0
20
40
60
80
100
120
140
160
180
Misorientation angle (°)
Correlated
UnCorrelated
Random
(Theoretical)

Fig. 5.31

Fig. 5.31 (previous pages)

EBSD analysis of plagioclase layer in amphibole-poor mylonite.

(a) *Light microscope image of the plagioclase layer, plane polarised light;*

(b) *Detail of the microstructure, in crossed polars. Location of EBSD map in white box.*

(c) *Inverse pole figure map with respect to the X sample direction, which corresponds to the stretching lineation of the mylonite. The map shows plagioclase parent grains (> 10 µm) surrounded by an aggregate of recrystallized grains (< 10 µm). The recrystallized grains are highlighted as a subset.*

(d) *Phase map of the plagioclase ribbon; plagioclase is shown in green; low angle (3-10°) subgrain boundaries are shown in white; albite-law twin boundaries in yellow; > 10° grain boundaries in black. Elongated grain marked with a star is highlighted for further reference.*

(e) *Local misorientation map, colour coded according to the degree of misorientation between each pixel and its neighbouring cluster of pixels within an area of 7x7 pixels; twin boundaries in grey; colour scale below. Note the abundance of intracrystalline misorientation bands. Arrows point to examples of subgrain development within parent grains.*

(f-h) *Pole figures of plagioclase, divided in datasets as detailed below. Crystallographic planes and directions marked with the asterisk (*) are the most common slip planes and directions of dislocation creep in literature (from Kruze et al., 2001); crystallographic planes and directions in red are those considered favourably oriented for slip based on the orientation of their maxima. All datasets are plotted in the upper and lower hemispheres as specified next to the figure, and in equal area projection. Kinematic reference frame is below each dataset. N is the number of grains.*

(f) *Pole figures of the elongated grain, marked with a star in d. The complete dataset of the grain is plotted.*

(g) *Pole figures of the large parent grains (all grains > 10 µm), one-point-per-grain. Colours correspond to those of the inverse pole figure map c.*

(h) *Pole figures of the recrystallized grains (< 10 µm), plotted as one-point-per-grain and contoured using a half-width of 15°. Strength of texture is given as m.u.d. Contours have a step-size of 0.5, starting from 1 m.u.d.*

(i) *Inverse pole figure plots, using the same datasets and parameters as used in f-h.*

(j) *Misorientation angle distribution of plagioclase (grains > 10 µm) for correlated and uncorrelated grain boundaries using one-point-per-boundary, plotted against the theoretical random curve. This relates to the misorientation axis-angle pair plots, showing the distribution of misorientation axis for misorientation of 3-10°, 10-40°, 40-140° and 140-180°, in sample coordinate and in crystal coordinate. N is the number of misorientation axes.*

Clinopyroxene:

A pyroxene-rich layer of the amphibole-poor mylonites was analysed with EBSD to evaluate the crystallographic relationship between a clinopyroxene porphyroclast and its surrounding aggregate of neoblastic clinopyroxenes (Fig. 5.32a). The clinopyroxene porphyroclast (labelled P_1) is oriented with the (001) plane subparallel to the foliation and with the [010] direction subparallel to the lineation (Fig. 5.32b and c). The adjacent clinopyroxene neoblasts have a CPO with the [100] axis oriented sub-parallel to the centre of the pole figure (corresponding to the Y-axis of the finite strain ellipsoid), and with the (010) and (001) planes forming girdles sub-parallel to the YZ plane and XZ plane of the finite strain ellipsoid, respectively (Fig. 5.32b). The [100] maxima of the neoblasts overlaps with the [100] orientation of the porphyroclast, whereas the other crystallographic directions do not.

The local misorientation map highlights the presence of internal substructures with local misorientations of just a few degrees (Fig. 5.32d). The pyroxene porphyroclast (labelled P_1) and some of the grains in the aggregate (labelled with stars) show an abundance of internal lattice distortions in the form of low-angle (2-3°) misorientation bands; whereas most grains are internally devoid of substructures. This result is consistent with the GOS map, which shows that most pyroxenes in the aggregate have mean misorientation of < 2°, while the porphyroclast P_1 and the grains with abundant substructures have mean misorientations > 2° (Fig. 5.32e).

The misorientation angle distribution of neoblastic pyroxenes shows an excess of misorientation boundaries < 75° and a deficit of boundaries > 75° for correlated pairs of

data, when compared to the theoretical random distribution curve (Fig. 5.32f). Instead, the misorientation angle distribution for random pairs is remarkably close to the theoretical random curve (Fig. 5.32f). Analysis of misorientation axis-angle pairs does not highlight any preferred misorientation axis. It seems that most misorientations occur around the [100] axes, but their distribution in the sample reference frame is random (Fig. 5.32f). No specific misorientation axis could be recognized for low angles (< 10°).

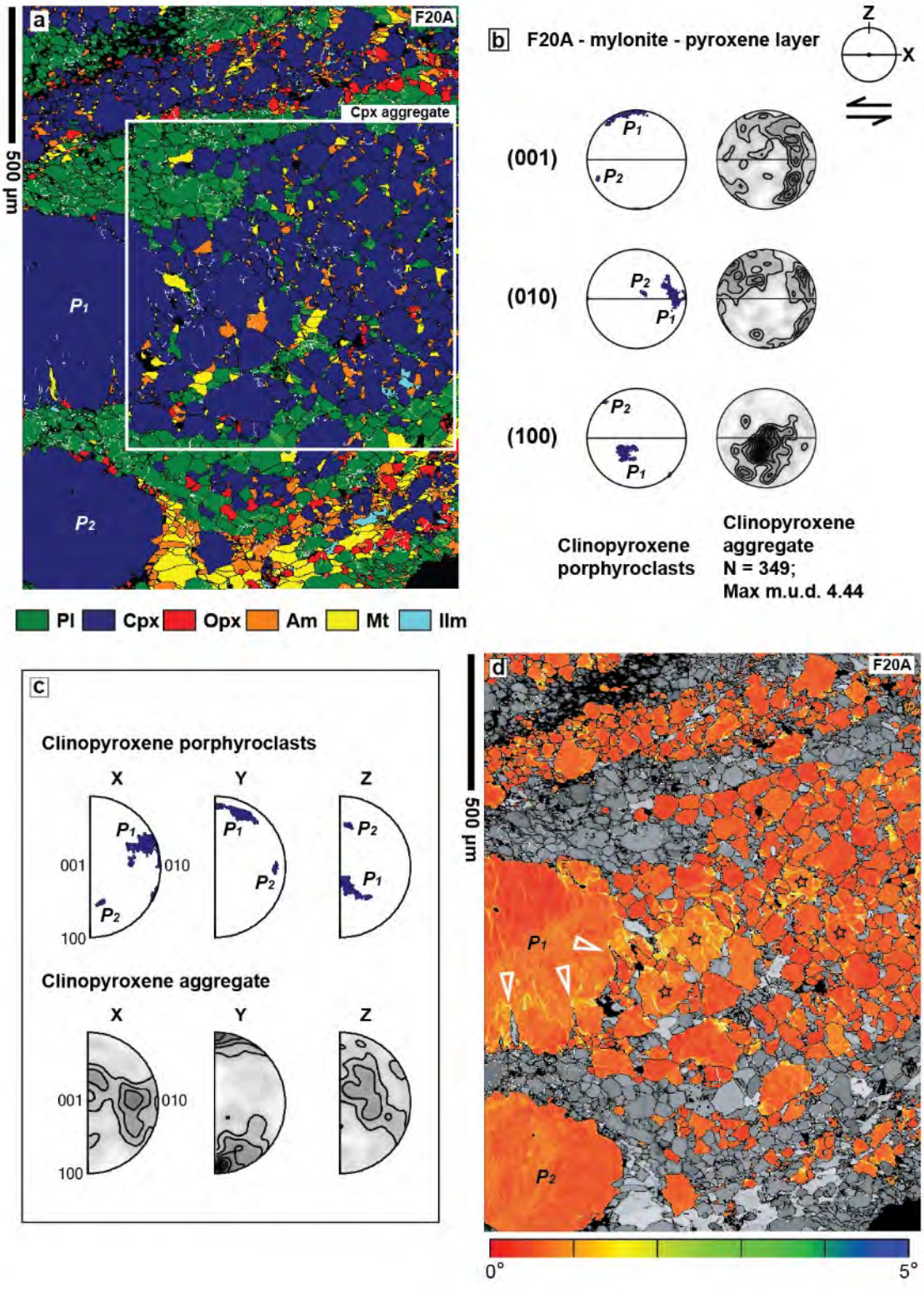

Fig. 5.32 (continued)

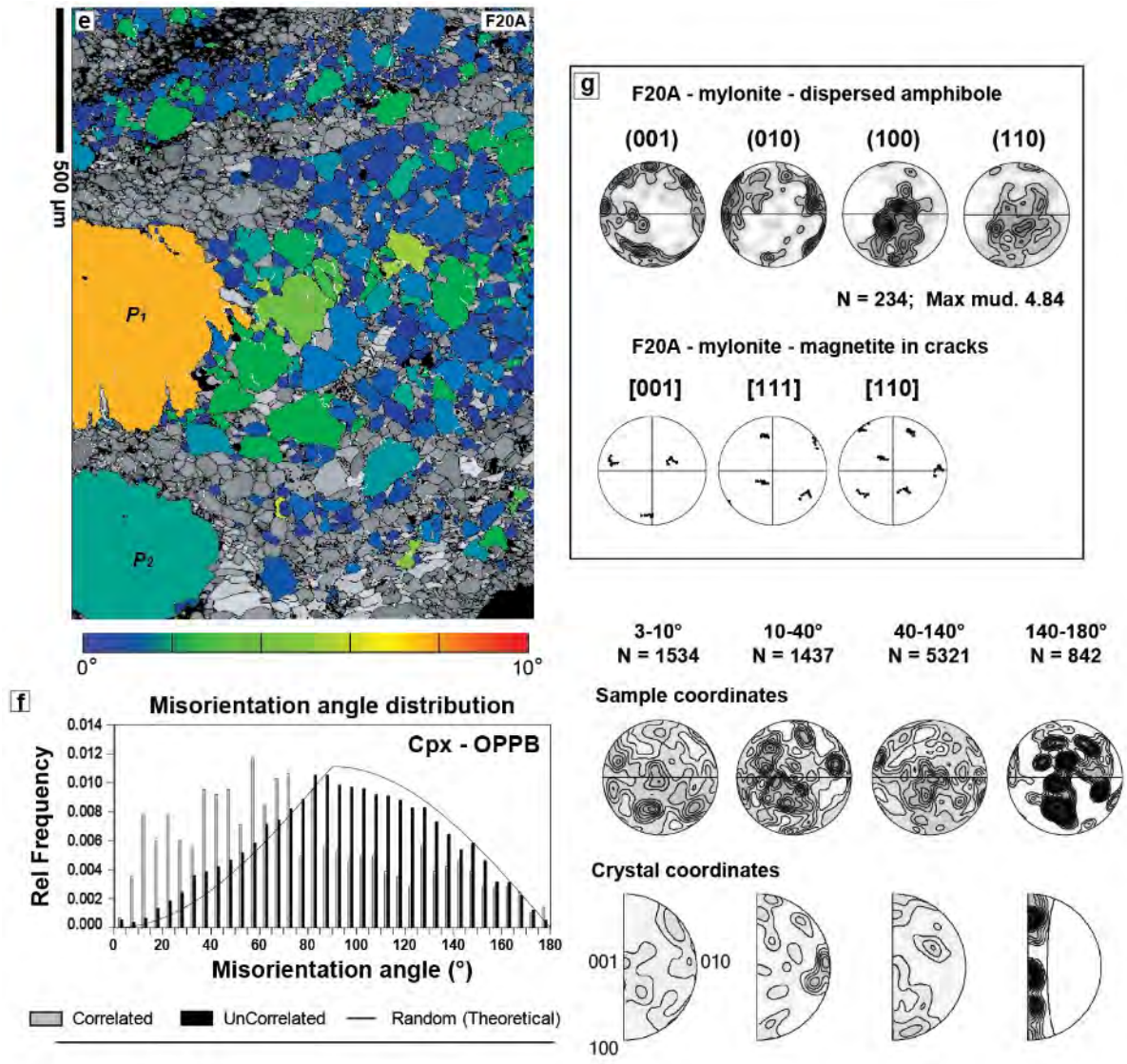

Fig. 5.32 (previous pages)

EBSD analysis of pyroxene-rich band in amphibole-poor mylonite.

***(a)** Phase map.*

***(b)** Pole figures of the porphyroclasts P1 and P2 (as determined by grain size) using the complete datasets of the grains; and of the pyroxene aggregate subset (area of white box in a), plotted as one-point-per-grain and contoured using a half-width of 15°. Strength of texture is given as m.u.d. Contours have a step-size of 0.5, starting from 1 m.u.d. N is the number of grains. Upper hemisphere, equal area projection. Kinematic reference frame below.*

***(c)** Inverse pole figure plots, using the same datasets and parameters as for b.*

***(d)** Local misorientation map, colour coded according to the degree of misorientation between each pixel and its neighbouring cluster of pixels within an area of 7x7 pixels. Grains marked with P1 and P2 are porphyroclasts, grains marked with stars are fragments, the remaining are*

neoblasts. Colour scale below. Low angle (3-10º) subgrain boundaries are shown in white; >10º grain boundaries in black.

(e) *Grain orientation spread map, where grains are colour coded according to their mean internal misorientation. Colour scale below.*

(f) *Misorientation angle distribution of the neoblastic clinopyroxene subset for correlated and uncorrelated grain boundaries using one-point-per-boundary, plotted against the theoretical random curve. This relates to the misorientation axis-angle pair plots, showing the distribution of misorientation axis for misorientation of 3-10°, 10-40°, 40-140° and 140-180°, in sample coordinate and in crystal coordinate. N is the number of misorientation axes.*

(g) *Pole figures of the "dispersed" amphibole found in between pyroxene neoblasts, plotted as one-point-per-grain and contoured using a half-width of 15°. Strength of texture is given as m.u.d. Contours have a step-size of 0.5, starting from 1 m.u.d. N is the number of grains. Upper hemisphere, equal area projection. The lower plot is of magnetite in the cracks of the porphyroclast P1.*

5.8.2 AMPHIBOLE-RICH ULTRAMYLONITES

As seen in section 5.3.2, amphibole-rich ultramylonites are the deformed equivalents of the amphibole-rich metagabbros. They are typically fine grained mixtures of the minerals plagioclase, amphibole, clinopyroxene, orthopyroxene, ilmenite, magnetite ± apatite; containing isolated porphyroclasts of amphibole, garnet and pyroxene. Two EBSD maps from the F20A ultramylonite were taken as representatives textures of the amphibole-rich metagabbros (Fig. 5.33a; Fig. 5.34a). These are the *F20A EBSD map 1* and *F20A EBSD map 2*, and their locations are shown in the microprobe map of Fig. 5.20.

Amphibole:

Ultramylonitic amphiboles show a weak (2.27 - 2.68 m.u.d) but clear CPO, with alignment of (100) and (110) planes subparallel to the foliation and alignment of [001] directions subparallel to the stretching lineation (Fig. 5.33b and c; Fig. 5.34b and c). Low angle boundaries (3-10°, in white) are locally visible; yet the majority of the grains show no internal substructures (Fig. 5.33f and Fig. 5.34f) and are virtually free of misorientations (mean misorientation < 2°, Fig. 5.33g and Fig. 5.34g). The misorientation angle distribution of uncorrelated pairs of ultramylonitic amphiboles neatly matches the theoretical random curve; whereas the misorientation angle distribution of correlated pairs shows an excess of misorientations for angles < 75° and < 55° and a general deficit in misorientations for angles >75° and > 55° (Fig. 5.33d and Fig. 5.34d respectively). In Fig. 5.34d, a peak of correlated misorientations is also shown for angles between 95°-105°.

The amphibole porphyroclast (labelled *P*) found within the ultramylonite is oriented with the (001) plane subparallel to the foliation and with the [010] direction subparallel to the stretching lineation (Fig. 5.34b and c). Internally, the porphyroclast is devoid of low angle subgrain boundaries (3-10°, in white), and in the local misorientation map has a speckled appearance which indicates discontinuous misorientations of 1-2° (Fig. 5.34f). Despite these scattered 1-2° misorientations, the entire porphyroclast has a mean internal misorientation < 2°, as shown in the GOS map (Fig. 5.34g).

The CPO of the fine grained amphibole differs from the crystallographic orientation of the amphibole porphyroclast (Fig. 5.34b and c). Furthermore, the fine grained amphiboles in proximity of the porphyroclast exhibit large misorientations (> ca. 30° and

up to 110°) from the crystallographic orientation of the porphyroclast (from the orientation of the red dot, Fig. 5.34e).

Pyroxenes:

Clinopyroxenes and orthopyroxenes in the ultramylonite lack a CPO (Fig. 5.33b and c). The crystallographic planes and axes are not systematically aligned with any of the sample's reference directions, and a number of weak maxima can be seen at random positions in the sample's coordinate system. Like amphibole, ultramylonitic clinopyroxene and orthopyroxene are mostly devoid of internal substructures (3-10° subgrain boundaries / misorientation bands) (Fig. 5.33f). This is confirmed by the GOS maps, which indicate that the majority of the grains have mean internal misorientations < 2° (Fig. 5.33g, blue grains). The few clinopyroxene and orthopyroxene grains which do contain subgrains have mean misorientation between 2-5° (Fig. 5.33g, green grains).

The misorientation angle distributions of the uncorrelated pairs, of both clinopyroxene and orthopyroxene, is remarkably close to the theoretical random curve (Fig. 5.33d). Instead, the misorientation angle distributions of the correlated pairs show an excess of misorientations for angles < 50° for clinopyorene and < 45° for orthopyroxene, and a general deficit in misorientations for angles >75° for clinopyroxene and > 55° for orthopyroxenes.

Plagioclase:

Plagioclase in the ultramylonite has a weak CPO (3.08 m.u.d.) defined by clusters of the following crystallographic planes and directions: (110), (011) (01-1), (111), (-11-1), [011], [01-1], [111], [-11-1], [-111] and [11-1] (Fig. 5.33b). Of the latter, the (110), (011) and

(111) planes cluster subparallel to the foliation, and the [01-1], [-11-1] and [11-1] directions cluster subparallel to the stretching lineation.

Compared to the other ultramylonitic phases, plagioclase grains shows more lattice distortions, in the form of low angle (2-3°) misorientation bands (Fig. 5.33g). Polysynthetic twins also occur (in green), whereas low-angle subgrain boundaries (between 3-10°) are uncommon. Polysynthetic twins result in plagioclase displaying large grain orientation spreads, with mean misorientations as high as 120° (Fig. 5.33g). Due to twinning, caution should be taken in the interpretation and comparison of plagioclase GOS with other phases' GOS.

The misorientation angle distribution for plagioclase uncorrelated pairs shows a strong fit to the theoretical random curve, in line with all the other phases of the ultramylonite (Fig. 5.33d). The misorientation angle distribution for correlated pairs shows an excess in misorientation angles < 55°, and a general deficit in misorientation angles > 55°. Furthermore, there is a peak of 175-180° misorientations.

Plots of plagioclase misorientation axis-angle pairs show that misorientation angles between 3-10°, and between 10-40°, produce a maximum aligned with the sample's Y-direction. Instead, misorientation angles > 40° show no maximum (Fig. 5.33e). For misorientation angles between 3-10°, the Y-maximum is produced mainly by the [100] axis, as seen in the crystal coordinate reference frame. Instead, for misorientation angles between 10-40°, and between 40-140°, there is no preferred misorientation axis. Finally, for misorientation angles between 140-180°, the dominant misorientation axis is the [010].

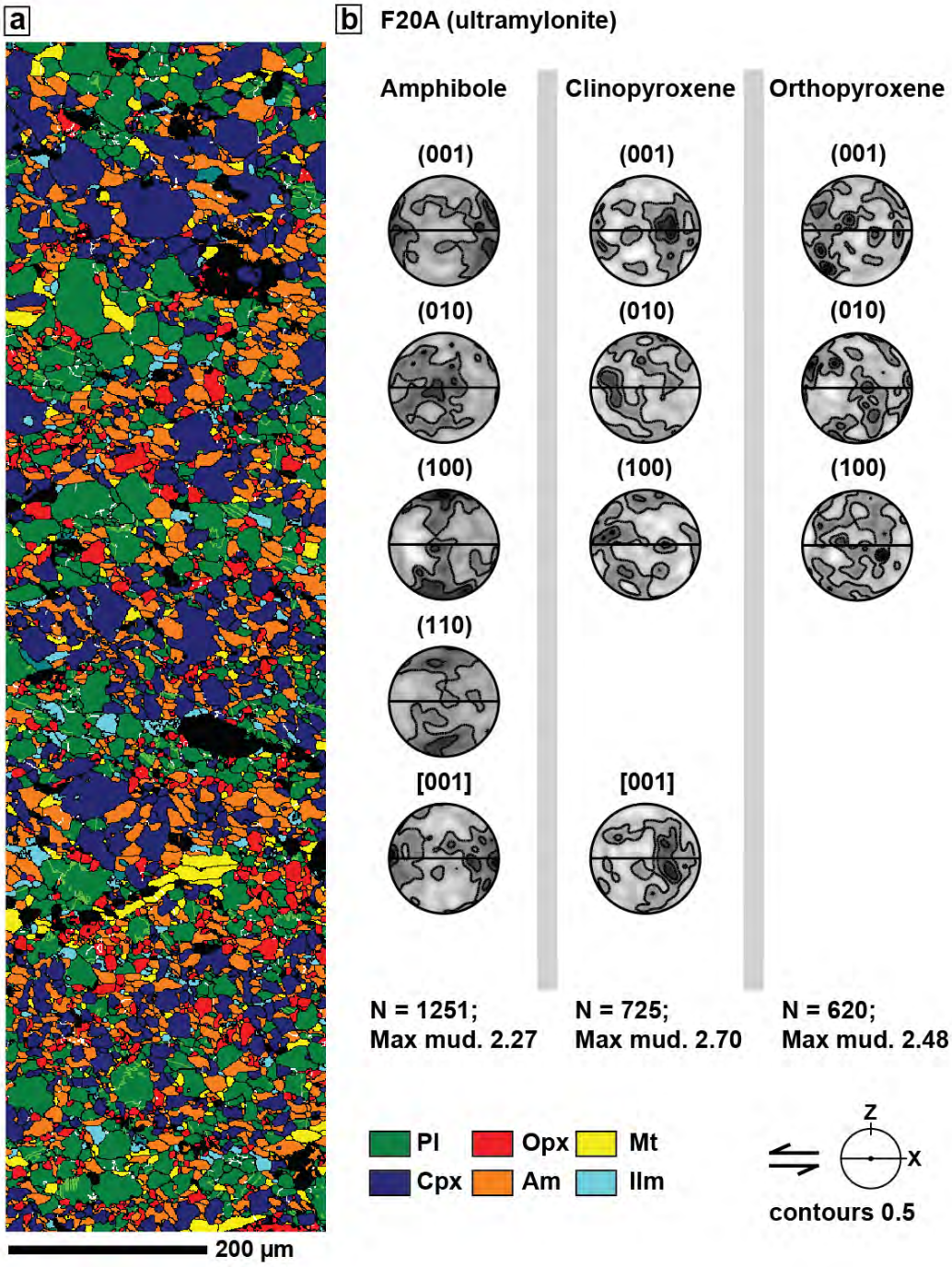

Fig. 5.33 (continued)

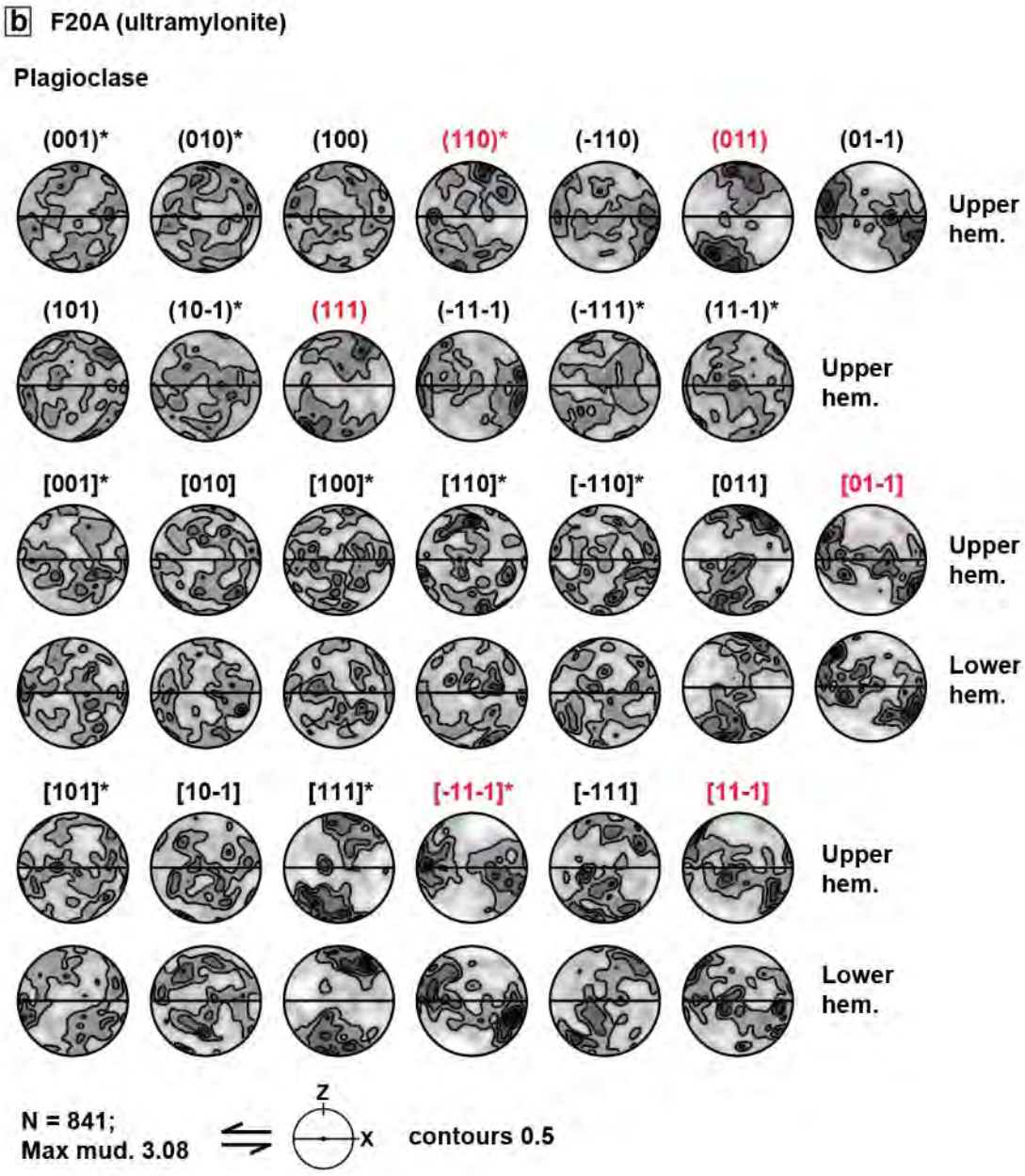

Fig. 5.33 (continued)

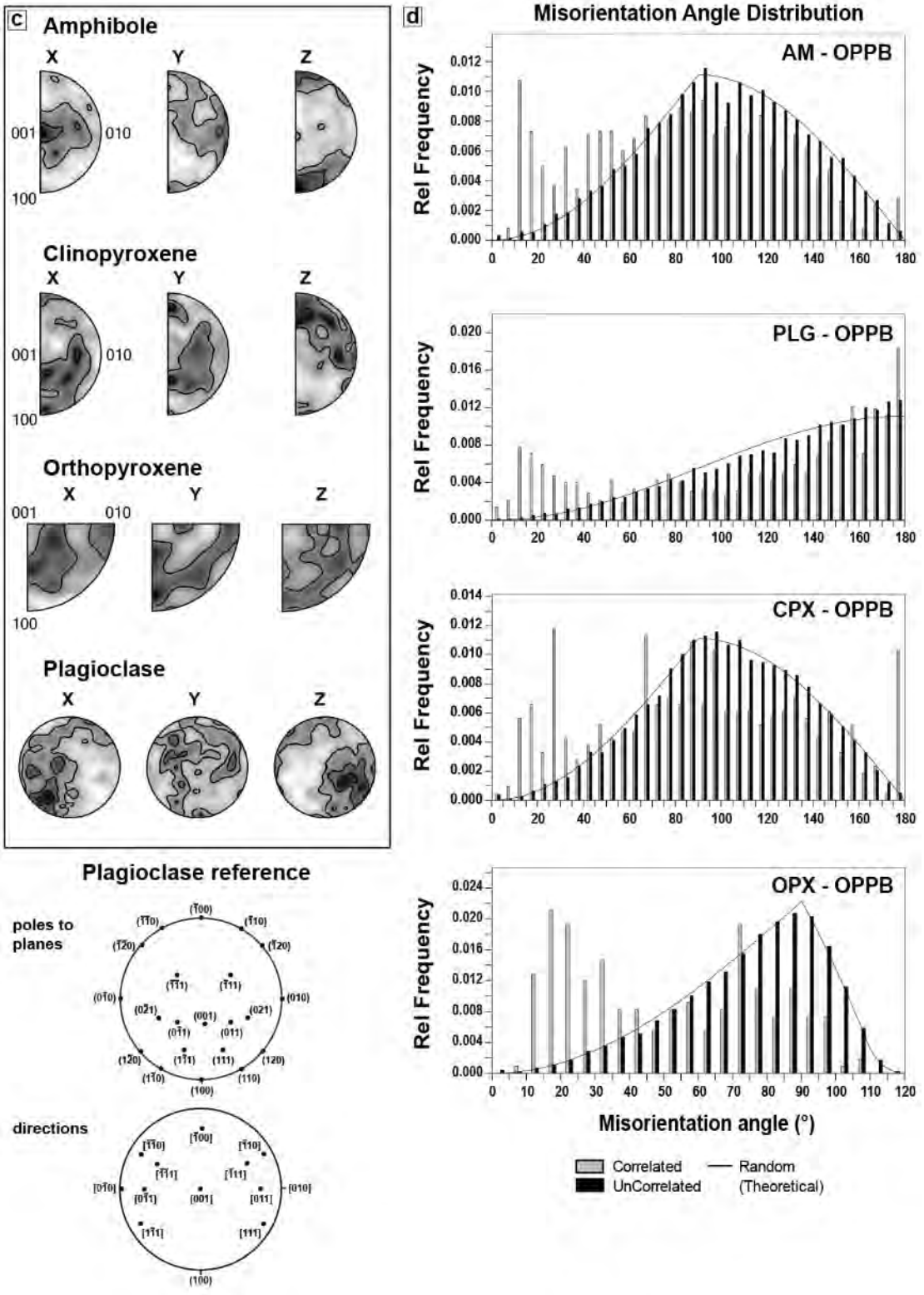

Fig. 5.33 (continued)

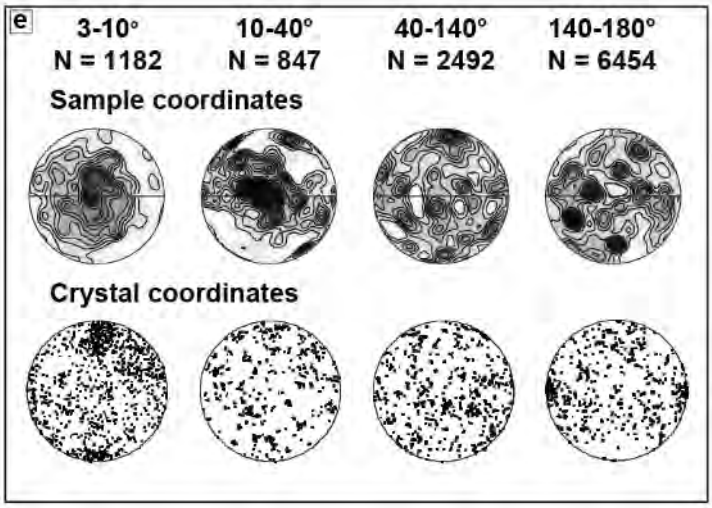

Fig. 5.33 (continued)

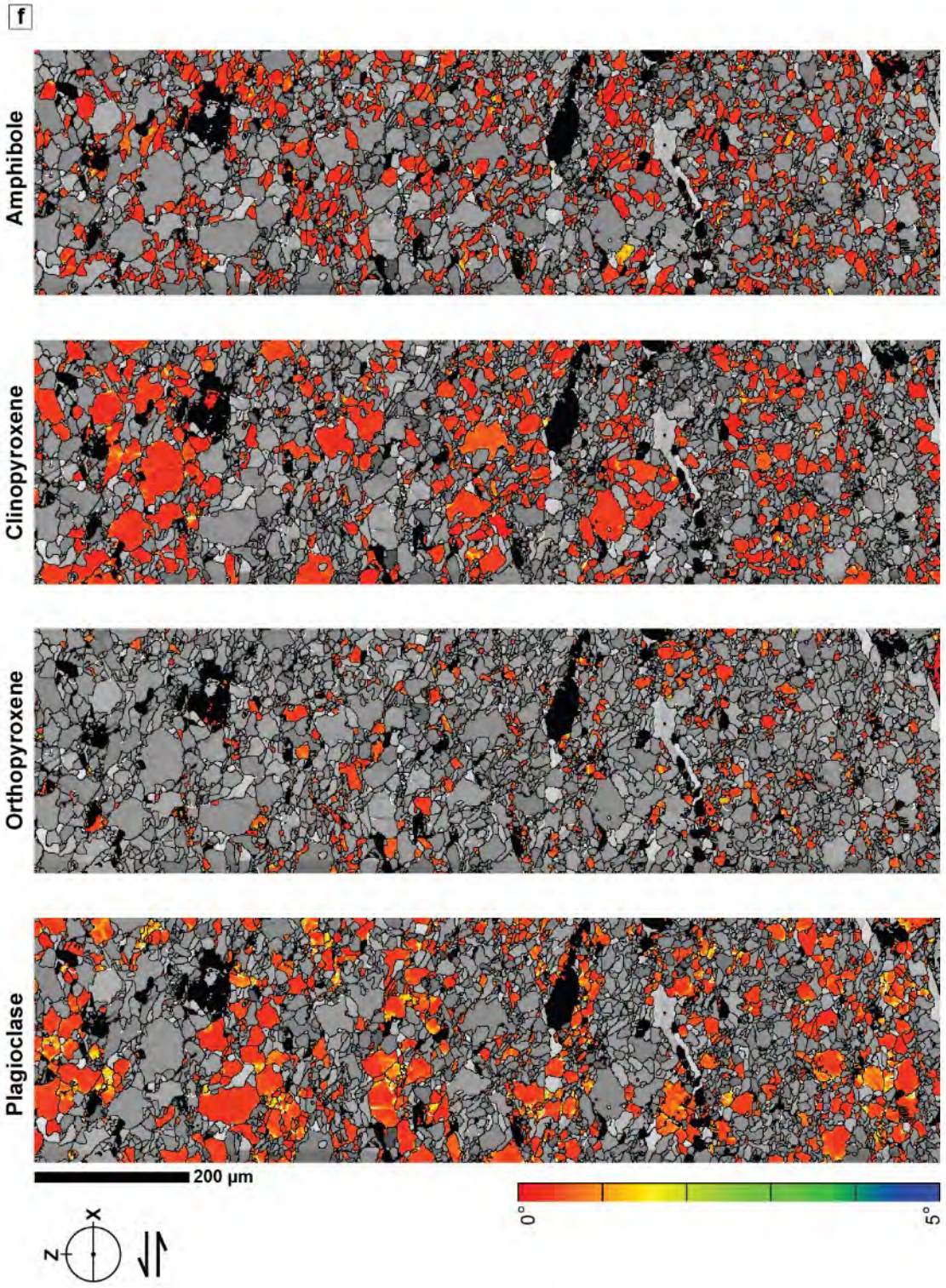

Fig. 5.33 (continued)

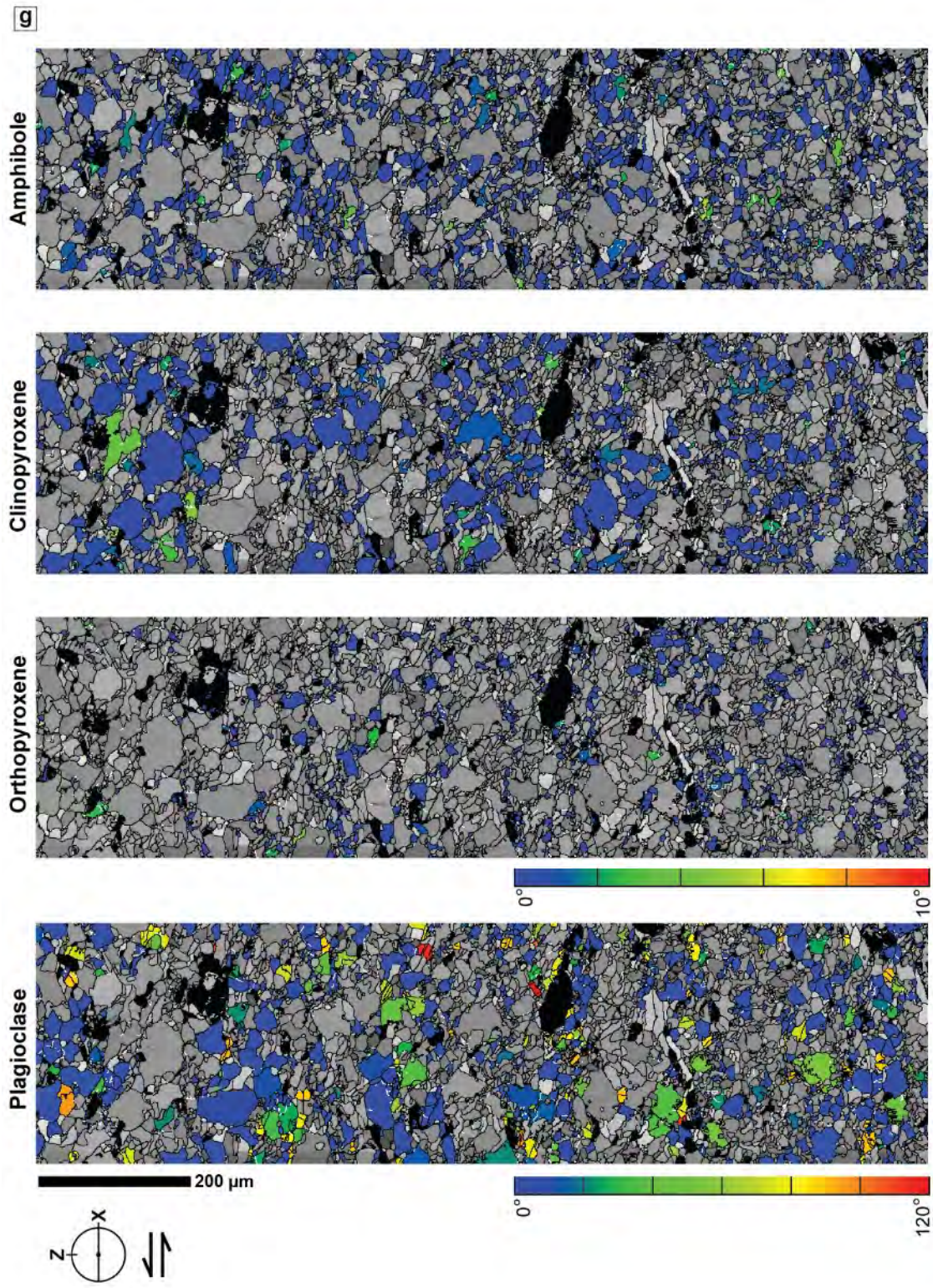
g
Amphibole
Clinopyroxene
Orthopyroxene
0°
10°
Plagioclase
200 µm
0°
120°
X
Z

Fig. 5.33

Fig. 5.33 (previous pages)

EBSD analysis of the amphibole-rich ultramylonites, F20A EBSD map 1.

(a) Phase map.

(b) Pole figures of amphibole, clinopyroxene, orthopyroxene and plagioclase, plotted as one-point-per-grain and contoured using a half-width of 15°. Strength of texture is given as m.u.d. Contours have a step-size of 0.5, starting from 1 m.u.d. Upper hemisphere unless specified otherwise. Equal area projection. Kinematic reference frame is given below. N is the number of grains. For plagioclase, the crystallographic planes and directions marked with an asterisk (*) are the most common slip planes and directions of dislocation creep from literature (from Kruze et al., 2001); crystallographic planes and directions in red are those considered favourably oriented for slip based on the orientation of their maxima. Plagioclase pole figures are plotted in the upper and lower hemispheres as indicated next to the figure.

(c) Inverse pole figure plots, using the same datasets and parameters as used in b.

(d) Misorientation angle distributions of amphibole, clinopyroxene, orthopyroxene and plagioclase for correlated and uncorrelated grain boundaries using one-point-per-boundary, plotted against the theoretical random curves.

(e) Misorientation axis-angle pair plots for plagioclase, showing the distribution of misorientation axis for misorientation of 3-10°, 10-40°, 40-140° and 140-180°, in sample coordinate and in crystal coordinate. N is the number of misorientation axes. The other phases are omitted as they show random distributions.

(f) Local misorientation maps, colour coded according to the degree of misorientation between each pixel and its neighbouring cluster of pixels within an area of 7x7 pixels; colour scale below.

(g) Grain orientation spread map, where grains are colour coded according to their mean internal misorientation. Colour scales below.

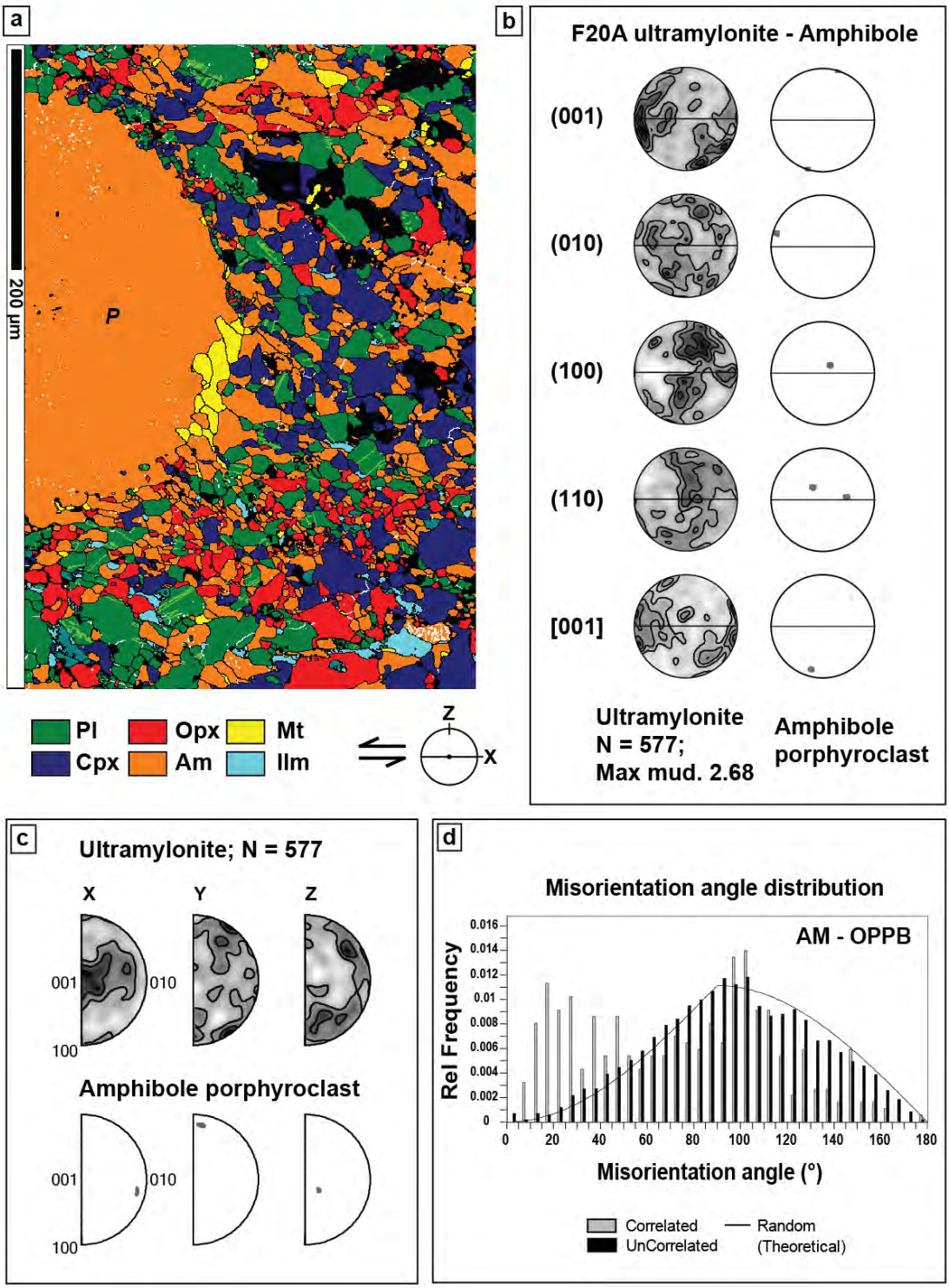

Fig. 5.34 (continued)

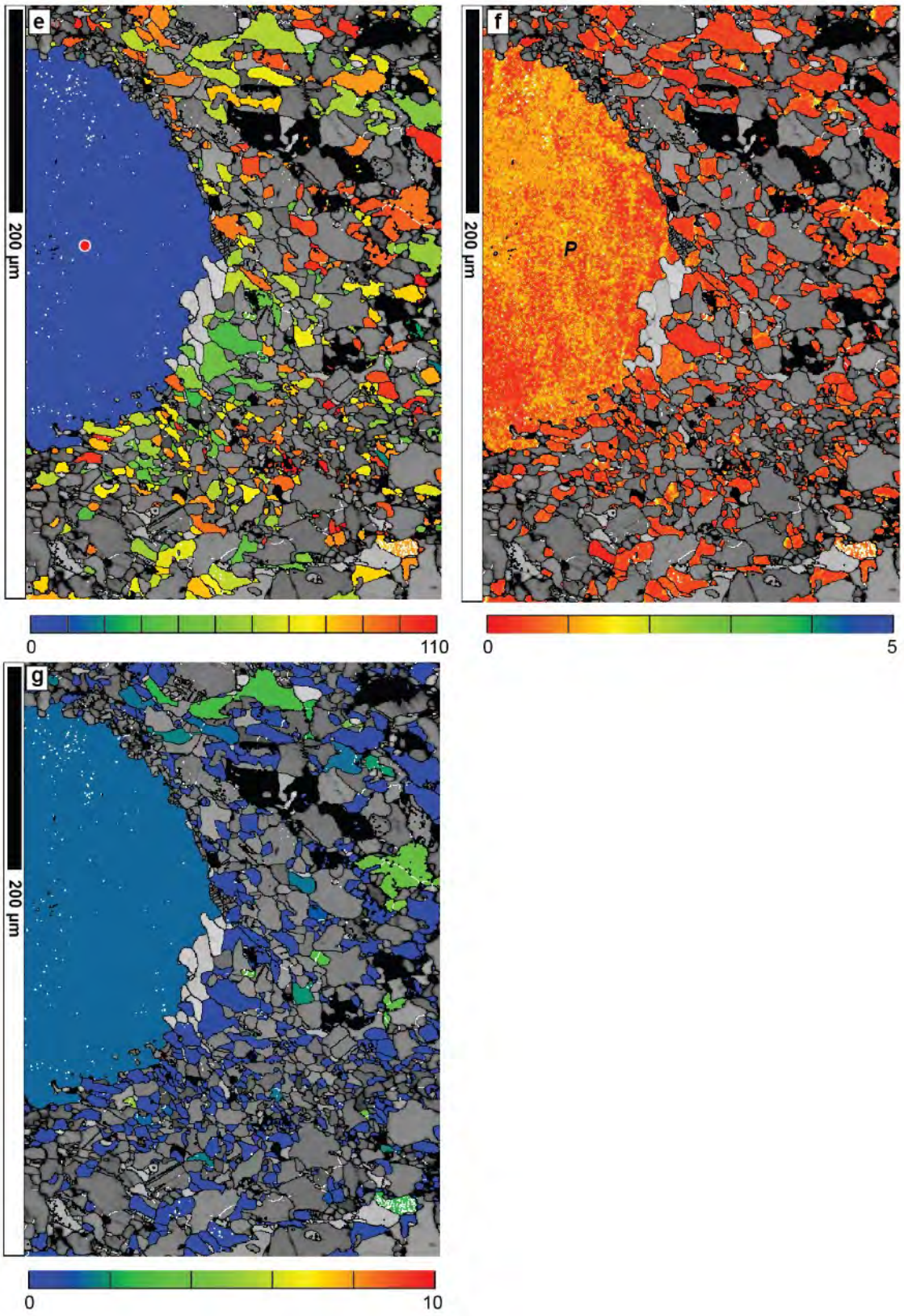

Fig. 5.34

Fig. 5.34 (previous pages)

EBSD analysis of the amphibole-rich ultramylonites, F20A EBSD map 2. (a) Phase map. (b) Pole figures of amphibole; Pole figure of amphibole porphyroclast P using the complete datasets of the grain; pole figure of the ultramylonitic amphibole, plotted as one-point-per-grain and contoured using a half-width of 15°. Strength of texture is given as m.u.d. Contours have a step-size of 0.5, starting from 1 m.u.d. Upper hemisphere, equal area projection. N is the number of grains. (c) Inverse pole figure plots, using the same datasets and parameters as used in b. (d) Misorientation angle distribution of amphibole, for correlated and uncorrelated grain boundaries using one-point-per-boundary, plotted against the theoretical random curve. (e) Texture component map, colour coded according to the misorientation from the red dot in the amphibole porphyroclast. Colour scale below. (f) Local misorientation map; as in *Fig. 5.33* (g) Grain orientation spread map; as in *Fig. 5.33*.

5.9 DEFORMATION MECHANISMS: AMPHIBOLE POOR VS. AMPHIBOLE RICH DOMAINS

This section will discuss the EBSD results of sheared amphibole-poor and amphibole-rich metagabbros, to shed light on the deformation mechanisms and processes that operated in these two microstructurally different domains.

5.9.1 AMPHIBOLE-POOR MYLONITES

Plagioclase:

In the banded mylonites derived from amphibole-poor metagabbros, plagioclase displays a classic core-and-mantle microstructure with larger, highly strained grains (10 – 100 µm in F10B) surrounded by a matrix of recrystallized grains (< 10 µm in F10B) (Fig. 5.31c, d and e).

On elongated plagioclase grains, the alignment of the [001] direction with the stretching lineation and the alignment of the (010) plane sub-parallel to the foliation is consistent with dislocation creep on the (010)[001] slip system (Fig. 5.31f). This slip system is known in literature as the dominant slip system in plagioclase, and is commonly found to operate in many natural samples (e.g. Baratoux et al., 2005; Kanagawa et al., 2008; Kruse et al., 2001; Kruse and Stünitz, 1999; Mehl and Hirth, 2008; Menegon et al., 2013).

If dislocation creep on the (010)[001] slip system was dominant on all plagioclase grains of the ribbon, then a strong CPO with alignment of [001] along the sample's X direction, and alignment of (010) along the sample's Z direction would be expected. However, the CPO of plagioclase parent grains (i.e. grains > 10 µm) is weak and shows a dispersion of

crystallographic data forming girdles (Fig. 5.31g). This dispersion results in multiple crystallographic planes and directions (i.e. the (010), (011), (111), (110) and [01-1], [11-1], [-11-1], [10-1], marked in red) to cluster subparallel to the foliation and stretching lineation, respectively (Fig. 5.31g). The dispersion of crystallographic data forming girdles, and the presence of several maxima along the X and Z directions, either indicates dislocation creep on multiple slip systems, or a contribution of dislocation accommodated grain boundary sliding (e.g. Miranda et al., 2016). Interestingly, also Kanagawa et al. (2008) finds a similar result, where elongated grains deform by (010)[001] slip system, while the recrystallized grains deform according to a different system (mainly the (001) ½ <1-10> ; Kanagawa et al., 2008).

The inverse pole figure plots of both the large parent grains and the recrystallized grains are similar to those of Baratoux et al., (2005) for gabbroic ultramylonites (their sample E3) (Fig. 5.31i). The latter were interpreted by Baratoux et al., (2005) as possible activation of the (021)½[1-12] slip system.

In the large parent grains (> 10 µm), polysynthetic twins and subgrain are widespread, and the subgrains have comparable grain sizes to the recrystallized grains (Fig. 5.31c, d and e). The recrystallized grains (< 10 µm) record the same CPO as the parent grains (> 10 µm). The host controlled crystallographic orientation of the recrystallized grains, combined with the abundance of subgrains of comparable grain size and absence of secondary phases, suggests that the recrystallized grains formed by subgrain rotation recrystallization. The high frequency of low-angle misorientations (< 40°, Fig. 5.31j) between correlated pairs is also consistent with intracrystalline plasticity and subgrain rotation recrystallization (e.g. Wheeler et al., 2001).

In addition, the misorientation axis-angle pairs of the large grains indicate that for misorientations < 40° degrees, rotation axes preferentially cluster around the sample's Y direction. In crystal coordinates, the latter correspond to a girdle containing the [100] and [001] directions (Fig. 5.31j). This could indicate that the most efficient slip systems during dislocation creep of plagioclase were those with misorientations axis subparallel to the bulk vorticity axis of the shear zone (i.e. to the Y direction), as recently observed for quartz (Ceccato et al., 2017). High angle rotations (> 140°) occurring around [010] axes aligned with Z are interpreted as the result of twinning on the albite law (Fig. 5.31j). However, clusters of misorientation axes close to Y persist also for misorientations > 140°, and possibly indicate a component of passive rotation of the recrystallized grains around the bulk vorticity axis (e.g. Ceccato et al., 2017; Menegon et al., 2013; Reddy and Buchan, 2005; van Daalen et al., 1999) (Fig. 5.31j).

In summary, EBSD analysis on a monophase plagioclase ribbons suggests dislocation creep on a combination of slip systems, including the (010)[001] slip system recognized for elongated grains. This result confirms previous studies of metagabbros which find monophase plagioclase layers to deform by crystal plasticity accompanied by dynamic recrystallization (Baratoux et al., 2005; Brodie and Rutter, 1987b; Kanagawa et al., 2008; Kenkmann and Dresen, 2002). This result closely matches with that of Kanagawa et al. (2008), who find different CPOs (and thus slip systems) between elongated plagioclase grains and recrystallized grains. Dislocation creep on multiple slip systems was accompanied by subgrain rotation recrystallization, as suggested by abundant subgrain development in the larger grains and on the host-control of the recrystallized grains.

Clinopyroxene:

Crystal plasticity in pyroxenes manifests as undulose extinctions and crystal bending (visible as spreads in orientations in the pole figures). Incipient microfractures, sub-perpendicular to the foliation, are visible along some porphyroclasts' rims, and are often filled by magnetite or amphibole (Fig. 5.32d, white arrows). Magnetite filling these cracks has a weak CPO with the [001] direction subparallel to the sample's stretching lineation, suggesting syn-kinematic oriented growth of magnetite during clinopyroxene microfracturing (Fig. 5.32g). The presence of microfractures suggests that dislocation glide was not associated with an efficient recovery in clinopyroxene.

Fragments of porphyroclasts can be distinguished from the neoblasts based on their different composition (with the neoblasts showing a marked decrease in Al_2O_3 content – Fig. 5.12b and Fig. 5.25), but an indication is also given by the degree of internal strain, which is larger in the fragments than in the neoblasts (Fig. 5.32d and e). In fact, the extent of intragranular lattice distortion is often considered to reflect the grains' deformation history; whereby relicts, porphyroclasts or fractured fragments display higher distortions than recrystallized or neocrystallized grains (as discussed in Cross et al., 2017 for quartz). The intensity of lattice distortions, calculated as the average internal misorientation within the grain, can therefore be used as a tool to discern two different population of grains with different deformation histories, such as porphyroclastic fragments from neocrystallized grains (Cross et al., 2017). The GOS map of Fig. 5.32e, can therefore help distinguish neoblasts with virtually no internal misorientation (i.e. mean misorientation < 2°), from presumed fragments with mean misorientations > 2°.

Presence of a CPO in clinopyroxene neoblasts and evidence of subgrain development in the porphyroclasts would be consistent with crystal plasticity and dynamic recrystallization. However, the porphyroclasts do not contain subgrains of the same size of the aggregate's grains, and contain very few, discontinuous low angle boundaries (Fig. 5.32d). The occurrence of amphibole and magnetite elongated parallel to the foliation in between fragments of clinopyroxene suggests that clinopyroxene porphyroclasts were subject to micro-fracturing and micro-boudinage during shearing.

Moreover, the CPO of the neoblasts is not consistent with CPOs produced by dislocation creep on clinopyroxene common slip systems reported in literature (Bascou et al., 2002; Bystricky and Mackwell, 2001; Godard and van Roermund, 1995; Mauler et al., 2000, see also Chapter 2, section 2.3.3). The strong (100) maximum of the neoblasts could be inherited from the porphyroclast, but the other crystallographic directions show remarkable dispersion from its orientation, suggesting that the two are unrelated (Fig. 5.32b). Therefore, the neoblasts' CPO could be the result of grains growing epitaxially by sharing the (100) planes of the fragments, possibly associated with a rotational component which causes the high (> 20°) misorientation angles between neighbour grains (Fig. 5.32f).

Based on the above, the neoblasts of clinopyroxene have been interpreted to form largely nucleation and growth along fractures and boudin necks (e.g. Stünitz, 1998) as the strain shadow stretch, with some grains growing epitaxially by sharing the (100) planes of the fragments.

In the mylonites derived from amphibole-poor metagabbros, amphibole found between clinopyroxene fragments is a reaction product as there are no porphyroclasts of

amphiboles as a source (Fig. 5.32g). Therefore, the CPO of amphibole is most likely the result of nucleation/oriented grain growth during deformation and not the result of crystal plasticity. This interpretation is in line with the one of Getsinger et al., (2013) and Getsinger and Hirth, (2014), and indicates grain scale mass transfer (Kilian et al., 2011; Menegon et al., 2015). Furthermore, the CPO of this dispersed amphibole is the same as the one in the ultramylonite.

5.9.2 AMPHIBOLE-RICH ULTRAMYLONITES

Amphibole:

In the amphibole-rich ultramylonites, amphibole displays a CPO with (100) planes and [001] directions aligned subparallel to foliation and lineation respectively (Fig. 5.33b and Fig. 5.34b). This CPO is consistent with CPOs frequently observed on natural and experimental samples, in both dislocation and diffusion creep regimes (e.g. dislocation: Harigane et al., 2008; diffusion: Getsinger and Hirth, 2014; Pearce et al., 2011). Previous studies on analogous shear zone from the Ivrea-Verbano Zone found amphibole at high T conditions to deform by dislocation creep, accompanied by dynamic recrystallization (Brodie 1981, Brodie and Rutter 1985). However, it is suggested here that dislocation creep was not the main deformation mechanism of amphibole porphyroclasts, and that dynamic recrystallization was not the main mechanisms of formation of the ultramylonitic amphibole. This conclusion is based on the following observations: 1) the amphibole porphyroclast shows no orientation spread and no evidence of subgrains (Fig. 5.34f and g), 2) the ultramylonitic amphiboles are largely misoriented (> 30°) from the porphyroclast's orientation - even those in contact with the porphyroclast's rim (Fig. 5.34e, orientation from red dot in porphyroclast) and 3) the CPO of the ultramylonitic

matrix is independent from the porphyroclast's orientation (Fig. 5.34b and c). Furthermore, amphibole porphyroclasts are often rimmed by orthopyroxene + plagioclase, suggesting reactions rather than dynamic recrystallization to take place during deformation (Fig. 5.22).

Therefore, the observed amphibole CPO is interpreted to have formed by anisotropic grain growth during diffusion-accommodated grain boundary sliding (Berger and Stünitz, 1996; Getsinger and Hirth, 2014). In the presence of grain boundary fluids (either aqueous or melt), this CPO could be the result of anisotropic grain growth during dissolution-precipitation creep (Imon et al., 2002, 2004; Pearce et al., 2011; Stokes et al., 2012; Wintsch and Yi, 2002).

Plagioclase:

In ultramylonitic plagioclase, the absence of CPOs commonly associated with the activity of slip systems (i.e. (010)[001], (010)[100] and (001)[100]: Kruse et al., 2001; Mehl and Hirth, 2008; Menegon et al., 2013; Stünitz et al., 2003) suggest that dislocation creep was not the dominant deformation mechanism of plagioclase in the Provola ultramylonites. In addition, it is unlikely that dynamic recrystallization alone (without the contribution of metamorphic reactions and of phase nucleation) could produce such a high degree of phase mixing (ca. 90 area% phase boundaries, Fig. 5.17), as also suggested by recent deformation experiments by Linckens et al. (2014). Dynamic recrystallization is also not expected to result in significant compositional variations (Poirier and Guillopé, 1979), which, on the contrary, are ubiquitous in the Provola shear zone (e.g. Fig. 5.26).

Grain size sensitive creep is commonly associated with a weak CPO, as well to a weakening of pre-existing CPO's (e.g. Karato, 2008). Indeed, ultramylonitic plagioclase displays a weak CPO, where the crystallographic planes and directions plagioclase are mostly randomly oriented (Fig. 5.33b). There are however some crystallographic planes and directions in plagioclase which do form clear maxima (i.e. the (110), (011) (01-1), (111), (-11-1) and the [011], [01-1], [111], [-11-1], [-111], [11-1] of Fig. 5.33b, marked in red). These could result from anisotropic grain growth, during diffusion-accomodated grain boundary sliding or during dissolution-precipitation creep – the latter assuming that a grain boundary fluid was present, as in Fukuda et al. (2013) and Pearce et al. (2011). The compositional variation between cores and rims of plagioclase grains in the ultramylonite (as in Fig. 5.26) is also consistent with anisotropic grain growth, as composition may readjust during diffusion creep (Pearce and Wheeler, 2010). Furthermore, the small grain size of the ultramylonitic plagioclase (20 µm on average) is consistent with deformation by grain size sensitive creep (diffusion creep + grain boundary sliding) (Mehl and Hirth, 2008; Rybacki and Dresen, 2004).

Based on the above, it is suggested that the plagioclase in the ultramylonite deformed primarily by grain size sensitive creep, possibly under fluid-present conditions. This result agrees with other studies of natural shear zones: e.g. Fukuda and Okudaira(2013); Kanagawa et al. (2008); Mehl and Hirth (2008); Miranda et al. (2016); Pearce et al. (2011); Raimbourg et al. (2008).

Pyroxenes:

Clino- and orthopyroxene in the ultramylonite lack a CPO, are mostly internally strain free and devoid of substructures, and have no preferential rotation axis in the axis-angle pairs

(the latter not shown). In addition, their grain size is consistently below 20µm. This suggests that they too were deforming by grain size sensitive creep, together with the other phases.

In summary, in the amphibole-rich ultramylonites, deformation is controlled by amphibole dehydration reactions that produce symplectites of fine grained clinopyroxene + plagioclase or orthopyroxene + plagioclase ± amphibole (Sections 5.3.2 and 5.12). Through symplectites formation, grain size is dramatically reduced and diffusion is enhanced, resulting in the activation of grain size sensitive creep (diffusion creep + grain boundary sliding).

Increasing temperature during prograde metamorphism promotes grain growth, which tends to remove evidence of the deformation mechanism (Brodie and Rutter, 1985; Vernon, 2004). This seems to be the reason why most studies of high-grade shear zones record deformation during retrograde conditions. In the Provola shear zone, the formation of symplectic intergrowths of 2+ phases during prograde metamorphism allows for the grain size to be sufficiently small for grain size sensitive mechanisms to be maintained, highlighting the importance of phase-mixing (Hobbs et al., 2010).

In the amphibole-rich domains, deformation by grain-size sensitive creep is invoked on the basis of the small grain size of all phases (below 20 µm on average, Fig. 5.16), on the high degree of phase mixing, and on the weak or absent CPO of all phases in the ultramylonite. At a typical geological strain rates of $10^{-12} – 10^{-14}$, grain size sensitive creep requires lower differential stresses than dislocation creep (e.g. Mehl and Hirth, 2008), which translates in weakening and strain localization in the amphibole-rich domains.

5.10 SIMS RESULTS: WATER CONTENTS IN NAMS OF THE PROVOLA SHEAR ZONE

Together with diffusion creep, water (aqueous fluid) is perhaps one of the most important causes of weakening and strain localization in the lower crust. Water can have multiple effects on deformation: it can increase the efficiency of dislocation creep and grain boundary diffusion (Kohlstedt, 2006), promote metamorphic reactions through enhanced chemical diffusion (e.g. Burlini and Bruhn, 2005), and cause partial melting by lowering the solidus of minerals (Kohlstedt, 2006; Seaman et al., 2013; Weinberg and Hasalová, 2015). The importance of water is such that it is suggested that the most important metamorphic reactions in the lower crust (i.e. the granulite - eclogite, the gabbro-eclogite and the eclogites-amphibolite transitions) are all triggered by hydrous fluids (e.g. Austrheim, 2013).

In the lower crust, water (i.e. aqueous fluid) can be stored in different ways. Water can be structurally bond to hydrous minerals (i.e. mainly biotite and amphiboles). This structurally-bond water can be liberated with dehydration reactions forming anhydrous granulites (e.g. Fyfe, 1973). In alternative, water can be incorporated as hydroxyl in the intracrystalline lattice of nominally anhydrous minerals (NAMs), either during magmatic crystallization or during subsequent metamorphism.

The presence or absence of water can have dramatic effects on the strength of rocks, and consequently on shear zone development. The presence of water is particularly important in the lower crust, because water is scarce compared to upper crustal levels and is unevenly distributed, causing significant rheological contrasts between dry and wet

lithologies (e.g. Austrheim, 2013; Getsinger et al., 2013; Menegon et al., 2011). Therefore, a better understanding of water distribution in the lower crust is essential for understanding where weakening occurs and the mechanisms responsible for lower crustal deformation.

In an attempt to contribute to this gap in knowledge, the intracrystalline water contents in pyroxenes and plagioclases of the Provola shear zone were measured with SIMS. The objective was to see how much water is stored in deformed nominally anhydrous minerals, and compare these results to published crustal water contents. The assumption behind this investigation is that shear zones minerals could have modified their intracrystalline water contents while deforming, thus providing clues to the water content of shear zones.

Three samples (F10B, F10A1, F32E) from the Provola shear zone were selected for SIMS analysis: sample F10B is an amphibole-poor mylonite, F10A1 is an amphibole-rich gabbro ultramylonite and F32E is a plagioclase-garnet lens (Fig. 5.35). The elements Si, Mg, Na, Li, K, Sr and Ca were simultaneously measured with H to evaluate if there was any systematic correlation between other elements and water content. Results are summarized in Table 5.6, and plotted as frequency distribution diagrams in Fig. 5.36. For the complete dataset and probing locations please refer to the Appendix, Appx. 8.

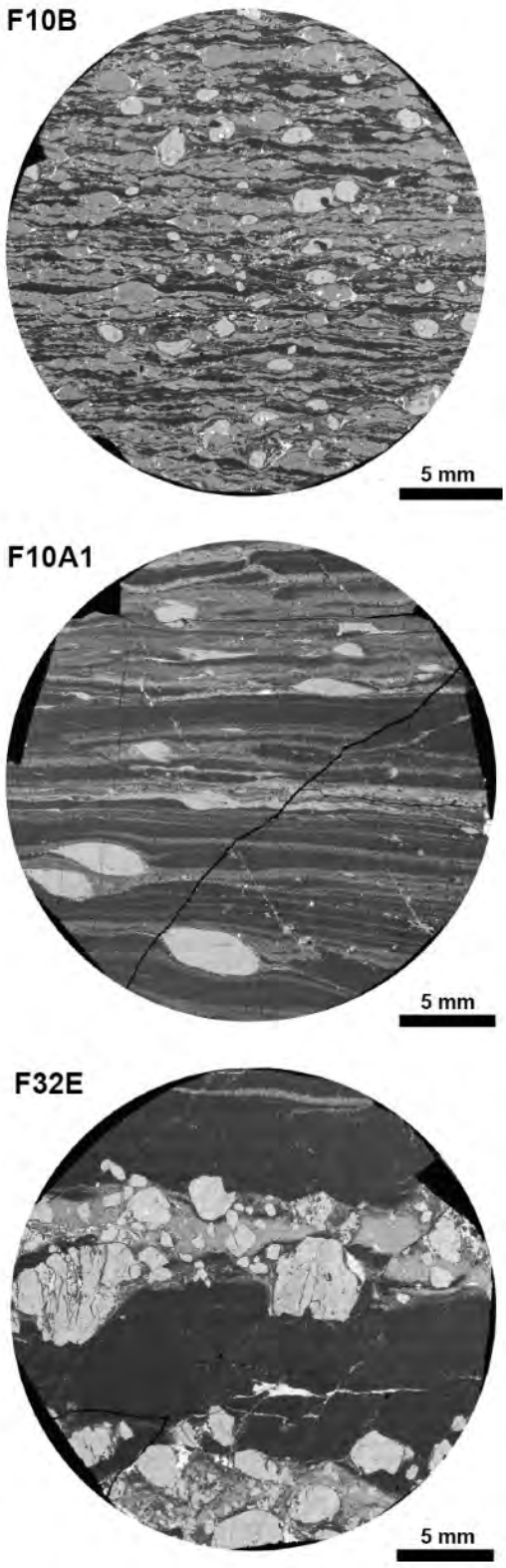

Fig. 5.35

BSE images of the samples for SIMS analyses. Enlarged versions with details of probing locations are shown in the Appendix, Appx. 8.

Clino- and orthopyroxenes were measured from the amphibole-poor metagabbro (mylonite sample F10B). Only porphyroclasts and inclusions in garnet were probed, due to the spot size of the SIMS. Results show that clinopyroxenes contain between 49 and 181 wt ppm H_2O, with a median value of 72 wt ppm H_2O, while orthopyroxenes contain between 8 and 61 wt ppm H_2O with a median of 10 wt ppm H_2O (Table 5.6 and Fig. 5.36a). These results seem to suggest that orthopyroxene incorporates less water than clinopyroxene, even though there are only a few data points available for orthopyroxene. The highest water contents were measured in clinopyroxene inclusions in garnets (Fig. 5.36a in light grey; probe locations in Appendix, Appx. 8, sample F10B – spots c1, c18, c20, c53, c53b). In addition, clinopyroxenes also show a positive correlation between their water contents and their Na, Li and Sr contents (Fig. 5.37).

	Samples	**F10B**	**F10A1**	**F32E**
Cpx*	Mean H2O	**86**	-	-
	Min	49	-	-
	Max	181	-	-
	Median	72	-	-
	N of grains	17	-	-
Opx*	Mean H2O	**22**	-	-
	Min	8	-	-
	Max	61	-	-
	Median	10	-	-
	N of grains	4	-	-
Pl	Mean H2O	**50**	**58**	**40**
	Min	12	6	6
	Max	280	156	177
	Median	15	17	22
	N of grains	12	9	17

*mineral corrections applied: clinopyroxene *2.11; orthopyroxene *0.92

Table 5.6

*SIMS results: intracrystalline water contents of clinopyroxene, orthopyroxene and plagioclase of the Provola shear zone. Results of clinopyroxene and orthopyroxene are corrected for mineralogy: clinopyroxene *2.11, orthopyroxene *0.92, whereas plagioclase has no available correction to date (see Chapter 3, section 3.7). Samples are shown in Fig. 5.35. See also Fig. 5.36 for results.*

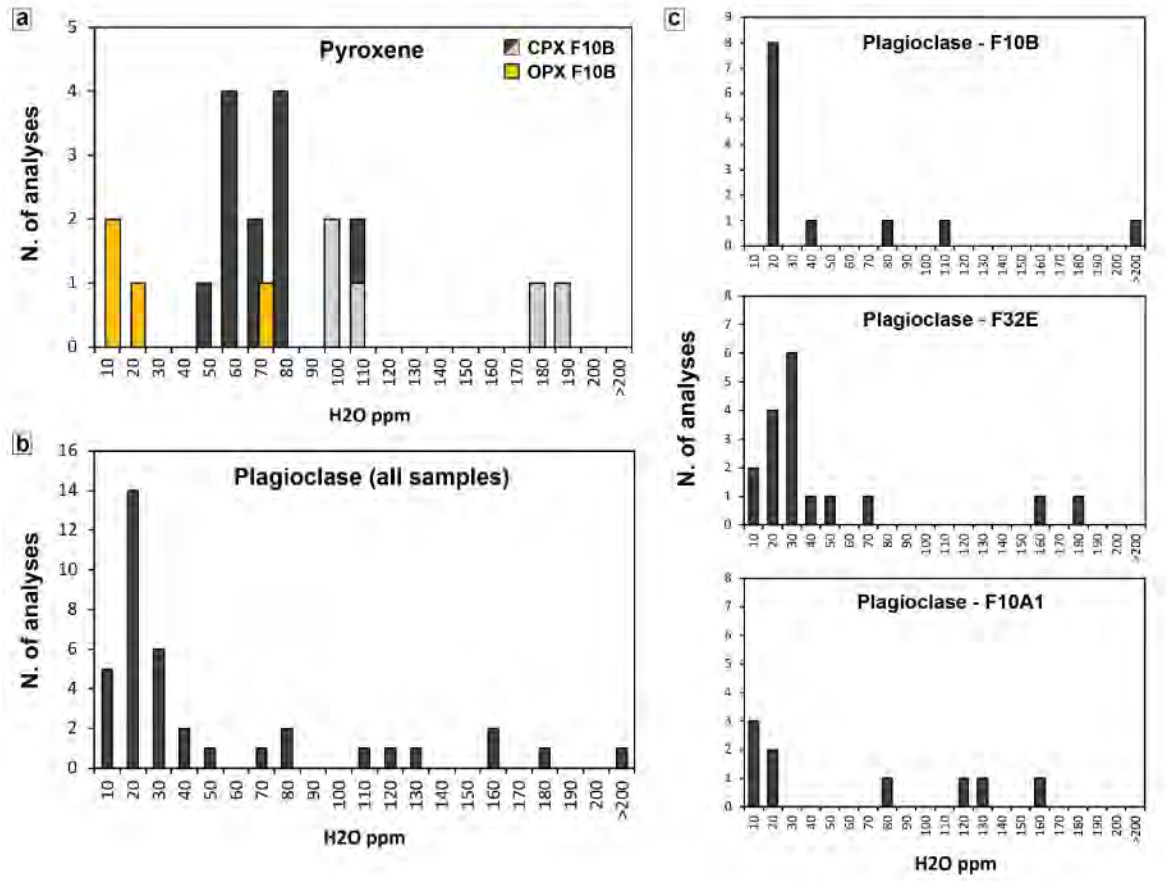

Fig. 5.36

*SIMS results: intracrystalline water contents of clinopyroxene, orthopyroxene and plagioclase, shown as frequency plots. Frequency is given as number of measurements. Results of clinopyroxene and orthopyroxene are corrected for mineralogy: clinopyroxene *2.11, orthopyroxene *0.92, whereas plagioclase has no available correction to date (see Chapter 3, section 3.7). See also Table 5.6 for results. (a) Intracrystalline water content in pyroxenes, sample F10B. Orthopyroxenes are plotted in yellow, clinopyroxenes are plotted in black and grey; the grey clinopyroxene are from inclusions in garnet porphyroclasts. (b) Intracrystalline water contents in plagioclase; all samples plotted together. (c) Intracrystalline water contents in plagioclase; separated by sample.*

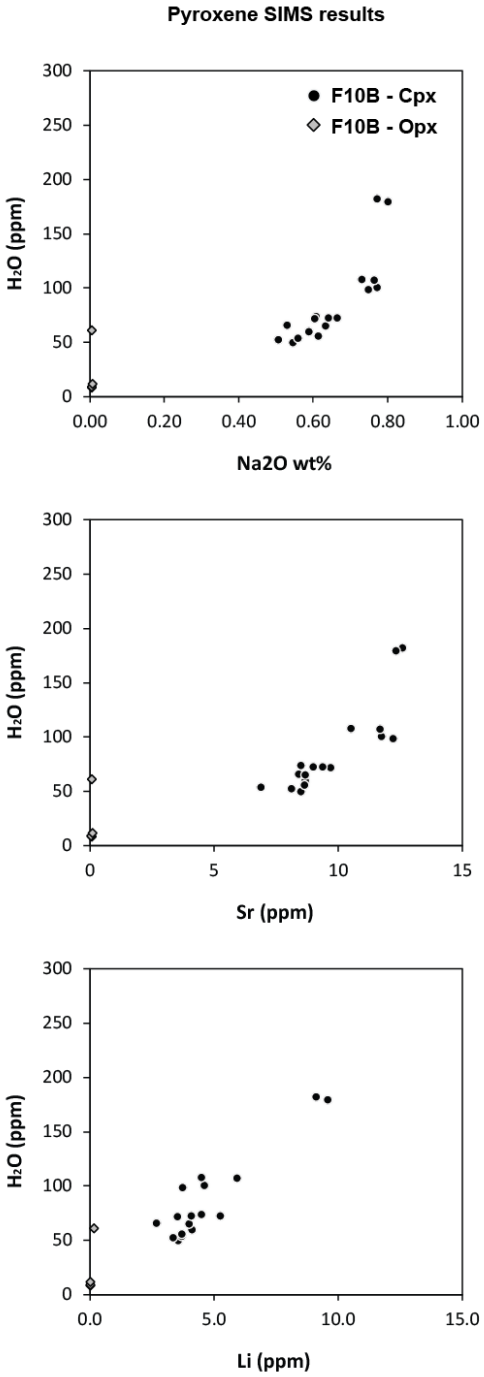

Fig. 5.37

Plots relating water content of pyroxenes of sample F10B to other elements concentration. A positive correlation can be observed between the water content and the Na, Sr and Li contents in clinopyroxenes.

Plagioclase grains were measured in all three samples. Probed grains were porphyroclasts or sufficiently large relict grains in the recrystallized matrix. Water concentrations in plagioclase range considerably, between 6 and 280 wt ppm H_2O. Nevertheless, taken cumulatively, 74% (28/38 measurements) of the analysed plagioclase grains contains less than 50 wt ppm H_2O, with a peak in values between 10 - 20 wt ppm H_2O, and a median of 19 wt ppm H_2O (Fig. 5.36b). When analysed individually, the amphibole-poor mylonitic sample F10B contains between 12 - 280 (median of 15) wt ppm H_2O, the amphibole-rich ultramylonitic sample F10A1 contains between 6 - 156 (median of 17) wt ppm H_2O, and the plagioclase – garnet sample F32E contains between 6-177 (median of 22) wt ppm H_2O (Table 5.6). Despite these wide ranges, all three samples individually show frequency peaks for water contents between 0-30 wt ppm H_2O (Fig. 5.36c), suggesting rather low water contents in plagioclase overall. It is worth noting, however, that there is still no mineral correction for H_2O content of plagioclase analysed with SIMS, therefore these absolute values should be taken with caution.

5.11 THE EFFECT OF NAM WATER ON DEFORMATION

It has been known for decades that water in NAMs has the potential to reduce creep strength dramatically by enhancing crystal plasticity, even if only present as a few parts per million (i.e. hydrolytic weakening effect: Kronenberg and Tullis, 1984; Stünitz et al., 2017). Water in NAMs is thought to reduce mineral strengths by promoting climb, and hence dislocation creep (Kohlstedt 2006; Chen et al., 2006). Experimental studies on the effect of water on the strength of pyroxenites indicate that water can increase dislocation creep rates in clinopyroxenes up to 100 times (Chen et al., 2006). The given explanation is that OH^- point defects cause an increase in the concentration and mobility of charged (ionized) jogs, and an increase in the concentration and diffusivity of charged ionic defects, and these enhance the rate of climb (Chen et al., 2006). The authors suggest that this weakening effect is most significant in clinopyroxene, while less so in plagioclase and olivine (Chen et al., 2006, and reference therein). Water in NAMs could also reduce mineral strengths by influencing the activity of slip systems, as was found by Jung et al. (2006) for olivine. Other authors suggest that during deformation, water in NAMs diffuses at phase boundaries and triggers partial melting by lowering the solidus (Seaman et al., 2013), or in alternative, that it promotes diffusion creep by "wetting" grain boundaries (Karato, 2008). It follows that measuring the water content in NAMs can give some insights on the fluids contents of the lower crust, and on its rheological effects.

As of today, most studies of water in NAMs have focused on mantle rocks (e.g. Bell and Rossman, 1992; Peslier, 2010; Skogby, 2006; Warren and Hauri, 2014) and only a handful have investigated lower-crustal rocks (e.g. Johnson, 2006; Menegon et al., 2011; Skogby et al., 1990; Xia et al., 2006, 2017; Yang et al., 2008). According to estimates of Warren

and Hauri (2014), upper mantle clinopyroxenes should incorporate between 191-764 ppm water, while orthopyroxenes 73-294 ppm. In the crust, the typical range has been estimated between 0-240 ppm (max: 466 ppm) for clinopyroxene and 26-117 ppm for orthopyroxene (max: 350 ppm) (Johnson, 2006).

Clinopyroxenes of the Provola shear zone were found to contain between 49-181 wt ppm H_2O, and orthopyroxenes between 8-61 wt ppm H_2O (Table 5.6, Fig. 5.36a). These results are in line with previous studies that found clinopyroxenes to systematically contain more water than orthopyroxenes at similar P, T conditions (e.g. Johnson, 2006; Peslier, 2010). Results also indicate that clinopyroxenes inclusions in garnet porphyroclasts (mylonite F10B sample) are generally richer in water than mylonitic pyroxenes. Several reasons could possibly explain this difference: 1) the different mineral chemistry of pyroxenes (especially their Al_2O_3 content) allowed for different quantities of water to be incorporated in the intracrystalline lattice; i.e. the more the Al_2O_3 content, the more the H_2O (e.g. Hauri et al., 2006; Skogby, 2006); or in alternative, 2) pyroxenes were depleted of water during deformation, either through crystal plasticity and recrystallization (as proposed by Finch et al. (2016) and reference therein for quartz and feldspar; and similarly by Seaman et al. 2013 for a lower crustal granitoid), or through partial melting (e.g. Peslier 2010). The fact that pyroxene inclusions in garnets were found to be richer in water than the mylonitic pyroxenes suggests that deformation played a role in water liberation. Release of intracrystalline water at grain boundaries during deformation has been recently proposed by Finch et al. (2016) as a means to produce thick ultramylonites.

Water contents in plagioclases of the Provola shear zone are more difficult to interpret. Values range from as low as 6 wt ppm H_2O to as high as 280 wt ppm H_2O, even though

low values (< 50 wt ppm) are most common (Table 5.6, Fig. 5.36b and Table in Appendix, Appx. 8). The high frequency of low values suggests that plagioclase in the lower crust contains very minor quantities of intracrystalline water. The presence of higher values (> 50 wt ppm, which makes the remaining 26% of the data) could be the result of either H_2O molecules, NH^{4+} ions, sub-microscopic fluid inclusions (< 1 µm in size) and/or alteration (Johnson 2006 and reference therein). Unfortunately, SIMS cannot discern the different hydrous species so the results are to be taken with this limitation in mind. The risk of alteration has nevertheless been minimized by inspection of the probing sites before and after the analyses, and by removal of results which displayed micro-cracks.

Overall, the Finero results indicate that lower crustal rocks store only limited amounts of water in NAMs (pyroxene and plagioclase) with values mostly below 200 wt ppm; and this result falls in the lower crustal range estimated in Johnson et al. (2006). Clinopyroxenes have been found to retain more water than orthopyroxenes; and plagioclases seem to have the largest distribution of water contents, even though most values cluster around 20 ppm.

DISCUSSION

5.12 METAMORPHIC REACTIONS AND DEFORMATION IN MAFIC ROCKS:

Metamorphic reactions occur when one or more phases are in thermodynamic disequilibrium with the surroundings. Disequilibrium is normally achieved either through changes in P-T conditions (e.g. Brodie, 1981; Newman et al., 1999; Stünitz and Tullis, 2001) or through chemical instabilities driven by the addition of a fluid (water or melt) to the system (e.g. Etheridge et al., 1983). Shear zones are ideal settings for chemical reactions to occur due to P-T changes during protracted shearing. In addition, shear zones are permeable pathways for fluids (water or melt) which enhance diffusion and consequently metamorphic reactions (e.g. Burlini and Bruhn, 2005). High grade, mafic and ultramafic lithologies are extremely valuable for understanding chemical reactions because reactions are often incomplete, and disequilibrium microstructures with products and reactants (such as, for example, corona reactions and symplectites) are often preserved (Vernon and Clarke, 2008). These in turn record the P-T conditions of shearing.

In the Provola shear zone there is multiple evidence of chemical (metamorphic) reactions in the form of symplectites or reaction rims. Symplectites are typically fine-grained vermicular intergrowths of two or more reaction products that form out of an unstable phase. Their formation is diffusion-controlled, so it is believed that symplectites grow from the outside inwards (Passchier and Trouw, 2005).

In the Provola shear zone, two types of symplectites were identified: (1) symplectites of clinopyroxene / orthopyroxene + plagioclase consuming amphibole porphyroclasts and (2) symplectites of orthopyroxene + plagioclase (± amphibole) consuming garnet porphyroclasts.

Garnet-derived orthopyroxene + plagioclase symplectites are frequent in granulite facies rocks and are commonly associated with (isothermal) decompression (Brodie, 1995; Brown, 2002; Dégi et al., 2009; Gross et al., 2009; Jones and Escher, 2002). They indicate one of the following retrograde reactions:

1) Grt + Qtz = Opx + Pl ± Mt
2) Grt + Cpx + Qtz = Opx + Pl ± Mt

(e.g. Prakash et al., 2007; Zhao et al., 2001)

In Finero, garnet-derived symplectites are equally present in the metagabbroic protomylonites, mylonite and ultramylonites (Fig. 5.10, Fig. 5.12d and Fig. 5.21). In the high-strain domains, the symplectites are asymmetrically distributed with respect to the shear plane, occurring in the extensional quadrants around garnet porphyroclasts. Their microstructural position indicates that they formed during deformation (Brodie, 1995; Rutter et al., 1993) (e.g. Fig. 5.12d).

Amphibole-derived orthopyroxene + plagioclase or clinopyroxene + plagioclase symplectites are found around porphyroclasts of amphiboles in amphibole-rich domains (Fig. 5.12d and Fig. 5.21). These symplectites are interpreted as the result of dehydration melting reactions consuming amphibole for pyroxene, and releasing fluid (melt) to the system (Vernon and Clarke, 2008). This is because at temperature and pressure

conditions of ca. 800 - 900 °C and 8 kbar, amphibole porphyroclasts undergo one of the following dehydration melting reactions, to produce a tonalitic (pl-rich) melt (Wolf and Wyllie, 1994) and a fine-grained intergrowth of peritectic plagioclase and pyroxene (clino- or ortho):

1) Hbl + Pl = Cpx (+ Grt) + Opx + Am [Ca-Am + Al-Am] + melt
   (Wolf and Wyllie, 1991, 1994)
2) Hbl + Qtz (in the form of Si) = Pl + Opx + Cpx (+ Grt) + melt
   (Vernon and Clarke, 2008; Weinberg and Hasalová, 2015)
3) Grt + Hbl = Opx + Pl + melt (Prakash et al., (2007) and reference therein)

These syn-kinematic dehydration melting reaction consuming amphibole are prograde reactions that occur for increasing temperatures (Brown, 2007; Vernon and Clarke, 2008). Dehydration melting can be also be triggered by decompression (e.g. Boriani and Villa, 1997; Brown, 2007).

In the Provola shear zone, amphibole-rich metagabbros preserve microstructural evidence of amphibole dehydration reactions, in the form of pyroxene + plagioclase rims, or symplectites (Fig. 5.15 and Fig. 5.22). These peritectic products are found around amphibole porphyroclasts, both in the weakly deformed domains and in the ultramylonitic domains. Peritectic garnet does not form in the Provola shear zone as a reaction product, suggesting that the dehydration reactions occurred at conditions of garnet instability.

Orthopyroxene + plagioclase rims/symplectites from amphiboles have been first described by Brodie and Rutter, (1985) and interpreted as post-shearing, high temperature reactions, or as a drop in P_{H2O}. This study instead interprets the amphibole-

derived symplectites to be pre- to- synkinematic reaction products, and attributes them a key role in weakening and strain localization of mafic lower crustal rocks (see section 5.13 that follows). It is worth mentioning here that partial melting in metabasic rocks of the Ivrea Zone was also observed elsewhere, e.g. in Val Strona di Omegna (Kunz et al., 2014).

The by-product of amphibole dehydration reactions is melt, as indicated by the reactions (1)-(3) above. If the melt produced by these reactions remained in the system, then some evidence of former melt would be expected in the microstructure. Yet, classic evidence of former melt, such as K-feldspar films, pools or patches (e.g. Holness and Sawyer, 2008; Weinberg and Hasalová, 2015), quartz along triple junctions, quartz beads or films along grains (e.g. Stuart et al., 2017; Weinberg and Hasalová, 2015) have not been observed in the amphibole-rich ultramylonites. It must be noted however that the formation and/or preservation of these phases depends on the chemistry of the rock. The Provola metagabbros are originally potassium poor and silica poor rocks (43-46 wt% SiO_2, compared to 51-53 wt% SiO_2 of quartz-bearing gabbros of Stuart et al. (2017) of which melt evidence is preserved (see Table 5.3). It is therefore possible that the K and Si that partitioned in the melt did not form K-feldspar and quartz phases for the P-T conditions experienced by the Provola shear zone. This aspect has being tested by extracting the melt composition from the pseudosection F20A (at two fixed P-T conditions), and using it to make another pseudosection to see what phase assemblages would form out of it. The work is still preliminary and is not shown here, but suggests that quartz forms only below 600 °C in these rocks.

It is here proposed that the melt that formed by dehydration melting of amphibole remained in the system, and back-reacted to form the ultramylonitic amphibole upon

cooling below the solidus (see section 5.7). Back-reactions upon cooling forming amphibole/biotite was investigated by Beard et al. (2004). Indeed, ultramylonitic amphiboles and the rims of amphibole porphyroclasts are richer in K_2O (ca. 0.3 wt% richer) than the cores of amphibole porphyroclasts, suggesting formation of secondary amphibole from a K_2O "enriched" melt (Fig. 5.26 and Tables in Appendix, Appx. 6). Furthermore, plagioclase grains in the ultramylonite show compositional variations from cores to rims, with rims being more anorthitic than cores, suggesting chemical re-equilibration with a fluid (Fig. 5.26).

If the melt produced by dehydration reactions of amphiboles escaped the system carrying the water with it, only limited rehydration reactions could have occurred (Brown, 2002; Sawyer, 2001), meaning that little or no secondary amphibole (i.e. ultramylonitic amphibole) could have formed in the ultramylonites. Hence, the presence of abundant secondary amphibole in the ultramylonites indicates that melt remained in the system until the solidus was crossed again precipitating amphibole (backreaction) (e.g. Grt + Cpx + Qtz + melt = Pl + Hbl ± Mt; Jones and Escher, 2002) or, in alternative, indicates that amphibole was a peritectic product alongside pyroxene of in-situ partial melting (e.g. Hbl + Pl = Cpx + Opx + Am + melt ; (Wolf and Wyllie, 1991, 1994). Melting in the presence of small amounts of water favours orthopyroxene-clinopyroxene formation over amphibole (< 3-5 wt%) (Weinberg and Hasalová, 2015).

The possibility of an externally derived fluid (as in case-study 1) is here argued against, because the bulk major chemistry of the rock is the same throughout all analysed samples, indicating limited metasomatism. In addition, influx of an external fluid could not explain the mineralogical control on strain partitioning and localization. In other

words, it would not explain why ultramylonites systematically occur in amphibole-rich domains where primary magmatic amphiboles are abundant.

5.13 Reaction weakening and strain localization in the Provola shear zone during prograde metamorphism

Syn-kinematic metamorphic reactions are known to play an important role in shear zone development, as they can significantly contribute to weakening and strain localization via production of a fine grained aggregate that deforms by grain size sensitive creep (e.g. Brodie and Rutter, 1987b; de Ronde et al., 2005; Kanagawa et al., 2008; Kenkmann and Dresen, 2002; Kilian et al., 2011; Kruse and Stünitz, 1999; Mehl and Hirth, 2008; Newman et al., 1999; Pearce et al., 2011; Pearce and Wheeler, 2011; Poirier, 1980; Raimbourg et al., 2008; Rutter and Brodie, 1988; Stünitz, 1998; Stünitz and Tullis, 2001; Urai et al., 1986; White et al., 1980). In addition, metamorphic reactions are an efficient mechanism for phase-mixing (e.g. Kenkmann and Dresen, 2002; Pearce et al., 2011; Stünitz, 1998; Stünitz and Tullis, 2001) which is crucial for weakening, because pinning of second phases prevents grain growth and thus stabilizes the fine-grained aggregate microstructure for diffusion creep processes to be maintained (e.g. Herwegh et al., 2011).

The Provola shear zone is an ideal example of how dehydration reactions can facilitate shearing and strain localization in the lower crust, and of how the presence or absence of the latter produces fundamentally different microstructures and rheological responses. In these rocks deforming at high P-T conditions, amphibole is the mineral that controls strain localization via syn-kinematic dehydration reactions. Dehydration of amphibole is an efficient weakening mechanism because of a double effect: it produces extremely fine-grained reaction products in the form of symplectites, while

simultaneously enhancing grain boundary diffusivity by liberating fluid to the system. These two effects together allow the fine-grained reaction products to form interconnected layers and activate diffusion creep (e.g. Dijkstra et al., 2002; Dimanov et al., 2000; Hirth and Kohlstedt, 1995; Rosenberg, 2001; Rosenberg and Handy, 2005; Rutter and Neumann, 1995; Závada et al., 2007; Zhou et al., 2012).

At the onset of deformation, these reactions were only local around amphibole porphyroclasts. Therefore, deformation was mainly accommodated by crystal plasticity and dynamic recrystallization of plagioclase (Kenkmann and Dresen, 2002). However, as shearing and reaction progressed, more reaction products merged to form interconnected networks of fine-grained material, triggering grain size sensitive creep. The weakening associated with these reactions far outweighed that of crystal plasticity in plagioclases, leading to strain localization in the fine-grained reaction products. This process eventually formed ultramylonites (Fig. 5.38b).

The absence of amphibole undergoing dehydration reactions had important implications for the microstructural evolution and strength of mafic lower crustal rocks. In the absence of fine-grained reaction products, deformation localized on the weakest phase plagioclase, which underwent crystal plasticity and dynamic recrystallization (Brodie and Rutter, 1987b; Kenkmann and Dresen, 2002)(Fig. 5.38a). No phase-mixing occurred within plagioclase ribbons as no plagioclase-consuming reactions were occurring in these layers during shearing. The stronger pyroxenes initially underwent a combination of (minor) crystal plasticity and micro-fracturing, followed by neocrystallization (e.g. Stünitz, 1998). Garnet-derived symplectites only marginally contributed to the weakening process, due to the amount and spatial distribution of garnet porphyroclasts that did not

allow the symplectic mixture to achieve interconnectivity. Furthermore, in a fluid (or melt) deficient environment, fluid-assisted diffusion is only minor or lacking, so that diffusion is slower overall (Karato, 2008).

In the Provola shear zone, amphibole-poor domains mostly failed to produce ultramylonites, because at the same P-T conditions, amphibole-rich domains were weaker due to grain size reduction and phase mixing, and higher fluid contents resulting from the dehydration reaction of amphibole (Fig. 5.38a vs. b). The strength contrast created between amphibole-poor and amphibole-rich domains (given by the different strain rates between the layers deforming by dislocation creep and those by diffusion creep, e.g. Mehl and Hirth, 2008) was thus responsible for strain partitioning and localization in amphibole-rich domains; and ultimately for the formation of an anastomosing shear zone at lower crustal conditions.

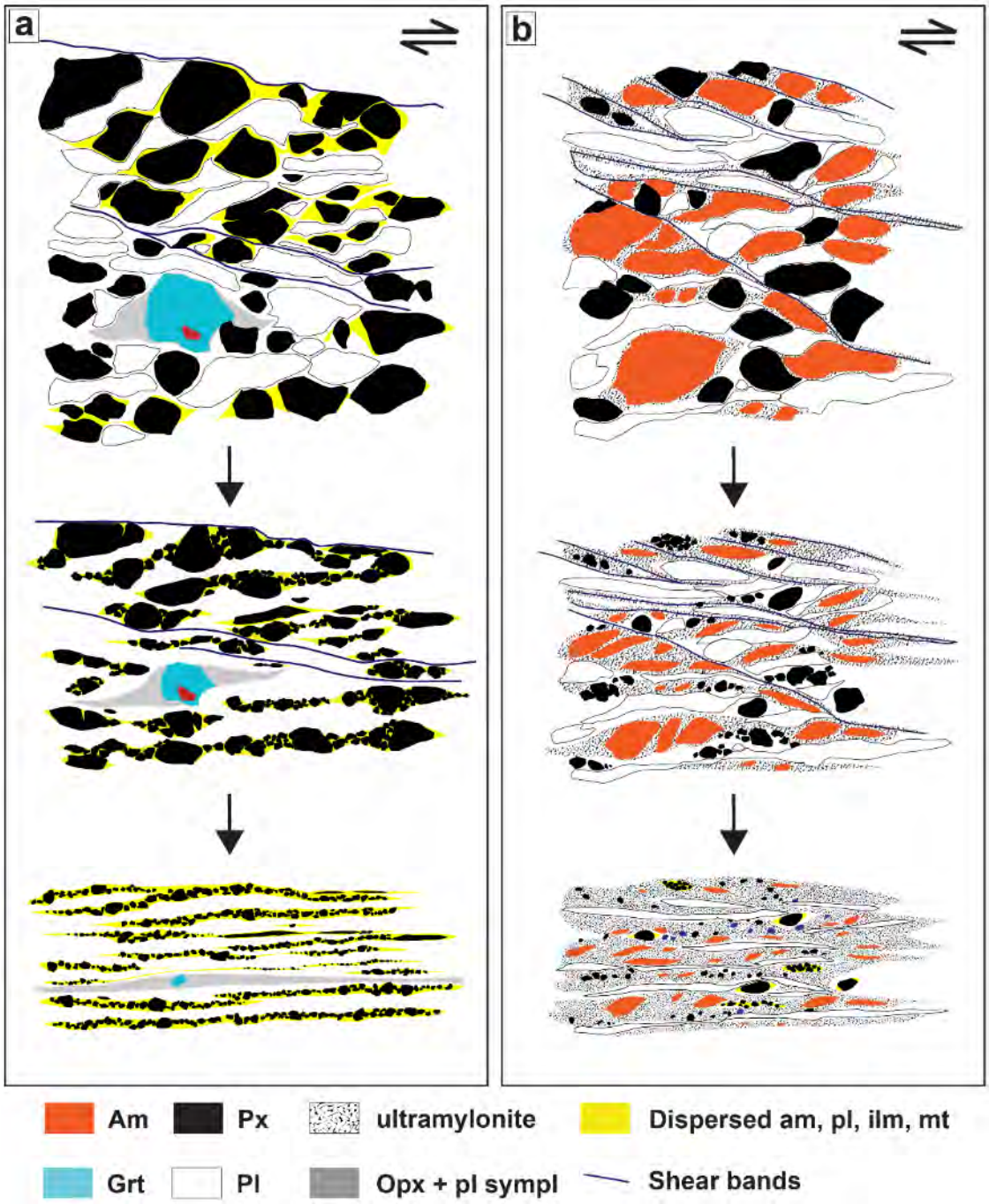
a
b
Am
Px
ultramylonite
Dispersed am, pl, ilm, mt
Grt
Pl
Opx + pl sympl
Shear bands

Fig. 5.38

Fig. 5.38 (previous page)

Summary sketch showing the microstructural evolutions of amphibole-poor and amphibole-rich domains with increasing strain. Legend below. (a) Amphibole-poor domain. No amphibole dehydration melting occurs. Deformation is controlled by the monophase ribbons of plagioclase, which deform by dislocation creep + dynamic recrystallization. Pyroxene undergoes a combination of microfracturing, followed by neocrystallization of neoblastic pyroxene. Garnets form symplectites of orthopyroxene + plagioclase. Even at high strains, phase mixing is limited, and the mineralogical banding is preserved (b) Amphibole-rich domain. Amphibole dehydration melting consumes amphibole porphyroclasts, forming symplectites of pyroxene + plagioclase. As this process continues, the fine grained reaction products form rheologically weaker interconnected layers which deform by grainsize sensitive creep. Pyroxenes porphyroclasts neocrystallize and are incorporated in the fine-grained aggregate.

This case study therefore clearly shows the importance of grain size reduction via dehydration reactions, and phase mixing, for strain partitioning and localization in the lower crust. Strain localization at these P-T conditions does not necessitate fluid percolation from outside sources, as dehydration reactions are sufficient for weakening. The formation of fine-grained reaction products is arguably the most important aspect of deformation under melt-present conditions as the weakening effect does not cease when temperatures drop below the solidus, thus shearing can protract at subsolidus conditions. In addition, the formation of fine-grained reaction products mean that even modest melt fractions are capable of a significant weakening. The latter is supported by recent experiments on creep of partially molten granulites, finding that as little as 2 vol% of melt at grain boundaries can produce strain rate enhancement of 5 times (Zhou et al., 2017).

5.14 The significance of the Provola shear zone for the tectono-metamorphic evolution of the Finero Complex, Ivrea Zone

High-T shear zones within the mafic complex of the Ivrea-Verbano zone have been recognised since the 1980's (e.g. the Forno-Anzola high-T shear zone, Brodie, 1981; Brodie and Rutter, 1987a, 1987b, Rutter et al., 2007, 1993). High-T shear zones not only provide valuable insights on the strength and rheology of the ductile lithosphere, but they are also crucial to explain the tectonic evolutions of rift systems and orogens (e.g. Beltrando et al., 2015). The metagabbroic high-T shear zones, preserved in the Mafic Complex of the Ivrea Zone are particularly valuable for the latter point. While high-T shear zones preserved in the mantle peridotites (e.g. Balmuccia, Finero, Lanzo) might have deformed in (at least) two instances (while residing in the mantle and after being emplaced in the lower crust), high-T shear zones which developed in the metagabbros of the Mafic Complex must have formed at lower crustal conditions, sometime between gabbro emplacement and exhumation to shallow mid-crustal levels.

According to the thermochronological results of Wolff et al. (2012), the Ivrea-Verbano Zone reached mid-crustal depths (9-12 km) and temperatures (ca. 300 °C) in the early Jurassic, and was later unaffected by the Alpine orogeny – meaning that temperatures were greenschist facies or lower since the Mesozoic. The latter brackets the activity of the high-T shear zones of the mafic complex between the Permian magmatic event (295-280Ma; Peressini et al., 2007) and the Early Jurassic.

Indeed, high-T shear zones in the Ivrea Zone have been genetically linked to heterogeneous regional stretching and decompression (crustal extension) following the Permian mafic intrusions in the lower crust (Brodie and Rutter, 1987a; Rutter et al., 2007,

1993). In the above studies, a definite age of shearing was not given, even though a late Permian – early Triassic activity was suggested as most probable. In alternative, it was also proposed that such high-T shear zones could represent deeper expressions of the Pogallo fault zone (Brodie and Rutter, 1987a), interpreted as an extensional mid-crustal fault zone active in the late Triassic – lower Jurassic times (Schmid et al., 1987; Zingg et al., 1990).

As of recently, limited age constrains are available for the timing of activity of these high-T shear zones, the most notable being the Ar-Ar datings of shear zone amphiboles by Brodie (1989), and the Ar-Ar dating of amphiboles by Boriani and Villa (1997). Results of Brodie (1989), from amphibole porphyroclasts and from a fine-grained aggregate of the Anzola-Rosarolo shear zone, yield ages between 215-203Ma. Similarly, results of Boriani and Villa (1997) yield ages between 217 ± 1 Ma. Based on these results, Beltrando et al. (2015) propose that the Anzola high-T shear zone was (at least partly) active in the 210 – 200 Ma interval (late Triassic). This time period coincides with a short-lived thermal anomaly, which is in turn coeval with early stages of rifting recorded both within the Adriatic Plate and along the future European margin of the Alpine Tethys (Beltrando et al., 2015). In other words, it is possible that (at least some) high-T shear zones preserved in the Ivrea-Verbano Zone are structures which have accommodated extension in the lower crust during (or just before) Jurassic rifting.

The Finero mafic complex has been considered part of the Permian magmatic event (Zingg et al., 1990) until recently, when new geochronological studies reassessed the emplacement of the Finero complex to be Middle Triassic (U/Pb zircon ages at 232 ±3 Ma) (Zanetti et al., 2013, 2014). The latter result implies that the high-T Provola shear

zone which reworked the rocks of the mafic complex is Middle Triassic in age or younger. Zanetti et al. (2013) have proposed this recrystallization (and shearing) event to have occurred in the Late Triassic, between 219 ± 3 and 205 ±3 Ma, and to represent the final stages of prolonged magmatic recrystallization and cooling of the mafic intrusion, aided by late-stage fluids (melts). Therefore, following this logic, the Provola shear zone was a *local* structure, formed by the anomalously high temperatures imposed by impulses of late-magmatic fluids in the lower crust following the gabbro emplacement – and not by a regional heating event.

However, ongoing studies suggest that the Provola shear zone, instead of being a local structure is rather a regional scale structure, genetically linked to the Anzola-Val Grande high-T shear zone described by Rutter et al. (2007). If this is the case, then the Provola shear could be one of the rift-related Jurassic shear zones which have accommodated extension in the lower crust during (or just before) Jurassic rifting, as proposed by Beltrando et al. (2015).

SUMMARY

In the Finero locality of the Ivrea zone, lower crustal shearing exploited a compositionally-layered mafic-ultramafic complex made of amphibole-rich and amphibole-poor metagabbros. Shearing was initiated after an increase in temperature above the solidus, starting from the post-intrusive granulite facies re-equilibration conditions of 900 °C and 9.7 kbar. Thermobarometric estimates using syn-kinematic amphibole-plagioclase pairs and orthopyroxene-clinopyroxene pairs indicate shearing conditions of both domains between 6.0 – 8.2 kbar and 700 – 900 °C. Both amphibole-poor and amphibole-rich

metagabbros were involved in the deformation, as evidenced by the same P-T conditions of deformation recorded using conventional thermobarometry, yet the different mineralogical assemblages resulted in different microstructural and rheological evolutions, with strain localization in the amphibole-rich domains.

In the amphibole-poor mylonites, mono-phase ribbons of plagioclase deformed by dislocation creep on multiple slip systems, including (but not limited to) the (010)[001] of elongated grains. Dislocation creep was accompanied by subgrain rotation recrystallization. Clinopyroxene porphyroclasts in pyroxene-rich layers initially deformed by crystal plasticity, followed by microfracturing and neocrystallization. This resulted in pyroxene-rich layers made of aggregates of neoblastic pyroxene.

In the amphibole-rich ultramylonites, the fine-grained (< 20 μm average grain size) polyphase matrix of clinopyroxene, amphibole, orthopyroxene, plagioclase, ilmenite, magnetite (± apatite) deformed by grain size sensitive creep (diffusion creep + grain boundary sliding), accompanied by anisotropic grain growth of amphibole and plagioclase grains. The weak CPO of the ultramylonitic plagioclase does not identify with any of the known CPOs formed by dislocation creep, and is thus interpreted as resulting from anisotropic grain growth during diffusion-accomodated grain boundary sliding. Similarly, the CPO of ultramylonitic amphibole, which shows an alignment of (100) subparallel to foliation and [001] subparallel to lineation, is interpreted as oriented grain growth during grain size sensitive creep. Ultramylonitic clinopyroxene and orthopyroxene grains instead show no CPO.

In the Provola shear zone, strain partitioned in the amphibole-rich domains of the layered complex, due to in-situ dehydration melting of primary (magmatic) amphiboles.

Amphibole dehydration melting formed fine-grained symplectites of pyroxene and plagioclase as dehydration reaction products. These products are preserved in the microstructure of amphibole-rich domains in the form of symplectites. Through dehydration melting reactions, amphibole-rich domains formed fine-grained interconnected networks of reaction products that deformed by grain size sensitive creep. On the contrary, amphibole-poor layers did not experience dehydration melting reactions, resulting in banded mylonites with relatively low degrees of phase mixing.

SIMS results on pyroxene and plagioclases of the Provola shear zone indicate that pyroxene and plagioclases store only limited amounts of intracrystalline water, with values mostly below 200 wt ppm H_2O. Results also indicated that clinopyroxene inclusions preserved in garnet porphyroclasts are richer in intracrystalline water than pyroxenes in the shear zone, suggesting water liberation during deformation.

This case study clearly underlines the importance of dehydration melting reactions for weakening and strain localization in mafic lower crustal lithologies. It follows that the presence of primary (i.e. magmatic) amphibole in the lower crust is key for weakening and strain localization of otherwise strong rocks. Strain localization at these P-T conditions does not necessitate fluid percolation from outside sources, as in-situ dehydration melting reactions forming a fine-grained aggregate of 2+ phases that deforms by grain size sensitive creep is sufficient for weakening.

6 CONCLUSIONS

6.1 OVERALL CONCLUSIONS

The two case-studies analysed in this PhD thesis are a window on natural processes occurring in the lower crust, providing evidence of the intimate link between chemical reactions (in the form of symplectites) and rheological weakening of mafic lower crustal rocks.

Both case studies find that rheological weakening of mafic lower crustal rocks occurs through chemical reactions which form a fine-grained mixture of 2+ phases. Fine-grained reaction products coalesce into interconnected networks of fine-grained material, causing a switch from grain size insensitive to grain-size sensitive creep; and this is a proven mechanism for weakening and strain localization in the ductile lithosphere (e.g. Brodie and Rutter, 1987; de Ronde et al., 2005; Kanagawa et al., 2008; Kenkmann and Dresen, 2002; Kilian et al., 2011; Kruse and Stünitz, 1999; Mehl and Hirth, 2008; Newman et al., 1999; Pearce et al., 2011; Pearce and Wheeler, 2011; Poirier, 1980; Raimbourg et al., 2008; Rutter and Brodie, 1988; Stünitz, 1998; Stünitz and Tullis, 2001; Urai et al., 1986; White et al., 1980).

In the first case-study (Seiland Igneous Province, Norwegian Caledonides) chemical reactions occurred by infiltration of felsic melt from adjacent partially-molten metapelites. This resulted in melt-rock interaction and formation of a fine-grained polyphase aggregate. In the second case study (Finero mafic complex, Italian Alps) chemical reactions occurred by in-situ dehydration melting of amphiboles, forming fine-grained symplectites of pyroxene + plagioclase. Therefore, both case-studies directly or

indirectly show that dehydration melting of hydrous minerals (biotite/amphibole) played a key role in rheological weakening of mafic lower crustal rocks. These examples also indicate that water does not necessarily need to infiltrate from shallower crustal levels - provided that hydrous minerals undergoing dehydration melting are present (either within the mafic rocks or within nearby metasediments). Weakening can therefore occur in pristine, strong, granular rocks without the need for prior fracturing and water ingress.

In addition, both case studies find weakening and strain localization of mafic lower crustal rocks to initiate during prograde metamorphism. Studies of natural lower crustal shear zones often associate weakening of mafic rocks with retrograde reactions rather than prograde reactions, with ingress of fluids and hydration along pre-existing shear zones (e.g. Baratoux et al., 2005; Brodie and Rutter, 1987; Harigane et al., 2008; Jamtveit et al., 2016; Kanagawa et al., 2008; Kenkmann and Dresen, 2002; Kruse and Stünitz, 1999). This PhD instead brings examples of prograde weakening, and suggests that pristine sections of lower crust can be weakened just via temperature or pressure perturbations that cause dehydration melting reactions, which in turn produce fine grained reaction products. Therefore, these two natural case studies of lower crustal deformation suggest that (at least some of) the fine grained polyphase ultramylonites that form at lower crustal conditions under prograde metamorphism are governed by chemical reactions, directly or indirectly linked with melt.

The Finero case-study (case study 2) also finds that pre-existing lithological (mineralogical) heterogeneities are crucial for strain partitioning and strain localization, even at lower crustal conditions. This study thus confirms the importance of precursor heterogeneities for shear zone nucleation and growth, as Pennacchioni and Mancktelow (2007) have proven for mid-crustal plutons.

Last but not least, the two case studies provide valuable information on texture (CPO) development and texture strength of lower crustal shear zones. The presence or absence of CPOs has important implications for seismological investigations of the structure and composition of the lower crust, as it was found experimentally that seismic wave velocities differ considerably according to the propagation directions in rocks with a CPO. The CPO of amphibole, in particular, has been identified as a major cause of seismic anisotropy and shear wave splitting in the lower crust (e.g. Barberini et al. 2007; Barroul and Kern, 1996; Ji et al., 2013; Meissner et al., 2006; Tatham et al., 2008). P-waves in amphibole rich rocks (e.g. amphibolites) propagate fastest when parallel to the sample's stretching lineation and slowest when perpendicular to the foliation – due to amphibole CPO showing an alignment of [100] directions parallel to the stretching lineation and of (100) planes parallel to the foliation (Ji et al., 2013). Likewise, shear wave splitting is greatest when the propagation direction lies in the foliation plane (Barroul and Kern 1996). The presence of plagioclase, quartz and clinopyroxene has been found to have a diminishing effect on the anisotropy induced by amphibole CPO (Ji et al., 2013). Therefore, seismic anisotropy and shear wave splitting can be used to identify crustal domains with strong crystallographic alignment of amphiboles, and thus indirectly provide information on the distribution of strain in the deeper levels of the crust. A better understanding of CPO development in the lower crust and how it relates to shear zones and strain localization is therefore essential for a correct interpretation of seismic anisotropy, and a better understanding of the structure and composition of lower crustal levels.

6.2 FUTURE WORK

This PhD research is far from being complete, as the complexity of natural systems mean that lots of aspects remain open to further analysis and discussion.

Two aspects that would benefit from further investigation are thermodynamic modelling using the mafic melt model of Green et al. (2016); and combining SIMS with detailed chemical analysis and EBSD. On the last point, additional investigations are planned regarding the intracrystalline water contents in nominally anhydrous minerals preserved in lower crustal shear zones. Microprobe analyses on the same grains probed with SIMS would determine whether any correlation exists between intracrystalline water content and mineral chemistry. Furthermore, EBSD on the same grains probed with SIMS could assess if there is any systematic correlation between slip systems and intracrystalline water contents. Another interesting aspect to investigate (not planned in the near future) would be to measure the matrix grains of the shear zones using the nano-SIMS, to test whether they contain more or less water than the porphyroclasts. The latter promises to be particularly challenging due to the fine grain size of the matrix; yet if successful it would provide valuable insights on the availability and distribution of water in lower crustal shear zones, and potentially discern whether water is expelled to grain boundaries and lost (as recent results of Finch et al., 2016 suggest), or incorporated during shearing.

Lastly, one of the current debates in the Ivrea Zone revolve around the timing of activity of the high-T shear zones, as their age determines whether they are genetically linked to Jurassic rifting, or not. A large dataset of radiometric datings exist for the Ivrea Zone (for a review, see Peressini et al., 2007; Zanetti et al., 2013; Wolff et al., 2012), nevertheless the results span considerably and only a few works, to my knowledge, directly date the shear zones (e.g. Anzola shear zone, Brodie et al., 1989). It would therefore be

scientifically relevant to date the Provola shear zone with one of the modern dating techniques now available. Zircons and amphiboles would be the obvious minerals of choice, but the former could yield ages of gabbro emplacement while the latter could yield mixing ages due to difficult separation between porphyroclasts and ultramylonitic amphiboles. A novel approach could be in-situ dating of the abundant apatites preserved in the mylonites and ultramylonites of the Provola shear zone, as their microstructural positions and habitus suggests that they could be syn-kinematic (e.g. Fig. 5.20). An age of 220 Ma or younger would confirm that the shear zone was a rift-related structure that accommodated at deeper structural levels the opening of the Alpine Tethys (Beltrando et al., 2015).

REFERENCES

Al-Merey, R., Karajou, J., Issa, H., 2005. X-ray fluorescence analysis of geological samples: exploring the effect of sample thickness on the accuracy of results. Appl. Radiat. Isot. 62, 501–508. https://doi.org/10.1016/j.apradiso.2004.04.020

Austrheim, H., 2013. Fluid and deformation induced metamorphic processes around Moho beneath continent collision zones: Examples from the exposed root zone of the Caledonian mountain belt, W-Norway. Tectonophysics, Moho: 100 years after Andrija Mohorovicic 609, 620–635. https://doi.org/10.1016/j.tecto.2013.08.030

Austrheim, H., 1987. Eclogitization of lower crustal granulites by fluid migration through shear zones. Earth Planet. Sci. Lett. 81, 221–232. https://doi.org/10.1016/0012-821X(87)90158-0

Baratoux, L., Schulmann, K., Ulrich, S., Lexa, O., 2005. Contrasting microstructures and deformation mechanisms in metagabbro mylonites contemporaneously deformed under different temperatures (c. 650 C and c. 750 C). Geol. Soc. Lond. Spec. Publ. 243, 97–125. https://doi.org/10.1144/GSL.SP.2005.243.01.09

Barberini, V. Burlini L., Zappone A., 2007. Elastic properties, fabric and seismic anisotropy of amphibolites and their contribution to the lower crust reflectivity. Tectonophysics 445, 227-244.

Barruol G., Kern H., 1996. Seismic anisotropy and shear-wave splitting in lower-crustal and upper-mantle rocks from the Ivrea Zone—experimental and calculated data. Physics of the Earth and Planetary Interiors. 95, 175-194.

Bascou, J., Barruol, G., Vauchez, A., Mainprice, D., Egydio-Silva, M., 2001. EBSD-measured lattice-preferred orientations and seismic properties of eclogites. Tectonophysics 342, 61–80.

Bascou, J., Tommasi, A., Mainprice, D., 2002. Plastic deformation and development of clinopyroxene lattice preferred orientations in eclogites. J. Struct. Geol. 24, 1357–1368.

Beard, J.S., Ragland, P.C., Rushmer, T., 2004. Hydration Crystallization Reactions between Anhydrous Minerals and Hydrous Melt to Yield Amphibole and Biotite in Igneous Rocks: Description and Implications. J. Geol. 112, 617–621. https://doi.org/10.1086/422670

Bell, D.R., Rossman, G.R., 1992. Water in Earth's Mantle: The Role of Nominally Anhydrous Minerals. Science 255, 1391–1397.

Beltrando, M., Stockli, D.F., Decarlis, A., Manatschal, G., 2015. A crustal-scale view at rift localization along the fossil Adriatic margin of the Alpine Tethys preserved in NW Italy. Tectonics 34, 2015TC003973. https://doi.org/10.1002/2015TC003973

Berger, A., Stünitz, H., 1996. Deformation mechanisms and reaction of hornblende: examples from the Bergell tonalite (Central Alps). Tectonophysics 257, 149–174. https://doi.org/10.1016/0040-1951(95)00125-5

Blenkinsop, T.G., 2000. Deformation Microstructures and Mechanisms in Minerals and Rocks. Springer Science & Business Media.

Bons, P.D., den Brok, B., 2000. Crystallographic preferred orientation development by dissolution–precipitation creep. J. Struct. Geol. 22, 1713–1722. https://doi.org/10.1016/S0191-8141(00)00075-4

Boriani, A., Burlini, L., Sacchi, R., 1990a. The Cossato-Mergozzo-Brissago Line and the Pogallo Line (Southern Alps, Northern Italy) and their relationships with the late-Hercynian magmatic and metamorphic events. Tectonophysics, The nature of the lower continental crust 182, 91–102. https://doi.org/10.1016/0040-1951(90)90344-8

Boriani, A., Burlini, L., Università degli studi di Milano-Bicocca, Dipartimento di scienze della terra, Centro di studio per la geodinamica alpina e quaternaria, Valle Cannobina (Italy : Commune), Istituto geografico militare (Italy), 1995. Carta geologica della Valle Cannobina = Geological map of Valle Cannobina.

Boriani, A., Giobbi, E., 2004. Does the basement of western southern Alps display a tilted section through the continental crust? A review and discussion. Period. Mineral. 73, 5–22.

Boriani, A., Origoni, E.G., Borghi, A., Caironi, V., 1990b. The evolution of the "Serie dei Laghi" (Strona-Ceneri and Scisti dei Laghi): the upper component of the Ivrea-Verbano crustal section; Southern Alps, North Italy and Ticino, Switzerland. Tectonophysics, The nature of the lower continental crust 182, 103–118. https://doi.org/10.1016/0040-1951(90)90345-9

Boriani, A., Villa, I.M., 1997. Geochronology of regional metamorphism in the Ivrea-Verbano zone and Serie dei Laghi, Italian Alps. Schweiz Miner. Petrogr Mitt 77, 381–401.

Bragg, W.H., Bragg, W.L., 1913. The Reflection of X-rays by Crystals. Proc. R. Soc. Lond. Ser. Contain. Pap. Math. Phys. Character 88, 428–438.

Brodie, K.H., 1995. The development of orientated symplectites during deformation. J. Metamorph. Geol. 13, 499–508. https://doi.org/10.1111/j.1525-1314.1995.tb00237.x

Brodie, K.H., 1981. Variation in amphibole and plagioclase composition with deformation. Tectonophysics, The Effect of Deformation on Rocks 78, 385–402. https://doi.org/10.1016/0040-1951(81)90021-4

Brodie, K.H., 1980. Shear zones in rocks Variations in mineral chemistry across a shear zone in phlogopite peridotite. J. Struct. Geol. 2, 265–272. https://doi.org/10.1016/0191-8141(80)90059-0

Brodie, K.H., Rutter, E.H., 1987a. Deep crustal extensional faulting of the Ivrea Zone of Northern Italy. Tectonophysics 140, 193–212.

Brodie, K.H., Rutter, E.H., 1987b. The role of transiently fine-grained reaction products in syntectonic metamorphism: natural and experimental examples. Can. J. Earth Sci. 24, 556–564. https://doi.org/10.1139/e87-054

Brodie, K.H., Rutter, E.H., 1985. On the relationship between deformation and metamorphism, with special reference to the behavior of basic rocks, in: Thompson, A.B., Rubie, D.C. (Eds.), Metamorphic Reactions, Advances in Physical Geochemistry. Springer New York, pp. 138–179. https://doi.org/10.1007/978-1-4612-5066-1_6

Brodie, K.H., Rutter, E.H., Rex, D., 1989. On the age of deep crustal extensional faulting in the Ivrea zone, northern Italy. Geol. Soc. Lond. Spec. Publ. 45, 203–210. https://doi.org/10.1144/GSL.SP.1989.045.01.11

Brown, M., 2007. Crustal melting and melt extraction, ascent and emplacement in orogens: mechanisms and consequences. J. Geol. Soc. 164, 709–730. https://doi.org/10.1144/0016-76492006-171

Brown, M., 2002. Retrograde processes in migmatites and granulites revisited. J. Metamorph. Geol. 20, 25–40. https://doi.org/10.1046/j.0263-4929.2001.00362.x

Bunge, H.J., 1982. Texture Analysis in Materials Science. Lond. Butterwoths.

Burg, J.-P., Arbaret, L., Chaudhry, N.M., Dawood, H., Hussain, S., Zeilinger, G., 2005. Shear strain localization from the upper mantle to the middle crust of the Kohistan Arc (Pakistan). Geol. Soc. Lond. Spec. Publ. 245, 25–38. https://doi.org/10.1144/GSL.SP.2005.245.01.02

Bürgmann, R., Dresen, G., 2008. Rheology of the Lower Crust and Upper Mantle: Evidence from Rock Mechanics, Geodesy, and Field Observations. Annu. Rev. Earth Planet. Sci. 36, 531–567. https://doi.org/10.1146/annurev.earth.36.031207.124326

Burlini, L., Bruhn, D., 2005. High-strain zones: laboratory perspectives on strain softening during ductile deformation. Geol. Soc. Lond. Spec. Publ. 245, 1–24. https://doi.org/10.1144/GSL.SP.2005.245.01.01

Burov, E.B., 2011. Rheology and strength of the lithosphere. Mar. Pet. Geol. 28, 1402–1443.

Burov, E.B., 2010. The equivalent elastic thickness (Te), seismicity and the long-term rheology of continental lithosphere: Time to burn-out “crème brûlée”? Tectonophysics 484, 4–26. https://doi.org/10.1016/j.tecto.2009.06.013

Byerlee, J., 1978. Friction of rocks. Pure Appl. Geophys. 116, 615–626. https://doi.org/10.1007/BF00876528

Bystricky, M., Mackwell, S., 2001. Creep of dry clinopyroxene aggregates. J. Geophys. Res. Solid Earth 106, 13443–13454. https://doi.org/10.1029/2001JB000333

Ceccato, A., Pennacchioni, G., Menegon, L., Bestmann, M., 2017. Crystallographic control and texture inheritance during mylonitization of coarse grained quartz veins. Lithos 290–291, 210–227. https://doi.org/10.1016/j.lithos.2017.08.005

Chen, S., Hiraga, T., Kohlstedt, D.L., 2006. Water weakening of clinopyroxene in the dislocation creep regime. J. Geophys. Res. 111. https://doi.org/10.1029/2005JB003885

Christensen, N.I., Fountain, D.M., 1975. Constitution of the Lower Continental Crust Based on Experimental Studies of Seismic Velocities in Granulite. Geol. Soc. Am. Bull. 86, 227–236. https://doi.org/10.1130/0016-7606(1975)86<227:COTLCC>2.0.CO;2

Christensen, N.I., Mooney, W.D., 1995. Seismic velocity structure and composition of the continental crust: A global view. J. Geophys. Res. Solid Earth 100, 9761–9788. https://doi.org/10.1029/95JB00259

Connolly, J.A.D., 1990. Multivariable phase-diagrams - an algorithm based on generalized thermodynamics. Am. J. Sci. 290, 666–718.

Connolly, J.A.D., 1990. Multivariable phase diagrams; an algorithm based on generalized thermodynamics. Am. J. Sci. 290, 666–718. https://doi.org/10.2475/ajs.290.6.666

Cross, A.J., Prior, D.J., Stipp, M., Kidder, S., 2017. The recrystallized grain size piezometer for quartz: An EBSD-based calibration. Geophys. Res. Lett. 44, 2017GL073836. https://doi.org/10.1002/2017GL073836

Dale, J., Powell, R., White, R.W., Elmer, F.L., Holland, T.J.B., 2005. A thermodynamic model for Ca–Na clinoamphiboles in Na2O–CaO–FeO–MgO–Al2O3–SiO2–H2O–O for petrological calculations. J. Metamorph. Geol. 23, 771–791. https://doi.org/10.1111/j.1525-1314.2005.00609.x

De Bresser, J., Ter Heege, J., Spiers, C., 2001. Grain size reduction by dynamic recrystallization: can it result in major rheological weakening? Int. J. Earth Sci. 90, 28–45. https://doi.org/10.1007/s005310000149

De Meer, S., Drury, M.R., De Bresser, J.H.P., Pennock, G.M., 2002. Current issues and new developments in deformation mechanisms, rheology and tectonics. Geol. Soc. Lond. Spec. Publ. 200, 1–27. https://doi.org/10.1144/GSL.SP.2001.200.01.01

de Ronde, A.A., Stünitz, H., Tullis, J., Heilbronner, R., 2005. Reaction-induced weakening of plagioclase–olivine composites. Tectonophysics 409, 85–106. https://doi.org/10.1016/j.tecto.2005.08.008

Deer, W. a, Howie, R. a, Zussman, J., 2013. Introduction to the Rock-Forming Minerals, Third edition. ed. Mineralogical Society, London.

Dégi, J., Abart, R., Török, K., Bali, E., Wirth, R., Rhede, D., 2009. Symplectite formation during decompression induced garnet breakdown in lower crustal mafic granulite xenoliths: mechanisms and rates. Contrib. Mineral. Petrol. 159, 293–314. https://doi.org/10.1007/s00410-009-0428-z

Degli Alessandrini, G., Menegon, L., Malaspina, N., Dijkstra, A.H., Anderson, M.W., 2017. Creep of mafic dykes infiltrated by melt in the lower continental crust (Seiland Igneous Province, Norway). Lithos 274–275, 169–187. https://doi.org/10.1016/j.lithos.2016.12.030

Dell`Angelo, L.N., Tullis, J., Yund, R.A., 1987. Transition from dislocation creep to melt-enhanced diffusion creep in fine-grained granitic aggregates. Tectonophysics 139, 325–332. https://doi.org/10.1016/0040-1951(87)90107-7

Dijkstra, A.H., Drury, M.R., Vissers, R.L.M., Newman, J., 2002. On the role of melt-rock reaction in mantle shear zone formation in the Othris Peridotite Massif (Greece). J. Struct. Geol. 24, 1431–1450. https://doi.org/10.1016/S0191-8141(01)00142-0

Dimanov, A., Dresen, G., 2005. Rheology of synthetic anorthite-diopside aggregates: Implications for ductile shear zones. J. Geophys. Res. 110. https://doi.org/10.1029/2004JB003431

Dimanov, A., Dresen, G., Wirth, R., 1998. High-temperature creep of partially molten plagioclase aggregates. J. Geophys. Res. Solid Earth 103, 9651–9664. https://doi.org/10.1029/97JB03742

Dimanov, A., Wirth, R., Dresen, G., 2000. The effect of melt distribution on the rheology of plagioclase rocks. Tectonophysics 328, 307–327. https://doi.org/10.1016/S0040-1951(00)00214-6

Dornbusch, H.-J., Weber, K., Skrotzki, W., 1994. Development of microstructure and texture in high-temperature mylonites from the Ivrea zone. Textures Geol. Mater. DGM Informationsgesellschaft 187–201.

Ellis, D.J., 1987. Origin and evolution of granulites in normal and thickened crusts. Geology 15, 167–170. https://doi.org/10.1130/0091-7613(1987)15<167:OAEOGI>2.0.CO;2

Elvevold, S., Reginiussen, H., Krogh, E.J., Bjorklund, F., 1994. Reworking of deep-seated gabbros and associated contact metamophosed paragneisses in the south-eastern part of the Seiland Igneous Province, northern Norway. J. Metamorph. Geol. 12, 000–000.

Engler, O., Randle, V., 2009. Introduction to Texture Analysis: Macrotexture, Microtexture, and Orientation Mapping, Second Edition. CRC Press.

Ernst, W.G., Liu, J., 1998. Experimental phase-equilibrium study of Al- and Ti-contents of calcic amphibole in MORB—A semiquantitative thermobarometer. Am. Mineral. 83, 952–969. https://doi.org/10.2138/am-1998-9-1004

Etheridge, M.A., Wall, V.J., Vernon, R.H., 1983. The role of the fluid phase during regional metamorphism and deformation. J. Metamorph. Geol. 1, 205–226. https://doi.org/10.1111/j.1525-1314.1983.tb00272.x

Evans, B., Renner, J., Hirth, G., 2001. A few remarks on the kinetics of static grain growth in rocks. Int. J. Earth Sci. 90, 88–103. https://doi.org/10.1007/s005310000150

Fagereng, Å., 2013. Fault segmentation, deep rift earthquakes and crustal rheology: Insights from the 2009 Karonga sequence and seismicity in the Rukwa–Malawi rift zone. Tectonophysics 601, 216–225. https://doi.org/10.1016/j.tecto.2013.05.012

Finch, M.A., Weinberg, R.F., Hunter, N.J.R., 2016. Water loss and the origin of thick ultramylonites. Geology 44, 599–602. https://doi.org/10.1130/G37972.1

Fitz Gerald, J.D., Mancktelow, N.S., Pennacchioni, G., Kunze, K., 2006. Ultrafine-grained quartz mylonites from high-grade shear zones: Evidence for strong dry middle to lower crust. Geology 34, 369–372. https://doi.org/10.1130/G22099.1

Fitz Gerald, J.D., Stünitz, H., 1993. Deformation of granitoids at low metamorphic grade. I: Reactions and grain size reduction. Tectonophysics 221, 269–297. https://doi.org/10.1016/0040-1951(93)90163-E

Fossen, H., Cavalcante, G.C.G., 2017. Shear zones – A review. Earth-Sci. Rev. 171, 434–455. https://doi.org/10.1016/j.earscirev.2017.05.002

Frost, R., Lindsley, D.H., 1992. Equilibria among Fe-Ti oxides, pyroxenes, olivine, and quartz: Part II. Application. Am. Mineral. 77, 1004–1020.

Fuhrman, M., Lindsley, D., 1988. Ternary - feldspar modeling and thermometry. Am. Mineral. 73, 201–215.

Fukuda, J., Okudaira, T., 2013. Grain-size-sensitive creep of plagioclase accompanied by solution–precipitation and mass transfer under mid-crustal conditions. J. Struct. Geol. 51, 61–73. https://doi.org/10.1016/j.jsg.2013.03.006

Fukuda, J., Okudaira, T., Satsukawa, T., Michibayashi, K., 2012. Solution–precipitation of K-feldspar in deformed granitoids and its relationship to the distribution of water. Tectonophysics 532–535, 175–185. https://doi.org/10.1016/j.tecto.2012.01.033

Fyfe, W.S., 1973. The Granulite Facies, Partial Melting and the Archaean Crust. Philos. Trans. R. Soc. Lond. Ser. Math. Phys. Sci. 273, 457–461.

Getsinger, A.J., Hirth, G., 2014. Amphibole fabric formation during diffusion creep and the rheology of shear zones. Geology 42, 535–538. https://doi.org/10.1130/G35327.1

Getsinger, A.J., Hirth, G., Stünitz, H., Goergen, E.T., 2013. Influence of water on rheology and strain localization in the lower continental crust: Water, Rheology, and Strain Localization. Geochem. Geophys. Geosystems 14, 2247–2264. https://doi.org/10.1002/ggge.20148

Godard, G., van Roermund, H.L., 1995. Deformation-induced clinopyroxene fabrics from eclogites. J. Struct. Geol. 17, 1425–1443.

Goetze, C., Evans, B., 1979. Stress and temperature in the bending lithosphere as constrained by experimental rock mechanics. Geophys. J. Int. 59, 463–478. https://doi.org/10.1111/j.1365-246X.1979.tb02567.x

Gómez-Barreiro, J., Lonardelli, I., Wenk, H.R., Dresen, G., Rybacki, E., Ren, Y., Tomé, C.N., 2007. Preferred orientation of anorthite deformed experimentally in Newtonian creep. Earth Planet. Sci. Lett. 264, 188–207. https://doi.org/10.1016/j.epsl.2007.09.018

Green, E.C.R., White, R.W., Diener, J.F.A., Powell, R., Holland, T.J.B., Palin, R.M., 2016. Activity–composition relations for the calculation of partial melting equilibria in metabasic rocks. J. Metamorph. Geol. 34, 845–869. https://doi.org/10.1111/jmg.12211

Griggs, D., 1967. Hydrolytic Weakening of Quartz and Other Silicates. Geophys. J. Int. 14, 19–31. https://doi.org/10.1111/j.1365-246X.1967.tb06218.x

Gross, A.O.M.S., Droop, G.T.R., Porcher, C.C., Fernandes, L.A.D., 2009. Petrology and thermobarometry of mafic granulites and migmatites from the Chafalote Metamorphic Suite: New insights into the Neoproterozoic P–T evolution of the Uruguayan—Sul-Rio-Grandense shield. Precambrian Res. 170, 157–174. https://doi.org/10.1016/j.precamres.2009.01.011

Gueydan, F., Leroy, Y.M., Jolivet, L., Agard, P., 2003. Analysis of continental midcrustal strain localization induced by microfracturing and reaction-softening. J. Geophys. Res. Solid Earth 108. https://doi.org/10.1029/2001JB000611

Gueydan, F., Précigout, J., Montési, L.G.J., 2014. Strain weakening enables continental plate tectonics. Tectonophysics, Observational and Modelling perspectives on the Mechanical properties of the Lithosphere 631, 189–196. https://doi.org/10.1016/j.tecto.2014.02.005

Hacker, B.R., Kelemen, P.B., Behn, M.D., 2015. Continental Lower Crust. Annu. Rev. Earth Planet. Sci. 43, 167–205. https://doi.org/10.1146/annurev-earth-050212-124117

Halfpenny, A., Prior, D.J., Wheeler, J., 2006. Analysis of dynamic recrystallization and nucleation in a quartzite mylonite. Tectonophysics, Deformation mechanisms, microstructure and rheology of rocks in nature and experiment 427, 3–14. https://doi.org/10.1016/j.tecto.2006.05.016

Handy, M.., Brun, J.-P., 2004. Seismicity, structure and strength of the continental lithosphere. Earth Planet. Sci. Lett. 223, 427–441. https://doi.org/10.1016/j.epsl.2004.04.021

Handy, M., Hirth, G., Hovius, N., 2007. Continental fault structure and rheology from the frictional-to-viscous transition downward.

Handy, M.R., Stunitz, H., 2002. Strain localization by fracturing and reaction weakening -- a mechanism for initiating exhumation of subcontinental mantle beneath rifted margins. Geol. Soc. Lond. Spec. Publ. 200, 387–407. https://doi.org/10.1144/GSL.SP.2001.200.01.22

Handy, M.R., Zingg, A., 1991. The tectonic and rheological evolution of an attenuated cross section of the continental crust: Ivrea crustal section, southern Alps, northwestern Italy and southern Switzerland. Geol. Soc. Am. Bull. 103, 236–253.

Hanmer, S., 2000. Matrix mosaics, brittle deformation, and elongate porphyroclasts: granulite facies microstructures in the Striding–Athabasca mylonite zone, western Canada. J. Struct. Geol. 22, 947–967.

Harigane, Y., Michibayashi, K., Ohara, Y., 2008. Shearing within lower crust during progressive retrogression: Structural analysis of gabbroic rocks from the Godzilla Mullion, an oceanic core complex in the Parece Vela backarc basin. Tectonophysics 457, 183–196. https://doi.org/10.1016/j.tecto.2008.06.009

Harley, S.L., 1989. The origins of granulites: a metamorphic perspective. Geol. Mag. 126, 215–247. https://doi.org/10.1017/S0016756800022330

Harlov, D.E., 2012. The potential role of fluids during regional granulite-facies dehydration in the lower crust. Geosci. Front., Charnockites and Charnockites 3, 813–827. https://doi.org/10.1016/j.gsf.2012.03.007

Hauri, E.H., Gaetani, G.A., Green, T.H., 2006. Partitioning of water during melting of the Earth's upper mantle at H2O-undersaturated conditions. Earth Planet. Sci. Lett. 248, 715–734. https://doi.org/10.1016/j.epsl.2006.06.014

Heilbronner, R., Barrett, S., 2014. Image Analysis in Earth Sciences. Springer Berlin Heidelberg, Berlin, Heidelberg.

Heilbronner, R., Barrett, S., 2013. Image Analysis in Earth Sciences: Microstructures and Textures of Earth Materials. Springer Science & Business Media.

Helmstaedt, H., Anderson, O.L., Gavasci, A.T., 1972. Petrofabric studies of eclogite, spinel-Websterite, and spinel-lherzolite Xenoliths from kimberlite-bearing breccia pipes in southeastern Utah and northeastern Arizona. J. Geophys. Res. 77, 4350–4365. https://doi.org/10.1029/JB077i023p04350

Herwegh, M., Linckens, J., Ebert, A., Berger, A., Brodhag, S.H., 2011. The role of second phases for controlling microstructural evolution in polymineralic rocks: A review. J. Struct. Geol. 33, 1728–1750. https://doi.org/10.1016/j.jsg.2011.08.011

Higgins, M., 2006. Quantitative Textural Measurements in Igneous and Metamorphic Petrology [WWW Document]. Camb. Univ. Press. URL http://www.cambridge.org/gb/academic/subjects/earth-and-environmental-science/mineralogy-petrology-and-volcanology/quantitative-textural-measurements-igneous-and-metamorphic-petrology.

Hippertt, J.F., 1994. Microstructures and c-axis fabrics indicative of quartz dissolution in sheared quartzites and phyllonites. Tectonophysics 229, 141–163. https://doi.org/10.1016/0040-1951(94)90026-4

Hippertt, J.F., Hongn, F.D., 1998. Deformation mechanisms in the mylonite/ultramylonite transition. J. Struct. Geol. 20, 1435–1448. https://doi.org/10.1016/S0191-8141(98)00047-9

Hirth, G., Kohlstedt, D.L., 1995a. Experimental constraints on the dynamics of the partially molten upper mantle: 2. Deformation in the dislocation creep regime. J. Geophys. Res. Solid Earth 100, 15441–15449. https://doi.org/10.1029/95JB01292

Hirth, G., Kohlstedt, D.L., 1995b. Experimental constraints on the dynamics of the partially molten upper mantle: Deformation in the diffusion creep regime. J. Geophys. Res. Solid Earth 100, 1981–2001. https://doi.org/10.1029/94JB02128

Hirth, G., Tullis, J., 1992. Dislocation creep regimes in quartz aggregates. J. Struct. Geol. 14, 145–159. https://doi.org/10.1016/0191-8141(92)90053-Y

Hobbs, B.E., Mühlhaus, H.-B., Ord, A., 1990. Instability, softening and localization of deformation. Geol. Soc. Lond. Spec. Publ. 54, 143–165. https://doi.org/10.1144/GSL.SP.1990.054.01.15

Hobbs, B.E., Ord, A., Spalla, M.I., Gosso, G., Zucali, M., 2010. The interaction of deformation and metamorphic reactions. Geol. Soc. Lond. Spec. Publ. 332, 189–223. https://doi.org/10.1144/SP332.12

Holland, T., Blundy, J., 1994. Non-ideal interactions in calcic amphiboles and their bearing on amphibole-plagioclase thermometry. Contrib. Mineral. Petrol. 116, 433–447. https://doi.org/10.1007/BF00310910

Holland, T., Powell, R., 2003. Activity–composition relations for phases in petrological calculations: an asymmetric multicomponent formulation. Contrib. Mineral. Petrol. 145, 492–501. https://doi.org/10.1007/s00410-003-0464-z

Holland, T.J.B., Powell, R., 2011. An improved and extended internally consistent thermodynamic dataset for phases of petrological interest, involving a new equation of state for solids. J. Metamorph. Geol. 29, 333–383. https://doi.org/10.1111/j.1525-1314.2010.00923.x

Holland, T.J.B., Powell, R., 1998a. An internally consistent thermodynamic data set for phases of petrological interest. J. Metamorph. Geol. 16, 309–343.

Holland, T.J.B., Powell, R., 1998b. An internally consistent thermodynamic data set for phases of petrological interest. J. Metamorph. Geol. 16, 309–43.

Holland, T.J.B., Powell, R., 1996. Thermodynamics of order-disorder in minerals. 2. Symmetric formalism applied to solid solutions. Am. Mineral. 81, 1425–1437.

Holness, M.B., Sawyer, E.W., 2008. On the Pseudomorphing of Melt-filled Pores During the Crystallization of Migmatites. J. Petrol. 49, 1343–1363. https://doi.org/10.1093/petrology/egn028

Holyoke, C.W., Tullis, J., 2006. Formation and maintenance of shear zones. Geology 34, 105–108. https://doi.org/10.1130/G22116.1

Imon, R., Okudaira, T., Fujimoto, A., 2002. Dissolution and precipitation processes in deformed amphibolites: an example from the ductile shear zone of the Ryoke metamorphic belt, SW Japan. J. Metamorph. Geol. 20, 297–308. https://doi.org/10.1046/j.1525-1314.2002.00367.x

Imon, R., Okudaira, T., Kanagawa, K., 2004. Development of shape- and lattice-preferred orientations of amphibole grains during initial cataclastic deformation and subsequent deformation by dissolution–precipitation creep in amphibolites from the Ryoke metamorphic belt, SW Japan. J. Struct. Geol. 26, 793–805. https://doi.org/10.1016/j.jsg.2003.09.004

Ishii, K., Sawaguchi, T., 2002. Lattice- and shape-preferred orientation of orthopyroxene porphyroclasts in peridotites: an application of two-dimensional numerical modeling. J. Struct. Geol. 24, 517–530. https://doi.org/10.1016/S0191-8141(01)00078-5

Jackson, J., 2002. Strength of the continental lithosphere: time to abandon the jelly sandwich? GSA Today 12, 4–10.

Jackson, J., McKenzie, D., Priestley, K., Emmerson, B., 2008. New views on the structure and rheology of the lithosphere. J. Geol. Soc. 165, 453–465. https://doi.org/10.1144/0016-76492007-109

Jackson, J.A., Austrheim, H., McKenzie, D., Priestley, K., 2004. Metastability, mechanical strength, and the support of mountain belts. Geology 32, 625. https://doi.org/10.1130/G20397.1

Jamtveit, B., Austrheim, H., Putnis, A., 2016. Disequilibrium metamorphism of stressed lithosphere. Earth-Sci. Rev. 154, 1–13. https://doi.org/10.1016/j.earscirev.2015.12.002

Janoušek, V., Farrow, C.M., Erban, V., 2006. Interpretation of Whole-rock Geochemical Data in Igneous Geochemistry: Introducing Geochemical Data Toolkit (GCDkit). J. Petrol. 47, 1255–1259. https://doi.org/10.1093/petrology/egl013

Ji, S., Shao, T., Michibayashi, K., Long, C., Wang, Q., Kondo, Y., Zhao, W., Wang, H., Salisbury, M.H., 2013. A new calibration of seismic velocities, anisotropy, fabrics, and elastic moduli of amphibole-rich rocks. J. Geoph Research. 118, 4699-4728

Johnson, E.A., 2006. Water in Nominally Anhydrous Crustal Minerals: Speciation, Concentration, and Geologic Significance. Rev. Mineral. Geochem. 62, 117–154. https://doi.org/10.2138/rmg.2006.62.6

Jones, K.A., Escher, J.C., 2002. Near-isothermal decompression within a clockwise P–T evolution recorded in migmatitic mafic granulites from Clavering Ø, NE Greenland: implications for the evolution of the Caledonides. J. Metamorph. Geol. 20, 365–378. https://doi.org/10.1046/j.1525-1314.2002.00375.x

Jung, H., Katayama, I., Jiang, Z., Hiraga, T., Karato, S., 2006. Effect of water and stress on the lattice-preferred orientation of olivine. Tectonophysics 421, 1–22. https://doi.org/10.1016/j.tecto.2006.02.011

Kaczmarek, M.-A., Tommasi, A., 2011. Anatomy of an extensional shear zone in the mantle, Lanzo massif, Italy. Geochem. Geophys. Geosystems 12, Q0AG06. https://doi.org/10.1029/2011GC003627

Kanagawa, K., Shimano, H., Hiroi, Y., 2008. Mylonitic deformation of gabbro in the lower crust: A case study from the Pankenushi gabbro in the Hidaka metamorphic belt of central Hokkaido, Japan. J. Struct. Geol. 30, 1150–1166. https://doi.org/10.1016/j.jsg.2008.05.007

Karato, S., 2010a. Rheology of the deep upper mantle and its implications for the preservation of the continental roots: A review. Tectonophysics, Insights into the Earth's Deep Lithosphere 481, 82–98. https://doi.org/10.1016/j.tecto.2009.04.011

Karato, S., 2010b. Rheology of the Earth's mantle: A historical review. Gondwana Res., A Tribute to Miyashiro 18, 17–45. https://doi.org/10.1016/j.gr.2010.03.004

Karato, S., 2008. Deformation of Earth Materials: An Introduction to the Rheology of Solid Earth. Cambridge University Press.

Kay, R.W., Kay, S.M., 1981. The nature of the lower continental crust: Inferences from geophysics, surface geology, and crustal xenoliths. Rev. Geophys. 19, 271–297. https://doi.org/10.1029/RG019i002p00271

Kenkmann, T., 2000. Processes controlling the shrinkage of porphyroclasts in gabbroic shear zones. J. Struct. Geol. 22, 471–487.

Kenkmann, T., Dresen, G., 2002. Dislocation microstructure and phase distribution in a lower crustal shear zone – an example from the Ivrea-Zone, Italy. Int. J. Earth Sci. 91, 445–458. https://doi.org/10.1007/s00531-001-0236-9

Kilian, R., Heilbronner, R., Stünitz, H., 2011a. Quartz grain size reduction in a granitoid rock and the transition from dislocation to diffusion creep. J. Struct. Geol. 33, 1265–1284. https://doi.org/10.1016/j.jsg.2011.05.004

Kilian, R., Heilbronner, R., Stünitz, H., 2011b. Quartz microstructures and crystallographic preferred orientation: Which shear sense do they indicate? J. Struct. Geol. 33, 1446–1466. https://doi.org/10.1016/j.jsg.2011.08.005

Kirby, S.H., 1980. Tectonic stresses in the lithosphere: Constraints provided by the experimental deformation of rocks. J. Geophys. Res. Solid Earth 85, 6353–6363. https://doi.org/10.1029/JB085iB11p06353

Klein, C., Dana, J. D., Hurlbut, C. S., 2002. Manual of Mineral Science (Manual of Mineralogy). 22nd Edition of the Manual of Mineral Science. Wiley.

Koepke, J., Feig, S.T., Snow, J., Freise, M., 2004. Petrogenesis of oceanic plagiogranites by partial melting of gabbros: an experimental study. Contrib. Mineral. Petrol. 146, 414–432. https://doi.org/10.1007/s00410-003-0511-9

Kohlstedt, D.L., 2006. The Role of Water in High-Temperature Rock Deformation. Rev. Mineral. Geochem. 62, 377–396. https://doi.org/10.2138/rmg.2006.62.16

Kohlstedt, D.L., Evans, B., Mackwell, S.J., 1995. Strength of the lithosphere: Constraints imposed by laboratory experiments. J. Geophys. Res. 100, 17,587-17,602.

Kronenberg, A.K., Tullis, J., 1984. Flow strengths of quartz aggregates: Grain size and pressure effects due to hydrolytic weakening. J. Geophys. Res. Solid Earth 89, 4281–4297. https://doi.org/10.1029/JB089iB06p04281

Kruse, R., Stünitz, H., 1999. Deformation mechanisms and phase distribution in mafic high-temperature mylonites from the Jotun Nappe, southern Norway. Tectonophysics 303, 223–249.

Kruse, R., Stünitz, H., Kunze, K., 2001. Dynamic recrystallization processes in plagioclase porphyroclasts. J. Struct. Geol. 23, 1781–1802.

Kunz, B.E., Johnson, T.E., White, R.W., Redler, C., 2014. Partial melting of metabasic rocks in Val Strona di Omegna, Ivrea Zone, northern Italy. Lithos 190–191, 1–12. https://doi.org/10.1016/j.lithos.2013.11.015

Lanari, P., Engi, M., 2017. Local bulk composition effects on metamorphic mineral assemblages. Rev. Mineral. Geochem. 83, 55–102.

Lanari, P., Vidal, O., De Andrade, V., Dubacq, B., Lewin, E., Grosch, E.G., Schwartz, S., 2014. XMapTools: A MATLAB©-based program for electron microprobe X-ray image processing and geothermobarometry. Comput. Geosci. 62, 227–240. https://doi.org/10.1016/j.cageo.2013.08.010

Langone, A., Padrón-Navarta José, A., Ji, W.-Q., Zanetti, A., Mazzucchelli, M., Tiepolo, M., Giovanardi, T., Bonazzi, M., 2017. Ductile–brittle deformation effects on crystal-chemistry and U–Pb ages of magmatic and metasomatic zircons from a dyke of the Finero Mafic Complex (Ivrea–Verbano Zone, Italian Alps). Lithos 284–285, 493–511. https://doi.org/10.1016/j.lithos.2017.04.020

Lesne, P., Kohn, S.C., Blundy, J., Witham, F., Botcharnikov, R.E., Behrens, H., 2011. Experimental Simulation of Closed-System Degassing in the System Basalt–H2O–CO2–S–Cl. J. Petrol. 52, 1737–1762. https://doi.org/10.1093/petrology/egr027

Linckens, J., Bruijn, R.H.C., Skemer, P., 2014. Dynamic recrystallization and phase mixing in experimentally deformed peridotite. Earth Planet. Sci. Lett. 388, 134–142. https://doi.org/10.1016/j.epsl.2013.11.037

Lindsley, D.H., Frost, B.R., 1992. Equilibria among Fe-Ti oxides, pyroxenes, olivine, and quartz; Part I, Theory. Am. Mineral. 77, 987–1003.

Liu, Y.-S., Gao, S., Jin, S.-Y., Hu, S.-H., Sun, M., Zhao, Z.-B., Feng, J.-L., 2001. Geochemistry of lower crustal xenoliths from Neogene Hannuoba basalt, North China craton: implications for petrogenesis and lower crustal composition. Geochim. Cosmochim. Acta 65, 2589–2604. https://doi.org/10.1016/S0016-7037(01)00609-3

Lloyd, G.E., Farmer, A.B., Mainprice, D., 1997. Misorientation analysis and the formation and orientation of subgrain and grain boundaries. Tectonophysics, The Adolphe Nicolas Volume 279, 55–78. https://doi.org/10.1016/S0040-1951(97)00115-7

Lu, M., Hofmann, A.W., Mazzucchelli, M., Rivalenti, G., 1997a. The mafic-ultramafic complex near Finero (Ivrea-Verbano Zone), I. Chemistry of MORB-like magmas. Chem. Geol. 140, 207–222. https://doi.org/10.1016/S0009-2541(97)00049-1

Lu, M., Hofmann, A.W., Mazzucchelli, M., Rivalenti, G., 1997b. The mafic-ultramafic complex near Finero (Ivrea-Verbano Zone), II. Geochronology and isotope geochemistry. Chem. Geol. 140, 223–235. https://doi.org/10.1016/S0009-2541(97)00050-8

Mackwell, S.J., Zimmerman, M.E., Kohlstedt, D.L., 1998. High-temperature deformation of dry diabase with application to tectonics on Venus. J. Geophys. Res. Solid Earth 103, 975–984. https://doi.org/10.1029/97JB02671

Maggi, A., Jackson, J.A., McKenzie, D., Priestley, K., 2000. Earthquake focal depths, effective elastic thickness, and the strength of the continental lithosphere. Geology 28, 495. https://doi.org/10.1130/0091-7613(2000)28<495:EFDEET>2.0.CO;2

Mancktelow, N.S., 2006. How ductile are ductile shear zones? Geology 34, 345–348. https://doi.org/10.1130/G22260.1

Mancktelow, N.S., Arbaret, L., Pennacchioni, G., 2002. Experimental observations on the effect of interface slip on rotation and stabilisation of rigid particles in simple shear and a comparison with natural mylonites. J. Struct. Geol. 24, 567–585.

Mancktelow, N.S., Pennacchioni, G., 2004. The influence of grain boundary fluids on the microstructure of quartz-feldspar mylonites. J. Struct. Geol. 26, 47–69. https://doi.org/10.1016/S0191-8141(03)00081-6

Matysiak, A.K., Trepmann, C.A., 2015. The deformation record of olivine in mylonitic peridotites from the Finero Complex, Ivrea Zone: Separate deformation cycles during exhumation: DEFORMATION OF OLIVINE IN MYLONITES. Tectonics 34, 2514–2533. https://doi.org/10.1002/2015TC003904

Matysiak, A.K., Trepmann, C.A., 2012. Crystal–plastic deformation and recrystallization of peridotite controlled by the seismic cycle. Tectonophysics 530–531, 111–127. https://doi.org/10.1016/j.tecto.2011.11.029

Mauler, A., Bystricky, M., Kunze, K., Mackwell, S., 2000. Microstructures and lattice preferred orientations in experimentally deformed clinopyroxene aggregates. J. Struct. Geol. 22, 1633–1648.

McKenzie, D., Jackson, J., 2002. Conditions for flow in the continental crust. Tectonics 21, 1055. https://doi.org/10.1029/2002TC001394

Meissner, R., Rabbel, W., Kern, H., 2006. Seismic lamination and anisotropy of the Lower Continental Crust. Tectonophysics, 416, 81-99.

Mehl, L., Hirth, G., 2008. Plagioclase preferred orientation in layered mylonites: Evaluation of flow laws for the lower crust. J. Geophys. Res. 113. https://doi.org/10.1029/2007JB005075

Menegon, L., Fusseis, F., Stünitz, H., Xiao, X., 2015. Creep cavitation bands control porosity and fluid flow in lower crustal shear zones. Geology 43, 227–230. https://doi.org/10.1130/G36307.1

Menegon, L., Nasipuri, P., Stünitz, H., Behrens, H., Ravna, E., 2011. Dry and strong quartz during deformation of the lower crust in the presence of melt. J. Geophys. Res. 116. https://doi.org/10.1029/2011JB008371

Menegon, L., Pennacchioni, G., Malaspina, N., Harris, K., Wood, E., 2017. Earthquakes as Precursors of Ductile Shear Zones in the Dry and Strong Lower Crust. Geochem. Geophys. Geosystems 1–19. https://doi.org/10.1002/2017GC007189

Menegon, L., Pennacchioni, G., Spiess, R., 2008. Dissolution-precipitation creep of K-feldspar in mid-crustal granite mylonites. J. Struct. Geol. 30, 565–579. https://doi.org/10.1016/j.jsg.2008.02.001

Menegon, L., Pennacchioni, G., Stünitz, H., 2006. Nucleation and growth of myrmekite during ductile shear deformation in metagranites. J. Metamorph. Geol. 24, 553–568. https://doi.org/10.1111/j.1525-1314.2006.00654.x

Menegon, L., Stünitz, H., Nasipuri, P., Heilbronner, R., Svahnberg, H., 2013. Transition from fracturing to viscous flow in granulite facies perthitic feldspar (Lofoten, Norway). J. Struct. Geol. 48, 95–112. https://doi.org/10.1016/j.jsg.2012.12.004

Miranda, E.A., Hirth, G., John, B.E., 2016. Microstructural evidence for the transition from dislocation creep to dislocation-accommodated grain boundary sliding in naturally deformed plagioclase. J. Struct. Geol. 92, 30–45. https://doi.org/10.1016/j.jsg.2016.09.002

Miranda, E.A., Klepeis, K.A., 2016. The interplay and effects of deformation and crystallized melt on the rheology of the lower continental crust, Fiordland, New Zealand. J. Struct. Geol. 93, 91–105. https://doi.org/10.1016/j.jsg.2016.09.007

Misra, S., Burlini, L., Burg, J.-P., 2009. Strain localization and melt segregation in deforming metapelites. Phys. Earth Planet. Inter. 177, 173–179. https://doi.org/10.1016/j.pepi.2009.08.011

Miyazaki, T., Sueyoshi, K., Hiraga, T., 2013. Olivine crystals align during diffusion creep of Earth/'s upper mantle. Nature 502, 321–326. https://doi.org/10.1038/nature12570

Mohn, G., Manatschal, G., Beltrando, M., Haupert, I., 2014. The role of rift-inherited hyper-extension in Alpine-type orogens. Terra Nova 26, 347–353. https://doi.org/10.1111/ter.12104

Morales, L.F.G., Boudier, F., Nicolas, A., 2011. Microstructures and crystallographic preferred orientation of anorthosites from Oman ophiolite and the dynamics of melt lenses. Tectonics 30, TC2011. https://doi.org/10.1029/2010TC002697

Mulch, A., Roseau, M., Dorr, W., Handy, M.R., 2002. The age and structure of dikes along the tectonic contact of the Ivrea-Verbano and Strona-Ceneri Zones (southern Alps, Northern Italy, Switzerland). Schweiz. Mineral. Petrogr. Mitteilungen 82, 55–76.

Negrini, M., Stünitz, H., Nasipuri, P., Morales, L.F.G., 2014. Semibrittle deformation and partial melting of perthitic K-feldspar: An experimental study: Deformation and melting of K-feldspar. J. Geophys. Res. 119. https://doi.org/10.1002/2013JB010573

Newman, J., Lamb, W.M., Drury, M.R., Vissers, R.L.M., 1999. Deformation processes in a peridotite shear zone: reaction-softening by an H2O-deficient, continuous net transfer reaction. Tectonophysics 303, 193–222. https://doi.org/10.1016/S0040-1951(98)00259-5

Nicolas, A., 1976. Crystalline Plasticity and Solid State Flow in Metamorphic Rocks. Wiley-Blackwell, London ; New York.

Nishikawa, S., Kikuchi, S., 1928. Diffraction of Cathode Rays by Mica. Nature 121, 1019. https://doi.org/10.1038/1211019a0

Okudaira, T., Jeřábek, P., Stünitz, H., Fusseis, F., 2015. High-temperature fracturing and subsequent grain-size-sensitive creep in lower crustal gabbros: Evidence for coseismic loading followed by creep during decaying stress in the lower crust? J. Geophys. Res. Solid Earth 120, 2014JB011708. https://doi.org/10.1002/2014JB011708

Palin, R. M., White R. W., Green E. C. R., Diener J. F. A., Powell R., Holland T. J. B, 2016. High-grade metamorphism and partial melting of basic and intermediate rocks. J. Metam. Geol., 34, 871-892. https://doi.org/10.1111/jmg.12212

Passchier, C.W., Trouw, R.A.J., 2005. Microtectonics, 2nd ed. 2005 edition. ed. Springer, Berlin ; New York.

Paterson, M.S., 2001. A granular flow theory for the deformation of partially molten rock. Tectonophysics 335, 51–61. https://doi.org/10.1016/S0040-1951(01)00045-2

Pearce, M.A., Wheeler, J., 2011. Grain growth and the lifetime of diffusion creep deformation. Geol. Soc. Lond. Spec. Publ. 360, 257–272. https://doi.org/10.1144/SP360.15

Pearce, M.A., Wheeler, J., 2010. Modelling grain-recycling zoning during metamorphism. J. Metamorph. Geol. 28, 423–437. https://doi.org/10.1111/j.1525-1314.2010.00872.x

Pearce, M.A., Wheeler, J., Prior, D.J., 2011. Relative strength of mafic and felsic rocks during amphibolite facies metamorphism and deformation. J. Struct. Geol. 33, 662–675. https://doi.org/10.1016/j.jsg.2011.01.002

Pennacchioni, G., Mancktelow, N.S., 2007. Nucleation and initial growth of a shear zone network within compositionally and structurally heterogeneous granitoids under amphibolite facies conditions. J. Struct. Geol. 29, 1757–1780. https://doi.org/10.1016/j.jsg.2007.06.002

Peressini, G., Quick, J.E., Sinigoi, S., Hofmann, A.W., Fanning, M., 2007. Duration of a Large Mafic Intrusion and Heat Transfer in the Lower Crust: a SHRIMP U-Pb Zircon Study in the Ivrea-Verbano Zone (Western Alps, Italy). J. Petrol. 48, 1185–1218. https://doi.org/10.1093/petrology/egm014

Peslier, A.H., 2010. A review of water contents of nominally anhydrous natural minerals in the mantles of Earth, Mars and the Moon. J. Volcanol. Geotherm. Res. 197, 239–258. https://doi.org/10.1016/j.jvolgeores.2009.10.006

Platt, J.P., 2015. Rheology of two-phase systems: A microphysical and observational approach. J. Struct. Geol. https://doi.org/10.1016/j.jsg.2015.05.003

Platt, J.P., Behr, W.M., 2011. Grainsize evolution in ductile shear zones: Implications for strain localization and the strength of the lithosphere. J. Struct. Geol. 33, 537–550. https://doi.org/10.1016/j.jsg.2011.01.018

Poirier, J.-P., 1985. Creep of Crystals: High-Temperature Deformation Processes in Metals, Ceramics and Minerals. Cambridge University Press.

Poirier, J.P., 1980. Shear localization and shear instability in materials in the ductile field. J. Struct. Geol., Shear zones in rocks 2, 135–142. https://doi.org/10.1016/0191-8141(80)90043-7

Poirier, J.P., Guillopé, M., 1979. Deformation induced recrystallization of minerals. Bull. Minéralogie 102, 67–74.

Prakash, D., Arima, M., Mohan, A., 2007. Ultrahigh-temperature mafic granulites from Panrimalai, south India: Constraints from phase equilibria and thermobarometry. J. Asian Earth Sci. 29, 41–61. https://doi.org/10.1016/j.jseaes.2006.01.002

Prior, D.J., Boyle, A.P., Brenker, F., Cheadle, M.C., Day, A., Lopez, G., Peruzzo, L., Potts, G.J., Reddy, S., Spiess, R., others, 1999. The application of electron backscatter diffraction and orientation contrast imaging in the SEM to textural problems in rocks. Am. Mineral. 84, 1741–1759.

Prior, D.J., Mariani, E., Wheeler, J., 2009. EBSD in the Earth Sciences: Applications, Common Practice, and Challenges. In: Schwartz A., Kumar M., Adams B., Field D. (eds), in: Electron Backscatter Diffraction in Materials Science. Springer, Boston, MA.

Prior, D.J., Wheeler, J., Peruzzo, L., Spiess, R., Storey, C., 2002. Some garnet microstructures: an illustration of the potential of orientation maps and misorientation analysis in microstructural studies. J. Struct. Geol., Micro structural Processes: A Special Issue in Honor of the Career Contributions of R.H. Vernon 24, 999–1011. https://doi.org/10.1016/S0191-8141(01)00087-6

Quick, J.E., Sinigoi, S., Mayer, A., 1995. Emplacement of mantle peridotite in the lower continental crust, Ivrea-Verbano zone, northwest Italy. Geology 23, 739–742.

Quick, J.E., Sinigoi, S., Mayer, A., 1994. Emplacement dynamics of a large mafic intrusion in the lower crust, Ivrea-Verbano Zone, northern Italy. J. Geophys. Res. Solid Earth 99, 21559–21573. https://doi.org/10.1029/94JB00113

Quick, J.E., Sinigoi, S., Peressini, G., Demarchi, G., Wooden, J.L., Sbisà, A., 2009. Magmatic plumbing of a large Permian caldera exposed to a depth of 25 km. Geology 37, 603–606. https://doi.org/10.1130/G30003A.1

Quick, J.E., Sinigoi, S., Snoke, A.W., Kalakay, T.J., Mayer, A., Peressini, G., 2003. Geologic map of the southern Ivrea-Verbano Zone, northwestern Italy. US Geol. Surv.

Raimbourg, H., Kogure, T., Toyoshima, T., 2011. Crystal bending, subgrain boundary development, and recrystallization in orthopyroxene during granulite-facies deformation. Contrib. Mineral. Petrol. 162, 1093–1111. https://doi.org/10.1007/s00410-011-0642-3

Raimbourg, H., Toyoshima, T., Harima, Y., Kimura, G., 2008. Grain-size reduction mechanisms and rheological consequences in high-temperature gabbro mylonites of Hidaka, Japan. Earth Planet. Sci. Lett. 267, 637–653. https://doi.org/10.1016/j.epsl.2007.12.012

Raj, R., Ashby, M.F., 1971. On grain boundary sliding and diffusional creep. Metall. Trans. 2, 1113–1127. https://doi.org/10.1007/BF02664244

Ramsay, J.G., 1980. Shear zone geometry: A review. J. Struct. Geol., Shear zones in rocks 2, 83–99. https://doi.org/10.1016/0191-8141(80)90038-3

Ranalli, G., 1995. Rheology of the Earth. Springer Science & Business Media.

Raterron, P., Detrez, F., Castelnau, O., Bollinger, C., Cordier, P., Merkel, S., 2014. Multiscale modeling of upper mantle plasticity: From single-crystal rheology to multiphase aggregate deformation. Phys. Earth Planet. Inter., High-Pressure Research in Earth Science: Crust, Mantle, and Core 228, 232–243. https://doi.org/10.1016/j.pepi.2013.11.012

Reddy, S.M., Buchan, C., 2005. Constraining kinematic rotation axes in high-strain zones: a potential microstructural method? Geol. Soc. Lond. Spec. Publ. 243, 1–10. https://doi.org/10.1144/GSL.SP.2005.243.01.02

Reed, S.J.B., 2005. Electron Microprobe Analysis and Scanning Electron Microscopy in Geology. Cambridge University Press.

Reginiussen, H., Ravna, E.J., Berglund, K., 1995. Mafic dykes from Øksfjord, Seiland Igneous Province, northern Norway: geochemistry and palaeotectonic significance. Geol. Mag. 132, 667–681.

Rivalenti, G., Garuti, G., Rossi, A., 1975. The origin of the Ivrea-Verbano Basic Formation (Western Italian Alps), Whole rock chemistry. Ital. J. Geosci. 94, 1149–1186.

Rivalenti, G., Garuti, G., Rossi, A., Siena, F., Sinigoi, S., 1981. Existence of different peridotite types and of a layered igneous complex in the Ivrea Zone of the Western Alps. J. Petrol. 22, 127–153.

Roberts, R.J., Corfu, F., Torsvik, T.H., Ashwal, L.D., Ramsay, D.M., 2006. Short-lived mafic magmatism at 560–570 Ma in the northern Norwegian Caledonides: U–Pb zircon ages from the Seiland Igneous Province. Geol. Mag. 143, 887. https://doi.org/10.1017/S0016756806002512

Rosenberg, C.L., 2001. Deformation of partially molten granite: a review and comparison of experimental and natural case studies. Int. J. Earth Sci. 90, 60–76. https://doi.org/10.1007/s005310000164

Rosenberg, C.L., Berger, A., 2001. Syntectonic melt pathways in granitic gneisses, and melt-induced transitions in deformation mechanisms. Phys. Chem. Earth Part Solid Earth Geod. 26, 287–293. https://doi.org/10.1016/S1464-1895(01)00058-8

Rosenberg, C.L., Handy, M.R., 2005. Experimental deformation of partially melted granite revisited: implications for the continental crust. J. Metamorph. Geol. 23, 19–28. https://doi.org/10.1111/j.1525-1314.2005.00555.x

Rudnick, R.L., Fountain, D.M., 1995. Nature and composition of the continental crust: A lower crustal perspective. Rev. Geophys. 33, 267–309. https://doi.org/10.1029/95RG01302

Rudnick, R.L., Gao, S., 2003. Composition of the Continental Crust. Treatise Geochem. 3, 1–64. https://doi.org/10.1016/B0-08-043751-6/03016-4

Rutter, E., Brodie, K., James, T., Burlini, L., 2007. Large-scale folding in the upper part of the Ivrea-Verbano zone, NW Italy. J. Struct. Geol. 29, 1–17. https://doi.org/10.1016/j.jsg.2006.08.013

Rutter, E.H., Brodie, K.H., 1988. The role of tectonic grain size reduction in the rheological stratification of the lithosphere. Geol. Rundsch. 77, 295–307. https://doi.org/10.1007/BF01848691

Rutter, E.H., Brodie, K.H., Evans, P.J., 1993. Structural geometry, lower crustal magmatic underplating and lithospheric stretching in the Ivrea-Verbano zone, northern Italy. J. Struct. Geol. 15, 647–662.

Rutter, E.H., Brodie, K.H., Irving, D.H., 2006. Flow of synthetic, wet, partially molten “granite” under undrained conditions: An experimental study. J. Geophys. Res. Solid Earth 111, B06407. https://doi.org/10.1029/2005JB004257

Rutter, E.H., Holdsworth, R.E., Knipe, R.J., 2001. The nature and tectonic significance of fault-zone weakening: an introduction. Geol. Soc. Lond. Spec. Publ. 186, 1–11. https://doi.org/10.1144/GSL.SP.2001.186.01.01

Rutter, E.H., Neumann, D.H.K., 1995. Experimental deformation of partially molten Westerly granite under fluid-absent conditions, with implications for the extraction of granitic magmas. J. Geophys. Res. Solid Earth 100, 15697–15715. https://doi.org/10.1029/94JB03388

Rybacki, E., Dresen, G., 2004. Deformation mechanism maps for feldspar rocks. Tectonophysics 382, 173–187. https://doi.org/10.1016/j.tecto.2004.01.006

Sawaguchi, T., Ishii, K., 2003. Three-dimensional numerical modeling of lattice- and shape-preferred orientation of orthopyroxene porphyroclasts in peridotites. J. Struct. Geol. 25, 1425–1444. https://doi.org/10.1016/S0191-8141(02)00199-2

Sawyer, E.W., 2001. Melt segregation in the continental crust: distribution and movement of melt in anatectic rocks. J. Metamorph. Geol. 19, 291–309. https://doi.org/10.1046/j.0263-4929.2000.00312.x

Schmid, S.M., 1993. Ivrea Zone and adjacent Southern Alpine basement. VON RAUMER JF NEUBAUER F Eds Pre-Mesoz. Geol. Alps 567–583.

Schmid, S.M., Fagenschuh, B., Kissling, E., Schuster, R., 2004. Tectonic map and overall architecture of the Alpine orogen. Eclogae Geol. Helvetiae 97, 93–117. https://doi.org/10.1007/s00015-004-1113-x

Schmid, S.M., Zingg, A., Handy, M., 1987. The kinematics of movements along the Insubric Line and the emplacement of the Ivrea Zone. Tectonophysics, Tectonic and Structural Processes on a Macro-,Meso-, and Micro-scale 135, 47–66. https://doi.org/10.1016/0040-1951(87)90151-X

Schmidt, M.W., 1992. Amphibole composition in tonalite as a function of pressure: an experimental calibration of the Al-in-hornblende barometer. Contrib. Mineral. Petrol. 110, 304–310. https://doi.org/10.1007/BF00310745

Seaman, S.J., Williams, M.L., Jercinovic, M.J., Koteas, G.C., Brown, L.B., 2013. Water in nominally anhydrous minerals: Implications for partial melting and strain localization in the lower crust. Geology 41, 1051–1054. https://doi.org/10.1130/G34435.1

Sen, C., Dunn, T., 1994. Dehydration melting of a basaltic composition amphibolite at 1.5 and 2.0 GPa: implications for the origin of adakites. Contrib. Mineral. Petrol. 117, 394–409. https://doi.org/10.1007/BF00307273

Siena, F., Coltorti, M., 1989. The petrogenesis of a hydrated mafic ultramafic complex and the role of amphibole fractionation at Finero (Italian Western Alps). NEUES Jahrb. Mineral.-MONATSHEFTE 6, 255–274.

Sills, J.D., 1984. Granulite facies metamorphism in the Ivrea Zone, NW Italy. Schweiz. Mineral. Petrogr. Mitteilungen 169–191.

Simpson, C., 1985. Deformation of granitic rocks across the brittle-ductile transition. J. Struct. Geol. 7, 503–511. https://doi.org/10.1016/0191-8141(85)90023-9

Sinigoi, S., Quick, J.E., Clemens-Knott, D., Mayer, A., Demarchi, G., Mazzucchelli, M., Negrini, L., Rivalenti, G., 1994. Chemical evolution of a large mafic intrusion in the lower crust, Ivrea-Verbano Zone, northern Italy. J. Geophys. Res. Solid Earth 99, 21575–21590. https://doi.org/10.1029/94JB00114

Skemer, P., Katayama, I., Jiang, Z., Karato, S., 2005. The misorientation index: Development of a new method for calculating the strength of lattice-preferred orientation. Tectonophysics 411, 157–167. https://doi.org/10.1016/j.tecto.2005.08.023

Skemer, P., Warren, J.M., Hansen, L.N., Hirth, G., Kelemen, P.B., 2013. The influence of water and LPO on the initiation and evolution of mantle shear zones. Earth Planet. Sci. Lett. 375, 222–233. https://doi.org/10.1016/j.epsl.2013.05.034

Skogby, H., 2006. Water in Natural Mantle Minerals I: Pyroxenes. Rev. Mineral. Geochem. 62, 155–167. https://doi.org/10.2138/rmg.2006.62.7

Skogby, H., Bell, D.R., Rossman, G.R., 1990. Hydroxide in pyroxene: Variations in the natural environment. Am. Mineral. 75, 764–774.

Snoke, A.W., Kalakay, T.J., Quick, J.E., Sinigoi, S., 1999. Development of a deep-crustal shear zone in response to syntectonic intrusion of mafic magma into the lower crust, Ivrea–Verbano zone, Italy. Earth Planet. Sci. Lett. 166, 31–45. https://doi.org/10.1016/S0012-821X(98)00280-5

Steck, A., Tieche, J.C., 1976. Carte geologique de l'antiforme peridotitique de Finero avec des observations sur les phases de deformation et de recristallisation. Bull. Suisse Mineral. Petrogr. 56, 501–512.

Stokes, M.R., Wintsch, R.P., Southworth, C.S., 2012. Deformation of amphibolites via dissolution-precipitation creep in the middle and lower crust: DISSOLUTION-PRECIPITATION CREEP IN AMPHIBOLE. J. Metamorph. Geol. 30, 723–737. https://doi.org/10.1111/j.1525-1314.2012.00989.x

Stuart, C.A., Daczko, N.R., Piazolo, S., 2017. Local partial melting of the lower crust triggered by hydration through melt–rock interaction: an example from Fiordland, New Zealand. J. Metamorph. Geol. 35, 213–230. https://doi.org/10.1111/jmg.12229

Stünitz, H., 1998. Syndeformational recrystallization - dynamic or compositionally induced? Contrib. Mineral. Petrol. 131, 219–236. https://doi.org/10.1007/s004100050390

Stünitz, H., Fitz Gerald, J.D., Tullis, J., 2003. Dislocation generation, slip systems, and dynamic recrystallization in experimentally deformed plagioclase single crystals. Tectonophysics 372, 215–233. https://doi.org/10.1016/S0040-1951(03)00241-5

Stünitz, H., Thust, A., Heilbronner, R., Behrens, H., Kilian, R., Tarantola, A., Fitz Gerald, J.D., 2017. Water redistribution in experimentally deformed natural milky quartz single crystals—Implications for H2O-weakening processes. J. Geophys. Res. Solid Earth 122, 2016JB013533. https://doi.org/10.1002/2016JB013533

Stünitz, H., Tullis, J., 2001. Weakening and strain localization produced by syn-deformational reaction of plagioclase. Int. J. Earth Sci. 90, 136–148. https://doi.org/10.1007/s005310000148

Sundberg, M., Cooper, R.F., 2008. Crystallographic preferred orientation produced by diffusional creep of harzburgite: Effects of chemical interactions among phases during plastic flow. J. Geophys. Res. Solid Earth 113, B12208. https://doi.org/10.1029/2008JB005618

Tatham D.J, G.E. Lloyd, G.E., Butler, R.W.H., Casey M. 2008. Amphibole and lower crustal seismic properties. Earth and Planetary Science Letters. 267, 118-128.

Tommasi, A., Langone, A., Padrón-Navarta, J.A., Zanetti, A., Vauchez, A., 2017. Hydrous melts weaken the mantle, crystallization of pargasite and phlogopite does not: Insights from a petrostructural study of the Finero peridotites, southern Alps. Earth Planet. Sci. Lett. 477, 59–72. https://doi.org/10.1016/j.epsl.2017.08.015

Touret, J.L.R., 2009. Mantle to lower-crust fluid/melt transfer through granulite metamorphism. Russ. Geol. Geophys., PETROLOGY OF THE LITHOSPHERE AND DIAMOND GENESIS (to the 100th Birthday of Academician Vladimir Stepanovich Sobolev) 50, 1052–1062. https://doi.org/10.1016/j.rgg.2009.11.004

Trepmann, C.A., Stöckhert, B., Dorner, D., Moghadam, R.H., Küster, M., Röller, K., 2007. Simulating coseismic deformation of quartz in the middle crust and fabric evolution during postseismic stress relaxation — An experimental study. Tectonophysics 442, 83–104. https://doi.org/10.1016/j.tecto.2007.05.005

Tullis, J., Snoke, A.W., Todd, V.R., 1982. Significance and petrogenesis of mylonitic rocks. Geology 10, 227. https://doi.org/10.1130/0091-7613(1982)10<227:SAPOMR>2.0.CO;2

Tullis, J., Yund, R.A., 1991. Diffusion creep in feldspar aggregates: experimental evidence. J. Struct. Geol. 13, 987–1000. https://doi.org/10.1016/0191-8141(91)90051-J

Tullis, J., Yund, R.A., 1985. Dynamic recrystallization of feldspar: A mechanism for ductile shear zone formation. Geology 13, 238–241. https://doi.org/10.1130/0091-7613(1985)13<238:DROFAM>2.0.CO;2

Ullemeyer, K., Leiss, B., Stipp, M., 2010. Textures and Microstructures in Peridotites from the Finero Complex (Ivrea Zone, Alps) and their Influence on the Elastic Rock Properties. Solid State Phenom. 160, 183–188. https://doi.org/10.4028/www.scientific.net/SSP.160.183

Ulrich, S., Mainprice, D., 2005. Does cation ordering in omphacite influence development of lattice-preferred orientation? J. Struct. Geol. 27, 419–431. https://doi.org/10.1016/j.jsg.2004.11.003

Urai, J.L., Means, W.D., Lister, G.S., 1986. Dynamic Recrystallization of Minerals, in: Hobbs, B.E., Heard, H.C. (Eds.), Mineral and Rock Deformation: Laboratory Studies: The Paterson Volume. American Geophysical Union, pp. 161–199. https://doi.org/10.1029/GM036p0161

van Daalen, M., Heilbronner, R., Kunze, K., 1999. Orientation analysis of localized shear deformation in quartz fibres at the brittle–ductile transition. Tectonophysics 303, 83–107.

Van der Molen, I., Paterson, M.S., 1979. Experimental deformation of partially-melted granite. Contrib. Mineral. Petrol. 70, 299–318. https://doi.org/10.1007/BF00375359

Vanderhaeghe, O., 2009. Migmatites, granites and orogeny: Flow modes of partially-molten rocks and magmas associated with melt/solid segregation in orogenic belts. Tectonophysics, Hot orogens 477, 119–134. https://doi.org/10.1016/j.tecto.2009.06.021

Vauchez, A., Tommasi, A., Mainprice, D., 2012. Faults (shear zones) in the Earth's mantle. Tectonophysics 558–559, 1–27. https://doi.org/10.1016/j.tecto.2012.06.006

Vernon, R.H., 2004. A Practical Guide to Rock Microstructure. Cambridge University Press.

Vernon, R.H., Clarke, G.L., 2008. Principles of Metamorphic Petrology. Cambridge University Press.

Viegas, G., Menegon, L., Archanjo, C., 2016. Brittle grain-size reduction of feldspar, phase mixing and strain localization in granitoids at mid-crustal conditions (Pernambuco shear zone, NE Brazil). Solid Earth 7, 375–396.

Voshage, H., Hofmann, A.W., Mazzucchelli, M., Rivalenti, G., Sinigoi, S., Raczek, I., Demarchi, G., 1990. Isotopic evidence from the Ivrea Zone for a hybrid lower crust formed by magmatic underplating. Nature 347, 731–736. https://doi.org/10.1038/347731a0

Wang, Y.F., Zhang, J.F., Jin, Z.M., Green, H.W., 2012. Mafic granulite rheology: Implications for a weak continental lower crust. Earth Planet. Sci. Lett. 353–354, 99–107. https://doi.org/10.1016/j.epsl.2012.08.004

Warren, J.M., Hauri, E.H., 2014. Pyroxenes as tracers of mantle water variations. J. Geophys. Res. Solid Earth 119, 1851–1881. https://doi.org/10.1002/2013JB010328

Warren, J.M., Hirth, G., 2006. Grain size sensitive deformation mechanisms in naturally deformed peridotites. Earth Planet. Sci. Lett. 248, 438–450. https://doi.org/10.1016/j.epsl.2006.06.006

Wedepohl, K.H., 1995. The composition of the continental crust. Geochim. Cosmochim. Acta 59, 1217–1232. https://doi.org/10.1016/0016-7037(95)00038-2

Weinberg, R.F., Hasalová, P., 2015. Water-fluxed melting of the continental crust: A review. Lithos 212–215, 158–188. https://doi.org/10.1016/j.lithos.2014.08.021

Wells, P.R.A., 1977. Pyroxene thermometry in simple and complex systems. Contrib. Mineral. Petrol. 62, 129–139. https://doi.org/10.1007/BF00372872

Wheeler, J., Prior, D., Jiang, Z., Spiess, R., Trimby, P., 2001. The petrological significance of misorientations between grains. Contrib. Mineral. Petrol. 141, 109–124. https://doi.org/10.1007/s004100000225

White, J.C., 1996. Transient discontinuities revisited: pseudotachylyte, plastic instability and the influence of low pore fluid pressure on deformation processes in the mid-crust. J. Struct. Geol. 18, 1471–1486. https://doi.org/10.1016/S0191-8141(96)00059-4

White, R.W., Powell, R., Clarke, G.L., 2002. The interpretation of reaction textures in Fe-rich metapelitic granulites of the Musgrave Block, central Australia: constraints from mineral equilibria calculations in the system K2O–FeO–MgO–Al2O3–SiO2–H2O–TiO2–Fe2O3. J. Metamorph. Geol. 20, 41–55. https://doi.org/10.1046/j.0263-4929.2001.00349.x

White, R.W., Powell, R., Holland, T.J.B., Johnson, T.E., Green, E.C.R., 2014. New mineral activity–composition relations for thermodynamic calculations in metapelitic systems. J. Metamorph. Geol. 32, 261–286. https://doi.org/10.1111/jmg.12071

White, S.H., Burrows, S.E., Carreras, J., Shaw, N.D., Humphreys, F.J., 1980. On mylonites in ductile shear zones. J. Struct. Geol., Shear zones in rocks 2, 175–187. https://doi.org/10.1016/0191-8141(80)90048-6

White, S.H., Knipe, R.J., 1978. Transformation- and reaction-enhanced ductility in rocks. J. Geol. Soc. 135, 513–516. https://doi.org/10.1144/gsjgs.135.5.0513

Wintsch, R.P., Yi, K., 2002. Dissolution and replacement creep: a significant deformation mechanism in mid-crustal rocks. J. Struct. Geol., Micro structural Processes: A Special Issue in Honor of the Career Contributions of R.H. Vernon 24, 1179–1193. https://doi.org/10.1016/S0191-8141(01)00100-6

Wolf, M.B., Wyllie, P.J., 1994. Dehydration-melting of amphibolite at 10 kbar: the effects of temperature and time. Contrib. Mineral. Petrol. 115, 369–383. https://doi.org/10.1007/BF00320972

Wolf, M.B., Wyllie, P.J., 1991. Dehydration-melting of solid amphibolite at 10 kbar: Textural development, liquid interconnectivity and applications to the segregation of magmas. Mineral. Petrol. 44, 151–179. https://doi.org/10.1007/BF01166961

Wolff, R., Dunkl, I., Kiesselbach, G., Wemmer, K., Siegesmund, S., 2012. Thermochronological constraints on the multiphase exhumation history of the Ivrea-Verbano Zone of the Southern Alps. Tectonophysics, Orogenic processes and structural heritage in Alpine-type mountain belts 579, 104–117. https://doi.org/10.1016/j.tecto.2012.03.019

Wood, B.J., Banno, S., 1973. Garnet-orthopyroxene and orthopyroxene-clinopyroxene relationships in simple and complex systems. Contrib. Mineral. Petrol. 42, 109–124. https://doi.org/10.1007/BF00371501

Wright, T.J., Elliott, J.R., Wang, H., Ryder, I., 2013. Earthquake cycle deformation and the Moho: Implications for the rheology of continental lithosphere. Tectonophysics 609, 504–523. https://doi.org/10.1016/j.tecto.2013.07.029

Xia, Q.-K., Liu, J., Kovács, I., Hao, Y.-T., Li, P., Yang, X.-Z., Chen, H., Sheng, Y.-M., 2017. Water in the upper mantle and deep crust of eastern China: concentration, distribution and implications. Natl. Sci. Rev. https://doi.org/10.1093/nsr/nwx016

Xia, Q.-K., Yang, X.-Z., Deloule, E., Sheng, Y.-M., Hao, Y.-T., 2006. Water in the lower crustal granulite xenoliths from Nushan, eastern China. J. Geophys. Res. 111. https://doi.org/10.1029/2006JB004296

Yang, X.-Z., Xia, Q.-K., Deloule, E., Dallai, L., Fan, Q.-C., Feng, M., 2008. Water in minerals of the continental lithospheric mantle and overlying lower crust: A comparative study of peridotite and granulite xenoliths from the North China Craton. Chem. Geol. 256, 33–45. https://doi.org/10.1016/j.chemgeo.2008.07.020

Yardley, B.W.D., Valley, J.W., 1997. The petrologic case for a dry lower crust. J. Geophys. Res. Solid Earth 102, 12173–12185. https://doi.org/10.1029/97JB00508

Yoshinobu, A.S., Hirth, G., 2002. Microstructural and experimental constraints on the rheology of partially molten gabbro beneath oceanic spreading centers. J. Struct. Geol., Micro structural Processes: A Special Issue in Honor of the Career Contributions of R.H. Vernon 24, 1101–1107. https://doi.org/10.1016/S0191-8141(01)00094-3

Zanetti, A., Giovanardi, T., Langone, A., Tiepolo, M., Wu, F.-Y., Dallai, L., Mazzucchelli, M., 2016. Origin and age of zircon-bearing chromitite layers from the Finero phlogopite peridotite (Ivrea–Verbano Zone, Western Alps) and geodynamic consequences. Lithos 262, 58–74. https://doi.org/10.1016/j.lithos.2016.06.015

Zanetti, A., Mazzucchelli, M., Sinigoi, S., Giovanardi, T., Peressini, G., Fanning, M., 2014. SHRIMP U-Pb Zircon Triassic Intrusion Age of the Finero Mafic Complex (Ivrea-Verbano Zone, Western Alps) and its Geodynamic Implications. J. Petrol. 55, 1239–1240. https://doi.org/10.1093/petrology/egu018

Zanetti, A., Mazzucchelli, M., Sinigoi, S., Giovanardi, T., Peressini, G., Fanning, M., 2013. SHRIMP U-Pb Zircon Triassic Intrusion Age of the Finero Mafic Complex (Ivrea-Verbano Zone, Western Alps) and its Geodynamic Implications. J. Petrol. 54, 2235–2265. https://doi.org/10.1093/petrology/egt046

Závada, P., Schulmann, K., Konopásek, J., Ulrich, S., Lexa, O., 2007. Extreme ductility of feldspar aggregates—Melt-enhanced grain boundary sliding and creep failure: Rheological implications for felsic lower crust. J. Geophys. Res. Solid Earth 112, B10210. https://doi.org/10.1029/2006JB004820

Zhao, G., Cawood, P.A., Wilde, S.A., Lu, L., 2001. High-pressure granulites (retrograded eclogites) from the Hengshan Complex, North China Craton: petrology and tectonic implications. J. Petrol. 42, 1141–1170.

Zhou, Y., Rybacki, E., Wirth, R., He, C., Dresen, G., 2012. Creep of partially molten fine-grained gabbro under dry conditions. J. Geophys. Res. Solid Earth 117, B05204. https://doi.org/10.1029/2011JB008646

Zhou, Y., Zhang, H., Yao, W., Dang, J., He, C., 2017. An experimental study on creep of partially molten granulite under high temperature and wet conditions. J. Asian Earth Sci., Deformation and rheology of the eastern Asian continent 139, 15–29. https://doi.org/10.1016/j.jseaes.2016.10.011

Zingg, A., 1983. The Ivrea and the Strona-Ceneri zones (Southern Alps, Ticino and N-Italy) - a review. Schweiz. Mineral. Petrogr. Mitteilungen 63, 361–392.

Zingg, A., Handy, M.R., Hunziker, J.C., Schmid, S.M., 1990. Tectonometamorphic history of the Ivrea Zone and its relationship to the crustal evolution of the Southern Alps. Tectonophysics 182, 169–192. https://doi.org/10.1016/0040-1951(90)90349-D

APPENDICES

APPX. 1: GPS COORDINATES (CASE-STUDY 2)

Case-study 2 table listing samples GPS coordinates and orientation (foliation and mineral stretching lineation).

Structural position		Way point	GPS coordinates WGS 84 (UTM 32T)		N points	Banding / Foliation		N points	Mineral Lineation		Samples
			E	N		Dip Dir.	Dip		Trend	Plunge	
Provola shear zone	External gabbro, SZ	6	464483	5105408	10	335	66	8	53	32	F06A, F06B, F06C, F06D, F06E
	External gabbro, SZ	10	464534	5105399	2	296	62	2	44	27	F10A, F10B
	External gabbro, SZ	11	464386	5105394	9	321	80	8	41	36	F11A, F11B, F11C, F11D, F11E, F11F
	External gabbro, SZ	12	464525	5105399	6	332	76	5	59	30	F12A, F12B, F12C, F12D, F12E, F12F
	External gabbro, SZ	20	464840	5105552	2	330	51	2	34	25	F20
	External gabbro, SZ	21			2	296	49	1	2	58	F21
	External gabbro, SZ	22	465016	5105374	1	340	74	1	52	30	F22
	External gabbro, SZ	31	464407	5105412	2	338	64	2	35	38	F31A, F31B
	External gabbro, SZ	32	464408	5105379	6	324	73	5	46	44	F32A, F32B, F32C, F32D, F32E
	External gabbro, SZ	33	464489	5105378	5	332	72	5	50	38	F33
	External gabbro, SZ	34	464687	5105372	1	345	70	1	52	38	-
External Gabbro unit	External gabbro	13	465234	5105047	4	332	73	2	55	40	-
	External gabbro	14	465160	5105011	5	330	84	5	64	38	F14A, F14B, F14C
	External gabbro	15	465098	5105515	5	322	79	2	40	44	-
	External gabbro	16	465165	5105486	2	343	70	2	67	48	-
	External gabbro	17	465246	5105434	1	326	72				F17
	External gabbro	18	465237	5105280	3	144	76	3	95	71	F18A, F18B, F18C
Internal Gabbro unit	Internal gabbro	7	464888	5105793	1	328	58	1	234	3	F07
	Internal gabbro	8	464824	5105720	1	318	84				-
	Internal gabbro	9	464765	5105718							-
	Internal gabbro	19	464891	5105787	2	331	58	2	46	15	F19
	Internal gabbro	24	463767	5106447	9	343	52	3	6	51	-
	Internal gabbro	25	464104	5106265	2	154	15	2	247	13	-
	Internal gabbro	26	464246	5106264	5	323	69	4	288	54	F26A, F26B
	Internal gabbro	27	464322	5106244	5	318	44	2	257	28	F27A, F27B, F27C
	Internal gabbro	28	464690	5105725	2	327	70	2	276	55	F28A, F28B
	Internal gabbro	29	464649	5105744							F29
	Internal gabbro	30	464524	5105723	1	136	28	1	90	20	F30
	Peridotite	23	463948	5105739							F23A, F23B, F23C, F23D

APPX. 2: THIN SECTION SCANS (CASE-STUDY 2)

Sample F22: amphibole-poor metagabbro; protomylonite. Scale bar 5mm.

Sample F33: amphibole-poor metagabbro (upper portion), protomylonite; amphibole-rich metagabbro (lower portion), protomylonites. Scale bar 5mm.

Sample F32A: amphibole-poor metagabbro (upper portion), mylonite. Amphibole-rich metagabbro (lower portion), ultramylonite. Scale bar 5mm.

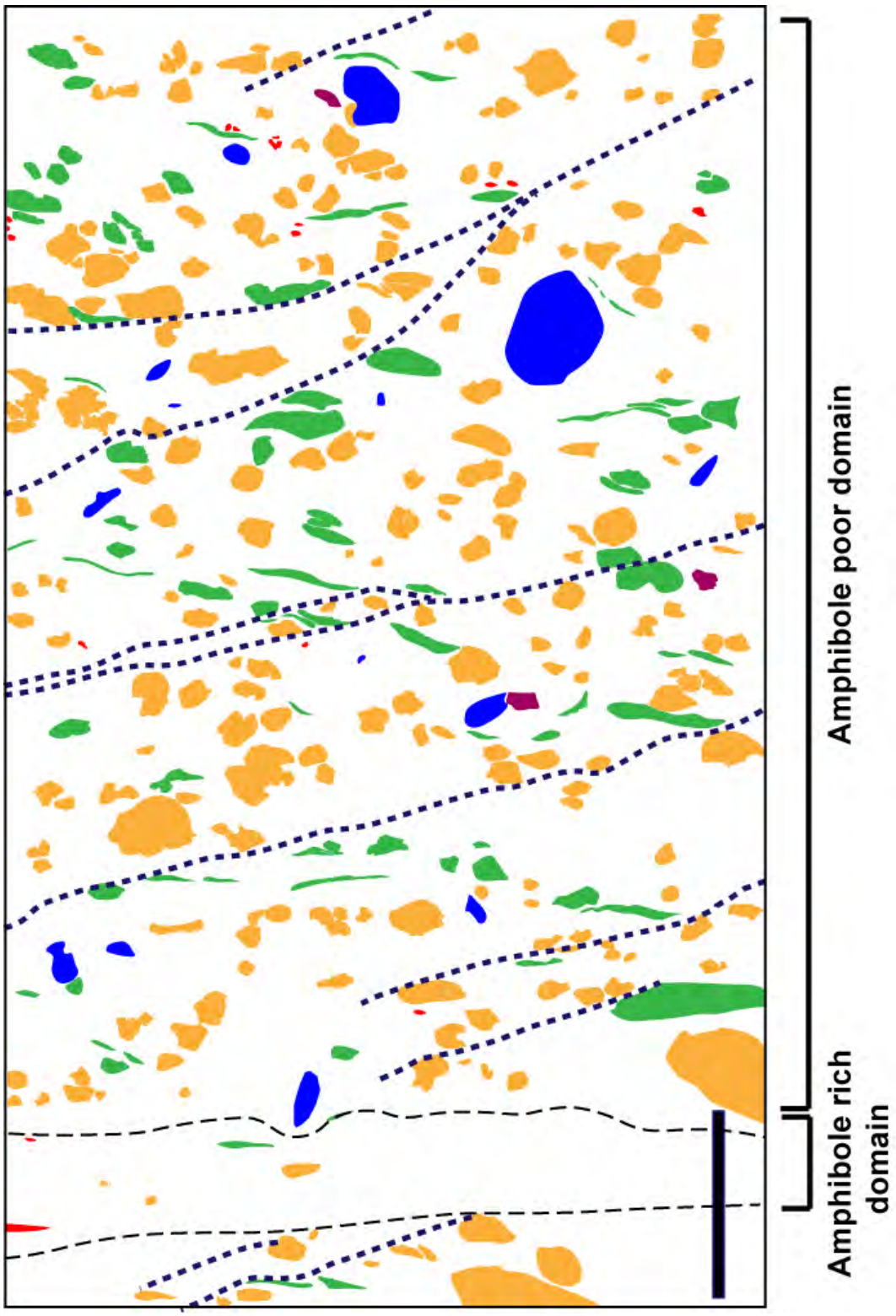

Sample F32A: Traced porphyroclasts. Orange - clinopyroxenes; green – orthopyroxene: blue - garnets; red – amphiboles; purple - plagioclase. Blue lines – shear bands; black lines separate ampihibole-rich to amphibole-poor domains.

Sample F20A: amphibole-rich metagabbro (upper portion), ultramylonite; amphibole-poor metagabbro (central portion), mylonite; amphibole-rich metagabbro (lower portion), ultramylonite. Scale bar 5mm.

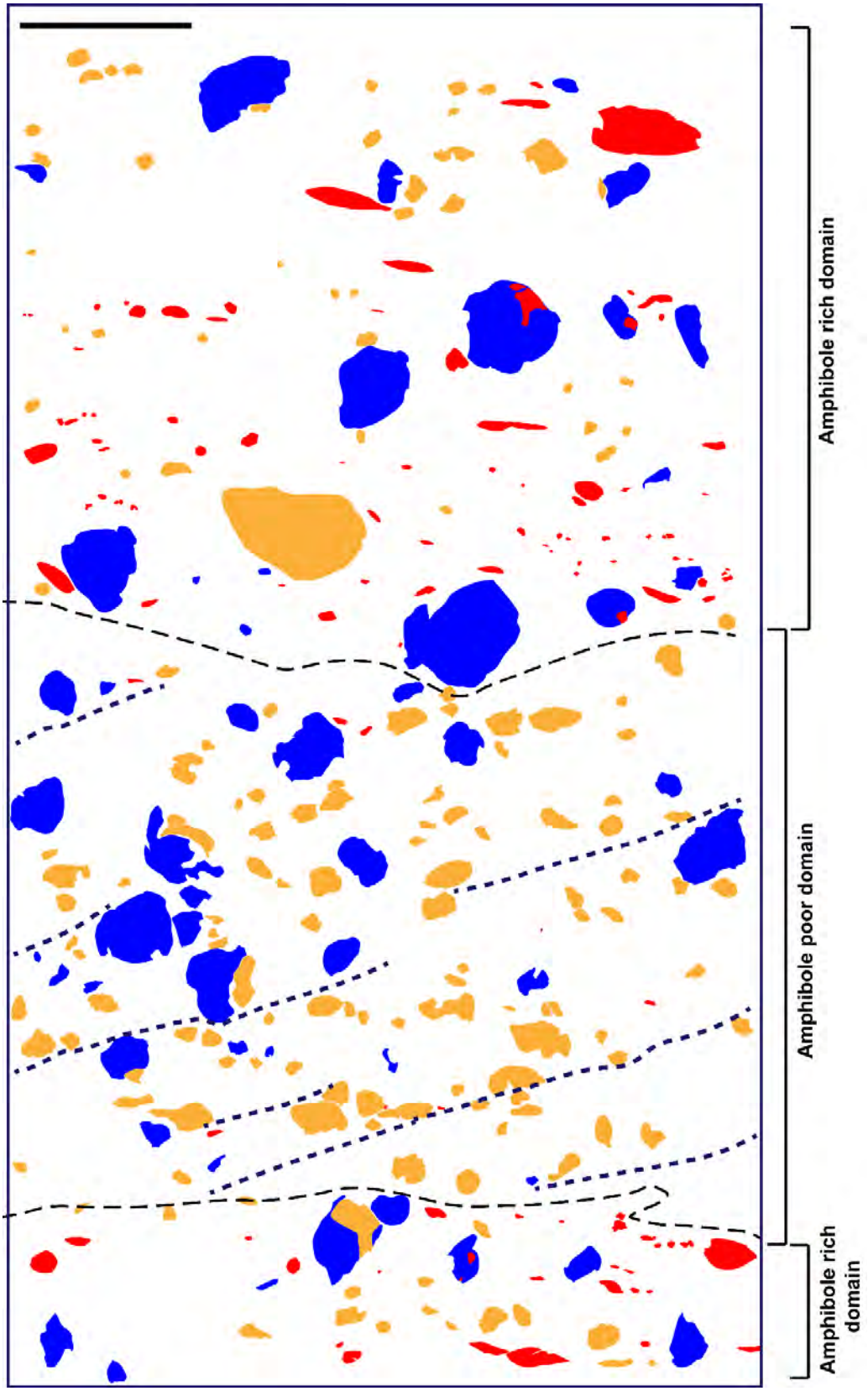

Sample F20A: Traced porphyroclasts. Orange - pyroxenes (clino-ortho); blue - garnets; red - amphiboles. Blue lines - shear bands; black lines separate amphibole-poor from amphibole-rich domains. Scale bar 5mm.

Sample F10B: Amphibole-poor metagabbro; mylonite. Scale bar 5mm.

Sample F32C: Amphibole-poor metagabbro (upper and lower portions), mylonite. Amphibole-rich metagabbro (centre), ultramylonite. The sample has strong greenschist facies alteration overprint. Scale bar 5mm.

Sample F12A: Amphibole-poor metagabbro, mylonite. The sample has greenschist facies alteration, and the foliation is crosscut by greenschist facies fractures. This figure is a scan.

F10A3: amphibole-rich metagabbro, ultramylonite. Scale bar 5mm.

Sample F10A1: amphibole-rich ultramylonite, with amphibole-rich and plagioclase layers. This figure is a scan. Scale bar 5mm.

Sample F32E: leucocratic garnet-plagioclase layer, with amphiboles. Scale bar 5mm.

APPX. 3: MAPS OF TABLE 5.1

Phase abundances (as area%) of amphibole-rich ultramylonites were calculated using the following microprobe and EBSD maps.

F32A - map1

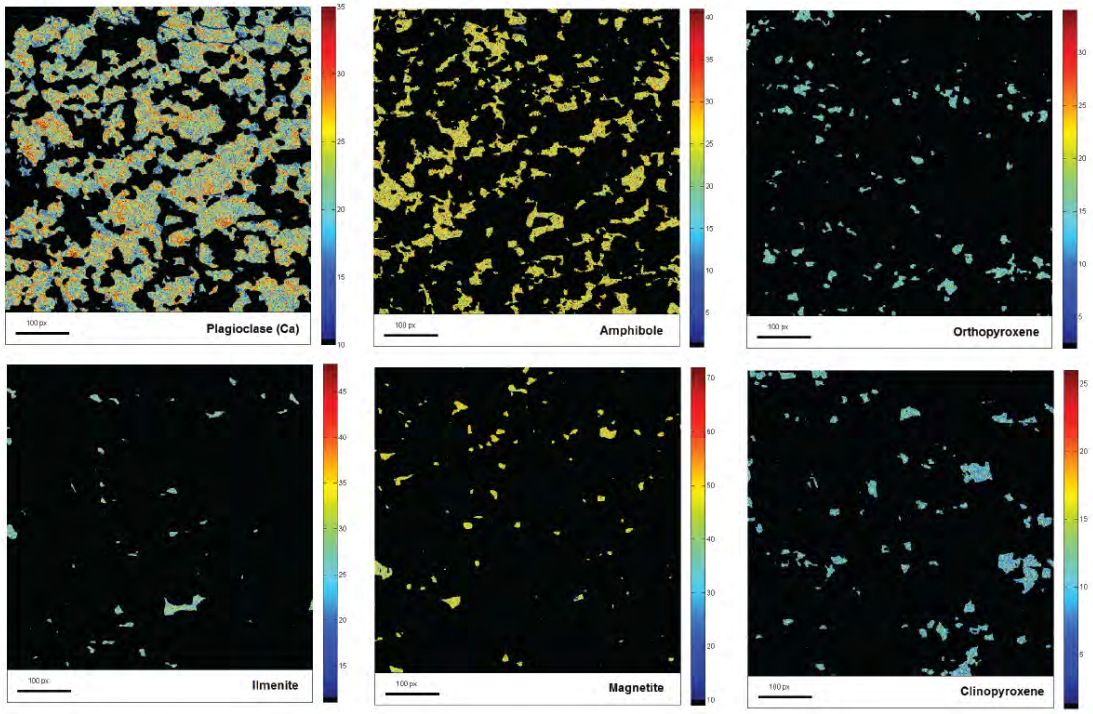

F20A - map1

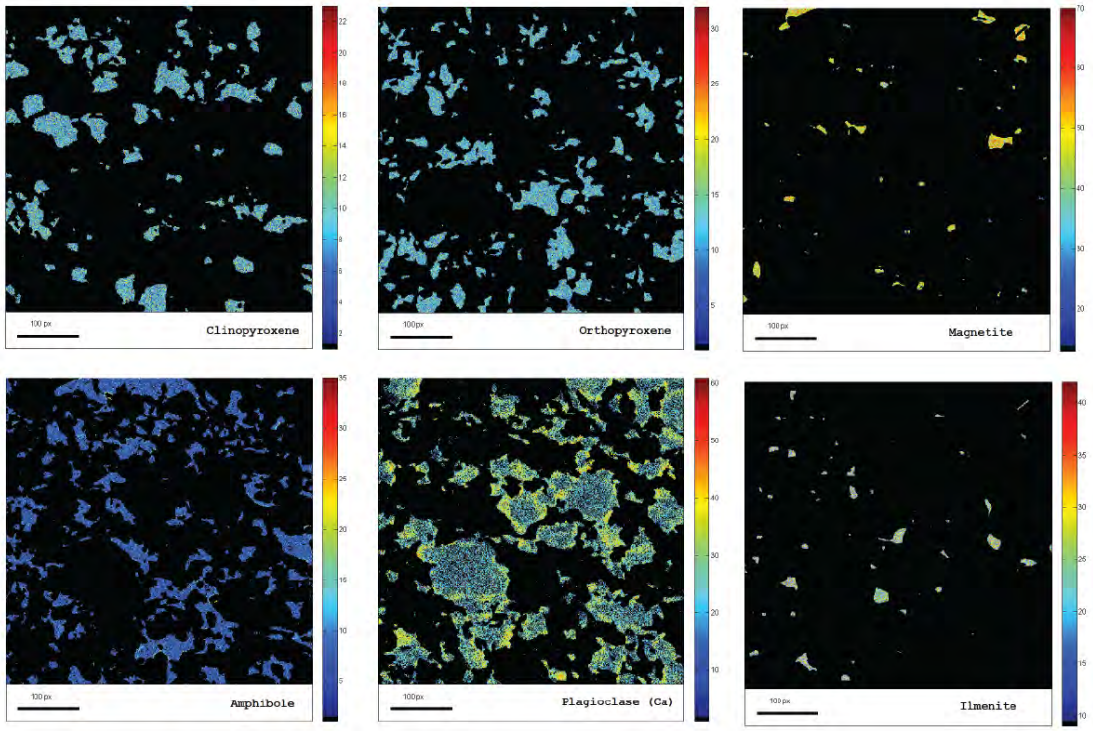

F20A - map3

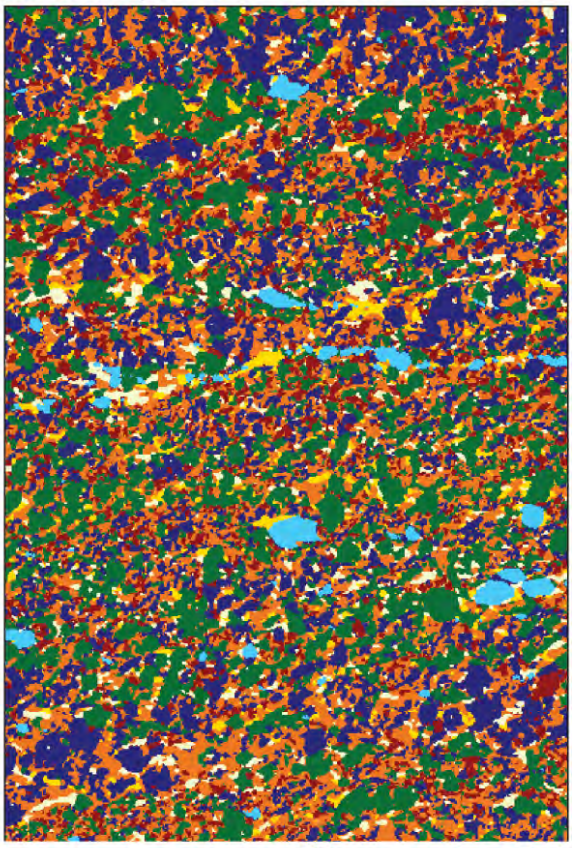

EBSD - F20A - map1

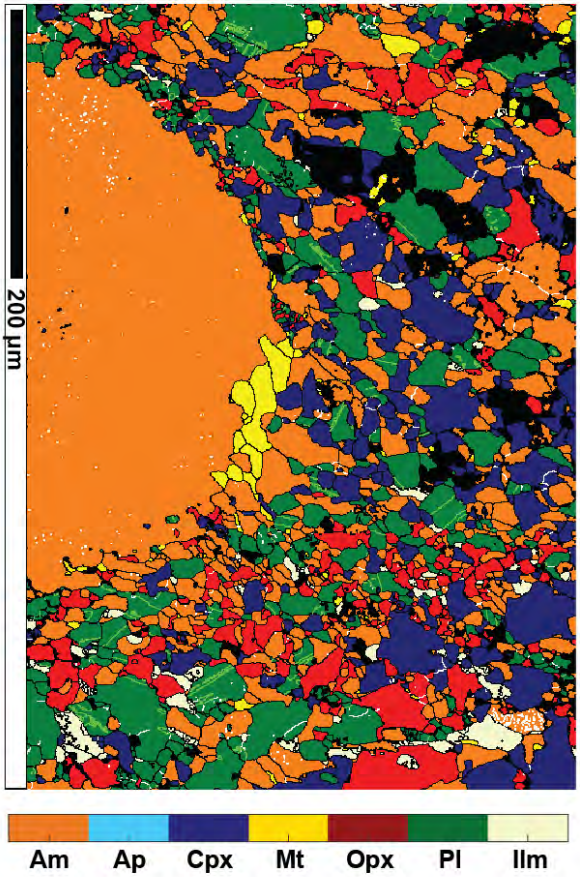

EBSD - F20A - map2

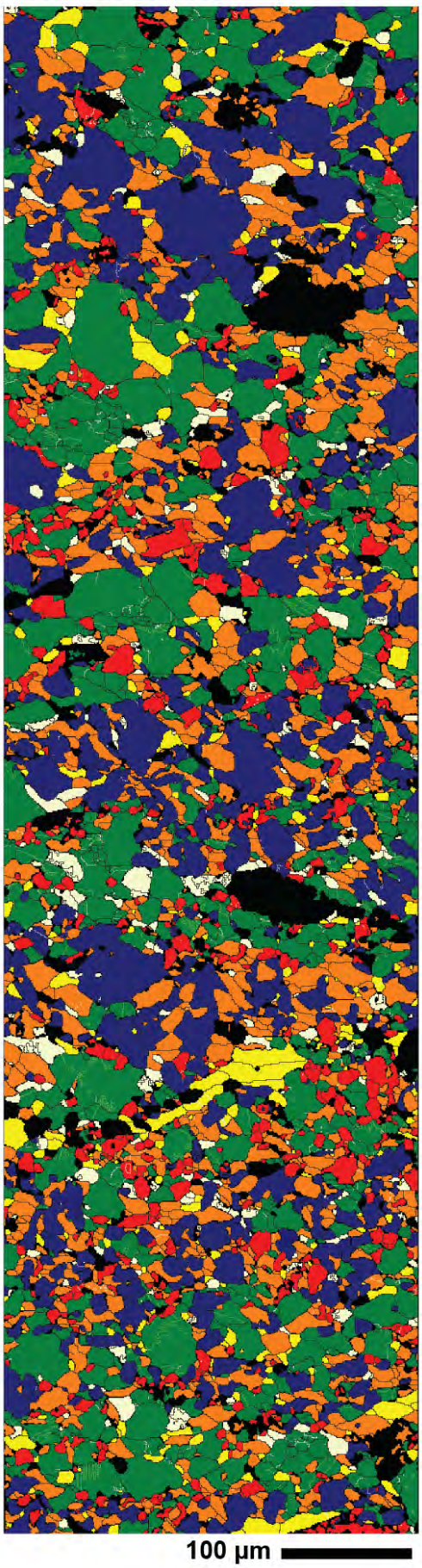

EBSD - F32A - map1

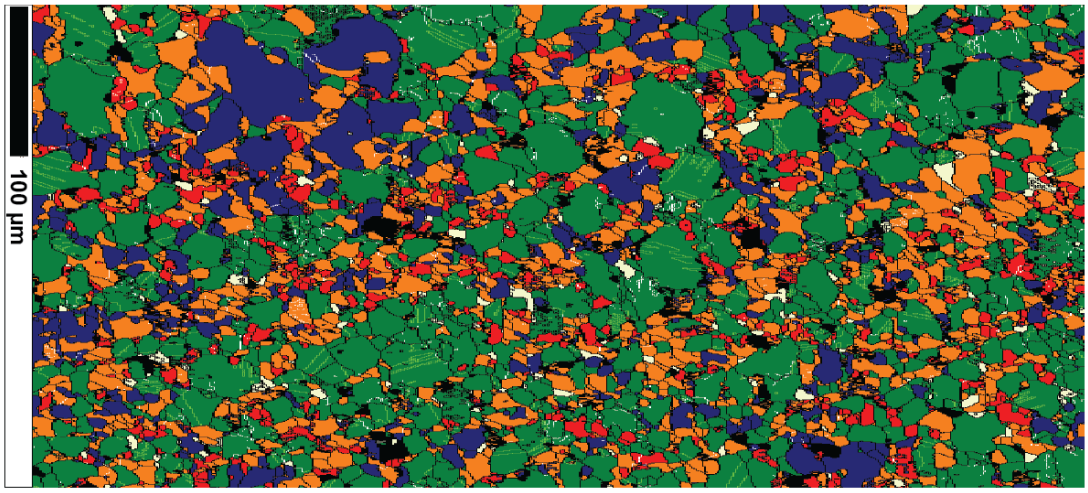

APPX. 4: PHASE ABUNDANCE, GRAIN AND PHASE BOUNDARIES IN F20A.

Images showing phase abundances and distribution in the ultramylonite F20A.

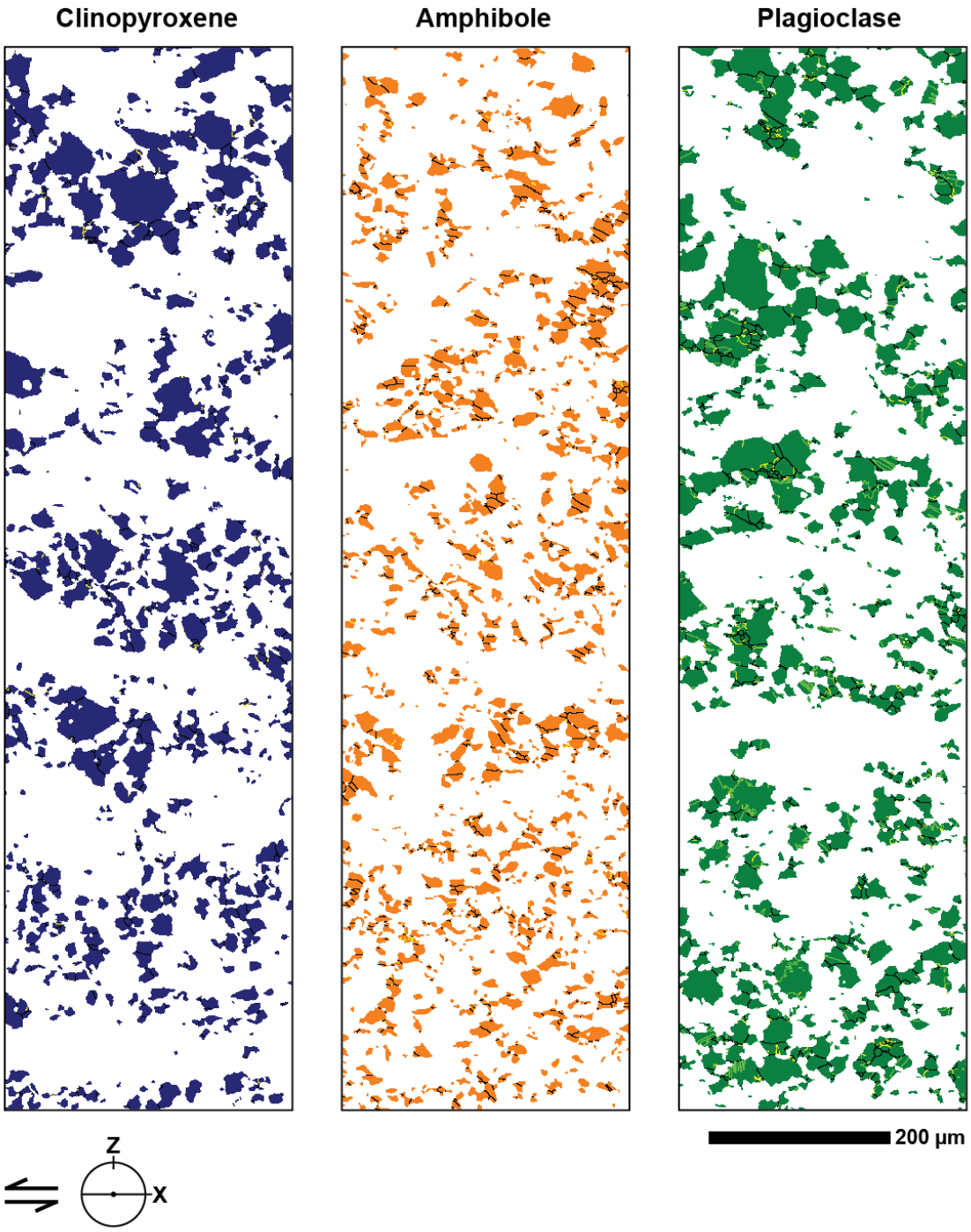

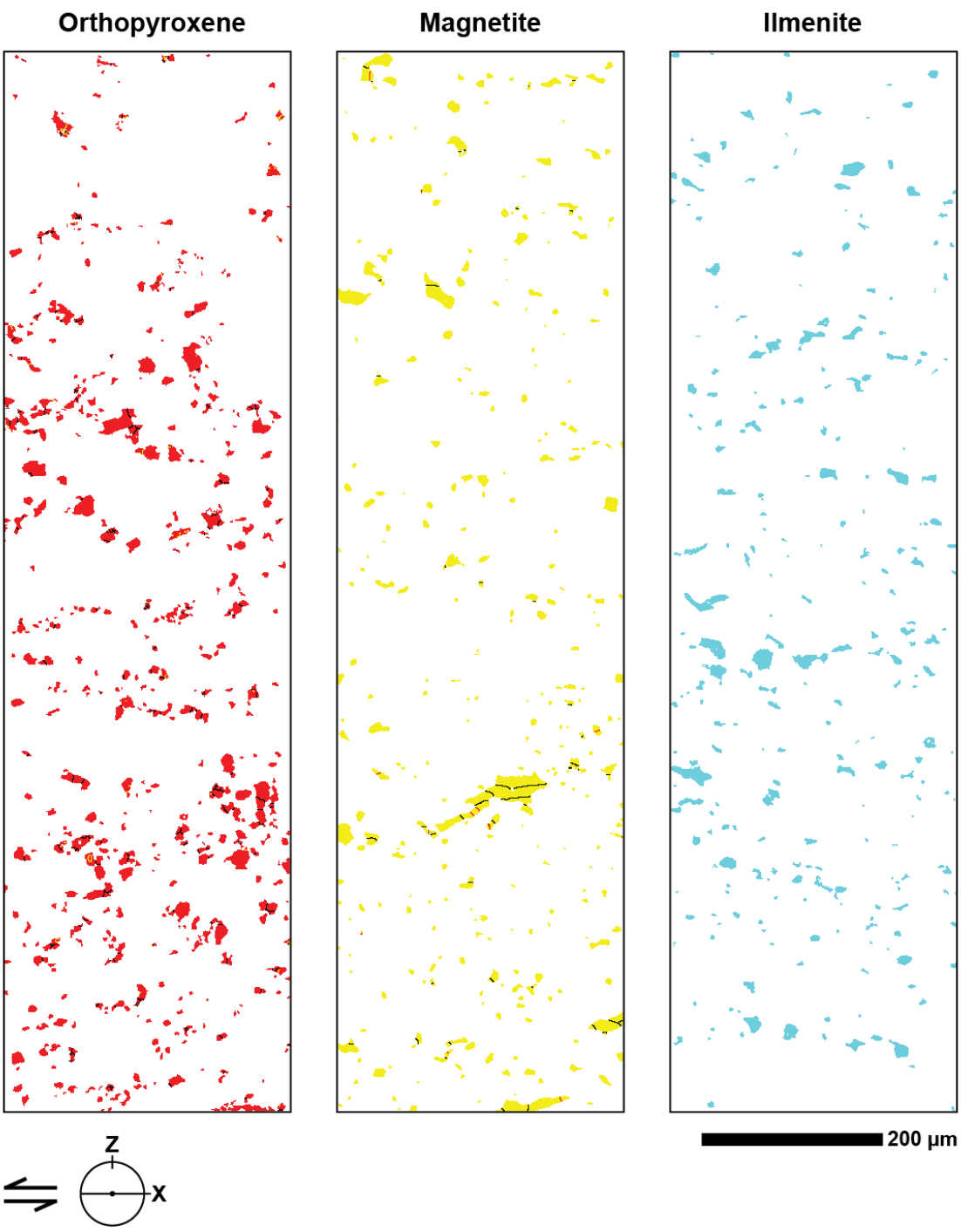
Orthopyroxene
Magnetite
Ilmenite
200 µm
Z
X

Grain vs. phase boundary of each phase in the ultramylonite F20A. Phase boundaries in red, grain boundaries in black. Grain boundaries are defined by EBSD, by a 10° misorientation. For more details, see Figure 5.17 in main body of text.

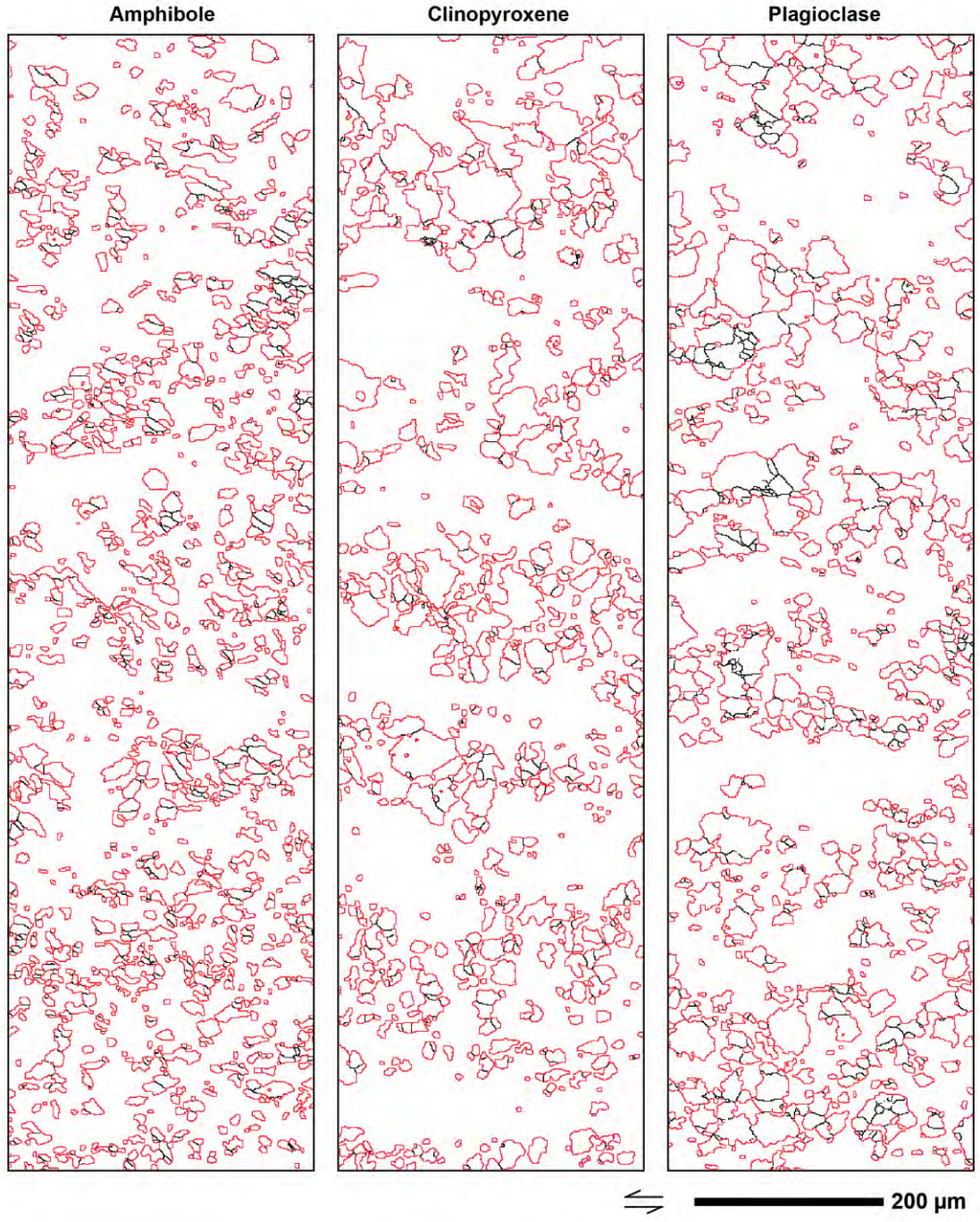

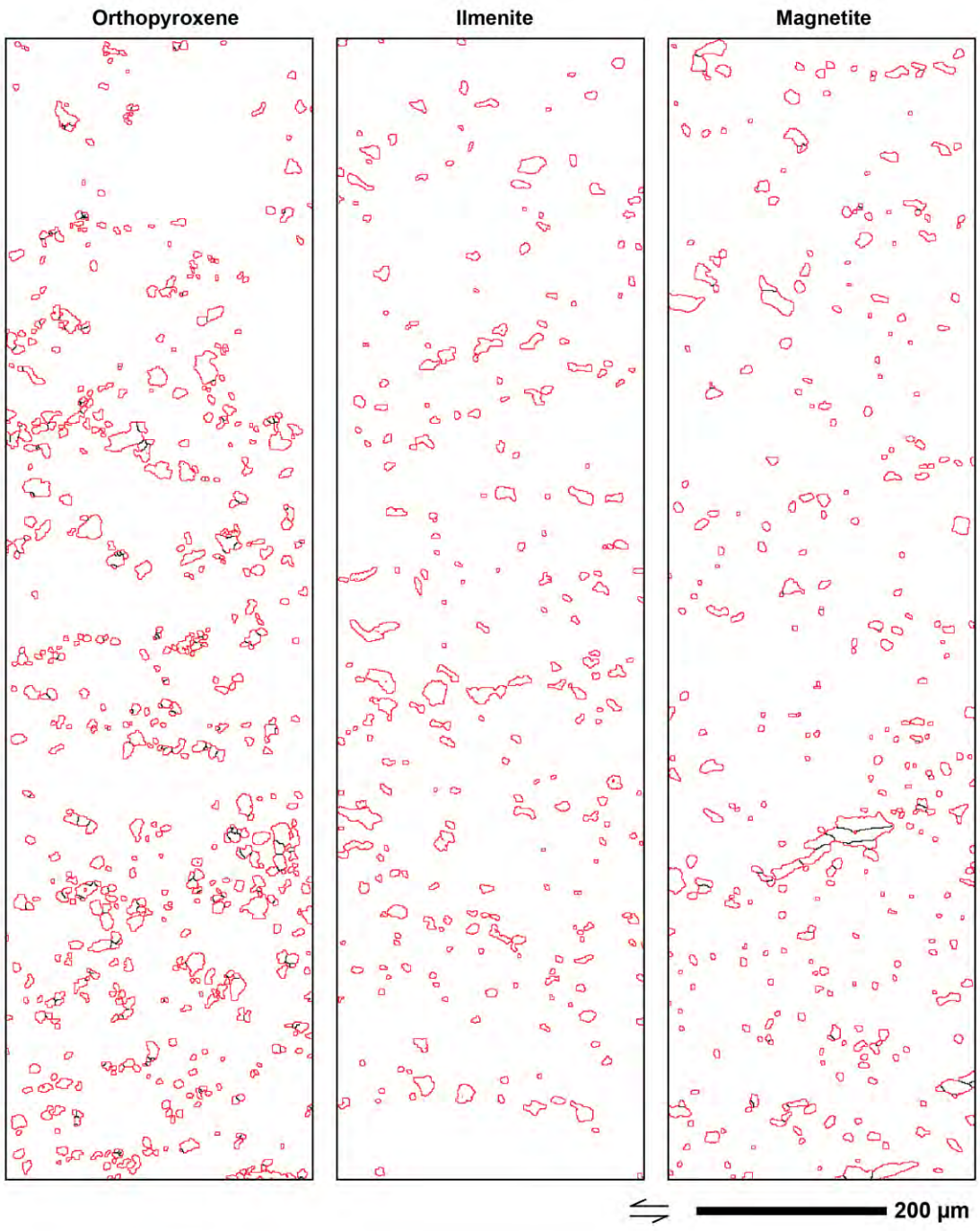
Orthopyroxene
Ilmenite
Magnetite
200 µm

APPX. 5: XRF ANALYSIS

Table of all XRF samples analysed for case-study 2, including samples from the internal gabbro unit.

XRF, Finero samples

Sample	F22	F17	F14B	F14A	F32 A	F10 B	F06D	F29	F07	PROTO A'	PROTO A''	PROTO C	PROTO D
Sample details	metagabbro, protomylonite	metagabbro, a bit altered	metagabbro layer in amphibolite	amphibolite	metagabbro, mylonite	metagabbro, mylonite	amphibole rich ultramylonite	metagabbro in Internal Gabbro Unit	metagabbro in Internal Gabbro Unit	hornblendite: hornblende + garnet	peridotite	amphibole rich metagabbro	pyroxenite: pyroxene + amphibole
Bulk rock oxide wt%													
SiO2	45.86	43.35	44.17	47.06	45.11	44.70	44.39	46.65	44.69	42.61	50.34	43.56	47.27
TiO2	3.34	3.37	2.01	1.54	2.95	2.72	2.09	0.33	0.26	0.12	0.04	0.18	0.63
Al2O3	12.94	12.69	13.09	16.26	13.37	13.27	18.23	19.96	15.94	18.00	7.26	23.07	9.87
Fe2O3	17.02	17.53	16.44	12.20	16.67	16.50	12.91	5.84	9.43	9.41	11.39	6.36	8.30
Mn3O4	0.29	0.28	0.54	0.45	0.30	0.28	0.21	0.10	0.18	0.19	0.17	0.11	0.18
MgO	8.01	7.66	7.83	3.71	7.95	7.10	6.38	9.83	14.66	15.98	24.01	9.97	14.49
CaO	9.95	10.97	11.64	15.21	9.96	12.33	10.13	13.58	12.25	10.60	5.88	13.21	16.75
Na2O	2.03	2.24	2.74	2.59	2.17	1.80	2.75	2.32	1.23	1.92	0.52	1.90	1.25
K2O	0.02	0.09	0.62	0.22	0.08	0.08	0.45	0.12	0.13	0.18	0.08	0.14	0.04
P2O5	0.32	0.32	0.19	0.21	0.32	0.23	0.10	0.00	0.00	0.00	0.00	0.01	0.00
SO3	0.20	0.63	0.01	0.00	0.43	0.03	0.27	0.06	0.15	0.00	0.27	0.03	0.13
V2O5	0.10	0.10	0.08	0.06	0.08	0.09	0.06	0.03	0.03	0.01	0.01	0.02	0.08
Cr2O3	0.02	0.02	0.02	0.02	0.02	0.02	0.03	0.11	0.11	0.03	0.06	0.04	0.22
SrO	0.00	0.01	0.03	0.08	0.01	0.02	0.06	0.03	0.01	0.03	0.00	0.09	0.01
ZrO2	0.02	0.02	0.01	0.02	0.03	0.02	0.01	0.00	0.00	-0.01	0.00	0.00	-0.01
BaO	0.00	0.00	0.01	0.01	0.00	0.00	0.02	0.00	0.00	0.00	0.00	0.00	0.00
NiO	0.01	0.01	0.01	0.01	0.01	0.01	0.01	0.02	0.02	0.02	0.04	0.02	0.02
CuO	0.01	0.01	0.00	0.01	0.02	0.00	0.01	0.00	0.01	0.00	0.01	0.00	0.01
ZnO	0.02	0.02	0.02	0.02	0.03	0.02	0.02	0.01	0.01	0.01	0.01	0.00	0.01
PbO	0.00	0.00	0.01	0.00	0.00	0.01	0.01	0.00	0.00	0.00	0.00	0.00	0.00
HfO2	0.00	0.00	0.00	0.00	0.00	0.00	0.00	0.00	0.00	0.00	0.00	0.00	0.00
Sum	**100.16**	**99.31**	**99.46**	**99.65**	**99.50**	**99.20**	**98.12**	**98.97**	**99.10**	**99.10**	**100.07**	**98.69**	**99.24**
FeO tot	15.32	15.78	14.79	10.97	15.00	14.85	11.61	5.25	8.49	8.46	10.24	5.72	7.47
MnO	0.27	0.26	0.51	0.42	0.28	0.26	0.20	0.10	0.17	0.17	0.16	0.10	0.17
LOI (balance)	-0.16	0.69	0.54	0.36	1.88	0.50	0.80	1.03	0.90	0.90	-0.07	1.31	0.76
LOI (manual)	**-0.06**	**0.67**	**0.24**	**0.04**	**0.30**	**0.09**	**0.97**	**0.72**	**0.96**	**0.97**	**0.90**	**1.21**	**0.46**

Table of XRF samples analysed for case-study 1.

XRF, Norway samples

	O34b.1	O34b.2
	metagabbro, with felsic	metagabbro, without felsic
oxide wt%		
SiO_2	52.12	47.39
TiO_2	2.50	3.14
Al_2O_3	15.04	14.13
Fe_2O_3	13.66	16.18
MnO	0.24	0.26
MgO	5.67	7.25
CaO	8.07	10.07
Na_2O	1.84	1.11
K_2O	0.80	0.13
P_2O_5	0.25	0.40
Sum	100.19	100.06
LOI	0.03	0.03
ppm		
S	121	259
Sc	26	32
V	342	440
Cr	178	197
Co	129	110
Ni	53	72
Cu	71	104
Zn	144	153
Ga	27	29
Rb	19	10
Sr	240	151
Y	54	56
Zr	286	170
Nb	12	9
Ba	557	245
La	23	<10
Ce	16	<10
Nd	29	40
Pb	51	23
Th	4	3
U	<3	<3

APPX. 6: MINERAL CHEMISTRY TABLES FROM MICROPROBE ANALYSIS

Major element (oxide wt%) microprobe analyses of clinopyroxene, orthopyroxene, plagioclase, amphibole and garnet, with corresponding mineral formula unit recalculations. Formula units are calculated based on 4 cations for clino-orthopyroxene, 5 for plagioclase, 13 for amphibole and 8 for garnet. End-member ratios of pyroxenes, plagioclases and garnets are shown below each measurement: Wollastonite (Wo), Enstatite (En), Ferrosilite (Fs), Albite (Ab), Anorthite (An), Orthoclase (Or), Almandine (Alm), Pyrope (Pyr), Grossular (Gr), Spessartine (Sp). The mg# is calculated as Mg/(Mg+ Fe_{tot}), and the Mg# as MgO/(MgO+ FeO_{tot}). Al(T) and Al(M1) are the Al in the tetrahedral and small octahedron structural sites, respectively. Tables are divided according to five subgroups (A-E) that reflect the different microstructural positions of the minerals. Each subgroup is divided according to sample.

***Table (A)**: Porphyroclasts (columns in white), and inclusions in garnet porphyroclasts (columns in grey).*

***Table (B)**: Recrystallized plagioclase grains in monophase ribbons, and neocrystallized pyroxene grains in pyroxene-rich layers of mylonites.*

***Table (C)**: Ultramylonites.*

***Table (D)**: Symplectic reactions from amphibole porphyroclasts (columns in white), and from garnet porphyroclasts (columns in grey).*

***Table (E)**: Dispersed grains in between pyroxene-neoblasts, and grains in shear bands.*

(A) Porphyroclasts and Inclusions

	Clinopyroxene																							
	F33		F10B							F20A						F32A								
wt%	F33-S10-cpx26	F33-cpx-incl	F10B-S2-cpx10	F10B-S6-cpx21	F10B-S3-cpx19	F10Bsite 1-px	F10Bsite 1-pxb	F10Bsite 1-pxc	F10Bsite 2-pxb	F20A-S2-cpx5	F20A-S7-cpx28	F20A-S9-cpx30	F20A-cpx-L4	F20A-cpx-L1	F20A-S4-cpx17	F32A-S4-cpx11	F32A-S7-cpx19	F32A-S8-cpx20	F32A-S10-cpx27	F32A-S13-cpx42	F32A-S15-cpx46	F32A-S18-cpx49	F32A-S19-cpx55
SiO_2	49.4	48.4	50.4	50.9	51.7	50.3	51.0	49.6	49.0	50.8	51.6	51.2	50.4	50.5	51.6	50.5	51.6	51.2	50.7	50.3	50.9	51.2	51.3
TiO_2	0.7	0.5	0.5	0.4	0.4	0.4	0.3	0.3	0.4	0.3	0.4	0.4	0.5	0.4	0.3	0.4	0.3	0.4	0.5	0.7	0.5	0.4	0.5
Al_2O_3	6.1	4.8	4.5	3.7	3.3	4.0	3.5	3.6	3.6	3.9	3.5	4.2	4.5	4.3	3.0	4.7	3.8	4.0	4.7	5.5	5.1	4.4	4.3
FeO	9.5	9.4	10.6	10.1	10.5	10.1	10.2	10.1	10.7	9.9	9.5	10.0	10.4	10.2	9.4	8.4	8.7	8.4	9.1	9.4	9.5	8.3	9.7
MnO	0.2	0.3	0.2	0.3	0.2	0.2	0.2	0.1	0.1	0.2	0.2	0.2	0.2	0.2	0.2	0.3	0.3	0.3	0.3	0.3	0.3	0.3	0.3
MgO	12.3	12.4	11.8	12.2	12.8	12.4	12.6	12.7	12.5	11.9	12.5	11.9	11.2	11.5	13.0	12.7	12.8	13.2	12.7	11.7	12.6	12.6	12.9
CaO	20.3	20.8	21.5	21.6	20.8	21.7	21.6	21.6	20.7	21.8	21.8	21.7	21.8	21.9	22.0	22.3	22.3	22.1	21.7	21.7	21.0	22.5	21.0
Na_2O	1.1	1.0	0.9	0.5	0.8	0.6	0.7	0.6	0.7	0.7	0.7	0.8	0.8	0.8	0.5	0.8	0.7	0.6	0.8	0.9	0.8	0.7	0.8
K_2O	0.0	0.0	0.0	0.0	0.0	0.0	0.0	0.0	0.0	0.0	0.0	0.0	0.0	0.0	0.0	0.0	0.0	0.0	0.0	0.0	0.0	0.0	0.0
Cr_2O_3	0.0	0.0	0.1	0.0	0.0	0.0	0.0	0.0	0.0	0.0	0.0	0.0	0.0	0.0	0.0	0.0	0.0	0.0	0.1	0.0	0.1	0.0	0.0
Tot	***99.7***	***97.7***	***100.5***	***99.7***	***100.5***	***99.7***	***100.1***	***98.7***	***97.8***	***99.6***	***100.2***	***100.5***	***99.8***	***99.9***	***99.9***	***100.1***	***100.7***	***100.2***	***100.6***	***100.4***	***100.7***	***100.3***	***100.7***
Si	1.84	1.84	1.87	1.91	1.92	1.88	1.90	1.87	1.87	1.91	1.92	1.90	1.89	1.89	1.92	1.87	1.90	1.90	1.87	1.87	1.88	1.90	1.89
Ti	0.02	0.01	0.01	0.01	0.01	0.01	0.01	0.01	0.01	0.01	0.01	0.01	0.01	0.01	0.01	0.01	0.01	0.01	0.01	0.02	0.01	0.01	0.01
Al	0.27	0.22	0.20	0.16	0.15	0.18	0.15	0.16	0.16	0.17	0.15	0.19	0.20	0.19	0.13	0.21	0.17	0.17	0.21	0.24	0.22	0.19	0.19
Fe tot	0.30	0.30	0.33	0.32	0.33	0.32	0.32	0.32	0.34	0.31	0.30	0.31	0.33	0.32	0.29	0.26	0.27	0.26	0.28	0.29	0.29	0.26	0.30
Mn	0.01	0.01	0.01	0.01	0.01	0.01	0.01	0.00	0.00	0.01	0.01	0.01	0.01	0.01	0.01	0.01	0.01	0.01	0.01	0.01	0.01	0.01	0.01
Mg	0.68	0.70	0.65	0.68	0.71	0.69	0.70	0.72	0.71	0.67	0.69	0.66	0.63	0.64	0.72	0.70	0.71	0.73	0.70	0.65	0.69	0.69	0.71
Ca	0.81	0.85	0.86	0.87	0.83	0.87	0.86	0.87	0.85	0.87	0.87	0.86	0.88	0.88	0.88	0.88	0.88	0.88	0.86	0.86	0.83	0.89	0.83
Na	0.08	0.07	0.06	0.04	0.06	0.04	0.05	0.05	0.06	0.05	0.05	0.06	0.06	0.05	0.04	0.05	0.05	0.04	0.06	0.07	0.06	0.05	0.06
K	0.00	0.00	0.00	0.00	0.00	0.00	0.00	0.00	0.00	0.00	0.00	0.00	0.00	0.00	0.00	0.00	0.00	0.00	0.00	0.00	0.00	0.00	0.00
Cr	0.00	0.00	0.00	0.00	0.00	0.00	0.00	0.00	0.00	0.00	0.00	0.00	0.00	0.00	0.00	0.00	0.00	0.00	0.00	0.00	0.00	0.00	0.00
SUM	***4.00***	***4.00***	***4.00***	***4.00***	***4.00***	***4.00***	***4.00***	***4.00***	***4.00***	***4.00***	***4.00***	***4.00***	***4.00***	***4.00***	***4.00***	***4.00***	***4.00***	***4.00***	***4.00***	***4.00***	***4.00***	***4.00***	***4.00***
Mg# totFe	69.8	70.1	66.5	68.3	68.6	68.5	68.7	69.3	67.6	68.1	70.0	68.0	65.7	66.8	71.2	72.9	72.4	73.8	71.5	69.0	70.3	73.0	70.3
MgO/(MgO +FeO)*100	56.5	56.8	52.6	54.7	55.0	55.0	55.2	55.8	53.9	54.5	56.7	54.4	51.8	53.0	58.1	60.2	59.5	61.2	58.4	55.5	57.0	60.3	57.0
Fe2+	0.19	0.15	0.25	0.28	0.27	0.24	0.24	0.20	0.20	0.26	0.26	0.27	0.28	0.26	0.25	0.18	0.21	0.20	0.21	0.23	0.24	0.21	0.24
Fe3+	0.10	0.15	0.08	0.03	0.06	0.08	0.08	0.12	0.14	0.05	0.04	0.04	0.05	0.05	0.04	0.08	0.06	0.06	0.07	0.06	0.05	0.05	0.06
Al (T)	0.16	0.16	0.13	0.09	0.08	0.12	0.10	0.13	0.13	0.09	0.08	0.10	0.11	0.11	0.08	0.13	0.10	0.10	0.13	0.13	0.12	0.10	0.11
Al (M1)	0.10	0.05	0.07	0.07	0.06	0.06	0.05	0.03	0.03	0.08	0.07	0.09	0.09	0.08	0.05	0.08	0.07	0.07	0.08	0.11	0.10	0.08	0.08
Wo	45.2	45.8	46.5	46.6	44.3	46.3	45.8	45.8	44.5	47.2	46.8	47.2	47.8	47.8	46.4	47.9	47.5	47.1	46.7	47.8	45.8	48.3	45.2
En	38.3	38.0	35.5	36.5	38.2	36.8	37.3	37.5	37.5	36.0	37.3	36.0	34.3	34.9	38.1	38.0	38.0	39.1	38.1	36.0	38.1	37.7	38.5
Fs	16.5	16.2	17.9	17.0	17.5	16.9	17.0	16.7	18.0	16.8	15.9	16.9	17.9	17.3	15.4	14.1	14.5	13.9	15.2	16.2	16.1	13.9	16.3

Table (A)

(A) Porphyroclasts and Inclusions

	Orthopyroxene									Amphibole - normalized to 13 cations, 23 oxygens. OH 2.00																
	F33		F10B	F20A	F32A					F33										F20A						F32A		
wt%	F33-S1-opx1	F33-S9-opx25	F10B-S4-opx20	F20A-S10-opx31	F32A-S5-opx16	F32A-S6-opx17	F32A-S13-opx35	F32A-S16-opx47	F32A-S19-opx54	F33-S1-am5	F33-S5-am17	F33-S7-am20	F33-symp4-p	F33-symp2-p	F33-porph	F33-symp1-p	F33-porph	F33-S9-am23	F20A-S11-am32	F20A-S12-am33	F20A-S1-am1	F20A-am55	F20A-S1-am2	F20A-S3-am14	F32A-S7-am18	F32A-S9-am25	F32A-S14-am45
SiO_2	52.2	54.6	52.3	52.2	53.2	52.9	53.3	52.9	52.8	42.7	42.3	42.7	40.7	40.2	40.5	41.4	40.5	42.6	43.0	42.5	42.4	42.1	42.2	43.2	44.2	44.0	42.6
TiO_2	0.1	0.1	0.1	0.1	0.1	0.0	0.1	0.0	0.1	2.3	2.5	2.5	3.4	4.2	2.9	3.5	2.8	2.6	2.3	2.4	2.5	2.6	2.1	2.3	2.0	2.4	2.5
Al_2O_3	2.8	0.7	1.6	1.9	2.0	2.2	2.2	2.5	2.9	13.0	13.1	12.6	13.1	13.1	12.8	12.5	12.8	13.1	12.5	12.5	12.2	12.4	13.4	12.1	11.5	11.8	12.7
FeO	21.3	19.3	26.0	25.4	22.3	21.6	21.8	21.3	20.9	13.6	13.0	13.0	12.0	11.4	13.7	11.2	12.8	12.6	14.5	14.7	14.9	14.2	14.6	14.6	12.7	11.4	12.9
MnO	0.7	0.7	0.5	0.6	0.7	0.6	0.7	0.7	0.8	0.2	0.2	0.2	0.1	0.1	0.2	0.2	0.2	0.2	0.2	0.2	0.2	0.1	0.1	0.1	0.2	0.2	0.2
MgO	23.3	25.4	20.6	20.4	23.2	23.2	23.0	23.1	23.2	12.7	12.3	12.9	12.5	12.3	12.0	12.9	12.4	12.8	11.9	11.5	11.5	11.1	11.7	12.0	13.1	13.5	12.6
CaO	0.4	0.4	0.5	0.6	0.4	0.5	0.5	0.4	0.5	11.1	11.1	11.2	11.7	11.6	11.2	11.6	11.3	11.5	11.2	11.2	11.1	11.7	11.4	11.3	11.6	11.4	11.3
Na_2O	0.0	0.0	0.0	0.0	0.0	0.0	0.0	0.0	0.1	2.9	3.1	2.8	2.9	3.0	2.8	2.8	2.9	2.9	3.0	2.8	2.9	2.8	2.9	2.8	2.5	2.5	2.8
K_2O	0.0	0.0	0.0	0.0	0.0	0.0	0.0	0.0	0.0	0.3	0.1	0.2	0.2	0.3	0.4	0.3	0.3	0.2	0.4	0.4	0.4	0.5	0.5	0.4	0.4	0.4	0.5
Cr_2O_3	0.1	0.0	0.0	0.0	0.0	0.0	0.0	0.0	0.0	0.0	0.0	0.1	0.1	0.2	0.0	0.1	0.1	0.0	0.0	0.0	0.0	0.0	0.0	0.0	0.0	0.0	0.1
Tot	***100.8***	***101.3***	***101.6***	***101.3***	***101.8***	***101.0***	***101.6***	***100.9***	***101.2***	***99.0***	***97.8***	***98.2***	***96.6***	***96.3***	***96.5***	***96.5***	***96.1***	***98.3***	***98.8***	***98.1***	***98.1***	***97.6***	***98.8***	***98.7***	***98.2***	***97.7***	***98.2***
Si	1.91	1.98	1.94	1.95	1.94	1.94	1.94	1.94	1.93	6.15	6.17	6.19	6.04	6.01	6.03	6.15	6.04	6.17	6.25	6.24	6.23	6.28	6.14	6.29	6.41	6.39	6.20
Ti	0.00	0.00	0.00	0.00	0.00	0.00	0.00	0.00	0.00	0.25	0.28	0.27	0.38	0.47	0.33	0.39	0.31	0.28	0.25	0.26	0.28	0.30	0.22	0.25	0.22	0.26	0.28
Al	0.12	0.03	0.07	0.08	0.09	0.09	0.09	0.11	0.13	2.20	2.26	2.15	2.30	2.30	2.24	2.19	2.25	2.23	2.14	2.16	2.12	2.18	2.31	2.07	1.97	2.01	2.18
Fe tot	0.65	0.58	0.81	0.79	0.68	0.66	0.66	0.65	0.64	1.64	1.59	1.58	1.49	1.42	1.70	1.39	1.60	1.52	1.76	1.80	1.83	1.77	1.78	1.77	1.54	1.39	1.57
Mn	0.02	0.02	0.02	0.02	0.02	0.02	0.02	0.02	0.02	0.03	0.03	0.03	0.02	0.02	0.03	0.02	0.02	0.02	0.02	0.02	0.02	0.02	0.01	0.02	0.03	0.02	0.03
Mg	1.27	1.37	1.14	1.13	1.26	1.27	1.25	1.27	1.26	2.73	2.68	2.78	2.76	2.74	2.67	2.86	2.76	2.76	2.58	2.52	2.52	2.46	2.53	2.60	2.84	2.92	2.73
Ca	0.02	0.02	0.02	0.02	0.02	0.02	0.02	0.01	0.02	1.72	1.73	1.73	1.86	1.85	1.79	1.85	1.81	1.79	1.74	1.75	1.75	1.87	1.77	1.76	1.80	1.78	1.76
Na	0.00	0.00	0.00	0.00	0.00	0.00	0.00	0.00	0.00	0.82	0.87	0.79	0.84	0.87	0.80	0.80	0.83	0.81	0.84	0.80	0.82	0.82	0.83	0.79	0.69	0.70	0.78
K	0.00	0.00	0.00	0.00	0.00	0.00	0.00	0.00	0.00	0.06	0.03	0.05	0.05	0.05	0.07	0.06	0.05	0.04	0.07	0.08	0.08	0.09	0.09	0.08	0.07	0.07	0.09
Cr	0.00	0.00	0.00	0.00	0.00	0.00	0.00	0.00	0.00	0.00	0.00	0.01	0.01	0.02	0.00	0.01	0.01	0.01	0.00	0.00	0.00	0.00	0.00	0.00	0.00	0.00	0.01
SUM	***4.00***	***4.00***	***4.00***	***4.00***	***4.00***	***4.00***	***4.00***	***4.00***	***4.00***	***13.00***	***13.00***	***13.00***	***13.00***	***12.98***	***13.00***	***13.00***	***13.00***	***13.00***	***13.00***	***13.00***	***13.00***	***13.00***	***13.00***	***13.00***	***13.00***	***13.00***	***13.00***
Mg# totFe	66.1	70.2	58.6	58.8	65.0	65.7	65.4	65.9	66.4	62.44	62.78	63.78	65.00	65.89	61.04	67.33	63.38	64.44	59.45	58.33	57.95	58.19	58.7	59.46	64.84	67.78	63.45
MgO/(MgO +FeO)*100	52.2	56.9	44.3	44.5	51.0	51.8	51.4	52.1	52.6	48.3	48.6	49.7	51.0	52.0	46.8	53.6	49.3	50.4	45.1	44.0	43.6	43.9	44.4	45.1	50.9	54.1	49.3
Fe2+	0.60	0.57	0.77	0.78	0.64	0.63	0.65	0.64	0.62	0.95	1.11	0.96	1.24	1.31	1.12	1.22	1.06	1.09	1.28	1.35	1.36	1.74	1.30	1.31	1.13	1.04	1.09
Fe3+	0.05	0.01	0.04	0.02	0.04	0.03	0.02	0.02	0.02	0.69	0.48	0.62	0.25	0.11	0.59	0.17	0.53	0.43	0.47	0.45	0.47	0.03	0.48	0.46	0.41	0.34	0.49
Al (T)	0.09	0.02	0.06	0.05	0.06	0.06	0.06	0.06	0.07	1.85	1.83	1.81	1.96	1.99	1.97	1.85	1.96	1.83	1.75	1.76	1.77	1.72	1.86	1.71	1.59	1.61	1.80
Al (M1)	0.03	0.01	0.01	0.03	0.02	0.03	0.04	0.04	0.05	0.35	0.43	0.34	0.35	0.32	0.27	0.34	0.30	0.41	0.39	0.40	0.35	0.46	0.45	0.36	0.38	0.40	0.38
Wo	0.8	0.9	1.0	1.2	0.8	0.9	1.1	0.8	1.1																		
En	65.6	69.6	58.0	58.1	64.4	65.1	64.7	65.4	65.7																		
Fs	33.6	29.6	41.0	40.7	34.7	34.0	34.3	33.8	33.2																		

(A) cont.

(A) Porphyroclasts and Inclusions

	Garnet										Plag					
	F10B				F20A				F32A		F33		F10B			
wt%	F10B-S3-grt18	F10B-1/1-1/4	F10B-6/1-6/4	F10B-7/1-7/2	F20A-S5-grt19	F20A-34/1-34/3	F20A-8/1-8/4	F20A-S8-grt29	F32A-S8-grt24		F33-S4-pl13	F33-Site5-Plag	F10Bsite 2-px	F10Bsite 3-pxa	F20A-plag-grt	F20A-grt1-line1
SiO_2	39.7	37.5	37.9	38.0	39.4	39.0	37.9	39.6	39.7		57.0	55.9	56.0	56.3	57.7	57.5
TiO_2	0.0	0.1	0.0	0.1	0.0	0.0	0.1	0.0	0.1		0.0	0.0	0.0	0.0	0.0	0.0
Al_2O_3	22.4	22.0	22.0	22.0	21.9	21.0	20.1	22.0	22.4		27.6	27.8	28.0	27.7	27.1	27.2
FeO	25.6	25.5	25.6	25.6	25.9	25.1	25.1	25.6	23.4		0.0	0.2	0.1	0.1	0.1	0.1
MnO	0.9	0.9	0.9	1.0	1.4	0.9	0.9	0.9	2.2		0.0	0.0	0.0	0.0	0.0	0.0
MgO	7.5	7.5	7.6	7.6	6.8	7.4	7.5	7.3	8.3		0.0	0.0	0.0	0.0	0.0	0.0
CaO	6.3	6.4	6.3	6.4	6.5	6.6	6.6	6.3	6.3		9.5	9.2	9.3	9.0	9.0	9.0
Na_2O	0.0	0.0	0.0	0.0	0.0	0.0	0.0	0.0	0.0		6.3	6.6	6.5	6.6	6.8	6.8
K_2O	0.0	0.0	0.0	0.0	0.0	0.0	0.0	0.0	0.0		0.0	0.1	0.2	0.2	0.1	0.1
Cr_2O_3	0.1	0.0	0.0	0.0	0.1	0.0	0.0	0.1	0.1		0.0	0.0	0.0	0.0	0.0	0.0
Tot	***102.4***	***99.9***	***100.4***	***100.7***	***101.9***	***100.1***	***98.2***	***101.9***	***102.5***		***100.5***	***99.8***	***100.0***	***100.0***	***100.8***	***100.8***
Si	2.99	2.90	2.91	2.91	3.00	3.01	2.98	3.00	2.98		2.54	2.50	2.50	2.52	2.56	2.55
Ti	0.00	0.00	0.00	0.00	0.00	0.00	0.00	0.00	0.00		0.00	0.00	0.00	0.00	0.00	0.00
Al	1.99	2.00	1.99	1.99	1.96	1.91	1.86	1.97	1.98		1.45	1.47	1.48	1.46	1.42	1.42
Fe tot	1.61	1.65	1.64	1.64	1.65	1.62	1.65	1.62	1.47		0.00	0.01	0.00	0.00	0.00	0.00
Mn	0.06	0.06	0.06	0.06	0.09	0.06	0.06	0.06	0.14		0.00	0.00	0.00	0.00	0.00	0.00
Mg	0.84	0.86	0.87	0.87	0.77	0.85	0.88	0.83	0.93		0.00	0.00	0.00	0.00	0.00	0.00
Ca	0.51	0.53	0.52	0.52	0.53	0.54	0.55	0.51	0.51		0.46	0.44	0.44	0.43	0.43	0.43
Na	-	-	-	-	-	-	-	-	-		0.54	0.57	0.56	0.57	0.58	0.58
K	-	-	-	-	-	-	-	-	-		0.00	0.00	0.01	0.01	0.01	0.00
Cr	0.00	0.00	0.00	0.00	0.00	0.00	0.00	0.00	0.00		0.00	0.00	0.00	0.00	0.00	0.00
SUM	***8.00***	***8.00***	***8.00***	***8.00***	***8.00***	***8.00***	***8.00***	***8.00***	***8.00***		***5.00***	***5.00***	***5.00***	***5.00***	***5.00***	***5.00***
Mg# totFe	34.4	34.4	34.6	34.5	31.9	34.4	34.8	33.9	38.8							
MgO/(MgO+FeO)*100	22.7	22.7	22.9	22.8	20.8	22.7	23.1	22.3	26.2							
Alm	53.4	53.1	53.2	53.1	54.3	52.7	52.5	53.6	48.2	**An**	45.5	43.4	43.7	42.7	42.2	42.2
Pyr	28.0	27.9	28.2	28.0	25.4	27.6	28.1	27.4	30.5	**Ab**	54.3	56.3	55.1	56.1	57.3	57.3
Gr	16.8	17.1	16.7	16.9	17.4	17.7	17.6	16.9	16.7	**Or**	0.2	0.4	1.2	1.2	0.5	0.4
Sp	1.8	1.9	2.0	2.0	2.9	2.0	1.9	2.0	4.6							

Table (A) cont.

(B) neoblastic polygonal aggregates

	Clinopyroxene														Orthopyroxene				
	F10B						F20A		F32A						F10B		F32A		
wt%	F10B-S1-cpx1	F10B-S1-cpx9	F10B-S2-cpx11	F10B-S2-cpx12	F10B-S6-cpx22	F10B-S7-cpx23	F20A-S2-cpx6	F20A-S2-cpx7	F32A-S3-cpx10	F32A-S10-cpx26	F32A-S13-cpx41	F32A-S18-cpx51	F32A-S18-cpx53	F32A-S20-cpx63	F10B-S1-opx2	F10B-S2-opx13	F32A-S3-opx9	F32A-S11-opx28	F32A-S13-opx36
SiO_2	51.7	52.7	52.1	52.8	53.2	52.2	53.2	52.7	53.3	53.0	51.0	53.1	52.7	53.1	52.3	52.9	53.5	54.5	54.1
TiO_2	0.2	0.2	0.1	0.1	0.1	0.3	0.2	0.2	0.2	0.3	0.4	0.2	0.3	0.2	0.0	0.0	0.0	0.0	0.1
Al_2O_3	2.6	2.0	2.0	2.5	1.6	2.4	1.7	2.2	1.5	2.3	4.5	2.6	2.7	2.2	1.4	0.7	1.5	0.9	0.8
FeO	9.5	8.5	9.7	10.4	9.0	9.2	9.1	9.4	6.7	8.0	9.3	8.1	7.8	7.7	25.2	25.5	21.4	21.6	21.1
MnO	0.2	0.2	0.2	0.2	0.2	0.2	0.3	0.2	0.3	0.3	0.3	0.3	0.3	0.4	0.6	0.6	0.7	0.8	0.6
MgO	13.4	13.7	13.4	12.8	13.5	13.1	13.5	13.6	15.0	13.9	12.7	13.6	14.0	14.1	20.8	20.8	23.6	24.2	24.0
CaO	21.9	22.5	22.1	21.6	22.4	22.0	22.1	22.2	23.2	22.1	21.6	22.1	22.6	22.5	0.6	0.5	0.5	0.3	0.4
Na_2O	0.4	0.4	0.5	0.5	0.5	0.5	0.4	0.5	0.4	0.6	0.8	0.6	0.5	0.5	0.0	0.0	0.0	0.0	0.0
K_2O	0.0	0.0	0.0	0.0	0.0	0.0	0.0	0.0	0.0	0.0	0.0	0.0	0.0	0.0	0.0	0.0	0.0	0.0	0.0
Cr_2O_3	0.0	0.0	0.0	0.0	0.0	0.0	0.0	0.0	0.0	0.0	0.1	0.1	0.0	0.0	0.0	0.0	0.0	0.0	0.0
Tot	***99.8***	***100.2***	***100.0***	***100.9***	***100.6***	***99.9***	***100.5***	***101.0***	***100.6***	***100.5***	***100.6***	***100.7***	***100.9***	***100.7***	***101.0***	***101.1***	***101.3***	***102.4***	***101.3***
Si	1.93	1.96	1.94	1.96	1.97	1.95	1.97	1.94	1.95	1.96	1.88	1.95	1.94	1.96	1.95	1.97	1.95	1.97	1.97
Ti	0.01	0.01	0.00	0.00	0.00	0.01	0.00	0.00	0.01	0.01	0.01	0.01	0.01	0.01	0.00	0.00	0.00	0.00	0.00
Al	0.11	0.09	0.09	0.11	0.07	0.11	0.07	0.10	0.06	0.10	0.20	0.11	0.12	0.09	0.06	0.03	0.06	0.04	0.04
Fe tot	0.29	0.26	0.30	0.32	0.28	0.29	0.28	0.29	0.20	0.25	0.29	0.25	0.24	0.24	0.79	0.79	0.65	0.65	0.64
Mn	0.01	0.00	0.01	0.01	0.01	0.01	0.01	0.01	0.01	0.01	0.01	0.01	0.01	0.01	0.02	0.02	0.02	0.02	0.02
Mg	0.74	0.76	0.74	0.71	0.74	0.73	0.75	0.75	0.82	0.76	0.70	0.75	0.76	0.77	1.16	1.16	1.28	1.30	1.31
Ca	0.87	0.89	0.88	0.86	0.89	0.88	0.88	0.88	0.91	0.87	0.86	0.87	0.89	0.89	0.02	0.02	0.02	0.01	0.02
Na	0.03	0.03	0.03	0.04	0.04	0.04	0.03	0.04	0.03	0.04	0.06	0.04	0.04	0.04	0.00	0.00	0.00	0.00	0.00
K	0.00	0.00	0.00	0.00	0.00	0.00	0.00	0.00	0.00	0.00	0.00	0.00	0.00	0.00	0.00	0.00	0.00	0.00	0.00
Cr	0.00	0.00	0.00	0.00	0.00	0.00	0.00	0.00	0.00	0.00	0.00	0.00	0.00	0.00	0.00	0.00	0.00	0.00	0.00
SUM	***4.00***	***4.00***	***4.00***	***4.00***	***4.00***	***4.00***	***4.00***	***4.00***	***4.00***	***4.00***	***4.00***	***4.00***	***4.00***	***4.00***	***4.00***	***4.00***	***4.00***	***4.00***	***4.00***
Mg# totFe	71.6	74.1	71.2	68.7	72.8	71.8	72.5	72.0	80.0	75.6	70.9	74.9	76.3	76.5	59.5	59.3	66.3	66.6	67.0
MgO/(MgO +FeO)*100	58.6	61.6	58.1	55.1	60.0	58.8	59.6	59.1	69.2	63.4	57.7	62.6	64.3	64.7	45.2	45.0	52.4	52.8	53.2
Fe2+	0.25	0.25	0.25	0.31	0.26	0.26	0.28	0.24	0.16	0.23	0.21	0.25	0.21	0.21	0.75	0.78	0.63	0.63	0.63
Fe3+	0.05	0.02	0.05	0.01	0.01	0.03	0.00	0.05	0.04	0.02	0.08	0.00	0.03	0.02	0.03	0.02	0.03	0.03	0.01
Al (T)	0.07	0.04	0.06	0.04	0.03	0.05	0.03	0.06	0.05	0.04	0.12	0.05	0.06	0.04	0.05	0.03	0.05	0.03	0.03
Al (M1)	0.04	0.05	0.03	0.06	0.04	0.05	0.05	0.04	0.02	0.06	0.08	0.07	0.05	0.05	0.01	0.01	0.02	0.01	0.01
Wo	45.7	46.7	45.8	45.4	46.5	46.3	46.0	45.8	47.1	46.4	46.5	46.7	47.0	46.8	1.1	1.0	1.0	0.7	0.9
En	38.8	39.5	38.6	37.5	38.9	38.5	39.1	39.0	42.3	40.5	37.9	40.0	40.4	40.7	58.8	58.7	65.6	66.2	66.4
Fs	15.4	13.8	15.6	17.1	14.6	15.1	14.9	15.2	10.6	13.1	15.6	13.4	12.6	12.5	40.0	40.3	33.4	33.2	32.7

Table (B)

(B) Recrystallized grains in monophase ribbons

	Plagioclase												
	F33	F20A	F10B					F32A					
wt%	F33-S4-pl12	F20A-S13-pl34	F10B-S1-pl3	F10B-S1-pl4	F10B-S1-pl5	F10B-S1-pl6	F10B-S1-pl7	F32A-S13-pl39	F32A-S13-pl40	F32A-S17-pl48	F32A-S19-pl60	F32A-S23-pl69	F32A-S24-pl70
SiO_2	57.1	58.3	54.6	56.3	55.7	56.4	55.3	56.5	56.1	57.1	56.3	56.6	56.9
TiO_2	0.0	0.0	0.0	0.0	0.0	0.0	0.0	0.0	0.0	0.0	0.0	0.0	0.0
Al_2O_3	27.4	26.4	28.8	27.7	27.3	27.8	28.5	28.0	27.8	27.7	28.4	27.9	27.8
FeO	0.0	0.0	0.0	0.0	0.1	0.1	0.2	0.2	0.1	0.0	0.1	0.1	0.1
MnO	0.0	0.0	0.0	0.0	0.0	0.0	0.0	0.0	0.1	0.0	0.0	0.0	0.0
MgO	0.0	0.0	0.0	0.0	0.0	0.0	0.0	0.0	0.0	0.0	0.0	0.0	0.0
CaO	9.6	8.3	11.2	9.9	10.0	10.0	10.8	10.2	10.2	9.7	10.3	10.1	9.8
Na_2O	6.3	6.8	5.3	5.9	5.8	6.0	5.5	5.8	5.9	6.4	6.0	5.9	6.2
K_2O	0.0	0.1	0.1	0.2	0.1	0.1	0.1	0.0	0.1	0.1	0.1	0.1	0.1
Cr_2O_3	0.0	0.0	0.0	0.0	0.0	0.0	0.0	0.0	0.0	0.1	0.0	0.1	0.0
Tot	***100.5***	***100.0***	***100.1***	***100.0***	***99.0***	***100.4***	***100.4***	***100.7***	***100.2***	***101.1***	***101.2***	***100.7***	***100.9***
Si	2.55	2.61	2.46	2.53	2.53	2.52	2.48	2.53	2.52	2.53	2.50	2.53	2.53
Ti	0.00	0.00	0.00	0.00	0.00	0.00	0.00	0.00	0.00	0.00	0.00	0.00	0.00
Al	1.44	1.39	1.53	1.47	1.46	1.47	1.50	1.47	1.47	1.45	1.48	1.47	1.46
Fe tot	0.00	0.00	0.00	0.00	0.00	0.00	0.01	0.01	0.00	0.00	0.01	0.00	0.00
Mn	0.00	0.00	0.00	0.00	0.00	0.00	0.00	0.00	0.00	0.00	0.00	0.00	0.00
Mg	0.00	0.00	0.00	0.00	0.00	0.00	0.00	0.00	0.00	0.00	0.00	0.00	0.00
Ca	0.46	0.40	0.54	0.48	0.49	0.48	0.52	0.49	0.49	0.46	0.49	0.48	0.47
Na	0.54	0.59	0.46	0.51	0.51	0.52	0.48	0.50	0.51	0.55	0.51	0.51	0.54
K	0.00	0.00	0.01	0.01	0.01	0.01	0.01	0.00	0.00	0.00	0.00	0.00	0.00
Cr	0.00	0.00	0.00	0.00	0.00	0.00	0.00	0.00	0.00	0.00	0.00	0.00	0.00
SUM	***5.00***	***5.00***	***5.00***	***5.00***	***5.00***	***5.00***	***5.00***	***5.00***	***5.00***	***5.00***	***5.00***	***5.00***	***5.00***
An	45.8	40.3	53.4	47.7	48.4	47.7	51.7	49.1	48.6	45.3	48.5	48.3	46.4
Ab	53.9	59.2	45.9	51.4	50.9	51.8	47.7	50.7	51.0	54.3	51.0	51.4	53.2
Or	0.2	0.5	0.7	0.9	0.7	0.5	0.6	0.2	0.4	0.5	0.5	0.32	0.4

Table (B) cont.

(C) Ultramylonite

Clinopyroxene

F20A

wt%	4 / 1 .	4 / 2 .	4 / 3 .	5 / 2 .	5 / 3 .	5 / 4 .	5 / 5 .	31 / 4 .	31 / 5 .	31 / 6 .	F20A-map-a	F20A-map-b	F20A-map-c	F20A-map-d	F20A-map-e	F20A-map-f	F20A-map-g	F20A-map-h
SiO_2	52.1	51.9	51.1	51.6	51.6	52.2	52.0	53.0	53.4	52.4	52.7	52.2	52.3	52.4	52.0	52.2	52.0	52.2
TiO_2	0.3	0.3	0.2	0.2	0.2	0.2	0.1	0.2	0.2	0.2	0.2	0.2	0.2	0.2	0.2	0.2	0.2	0.2
Al_2O_3	1.9	2.2	2.4	1.9	1.8	1.4	1.3	1.8	5.7	1.9	1.8	2.0	2.3	2.2	1.7	2.0	1.7	1.7
FeO	9.8	8.6	9.8	8.9	8.8	8.8	8.4	8.5	7.5	8.8	8.3	9.3	8.8	8.9	9.1	9.0	9.0	8.8
MnO	0.3	0.2	0.2	0.2	0.3	0.2	0.2	0.2	0.1	0.2	0.2	0.2	0.2	0.2	0.2	0.2	0.2	0.2
MgO	13.6	13.0	12.9	13.2	13.3	13.5	13.7	13.5	12.2	13.3	13.7	13.1	13.5	13.5	13.2	13.3	13.3	13.4
CaO	21.1	23.4	22.9	23.0	23.0	23.0	23.3	23.5	21.5	23.0	24.0	23.4	23.6	23.1	23.1	23.4	23.3	23.6
Na_2O	0.4	0.4	0.4	0.5	0.4	0.4	0.4	0.4	1.1	0.5	0.4	0.5	0.5	0.5	0.4	0.4	0.4	0.4
K_2O	0.0	0.0	0.0	0.0	0.0	0.0	0.0	0.0	0.0	0.0	0.0	0.0	0.0	0.0	0.0	0.0	0.0	0.0
Cr_2O_3	0.0	0.0	0.0	0.0	0.0	0.0	0.0	0.0	0.0	0.0	-	-	-	-	-	-	-	-
Tot	***99.4***	***99.9***	***100.0***	***99.5***	***99.4***	***99.8***	***99.4***	***101.0***	***101.6***	***100.4***	***101.4***	***100.8***	***101.5***	***101.0***	***100.0***	***100.7***	***100.0***	***100.6***
Si	1.95	1.93	1.91	1.93	1.93	1.95	1.94	1.95	1.94	1.95	1.93	1.93	1.92	1.93	1.94	1.93	1.94	1.93
Ti	0.01	0.01	0.01	0.01	0.01	0.00	0.00	0.01	0.01	0.01	0.01	0.01	0.01	0.01	0.01	0.01	0.01	0.01
Al	0.08	0.10	0.11	0.08	0.08	0.06	0.06	0.08	0.24	0.08	0.08	0.09	0.10	0.09	0.08	0.09	0.07	0.07
Fe tot	0.31	0.27	0.30	0.28	0.28	0.28	0.26	0.26	0.23	0.27	0.25	0.29	0.27	0.27	0.28	0.28	0.28	0.27
Mn	0.01	0.01	0.01	0.01	0.01	0.01	0.01	0.01	0.00	0.01	0.01	0.01	0.01	0.01	0.01	0.01	0.01	0.01
Mg	0.76	0.72	0.72	0.74	0.74	0.75	0.76	0.74	0.66	0.73	0.75	0.72	0.74	0.74	0.73	0.73	0.74	0.74
Ca	0.85	0.93	0.92	0.92	0.92	0.92	0.93	0.93	0.84	0.92	0.94	0.93	0.93	0.91	0.92	0.93	0.93	0.94
Na	0.03	0.03	0.03	0.03	0.03	0.03	0.03	0.03	0.08	0.03	0.03	0.03	0.03	0.03	0.03	0.03	0.03	0.03
K	0.00	0.00	0.00	0.00	0.00	0.00	0.00	0.00	0.00	0.00	0.00	0.00	0.00	0.00	0.00	0.00	0.00	0.00
Cr	0.00	0.00	0.00	0.00	0.00	0.00	0.00	0.00	0.00	0.00	0.00	0.00	0.00	0.00	0.00	0.00	0.00	0.00
SUM	***4.00***	***4.00***	***4.00***	***4.00***	***4.00***	***4.00***	***4.00***	***4.00***	***4.00***	***4.00***	***4.00***	***4.00***	***4.00***	***4.00***	***4.00***	***4.00***	***4.00***	***4.00***
Mg# totFe	71.3	73.0	70.2	72.5	72.8	73.2	74.4	73.9	74.3	72.8	80.6	77.1	79.9	78.1	77.1	77.7	77.8	79.2
MgO/(MgO+FeO)*100	58.3	60.3	56.9	59.7	60.1	60.5	62.0	61.4	61.8	60.0	62.4	58.4	60.4	60.3	59.1	59.6	59.7	60.3
Fe2+	0.28	0.21	0.21	0.20	0.20	0.21	0.19	0.22	0.23	0.23	0.18	0.21	0.19	0.21	0.22	0.21	0.21	0.19
Fe3+	0.02	0.05	0.09	0.08	0.08	0.07	0.07	0.04	0.00	0.05	0.07	0.07	0.09	0.07	0.07	0.07	0.07	0.08
Al (T)	0.05	0.07	0.09	0.07	0.07	0.05	0.06	0.05	0.06	0.05	0.07	0.07	0.08	0.07	0.06	0.07	0.06	0.07
Al (M1)	0.04	0.03	0.01	0.01	0.01	0.01	0.00	0.03	0.19	0.03	0.01	0.02	0.02	0.02	0.02	0.02	0.01	0.01
Wo	44.2	48.5	47.3	47.7	47.5	47.2	47.7	48.1	48.5	47.6	48.4	47.9	47.9	47.4	47.6	47.9	47.8	48.0
En	39.8	37.6	37.0	38.0	38.2	38.7	38.9	38.3	38.2	38.2	38.5	37.2	38.1	38.5	37.8	37.7	37.9	37.9
Fs	16.0	13.9	15.7	14.4	14.2	14.1	13.4	13.5	13.3	14.2	13.0	14.8	14.0	14.2	14.7	14.3	14.3	14.0

Table (C) cont.

(C) Ultramylonite

Orthopyroxene

	F20A																		F32A
wt%	F20A-S1-opx3	F20A-S4-opx15	7/1.	7/2.	7/3.	7/4.	7/5.	7/6.	2/1.	2/2.	2/5.	F20A-opx-map-a	F20A-opx-map-c	F20A-opx-map-d	F20A-opx-map-e	F20A-opx-map-f	F20A-opx-map-g	F20A-opx-map-h	F32A-S14-opx43
SiO_2	52.0	53.9	52.3	51.9	51.8	52.2	52.1	51.9	51.5	51.6	52.2	52.4	51.3	52.9	51.9	51.3	51.5	53.4	53.6
TiO_2	0.1	0.1	0.1	0.1	0.1	0.1	0.1	0.2	0.1	0.1	0.1	0.1	0.1	0.1	0.1	0.1	0.1	0.1	0.1
Al_2O_3	1.5	0.9	1.0	1.4	1.3	1.2	1.4	1.5	1.3	1.1	1.2	0.7	0.7	0.8	0.9	2.2	1.1	0.8	1.0
FeO	26.6	25.2	24.9	25.0	24.8	24.9	24.6	24.8	25.0	24.8	24.8	26.4	28.3	25.8	26.1	25.6	26.2	25.8	21.7
MnO	0.6	0.6	0.5	0.6	0.5	0.6	0.5	0.6	0.5	0.6	0.6	0.6	0.6	0.6	0.6	0.6	0.6	0.5	0.7
MgO	20.2	20.9	19.8	19.5	19.6	19.6	19.8	19.5	19.4	19.5	19.9	21.0	20.3	21.1	20.2	18.5	19.6	20.5	23.8
CaO	0.5	0.4	0.5	0.5	0.5	0.5	0.4	0.5	0.4	0.5	0.8	0.2	0.4	0.5	0.7	0.5	0.5	0.6	0.4
Na_2O	0.0	0.0	0.0	0.0	0.0	0.0	0.0	0.0	0.1	0.0	0.0	0.0	0.0	0.0	0.0	0.0	0.0	0.0	0.0
K_2O	0.0	0.0	0.0	0.0	0.0	0.0	0.0	0.0	0.0	0.0	0.0	0.0	0.0	0.0	0.0	0.0	0.0	0.0	0.0
Cr_2O_3	0.1	0.0	0.0	0.0	0.0	0.0	0.0	0.0	0.0	0.0	0.0	-	-	-	-	-	-	-	0.2
Tot	***101.5***	***102.0***	***99.1***	***99.0***	***98.6***	***99.1***	***98.9***	***98.9***	***98.1***	***98.2***	***99.6***	***101.4***	***101.7***	***101.7***	***100.6***	***98.7***	***99.5***	***101.7***	***101.5***
Si	1.94	1.99	1.99	1.98	1.99	1.99	1.99	1.99	1.98	1.99	1.98	1.95	1.91	1.96	1.95	1.97	1.96	1.99	1.96
Ti	0.00	0.00	0.00	0.00	0.00	0.00	0.00	0.00	0.00	0.00	0.00	0.00	0.00	0.00	0.00	0.00	0.00	0.00	0.00
Al	0.07	0.04	0.05	0.06	0.06	0.06	0.06	0.07	0.06	0.05	0.05	0.03	0.03	0.03	0.04	0.10	0.05	0.03	0.04
Fe tot	0.83	0.78	0.79	0.80	0.80	0.79	0.78	0.79	0.80	0.80	0.78	0.82	0.88	0.80	0.82	0.82	0.84	0.80	0.66
Mn	0.02	0.02	0.02	0.02	0.02	0.02	0.02	0.02	0.02	0.02	0.02	0.02	0.02	0.02	0.02	0.02	0.02	0.02	0.02
Mg	1.12	1.15	1.12	1.11	1.12	1.12	1.13	1.11	1.11	1.12	1.13	1.17	1.13	1.16	1.13	1.06	1.11	1.14	1.29
Ca	0.02	0.02	0.02	0.02	0.02	0.02	0.02	0.02	0.02	0.02	0.03	0.01	0.02	0.02	0.03	0.02	0.02	0.02	0.01
Na	0.00	0.00	0.00	0.00	0.00	0.00	0.00	0.00	0.00	0.00	0.00	0.00	0.00	0.00	0.00	0.00	0.00	0.00	0.00
K	0.00	0.00	0.00	0.00	0.00	0.00	0.00	0.00	0.00	0.00	0.00	0.00	0.00	0.00	0.00	0.00	0.00	0.00	0.00
Cr	0.00	0.00	0.00	0.00	0.00	0.00	0.00	0.00	0.00	0.00	0.00	0.00	0.00	0.00	0.00	0.00	0.00	0.00	0.01
SUM	***4.00***	***4.00***	***4.00***	***4.00***	***4.00***	***4.00***	***4.00***	***4.00***	***4.00***	***4.00***	***4.00***	***4.00***	***4.00***	***4.00***	***4.00***	***4.00***	***4.00***	***4.00***	***4.00***
Mg# totFe	57.6	59.7	58.6	58.3	58.4	58.4	59.0	58.4	58.1	58.3	59.0	58.7	56.1	59.2	58.0	56.3	57.1	58.6	66.1
MgO/(MgO+FeO)*100	43.2	45.4	44.3	43.9	44.1	44.1	44.6	44.0	43.7	44.0	44.6	44.4	41.8	44.9	43.6	41.9	42.7	44.3	52.3
Fe2+	0.78	0.78	0.79	0.80	0.80	0.79	0.78	0.79	0.80	0.80	0.78	0.76	0.75	0.76	0.77	0.82	0.81	0.80	0.63
Fe3+	0.05	0.00	0.00	0.00	0.00	0.00	0.00	0.00	0.00	0.00	0.00	0.07	0.13	0.04	0.05	0.00	0.02	0.00	0.04
Al (T)	0.06	0.01	0.01	0.02	0.01	0.01	0.01	0.01	0.02	0.01	0.02	0.03	0.03	0.03	0.04	0.03	0.04	0.01	0.04
Al (M1)	0.00	0.03	0.04	0.05	0.05	0.05	0.05	0.05	0.04	0.04	0.03	0.00	0.00	0.00	0.00	0.07	0.01	0.02	0.00
Wo	0.9	0.8	1.0	1.1	1.0	1.1	0.9	1.1	0.9	1.2	1.6	0.3	0.8	0.9	1.5	1.1	1.0	1.1	0.7
En	57.0	59.2	58.1	57.6	57.8	57.8	58.4	57.8	57.6	57.7	58.0	58.5	55.7	58.7	57.1	55.7	56.5	57.9	65.6
Fs	42.1	40.0	40.9	41.3	41.1	41.1	40.6	41.2	41.5	41.2	40.4	41.2	43.5	40.4	41.4	43.2	42.5	40.9	33.6

Table (C) cont.

(C) Ultramylonite

Amphibole

	F20A																	F32A		
wt%	31 / 1 .	31 / 2 .	31 / 3 .	31 / 7 .	31 / 9 .	31 / 10 .	F20A-amph-a	F20A-amph-b	F20A-amph-c	F20A-amph-d	F20A-amph-e	F20A-amph-f	F20A-amph-g	F20A-amph-h	F20A-amph-i	F20A-amph-j	F20A-S1-amph4	F32A-S1-cpx2-AMPH	F32A-S1-amph4	F32A-S14-amph44
SiO_2	44.1	43.0	42.7	42.9	42.1	42.1	41.6	42.0	41.9	41.9	41.3	42.4	42.4	41.2	41.4	43.7	42.8	44.6	44.1	44.6
TiO_2	1.6	1.9	2.0	2.0	2.2	2.1	2.7	2.2	2.5	2.2	1.9	2.3	2.3	2.4	3.0	2.0	2.0	1.8	2.2	1.7
Al_2O_3	9.6	12.0	12.8	11.9	12.7	13.3	13.5	12.6	12.6	12.9	12.4	12.7	12.7	12.8	12.9	12.6	13.0	11.8	11.3	11.5
FeO	13.6	13.7	13.9	13.3	14.2	13.7	14.1	13.8	14.5	13.5	14.0	13.6	14.0	13.4	14.4	12.9	14.1	11.1	11.5	11.1
MnO	0.1	0.1	0.1	0.1	0.1	0.1	0.1	0.1	0.1	0.1	0.2	0.1	0.1	0.1	0.1	0.1	0.1	0.1	0.1	0.1
MgO	12.2	11.7	11.1	11.1	11.0	10.9	10.6	11.1	10.5	11.0	10.8	11.2	11.3	10.7	10.5	10.8	11.9	13.7	13.8	13.8
CaO	12.9	12.1	12.4	13.2	11.8	12.2	11.7	11.6	11.4	11.4	11.6	11.6	11.6	12.5	11.7	12.1	11.5	12.0	11.9	11.8
Na_2O	2.1	2.3	2.5	2.5	2.5	2.5	2.9	2.7	2.5	2.6	2.4	2.6	2.8	2.5	2.8	2.7	2.7	2.1	2.0	2.2
K_2O	0.4	0.5	0.6	0.5	0.6	0.6	0.6	0.6	0.6	0.6	0.6	0.5	0.5	0.6	0.6	0.6	0.5	0.7	0.6	0.6
Cr_2O_3	0.0	0.0	0.1	0.0	0.0	0.0	-	-	-	-	-	-	-	-	-	-	0.1	0.1	0.1	0.1
Tot	***96.61***	***97.5***	***98.15***	***97.48***	***97.23***	***97.54***	***97.78***	***96.59***	***96.65***	***96.38***	***95.15***	***97.09***	***97.85***	***96.25***	***97.38***	***97.55***	***98.7***	***98.1***	***97.6***	***97.5***
Si	6.62	6.38	6.31	6.39	6.28	6.27	6.19	6.30	6.29	6.28	6.30	6.32	6.28	6.22	6.20	6.46	6.22	6.46	6.41	6.48
Ti	0.19	0.21	0.23	0.23	0.25	0.23	0.31	0.25	0.28	0.25	0.22	0.26	0.26	0.28	0.34	0.22	0.22	0.20	0.24	0.19
Al	1.70	2.11	2.24	2.08	2.24	2.33	2.37	2.22	2.22	2.29	2.23	2.23	2.21	2.28	2.27	2.20	2.23	2.02	1.93	1.97
Fe tot	1.70	1.70	1.72	1.66	1.78	1.71	1.75	1.73	1.82	1.70	1.78	1.69	1.73	1.70	1.81	1.60	1.72	1.35	1.40	1.35
Mn	0.01	0.02	0.02	0.01	0.01	0.01	0.02	0.02	0.02	0.02	0.02	0.02	0.02	0.02	0.02	0.02	0.02	0.02	0.01	0.02
Mg	2.72	2.59	2.44	2.46	2.45	2.41	2.36	2.48	2.36	2.46	2.45	2.48	2.50	2.41	2.35	2.38	2.58	2.96	3.00	2.99
Ca	2.08	1.92	1.97	2.11	1.89	1.94	1.86	1.86	1.83	1.84	1.90	1.85	1.85	2.02	1.88	1.91	1.80	1.86	1.86	1.83
Na	0.62	0.67	0.71	0.71	0.71	0.73	0.82	0.78	0.72	0.75	0.71	0.76	0.79	0.73	0.81	0.77	0.76	0.59	0.58	0.62
K	0.07	0.10	0.10	0.10	0.11	0.11	0.11	0.11	0.12	0.11	0.12	0.10	0.10	0.11	0.11	0.11	0.09	0.13	0.11	0.12
Cr	0.00	0.00	0.01	0.00	0.00	0.00	-	-	-	-	-	-	-	-	-	-	0.01	0.00	0.01	0.01
SUM	***12.93***	***13.00***	***12.96***	***12.83***	***13.00***	***12.97***	***13.00***	***13.00***	***13.00***	***13.00***	***13.00***	***13.00***	***13.00***	***12.91***	***12.99***	***12.87***	***13.00***	***13.00***	***13.00***	***13.00***
Mg# totFe	61.5	60.3	58.7	59.7	57.9	58.5	57.3	59.0	56.4	59.2	57.9	59.5	59.1	58.6	56.4	59.8	60.1	68.7	68.2	68.9
MgO/(MgO +FeO)*100	47.3	46.0	44.4	45.4	43.6	44.2	43.0	44.7	42.1	44.8	43.6	45.1	44.7	44.3	42.1	45.5	45.8	55.2	54.6	55.4
Fe2+	1.70	1.61	1.72	1.66	1.68	1.71	1.75	1.66	1.70	1.60	1.68	1.64	1.61	1.70	1.81	1.60	1.29	1.13	1.04	1.05
Fe3+	0.00	0.09	0.00	0.00	0.10	0.00	0.00	0.06	0.12	0.10	0.10	0.05	0.13	0.00	0.00	0.00	0.42	0.22	0.36	0.30
Al (T)	1.38	1.62	1.69	1.61	1.72	1.73	1.81	1.70	1.71	1.72	1.70	1.68	1.72	1.78	1.80	1.54	1.78	1.54	1.59	1.52
Al (M1)	0.31	0.48	0.55	0.47	0.52	0.60	0.56	0.53	0.51	0.57	0.52	0.55	0.49	0.51	0.48	0.66	0.45	0.48	0.34	0.45

Table (C) cont.

(C) Ultramylonite

Plagioclase

	F20A																										F32A	
wt%	F20A-pl-35.1	F20A-pl-35.2	F20A-pl-35.3	F20A-pl-35.4	F20A-pl-35.5	F20A-pl-36.1	F20A-pl-36.2	F20A-pl-36.3	F20A-pl-36.4	F20A-pl-36.5	F20A-pl-36.6	F20A-pl-36.7	F20A-pl-36.8	F20A-pl-39.1	F20A-pl-39.2	F20A-pl-39.3	F20A-pl-39.4	F20A-pl-a	F20A-pl-b	F20A-pl-c	F20A-pl-d	F20A-pl-e	F20A-pl-f	F20A-pl-g	F20A-pl-h	F20A-pl-i	F20A-pl-j	F32A-S1-pl3	F32A-S22-pl68
SiO_2	53.2	52.3	52.2	52.4	52.4	54.7	51.7	52.6	52.6	54.4	54.6	54.6	53.8	53.3	53.3	53.3	53.5	54.6	53.7	53.6	53.6	53.6	54.5	54.3	53.7	55.7	53.7	56.7	53.7
TiO_2	0.0	0.0	0.0	0.0	0.0	0.0	0.0	0.0	0.0	0.0	0.0	0.0	0.0	0.0	0.0	0.0	0.1	0.0	0.0	0.0	0.0	0.0	0.0	0.0	0.0	0.0	0.0	0.0	0.1
Al_2O_3	30.7	31.0	31.0	30.7	30.9	29.4	31.8	31.1	31.1	29.6	29.6	29.7	30.0	29.5	29.5	29.6	29.4	29.8	29.0	29.0	28.4	28.5	28.9	29.5	30.0	28.6	28.8	27.5	29.6
FeO	0.4	0.3	0.3	0.3	0.4	0.3	0.3	0.2	0.3	0.3	0.3	0.3	0.3	0.4	0.4	0.3	0.4	0.4	0.3	0.4	0.7	0.5	0.4	0.4	0.4	0.3	0.5	0.2	0.2
MnO	0.0	0.0	0.0	0.0	0.0	0.0	0.0	0.0	0.0	0.0	0.0	0.0	0.0	0.0	0.0	0.0	0.0	0.0	0.0	0.0	0.0	0.0	0.0	0.0	0.0	0.0	0.0	0.0	0.0
MgO	0.0	0.0	0.0	0.0	0.0	0.0	0.0	0.0	0.0	0.0	0.0	0.0	0.0	0.0	0.0	0.0	0.0	0.0	0.0	0.0	0.0	0.0	0.0	0.0	0.0	0.0	0.0	0.0	0.0
CaO	12.8	13.5	13.5	13.4	13.3	11.4	13.9	13.2	13.2	11.6	11.7	11.7	12.1	12.0	12.1	12.0	11.8	10.8	11.3	11.3	11.2	11.0	10.9	10.9	11.7	10.2	11.1	9.7	12.2
Na_2O	4.7	4.4	4.4	4.3	4.2	5.5	3.8	4.4	4.3	5.3	5.3	5.3	5.2	5.0	5.0	5.1	5.2	5.7	5.4	5.3	5.3	5.4	5.7	5.7	5.1	6.2	5.4	6.1	4.8
K_2O	0.0	0.0	0.0	0.0	0.0	0.0	0.0	0.0	0.0	0.0	0.0	0.0	0.0	0.0	0.0	0.0	0.0	0.0	0.0	0.0	0.0	0.0	0.0	0.0	0.0	0.0	0.0	0.0	0.1
Cr_2O_3	0.0	0.0	0.0	0.0	0.0	0.0	0.0	0.0	0.0	0.0	0.0	0.0	0.0	0.0	0.0	0.0	0.0	0.0	0.0	0.0	0.0	0.0	0.0	0.0	0.0	0.0	0.0	0.0	0.0
Tot	***101.9***	***101.5***	***101.5***	***101.2***	***101.2***	***101.4***	***101.6***	***101.6***	***101.5***	***101.2***	***101.6***	***101.7***	***101.4***	***100.3***	***100.3***	***100.4***	***100.5***	***101.4***	***99.7***	***99.6***	***99.3***	***99.1***	***100.4***	***100.8***	***100.9***	***100.9***	***99.7***	***100.4***	***100.4***
Si	2.36	2.33	2.33	2.35	2.35	2.43	2.31	2.34	2.35	2.42	2.42	2.42	2.39	2.40	2.40	2.40	2.40	2.42	2.43	2.43	2.44	2.44	2.44	2.42	2.40	2.47	2.43	2.54	2.42
Ti	0.00	0.00	0.00	0.00	0.00	0.00	0.00	0.00	0.00	0.00	0.00	0.00	0.00	0.00	0.00	0.00	0.00	0.00	0.00	0.00	0.00	0.00	0.00	0.00	0.00	0.00	0.00	0.00	0.00
Al	1.61	1.63	1.63	1.62	1.63	1.54	1.67	1.63	1.64	1.55	1.55	1.55	1.57	1.57	1.57	1.57	1.56	1.56	1.54	1.54	1.52	1.53	1.53	1.55	1.58	1.50	1.53	1.45	1.57
Fe tot	0.01	0.01	0.01	0.01	0.01	0.01	0.01	0.01	0.01	0.01	0.01	0.01	0.01	0.01	0.01	0.01	0.01	0.01	0.01	0.01	0.03	0.02	0.02	0.01	0.01	0.01	0.02	0.01	0.01
Mn	0.00	0.00	0.00	0.00	0.00	0.00	0.00	0.00	0.00	0.00	0.00	0.00	0.00	0.00	0.00	0.00	0.00	0.00	0.00	0.00	0.00	0.00	0.00	0.00	0.00	0.00	0.00	0.00	0.00
Mg	0.00	0.00	0.00	0.00	0.00	0.00	0.00	0.00	0.00	0.00	0.00	0.00	0.00	0.00	0.00	0.00	0.00	0.00	0.00	0.00	0.00	0.00	0.00	0.00	0.00	0.00	0.00	0.00	0.00
Ca	0.61	0.64	0.64	0.65	0.64	0.54	0.67	0.63	0.63	0.55	0.56	0.56	0.58	0.58	0.58	0.58	0.57	0.51	0.55	0.55	0.54	0.54	0.52	0.52	0.56	0.48	0.54	0.47	0.59
Na	0.40	0.38	0.38	0.37	0.37	0.48	0.33	0.38	0.38	0.46	0.46	0.46	0.45	0.44	0.44	0.45	0.45	0.49	0.47	0.46	0.47	0.48	0.49	0.49	0.44	0.53	0.48	0.53	0.41
K	0.00	0.00	0.00	0.00	0.00	0.00	0.00	0.00	0.00	0.00	0.00	0.00	0.00	0.00	0.00	0.00	0.00	0.00	0.00	0.00	0.00	0.00	0.00	0.00	0.00	0.00	0.00	0.00	0.00
Cr	0.00	0.00	0.00	0.00	0.00	0.00	0.00	0.00	0.00	0.00	0.00	0.00	0.00	0.00	0.00	0.00	0.00	0.00	0.00	0.00	0.00	0.00	0.00	0.00	0.00	0.00	0.00	0.00	0.00
SUM	***5.00***	***5.00***	***5.00***	***5.00***	***5.00***	***5.00***	***5.00***	***5.00***	***5.00***	***5.00***	***5.00***	***5.00***	***5.00***	***5.00***	***5.00***	***5.00***	***5.00***	***5.00***	***5.00***	***5.00***	***5.00***	***5.00***	***5.00***	***5.00***	***5.00***	***5.00***	***5.00***	***5.00***	***5.00***
An	59.9	62.7	62.8	63.3	63.3	53.2	66.6	62.3	62.5	54.5	54.9	54.6	56.3	56.9	56.9	56.2	55.5	51.0	53.7	53.9	53.8	52.7	51.2	51.3	55.7	47.5	53.0	46.7	58.4
Ab	40.0	37.2	37.0	36.5	36.6	46.6	33.3	37.5	37.3	45.3	44.9	45.2	43.5	43.0	42.9	43.5	44.4	48.8	46.2	45.9	46.1	47.1	48.6	48.5	44.1	52.4	46.9	53.1	41.3
Or	0.2	0.1	0.2	0.2	0.2	0.2	0.2	0.2	0.2	0.2	0.2	0.3	0.2	0.1	0.2	0.3	0.2	0.2	0.2	0.2	0.2	0.1	0.2	0.2	0.2	0.2	0.2	0.2	0.4

Table (C) cont.

(D) Symplectites

	Clinopyroxene								Orthopyroxene															
	F20A	F33							F33												F10B	F20A		F32A	
wt%	F20A-S3-cpx11	F33-symp-2.a	F33-symp-2.b	F33-symp-2.c	F33-symp-2.d	F33-symp-1.a	F33-symp-4.a	F33-symp-4.b	F33-S8-opx22	F33-symp4-1/1.	F33-symp4-2/2.	F33-symp4-2/3.	F33-symp4-2/4.	F33-symp2-17/1.	F33-symp2-18/1.	F33-symp1-26/1.	F33-symp1-26/2.	F33-symp1-26/3.	F33-symp1-26/5.	F33-symp1-26/6.	F33-S5-opx14	F10B-S3-opx16	F20A-S3-opx12	F20A-S5-opx21	F32A-S2-opx6	F32A-S8-opx21
SiO_2	52.9	53.0	50.4	50.4	50.7	51.1	53.9	51.8	54.7	53.0	53.0	52.8	53.2	51.4	51.6	52.3	52.5	53.7	51.8	51.8	54.0	52.4	52.6	52.6	53.3	53.5
TiO_2	0.3	0.2	0.4	0.4	0.5	0.6	0.2	0.4	0.1	0.1	0.1	0.1	0.1	0.2	0.1	0.1	0.1	0.1	0.1	0.1	0.5	0.0	0.1	0.1	0.0	0.0
Al_2O_3	2.4	5.3	2.7	2.8	3.9	2.4	5.1	3.2	1.3	0.9	1.0	1.2	3.1	1.3	1.4	1.4	1.1	1.9	1.9	1.5	1.4	2.1	1.6	1.8	2.4	1.6
FeO	8.9	5.4	6.1	6.2	6.0	5.8	5.8	6.3	19.8	20.2	20.2	20.1	20.0	20.5	20.4	19.1	19.0	18.2	19.1	18.9	19.7	25.1	25.2	24.0	20.7	21.1
MnO	0.2	0.2	0.2	0.2	0.2	0.2	0.2	0.2	0.7	0.6	0.6	0.6	0.6	0.6	0.6	0.5	0.5	0.6	0.6	0.5	0.6	0.7	0.6	0.5	0.7	0.7
MgO	13.3	14.4	14.6	14.5	14.1	14.8	13.0	13.9	24.7	24.1	24.0	23.9	23.5	23.8	23.6	24.7	24.7	24.0	24.6	25.0	24.8	20.3	20.4	21.2	23.9	23.6
CaO	22.2	22.3	22.5	22.5	22.8	23.0	21.1	22.1	0.5	0.4	0.5	0.4	1.0	0.5	0.5	0.4	0.4	0.9	0.5	0.4	0.4	0.5	0.5	0.6	0.3	0.3
Na_2O	0.5	0.8	0.6	0.6	0.6	0.5	0.8	0.6	0.1	0.0	0.0	0.0	0.2	0.0	0.0	0.0	0.0	0.1	0.0	0.0	0.1	0.0	0.0	0.0	0.0	0.0
K_2O	0.0	0.0	0.0	0.0	0.0	0.0	0.0	0.0	0.0	0.0	0.0	0.0	0.0	0.0	0.0	0.0	0.0	0.0	0.0	0.0	0.0	0.0	0.0	0.0	0.0	0.0
Cr_2O_3	0.0	0.1	0.2	0.2	0.3	0.1	0.0	0.0	0.0	0.0	0.0	0.0	0.1	0.0	0.0	0.1	0.0	0.0	0.0	0.0	0.0	0.0	0.0	0.1	0.0	0.1
Tot	***100.8***	***101.7***	***97.6***	***97.8***	***99.2***	***98.4***	***100.1***	***98.6***	***101.9***	***99.3***	***99.4***	***99.2***	***101.7***	***98.3***	***98.2***	***98.5***	***98.3***	***99.5***	***98.6***	***98.2***	***101.4***	***101.0***	***101.2***	***100.9***	***101.3***	***100.9***
Si	1.96	1.91	1.90	1.89	1.88	1.91	1.99	1.94	1.97	1.96	1.96	1.96	1.92	1.93	1.93	1.94	1.95	1.98	1.92	1.93	1.96	1.96	1.96	1.96	1.94	1.96
Ti	0.01	0.01	0.01	0.01	0.01	0.02	0.01	0.01	0.00	0.00	0.00	0.00	0.00	0.00	0.00	0.00	0.00	0.00	0.00	0.00	0.01	0.00	0.00	0.00	0.00	0.00
Al	0.10	0.22	0.12	0.13	0.17	0.11	0.22	0.14	0.06	0.04	0.04	0.05	0.13	0.06	0.06	0.06	0.05	0.08	0.08	0.07	0.06	0.09	0.07	0.08	0.10	0.07
Fe tot	0.27	0.16	0.19	0.19	0.19	0.18	0.18	0.20	0.60	0.63	0.62	0.62	0.60	0.64	0.64	0.59	0.59	0.56	0.59	0.59	0.60	0.78	0.79	0.75	0.63	0.65
Mn	0.01	0.01	0.01	0.01	0.01	0.01	0.01	0.01	0.02	0.02	0.02	0.02	0.02	0.02	0.02	0.02	0.02	0.02	0.02	0.02	0.02	0.02	0.02	0.02	0.02	0.02
Mg	0.73	0.78	0.82	0.81	0.78	0.82	0.71	0.78	1.33	1.33	1.33	1.32	1.27	1.33	1.32	1.37	1.37	1.32	1.36	1.39	1.34	1.13	1.14	1.17	1.30	1.29
Ca	0.88	0.86	0.91	0.91	0.91	0.92	0.83	0.89	0.02	0.02	0.02	0.02	0.04	0.02	0.02	0.02	0.01	0.03	0.02	0.02	0.01	0.02	0.02	0.02	0.01	0.01
Na	0.03	0.06	0.04	0.05	0.04	0.04	0.05	0.04	0.01	0.00	0.00	0.00	0.02	0.00	0.00	0.00	0.00	0.01	0.00	0.00	0.00	0.00	0.00	0.00	0.00	0.00
K	0.00	0.00	0.00	0.00	0.00	0.00	0.00	0.00	0.00	0.00	0.00	0.00	0.00	0.00	0.00	0.00	0.00	0.00	0.00	0.00	0.00	0.00	0.00	0.00	0.00	0.00
Cr	0.00	0.00	0.00	0.01	0.01	0.00	0.00	0.00	0.00	0.00	0.00	0.00	0.00	0.00	0.00	0.00	0.00	0.00	0.00	0.00	0.00	0.00	0.00	0.00	0.00	0.00
SUM	***4.00***	***4.00***	***4.00***	***4.00***	***4.00***	***4.00***	***4.00***	***4.00***	***4.00***	***4.00***	***4.00***	***4.00***	***4.00***	***4.00***	***4.00***	***4.00***	***4.00***	***4.00***	***4.00***	***4.00***	***4.00***	***4.00***	***4.00***	***4.00***	***4.00***	***4.00***
Mg# totFe	72.8	82.7	81.1	80.8	80.7	81.8	79.9	79.8	69.0	68.0	68.0	67.9	67.7	67.5	67.4	69.8	69.9	70.2	69.7	70.2	69.2	59.1	59.1	61.1	67.3	66.5
MgO/(MgO+FeO)*100	60.0	72.9	70.6	70.3	70.1	71.7	69.1	68.8	55.5	54.4	54.4	54.3	54.0	53.8	53.7	56.4	56.6	56.9	56.3	56.9	55.8	44.8	44.8	46.8	53.6	52.7
Fe2+	0.27	0.16	0.09	0.09	0.11	0.10	0.18	0.20	0.60	0.60	0.60	0.60	0.57	0.56	0.57	0.54	0.55	0.56	0.52	0.51	0.59	0.78	0.78	0.75	0.61	0.64
Fe3+	0.00	0.00	0.10	0.11	0.07	0.08	0.00	0.00	0.00	0.02	0.03	0.02	0.03	0.08	0.07	0.05	0.04	0.00	0.07	0.08	0.01	0.00	0.00	0.00	0.02	0.01
Al (T)	0.04	0.09	0.10	0.11	0.12	0.09	0.01	0.06	0.03	0.04	0.04	0.04	0.08	0.06	0.06	0.06	0.05	0.02	0.08	0.07	0.04	0.04	0.04	0.04	0.06	0.04
Al (M1)	0.06	0.13	0.02	0.02	0.05	0.01	0.21	0.08	0.03	0.00	0.01	0.01	0.05	0.00	0.00	0.00	0.00	0.06	0.01	0.00	0.01	0.05	0.03	0.04	0.04	0.03
Wo	46.5	47.9	47.4	47.3	48.4	47.8	48.2	47.7	1.0	0.9	0.9	0.9	2.0	1.0	1.1	0.8	0.7	1.8	1.0	0.8	0.7	1.1	1.1	1.2	0.6	0.7
En	38.9	43.1	42.7	42.6	41.7	42.7	41.4	41.7	68.3	67.4	67.4	67.4	66.3	66.8	66.7	69.2	69.4	68.9	68.9	69.7	68.7	58.4	58.5	60.4	66.9	66.1
Fs	14.6	9.0	10.0	10.1	10.0	9.5	10.4	10.6	30.7	31.7	31.7	31.8	31.7	32.2	32.2	30.0	29.9	29.3	30.0	29.6	30.6	40.5	40.5	38.4	32.5	33.2

(D) Symplectites

	Plagioclase																									Amph	
	F33																				F10B		F20A		F32A			F20A	F32A
wt%	F33-S6-pl19	F33-symp-2-12 / 1 .	F33-symp-2-12 / 3 .	F33-symp-2b-19 / 1 .	F33-symp-2b-19 / 2 .	F33-symp-2b-19 / 3 .	F33-symp-2b-19 / 4 .	F33-symp-2b-19 / 5 .	F33-symp-2b-19 / 6 .	F33-symp-1-25 / 1 .	F33-symp-1-25 / 3 .	F33-symp-1-25 / 4 .	F33-symp-1-25 / 5 .	F33-symp-1-25 / 6 .	F33-symp-1-25 / 7 .	F33-symp-1-25 / 8 .	F33-symp-4-3 / 1 .	F33-symp-4-4 / 1 .	F33-symp-4-4 / 2 .	F33-symp-4-4 / 4 .	F10B-S3-pl15	F10B-S3-pl17	F20A-S3-pl13	F20A-S5-pl22	F32A-S2-pl5	F32A-S8-pl23	F32A-S19-pl59	F20A-S5-am20	F32A-S8-am22
SiO_2	46.7	55.5	51.0	54.0	54.6	54.7	53.0	53.1	53.2	54.2	53.8	55.8	54.9	55.0	54.7	54.1	53.6	52.6	51.7	48.5	49.5	50.3	57.4	51.1	48.8	48.8	53.4	42.7	43.9
TiO_2	0.0	0.0	0.1	0.0	0.0	0.0	0.0	0.0	0.0	0.1	2.5	0.1	0.1	0.0	0.0	0.0	0.0	0.1	0.1	0.0	0.0	0.0	0.0	0.0	0.0	0.0	0.1	1.5	0.8
Al_2O_3	34.0	28.5	28.7	29.2	28.7	28.6	29.8	29.9	29.8	28.8	27.5	28.6	28.1	27.7	28.5	28.5	29.9	31.2	31.7	32.2	32.2	32.0	27.0	31.1	32.5	32.7	30.4	13.1	12.4
FeO	0.4	0.3	2.4	0.6	0.3	0.3	0.3	0.3	0.3	0.5	1.1	0.3	0.3	0.3	0.3	0.3	0.3	0.4	0.4	1.0	0.3	0.3	0.4	0.3	0.7	0.5	0.3	13.0	12.1
MnO	0.1	0.0	0.0	0.0	0.0	0.0	0.0	0.0	0.0	0.0	0.1	0.0	0.0	0.0	0.0	0.0	0.0	0.0	0.0	0.0	0.0	0.0	0.0	0.0	0.0	0.0	0.0	0.1	0.2
MgO	0.1	0.0	2.6	0.1	0.0	0.0	0.0	0.0	0.0	0.1	0.1	0.0	0.0	0.0	0.0	0.0	0.0	0.0	0.1	0.8	0.0	0.0	0.0	0.0	0.0	0.0	0.0	12.6	14.3
CaO	17.4	9.8	10.2	10.5	10.2	10.1	11.2	11.3	11.3	10.1	9.6	9.5	9.4	9.3	9.6	10.1	11.5	13.0	13.2	15.1	15.1	14.8	9.3	14.2	15.7	16.1	12.6	11.5	11.0
Na_2O	1.6	6.2	4.7	5.5	5.9	6.1	5.4	5.2	5.2	6.0	6.2	5.9	6.2	6.5	6.3	6.1	5.0	4.4	3.8	2.4	2.9	3.1	6.4	3.5	2.8	2.5	4.6	2.7	2.3
K_2O	0.0	0.0	0.0	0.1	0.0	0.0	0.0	0.0	0.0	0.0	0.1	0.0	0.0	0.0	0.0	0.0	0.0	0.0	0.0	0.0	0.0	0.1	0.0	0.0	0.0	0.0	0.0	0.5	0.4
Cr_2O_3	0.0	0.0	0.1	0.0	0.0	0.0	0.0	0.0	0.0	0.0	0.0	0.0	0.0	0.0	0.0	0.0	0.0	0.1	0.0	0.0	0.0	0.0	0.0	0.0	0.0	0.0	0.0	0.1	0.1
Tot	***100.3***	***100.4***	***99.8***	***99.9***	***99.8***	***99.8***	***99.8***	***99.9***	***99.8***	***99.8***	***101.0***	***100.2***	***99.1***	***98.8***	***99.4***	***99.2***	***100.5***	***101.7***	***101.1***	***100.0***	***100.0***	***100.6***	***100.6***	***100.3***	***100.4***	***100.6***	***101.4***	***97.6***	***97.4***
Si	2.14	2.48	2.30	2.43	2.46	2.45	2.39	2.40	2.40	2.43	2.41	2.50	2.49	2.49	2.46	2.44	2.41	2.35	2.32	2.22	2.26	2.28	2.56	2.32	2.22	2.22	2.38	6.24	6.29
Ti	0.00	0.00	0.00	0.00	0.00	0.00	0.00	0.00	0.00	0.00	0.08	0.00	0.00	0.00	0.00	0.00	0.00	0.00	0.00	0.00	0.00	0.00	0.00	0.00	0.00	0.00	0.00	0.16	0.09
Al	1.84	1.50	1.52	1.55	1.52	1.52	1.58	1.59	1.59	1.53	1.45	1.51	1.50	1.48	1.51	1.52	1.58	1.64	1.68	1.74	1.73	1.71	1.42	1.67	1.74	1.75	1.60	2.25	2.10
Fe tot	0.02	0.01	0.09	0.02	0.01	0.01	0.01	0.01	0.01	0.02	0.04	0.01	0.01	0.01	0.01	0.01	0.01	0.01	0.02	0.04	0.01	0.01	0.01	0.01	0.02	0.02	0.01	1.59	1.45
Mn	0.00	0.00	0.00	0.00	0.00	0.00	0.00	0.00	0.00	0.00	0.00	0.00	0.00	0.00	0.00	0.00	0.00	0.00	0.00	0.00	0.00	0.00	0.00	0.00	0.00	0.00	0.00	0.01	0.03
Mg	0.01	0.00	0.18	0.01	0.00	0.00	0.00	0.00	0.00	0.00	0.01	0.00	0.00	0.00	0.00	0.00	0.00	0.00	0.01	0.05	0.00	0.00	0.00	0.00	0.00	0.00	0.00	2.74	3.05
Ca	0.85	0.47	0.49	0.50	0.49	0.48	0.54	0.54	0.55	0.49	0.46	0.46	0.46	0.45	0.46	0.49	0.55	0.62	0.64	0.74	0.74	0.72	0.44	0.69	0.76	0.78	0.60	1.79	1.69
Na	0.14	0.54	0.41	0.48	0.51	0.53	0.47	0.46	0.45	0.53	0.54	0.51	0.54	0.57	0.55	0.53	0.44	0.38	0.33	0.21	0.26	0.28	0.56	0.31	0.25	0.22	0.40	0.75	0.64
K	0.00	0.00	0.00	0.00	0.00	0.00	0.00	0.00	0.00	0.00	0.00	0.00	0.00	0.00	0.00	0.00	0.00	0.00	0.00	0.00	0.00	0.00	0.00	0.00	0.00	0.00	0.00	0.08	0.07
Cr	0.00	0.00	0.00	0.00	0.00	0.00	0.00	0.00	0.00	0.00	0.00	0.00	0.00	0.00	0.00	0.00	0.00	0.00	0.00	0.00	0.00	0.00	0.00	0.00	0.00	0.00	0.00	0.01	0.00
SUM	***5.00***	***5.00***	***5.00***	***5.00***	***5.00***	***5.00***	***5.00***	***5.00***	***5.00***	***5.00***	***5.00***	***5.00***	***5.00***	***5.00***	***5.00***	***5.00***	***5.00***	***5.00***	***5.00***	***5.00***	***5.00***	***5.00***	***5.00***	***5.00***	***5.00***	***5.00***	***5.00***	***13.00***	***13.00***
Mg# totFe																												63.3	67.8
MgO/(MgO +FeO)*100																												49.2	54.2
Fe2+																												1.07	0.39
Fe3+																												0.51	1.06
Al (T)																												1.76	1.71
Al (M1)																												0.49	0.39
An	85.7	46.6	54.4	50.9	48.8	47.5	53.4	54.3	54.6	48.0	45.8	47.1	45.7	44.4	45.8	47.9	55.9	61.9	65.4	77.7	73.9	71.9	44.2	69.0	75.5	77.7	60.3		
Ab	14.2	53.3	45.4	48.8	51.1	52.3	46.3	45.6	45.2	52.0	53.9	52.9	54.2	55.5	54.1	52.0	44.0	38.0	34.4	22.2	25.9	27.7	55.6	31.0	24.5	22.2	39.5		
Or	0.1	0.2	0.2	0.3	0.2	0.2	0.2	0.2	0.2	0.1	0.3	0.0	0.1	0.1	0.1	0.1	0.1	0.1	0.2	0.1	0.2	0.4	0.2	0.1	0.1	0.1	0.2		

(D) cont.

	(E) Matrix / Intestitial																							
	Clinopyroxene									Orthopyroxene														
	F33			F20A		F32A				F33		F20A			F10B				F32A					
wt%	F33-S2-cpx7	F33-S1-cpx10	F33-S5-cpx15	F20A-S6-cpx23	F20A-S6-cpx26	F32A-S4-cpx12	F32A-S11-cpx29	F32A-S13-cpx37	F32A-S21-cpx66	F33-S1-opx9	F33-S5-opx14	F20A-S4-opx15	F20A-S1-opx3	F20A-S6-opx25	F10B-S1-opx2	F10B-S1-opx8	F10B-S2-opx13	F10B-S7-opx25	F32A-S4-opx14	F32A-S8-opx21	F32A-S11-opx28	F32A-S11-opx32	F32A-S19-opx57	F32A-S21-opx64
SiO_2	54.6	54.6	54.6	53.2	53.1	53.2	53.0	53.9	53.2	54.3	54.0	53.9	52.0	52.9	52.3	52.8	52.9	52.8	53.3	53.5	54.5	54.3	53.9	54.5
TiO_2	0.2	0.1	0.1	0.1	0.2	0.3	0.3	0.2	0.2	0.0	0.5	0.1	0.1	0.1	0.0	0.1	0.0	0.1	0.1	0.0	0.0	0.1	0.1	0.1
Al_2O_3	1.9	1.2	0.9	1.8	1.7	2.4	2.4	1.7	1.5	0.4	1.4	0.9	1.5	1.5	1.4	0.9	0.7	0.8	1.7	1.6	0.9	1.0	1.5	0.9
FeO	6.8	6.4	5.8	8.9	8.6	7.4	8.1	7.5	7.2	20.7	19.7	25.2	26.6	25.3	25.2	24.7	25.5	25.4	21.0	21.1	21.6	21.1	19.6	21.2
MnO	0.2	0.3	0.2	0.3	0.2	0.3	0.3	0.3	0.3	0.6	0.6	0.6	0.6	0.6	0.6	0.6	0.6	0.7	0.7	0.7	0.8	0.9	0.9	0.7
MgO	14.9	15.1	15.4	13.8	13.8	14.3	14.2	14.9	14.7	24.5	24.8	20.9	20.2	20.5	20.8	20.9	20.8	20.7	23.4	23.6	24.2	23.5	25.0	24.7
CaO	22.4	22.8	23.5	22.5	22.3	22.6	22.4	23.3	22.7	0.5	0.4	0.4	0.5	0.4	0.6	0.5	0.5	0.6	0.4	0.3	0.3	0.4	0.4	0.5
Na_2O	0.4	0.5	0.3	0.4	0.5	0.5	0.6	0.5	0.5	0.0	0.1	0.0	0.0	0.0	0.0	0.0	0.0	0.0	0.1	0.0	0.0	0.0	0.0	0.0
K_2O	0.0	0.0	0.0	0.0	0.0	0.0	0.0	0.0	0.0	0.0	0.0	0.0	0.0	0.0	0.0	0.0	0.0	0.0	0.0	0.0	0.0	0.0	0.0	0.0
Cr_2O_3	0.0	0.0	0.0	0.1	0.0	0.1	0.0	0.0	0.0	0.0	0.0	0.0	0.1	0.0	0.0	0.0	0.0	0.0	0.1	0.1	0.0	0.0	0.0	0.0
Tot	***101.4***	***101.0***	***100.9***	***101.0***	***100.4***	***101.0***	***101.2***	***102.2***	***100.3***	***101.1***	***101.4***	***102.0***	***101.5***	***101.4***	***101.0***	***100.6***	***101.1***	***101.0***	***100.9***	***100.9***	***102.4***	***101.4***	***101.5***	***102.6***
Si	1.99	2.00	1.99	1.96	1.97	1.95	1.94	1.95	1.96	1.98	1.96	1.99	1.94	1.97	1.95	1.98	1.97	1.97	1.95	1.96	1.97	1.98	1.95	1.96
Ti	0.00	0.00	0.00	0.00	0.00	0.01	0.01	0.00	0.01	0.00	0.01	0.00	0.00	0.00	0.00	0.00	0.00	0.00	0.00	0.00	0.00	0.00	0.00	0.00
Al	0.08	0.05	0.04	0.08	0.08	0.10	0.10	0.07	0.07	0.02	0.06	0.04	0.07	0.07	0.06	0.04	0.03	0.03	0.07	0.07	0.04	0.04	0.07	0.04
Fe tot	0.21	0.19	0.18	0.27	0.27	0.23	0.25	0.23	0.22	0.63	0.60	0.78	0.83	0.79	0.79	0.77	0.79	0.79	0.64	0.65	0.65	0.65	0.59	0.64
Mn	0.01	0.01	0.01	0.01	0.01	0.01	0.01	0.01	0.01	0.02	0.02	0.02	0.02	0.02	0.02	0.02	0.02	0.02	0.02	0.02	0.02	0.03	0.03	0.02
Mg	0.81	0.82	0.84	0.76	0.76	0.78	0.77	0.80	0.80	1.33	1.34	1.15	1.12	1.14	1.16	1.17	1.16	1.15	1.28	1.29	1.30	1.28	1.35	1.32
Ca	0.87	0.89	0.92	0.89	0.89	0.89	0.88	0.90	0.90	0.02	0.01	0.02	0.02	0.02	0.02	0.02	0.02	0.02	0.02	0.01	0.01	0.02	0.01	0.02
Na	0.03	0.03	0.02	0.03	0.03	0.04	0.04	0.04	0.04	0.00	0.00	0.00	0.00	0.00	0.00	0.00	0.00	0.00	0.00	0.00	0.00	0.00	0.00	0.00
K	0.00	0.00	0.00	0.00	0.00	0.00	0.00	0.00	0.00	0.00	0.00	0.00	0.00	0.00	0.00	0.00	0.00	0.00	0.00	0.00	0.00	0.00	0.00	0.00
Cr	0.00	0.00	0.00	0.00	0.00	0.00	0.00	0.00	0.00	0.00	0.00	0.00	0.00	0.00	0.00	0.00	0.00	0.00	0.00	0.00	0.00	0.00	0.00	0.00
SUM	***4.00***	***4.00***	***4.00***	***4.00***	***4.00***	***4.00***	***4.00***	***4.00***	***4.00***	***4.00***	***4.00***	***4.00***	***4.00***	***4.00***	***4.00***	***4.00***	***4.00***	***4.00***	***4.00***	***4.00***	***4.00***	***4.00***	***4.00***	***4.00***
Mg# totFe	79.7	80.9	82.5	73.5	74.1	77.4	75.8	77.9	78.4	67.9	69.2	59.7	57.6	59.1	59.5	60.1	59.3	59.2	66.5	66.5	66.6	66.5	69.5	67.6
MgO/(MgO+FeO)*100	68.8	70.4	72.6	60.8	61.6	65.8	63.7	66.5	67.0	54.2	55.8	45.4	43.2	44.8	45.2	45.8	45.0	44.9	52.6	52.7	52.8	52.7	56.1	53.9
Fe2+	0.21	0.19	0.18	0.25	0.25	0.2	0.2	0.16	0.19	0.61	0.59	0.78	0.78	0.79	0.8	0.77	0.78	0.8	0.63	0.64	0.63	0.65	0.56	0.59
Fe3+	0.00	0.00	0.00	0.02	0.02	0.02	0.04	0.06	0.04	0.02	0.01	0.00	0.05	0.00	0.03	0.00	0.02	0.02	0.01	0.01	0.03	0.00	0.04	0.04
Al (T)	0.01	0.00	0.01	0.04	0.03	0.05	0.06	0.05	0.04	0.02	0.04	0.01	0.06	0.03	0.05	0.02	0.03	0.03	0.05	0.04	0.03	0.02	0.05	0.04
Al (M1)	0.07	0.05	0.03	0.04	0.04	0.05	0.05	0.02	0.03	0.00	0.01	0.03	0.00	0.04	0.01	0.02	0.01	0.01	0.03	0.03	0.01	0.03	0.01	0.00
Wo	46.2	46.8	47.4	46.3	46.4	46.9	46.3	46.6	46.6	1.0	0.7	0.8	0.9	0.9	1.15	1.1	1.0	1.19	0.9	0.7	0.7	0.8	0.7	1.0
En	42.8	43.0	43.4	39.5	39.7	41.1	40.7	41.6	41.9	67.2	68.7	59.2	57.0	58.6	58.8	59.5	58.7	58.5	65.9	66.1	66.2	65.9	69.0	66.9
Fs	10.9	10.2	9.2	14.3	13.9	12.0	13.0	11.8	11.6	31.8	30.6	40.0	42.1	40.5	40.0	39.4	40.3	40.3	33.2	33.2	33.2	33.2	30.3	32.1

Table (E)

(E) Matrix / Intestitial

	Plagioclase									Amphibole																
	F33		F20A		F10B	F32A				F33					F20A			F10B	F32A							
wt%	F33-S1-pl11	F33-S1-pl4	F20A-S4-pl18	F20A-S6-pl27	F10B-S7-pl26	F32A-S4-pl15	F32A-S12-pl34	F32A-S19-pl58	F32A-S21-pl67	F33-S1-am8	F33-S1-am2	F33-S8-am21	F33-S5-am16	F33-S1-am3	F20A-S2-am8	F20A-S2-am9	F20A-S6-am24	F10B-S7-am24	F32A-S3-am8	F32A-S4-am13	F32A-S11-am30	F32A-S12-am31	F32A-S12-am33	F32A-S13-am38	F32A-S18-am50	F32A-S18-am52	F32A-S19-am56	F32A-S20-am61	F32A-S20-am62	F32A-S21-am65
SiO_2	56.7	56.2	59.9	55.0	51.9	52.1	55.3	48.0	56.3	44.6	42.8	42.6	46.0	43.8	42.2	42.3	42.7	40.7	46.0	44.3	44.9	44.0	44.8	44.8	43.9	44.3	46.9	45.3	44.5	44.1
TiO_2	0.0	0.1	0.0	0.0	0.0	0.0	0.0	0.0	0.1	2.3	2.4	3.0	1.6	2.1	1.8	2.7	2.1	4.0	1.3	1.4	1.4	2.3	2.1	1.9	2.1	2.0	0.3	2.0	2.1	2.2
Al_2O_3	27.9	28.0	25.3	28.9	31.0	30.1	28.2	33.3	28.2	11.5	12.9	13.2	11.4	12.7	12.5	12.8	12.5	13.1	10.1	11.3	11.3	11.4	11.2	11.2	11.5	12.0	10.0	10.9	11.6	11.4
FeO	0.3	0.3	0.5	0.4	0.6	0.6	0.4	0.8	0.4	10.5	12.4	11.7	9.3	11.8	14.7	14.5	13.5	14.6	11.0	11.3	11.3	11.6	11.1	11.2	13.1	11.3	10.0	10.1	11.4	11.7
MnO	0.0	0.0	0.0	0.0	0.0	0.0	0.0	0.0	0.0	0.2	0.1	0.1	0.1	0.1	0.1	0.2	0.1	0.2	0.2	0.2	0.1	0.2	0.1	0.2	0.2	0.2	0.2	0.2	0.2	0.2
MgO	0.0	0.0	0.0	0.0	0.0	0.0	0.0	0.0	0.0	14.1	12.8	12.9	15.0	13.5	12.1	11.1	12.4	10.4	15.1	14.2	14.5	13.8	14.0	14.6	12.9	14.1	16.4	14.7	13.7	13.9
CaO	9.9	10.3	7.5	11.2	13.6	12.9	11.0	16.2	10.0	11.9	11.7	11.7	12.1	11.8	11.5	11.4	11.6	11.6	11.9	11.7	11.8	11.6	11.8	11.8	11.5	11.8	11.4	12.1	11.7	11.5
Na_2O	6.3	6.0	7.7	5.4	4.1	4.2	5.6	2.2	5.9	2.5	2.6	2.9	2.2	2.5	2.9	3.2	2.7	2.6	2.1	2.2	2.4	2.2	2.2	2.4	2.5	2.4	2.1	2.1	2.4	2.2
K_2O	0.0	0.0	0.0	0.0	0.1	0.0	0.1	0.0	0.0	0.3	0.5	0.3	0.1	0.5	0.4	0.3	0.4	1.4	0.2	0.5	0.3	0.6	0.5	0.4	0.4	0.6	0.1	0.4	0.4	0.5
Cr_2O_3	0.0	0.0	0.0	0.0	0.0	0.0	0.0	0.0	0.0	0.1	0.0	0.1	0.0	0.1	0.0	0.0	0.0	0.1	0.0	0.1	0.0	0.0	0.0	0.0	0.1	0.0	0.1	0.0	0.1	0.2
Tot	***101.3***	***100.8***	***100.9***	***100.9***	***101.2***	***100.1***	***100.6***	***100.6***	***100.9***	***98.0***	***98.3***	***98.5***	***97.9***	***98.9***	***98.3***	***98.4***	***98.2***	***98.7***	***97.8***	***97.1***	***97.8***	***97.7***	***97.9***	***98.7***	***98.1***	***98.6***	***97.4***	***97.7***	***98.1***	***97.9***
Si	2.51	2.50	2.66	2.46	2.33	2.36	2.48	2.19	2.51	6.45	6.22	6.18	6.57	6.29	6.18	6.23	6.23	6.06	6.60	6.44	6.46	6.38	6.48	6.41	6.39	6.35	6.63	6.54	6.44	6.36
Ti	0.00	0.00	0.00	0.00	0.00	0.00	0.00	0.00	0.00	0.25	0.26	0.32	0.17	0.23	0.20	0.29	0.23	0.45	0.14	0.16	0.15	0.25	0.23	0.20	0.23	0.22	0.03	0.22	0.22	0.24
Al	1.46	1.47	1.32	1.52	1.64	1.61	1.49	1.79	1.48	1.97	2.22	2.26	1.93	2.15	2.15	2.23	2.15	2.30	1.70	1.92	1.91	1.96	1.91	1.89	1.97	2.03	1.66	1.84	1.97	1.94
Fe tot	0.01	0.01	0.02	0.01	0.02	0.02	0.02	0.03	0.02	1.26	1.51	1.42	1.11	1.42	1.80	1.78	1.65	1.82	1.31	1.37	1.36	1.40	1.34	1.34	1.59	1.35	1.18	1.22	1.38	1.41
Mn	0.00	0.00	0.00	0.00	0.00	0.00	0.00	0.00	0.00	0.03	0.02	0.02	0.02	0.01	0.02	0.02	0.02	0.02	0.02	0.02	0.01	0.02	0.02	0.03	0.03	0.02	0.03	0.02	0.02	0.02
Mg	0.00	0.00	0.00	0.00	0.00	0.00	0.00	0.00	0.00	3.03	2.78	2.79	3.20	2.89	2.64	2.44	2.71	2.30	3.23	3.08	3.10	2.98	3.02	3.12	2.79	3.02	3.45	3.17	2.95	3.00
Ca	0.47	0.49	0.35	0.54	0.65	0.63	0.53	0.79	0.48	1.84	1.83	1.81	1.85	1.82	1.80	1.80	1.81	1.86	1.83	1.82	1.81	1.81	1.82	1.80	1.79	1.82	1.73	1.87	1.82	1.78
Na	0.54	0.52	0.66	0.47	0.35	0.37	0.48	0.19	0.51	0.71	0.73	0.82	0.60	0.69	0.81	0.90	0.78	0.75	0.58	0.61	0.66	0.62	0.61	0.67	0.69	0.66	0.57	0.58	0.68	0.61
K	0.00	0.00	0.00	0.00	0.00	0.00	0.00	0.00	0.00	0.06	0.09	0.05	0.03	0.10	0.07	0.06	0.08	0.27	0.04	0.09	0.05	0.11	0.10	0.08	0.07	0.11	0.02	0.07	0.08	0.08
Cr	0.00	0.00	0.00	0.00	0.00	0.00	0.00	0.00	0.00	0.01	0.00	0.01	0.00	0.01	0.01	0.00	0.01	0.01	0.00	0.01	0.00	0.00	0.00	0.01	0.01	0.00	0.01	0.00	0.01	0.02
SUM	***5.00***	***5.00***	***5.00***	***5.00***	***5.00***	***5.00***	***5.00***	***5.00***	***5.00***	***13.00***	***13.00***	***13.00***	***13.00***	***13.00***	***13.00***	***13.00***	***13.00***	***12.97***	***13.00***	***13.00***	***13.00***	***13.00***	***13.00***	***13.00***	***13.00***	***13.00***	***13.00***	***13.00***	***13.00***	***13.00***
Mg# totFe										70.6	64.8	66.3	74.3	67.1	59.4	57.8	62.1	55.9	71.1	69.2	69.5	68.0	69.3	69.9	63.7	69.1	74.5	72.2	68.1	67.9
MgO/(MgO+FeO)*100										57.4	50.8	52.5	61.8	53.3	45.1	43.4	47.9	41.5	58.0	55.8	56.1	54.4	55.8	56.6	49.6	55.6	62.1	59.3	54.5	54.3
Fe2+										1.09	1.2	1.2	0.85	1.04	1.2	1.6	1.22	1.8	0.77	0.82	0.84	0.98	1.01	0.81	1.14	0.94	0.23	0.97	1.09	0.84
Fe3+										0.17	0.36	0.22	0.26	0.37	0.57	0.14	0.43	0.00	0.5	0.5	0.5	0.4	0.3	0.5	0.4	0.4	1.0	0.2	0.3	0.58
Al (T)										1.55	1.78	1.82	1.43	1.71	1.82	1.77	1.77	1.94	1.40	1.56	1.54	1.62	1.52	1.59	1.61	1.65	1.37	1.46	1.56	1.64
Al (M1)										0.42	0.43	0.44	0.49	0.44	0.34	0.46	0.39	0.37	0.30	0.36	0.37	0.34	0.39	0.30	0.36	0.39	0.30	0.38	0.42	0.30
An	46.4	48.6	35.0	53.5	64.6	62.6	51.9	80.5	48.4																					
Ab	53.3	51.2	64.9	46.3	34.9	37.2	47.6	19.4	51.4																					
Or	0.2	0.1	0.1	0.1	0.4	0.2	0.5	0.1	0.2																					

(E) cont.

Microprobe locations

Location of microprobe analyses. The numbers stand for sites, and correspond to the SEM - BSE images below (S=site. S1, S2 etc).

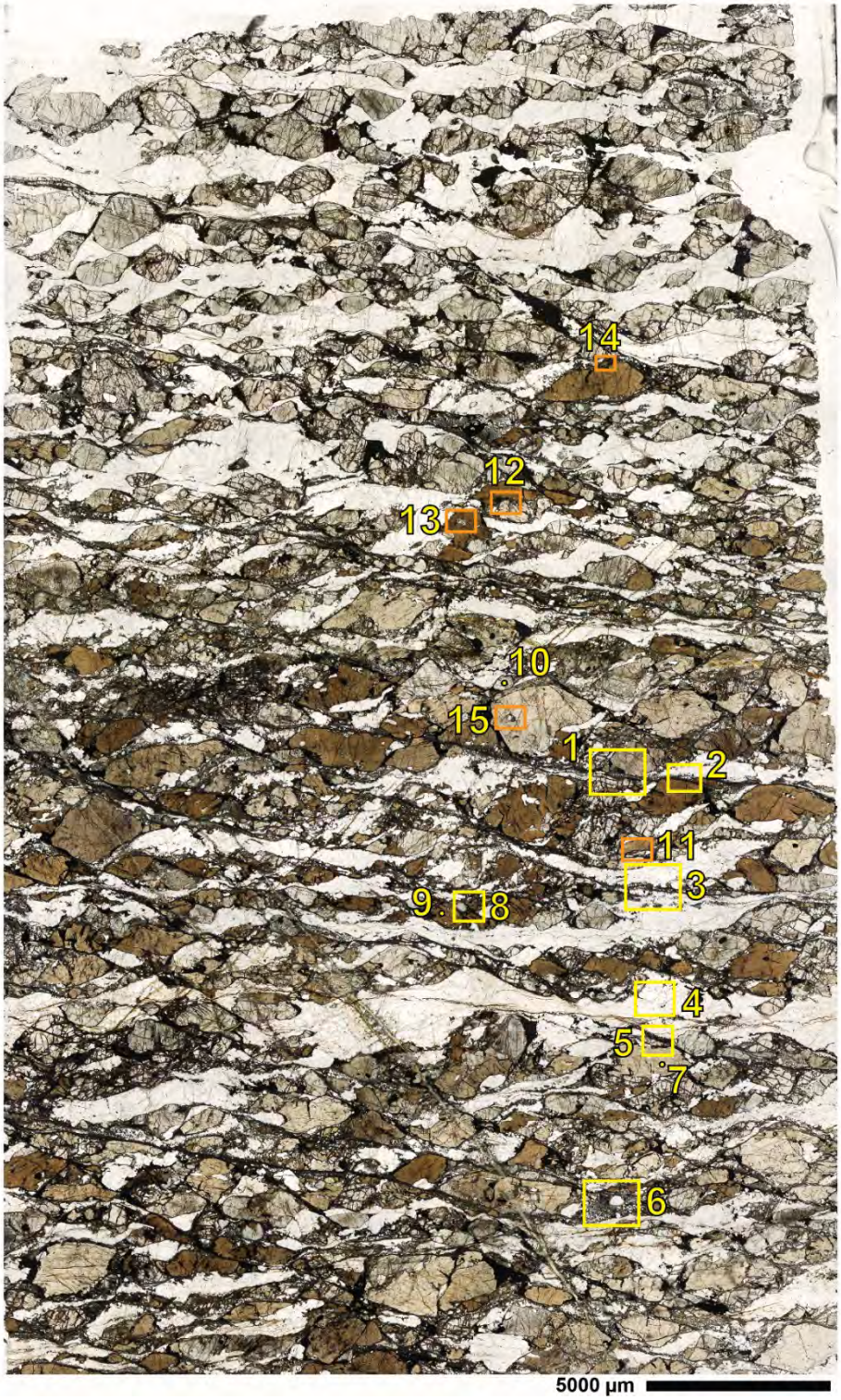

Sample F33

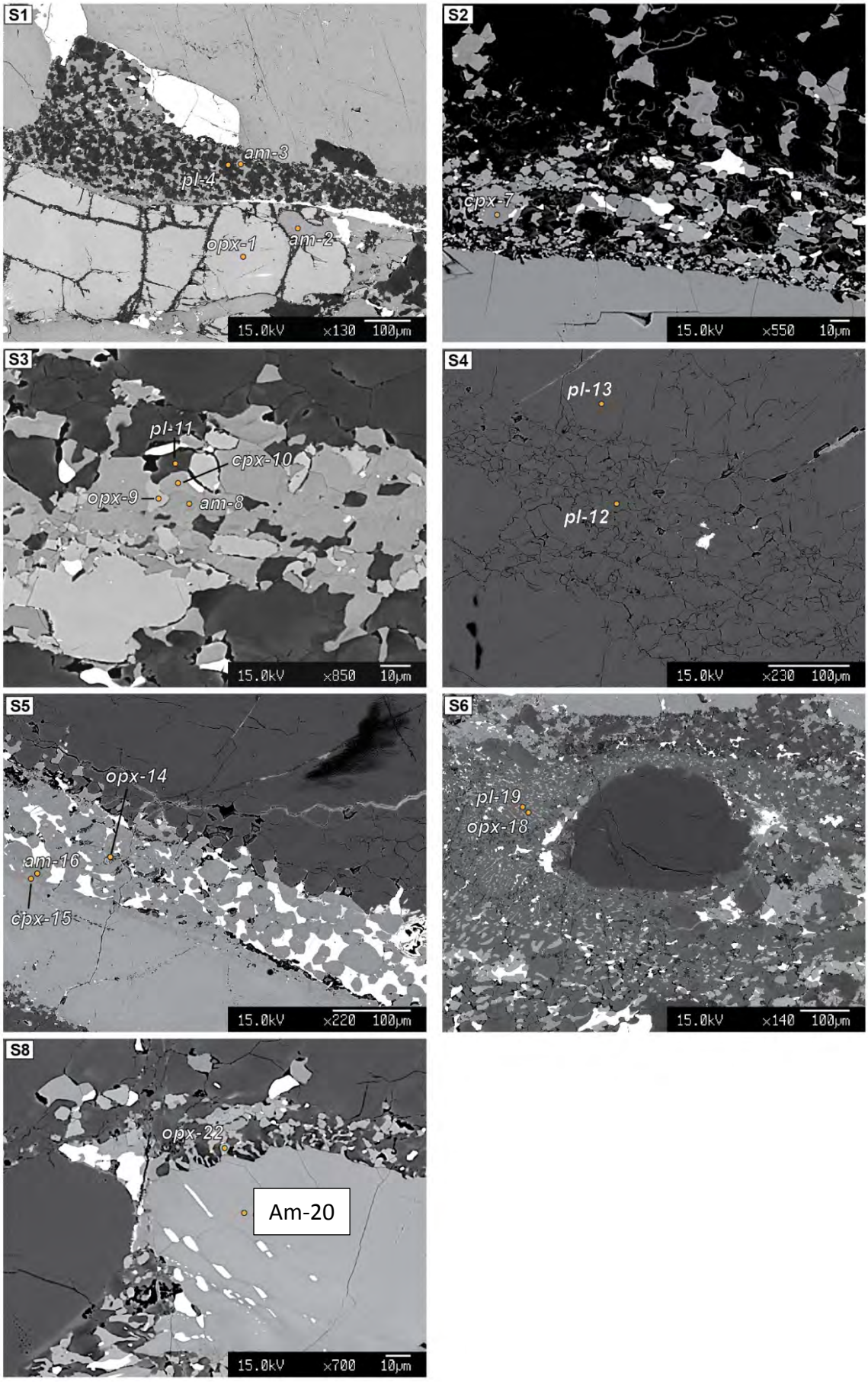
S1
am-3
pl-4
opx-1
am-2
15.0kV ×130 100µm
S2
cpx-7
15.0kV ×550 10µm
S3
pl-11
cpx-10
opx-9
am-8
15.0kV ×850 10µm
S4
pl-13
pl-12
15.0kV ×230 100µm
S5
opx-14
am-16
cpx-15
15.0kV ×220 100µm
S6
pl-19
opx-18
15.0kV ×140 100µm
S8
opx-22
Am-20
15.0kV ×700 10µm

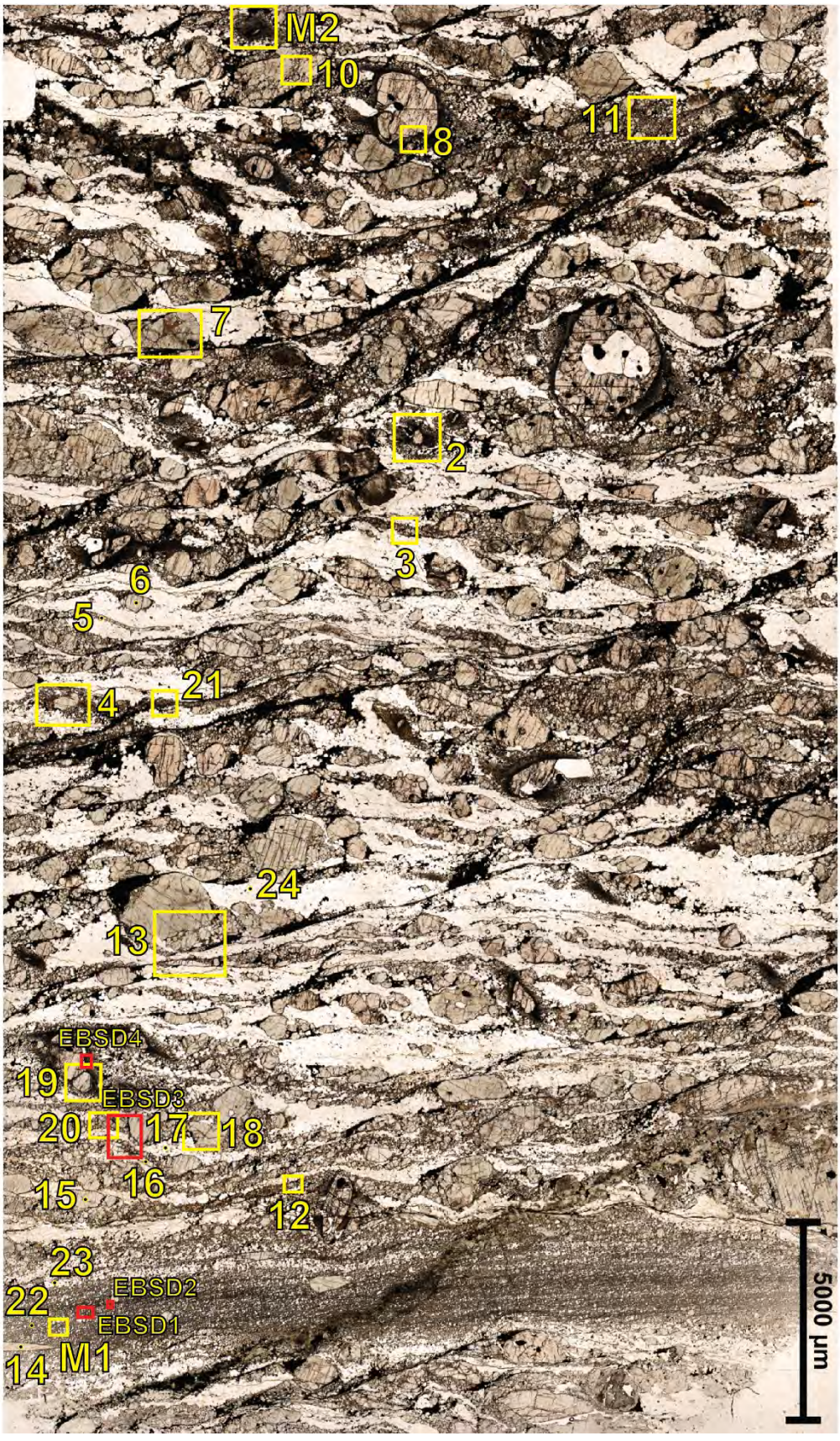

Sample F32A. In red, EBSD locations.

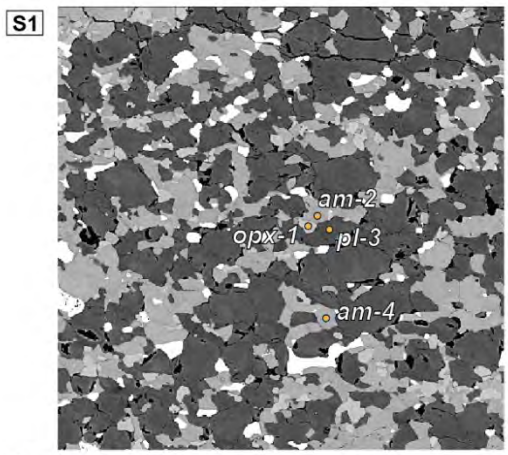
S1
am-2
opx-1
pl-3
am-4

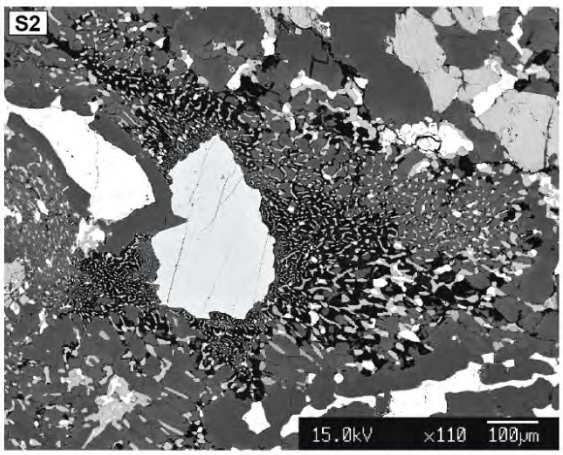
S2
15.0kV ×110 100µm

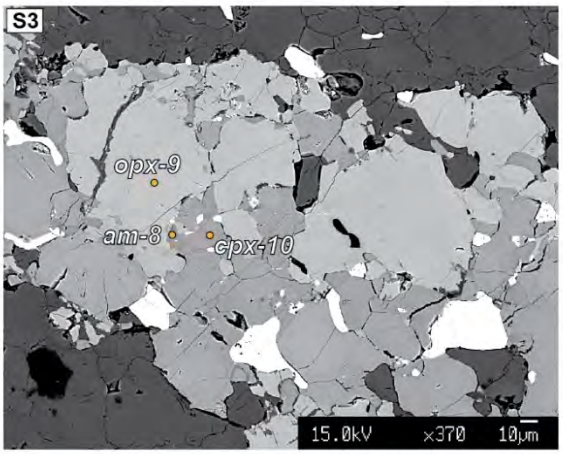
S3
opx-9
am-8
cpx-10
15.0kV ×370 10µm

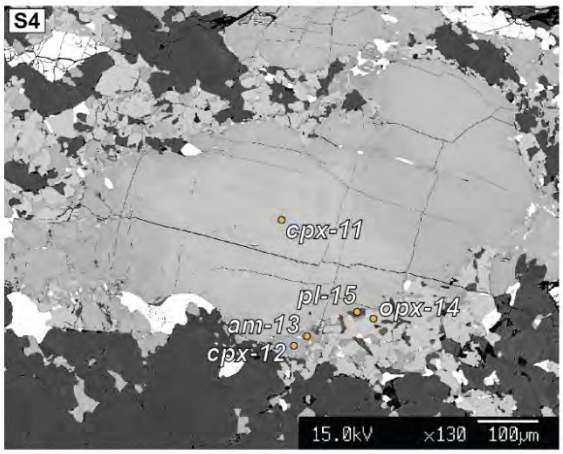
S4
cpx-11
pl-15
opx-14
am-13
cpx-12
15.0kV ×130 100µm

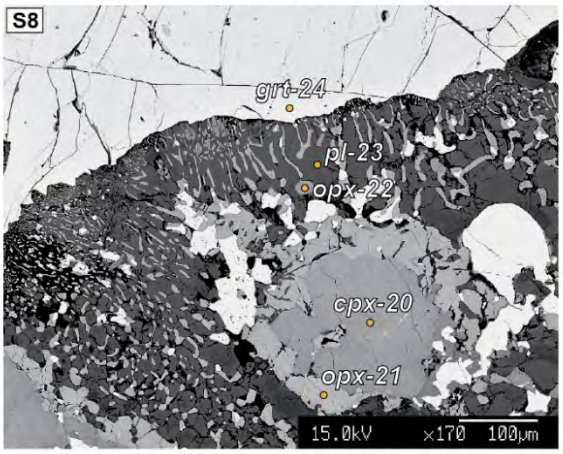
S8
grt-24
pl-23
opx-22
cpx-20
opx-21
15.0kV ×170 100µm

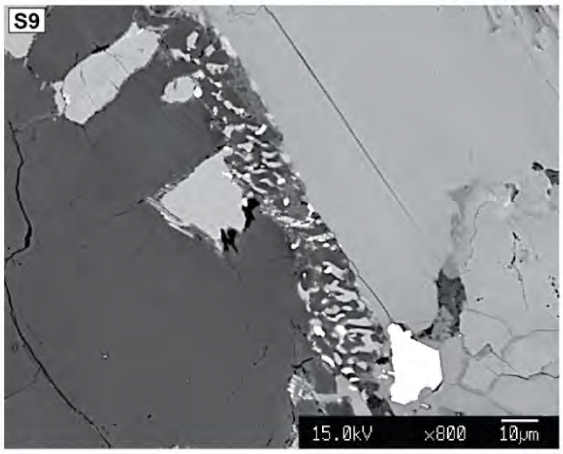
S9
15.0kV ×800 10µm

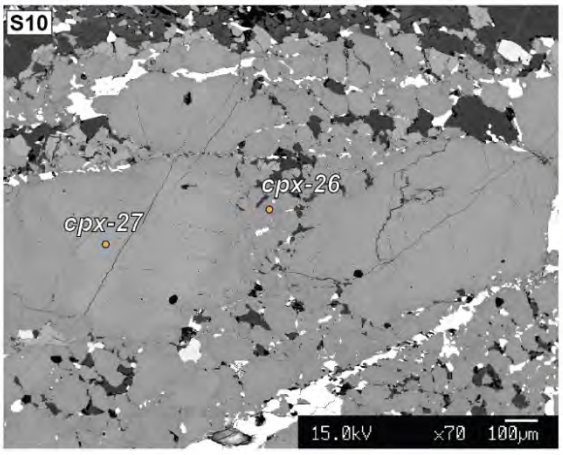
S10
cpx-26
cpx-27
15.0kV ×70 100µm

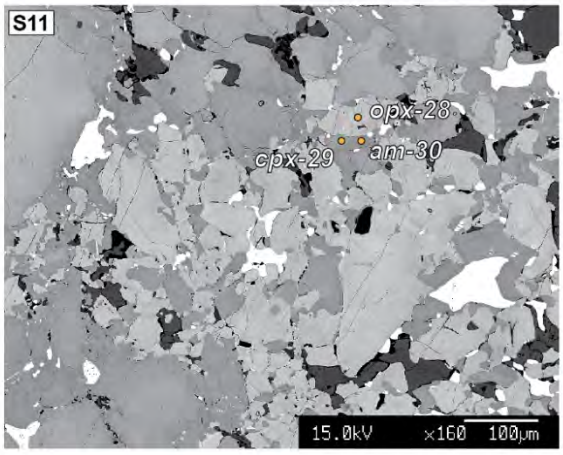
S11
opx-28
cpx-29
am-30
15.0kV ×160 100µm

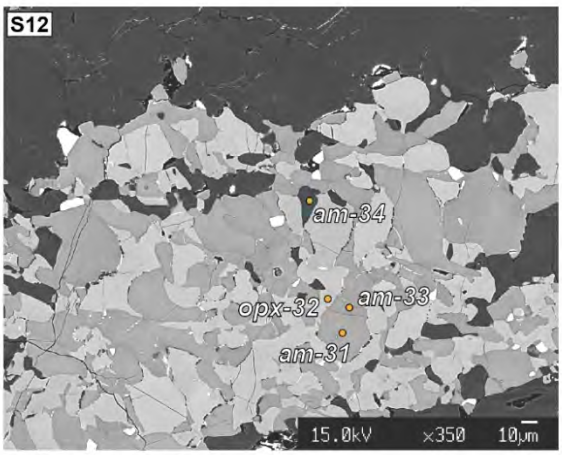
S12
am-34
opx-32
am-33
am-31
15.0kV ×350 10µm

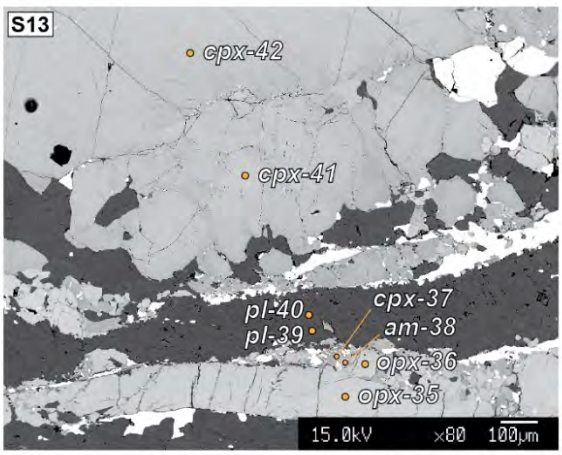
S13
cpx-42
cpx-41
pl-40
pl-39
cpx-37
am-38
opx-36
opx-35
15.0kV ×80 100µm

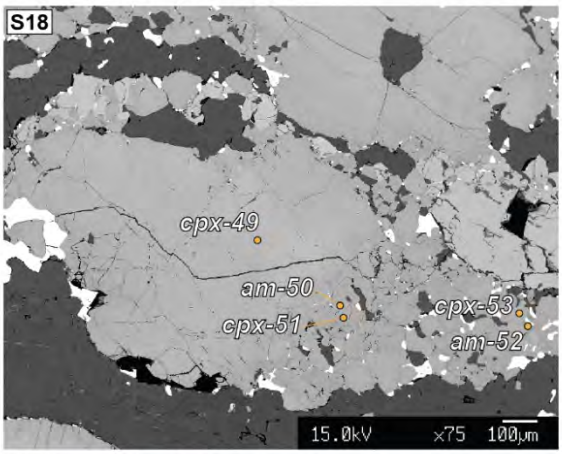
S18
cpx-49
am-50
cpx-51
cpx-53
am-52
15.0kV ×75 100µm

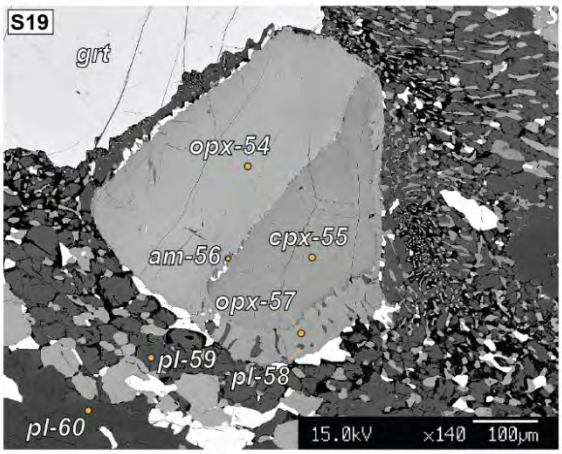
S19
grt
opx-54
am-56
cpx-55
opx-57
pl-59
pl-58
pl-60
15.0kV ×140 100µm

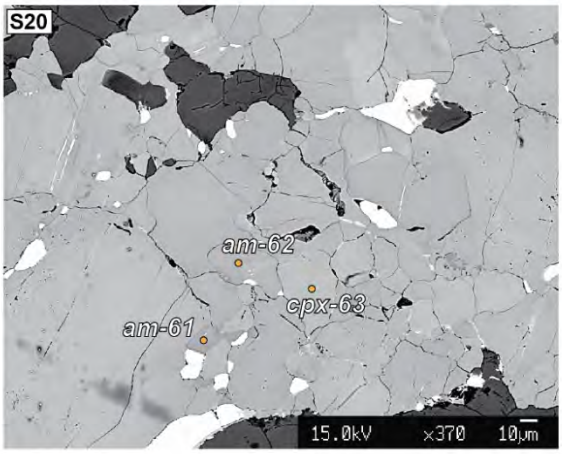
S20
am-62
cpx-63
am-61
15.0kV ×370 10µm


S21
opx-64
cpx-66
am-65
am
pl-67
15.0kV ×430 10µm

Sample F20A

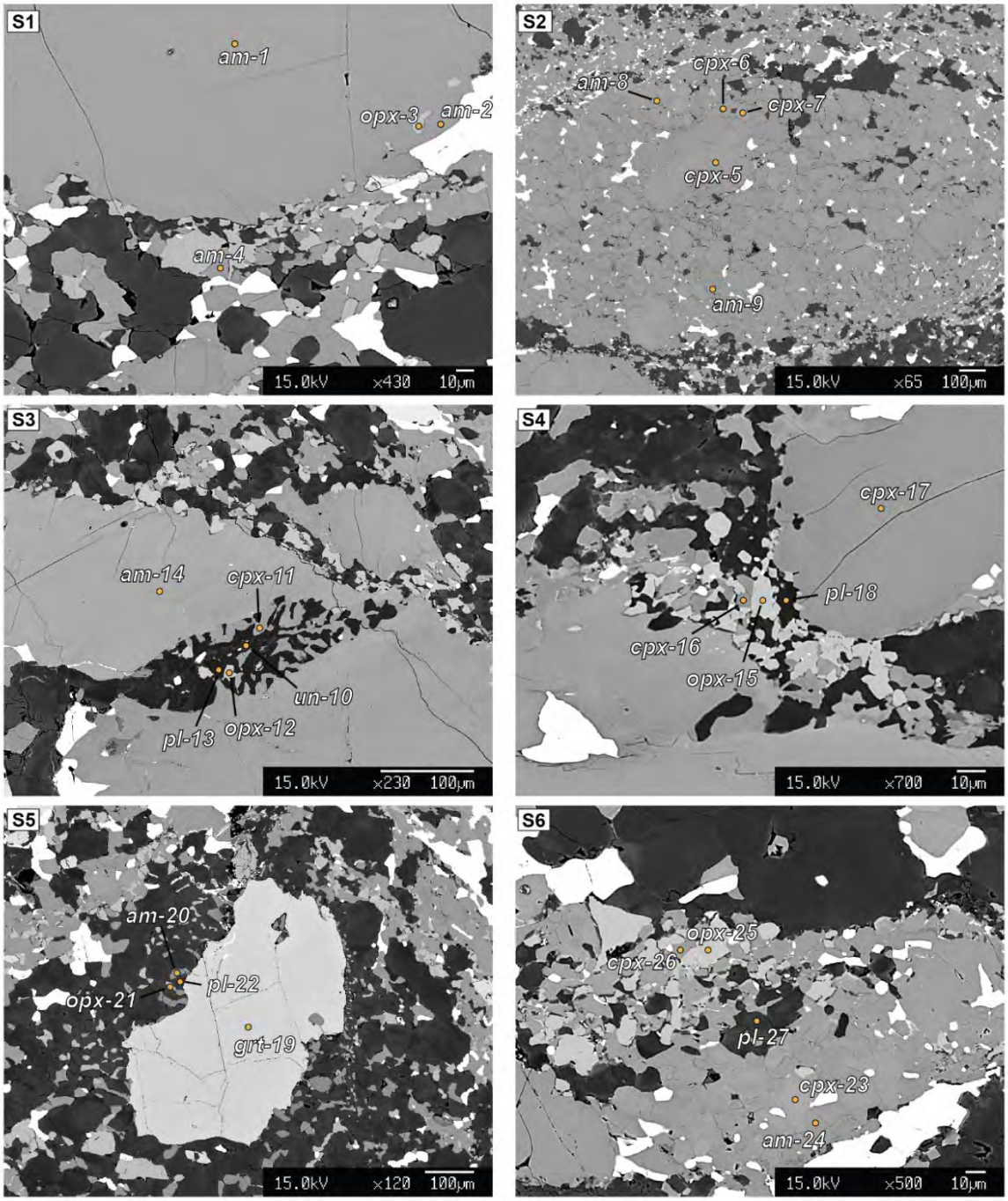
S1
am-1
opx-3
am-2
am-4
15.0kV ×430 10µm
S2
cpx-6
am-8
cpx-7
cpx-5
am-9
15.0kV ×65 100µm
S3
am-14
cpx-11
un-10
pl-13
opx-12
15.0kV ×230 100µm
S4
cpx-17
pl-18
cpx-16
opx-15
15.0kV ×700 10µm
S5
am-20
pl-22
opx-21
grt-19
15.0kV ×120 100µm
S6
opx-25
cpx-26
pl-27
cpx-23
am-24
15.0kV ×500 10µm

Sample F10B

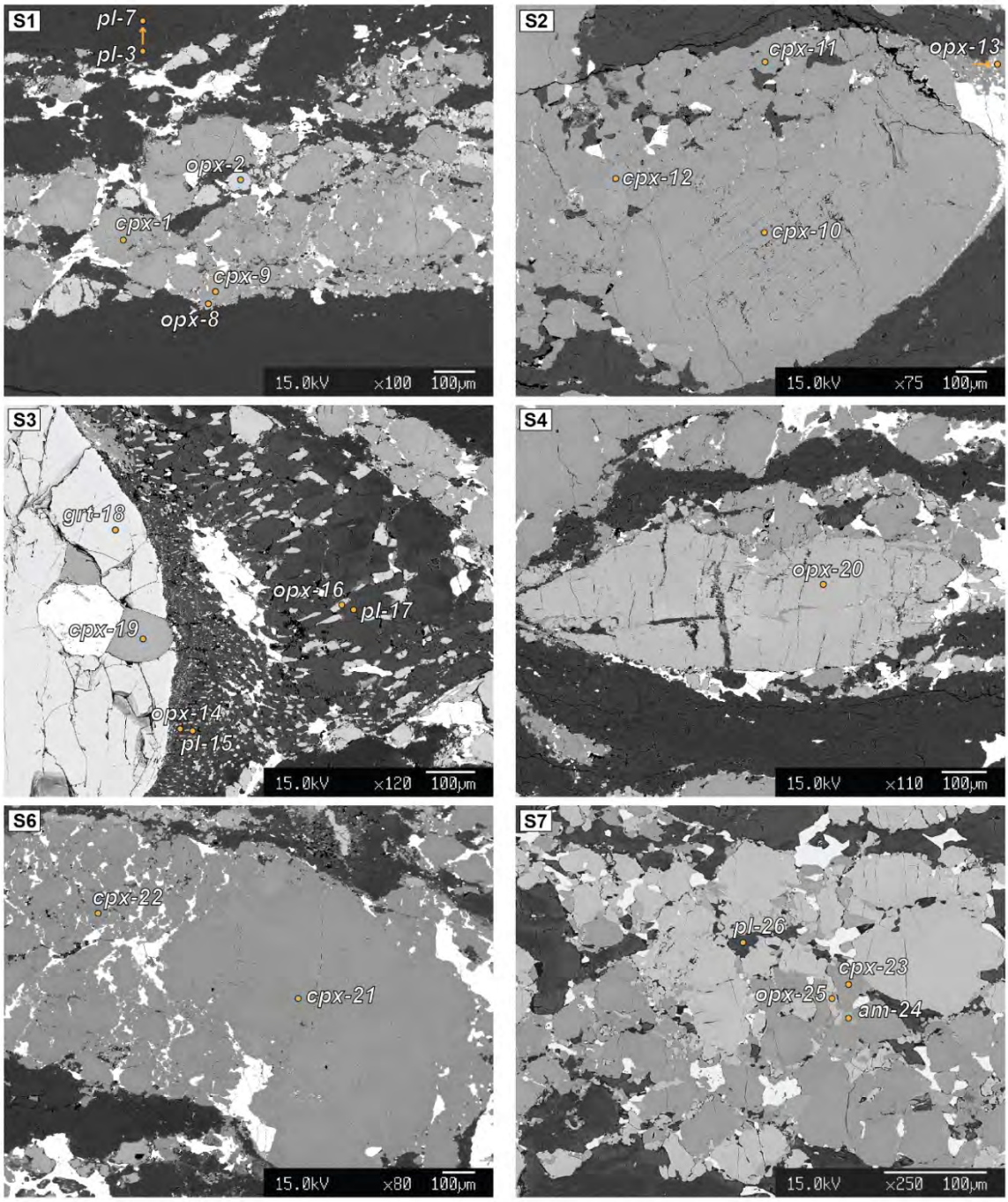
S1
pl-7
pl-3
opx-2
cpx-1
cpx-9
opx-8
15.0kV ×100 100µm
S2
cpx-11
opx-13
cpx-12
cpx-10
15.0kV ×75 100µm
S3
grt-18
opx-16
pl-17
cpx-19
opx-14
pl-15
15.0kV ×120 100µm
S4
opx-20
15.0kV ×110 100µm
S6
cpx-22
cpx-21
15.0kV ×80 100µm
S7
pl-26
cpx-23
opx-25
am-24
15.0kV ×250 100µm

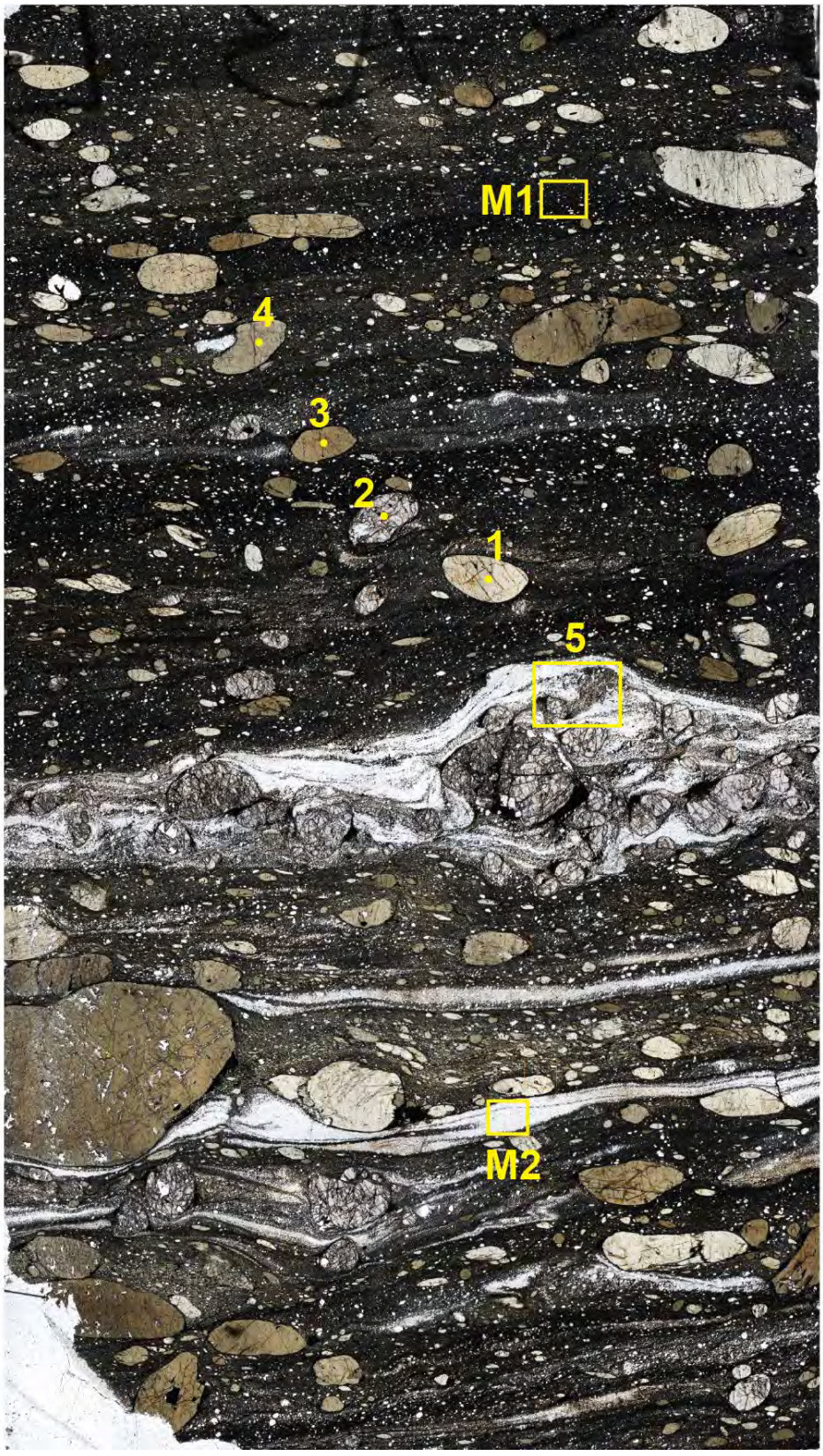

Sample F10A3.

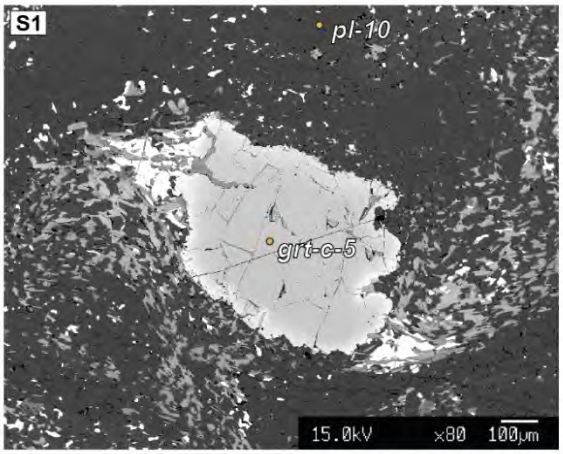
S1
pl-10
grt-c-5
15.0kV ×80 100µm

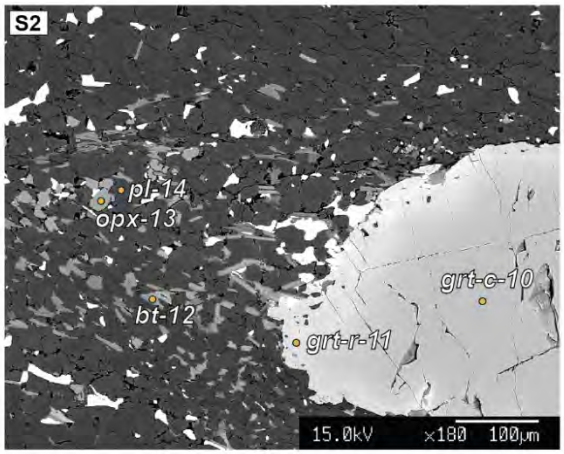
S2
pl-14
opx-13
bt-12
grt-r-11
grt-c-10
15.0kV ×180 100µm

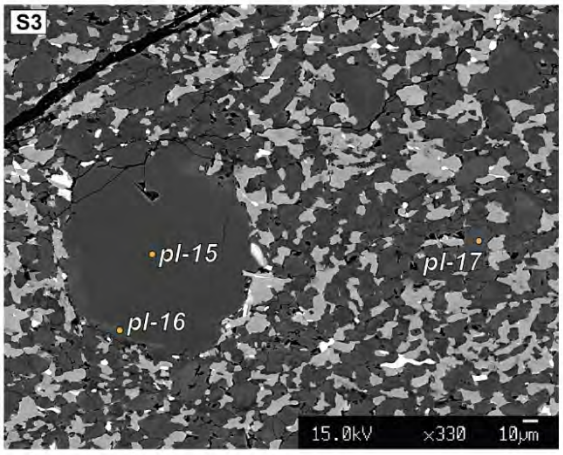
S3
pl-15
pl-16
pl-17
15.0kV ×330 10µm

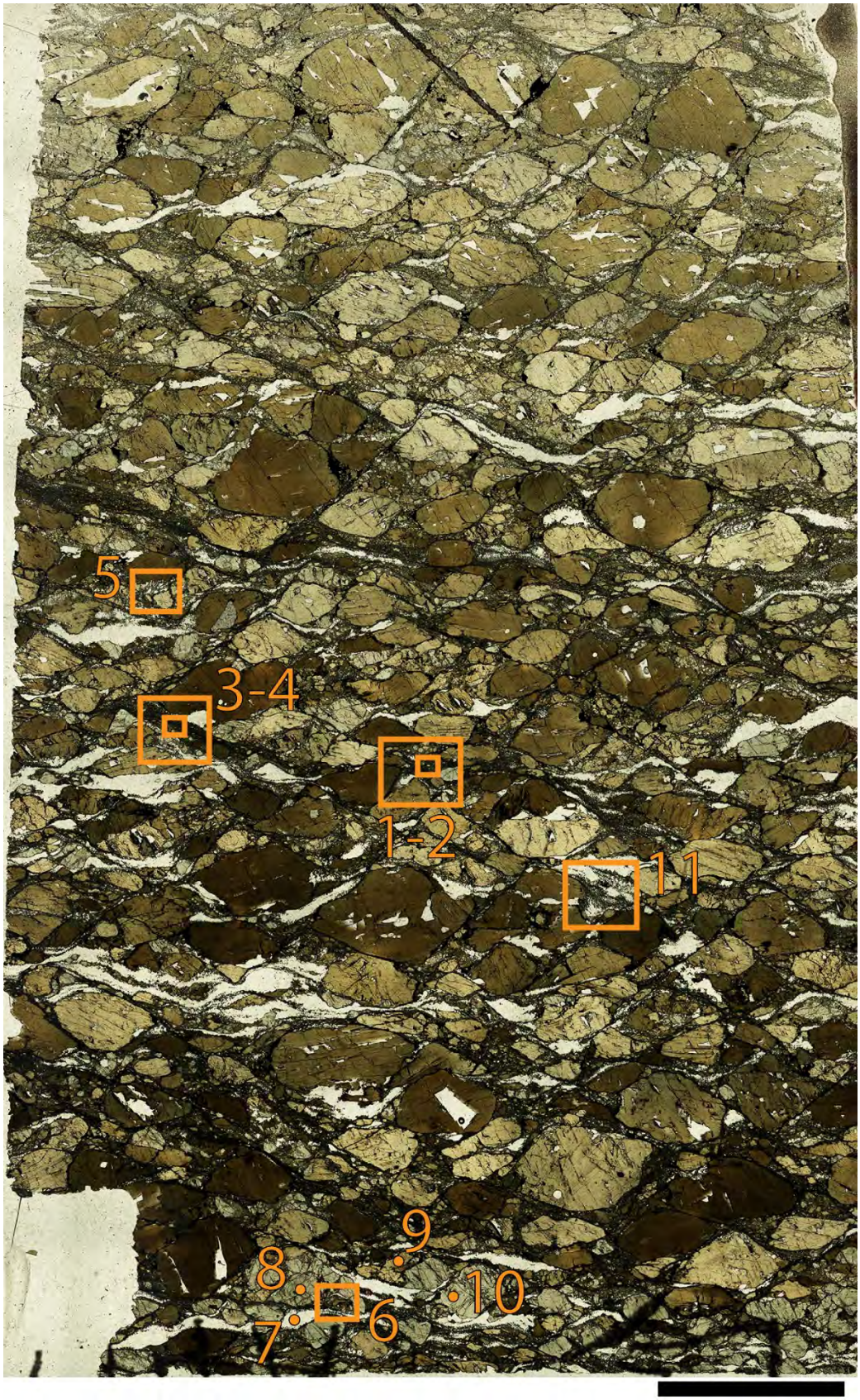

Sample F14B

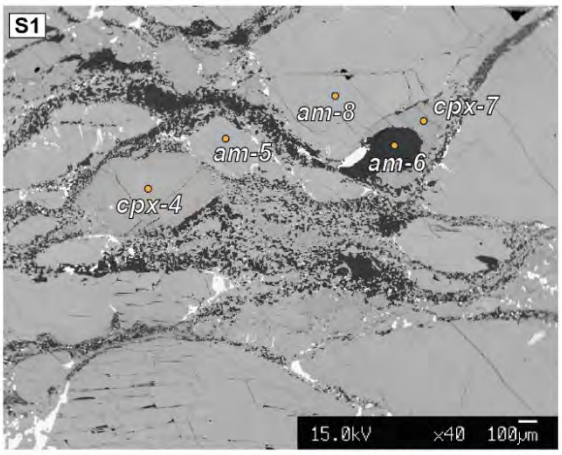
S1
am-8
cpx-7
am-5
am-6
cpx-4
15.0kV ×40 100µm

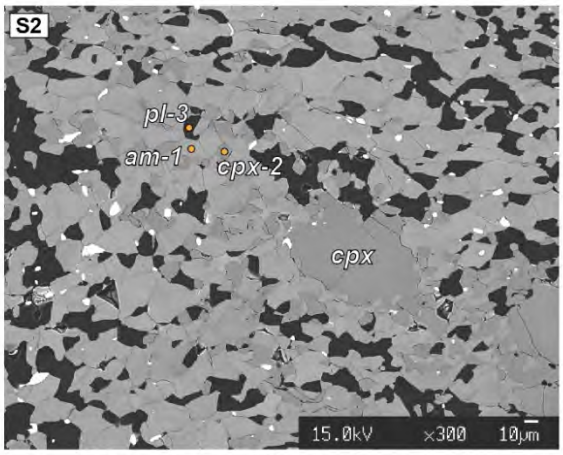
S2
pl-3
am-1
cpx-2
cpx
15.0kV ×300 10µm

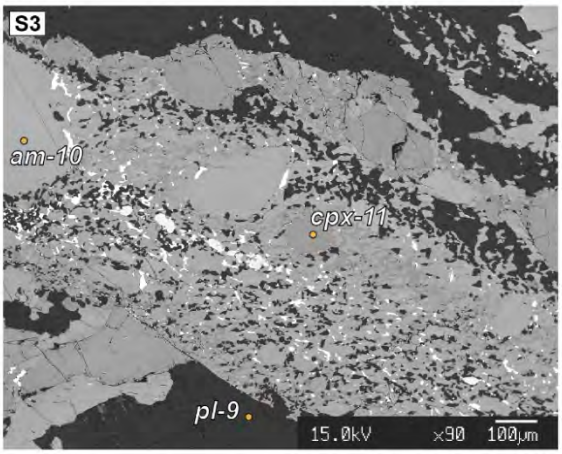
S3
am-10
cpx-11
pl-9
15.0kV ×90 100µm

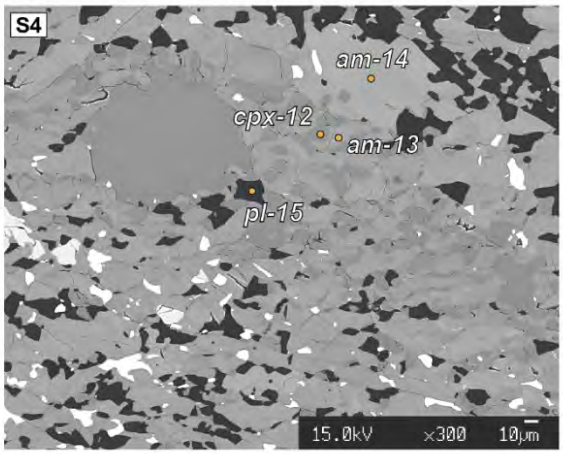
S4
am-14
cpx-12
am-13
pl-15
15.0kV ×300 10µm

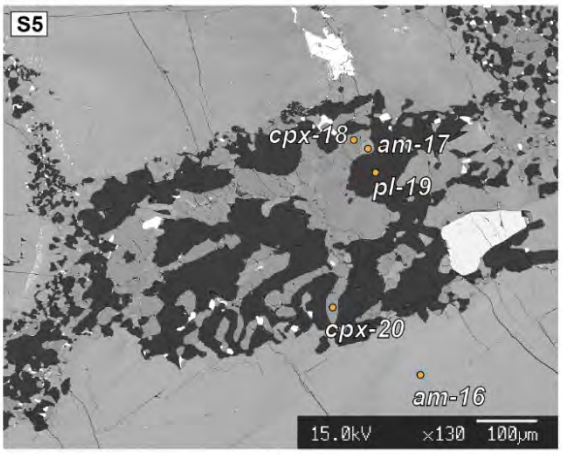
S5
cpx-18
am-17
pl-19
cpx-20
am-16
15.0kV ×130 100µm

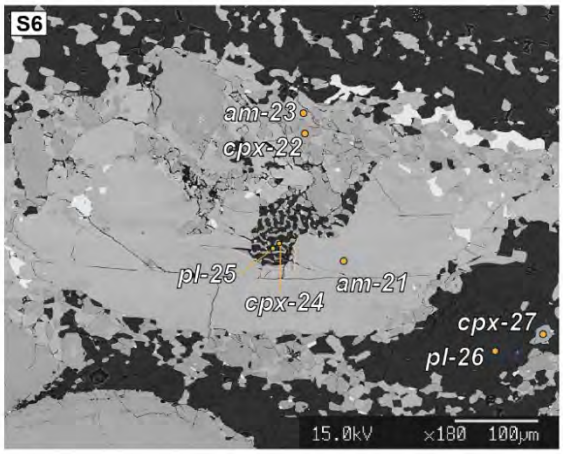
S6
am-23
cpx-22
pl-25
am-21
cpx-24
cpx-27
pl-26
15.0kV ×180 100µm

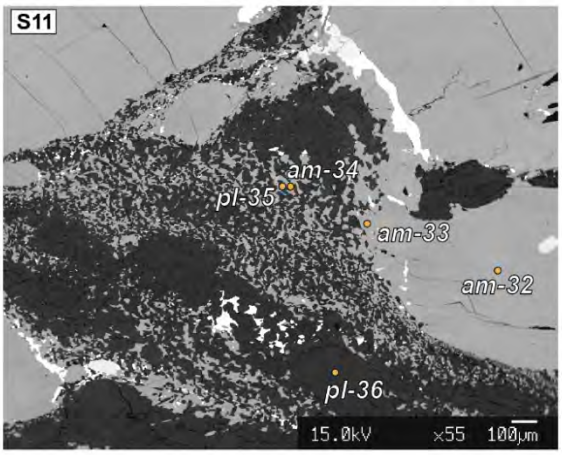
S11
am-34
pl-35
am-33
am-32
pl-36
15.0kV ×55 100µm

APPX. 7: EBSD EXTRA

Pole figures of plagioclase in the mylonite F20A, plotted as one-point-per-grain and contoured using a half-width of 15°. Strength of texture is given as m.u.d. Contours have a step-size of 0.5, starting from 1 m.u.d. Crystallographic planes and directions marked with the asterisk (*) are the most common slip planes and directions of dislocation creep in literature (from Kruze et al., 2001); crystallographic planes and directions in red are those considered favourably oriented for slip based on the orientation of their maxima. All datasets are plotted in the upper and lower hemispheres as specified next to the figure, and in equal area projection. Kinematic reference frame is given below each dataset. N is the number of grains.

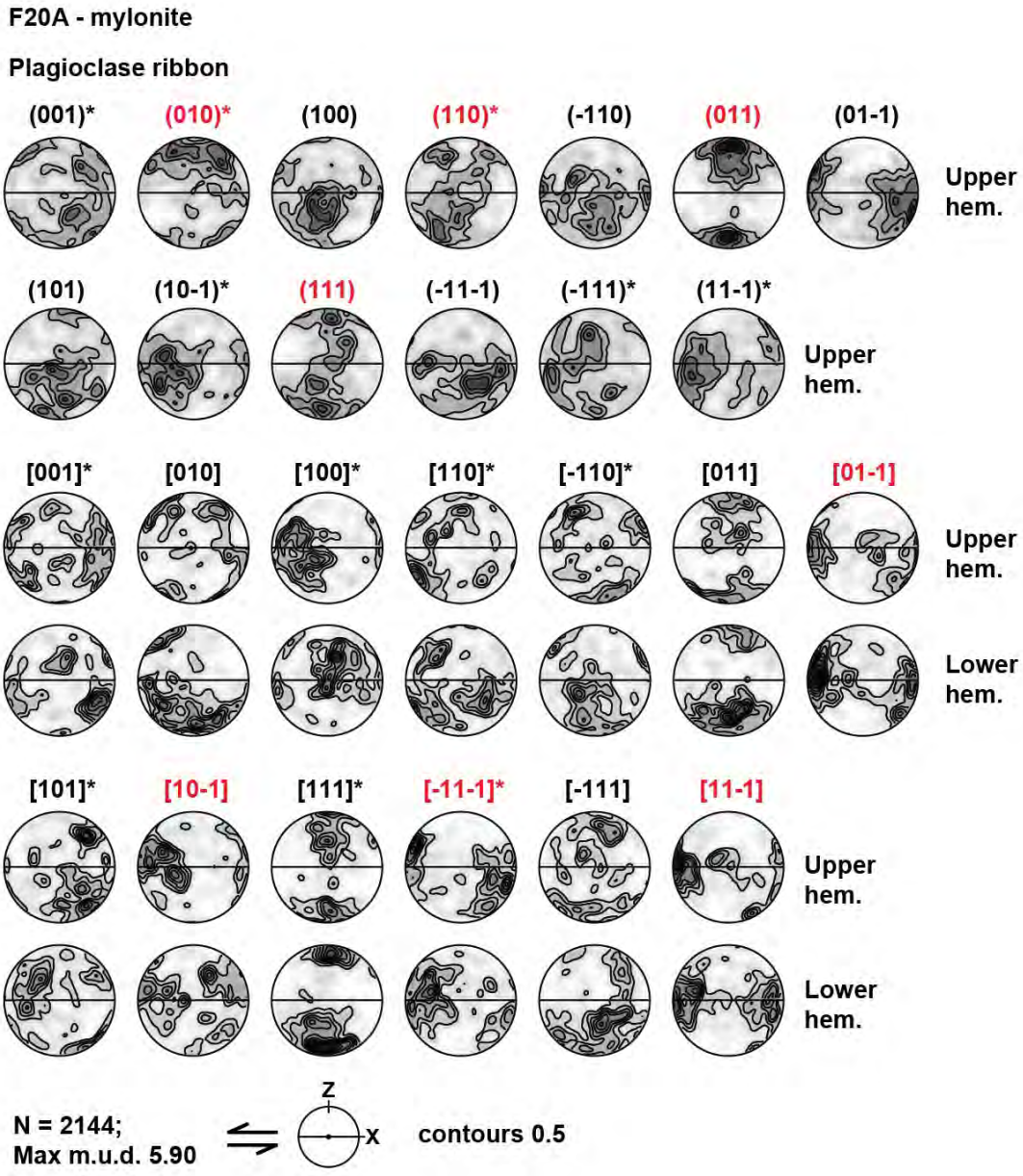

APPX. 8: SIMS ANALYSIS

BSE images of samples used for SIMS analyses, with overview of probing locations. The letters stand for the different minerals: p= plagioclase, c=clinopyroxene, o=orthopyroxene, g=garnet, a=amphibole, q=quartz. SIMS results are given in the tables below.

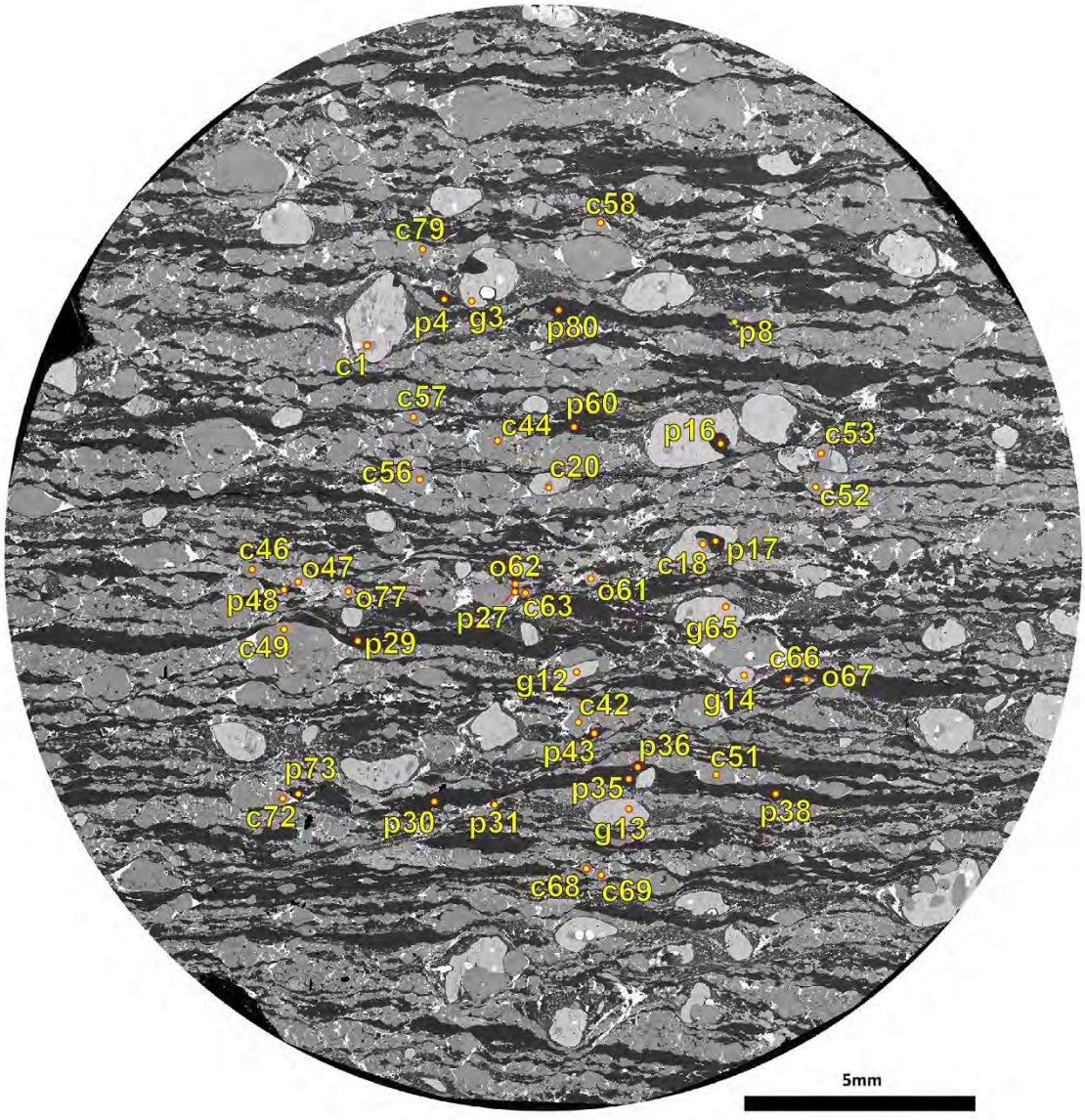

Sample F10B: metagabbroic mylonite from the Provola shear zone (Finero, Italy).

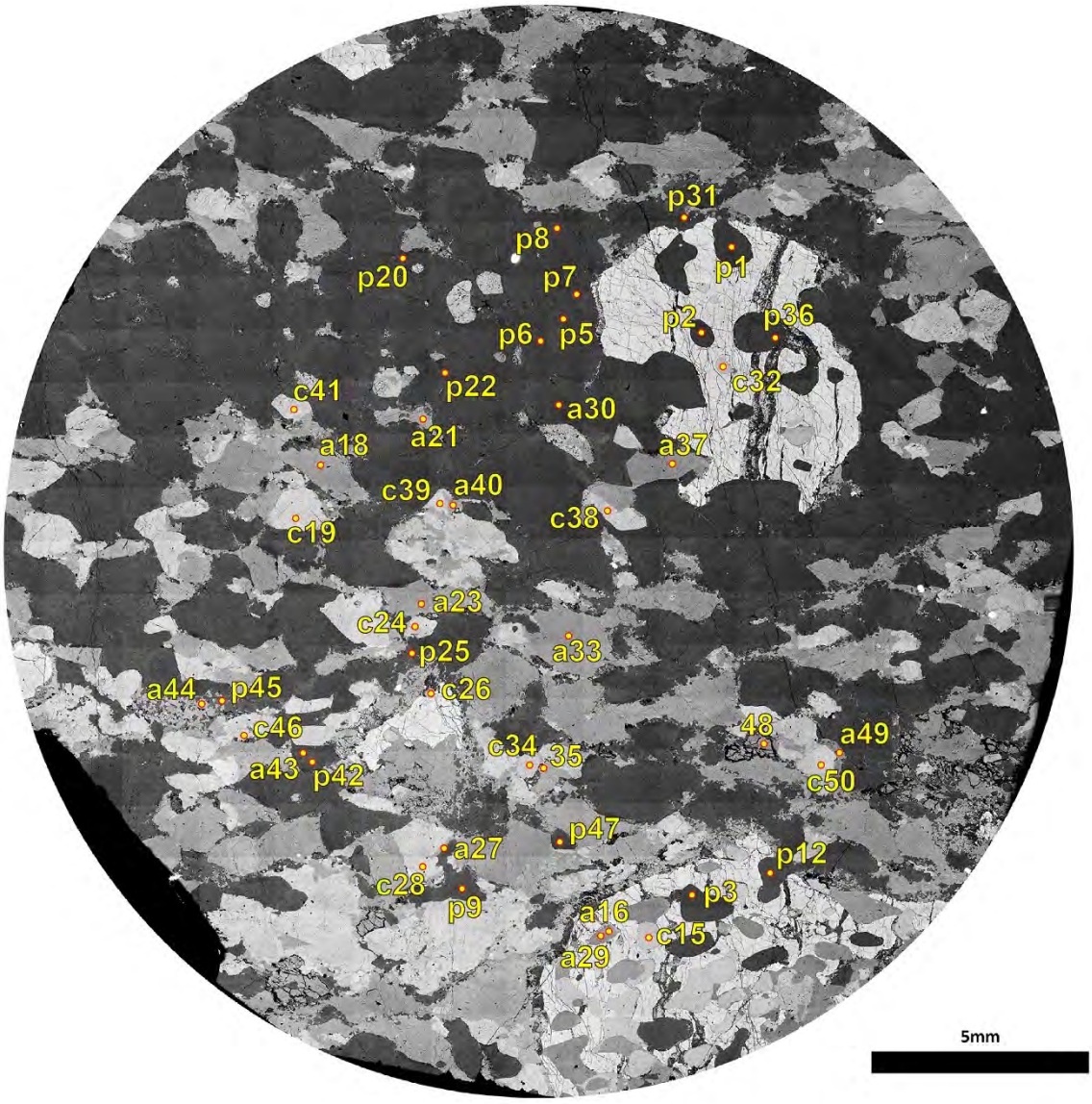

Sample F29: undeformed metagabbro from the Internal Gabbro Unit (Finero, Italy).

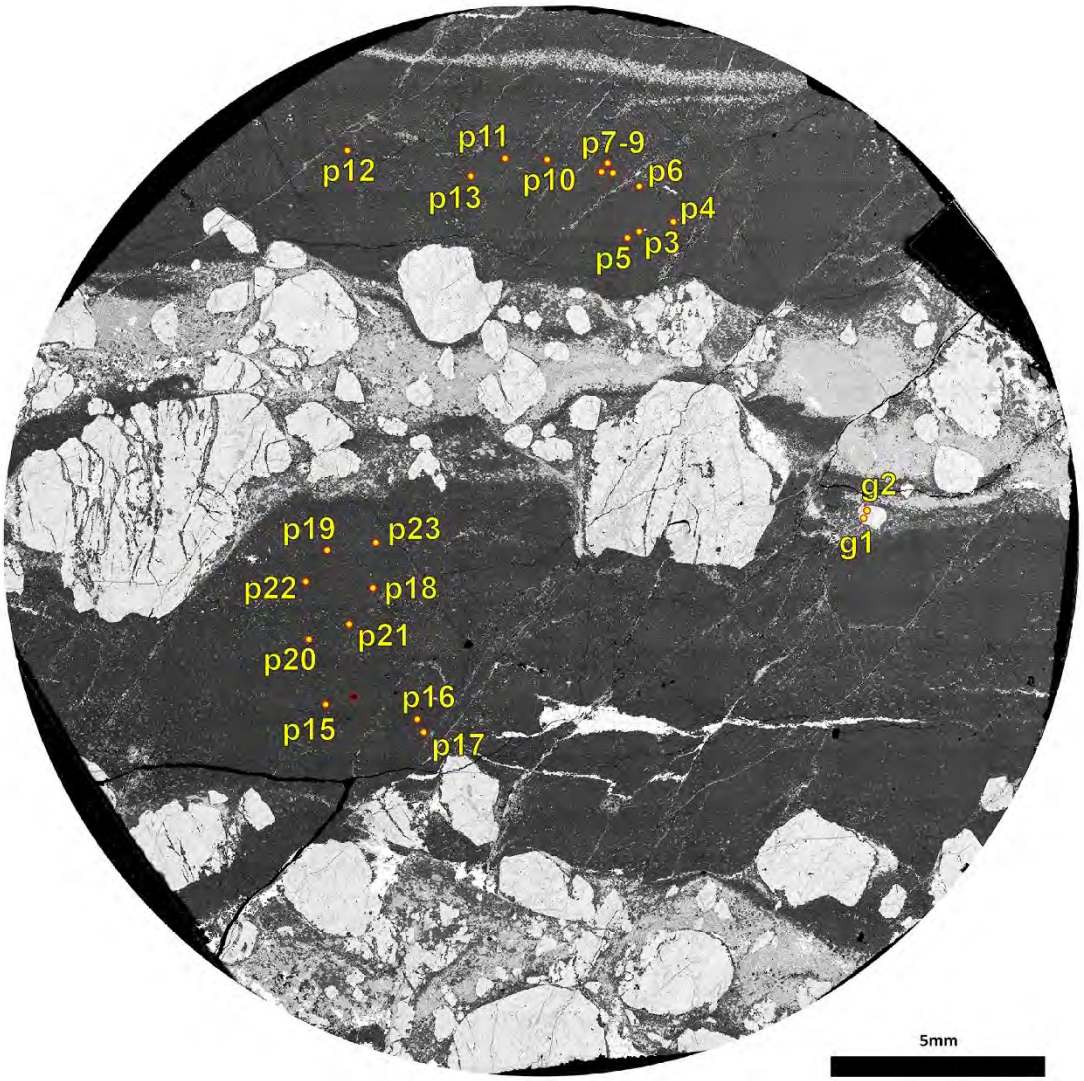

Sample F32E: Plagioclase-garnet layer from the Provola shear zone (Finero, Italy).

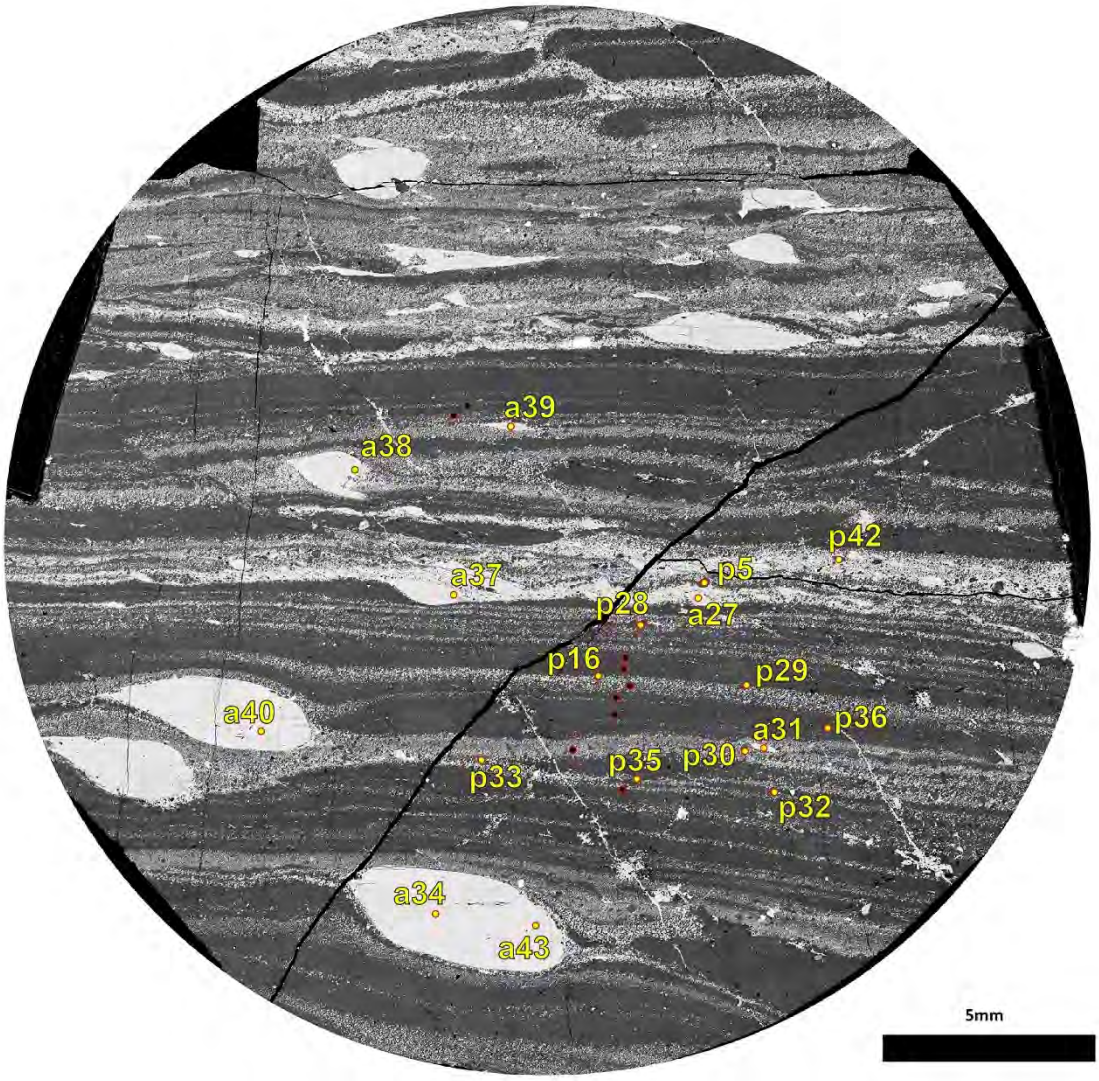

Sample F10A1: plagioclase-amphibole ultramylonite from the Provola shear zone (Finero, Italy).

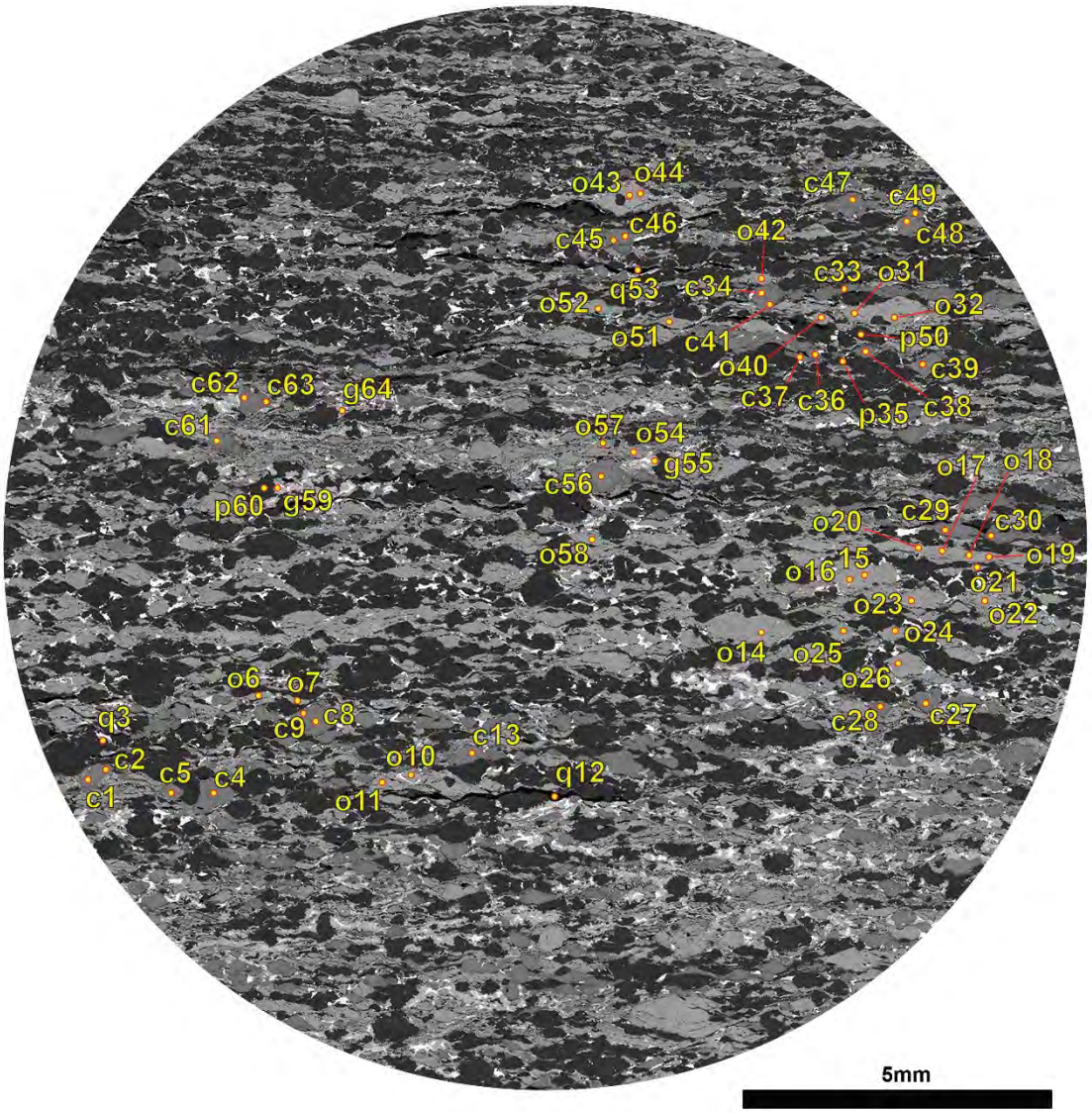

Sample O34b: sheared metagabbroic dyke (SIP, Norway).

SIMS results Table, Finero

*Finero SIMS results. H/Si: ratio between H counts (average of last 15 cycles) and Si counts (average of last 15 cycles), minus the background. H2O results are corrected for mineralogy: clinopyroxene *2.11, orthopyroxene *0.92, amphibole *1.17. SiO2 wt% values are obtained from microprobe; the other oxides are calculated as ratios of the SiO2 content.*

Clinopyroxene

Sample	Grain	H_2O ppm	H/Si	SiO_2 wt%	Na_2O ppm	K_2O ppm	CaO wt%	MgO wt%	Sr ppm	Li ppm
F10B	Cpx_42	49	0.00102	52.20	5479	1	24.8969	14.0599	9	4
F10B	Cpx_63	59	0.00122	52.20	5910	1	25.0784	13.9189	9	4
F10B	Cpx_44	53	0.00109	52.20	5620	1	25.7296	14.0424	7	4
F10B	Cpx_66	52	0.00109	52.20	5084	1	25.5116	14.0786	8	3
F10B	Cpx_46	55	0.00116	52.20	6164	1	25.2566	13.9616	9	4
F10B	Cpx_69	65	0.00133	52.20	5322	1	25.3011	14.1202	8	3
F10B	Cpx_72	73	0.00151	52.20	6094	3	25.2971	13.9037	9	5
F10B	Cpx_52	65	0.00136	52.20	6345	1	25.2388	13.7642	9	4
F10B	Cpx_79	71	0.00146	52.20	6069	1	25.2490	13.9492	10	4
F10B	Cpx_57	72	0.00146	52.20	6428	1	25.5443	13.7713	9	5
F10B	Cpx_56	72	0.00147	52.20	6662	2	25.2595	13.8478	9	4
F10B	Cpx_53	98	0.00206	52.20	7509	5	24.9122	14.0051	12	4
F10B	Cpx_53b	100	0.00210	52.20	7730	3	24.6057	13.9233	12	5
F10B	Cpx_01	107	0.00218	52.20	7657	2	24.9876	13.9942	12	6
F10B	Cpx_49	108	0.00227	52.20	7335	2	25.0942	13.7454	11	5
F10B	Cpx_18	181	0.00376	52.20	7745	3	25.0410	13.8778	13	9
F10B	Cpx_20	179	0.00365	52.20	8032	2	25.2009	14.0477	12	10
F29	Cpx_46	190	0.00417	52.20	6020	1	24.3886	15.4036	15	5
F29	Cpx_34	206	0.00496	52.20	7274	1	24.0698	15.2110	19	8
F29	Cpx_19	297	0.00652	52.20	8314	1	22.2124	15.5962	20	10
F29	Cpx_38	318	0.00699	52.20	7709	1	24.1581	15.1504	19	7
F29	Cpx_15	261	0.00627	52.20	7717	1	23.4047	15.3116	22	9
F29	Cpx_32	261	0.00629	52.20	6874	1	24.3871	15.3525	21	8
F29	Cpx_26	358	0.00754	52.20	7792	1	24.3336	14.9169	23	10
F29	Cpx_28	382	0.00803	52.20	8012	1	23.5348	15.1415	18	8
F29	Cpx_39	477	0.01047	52.20	7616	6	24.4525	14.9470	17	7
F29	Cpx_50	500	0.01099	52.20	9151	1	24.2203	14.6121	20	9
F29	Cpx_41	616	0.01354	52.20	8015	10	24.2335	15.1014	19	7

Orthopyroxene

Sample	Grain	H_2O ppm	H/Si	SiO_2 wt%	Na_2O wt%	K_2O ppm	CaO wt%	MgO wt%	Sr ppm	Li ppm
F10B	Opx_61	8	0.00041	53.20	57	0	0.8828	22.9230	0	0
F10B	Opx_77	9	0.00042	53.20	63	0	0.9104	22.7811	0	0
F10B	Opx_67	11	0.00055	53.20	73	0	0.9436	22.6807	0	0
F10B	Opx_62	61	0.00291	53.20	59	2	0.8519	22.8553	0	0

Plagioclase

Sample	Grain	H_2O ppm	H/Si	SiO_2 wt%	Na_2O wt%	K_2O ppm	CaO wt%	MgO ppm	Sr ppm	Li ppm
F10B	Plg_43	12	0.00052	58.00	5.5514	1269	10.2274	16	270	0
F10B	Plg_73	12	0.00053	58.00	5.4730	1088	10.2606	14	293	0
F10B	Plg_16	13	0.00057	58.00	5.9352	1436	9.6114	30	248	0
F10B	Plg_80	12	0.00052	58.00	5.9103	1541	9.8162	23	232	0
F10B	Plg_38	13	0.00059	58.00	5.7554	1508	9.7159	13	272	0
F10B	Plg_04	14	0.00061	58.00	5.5549	1181	10.2049	26	244	0
F10B	Plg_35	15	0.00066	58.00	5.7119	1336	9.9723	17	293	0
F10B	Plg_60	15	0.00067	58.00	5.6918	1295	9.9687	17	242	0
F10B	Plg_48	39	0.00171	58.00	5.4605	1244	10.4438	11	286	0
F10B	Plg_29	78	0.00340	58.00	5.8117	1466	9.7415	20	289	0
F10B	Plg_36	102	0.00445	58.00	5.9449	1540	9.4474	18	273	0
F10B	Plg_30	280	0.01225	58.00	5.2495	1321	10.4029	15	244	0

F29	Plg_01	15	0.00066	58.00	3.2109	164	14.7583	35	639	0
F29	Plg_03	13	0.00066	58.00	3.1924	139	14.5339	63	611	0
F29	Plg_12	14	0.00072	58.00	3.0698	128	14.8361	47	610	0
F29	Plg_43	18	0.00081	58.00	3.2286	98	14.7888	16	591	0
F29	Plg_02	19	0.00087	58.00	3.2555	172	14.6502	76	637	0
F29	Plg_20	20	0.00087	58.00	4.8160	255	11.5497	49	625	0
F29	Plg_05	20	0.00089	58.00	3.0544	161	14.8929	48	619	0
F29	Plg_09	18	0.00092	58.00	3.1261	123	14.7622	27	581	0
F29	Plg_42	23	0.00105	58.00	3.1879	115	14.6602	26	589	0
F29	Plg_07	24	0.00108	58.00	3.3887	152	14.3948	20	582	0
F29	Plg_36	28	0.00129	58.00	3.3092	150	14.6954	36	604	0
F29	Plg_30	23	0.00116	58.00	3.3360	187	14.5767	54	637	0
F29	Plg_22	32	0.00141	58.00	3.1964	166	14.6700	45	608	0
F29	Plg_08	39	0.00173	58.00	3.0279	132	15.2934	36	618	0
F29	Plg_47	44	0.00203	58.00	3.1491	120	14.8050	27	596	0
F29	Plg_45	52	0.00241	58.00	1.9109	56	17.8894	12	578	0
F29	Plg_31	53	0.00268	58.00	2.8078	100	15.7846	20	589	0
F10A1	Plg_35	6	0.00029	58.00	5.0958	839	10.6835	9	977	0
F10A1	Plg_33	7	0.00035	58.00	5.1516	1110	10.6090	15	932	0
F10A1	Plg_29	9	0.00047	58.00	5.2608	1147	10.4550	13	948	0
F10A1	Plg_32	14	0.00073	58.00	5.2340	1061	10.4522	12	990	0
F10A1	Plg_05	17	0.00085	58.00	5.2399	875	10.4908	15	968	0
F10A1	Plg_28	72	0.00365	58.00	5.1150	712	10.7921	7	935	0
F10A1	Plg_m1	115	0.00533	58.00	5.5171	551	10.3854	5	1002	1
F10A1	Plg_16	129	0.00656	58.00	5.5105	602	10.4185	3	1017	0
F10A1	Plg_30	156	0.00794	58.00	5.5140	820	10.2313	15	1006	0
F32E	Plg_20	6	0.00025	58.00	5.3182	900	10.6086	18	950	0
F32E	Plg_17	9	0.00039	58.00	5.2747	842	10.7421	14	953	0
F32E	Plg_16	11	0.00049	58.00	5.2825	848	10.5393	21	979	0
F32E	Plg_05	12	0.00052	58.00	5.0634	679	11.2243	19	984	0
F32E	Plg_06	13	0.00055	58.00	5.0103	806	11.3555	43	1024	0
F32E	Plg_11	13	0.00057	58.00	5.2123	910	10.7787	43	992	0
F32E	Plg_15	21	0.00089	58.00	5.2273	543	10.6879	16	967	0
F32E	Plg_23	22	0.00094	58.00	5.3234	543	10.7297	16	1006	0
F32E	Plg_07	22	0.00096	58.00	4.4482	524	12.2903	25	1009	0
F32E	Plg_18	25	0.00107	58.00	4.8866	640	11.2491	29	1048	0
F32E	Plg_13	26	0.00111	58.00	5.2241	986	10.5603	34	955	0
F32E	Plg_08	26	0.00112	58.00	5.3664	768	10.6954	32	976	0
F32E	Plg_10	31	0.00133	58.00	5.3359	466	10.5996	36	962	0
F32E	Plg_09	45	0.00194	58.00	5.1793	518	11.0939	34	1020	0
F32E	Plg_03	69	0.00300	58.00	5.2877	459	10.7959	16	986	0
F32E	Plg_12	153	0.00661	58.00	5.4048	939	10.4422	43	987	0
F32E	Plg_22	177	0.00764	58.00	5.2527	552	10.7493	21	941	0

Amphibole

Sample	Grain	H_2O ppm	H/Si	SiO_2 wt%	Na_2O wt%	K_2O ppm	CaO wt%	MgO wt%	Sr ppm	Li ppm
F29	Amph_40	20006	0.79235	43.10	3.1079	2352	12.8418	16.2911	40	1
F29	Amph_18	20219	0.80079	43.10	3.2383	2294	12.7430	16.4496	58	2
F29	Amph_37	20852	0.82589	43.10	3.2158	2228	12.5404	16.4443	55	2
F29	Amph_23	21658	0.82234	43.10	3.0006	2159	12.6517	16.3654	47	1
F29	Amph_44	23352	0.92487	43.10	3.3088	2073	12.7066	16.2967	32	2
F29	Amph_33	19108	0.82903	43.10	3.2007	2169	12.5786	16.5605	54	1
F29	Amph_21	23324	0.88562	43.10	2.9989	2382	12.7581	16.6720	43	1
F29	Amph_29	24049	0.91315	43.10	3.1339	1761	11.9791	16.5277	57	3
F29	Amph_27	24419	0.92718	43.10	3.0357	2199	12.8168	16.4889	41	1
F10A1	Amph_43	14670	0.58103	43.10	2.2405	9758	13.3033	13.1403	150	1
F10A1	Amph_34	13715	0.59503	43.10	2.1865	9443	13.1498	13.1823	152	1
F10A1	Amph_38	14874	0.64531	43.10	1.9255	9266	12.8460	13.2753	82	1
F10A1	Amph_37	15404	0.66833	43.10	2.0530	10586	13.3436	12.8719	116	2
F10A1	Amph_27	15522	0.67344	43.10	2.1464	11572	13.6329	13.1124	118	1
F10A1	Amph_40	15637	0.67843	43.10	2.1761	9490	13.0683	13.1528	129	1
F10A1	Amph_31	15774	0.68437	43.10	2.0322	10597	13.4165	13.0092	98	1
F10A1	Amph_39	16561	0.71853	43.10	2.0620	10049	13.2730	12.8974	98	2

*Norway SIMS results (all data). H/Si: ratio between H counts (average of last 15 cycles) and Si counts (average of last 15 cycles), minus the background. H2O results are corrected for mineralogy: clinopyroxene *2.11, orthopyroxene *0.92, amphibole *1.17. SiO2 wt% values are obtained from microprobe; the other oxides are calculated as ratios of the SiO2 content.*

Clinopyroxene

Sample	Grain	H_2O ppm	H/Si	SiO_2 wt%	Na_2O ppm	K_2O ppm	TiO2 wt%
O34b	Cpx_47	80	0.00129	51.80	3883	2	0.2342
O34b	Cpx_28	95	0.00167	51.80	5126	3	0.3300
O34b	Cpx_49	101	0.00162	51.80	4123	3	0.2259
O34b	Cpx_05	107	0.00187	51.80	4535	4	0.1871
O34b	Cpx_46	112	0.00181	51.80	4583	2	0.3315
O34b	Cpx_13	113	0.00199	51.80	3556	4	0.3283
O34b	Cpx_09	116	0.00204	51.80	3860	2	0.2145
O34b	Cpx_02	119	0.00209	51.80	4779	3	0.4978
O34b	Cpx_27	121	0.00212	51.80	5266	3	0.2188
O34b	Cpx_45	124	0.00199	51.80	4382	3	0.5380
O34b	Cpx_33	137	0.00241	51.80	5376	6	0.4094
O34b	Cpx_04	137	0.00241	51.80	4062	3	0.3879
O34b	Cpx_39	138	0.00222	51.80	3599	2	0.2894
O34b	Cpx_61	140	0.00225	51.80	4540	2	0.2231
O34b	Cpx_29	149	0.00261	51.80	4898	17	0.4797
O34b	Cpx_30	153	0.00268	51.80	3503	3	0.3991
O34b	Cpx_41	163	0.00261	51.80	3683	15	0.5308
O34b	Cpx_63	165	0.00266	51.80	5495	5	0.2285
O34b	Cpx_48	172	0.00277	51.80	3758	4	0.5205
O34b	Cpx_37	176	0.00283	51.80	4153	9	0.2362
O34b	Cpx_01	196	0.00343	51.80	3942	3	0.1964
O34b	Cpx_34	210	0.00369	51.80	3551	4	0.4375
O34b	Cpx_56	218	0.00350	51.80	3010	3	0.5344
O34b	Cpx_08	230	0.00404	51.80	4532	6	0.2363
O34b	Cpx_38	294	0.00472	51.80	4474	12	0.4349
O34b	Cpx_62	357	0.00573	51.80	4520	15	0.1502

Orthopyroxene

Sample	Grain	H_2O ppm	H/Si	SiO_2 wt%	Na_2O ppm	K_2O ppm	TiO2 wt%
O34b	Opx_26	9	0.00036	51.20	95	0	0.1135
O34b	Opx_51	9	0.00035	51.20	95	1	0.0827
O34b	Opx_23	9	0.00038	51.20	99	0	0.1091
O34b	Opx_40	10	0.00038	51.20	114	1	0.0917
O34b	Opx_22	11	0.00044	51.20	103	0	0.1048
O34b	Opx_44	12	0.00043	51.20	81	1	0.0697
O34b	Opx_32	12	0.00048	51.20	96	0	0.1305
O34b	Opx_06	12	0.00049	51.20	106	1	0.0818
O34b	Opx_19	12	0.00050	51.20	171	0	0.1263
O34b	Opx_52	13	0.00047	51.20	104	1	0.1312
O34b	Opx_24	13	0.00052	51.20	87	0	0.1101
O34b	Opx_20	14	0.00058	51.20	150	0	0.1277
O34b	Opx_25	15	0.00062	51.20	92	1	0.0995
O34b	Opx_31	16	0.00063	51.20	145	1	0.1368
O34b	Opx_15	17	0.00070	51.20	136	0	0.1101

O34b	Opx_14	18	0.00071	51.20	87	0	0.0869
O34b	Opx_16	18	0.00074	51.20	142	0	0.1355
O34b	Opx_21	19	0.00078	51.20	34	4	0.1066
O34b	Opx_54	24	0.00087	51.20	78	2	0.1091
O34b	Opx_43	26	0.00097	51.20	264	2	0.0413
O34b	Opx_18	42	0.00168	51.20	146	1	0.1305
O34b	Opx_11	50	0.00203	51.20	91	2	0.2954
O34b	Opx_57	99	0.00363	51.20	177	7	0.1639
O34b	Opx_07	134	0.00541	51.20	74	7	0.0574
O34b	Opx_10	189	0.00761	51.20	204	23	0.0968
O34b	Opx_58	220	0.00810	51.20	141	20	0.0930
O34b	Opx_42	351	0.01295	51.20	140	47	0.1152

Plagioclase

Sample	Grain	H_2O ppm	H/Si	SiO_2 wt%	Na_2O ppm	K_2O ppm	TiO2 wt%
O34b	Plg_60	9	0.00030	48.50	20445	786	0.0050
O34b	Plg_50	10	0.00035	48.50	19229	752	0.0041
O34b	Plg_35	24	0.00082	48.50	20819	636	0.0015

Quartz

Sample	Grain	H_2O ppm	H/Si	SiO_2 wt%	Na_2O ppm	K_2O ppm	TiO2 wt%
O34b	Qtz_53	22	0.00075	100	3	2	0.0179
O34b	Qtz_12	32	0.00118	100	1	1	0.0075
O34b	Qtz_03	252	0.00932	100	1	1	0.0021

APPX. 9: THERMODYNAMIC EXTRA

Compositional ispleth extracted from the pseudosection F20A. (a) isopleths of Al_2O_3 in clinopyroxene grains of the ultramylonite. Shaded area corresponds to the range of Al2O3 contents in ultramylonitic clinopyroxenes of sample F20A. (b) isopleths of Anorthite content, of plagioclase of the ultramylonite.

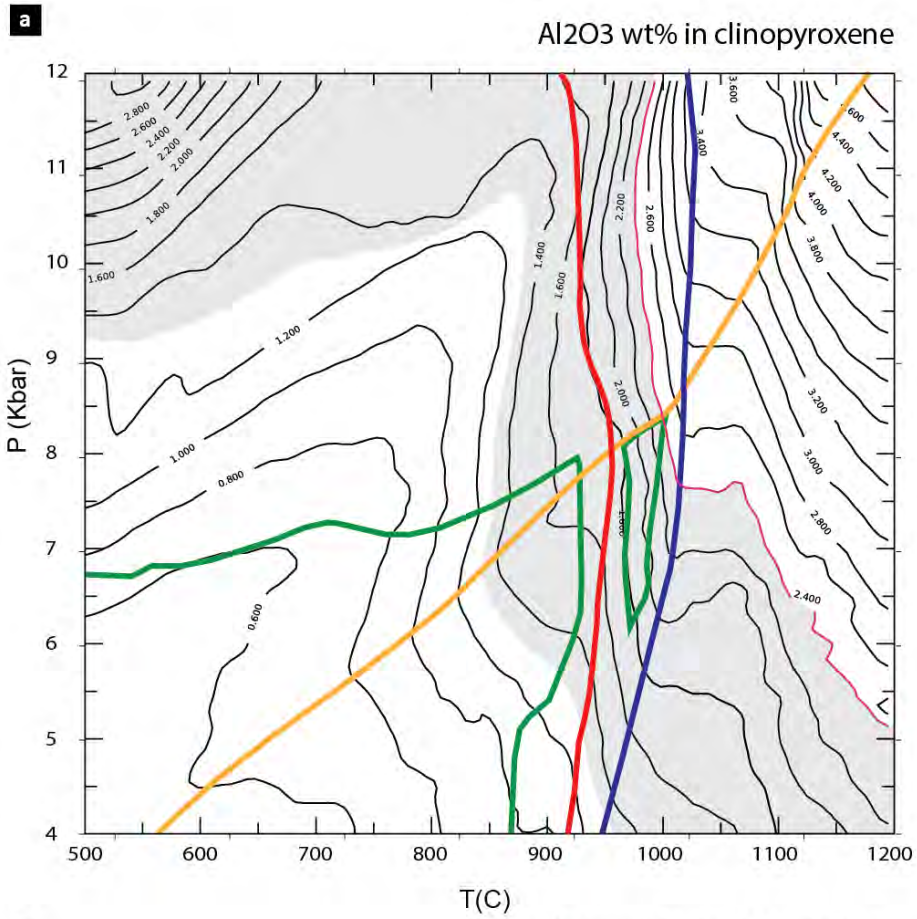
a
Al2O3 wt% in clinopyroxene
P (Kbar)
T(C)
12
11
10
9
8
7
6
5
4
500
600
700
800
900
1000
1100
1200

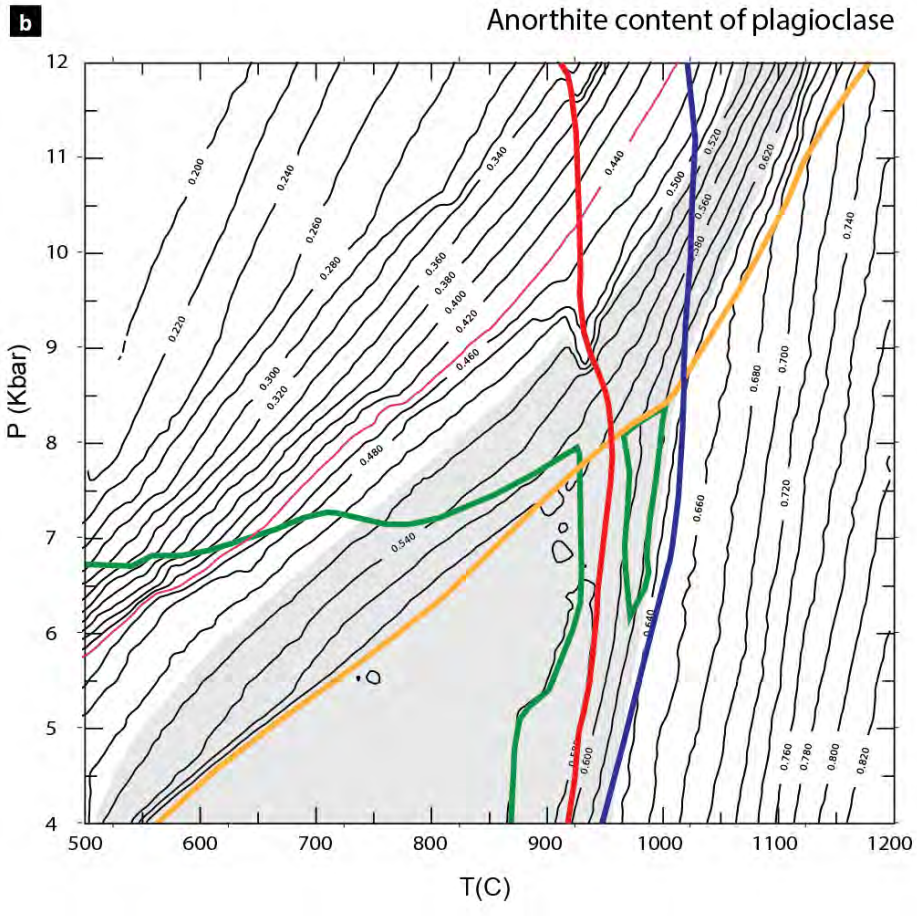
b
Anorthite content of plagioclase
P (Kbar)
T(C)
12
11
10
9
8
7
6
5
4
500
600
700
800
900
1000
1100
1200